Modélisation Eulérienne multi-fluide unifiée à deux échelles des écoulements diphasiques à phases séparées et dispersées

Arthur Loison

INSTITUT POLYTECHNIQUE DE PARIS

NNT : 2024IPPAX009

Thèse de doctorat

Unified two-scale Eulerian multi-fluid modeling of separated and dispersed two-phase flows

Thèse de doctorat de l'Institut Polytechnique de Paris
préparée à École polytechnique

École doctorale n°574 École doctorale de mathématiques Hadamard (EDMH)
Spécialité de doctorat: Mathématiques appliquées

Thèse présentée et soutenue à Palaiseau, le 27 Mars 2024, par

ARTHUR LOISON

Composition du Jury :

Pauline Lafitte Professeure, CentraleSupelec	Présidente
Hélène Mathis Professeure, Université de Montpellier	Rapporteure
Sergey Gavrilyuk Professeur, Aix-Marseille Université	Rapporteur
Maren Hantke Wissenschaftliche Mitarbeiterin, Uni Halle	Examinatrice
Jean-Marc Hérard Ingénieur de recherche, EDF R&D	Examinateur
Vincent Perrier Chargé de recherche, INRIA - Université de Pau	Examinateur
Marc Massot Professeur, École polytechnique	Directeur de thèse
Marica Pelanti Maître de Conférences, ENSTA Paris	Invitée
François-Xavier Demoulin Professeur, Université de Rouen Normandie	Invité

Encadrement de thèse :

Samuel Kokh
CEA Saclay

Teddy Pichard
CMAP, École polytechnique

Remerciements

Je tiens à remercier l'ensemble du jury d'avoir accepté de participer à ma soutenance et tout particulièrement Hélène Mathis et Sergey Gavrilyuk d'avoir rapporté ma thèse et qui, par leur lecture détaillée, leur remarques et suggestions m'ont permis de prendre une hauteur supplémentaire sur mes recherches.

Je remercie ensuite mon équipe encadrante constituée de Marc Massot, Teddy Pichard et Samuel Kokh pour m'avoir accompagné au cours de ses trois dernières années, pour leur bienveillance, leurs conseils et leurs enseignements. Au delà de toutes les connaissances que vous avez pu me transmettre, je retiendrais la qualité des nombreuses discussions que l'on a pu avoir sur le plan scientifique, la satisfaction de partager de nouvelles idées, mais aussi les séances de calcul hasardeuses à la recherche de nouveaux modèles. Merci aussi pour toutes les rencontres que vous avez pu rendre possibles lors de toutes ces conférences, séminaires et séances de travail avec d'autres équipes de recherche notamment avec l'ONERA, le CEA ou le CORIA.

Cette thèse a aussi été rendue possible grâce aux doctorants, post-doctorants et ex-docteurs de l'équipe avec des mentions spéciales pour Katia et Giuseppe avec qui on a partagé de nombreuses réflexions sur la modélisation des petites échelles, pour Ward toujours prêt à discuter longue;ent de physique, de modèles diphasiques, de schémas numériques (ou à gérer l'orga au pied levé) et qui m'a aide dans la finalisation de ce manuscrit par sa fine relecture, à Thomas et Louis pour m'avoir accueilli, aiguillé dans l'équipe, au labo et en conférences, et qui ont été de bons partenaires de recherche, à Ruben pour m'avoir transmis ses travaux de grande qualité sur le développement du solveur fluide et aussi aux précédents doctorants de l'équipe dont les travaux de thèse ont ouvert la voie à toutes les idées que j'ai pu avoir lors de cette thèse.

Merci aussi à toute l'équipe HPC@Maths pour les collaborations, les discussions, les coups de pouce, pour avoir animé la vie scientifique et sociale de l'équipe avec les séminaires et pots.

Un grand merci à l'équipe administrative aussi pour l'organisation de nombreux événements conviviaux au sein du labo et des déplacements en conférence.

Dédicace aux anciens et nouveaux co-bureaux notamment à Clément et Baptiste et aux autres doctorants de la team Josselin pour la bonne ambiance même si ça parlait plus UQ qu'autre chose. Même après votre départ ça n'a pas arrêté et me voilà moi-même parti pour en faire, les EDPistes ne gagneront jamais cette guerre.

Coucou aussi à tous les sportifs du CMAP, Manon, Corentin, Jessie, Yoann et Louis, pour les séances de course à pied, de piscine et d'escalade (sans oublier Leïla la reine du trail pour discuter course à pied même si on a pas trop eu l'occasion de courir ensemble).

Un merci aussi à Armand, Madeleine, Solange, Antoine et à tous les doctorants, chercheurs et ingénieurs du

CMAP pour l'ambiance chaleureuse, les discussions et séminaires qui permettent une ouverture exceptionnelle sur tous les domaines des mathématiques appliquées !

Mes respects à mes amis doctorants Palaisiens de la DGA d'avoir partagé ses quelques années supplémentaires sur le plateau, avec mention spéciale pour Rodolphe qui a lui aussi partagé l'immense plaisir d'étudier les gouttes !

Merci à mes amis et ma famille pour votre soutin et pour votre curiosité sur mes recherches parfois un peu fumeuses. J'espère que vous en savez (un peu) plus aujourd'hui !

Enfin, merci à Philippine qui n'a pas simplement partagé l'aventure qu'a été cette thèse mais tout simplement a partagé ma vie depuis maintenant de nombreuses années et sans qui je n'aurai sans doute pas le courage ni la force d'entreprendre d'aussi grands projets !

Abstract

Liquid-gas two-phase flows are present in numerous industrial applications such as aerospace propulsion, nuclear hydraulics or bubble column reactors in the chemical industry. The simulation of such flows is of primary interest for their understanding and optimization. However, the dynamics of the interface separating the gas from the liquid can present a multiscale dynamics and thus makes simulations of industrial processes computationally too expensive. Some modelling efforts have been conducted on the development of cheaper multi-fluid models adapted to particular interface dynamics regime, e.g. in the separated regime where the fluids are separated by a single smooth surface or in the disperse regime where there are inclusions of one fluid carried by the other. Attempts of coupling between these models have showed some progress to simulate multiscale flows like atomization, but usually have physical or mathematical drawbacks. This thesis then pursues the goal of proposing a unified two-scale modelling framework with appropriate numerical methods adapted to this multiscale interface dynamics which goes from a separated to a disperse regime. The main contributions related to this modelling effort are : 1- The combination of compressible multi-fluid models of the literature adapted to either the separated or the disperse regime into a unified two-scale multi-fluid model relying on Hamilton's Stationary Action Principle; 2- The local coupling of the models with an inter-scale mass transfer both regularizing the large-scale inter face and modelling mixed regime phenomena such as in primary break-up; 3- Enhancing the small-scale models for the disperse regimes by adding the dynamics of geometric quantities for oscillating droplets and pulsating bubbles, built as moments of a kinetic description. From the numerical perspective, finite-volume schemes and relaxation methods are used to solve the system of conservative laws of the models. Eventually, simulations with the open-source finite solver `Josiepy` demonstrates the regularization properties of the model on a set of well-chosen numerical setups leading to multi-scale interface dynamics.

Résumé

Les écoulements diphasiques liquide-gaz sont présents dans de nombreuses applications industrielles telles que la propulsion aérospatiale, l'hydraulique nucléaire ou les colonnes à bulles dans l'industrie chimique. La simulation de ces écoulements est d'un intérêt primordial pour leur compréhension et leur optimisation. Cependant, la dynamique de l'interface séparant le gaz du liquide peut avoir une dynamique multi-échelle et rend alors sa simulation trop coûteuse en calcul dans un contexte industriel. Une classe de modèles - dits multi-fluides - sont moins coûteux pour des régimes particuliers de dynamique d'interface, par exemple lorsque les fluides s'écoulent de part et d'autre d'une unique interface lisse dans un régime séparé ou lorsque l'un des deux fluides est sous formes d'inclusions (gouttes ou bulles) portées par l'autre fluide dans un régime dispersé. Le couplage de ces modèles a été proposé pour des écoulements multi-échelles comme l'atomisation liquide, mais un tel couplage est souvent difficile à mettre en place du point de vue de la modélisation physique ou de ses propriétés mathématiques. Cette thèse répond à cette problématique en proposant un cadre de modélisation unifiée à deux échelles ainsi que des schémas numériques robustes. Les principales contributions liées à cette modélisation sont : 1- La combinaison de modèles multi-fluides compressibles de la littérature, adaptés soit au régime séparé soit au régime dispersé, en un modèle multi-fluide unifié à deux échelles grâce au principe d'action stationnaire de Hamilton ; 2- Le couplage local des modèles avec un transfert de masse inter-échelle régularisant l'interface à grande échelle en conservant l'énergie capillaire et modélisant les phénomènes de régime mixte présents dans l'atomisation primaire ; 3- L'amélioration des modèles à petite échelle pour les régimes dispersés en ajoutant la dynamique de quantités géométriques pour des gouttes oscillantes ou des bulles pulsantes, construites comme des moments d'une description cinétique. D'un point de vue numérique, des schémas volumes-finis adaptés aux systèmes de lois de conservation avec relaxations ont été implémentés dans le solveur open-source `Josiepy`. Enfin, des simulations démonstratives des propriétés de régularisation du modèle sont proposées sur des configurations numériques conduisant à des dynamiques d'interface multi-échelles.

Contents

Introduction

Industrial and scientific context

Two-phase flows of liquid and gaseous phases appear in a variety of industrial applications. On the one hand, some processes explicitly requires the interaction of a liquid and a gaseous phase across an interface, like a chemical reaction or a phase transition. The amount of interface area present in the flow is then a critical parameter of these processes. On the other hand, other flows can be globally driven by the motion of the interface, like the sloshing in a container or the interaction of a hot gaseous flow with a liquid interface at rest (Chanteperdrix, 2004; Haegeman et al., 2024). Other configurations are sensitive to both aspects such as atomization of a liquid jet into a spray or bubbly flows. For introductory purposes, let us detail the flow mechanisms and physics phenomena associated with these two configurations.

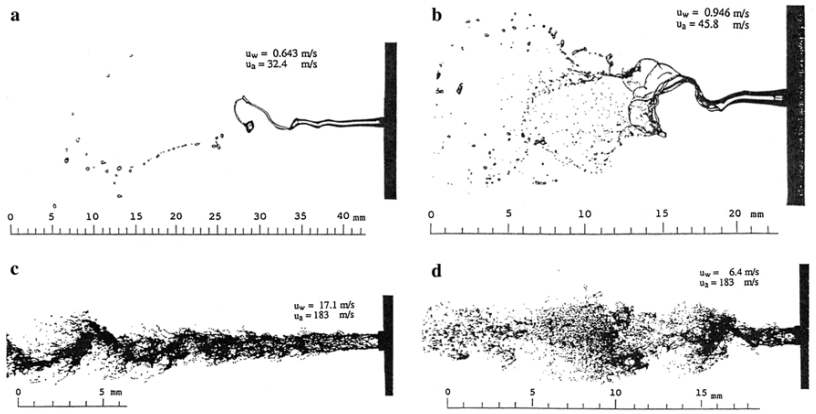

Figure 0.1: Air-assisted atomization of a liquid jet of water for different velocities of the injected air u_a and water u_w from Farago and Chigier (1992).

If one considers the atomization of a jet in a combustion chamber, the liquid fuel is injected through a nozzle and the combustion can take place after the evaporation of the resulting droplets such as in diesel-like engines (Kah, 2010; Bode et al., 2014; Oguz, 2014; Essadki, 2018) or cryogenic flames for aerospace propulsion (Habiballah et al., 2006; Cordesse, 2020; Granger et al., 2023; Haegeman, 2025). As the phase change occurs at the interface between the liquid and the gas, the time rate of this transition is controlled by the amount of interface area present in the reactor. In order to control the timescale of the phase transition, large or small droplets are produced by triggering different regimes of atomization spanning a wide range of Weber and Reynolds numbers (see Figure 0.1) by selecting different injection velocities or nozzle geometries (Reitz and Bracco, 1979; Janodet et al., 2022). However,

the prediction of the statistical distribution in sizes of the resulting droplets is very challenging and depends on each experimental setup. Indeed, this size distribution is obtained as the consequence of numerous complex mechanisms encompassing interface instability, formation of filaments or thin surfaces, appearance of holes, filament and droplet break-up, coalescence. Therefore, extensive experimental studies have been conducted to better understand the overall dynamics of the atomization (Farago and Chigier, 1992; Faeth, 1996; Marmottant and Villermaux, 2004; Mayer and Branam, 2004; Dumouchel, 2008; Jain et al., 2015; Warncke et al., 2017; Sharma et al., 2021; Aliseda and Heindel, 2021). The investigation of such mechanisms is showed to be very complex such that these experimental studies are also complemented with numerical ones to better capture the dynamics at play (Deberne et al., 2024; Ferrando et al., 2023).

Let us then discuss the case of bubbly flows where the reaction between the two phases can occur at the interface between the two phases or in the liquid phase after dissolution (Orejas, 1999). In this context, bubble columns are very practical as the gas is injected at the bottom of the liquid column and the bubbles are naturally agitated within the liquid phase thanks to their unstable upward displacement under buoyancy forces (see Figure 0.2). Although the experimental setup is quite simple, it may bring into play several flow regimes that remain an active research topic nowadays (Zehner and Kraum, 2000; Risso, 2018; Zamansky et al., 2023). Indeed, the dynamics of a single bubble is quite complex as it is highly deformable under the stress enforced by the flow (Lalanne et al., 2013). The drag endured by the bubble then changes in time, modifying its trajectory within the liquid phase (Ern et al., 2012). The shape of the bubble also impacts in return the local flow and can generate turbulence. Furthermore, the overall dynamics of the bubbly flow shows collective behaviours through the coalescence of bubbles, the segregation of the bubbles and added-mass effect, which all depend on the average gaseous volume occupation in the reactor and the sizes of the bubbles. Remark however that the bubbly flow notably differs from the atomization process as of the gaseous inclusions are directly injected within the flow but predicting the interface area density is still of major interest.

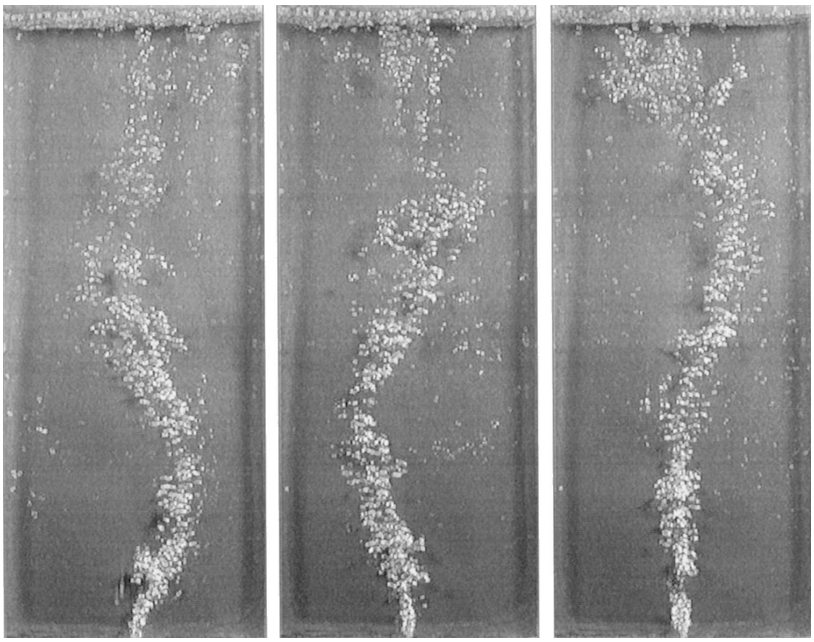

Figure 0.2: Lateral oscillation in a bubble column (Becker et al., 1999).

Conversely, some two-phase flow phenomena are sometimes unwanted. One example is the “boiling crisis” in some heat exchangers when the water boiling goes from a *nucleation* regime with small bubbles appearing in the liquid to a *film* regime where a thin layer of vapour separates the liquid phase from the heater. Indeed, such phase change phenomenon prevents the cooling by the liquid which is replaced by the vapour that insulates the heater (Theofanous et al., 2002) and may cause damage to the heater surface. Another drawback of the presence of a

two-phase flow sometimes lies in the cavitation phenomenon when small bubbles appear in the liquid phase under a sudden depressurization. The following implosion of the bubble can then cause damage on neighbouring surfaces or generates acoustic waves. These two issues are critical for the submarines as it prematurely damages the helix propellers or decreases the stealth of the ships.

Finally, all these phenomena occur at length- and time-scales encompassing several orders of magnitude. Therefore, we will qualify these two-phase flows as *multiscale*. In this manuscript, we are particularly interested in the atomization process with compressible phases as it is the perfect example of a multiscale flow with different interface regimes. The length-scales span over several orders of magnitude, from the size of the injection nozzle to the smallest droplets in the flow downstream.

A broad classification of the interface regime is proposed in Ishii and Hibiki (1975), and, as far as the atomization is concerned, we identify the following regimes:

- The *separated regime* describes a sufficiently regular interface such that the length-scale of the interface dynamics is comparable or larger than the length-scales of the bulk phase, and no arbitrary small length-scales arise from the flow dynamics.
- The *mixed regime* involves arbitrarily small length-scales as the interface surface undergoes topological changes through pinching, filament break-up or apparition of holes. Such regime encompasses the *primary break-up* when the first liquid inclusions appear.
- The *disperse regime* corresponds only to small inclusions of one phase (here the liquid) carried by the other (the gas), where the inclusions can break up again in smaller ones (also known as *secondary break-up*), or coalesce with other inclusions. Due to the large number of inclusions, this regime is often described statistically through a distribution over a phase-space characterizing the inclusions: size, shape, velocity, temperature, ...

These regimes are schematically represented in Figure 0.3.

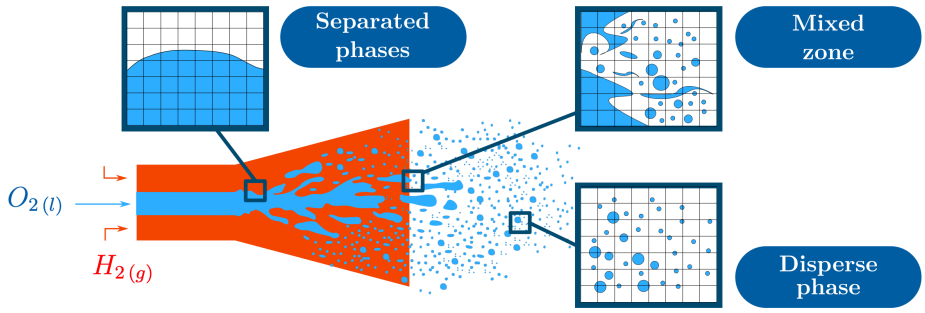

Figure 0.3: Schematic representation of an atomization of cryogenic injectors in aerospace engines (Cordesse, 2020).

With such different interface regimes, it is common to focus on a single regime to capture a smaller amount of phenomena, that can be efficiently described. Consequently, numerous models have been developed to tackle each of these regimes.

A wide variety of two-phase flow models

Different length-scales and different models

The choice of the two-phase flow model is usually adapted to the regime of interest and proposes different levels of details for the description of the interface, both its dynamics and capillarity phenomena. Let us briefly describe each class of models from the smallest length-scale level of description of the interface to the largest.

When including in the modelling the full spectrum of length-scales, a family of models that can be referred to as *Phase Field Diffuse Interface Model (DIM)* that proposes to describe continuously the transition from one phase to

the other and involves a potentially very small length scale, which will have to be resolved, which is the thickness of the interface. Many models fall within this category, such as Cahn-Hilliard models (Cahn and Hilliard, 1958), Korteweg materials (Korteweg, 1901; Dunn, 1986; Dunn and Serrin, 1986) or second-gradient models (Gouin, 1996; Seppecher, 2002). Despite relying on a solid thermodynamic model (see the recent derivation from the kinetic level of description by Giovangigli (2021)) and thus a proper mathematical structure (Giovangigli et al., 2023), they are of limited use in ambient conditions, where the physical thickness of the interface only reaches a few nanometers.

At a larger scale, that is if the thickness of the interface is not described in the model, *sharp interface models* (Sussman et al., 1994; Vaudor et al., 2017) enable a non-ambiguous location of the interface as a discontinuity of the material properties. These strategies can be viewed as the coupling of single-fluid systems across a sharp and moving boundary. Therefore, the chosen numerical schemes must track the location of the interface during the simulations. For instance, in Volume Of Fluid (VOF) methods (Rudman, 1998; Gueyffier et al., 1999; Scardovelli and Zaleski, 1999) or Front-Tracking methods (Chern et al., 1986; Unverdi and Tryggvason, 1992; Popinet and Zaleski, 1999; Glimm et al., 2000), the location of the interface is tracked with an advected colour function, Level-Set methods use distance functions (Sussman et al., 1994; Desjardins and Moureau, 2010), or Coupled Level-Set VOF methods combines the advantages of each method, which are respectively a fine description of geometric properties and better mass conservation (Sussman and Puckett, 2000; Ménard et al., 2007; Vaudor et al., 2017). These approaches are sometimes used in what can be referred to as Direct Numerical Simulations (DNS) regarding the capture of the interface although resolving the scales cannot always be guaranteed. However, for cases involving multiple interface topology regimes, implementing these approaches requires to reconstruct the interface at all relevant scales. This can lead to an unreasonably high computational cost for challenging setups such as atomizations where mesh convergence can rarely be reached (Herrmann, 2009; Shinjo and Umemura, 2010; Ling et al., 2017) (see Figure 0.4). Despite its inherent high computational cost, it remains a well-adopted technique to investigate the atomization process (Janodet et al., 2022) or focus on elementary, but complex, two-phase flow phenomena such as droplet break-up, apparition of holes (Chirco et al., 2022), or turbulence (Martinez et al., 2021).

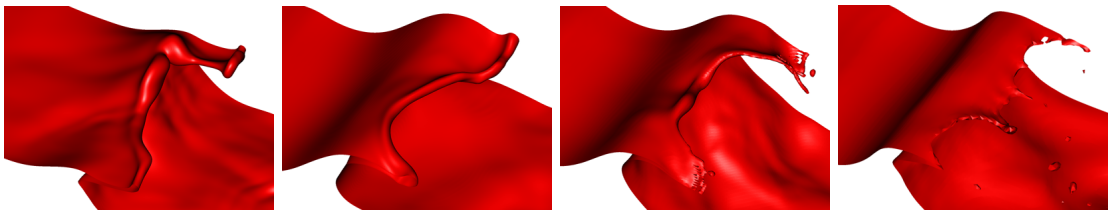

Figure 0.4: Resolution of a thin wave crest for different mesh resolutions from coarse (left) to fine (right) (Ling et al., 2017).

The disperse regime is also very challenging for the DNS approach, despite the presence of a unique flow regime, the length-scale of the flow around or within the carried inclusions can be much smaller, with several orders of magnitude. If capturing the collective behaviour of the disperse flow is at stake, such approach becomes intractable because of the large amount of inclusions. Therefore, some dedicated models have been proposed to tackle this specific regime, for instance with Particle Resolved DNS or PR-DNS (Uhlmann, 2005; Uhlmann et al., 2023) where the interaction between the fluid and rigid particles are solved with an immersed boundary approach in an incompressible context.

Another class of models are the kinetic models have been derived with the assumption of point particles described with a Number Density Function (NDF) which accounts for the inclusions characteristics (*e.g.* in sizes, shapes, temperatures). While most models assume spherical droplets with static interface shape (Williams, 1958; Dufour and Villedieu, 2005; Essadki et al., 2018; Fox et al., 2020), others aim at modelling interface dynamics of the inclusions, *e.g.* with droplet oscillation (O'Rourke and Amsden, 1987), resulting either from the mixed regime or from agitated downstream by the gaseous flow. Analogously with the kinetic theory for gas dynamics modelling, a Population Balance Equation (PBE) describe the dynamics of the NDF *e.g.* Williams (1958). It results in a high-dimensional model which is difficult to solve with usual deterministic discretization techniques. One possibility is to do a statistical sampling of the inclusion distribution with the Lagrangian tracking of numerous inclusions (Amsden et al., 1989). Otherwise, a method of moments can then be used to reduce this high dimensional problem into an

Eulerian reduced-order model with the transport of a finite set of moments which gathers statistical information about the NDF (Massot et al., 1998; Laurent and Massot, 2001; Fox and Marchisio, 2007; Massot, 2007; Doisneau et al., 2013).

Multi-fluid models

Another class of models, can efficiently reduce the complexity associated with the interface length-scale, the *multi-fluid models*, which are typically obtained after an averaging process (Drew, 1990; Saurel and Abgrall, 1999). These models stand at a relatively large scale to capture a specific interface regime, a portion of a smooth interface or a collection of inclusions. This allows building reduced-order models for the interface dynamics and description, usually with the advection of a single scalar information. However, various challenges arise with this approach such as the proper modelling of capillarity depending on the flow regime or the description of the local thermodynamics between the two fluids. In the separated regime, one can adopt a *multi-fluid DIM* where both immiscible phases coexist within an artificial mixture, and one usually considers the interface to be approximately captured in the computational domain by the transition zone from 0 to 1 of a colour function that also provides an estimator of the interface area density (IAD). Remark that such a model, except if some specific interface compression techniques are added to the model (Shukla et al., 2010), does not involve any interface thickness length scale as opposed to phase-field DIM. Regarding the modelling of capillarity, the Continuum Surface Force (CSF) model of Brackbill (Brackbill et al., 1992) accounts for the capillarity forces as a source term based on the colour function. Therefore, this allows a volume-based approach of a surface-based phenomena, making it compatible with the multi-fluid framework. An alternate approach involves an equivalent flux form referred to as the Continuum Surface Stress (CSS) model (Lafaurie et al., 1994; Gueyffier et al., 1999; Perigaud and Saurel, 2005; Grenier et al., 2013; Schmidmayer et al., 2017). Other methods based on *second-gradient DIM* (Jamet et al., 2001; Bueno and Gomez, 2016) are reminiscent of the Phase Field (Cahn and Hilliard, 1958; Jacqmin, 1999) approach. They rely on an adapted thermodynamic model in order to control the thickness of the interface. However, both *multi-fluid DIM* or *second-gradient DIM* methods cannot be used to capture fine geometric details that are smaller than the resolution of the bulk scale, potentially related to the interface width in the second-gradient approach. Then, the multi-fluid approach naturally introduces the notion of *large-scale* dynamics which corresponds to the dynamics of the interface that can be located by the colour function field while *small-scale* dynamics corresponds to the under-resolved features or small fluid inclusions that are naturally out of reach for amenable mesh resolution.

In the disperse regime, the exact locations of the droplets or bubbles are unknown, and a mixture description with the sole volume fraction can be retained in a *multi-fluid disperse model* (Baer and Nunziato, 1986; Raviart and Sainsaulieu, 1995; Saurel et al., 2017; Drui et al., 2019; Fox et al., 2020). In such regime, capillarity effects are often not considered as the particles are assumed spherical with no intrinsic dynamics.

Regarding the thermodynamics associated with the multi-fluid approach, the local description of the medium can encompass several disequilibria between averaged pressures, averaged velocities and averaged temperatures. Such disequilibria naturally appear when deriving the model with the classic averaging of the local equations (Drew, 1983). The thermodynamics of the model is tuned either by closing some averaged quantities or by assuming partial or total equilibria. At one end of the spectrum stands full-disequilibrium two-velocity two-pressure models, also known as seven-equation models (volume fraction, and for each phase, density, velocity, energy) with for instance the models in Baer and Nunziato (1986); Saurel and Abgrall (1999); Coquel et al. (2002); Guillemaud (2007b). At the other end of the spectrum, one can consider the four-equation model where full equilibrium is considered for pressure, velocity and temperature (Le Touze, 2015; Haegeman et al., 2024). Partial equilibrium or models with relaxation source terms can also be considered, and leads to six- and five-equation models (Kapila et al., 2001). Let us underline that these models do not all share the same mathematical structure regarding hyperbolicity or the definition of jump relations in presence of discontinuous solutions (Coquel et al., 2002). Moreover, the right definition of the relaxation source terms is a non-trivial task as different time-scales are involved, and cannot always be considered for any amplitude of disequilibrium (Jomée, 2023; Bussac, 2023). Such issue is currently under consideration in the PhD thesis of Haegeman (2025).

Derivation of multi-fluid models with Hamilton's Stationary Action Principle

As mentioned before, the multi-fluid models can be derived through a classic averaging of the local equations (Drew, 1983) but involve many averaged terms, the expression of which is unknown and are usually difficult to close. Another derivation technique, a variational method, is the Hamilton's Stationary Action Principle (SAP). Hamilton's SAP, or Least Action Principle, derives the equation of the motion thanks to an extremization problem. The strength of this approach relies on the genericity of its modelling framework, which encompasses a wide spectrum of physical theories from quantum physics (Dirac, 1933; Feynman, 1948; Schwinger, 1963) to general relativity (Dirac, 1974), and of course Newtonian mechanics with the seminal works of Maupertuis, Euler and Lagrange. These works were later interpreted within the new Hamiltonian framework by both Hamilton and Jacobi. This approach allows deriving the equations of motion from a single scalar function the Lagrangian $\mathcal{L}$ defined as the difference between the kinetic and potential energies

$$\mathcal{L} = E_{kin} - E_{pot}. \tag{1}$$

The associated action $\mathcal{A}$ is then extremized over a space-time domain Ω using a variational operator δ over family of trajectories,

$$\delta\mathcal{A} = 0, \qquad \mathcal{A} = \int_{\Omega} \mathcal{L}. \tag{2}$$

In the context of discrete mechanical system, the Hamilton's SAP boils down to a set of Euler-Lagrange equations Bourguignon (2007). Inspired by its use for electrodynamics by Eckart (1938), it has later been applied to continuum mechanics for the dynamics of solids or fluids (Herivel, 1955; Serrin, 1959; Eckart, 1960; Sedov, 1965; Salmon, 1983; Bedford, 1985; Berdichevsky, 2009; Gouin, 2020), and the specific application to multi-fluid systems was then proposed with the works of Bedford and Drumheller (1978); Geurst (1986); Truskinovsky (1991); Gavrilyuk and Gouin (1999).

The two-phase modelling strategy with Hamilton's SAP relies on the *a priori* knowledge of the energies of a *restricted amount of physical phenomena* that we want to model in order to include them in the Lagrangian energy. Thus, it differs from the averaging approach which consider *a priori all the physical phenomena*, and the restriction to specific phenomena is carried out *a posteriori*, through the closure of averaged terms. Numerous models have recently been derived with Hamilton's SAP as it provides a systematic methodology to derive models once the energies at stake are identified, for instance bubbly flows or capillarity (Gavrilyuk, 2011; Drui et al., 2019; Schmidmayer et al., 2017). However, such models are dedicated to the description of a single flow regime except for recent attempts of multi-regime models (Cordesse, 2020; Di Battista, 2021) that are notably discussed hereafter.

Multi-regime strategies

In order to adapt the modelling choices to the various flow regimes in a single computational domain, Eulerian-Eulerian (Le Touze et al., 2020) or Eulerian-Lagrangian (Herrmann, 2010; Tomar et al., 2010) coupling strategies have been developed, but the transfers between models, with either full-volume coupling or through a preset interface (see Figure 0.5), suffer from multiple drawbacks beyond the usual heuristics parametrizing the transfer. First, when a coupling interface is chosen, its *a priori* setup is difficult to manage, and the mathematical properties of the overall system is usually hard to study. Second, when a full-volume coupling is considered, the mass transfer from one model to another locally changes the local volume occupation and liquid density in each model, such that unphysical pressure variations are generated in return (Le Touze, 2015). Such mass transfer is consequently restricted to regions where the liquid volume fractions are relatively small.

Another strategy lies in Large-Eddy Simulation (LES), where the averaged equations are filtered so that the under-resolved small scales are modelled. Such an approach, is typically used to model turbulence, but has also been introduced for filtering interface length-scales (Toutant, 2006; Ménard et al., 2007; Herrmann, 2015). Similarly to the averaging of the equations, these models require the closure of the filtered term either with heuristics or assuming a small-scale model for the interface dynamics. However, this task is all the more difficult in the turbulent context considered by LES as both the turbulence in the neighbourhood of an interface and the small-scale dynamics of the interface are coupled and lead to unclosed terms (Chesnel et al., 2011; Vaudor et al., 2017). Thus, the

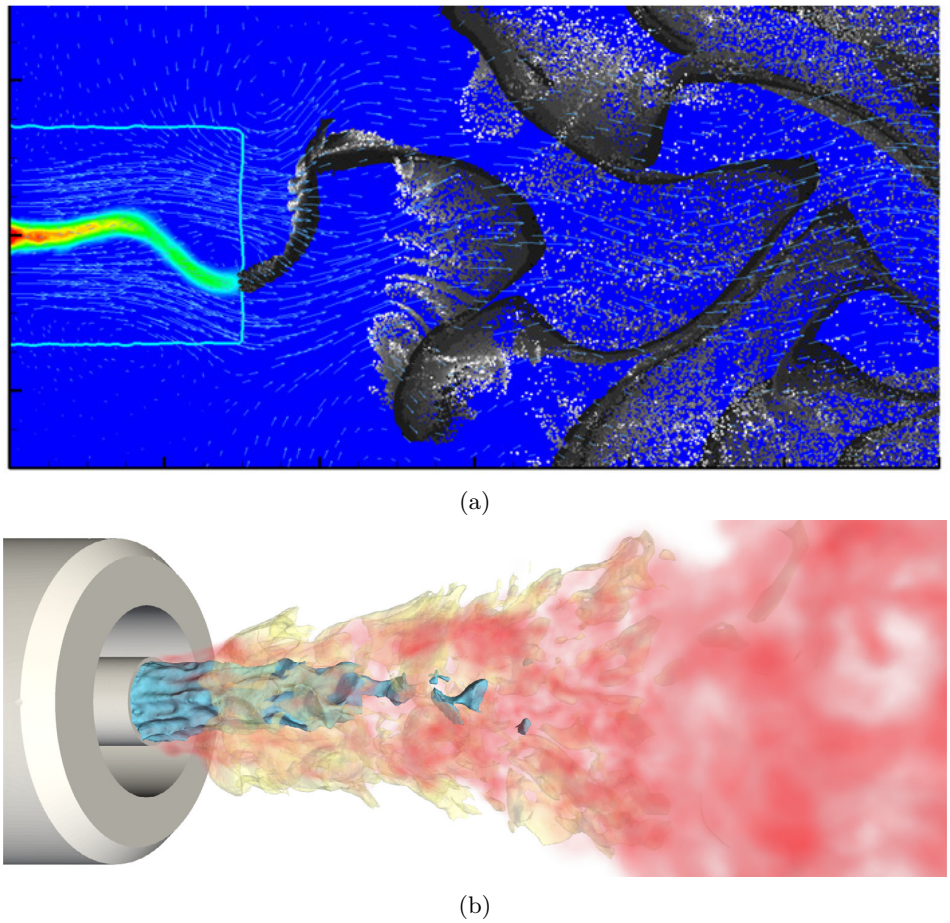

(a)

(b)

Figure 0.5: (a) An Eulerian-Lagrangian two-dimensional simulation of the atomization of a liquid sheet (Zuzio et al., 2013). The coupling occurs through a fixed surface (the light-blue square shape). (b) An Eulerian-Eulerian three-dimensional simulation of the atomization of a liquid injection (Le Touze et al., 2020). An iso-contour of the dense volume fraction of the separated phase is plotted in blue and a disperse volume fraction field of the disperse phase is plot red.

concomitant modelling of both phenomena is a challenging task, and we follow here another modelling strategy out of the turbulence context.

Finally, the *two-scale modelling* combines two models: one for the large scale and one for the small scale where the reduced-order model of the small-scale dynamics is included in the derivation of the two-phase model. Some attempts of formulating such models have been proposed by Bedford and Drumheller (1978); Gavrilyuk and Saurel (2002); Drui et al. (2019) using the Hamilton's SAP. However, they only account for a disperse flow regime of bubbles in a carrier liquid phase. Then, attempts of unified models describing both the separated and disperse regime have been proposed in Devassy et al. (2015); Drui (2017); Cordesse et al. (2019, 2020); Di Battista (2021), with the introduction of some small-scale geometric quantities. In these last two works, Hamilton's SAP has been used to combine a *large-scale* multi-fluid DIM model, adapted to the separated phase regime above a preset length threshold with the dynamics of geometric quantities describing the small interface length-scales. Furthermore, it has been showed that some well-chosen geometric quantities can be linked to statistical moments of the size distribution of the inclusions in the disperse regime (Essadki et al., 2016). This suggests a possible coupling of these two-scale models with disperse models. However, the two-scale modelling approach still suffers from limitations preventing its use for effective simulations of flows with multiple regimes, namely:

- no transfer from one scale to another is considered, preventing the presence of transition from one regime to another;
- no control over the length-scales associated with each regime in the models;
- only spherical static inclusions in small-scale models, that is not realistic enough nearer to the transitional mixed regimes where inclusions are deformed with their own dynamics of interface;
- no consistent capillarity models at both scales, which are required to balance the energies when topological changes of the interface occur.

The work proposed in this manuscript follows this two-scale modelling strategy and offers solution to overcome these modelling hurdles with a two-scale multi-regime regime approach or *two-scale unified model* that aims at both the description of the multiple two-phase flow regimes within a unique set of equations and subsequent simulations.

Numerical schemes

In our context of compressible two-phase flows, the employed numerical schemes are built for a specific family of partial differential equations: the systems of conservation laws. Such systems read

$$\partial_t \boldsymbol{q} + \boldsymbol{\nabla} \cdot \boldsymbol{F}(\boldsymbol{q}) = 0, \tag{3}$$

with $\boldsymbol{q}$ a set of conserved variables and $\boldsymbol{F}(\boldsymbol{q})$ a vector-valued function of the conserved variables. A particular property of such systems relies on the existence of discontinuous weak solutions accounting for either shocks or material contacts (Lax, 1957; Godlewski and Raviart, 1991). Such a property restricts the choice of numerical methods to conservative ones based on a consistent discretization of the flux divergence at the interface of the computational cell. This corresponds to a class of methods called *finite-volume scheme* and many schemes can be interpreted in that framework, but we underline that a natural conservative extension of the upwind scheme was first proposed by (Godunov and Bohachevsky, 1959). Such a method allows the resolution of the weak solution without introducing artificial viscosity, but requires solving a non-linear problem between two constant states, also known as the *Riemann problem*. Then, numerous strategies have been proposed to either build high-order extension of the Godunov scheme, *e.g.* MUSCL schemes (Van Leer, 1979), ENO/WENO schemes (Harten et al., 1987), or approximated Riemann solvers to avoid the costly solution of a Riemann problem, *e.g.* Rusanov (Rusanov, 1961), HLL (Harten et al., 1983), and Roe schemes (Roe, 1981).

However, some two-phase flow DIM do not match the form (3) but also include other first-order partial differential terms called *non-conservative* terms (Baer and Nunziato, 1986; Saurel and Abgrall, 1999; Kapila et al., 2001), higher-order partial differential terms called *dispersive* terms (Schmidmayer et al., 2017; Tkachenko et al., 2023), additional algebraic equations (Chanteperdrix et al., 2002) or relaxation source terms (Baer and Nunziato, 1986; Downar-Zapolski et al., 1996; Hérard, 2007; Jomée, 2023; Bussac, 2023). Note that no general theory is available for the study of such features, only some case-dependent theoretical elements are available. We mention here some theoretical results for non-conservative models (Coquel et al., 2002; Gallouët et al., 2004; Forestier and Gavrilyuk, 2011; Cordesse and Massot, 2020) or for relaxation source terms (Liu, 1987; Bouchut, 1999), but the lack of global proper mathematical theory for systems involving such terms in the general case makes the derivation of numerical schemes model-dependent and are discussed in each of the reference aforementioned.

Besides, some multi-fluid disperse models rely on a kinetic equation and a method of moments, as McGraw (1997); Dufour and Villedieu (2005); Marchisio and Fox (2005); Massot et al. (2010); Essadki et al. (2018); Fox et al. (2022) and must satisfy supplementary *realizability conditions* (Akhiezer, 1965; Schmüdgen, 2017) that must be preserved at the discrete numerical level to ensure the existence of a corresponding positive distribution. *Realizable numerical schemes* on moments (Perthame, 1990; Bouchut, 1994; Bouchut et al., 2003; Essadki, 2018; Ait-Ameur et al., 2024) preserve this property through the use of the underlying kinetic equation in the construction of the numerical schemes.

In the context of such an abundant literature of models and numerical schemes, we require a fast-prototyping solver to rapidly implement, couple and test models and their dedicated schemes. Therefore, the open-source solver Josiepy (2023), initiated by the PhD thesis of Di Battista (2021) has been chosen to fulfil this task and consists in

a structured finite-volume solver. The modularity of the implementation enables to efficiently reproduce a hierarchy of two-phase models derived thanks to Hamilton's SAP in this manuscript.

Overview of the manuscript

The coupling process offered by two-scale unified models is a cornerstone for two-scale models as it allows describing the transition between the different regimes, while ensuring critical properties such as energy conservation or a dissipative structure. In the first part of this manuscript, the modelling tools for the derivation of unified models are provided along with numerous building block models, which can be combined with each other to design the most adequate model for a given two-phase flow. The second part of the manuscript is dedicated to the numerical methods associated with the two-scale unified model. Moreover, simulations designed to assess the potential of the modelling approach are proposed on demonstrative test-cases.

In Chapter 1, an overview of the derivation techniques leading to multi-fluid models is provided, and key systems are identified in separated and disperse regimes that will be used as building blocks for the upcoming two-scale models. In Section 1.1, some mathematical properties of conservation laws are recalled before presenting the derivation of several models of the literature. Despite an incomplete mathematical theory for systems of conservation laws, the models always seek to satisfy the key mathematical properties that are required for well-posedness in simpler context such as scalar equations, namely the hyperbolicity of the system, the existence of a supplementary conservation equation and well-defined Rankine-Hugoniot jump relations. We highlight how the quest of a two-phase flow model with such properties has influenced the various derivation techniques of the literature. Furthermore, we emphasize another modelling challenge, mainly through the presentation of averaged models, that lies in the coupling between the dynamics of each phase and the interface. The difficult modelling step for such models particularly lies in establishing the *a posteriori* closure of averaged terms. Indeed, without any assumption made on the interface regime, a generic closure is most probably out of reach. Conversely, the derivation of two-phase flow models with Hamilton's SAP detailed in Section 1.2 requires an *a priori* knowledge of the two-phase flow regime. The method relies on the identification of the Lagrangian energy, *i.e.* kinetic minus potential energies, locally present in the flow and should gather any knowledge about the specific flow regime under consideration. In order to both assess the methodology and demonstrate the flexibility of the method, examples of two-phase flows are derived with Hamilton's SAP for both the separated regime in Section 1.3 and the disperse regime in Section 1.4. Moreover, while the Sections 1.1-1.2-1.3 offers an interesting perspective on multi-fluid models of the literature, an original perspective is drawn in Section 1.4 regarding the derivation of two-velocity models with Hamilton's SAP through the accounting of added-mass effects.

Chapter 2 is dedicated to the reduced-order modelling of the small-scale dynamics, mainly based on the assumption of a small-scale disperse regime. Extending the works of Essadki et al. (2016) for polydisperse spherical inclusions, the goal is to characterize other small-scale configurations, not just static but also with a dynamical model, using appropriate geometric quantities. As we extensively use geometric quantities and their associated kinematic relations, we propose in Section 2.1 a detailed presentation of the geometric quantities through introductory concepts of differential geometry. A specific emphasis is set on the kinematic relations for closed shapes as it characterizes the interface movement of inclusions such as droplets or bubbles. In Section 2.2, we formalize the Geometric Method of Moments (GeoMOM), a small-scale modelling approach, based on the method of moments of a kinetic model, that allows to describe the collective dynamics of inclusions (droplets or bubbles) with geometric quantities. Remark that, thanks to the use of geometric quantities rather than statistical moments, such a method particularly enables the use of the resulting models anywhere in the flow regardless of the assumption on the disperse nature of the small-scale dynamics. This geometric information is then included within the framework of the Hamilton's SAP at two levels. First, the energies related to the collection of inclusions are expressed with these geometric quantities and added in the total Lagrangian. Second, kinematic constraints between the geometric quantities are also enforced in the variational process leading to the equations of motion. This approach is then applied to propose new models for bubbly flows and oscillations of deformed liquid droplets. This latter model with deformed inclusions answers a first limitation in existing two-scale models where only static droplets are accounted for, and it has lead to a contribution

Loison et al. (2023b). It notably makes a step towards the description of mixed regime by both providing a simple model for detached filaments and showing that handling some cases requires new *oriented* geometric quantities. Indeed, these models provide clues on the right variables to use for the modelling of more complex interface dynamics by first identifying the ones required for the minimal models – pulsating bubbles and oscillating droplets.

Chapter 3 holds the key elements for the derivation of two-scale unified models and stands as a major contribution of this manuscript. Indeed, it provides an answer to the remaining limitations of two-scale models aforementioned by showing how the models for both separated and disperse regimes can be combined in a single one and how we model the interaction between each other. We proceed in three steps: 1- building a unified model with the addition of the small-scale liquid phase as a third phase, 2- introducing an inter-scale mass transfer complying with a dissipative structure, 3- defining a modelling length-scale separating the two scales of the model *via* a regularizing of the large-scale interface. In Section 3.1, the usual concept of two-phase mixture for two-fluid models is first extended into a unified two-scale two-phase mixture. Taking advantage of Hamilton's SAP flexibility, classic separated multi-fluid models and the newly proposed disperse models are combined in a single set of conservation laws. This way, we overcome the issues of unphysical pressure variations arising with coupling techniques when the volume of one phase is transferred to the other model. Section 3.2 then details the inter-scale transfer between the two scales within the unified model through the addition of mass exchanges. The mathematical admissibility of such exchanges is assessed as either a simple energy redistribution within the model or a dissipative process complying with the second principle of thermodynamics. With the geometric quantities and their associated small-scale models introduced in Chapter 2, we assess the modelling capabilities of such inter-scale processes with the identification of parameters that can be tuned to model the primary break-up phenomena. Polydispersion in sizes of the droplets or their deformations resulting from the break-up of filaments can be encompassed in this approach. Finally, an innovative interface regularizing process (Loison et al., 2023a) is introduced in Section 3.3 to both locate where the inter-scale transfers are triggered and keep the large-scale interface from developing length-scales below a preset size threshold. A key feature of this regularization lies in its local nature that differs from usual non-local mass re-distribution processes and in its interpretation as a local energy re-distribution between the large- and small-scale models that preserves the mathematical properties of the model. Moreover, it is important to note that the length-scale threshold is also introduced as a preset value and does not rely on the numerical cell size. Note that this inter-scale transfer and regularization process are tuned by the modeller as a mean to model the complex phenomena arising in the mixed regime.

Thanks to these new advances regarding inter-scale mass transfers, relevant simulations of two-scale two-phase flows are presented in the second part of this manuscript.

In Chapter 4, we introduce the numerical strategies to solve the different parts of the two-scale unified models. Section 4.1 focuses on a two-scale model with the regularization process connecting the large-scale flow model to a simple small-scale model only accounting for a disperse regime characterized by its volume fraction and its interface area density. This model involves a set of partial differential equations that can be split into terms of different natures with time splitting techniques (Hundsdorfer and Verwer, 2003; Duarte, 2011). Due to the discontinuous nature of the solutions, we solve numerically these equations with a Finite-Volume approach. More specifically, we separate the convective-related part of the system from the capillarity-related one. This enables the use of classic schemes (LeVeque, 1992; Godlewski and Raviart, 1996; Toro, 2009) such as the Godunov method that uses the exact solution of the two-scale Riemann problem. The capillarity is present both in both the conservative fluxes in the momentum equation and in a local Laplace pressure jump that is solved with a relaxation procedure. While the fluxes are classically discretized with an arithmetic average of gradients, the Laplace pressure jump cannot be solved with a usual relaxation procedure on the volume fraction, like Rosenbrock methods for Differential Algebraic Equations (Hairer and Wanner, 1996; Hundsdorfer and Verwer, 2003). Indeed, the relaxation source terms not only depends on the volume fraction but also on its spatial derivatives. Therefore, an original implicit-explicit relaxation procedure is then proposed to extend the usual Newton-Raphson method. This requires to solve the Laplace equation with respect of a fictitious time by means of an explicit integration of the source terms with spatial derivatives. This approach allows

to preserve the low complexity of the procedure in comparison with a relaxation procedure that implicitly couples each cell with its neighbour. We propose in Section 4.2 a numerical scheme dedicated for the small-scale model with oscillating droplets. This model is here treated separately to address the realizability issue associated with the geometric quantities, *i.e.* the possibility of reconstructing a distribution represented by the moments related to the geometric quantities obtained by GeoMOM. A specific kinetic scheme is chosen to preserve the realizability properties thanks to the exact solution of the kinetic equation associated with the dynamics of the polydisperse inclusions.

In Chapter 5, we validate the implementation for the discretization methods and some basic model properties. This test cases all result from personal contributions of the author in the open-source solver `Josiepy`[1]. This chapter considers each sub-model separately before integrating them all together in a full two-scale simulation in Chapter 6. In Section 5.1, we start by assessing the convergence rate of the second-order MUSCL extension of Godunov schemes for smooth solutions. Both material advection and sound propagation test cases are set up for the convective part of the two-scale models. The simulation of sound propagation enables to verify that the instantaneous relaxation of the one velocity/two-pressure model solves the one velocity/one pressure model and that the small-scale volume fraction modifies the sound propagation velocity. The study of Riemann problems is proposed in Section 5.2 to validate that the implemented finite-volume scheme and Riemann solvers are indeed solving the corresponding exact solutions. We pursue in Section 5.3 by illustrating the effect of capillarity fluxes and local Laplace equation on the case of a static droplet initialized out of the correct global Laplace pressure jump. The simulation of this test-case reveals to be challenging as the mean curvature of the equilibrium circle shape is complex to compute accurately on a Cartesian mesh. Finally, Section 5.4 assesses the proper dynamics for a spray of oscillating droplets without global motion including possible external source terms.

In Chapter 6, we propose numerical studies that illustrate the potential of both the two-scale model with regularization and the small-scale model of oscillating droplets in a physical context. In Section 6.1, we first consider a compressible liquid column deformed by an impacting compressible gaseous flow. This setup has been chosen as it develops filaments on each side of the column such that a basic multiscale interface dynamics appear. Then, it allows us to demonstrate the efficiency of the regularization process of the large-scale interface. Moreover, we indicate how the parametrization of the source terms enables the modelling of the evolution of interface geometry, particularly the IAD, as the transfer occurs. A comparison is proposed with a simulation of higher fidelity coming from another implementation of the test-case. More specifically, we estimate the source terms parameters that must be chosen to get the same geometric characteristics. This illustrates the modelling potential for regime transition within the two-scale unified approach. We finally propose in Section 6.2, one-dimensional simulations of a spray of oscillating droplets that are agitated by an external source term mimicking the effect of velocity drag on oscillations. Although this test can be considered elementary, it shows us the rich description contained in the model, especially regarding the dynamics of geometric quantities Moreover, this model should also be considered as another building blocks which aims to be added in a complete configuration involving all the modelling ingredients

The manuscript ends with conclusive remarks, outlooks and works in progress towards richer two-scale unified models. The preparation of this thesis has also led to scientific communications, collaborations and contributions which are listed in the next section.

[1] https://github.com/hpc-maths/josiepy

Introduction

Contexte industriel et scientifique

Les écoulements diphasiques composés de phases liquides et gazeuses apparaissent dans diverses applications industrielles. Certains processus impliquent directement l'interaction d'une phase liquide et d'une phase gazeuse à travers une interface, comme pour une réaction chimique ou une transition de phase. La surface déployée par l'interface présente alors dans l'écoulement est alors un paramètre critique de ces processus. D'autres processus sont eux complètement influencés par le mouvement de l'interface, comme le ballottement dans un réservoir (Chanteperdrix, 2004; Haegeman et al., 2024). D'autres configurations sont, elles, sensibles aux deux aspects, comme l'atomisation d'un jet de liquide en un spray ou les écoulements à bulles. À titre introductif, détaillons les mécanismes d'écoulement et les phénomènes physiques associés à ces deux configurations.

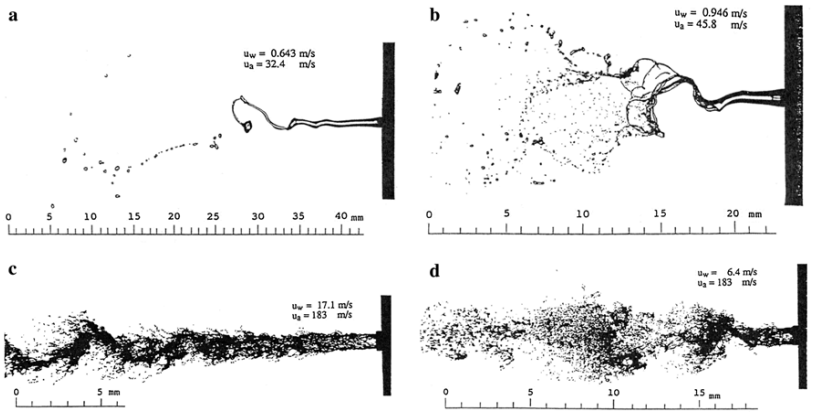

Figure 0.6: A atomisation assistée d'un jet d'eau liquide pour différentes vitesses de l'air injecté u_a et de l'eau u_w de Farago and Chigier (1992).

Pour l'atomisation d'un jet dans une chambre à combustion, le carburant liquide est injecté par une buse, se disperse en gouttelettes et la combustion a ensuite lieu après l'évaporation des gouttelettes obtenues, comme pour les moteurs diesel (Kah, 2010; Bode et al., 2014; Oguz, 2014; Essadki, 2018) ou les flammes cryogéniques pour la propulsion aérospatiale (Habiballah et al., 2006; Cordesse, 2020; Granger et al., 2023; Haegeman, 2025). Du fait que le changement de phase se produit à l'interface entre le liquide et le gaz, la vitesse de cette transition de phase est contrôlée par la quantité de surface interfaciale présente dans le réacteur. Afin de contrôler la vitesse de la transition de phase, on peut choisir de produire des gouttelettes plus ou moins grosses en déclenchant différents régimes d'atomisation sur de grandes plages de nombres de Weber et nombres de Reynolds (voir la Figure 0.6) en sélectionnant

différentes vitesses d'injection ou géométries de buse (Reitz and Bracco, 1979; Janodet et al., 2022). Cependant, prédir la distribution statistique en tailles des gouttelettes est très difficile et dépend de chaque dispositif expérimental. En effet, cette distribution en taille résulte de nombreux mécanismes complexes comprenant l'instabilité de l'interface, la formation de filaments ou de surfaces minces, l'apparition de trous, la rupture des filaments et des gouttelettes, la coalescence. Ainsi, de nombreuses études expérimentales approfondies ont été menées pour mieux comprendre la dynamique globale de l'atomisation (Farago and Chigier, 1992; Faeth, 1996; Marmottant and Villermaux, 2004; Mayer and Branam, 2004; Dumouchel, 2008; Jain et al., 2015; Warncke et al., 2017; Sharma et al., 2021; Aliseda and Heindel, 2021). L'étude de tels mécanismes est souvent très complexe, de sorte que ces dispositifs expérimentaux sont également complétées par des études numériques afin de mieux saisir la dynamique en jeu (Deberne et al., 2024; Ferrando et al., 2023).

Examinons maintenant le cas des écoulements à bulles où la réaction entre les deux phases se produit à l'interface entre les deux phases ou bien dans la phase liquide après dissolution (Orejas, 1999). Pour une telle interaction, les colonnes à bulles sont très pratiques car le gaz est injecté au bas de la colonne de liquide et les bulles sont naturellement agitées dans la phase liquide grâce à leur déplacement instable vers le haut sous l'effet de la poussée d'Archimède (voir la Figure 0.7). Bien que le dispositif expérimental soit assez simple, il peut mettre en jeu plusieurs régimes d'écoulement qui restent un sujet de recherche aujourd'hui encore très actif (Zehner and Kraum, 2000; Risso, 2018; Zamansky et al., 2023). En effet, rien que la dynamique d'une seule bulle est déjà assez complexe car elle se déforme facilement sous les contraintes imposées par l'écoulement (Lalanne et al., 2013). La traînée subie par la bulle peut alors changer au cours du temps, modifiant sa trajectoire dans la phase liquide (Ern et al., 2012). La forme de la bulle impacte également en retour l'écoulement local et peut générer des phénomènes turbulences. De plus, la dynamique globale de l'écoulement à bulles présente des comportements collectifs à travers la coalescence des bulles, la ségrégation des bulles et l'effet de masse ajoutée, qui dépendent tous de l'occupation moyenne du volume gazeux dans le réacteur et de la taille des bulles. Il convient toutefois de noter que l'écoulement à bulles diffère notablement du processus d'atomisation, car les inclusions gazeuses sont directement injectées dans l'écoulement sans régime de transition pour les créer. Toutefois, la prédiction de la densité d'aire interfaciale dans l'écoulement reste d'un interet majeur.

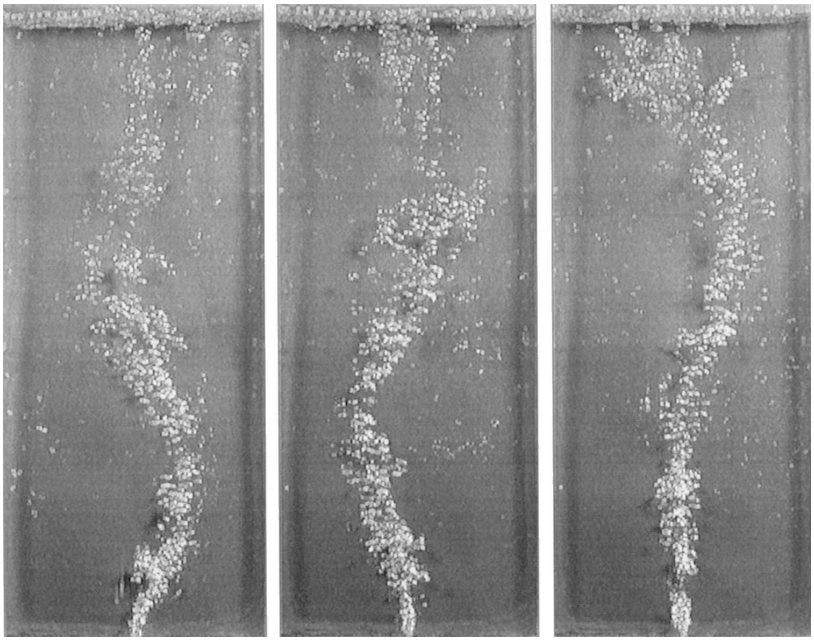

Figure 0.7: L'oscillation latérale dans une colonne de bulles (Becker et al., 1999).

Néanmoins, il existe aussi certains phénomènes d'écoulement diphasique qui présentent parfois des effets indésirables. Un exemple est la "crise d'ébullition" dans certains échangeurs de chaleur, lorsque l'ébullition de l'eau passe

d'un régime dit de *nucléation* avec l'apparition de petites bulles dans le liquide à un régime *film* où une fine couche de vapeur sépare la phase liquide de la paroi chauffante. En effet, ce phénomène de changement de phase empêche le bon transfert de chaleur avec le liquide qui est remplacé par la vapeur, isole le dispositif de chauffage (Theofanous et al., 2002) et peut endommager la surface du dispositif de chauffage qui n'est plus suffisamment refroidi. Un autre inconvénient de la présence impliquant un écoulement diphasique réside dans le phénomène de cavitation, lorsque de petites bulles apparaissent dans la phase liquide sous l'effet d'une dépressurisation brutale. L'implosion de la bulle qui s'ensuit peut alors causer des dommages sur les surfaces voisines ou générer des ondes acoustiques. Ces deux problèmes sont critiques, notamment pour les sous-marins, car ils endommagent prématurément les hélices des propulseurs ou réduisent leur furtivité.

Enfin, notons que tous ces phénomènes se produisent à des échelles de longueur et de temps qui s'étalent sur plusieurs ordres de grandeur. C'est pourquoi nous qualifierons ces écoulements diphasiques de *multiscale*. Dans ce manuscrit, nous nous intéressons particulièrement au processus d'atomisation avec des phases compressibles car il s'agit d'un bon exemple réunissant une grande partie de la compléxité d'un écoulement multi-échelle avec différents régimes d'interface. Dans ces dispositifs, les échelles de longueur s'étendent en effet sur plusieurs ordres de grandeur: de la taille de la buse d'injection aux plus petites gouttelettes dans l'écoulement en aval.

Une classification générale du régime lié à interface est proposée dans Ishii and Hibiki (1975), et, en ce qui concerne l'atomisation, nous identifions les régimes suivants:

- Le *régime séparé* décrit une interface suffisamment régulière pour que l'échelle de longueur lié à la dynamique de l'interface soit comparable ou plus grande que les échelles de longueur de la phase globale, et qu'aucune petite échelle, arbitrairement petite, ne puisse résulter de la dynamique de l'écoulement.

- Le régime *mixte* implique des échelles de longueur arbitrairement petites car la surface de l'interface subit des changements topologiques par pincement, rupture de filaments ou apparition de trous. Ce régime inclut notamment *l'atomisation primaire* lorsque les premières inclusions liquides apparaissent.

- Le *régime dispersé* correspond uniquement à de petites inclusions d'une phase (ici le liquide) transportées par l'autre (le gaz), où les inclusions peuvent alors se diviser à nouveau en plus petites (phénomène également appelé *atomisation secondaire*), ou coalescer avec d'autres inclusions. En raison du grand nombre d'inclusions, ce régime est souvent décrit statistiquement par une distribution sur un espace de phase caractérisant les inclusions : taille, forme, vitesse, température, ….

Ces régimes sont représentés schématiquement dans la Figure 0.8.

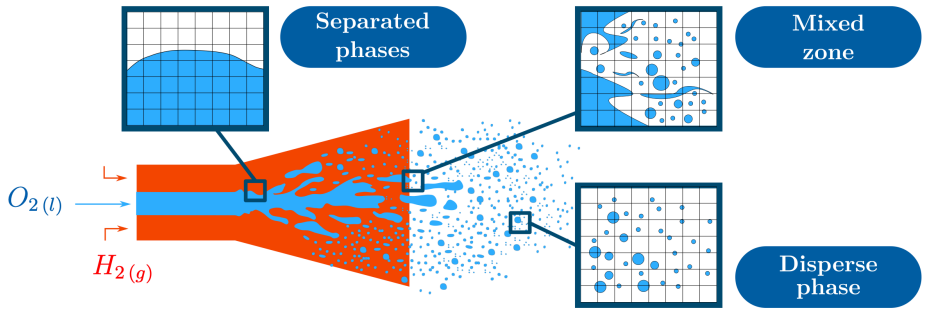

Figure 0.8: Représentation schématique d'une atomisation d'injecteurs cryogéniques dans les moteurs aérospatiaux (Cordesse, 2020).

Avec des régimes d'interface aussi différents, il est courant de se concentrer sur un seul régime pour représenter un plus petit nombre de phénomènes, qui peuvent être décrits alors de manière efficace. Par conséquent, de nombreux modèles ont été développés pour traiter chacun de ces régimes.

Une grande variété de modèles d'écoulement diphasique

Différentes échelles de longueur et différents modèles

Le choix du modèle d'écoulement diphasique est généralement adapté à un régime d'intérêt et peut proposer différents niveaux de détails pour la description de l'interface, à la fois sa dynamique et les phénomènes de capillarité qui y sont attachés. Décrivons brièvement chaque classe de modèles, partant du plus petit niveau de description de l'interface au plus grand.

Si l'on inclut dans la modélisation l'ensemble des échelles de longueur, on obtient une famille de modèles que l'on peut nommer *modèles d'interface diffuse à champs de phase* et qui propose de décrire en continu la transition d'une phase à l'autre et implique une échelle de longueur potentiellement très petite, l'épaisseur de l'interface, qui devra être résolue. De nombreux modèles entrent dans cette catégorie, tels que les modèles de Cahn-Hilliard (Cahn and Hilliard, 1958), ceux de Korteweg (Korteweg, 1901; Dunn, 1986; Dunn and Serrin, 1986) ou les modèles de second gradient (Gouin, 1996; Seppecher, 2002). Bien qu'ils s'appuient sur un modèle thermodynamiquement solide (voir la récente dérivation à partir niveau de description cinétique par Giovangigli (2021)) et donc une structure mathématique appropriée (Giovangigli et al., 2023), elles sont d'une utilité limitée dans des conditions ambiantes, où l'épaisseur physique de l'interface n'atteint que quelques nanomètres.

À plus grande échelle, c'est-à-dire si l'épaisseur de l'interface n'est pas décrite dans le modèle, les *modèles à interface résolues* (Sussman et al., 1994; Vaudor et al., 2017) permettent une localisation précise de l'interface avec une discontinuité des propriétés entre les fluides. Ces stratégies peuvent être considérées comme un couplage de systèmes monophasiques à travers une frontière dynamique. Par conséquent, les schémas numériques choisis doivent suivre l'emplacement de l'interface pendant les simulations. Parmi ces méthodes on trouve les méthodes de type *Volume Of Fluid* (Rudman, 1998; Gueyffier et al., 1999; Scardovelli and Zaleski, 1999) ou les méthodes de *Front Tracking* (Chern et al., 1986; Unverdi and Tryggvason, 1992; Popinet and Zaleski, 1999; Glimm et al., 2000) pour lesquelles l'emplacement de l'interface est suivi à l'aide d'une fonction de couleur advectée, les méthodes *Level-Set* utilisent des fonctions de distance (Sussman et al., 1994; Desjardins and Moureau, 2010), ou les méthodes *Coupled Level-Set VOF* qui combinent les avantages de chaque méthode, qui sont respectivement une description plus précise des propriétés géométriques et une meilleure conservation de la masse (Sussman and Puckett, 2000; Ménard et al., 2007; Vaudor et al., 2017). Ces approches sont parfois utilisées dans ce que l'on peut appeler les simulations numériques directes ou *DNS* car elles permettent la localisation précise de l'interface, bien que la résolution de toutes les échelles associées ne puisse pas toujours être garantie. Dans les cas impliquant plusieurs régimes de topologie d'interface, la mise en œuvre de ces approches nécessite de reconstruire l'interface à toutes les échelles pertinentes. Cela peut entraîner alors un coût de calcul déraisonnablement élevé pour des configurations complexes telles que les atomisations où la convergence du maillage est rarement atteinte (Herrmann, 2009; Shinjo and Umemura, 2010; Ling et al., 2017) (voir la Figure 0.9). Malgré son coût de calcul élevé inhérent, elle reste une technique fréquemment adoptée pour étudier le processus d'atomisation (Janodet et al., 2022) ou se concentrer sur des phénomènes d'écoulement diphasique élémentaires, mais complexes, tels que la rupture des gouttelettes, l'apparition de trous (Chirco et al., 2022), ou la turbulence (Martinez et al., 2021).

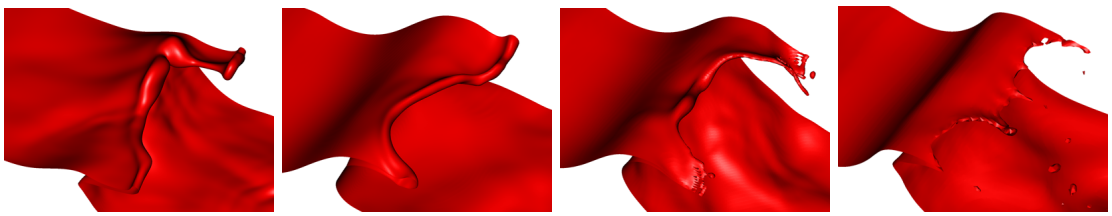

Figure 0.9: Résolution d'une fine crête de vague pour différentes résolutions de maillage, de grossier (à gauche) à fin (à droite) (Ling et al., 2017).

Le régime dispersé est également très difficile pour l'approche DNS car, malgré la présence d'un régime d'écoulement unique, l'échelle de longueur de l'écoulement autour ou à l'intérieur des inclusions transportées peut être beaucoup

plus petite de plusieurs ordres de grandeur. De plus, s'il s'agit d'étudier le comportement collectif de l'écoulement dispersé, cette approche devient alors impossible à mettre en œuvre en raison du grand nombre d'inclusions. Par conséquent, certains modèles dédiés ont été proposés pour aborder ce régime spécifique, par exemple avec Particle Resolved DNS ou PR-DNS (Uhlmann, 2005; Uhlmann et al., 2023) où l'interaction entre le fluide et les particules rigides est résolue avec une approche de frontière immergée dans un contexte incompressible.

Une autre classe de modèles, dits cinétiques, ont, eux, été dérivés dans l'hypothèse de particules ponctuelles décrites par une fonction de distribution qui tient compte des caractéristiques des inclusions (taille, forme, température, etc.). Alors que la plupart des modèles supposent des gouttelettes sphériques avec une forme d'interface statique (Williams, 1958; Dufour and Villedieu, 2005; Essadki et al., 2018; Fox et al., 2020), d'autres visent aussi à modéliser la dynamique de l'interface des inclusions, *e.g.* avec l'oscillation des gouttelettes (O'Rourke and Amsden, 1987), résultant soit du régime mixte, soit d'une agitation uléerieure par l'écoulement du gaz. De manière analogue à théorie cinétique pour la dynamique des gaz, une équation de transport dans l'espace physique et l'espace des phases *i.e.* des caractéristiques, permet de décrire la dynamique de la distributioon *e.g.* Williams (1958). Il en résulte un modèle à grande dimension qui est difficile à résoudre avec les techniques de discrétisation habituelles. Afin de palier à cette difficulté, une possibilité est d'effectuer un échantillonnage statistique de la distribution avec un suivi Lagrangien d'un grand nombre d'inclusions (Amsden et al., 1989). Une autre possibilité consiste à utiliser une méthode aux moments pour réduire ce problème de grande dimension en un modèle Eulérien d'ordre réduit de faible dimension avec le transport d'un nombre fini de moments qui rassemble des informations statistiques pertinente sur la distribution des inclusions (Massot et al., 1998; Laurent and Massot, 2001; Fox and Marchisio, 2007; Massot, 2007; Doisneau et al., 2013).

Modèles multi-fluides

Une autre classe de modèles peut aussi réduire efficacement la complexité associée à l'échelle de longueur de l'interface, les *modèles multi-fluides*, qui sont généralement obtenus après un processus de moyennisation (Drew, 1990; Saurel and Abgrall, 1999). Ces modèles se positionnent à une échelle relativement grande pour capturer un régime d'interface spécifique, comme une zone où l'interface lisse ou une collection d'inclusions. Cela permet de construire des modèles d'ordre réduit pour la dynamique et la description de l'interface, généralement avec l'advection d'un champ scalaire unique. Cependant, cette approche pose aussi différents problèmes, tels que la modélisation correcte de la capillarité en fonction du régime d'écoulement ou la description de la thermodynamique locale entre les deux fluides. Dans le régime séparé, on peut adopter un *modèle à interface diffuse multi-fluide* où les deux phases non miscibles coexistent dans un mélange artificiel, et on considère généralement que l'interface est approximativement capturée dans le domaine de calcul par la zone de transition de 0 à 1 d'une fonction couleur qui fournit également un estimateur de la densité d'aire interfaciale. Il convient alors de noter qu'un tel modèle, sauf si certaines techniques spécifiques de compression de l'interface sont ajoutées au modèle (Shukla et al., 2010), n'implique pas d'échelle de longueur liée à l'épaisseur de l'interface, contrairement au modèles à interface diffuse à champ de phase. En ce qui concerne la modélisation de la capillarité, le modèle *Continuum Surface Force* de Brackbill (Brackbill et al., 1992) tient compte des forces de capillarité en tant que terme source basé sur la fonction couleur. Cela permet donc une approche volumique d'un phénomène surfacique, ce qui le rend compatible avec le cadre multi-fluide. Une autre approche équivalente au modèle précédent permet une formulation sous la forme d'un flux conservatif (Lafaurie et al., 1994; Gueyffier et al., 1999; Perigaud and Saurel, 2005; Grenier et al., 2013; Schmidmayer et al., 2017). D'autres méthodes basées sur les *modèles à interface diffuse de type second gradient* (Jamet et al., 2001; Bueno and Gomez, 2016) rappellent l'approche utilisée pour les modèles à champ de phase (Cahn and Hilliard, 1958; Jacqmin, 1999). Elles s'appuient sur un modèle thermodynamique modifié afin de contrôler l'épaisseur de l'interface. Cependant, les méthodes à interface diffuse ou type second gradient ne peuvent pas être utilisées pour capturer les détails géométriques fins qui sont plus petits que la résolution de l'épaisseur de l'interface. Enfin, l'approche multi-fluide introduit naturellement la notion de dynamique *grande échelle* qui correspond à la dynamique de l'interface qui peut être localisée par le champ de la fonction de couleur tandis que *petite échelle* correspond aux caractéristiques non résolues ou aux petites inclusions fluides qui sont naturellement hors de portée de la résolution du maillage.

Dans le régime dispersé, les emplacements exacts des gouttelettes ou des bulles ne sont pas nécessaires, et une description du mélange local avec la seule fraction de volume peut suffire dans un *modèle multi-fluide dispersé* (Baer

and Nunziato, 1986; Raviart and Sainsaulieu, 1995; Saurel et al., 2017; Drui et al., 2019; Fox et al., 2020). Dans ce régime, les effets de capillarité ne sont souvent pas pris en compte car les inclusions ou particules sont supposées sphériques sans dynamique intrinsèque.

Maintenant, en ce qui concerne la thermodynamique associée à l'approche multi-fluide, la description locale du mélange peut tenir compte de plusieurs déséquilibres entre chaque phase notamment entre les pressions moyennes, les vitesses moyennes et les températures moyennes. Ces déséquilibres apparaissent naturellement lors de la dérivation du modèle avec la moyennisation des équations locales (Drew, 1983). La thermodynamique du modèle est alors fixée soit en fermant certaines quantités moyennées, soit en supposant des équilibres partiels ou totaux entre les phases. D'une part, on trouve les modèles avec un déséquilibre complet à deux vitesses et deux pressions, également connus sous le nom de modèles à sept équations (fraction volumique, et pour chaque phase, densité, vitesse, énergie), avec par exemple les modèles de Baer and Nunziato (1986); Saurel and Abgrall (1999); Coquel et al. (2002); Guillemaud (2007b). D'autre part, on peut considérer le modèle à quatre équations où l'équilibre complet est pris en compte pour la pression, la vitesse et la température (Le Touze, 2015; Haegeman et al., 2024). La considération d'équilibres partiels ou des modèles avec des termes de source de relaxation peuvent également être considérés, et conduisent à des modèles à six et cinq équations (Kapila et al., 2001). Soulignons que ces modèles ne partagent pas tous la même structure mathématique en ce qui concerne l'hyperbolicité ou la définition des relations de saut en présence de solutions discontinues (Coquel et al., 2002). En outre, la bonne définition des termes sources de relaxation n'est pas évidente car différentes échelles de temps sont impliquées et ne peuvent pas toujours être prises en compte pour toute amplitude de déséquilibre (Jomée, 2023; Bussac, 2023). Cette question est actuellement à l'étude dans la thèse de doctorat de Haegeman (2025).

Dérivation des modèles multi-fluides avec le principe de moindre action de Hamilton

Comme indiqué précédemment, les modèles multi-fluides peuvent être dérivés par une moyennisation des équations locales (Drew, 1983) mais ils impliquent de nombreux termes moyennés, dont l'expression est inconnue et qui sont généralement difficiles à exprimer. Une autre technique de dérivation, une méthode variationnelle, est le principe de moindre action de Hamilton. Le principe de moindre action, permet de dériver l'équation du mouvement grâce à un problème d'extrémisation. La force de cette approche repose sur la généricité de son cadre de modélisation, qui englobe un large spectre de théories physiques allant de la physique quantique (Dirac, 1933; Feynman, 1948; Schwinger, 1963) à la relativité générale (Dirac, 1974), et bien sûr la mécanique newtonienne avec les travaux fondateurs de Maupertuis, d'Euler et de Lagrange. Ces travaux ont ensuite été interprétés dans le nouveau cadre hamiltonien par Hamilton et Jacobi. Cette approche permet de dériver les équations du mouvement à partir d'une seule fonction scalaire, le lagrangien $\mathcal{L}$ défini comme la différence entre l'énergie cinétique et l'énergie potentielle.

$$\mathcal{L} = E_{kin} - E_{pot}. \tag{4}$$

L'action associée $\mathcal{A}$ est alors extrémisée sur un domaine spatio-temporel Ω à l'aide d'un opérateur variationnel δ sur une famille de trajectoires,

$$\delta\mathcal{A} = 0, \qquad \mathcal{A} = \int_{\Omega} \mathcal{L}. \tag{5}$$

Dans le contexte d'un système mécanique discret, la principe de moindre action se résume à un ensemble d'équations d'Euler-Lagrange Bourguignon (2007). Inspiré par son utilisation en électrodynamique par Eckart (1938), il a ensuite été appliqué à la mécanique des milieux continus pour la dynamique des solides ou des fluides (Herivel, 1955; Serrin, 1959; Eckart, 1960; Sedov, 1965; Salmon, 1983; Bedford, 1985; Berdichevsky, 2009; Gouin, 2020), et l'application spécifique aux systèmes multi-fluides a ensuite été proposée avec les travaux de Bedford and Drumheller (1978); Geurst (1986); Truskinovsky (1991); Gavrilyuk and Gouin (1999).

La stratégie de modélisation diphasique avec le principe de moindre action de Hamilton repose sur la connaissance *a priori* des énergies d'un *nombre restreint de phénomènes physiques* que nous voulons modéliser afin de les inclure dans l'énergie lagrangienne. Elle diffère donc de l'approche par moyennisation qui considère *a priori tous les phénomènes physiques*, et la restriction à des phénomènes spécifiques est effectuée *a posteriori*, par le biais de la fermeture des termes moyennés. De nombreux modèles ont récemment été dérivés avec le principe de moindre action,

car il fournit une méthodologie systématique pour dériver des modèles une fois que les énergies en jeu sont identifiées, par exemple les écoulements à bulles ou la capillarité (Gavrilyuk, 2011; Drui et al., 2019; Schmidmayer et al., 2017). Cependant, ces modèles sont souvent dédiés à la description d'un seul régime d'écoulement, à l'exception de propositions récentes de modèles multi-régimes (Cordesse, 2020; Di Battista, 2021) que l'on va maintenant discuter.

Stratégies multi-régimes

Afin d'adapter les choix de modélisation aux différents régimes d'écoulement dans un même domaine de calcul, des stratégies de couplage ont été développées (Herrmann, 2010; Le Touze et al., 2020), mais les transferts entre modèles, soit avec un couplage volumique, soit à travers une interface prédéfinie (voir Figure 0.10), souffrent de plusieurs inconvénients au-delà de l'utilisation habituelle d'heuristiques qui paramétrisent un tel transfert. Premièrement, lorsqu'une interface de couplage est choisie, sa localisation *a priori* est difficile à gérer, et les propriétés mathématiques du système global sont généralement difficiles à étudier. Deuxièmement, lorsqu'un couplage volumique est considéré, le transfert de masse d'un modèle à l'autre modifie localement l'occupation du volume et la densité du liquide dans chaque modèle, de sorte que des variations de pression non physiques sont générées en retour (Le Touze, 2015). Ce transfert de masse est par conséquent limité aux régions où les fractions de volume de liquide sont relativement faibles.

Une autre stratégie consiste à utiliser la simulation LES, où les équations moyennes sont filtrées de manière à modéliser les petites échelles non résolues. Une telle approche est généralement utilisée pour modéliser la turbulence, mais elle a également été introduite pour filtrer les échelles de longueur des interfaces (Herrmann, 2015; Toutant, 2006). De même que pour la moyennisation des équations, ces modèles nécessitent la fermeture du terme filtré, soit à l'aide d'heuristiques, soit en supposant un modèle à petite échelle pour la dynamique de l'interface. Cependant, cette tâche est d'autant plus difficile que, dans le contexte turbulent considéré par la LES, la turbulence au voisinage d'une interface et la dynamique à petite échelle de l'interface sont couplées et conduisent à des termes complexes et non fermés (Chesnel et al., 2011). Ainsi, la modélisation concomitante des deux phénomènes est une tâche difficile, et nous suivons ici une autre stratégie de modélisation hors du contexte de la turbulence.

Enfin, la *modélisation à deux échelles* combine deux modèles : un pour la grande échelle et un pour la petite échelle où le modèle d'ordre réduit de la dynamique à petite échelle est inclus dans la dérivation du modèle à deux phases. Certaines tentatives de formulation de ces modèles ont été proposées par Bedford and Drumheller (1978); Gavrilyuk and Saurel (2002); Drui et al. (2019) à l'aide du principe de moidre action. Cependant, ils ne prennent en compte qu'un régime d'écoulement dispersé de bulles dans une phase liquide porteuse. Ensuite, des tentatives de modèles unifiés décrivant à la fois le régime séparé et dispersé ont été proposées dans Devassy et al. (2015); Drui (2017); Cordesse et al. (2019, 2020); Di Battista (2021), avec l'introduction de certaines quantités géométriques à petite échelle. Dans ces deux derniers travaux, le principe de moindre action a été utilisé pour combiner un modèle multi-fluide à interface diffuse de *grande échelle*, adapté au régime de phase séparée au-dessus d'une échelle de longueur prédéfinie avec la dynamique des quantités géométriques décrivant les petites échelles de longueur de l'interface. En outre, il a été montré que certaines quantités géométriques bien choisies peuvent être liées aux moments statistiques de la distribution de la taille des inclusions dans le régime dispersé (Essadki et al., 2016). Cela suggère un couplage possible de ces modèles à deux échelles avec des modèles dispersés. Cependant, l'approche de modélisation à deux échelles souffre encore de limitations empêchant son utilisation pour des simulations d'écoulements à régimes multiples, notamment :

- le transfert d'une échelle à l'autre qui n'est pas pris en compte, et qui empêche la présence d'une transition d'un régime à l'autre ;
- l'absence de contrôle sur les échelles de longueur associées à chaque régime dans les modèles ;
- la seule description sphérique et statique des inclusions dans les modèles à petite échelle, ce qui n'est pas assez réaliste à proximité des régimes mixtes transitoires où les inclusions sont déformées avec leur propre dynamique d'interface ;
- l'absence de modèles de capillarité cohérents aux deux échelles, qui sont nécessaires pour équilibrer les énergies lorsque des changements topologiques de l'interface se produisent.

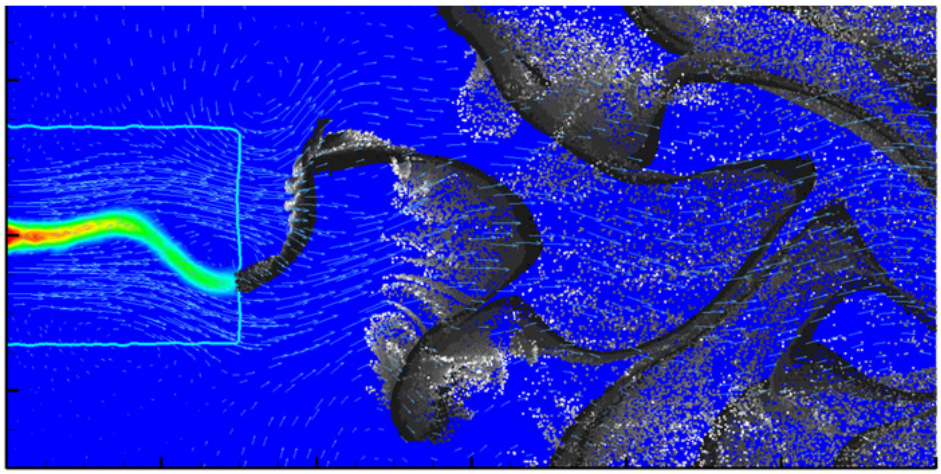

(a)

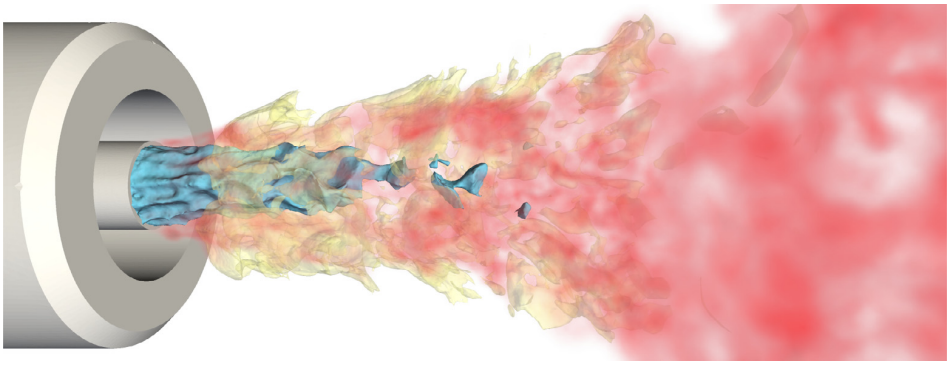

(b)

Figure 0.10: (a) Une simulation eulérienne-lagrangienne bidimensionnelle de l'atomisation d'une feuille de liquide (Zuzio et al., 2013). Le couplage se produit à travers une surface fixe (la forme carrée bleu clair). (b) Simulation tridimensionnelle eulérienne-eulérienne de l'atomisation d'une injection de liquide (Le Touze et al., 2020). Un iso-contour de la fraction volumique dense de la phase séparée est tracé en bleu et un champ de fraction volumique dispersée de la phase dispersée est tracé en rouge.

Le travail proposé dans ce manuscrit suit cette stratégie de modélisation à deux échelles et offre une solution pour surmonter ces obstacles de modélisation avec une approche de régime multi-régime à deux échelles ou *modèle unifié à deux échelles* qui vise à la fois la description des multiples régimes d'écoulement diphasique dans un ensemble unique d'équations et de simulations ultérieures.

Schémas numériques

Dans notre contexte d'écoulements compressibles à deux phases, les schémas numériques employés sont construits pour une famille spécifique d'équations aux dérivées partielles : les systèmes de lois de conservation. De tels systèmes s'écrivent

$$\partial_t \boldsymbol{q} + \boldsymbol{\nabla} \cdot \boldsymbol{F}(\boldsymbol{q}) = 0, \tag{6}$$

avec $\boldsymbol{q}$ un ensemble de variables conservées et $\boldsymbol{F}(\boldsymbol{q})$ une fonction flux des variables conservées. Une propriété particulière de ces systèmes repose sur l'existence de solutions faibles discontinues qui décrivent soit des chocs, soit des discontinuités matérielles (Lax, 1957; Godlewski and Raviart, 1991). Une telle propriété restreint le choix des

méthodes numériques à des méthodes conservatrices basées sur une discrétisation cohérente de la divergence du flux à l'interface du volume de controle. Cela correspond à une classe de méthodes appelées *schémas de volumes finis* et de nombreux schémas peuvent être interprétés dans ce cadre, mais notons tout d'aborf l'extension conservative du schéma Upwind a été proposée pour la première fois par (Godunov and Bohachevsky, 1959). Une telle méthode permet la résolution de la solution faible sans introduire de viscosité artificielle, mais nécessite la résolution d'un problème non linéaire entre deux états constants, dit *problème de Riemann*. Par la suite, de nombreuses stratégies ont été proposées pour construire une extension d'ordre élevé du schéma de Godunov, *e.g.* les schémas MUSCL (Van Leer, 1979), les schémas ENO/WENO (Harten et al., 1987), ou des solveurs de Riemann approchés pour éviter la résolution coûteuse d'un problème de Riemann, comme le schéma de Rusanov (Rusanov, 1961), HLL (Harten et al., 1983), et les schémas de Roe (Roe, 1981).

Cependant, certains modèles diphasique à interface diffuse ne correspondent pas à la forme conservative (6) mais incluent également d'autres termes différentiels du premier ordre appelés termes *non-conservatifs* (Baer and Nunziato, 1986; Saurel and Abgrall, 1999; Kapila et al., 2001), des termes différentiels d'ordre supérieur appelés termes *dispersifs* (Schmidmayer et al., 2017; Tkachenko et al., 2023), des équations algébriques supplémentaires (Chanteperdrix et al., 2002) ou des termes sources de relaxation (Baer and Nunziato, 1986; Downar-Zapolski et al., 1996; Hérard, 2007; Jomée, 2023; Bussac, 2023). Il est important de noter qu'il n'existe pas de théorie générale pour l'étude de ces systèmes, mais seulement quelques éléments théoriques au cas par cas pour chaque modèle. Nous mentionnons ici quelques résultats théoriques pour des modèles non conservatifs (Coquel et al., 2002; Gallouët et al., 2004; Forestier and Gavrilyuk, 2011; Cordesse and Massot, 2020) ou pour l'étude des termes sources de relaxation (Liu, 1987; Bouchut, 1999), mais l'absence d'une théorie mathématique globale appropriée pour les systèmes impliquant de tels termes rend la dérivation de schémas numériques dépendante du modèle et est discutée dans chacune des références susmentionnées.

En outre, certains modèles multi-fluides dispersés reposent sur une équation cinétique et une méthode des moments (McGraw, 1997; Dufour and Villedieu, 2005; Marchisio and Fox, 2005; Massot et al., 2010; Essadki et al., 2018; Fox et al., 2022) et doivent satisfaire des *conditions de réalisabilité* supplémentaires (Akhiezer, 1965; Schmüdgen, 2017) qui doivent être préservées au niveau numérique discret pour garantir l'existence d'une distribution positive correspondante. Les *schémas numériques réalisables* sur les moments (Perthame, 1990; Bouchut, 1994; Bouchut et al., 2003; Essadki, 2018; Ait-Ameur et al., 2024) préservent notamment cette propriété grâce à l'utilisation de l'équation cinétique sous-jacente dans la construction des schémas numériques.

Dans le contexte d'une littérature aussi abondante de modèles et de schémas numériques, nous avons alors besoin d'un solveur de prototypage rapide pour mettre en œuvre, coupler et tester rapidement les modèles et les schémas dédiés. Par conséquent, le solveur open-source Josiepy (2023), initié par la thèse de Di Battista (2021) a été choisi pour remplir cette tâche et consiste en un solveur structuré de volumes finis. La modularité de l'implémentation permet de reproduire efficacement la hiérarchie de modèles diphasiques dérivés dans ce manuscrit grâce au principe de moindre action.

Vue d'ensemble du manuscrit

Le processus de couplage offert par les modèles unifiés à deux échelles est une étape décisive pour les modèles à deux échelles car il permet de décrire la transition entre les différents régimes, tout en assurant des propriétés importantes telles que la conservation de l'énergie ou une structure dissipative. Dans la première partie de ce manuscrit, les outils de modélisation pour la dérivation de modèles unifiés sont fournis avec de nombreux modèles de base, qui peuvent être combinés les uns avec les autres pour concevoir le modèle le plus adéquat à un écoulement diphasique donné. La deuxième partie du manuscrit est consacrée aux méthodes numériques associées au modèle unifié à deux échelles. Enfin, des simulations conçues pour évaluer le potentiel de cette approche de modélisation unifiée à deux échelles sont proposées sur des cas-tests démonstratifs.

Le chapitre 1 présente une vue d'ensemble des techniques de dérivation conduisant à des modèles multi-fluides, et identifie les systèmes clés dans les régimes séparés et dispersés qui seront utilisés comme éléments de base pour les modèles à deux échelles à venir. Dans la section 1.1, certaines propriétés mathématiques des lois de conservation

sont rappelées avant de présenter la dérivation de plusieurs modèles de la littérature. Malgré une théorie mathématique incomplète pour les systèmes de lois de conservation, les modèles cherchent toujours à satisfaire les propriétés mathématiques clés qui sont requises pour la bonne pose dans un contexte plus simple tel que les équations scalaires, à savoir l'existence d'une équation de conservation supplémentaire avec des relations de saut de Rankine-Hugoniot bien définies. Nous soulignons comment la recherche d'un modèle d'écoulement diphasique avec de telles propriétés a influencé les différentes techniques de dérivation de la littérature. En outre, nous mettons l'accent sur un autre défi de modélisation, principalement à travers la présentation de modèles moyennés, qui réside dans le couplage entre la dynamique de chaque phase et l'interface. L'étape difficile de modélisation pour de tels modèles réside en particulier dans l'établissement de la fermeture *a posteriori* des termes moyennés. En effet, en l'absence de toute hypothèse sur le régime de l'interface, une fermeture générique est très probablement hors de portée. Inversement, la dérivation des modèles d'écoulement diphasique avec le principe de moindre action, détaillée dans la section 1.2, nécessite une connaissance *a priori* du régime d'écoulement diphasique. La méthode repose sur l'identification de l'énergie lagrangienne, c'est-à-dire l'énergie cinétique moins l'énergie potentielle, présente localement dans l'écoulement et doit rassembler toutes les connaissances sur le régime d'écoulement spécifique considéré. Afin d'évaluer la méthodologie et de démontrer sa flexibilité, des exemples d'écoulements diphasiques sont dérivés avec le principe de moindre action pour le régime séparé dans la section 1.3 et le régime dispersé dans la section 1.4. En outre, alors que les sections 1.1-1.2-1.3 offrent une perspective intéressante sur les modèles multifluides de la littérature, une perspective originale est dessinée dans la section 1.4 concernant la dérivation des modèles à deux vitesses avec le principe de moindre action par la prise en compte des effets de la masse ajoutée.

Le chapitre 2 est consacré à la modélisation d'ordre réduit de la dynamique à petite échelle, principalement basée sur l'hypothèse d'un régime dispersé à petite échelle. En prolongeant les travaux de Essadki et al. (2016) pour les inclusions sphériques polydisperses, l'objectif est de caractériser d'autres configurations à petite échelle, non seulement statiques mais aussi avec un modèle dynamique, en utilisant des quantités géométriques appropriées. Comme nous utilisons largement les grandeurs géométriques et les relations cinématiques qui leur sont associées, nous proposons dans la section 2.1 une présentation détaillée des grandeurs géométriques à l'aide de concepts d'introduction à la géométrie différentielle. Un accent particulier est mis sur les relations cinématiques pour les formes fermées, car elles caractérisent le mouvement d'interface des inclusions telles que les gouttelettes ou les bulles. Dans la section 2.2, nous formalisons la méthode géométrique des moments (GeoMOM), une approche de modélisation à petite échelle, basée sur la méthode des moments d'un modèle cinétique, qui permet de décrire la dynamique collective des inclusions (gouttelettes ou bulles) avec des quantités géométriques. Il est à noter que, grâce à l'utilisation de grandeurs géométriques plutôt que de moments statistiques, une telle méthode permet notamment d'utiliser les modèles résultants n'importe où dans l'écoulement, quelle que soit l'hypothèse sur la nature dispersée de la dynamique à petite échelle. Cette information géométrique est ensuite incluse dans le cadre du principe de moindre action à deux niveaux. Premièrement, les énergies liées à la collection d'inclusions sont exprimées avec ces quantités géométriques et ajoutées au lagrangien total. Deuxièmement, les contraintes cinématiques entre les quantités géométriques sont également appliquées dans le processus variationnel menant aux équations du mouvement. Cette approche est ensuite appliquée pour proposer de nouveaux modèles pour les écoulements bulleux et les oscillations de gouttelettes de liquide déformées. Ce dernier modèle avec des inclusions déformées répond à une première limitation des modèles à deux échelles existants où seules les gouttelettes statiques sont prises en compte, et il a conduit à une contribution Loison et al. (2023b). Il fait notamment un pas vers la description du régime mixte en fournissant à la fois un modèle simple pour les filaments détachés et en montrant que le traitement de certains cas nécessite de nouvelles quantités géométriques *orientées*. En effet, ces modèles fournissent des indices sur les bonnes variables à utiliser pour la modélisation de dynamiques d'interface plus complexes en identifiant d'abord celles requises pour les modèles minimaux - commes les bulles pulsantes et gouttelettes oscillantes.

Le chapitre 3 contient les éléments clés pour la dérivation des modèles unifiés à deux échelles et constitue une contribution majeure de ce manuscrit. En effet, il apporte une réponse aux limitations restantes des modèles à deux échelles mentionnées ci-dessus en montrant comment les modèles pour les régimes séparés et dispersés peuvent être combinés en un seul et comment nous modélisons l'interaction entre ceux-ci. Nous procédons en trois étapes

: 1- construction d'un modèle unifié avec l'ajout de la phase liquide à petite échelle comme troisième phase, 2- introduction d'un transfert de masse inter-échelle conforme à une structure dissipative, 3- définition d'une échelle de longueur de modélisation séparant les deux échelles du modèle *via* une régularisation de l'interface à grande échelle. Dans la section 3.1, le concept habituel de mélange biphasique pour les modèles à deux fluides est d'abord étendu à un mélange biphasique unifié à deux échelles. En tirant parti de la flexibilité du principe de moindre action, les modèles multi-fluides séparés classiques et les modèles dispersés nouvellement proposés sont combinés en un seul ensemble de lois de conservation. De cette manière, nous surmontons les problèmes de variations de pression non physiques découlant des techniques de couplage lorsque le volume d'une phase est transféré dans l'autre modèle. La section 3.2 détaille ensuite le transfert entre les deux échelles au sein du modèle unifié par l'ajout d'échanges de masse. L'admissibilité, du point de vue mathématique ,de ces échanges est évaluée comme une simple redistribution d'énergie au sein du modèle ou comme un processus dissipatif conforme au deuxième principe de la thermodynamique. Avec les quantités géométriques et leurs modèles associés à petite échelle introduits au chapitre 2, nous évaluons les capacités de modélisation de ces processus inter-échelles avec l'identification des paramètres qui peuvent être ajustés pour modéliser les phénomènes de rupture primaire. La polydispersion des tailles des gouttelettes ou leurs déformations résultant de la rupture des filaments peuvent être prises en compte dans cette approche. Enfin, un processus innovant de régularisation de l'interface (Loison et al., 2023a) est introduit dans la section 3.3 pour localiser l'endroit où les transferts inter-échelles sont déclenchés et empêcher l'interface à grande échelle de développer des échelles de longueur inférieures à un seuil de taille prédéfini. L'une des principales caractéristiques de cette régularisation réside dans sa nature locale, qui diffère des processus habituels de redistribution de masse non locale, et dans son interprétation en tant que redistribution locale d'énergie entre les modèles à grande et à petite échelle, qui préserve les propriétés mathématiques du modèle. En outre, il est important de noter que le seuil de l'échelle de longueur est également introduit comme une valeur prédéfinie et ne dépend pas de la taille de la cellule numérique. Il convient de noter que ce transfert inter-échelle et ce processus de régularisation sont réglés par le modélisateur afin de modéliser les phénomènes complexes qui se produisent dans le régime mixte.

Grâce à ces nouvelles avancées concernant les transferts de masse inter-échelles, des simulations pertinentes d'écoulements diphasiques à deux échelles sont présentées dans la deuxième partie de ce manuscrit.

Dans le chapitre 4, nous présentons les stratégies numériques permettant de résoudre les différentes parties des modèles unifiés à deux échelles. La section 4.1 se concentre sur un modèle à deux échelles avec le processus de régularisation reliant le modèle d'écoulement à grande échelle à un modèle simple à petite échelle ne prenant en compte qu'un régime dispersé caractérisé par sa fraction de volume et la densité de sa zone d'interface. Ce modèle implique un ensemble d'équations aux dérivées partielles qui peuvent être divisées en termes de nature différente grâce à des techniques de division temporelle (Hundsdorfer and Verwer, 2003; Duarte, 2011). En raison de la nature discontinue des solutions, nous résolvons numériquement ces équations à l'aide d'une approche à volumes finis. Plus précisément, nous séparons la partie du système liée à la convection de celle liée à la capillarité. Cela permet d'utiliser des schémas classiques (LeVeque, 1992; Godlewski and Raviart, 1996; Toro, 2009) tels que la méthode de Godunov qui utilise la solution exacte du problème de Riemann à deux échelles. La capillarité est présente à la fois dans les flux conservatifs de l'équation de quantité de mouvement et dans un saut de pression de Laplace local qui est résolu par une procédure de relaxation. Alors que les flux sont discrétisés classiquement avec une moyenne arithmétique des gradients, le saut de pression de Laplace ne peut pas être résolu avec une procédure de relaxation habituelle sur la fraction de volume, comme les méthodes de Rosenbrock pour les équations algébriques différentielles (Hairer and Wanner, 1996; Hundsdorfer and Verwer, 2003). En effet, les termes sources de relaxation dépendent non seulement de la fraction volumique mais aussi de ses dérivées spatiales. Par conséquent, une procédure originale de relaxation implicite-explicite est proposée pour étendre la méthode habituelle de Newton-Raphson. Cela nécessite de résoudre l'équation de Laplace en fonction d'un temps fictif au moyen d'une intégration explicite des termes sources avec les dérivées spatiales. Cette approche permet de préserver la faible complexité de la procédure par rapport à une procédure de relaxation qui couple implicitement chaque cellule avec sa voisine. Nous proposons dans la section 4.2 un schéma numérique dédié au modèle à petite échelle avec des gouttelettes oscillantes. Ce modèle est traité séparément pour résoudre le problème de réalisabilité associé aux quantités géométriques, c'est-à-dire la possibilité

de reconstruire une distribution représentée par les moments liés aux quantités géométriques obtenues par GeoMOM. Un schéma cinétique spécifique est choisi pour préserver les propriétés de réalisabilité grâce à la solution exacte de l'équation cinétique associée à la dynamique des inclusions polydisperses.

Dans le chapitre 5, nous validons la mise en œuvre des méthodes de discrétisation et certaines propriétés de base du modèle. Ces cas de test résultent tous de contributions personnelles de l'auteur au solveur open-source `Josiepy`[2]. Ce chapitre examine chaque sous-modèle séparément avant de les intégrer tous ensemble dans une simulation complète à deux échelles au chapitre 6. Dans la section 5.1, nous commençons par évaluer le taux de convergence de l'extension MUSCL du deuxième ordre des schémas de Godunov pour les solutions lisses. Des cas d'essai d'advection de matière et de propagation du son sont mis en place pour la partie convective des modèles à deux échelles. La simulation de la propagation du son permet de vérifier que la relaxation instantanée du modèle à une vitesse/deux pressions résout le modèle à une vitesse/une pression et que la fraction de volume à petite échelle modifie la vitesse de propagation du son. L'étude des problèmes de Riemann est proposée dans la section 5.2 pour valider que le schéma de volumes finis et les solveurs de Riemann mis en œuvre résolvent effectivement les solutions exactes correspondantes. Nous poursuivons dans la section 5.3 en illustrant l'effet des flux de capillarité et de l'équation de Laplace locale sur le cas d'une goutte statique initialisée hors du saut de pression de Laplace global correct. La simulation de ce cas-test s'avère difficile car la courbure moyenne de la forme du cercle d'équilibre est complexe à calculer avec précision sur un maillage cartésien. Enfin, la section 5.4 évalue la dynamique appropriée pour un spray de gouttelettes oscillantes sans mouvement global, y compris d'éventuels termes de source externe.

Au chapitre 6, nous proposons des études numériques qui illustrent le potentiel du modèle à deux échelles avec régularisation et du modèle à petite échelle de gouttelettes oscillantes dans un contexte physique. Dans la section 6.1, nous considérons tout d'abord une colonne de liquide compressible déformée par un écoulement gazeux compressible impactant. Cette configuration a été choisie parce qu'elle développe des filaments de chaque côté de la colonne, de sorte qu'une dynamique d'interface multi-échelle de base apparaît. Il nous permet ensuite de démontrer l'efficacité du processus de régularisation de l'interface à grande échelle. De plus, nous indiquons comment la paramétrisation des termes sources permet de modéliser l'évolution de la géométrie de l'interface, en particulier la densité d'aire interfaciale, au fur et à mesure que le transfert se produit. Une comparaison est proposée avec une simulation plus fidèle provenant d'une autre implémentation du cas-test. Plus précisément, nous estimons les paramètres des termes sources qui doivent être choisis pour obtenir les mêmes caractéristiques géométriques. Cela illustre le potentiel de modélisation de la transition de régime dans le cadre de l'approche unifiée à deux échelles. Nous proposons enfin, dans la section 6.2, des simulations unidimensionnelles d'un jet de gouttelettes oscillantes agitées par un terme source externe imitant l'effet de la traînée de vitesse sur les oscillations. Bien que ce test puisse être considéré comme élémentaire, il nous montre la richesse de la description contenue dans le modèle, en particulier en ce qui concerne la dynamique des quantités géométriques.

Le manuscrit se termine par quelques conclusions, des perspectives et la synthèse travaux en cours vers la modélisation des modèles unifiés à deux échelles plus riches. La préparation de cette thèse a également donné lieu à des communications scientifiques, des collaborations et des contributions qui sont énumérées dans la section suivante.

[2] https://github.com/hpc-maths/josiepy

Scientific outreach

Research context and scientific partnership

This PhD thesis has been conducted in the CMAP laboratory at Ecole polytechnique (Palaiseau, France) under the joint supervision of Samuel Kokh (CEA Saclay), Marc Massot (CMAP) and Teddy Pichard (CMAP), and has been funded both by the French Department of Higher Education and Research and the French Department of Defence (Defence Innovation Agency). This PhD thesis is part of a long-term research effort on the modelling of liquid-gas two-phase flows, notably with the PhD thesis of :

- Drui, Florence. « Eulerian modeling and simulations of separated and disperse two-phase flows: development of a unified modeling approach and associated numerical methods for highly parallel computations ». Université Paris-Saclay, 2017. tel-01618320v1.
- Essadki, Mohamed. « Contribution à la modélisation eulérienne unifiée de l'injection: de la zone dense au spray polydispersé ». Université Paris-Saclay, 2018. tel-01928584v1.
- Cordesse, Pierre. « Contribution to the study of combustion instabilities in cryotechnic rocket engines: coupling diffuse interface models with kinetic-based moment methods for primary atomization simulations ». Université Paris-Saclay, 2020. tel-02948195v1.
- Di Battista, Ruben. « Towards a unified eulerian modeling framework for two-phase flow: geometrical subscale phenomena and associated highly-scalable numerical methods ». Institut Polytechnique de Paris, 2021. tel-03496405v1.

The scientific research team on the modelling topics extends to Giuseppe Orlando (visiting PhD candidate of the MOX laboratory, Polimi and post-doctoral student at CMAP), Katia Ait-Ameur (post-doctoral student at CMAP) and Ward Haegeman (PhD candidate at CMAP and ONERA). Finally, a software development support has been provided by Ruben Di Battista (PhD candidate at CMAP) who started the development of `Josiepy` and the research engineers of the HPC@Maths team at CMAP, namely Loïc Gouarin and Pierre Matalon. High fidelity simulations have also been provided by Thibaut Menard (CORIA laboratory) with the code `ARCHER` and by Nicolas Grenier (research engineer at CMAP and Paris-Saclay University) for comparison purposes.

Scientific contributions and communications

Scientific contributions

This work has lead to several contributions and communications which are gathered below and recalled in the introductions of the appropriated chapters in the manuscript.

Accepted

- Loison, Arthur, Kokh, Samuel, Pichard, Teddy, and Massot, Marc. "A unified two-scale gas-liquid multi-fluid model with capillarity and interface regularization through a mass transfer between scales ". International Journal of Multiphase Flow, 2024. https://doi.org/10.1016/j.ijmultiphaseflow.2024.104857.

Submitted

- Loison, Arthur, Kokh, Samuel, Pichard, Teddy, and Massot, Marc. " Two-scale modelling of two-phase flows based on the Stationary Action Principle and a Geometric Method Of Moments". arXiv, 2023. https://doi.org/10.48550/arXiv.2308.15641.

In preparation

- Orlando, Giuseppe, Loison, Arthur, Barbante, Paolo Francesco, et Massot, Marc. "Derivation of a dynamic relation for the interfacial area density in two-phase flows through the Stationary Action Principle", *In preparation.*
- Loison, Arthur, Kokh, Samuel, Pichard, Teddy, and Massot, Marc. "Derivation of a disperse two-velocity model accounting for added-mass through the Stationary Action Principle", *In preparation.*
- Ait-Ameur, Katia, Loison, Arthur, Pichard, Teddy, and Massot, Marc. "Simulation of polydisperse oscillating droplets with kinetic schemes for geometric moment equations", *In preparation.*

Communications

Oral communications

The following communications are listed in chronological order :

- "Two-phase separated and disperse flow : towards a two-scale diffuse interface models with geometrical variables" – Workshop "Modèles et méthodes pour les équations cinétiques" – 20/10/2021 – Bordeaux, France – https://www.math.u-bordeaux.fr/~sbrull/etudiant.html
- "Two-phase separated and disperse flow : towards a two-scale diffuse interface models with geometrical variables" – Biennale SMAI 2021 – 21/06/2021 – La-Grande-Motte, France – https://smai2021.math.univ-toulouse.fr/
- "Two-scale dynamic polydisperse reduced order model for two-phase flows" – Fourth Workshop on Compressible Multiphase Flows – 30/05/2022 – Strasbourg, France – https://indico.math.cnrs.fr/event/7728/
- "Two-phase flow reduced-order model with polydisperse oscillating droplets" – ECCOMAS CONGRESS 2022 – 05/06/2022 – Oslo, Norway – http://eccomas2022.org
- "Modélisation d'écoulements diphasiques à l'aide d'une approche deux-échelles et d'un modèle réduit de gouttes oscillantes polydispersées" – CANUM 2020/2022 – 16/06/2022 – Evian-les-bains, France – https://canum2020.math.cnrs.fr
- "Kinetic-based two-phase flow models: a reduced-order model of polydisperse oscillating droplets with geometrical variables" – RGD 2022 – 08/07/2022 – Seoul, South Korea – http://www.rgd32.org
- "Two-phase flow reduced-order model: A two-scale model of polydisperse oscillating droplets" – ICNMMF-4 – 28/09/2022 – Venice, Italy – https://sites.psu.edu/icnmmf4/
- "Kinetic-based two-phase flow model: a reduced-order model of polydisperse oscillating droplets with geometrical variables" – CSE23 – 02/03/2023 – Amsterdam, Netherlands – https://www.siam.org/conferences/cm/conference/cse23

- "Small-scale modelling of interface dynamics in two-phase flows: a kinetic approach based on a geometric method of moments" – University of Kyoto (Thermal Science and Engineering Laboratory) – 31/03/2023 – Kyoto, Japan
- "A two-scale two-phase flow model with capillarity - subscale reduced-order model using a geometric method of moments" – ICMF 2023 – 05/04/2023 – Kobe, Japan – http://www.jsmf.gr.jp/icmf2022
- "Simulation of polydisperse oscillating droplets through high order numerical methods for geometric moment equations" (presented by Katia Ait-Ameur)– ICMF 2023 – 05/04/2023 – Kobe, Japan – http://www.jsmf.gr.jp/icmf2022
- "Two-scale model for two-phase flows with capillarity and scale transfer" – JAXA – 10/04/2023 – Tokyo, Japan

Posters

- "Two-phase flow reduced-order model : A two-scale model with polydisperse oscillating droplets" – Seminar CEA SMAI/GAMNI "La mécanique des fluides numérique" – 24/01/2022 – Paris, France – http://www.cmap.polytechnique.fr/~allaire/gamni/semihp22.html
- "Two-phase flow reduced-order model : A two-scale model with polydisperse oscillating droplets" – Journée CIEDS – 18/05/2022 – Palaiseau, France
- "Modélisation d'écoulements diphasique multi-échelles" – Operation CIEDS – 29/06/2023 – Palaiseau, France – https://www.ip-paris.fr/actualites/operation-cieds-2023-une-journee-sur-la-defense-et-la-securite

Notations and list of abbreviations

In this manuscript, the vectors and matrices are denoted in bold.

The partial derivative of a function f with respect to x is denoted with $\partial_x f$. The partial derivative with respect to a vector $\boldsymbol{v}$ is sometimes denoted with the operator $\boldsymbol{\nabla}_{\boldsymbol{v}}$. If such operator is not indexed, it is a partial derivation with respect to the Eulerian coordinates $\boldsymbol{x}$. Given a velocity fields $\boldsymbol{u}$, we denote the material derivative $D_t(\cdot) := \partial_t(\cdot) + \boldsymbol{u} \cdot \boldsymbol{\nabla}(\cdot)$.

Furthermore, for clarity purposes, some operation on vectors and matrices are sometimes written with the summation convention on repeated indexes.

We notably underline that the divergence of a matrix $\mathbf{A}$ is a vector denoted $\boldsymbol{\nabla} \cdot \mathbf{A}$ which here evaluates to $\boldsymbol{\nabla} \cdot \mathbf{A} = (\partial_{x_j} A_{ij})$ with the summation on repeated indexes. The double scalar product of two matrices $\boldsymbol{A}$ and $\boldsymbol{B}$ is $\boldsymbol{A} : \boldsymbol{B} = A_{ij} B_{ij}$. The gradient of a vector $\boldsymbol{a}$ is $\boldsymbol{\nabla a} = \partial_{x_j} a_i$.

List of abbreviations

CFL	Courant-Friedrichs-Lewy
CSF/CSS	Continuum Surface Force/Stress
DIM	Diffuse Interface Model
DNS	Direct Numerical Simulation
DSDF	Discrete Surface Density Function
EEC	Entropy Extension Criterion
EOS	Equation Of State
FV	Finite-Volume
GeoMOM	Geometric Method of Moments
IAD	Interface Area Density
ImEx	Implicit-Explicit
LES	Large-Eddy Simulation
NDF	Number Density Function
ODE	Ordinary Differential Equation
PBE	Population Balance Equation
PDE	Partial Differential Equations
SAP	Stationary Action Principle
SDF	Surface Density Function
TAB	Taylor Analogy Breakup

Part I

Modelling

CHAPTER 1

Multi-fluid modelling

The resolution of the two-phase models by solving the fluid equations on each side of the interface have showed inherent bottlenecks in the context of multiscale interface dynamics as previously discussed in the introduction of this manuscript. Therefore, we propose now to focus on the multi-fluid class of models as they appear as a possible answer to the complexity of the interface dynamics. Furthermore, these models often takes the form of a system of conservation laws which can be analysed following the theory of Lax (1957). Instead of directly solving some single-fluid, local and instantaneous equations, *e.g.* Navier-Stokes, for each fluid on each side of a moving boundary (the interface), multi-fluid models typically assume a particular regime of the interface, separated or disperse, and respectively describe at a same location an artificial mixture of the two-phases or inclusions of one fluid into the other. We respectively denote these two classes of models as *multi-fluid diffuse interface models* and *multi-fluid disperse models*.

The multi-fluid DIM can result from an averaging process as proposed by Drew (1983). Such averaging is performed on a single set of the local instantaneous equations thanks to the introduction of an indicator function locating each fluid. Then, the interface is located through the volume fraction defined as the average of this indicator function. This averaging process then provides a diffuse interface model made of a set of partial differential equations for artificial two-phase fluid particles where the two fluid phases coexist even though they are not miscible. Such an approach naturally discards the challenging interface dynamics, which is now accessed through the volume fraction field. However, this approach also comes with its own challenges. First, the averaging procedure produces unclosed averaged terms, classically the *interface velocity and pressure*, which gathers in a concise formulation the complexity of the interaction between the two fluids across the interface (Saurel and Abgrall, 1999). The closure of these terms is mostly sought such that the model is hyperbolic with coherent jump relation, notably in the case of a non-conservative form of the system (Coquel et al., 2002). Second, there is no sound and generic thermodynamic theory to help us to choose the right closures in the equations on energy as the thermodynamic processes between the phases depend on the structure of the interface separating the fluids. Third, the transition from a flow regime to another is not clear as the diffuse interface model spreads the interface over a distance below which the interface dynamics in not accessible.

The multi-fluid disperse models offer a different perspective as the two-phase mixture is not artificial anymore, but consists in a collection of inclusions of one fluid carried by another fluid. Then, instead of describing the fine details of the flow around the inclusions, *i.e.* the *small-scale* dynamics, only the dynamics of the volume fraction occupied by the inclusions is followed in time. Typical setups involve solid particles/incompressible droplets (Marble, 1963; Baer and Nunziato, 1986; Saurel et al., 2017) or compressible bubbles (Bedford and Drumheller, 1978; Biesheuvel and Wijngaarden, 1984; Gavrilyuk and Saurel, 2002; Drui et al., 2019). More complex models, where more quantities than just the volume fraction are used to represent the collection of droplets, are the subject of Chapter 2. Another challenge associated with this second class of models is the hyperbolicity of the two-velocity models which requires considering ad-hoc interaction terms, either pressure (Raviart and Sainsaulieu, 1995) or energy (Gavrilyuk, 2020).

If not considering a particular separated or disperse regime, there is no all-regime multi-fluid models in the literature, and only the coupling of models in different region of the flows are possible (Le Touze, 2015). A key modelling contribution towards the derivation of such all-regime model is later proposed in Chapter 3.

The purpose of this first chapter is to offer an overview of multi-fluid modelling techniques of the literature and motivate the upcoming extensive use of a variational method, the Hamilton's SAP, by assessing its flexibility with the derivation of two-phase models for different regimes. The overview of the main multi-fluid model derivation techniques is provided in Section 1.1 along with a presentation of some theoretical properties of such systems. Then, a specific focus is set in Section 1.2 on Hamilton's Stationary Action Principle (SAP) approach, a variational derivation strategy based on the knowledge of the energies of the flow. We illustrate the advantage of this technique through the detailed derivation of the Euler equations along with the methodology to add dissipative source terms consistently with the second principle of thermodynamics. Then, we propose the derivation of multi-fluid models with Hamilton's SAP for separated regime in Section 1.3 and the disperse regime in Section 1.4. While classic models of the literature are derived in the separated regime, a new modelling approach based on added-mass is proposed for the derivation of a hyperbolic multi-fluid disperse model and a contribution associated with this model is currently under preparation:

- Loison, Arthur, Teddy Pichard, Samuel Kokh, and Marc Massot. "Derivation of a disperse two-velocity model accounting for added-mass through the Stationary Action Principle", *In preparation.*

1.1 Overview of multi-fluid modelling approaches

The derivation of multi-fluid models can be achieved in several ways, and we propose here to detail the *averaging approach* and the *Landau approach* as they have led to numerous multi-fluid models of the literature.

The averaging approach relies on the definition of an averaging operator, over space, time or different realizations of a statistical process. The single-fluid models such as Euler or Navier-Stokes equations are averaged to provide the multi-fluid models. These latter models involve complex averaged terms, which require to be expressed using the averaged state to obtain a closed model. The Landau approach directly assumes a set of state variables, and the equations of evolutions are obtained by enforcing Galilean invariance and thermodynamic principles.

All these approaches lead to multi-fluid models involving conservation laws, sometimes supplementary non-conservative terms. Then, we propose to recall some mathematical properties associated with such systems in Section 1.1.1. We expect some of them to be satisfied for the obtention of physically relevant multi-fluid models, and they will guide us for the closure of averaged models presented in Section 1.1.2 and the models derived with the Landau approach in Section 1.1.3.

1.1.1 Systems of conservation laws

In this section, we provide some definitions, properties and theorems associated with the study of systems of conservation laws. Let us write a system of p conservation laws in dimension d. Given a vector-valued function $\boldsymbol{q} \in \Omega \subset \mathbb{R}^p$ from the space-time domain $\mathbb{R}^d \times (0, +\infty)$ to Ω, smooth flux functions $\boldsymbol{F}$ from Ω to $\mathbb{R}^p$, and source terms $\boldsymbol{S}$ from Ω to $\mathbb{R}^p$, the system of conservation laws reads

$$\partial_t \boldsymbol{q} + \boldsymbol{\nabla} \cdot (\boldsymbol{F}(\boldsymbol{q})) = \boldsymbol{S}(\boldsymbol{q}), \tag{1.1}$$

which locally translates the integral balance of advected quantities within an arbitrary control volume.

1.1.1.1 The theory of Lax

Let us first recall fundamental elements of the Lax's theory (Lax, 1957) which focuses on systems of conservation laws of the form

$$\partial_t \boldsymbol{q} + \sum_{j=1,\dots,d} \partial_{x_j}(\boldsymbol{F}_j(\boldsymbol{q})) = \boldsymbol{0}, \tag{1.2}$$

where we decomposed the flux in each direction $\boldsymbol{F} = (\boldsymbol{F}_1, \dots, \boldsymbol{F}_d)$. Note that we only provide here the key properties that we will use for the further modelling work proposed in this manuscript. For a more comprehensive presentation of the systems of conservation, we refer the reader to Godlewski and Raviart (1991); Smoller (1994); Dafermos (2005). First, a system of conservation laws is said *hyperbolic* if it satisfies Property 1 *i.e.* the eigenvalues of the Jacobian of the flux functions has p real eigenvalues and p linearly independent eigenvectors. If all the eigenvalues are distinct, the system is said to be *strictly hyperbolic*. Such property is critical as it has been showed to be a necessary condition for the well-posedness of the system of conservation laws (Métivier, 2005).

Property 1 (Hyperbolicity)

Consider the system of conservation laws (1.2). For each direction $j = 1, ..., d$, we define the Jacobian of the fluxes $\boldsymbol{F} = (F_{ij})_{1\leq i\leq p, 1\leq j\leq d}$ by

$$\boldsymbol{A}_j = \left(\frac{\partial F_{ij}}{\partial q_k}\right)$$

The system is called hyperbolic if, for any direction $\boldsymbol{\omega} \in \mathbb{S}^{d-1}$, the matrix

$$\boldsymbol{A} = \sum_{j=1,...,d} \omega_j \boldsymbol{A}_j,$$

has p real eigenvalues $\lambda_1 \leq ... \leq \lambda_p$ and p linearly independent eigenvectors $\boldsymbol{r}_1 \leq ... \leq \boldsymbol{r}_p$ such that for $k = 1, ..., p$,

$$\boldsymbol{A}\boldsymbol{r}_k = \lambda_k \boldsymbol{r}_k.$$

Remark that the study of hyperbolicity of system (1.1) does not depend on the source terms and that only one arbitrarily chosen direction can be considered as the divergence operator is rotational invariant. In the following, the hyperbolicity of the system of conservation laws is always assumed.

We are now interested in the solution of the Cauchy problem associated with (1.2). It is well known that even for smooth initial datum, the solution can develop discontinuities in finite time and that one should define a notion of weak solution for system (1.2), as recalled in Definition 1.

Definition 1 (Weak solution)

Consider a Cauchy problem of system (1.2) with initial datum $\boldsymbol{q}_0 \in L^\infty_{loc}(\mathbb{R}^d)^p$. Denote $C^\infty_c(\mathbb{R}^d \times (0, +\infty))^p$ the ensemble of smooth functions with compact support. A function $\boldsymbol{q} \in L^\infty_{loc}(\mathbb{R}^d \times [0, +\infty))^p$ is called a weak solution of the Cauchy problem if $\boldsymbol{q}(\boldsymbol{x}, t) \in \Omega$ almost everywhere and, for any test-function $\boldsymbol{\phi} \in C^\infty_c(\mathbb{R}^d \times (0, +\infty))^p$, $\boldsymbol{q}$ satisfies

$$\int_0^\infty \int_{\mathbb{R}^d} [\boldsymbol{q} \cdot \partial_t \boldsymbol{\phi} + (\boldsymbol{F}(\boldsymbol{q}) \cdot \boldsymbol{\nabla})\boldsymbol{\phi}]\, d\boldsymbol{x}\, dt + \int_{\mathbb{R}^d} \boldsymbol{q}_0 \cdot \boldsymbol{\phi} d\boldsymbol{x} = 0.$$

Now considering a C^1-piecewise weak solution of (1.2) separated by discontinuity, one can show that for each surface of discontinuities, the weak solution satisfies the Rankine-Hugoniot jump conditions given in Theorem 1.

Theorem 1 (Rankine-Hugoniot jump conditions)

Given $\boldsymbol{q}$ a C^1-piecewise weak solution of (1.2), then :

- $\boldsymbol{q}$ is a classic solution of (1.2) where $\boldsymbol{q}$ is C^1;
- for each time-space surface discontinuity, at every location along the surface oriented by its local normal $\boldsymbol{n} = (n_t, \boldsymbol{n_x})$, and denoting $\boldsymbol{q}^-$ and $\boldsymbol{q}^+$ the solution on each side, we have

$$(\boldsymbol{q}^+ - \boldsymbol{q}^-)n_t + (\boldsymbol{F}(\boldsymbol{q}^+) - \boldsymbol{F}(\boldsymbol{q}^-)) \cdot \boldsymbol{n_x} = \boldsymbol{0}.$$

Remark that, in the one-dimensional case, the Rankine-Hugoniot jump involves the velocity of the discontinuity s with $(\boldsymbol{q}^+ - \boldsymbol{q}^-)s = (\boldsymbol{F}(\boldsymbol{q}^+) - \boldsymbol{F}(\boldsymbol{q}^-))$. It is also well known that the system of conservation laws (1.2) can admit several weak solutions. In the scalar case *i.e.* $p = 1$, uniqueness is recovered in Theorem 2 by introducing the notion of mathematical entropy in Definition 2 and entropy solution in Definition 3.

<table>
<tr><th></th><th>$d = 1$</th><th></th><th>$d \geq 2$</th></tr>
<tr><td>$p = 1$</td><td colspan="3">$q_0 \in L^\infty_{loc}(\mathbb{R}^d)$
Existence, uniqueness</td></tr>
<tr><td>$p = 2$</td><td>$\boldsymbol{q}_0 \in L^\infty_{loc}(\mathbb{R}^d)^2$ +
geometric assumption
Existence</td><td>$TV(\boldsymbol{q}_0) \ll 1$</td><td rowspan="2">Terra incognita</td></tr>
<tr><td>$p \geq 3$</td><td colspan="2">Existence
Uniqueness</td></tr>
</table>

Table 1.1: Existence and uniqueness results for Cauchy problems of conservation laws reproduced from Serre (2001). See the references therein for the proofs of these results.

Definition 2 (Mathematical entropy)

A convex function $\mathcal{H} : \Omega \to \mathbb{R}$ is called a mathematical entropy of system (1.2) if there exists function $\boldsymbol{\mathcal{G}_j}$ such that for $j = 1, ..., d$,

$$(\partial_{\boldsymbol{q}} \mathcal{H}) \boldsymbol{A}_j = \partial_{\boldsymbol{q}} \mathcal{G}_j.$$

Definition 3 (Entropy solutions)

A weak solution $\boldsymbol{q}$ is called an entropy solution if it satisfies

$$\partial_t \mathcal{H} + \sum_{j=1,...,d} \partial_{x_j} \mathcal{G}_j \leq 0,$$

for every mathematical entropy $\mathcal{H}$ of (1.2).

Theorem 2 (Uniqueness of the entropy solution in the scalar case)

If $p = 1$, and $\boldsymbol{q}_0 \in L^\infty_{loc}(\mathbb{R}^d)^p$ the entropy solution q, in the sense of distribution, of the strictly hyperbolic system

$$\partial_t q + \partial_x F(q) = 0, \quad q(t = 0) = \boldsymbol{q}_0,$$

is unique.

The proof of this theorem can be found in Kruzhkov (1969). For general cases $p \geq 1$, the existence and uniqueness of the entropy solution is not proven. We reproduce below in Table 1.1 a summarized list of results regarding the existence and uniqueness of the Cauchy Problem associated with the conservation equation (1.1). As a consequence of this lack of results for the existence and uniqueness for general systems of conservation laws, we identify two requirements for the following modelling work: the hyperbolicity of the system and the existence of a mathematical entropy $\mathcal{H}$ and fluxes $\mathcal{G}_j$ such that

$$\partial_t \mathcal{H} + \sum_{j=1,...,d} \partial_{x_j} \mathcal{G}_j \leq 0. \tag{1.3}$$

For systems of conservation laws, providing a mathematical entropy is *a priori* neither trivial nor guaranteed, but for some physical systems, it is linked to the physical notion of entropy.

1.1.1.2 Non-conservative terms

In many models, some non-conservative terms are present in the following form

$$\partial_t \boldsymbol{q} + \boldsymbol{\nabla} \cdot \boldsymbol{F}(\boldsymbol{q}) + \boldsymbol{B}(\boldsymbol{q}) \cdot \boldsymbol{\nabla} \boldsymbol{q} = \boldsymbol{0}. \tag{1.4}$$

The first question lies in the proper definition of the weak solutions in the presence of the non-conservative product. One approach was given by Dal Maso's theory (Dal Maso et al., 1995; Parés, 2006; Castro et al., 2008) by introducing path-integral in the Rankine-Hugoniot jump conditions. However, the associated path-conservative schemes are difficult to implement successfully (Abgrall and Karni, 2010) as some numerical schemes do not systematically recover the exact solution for the Euler model. Another approach can be found in Raviart and Sainsaulieu (1995); Wargnier et al. (2020), where the jump relations are obtained by connecting the states through travelling waves with vanishing diffusion terms. Finally, following the works in Seguin (2002); Gallouët et al. (2004); Guillemaud (2007a) some systems see their non-conservative products well-defined as both quantities involved in the product are not simultaneously discontinuous such that Rankine-Hugoniot jump conditions are well-defined too.

Other works are related to the study of first-order non-conservative term such as Forestier and Gavrilyuk (2011) where a hyperbolic criterion is given for system admitting a supplementary conservation law, or Cordesse and Massot (2020) where criteria for finding a supplementary conservation equation are given.

As modelling requirements when dealing with non-conservative systems, we will focus on the eigen-structure study and the existence of an entropy evolution equation. The issue of giving a proper definition for the non-conservative products is not of prime interest in this work, and will be discussed on a case-by-case basis In order to avoid such issues, most of our model relies on simplified barotropic Equation of States (EOS) under either isentropic or isothermal assumptions and a single velocity for both phases.

1.1.1.3 Relaxation source terms

Some models derived in this work are endowed with dissipative processes that act through source terms of the following form

$$\partial_t \boldsymbol{q} + \boldsymbol{\nabla} \cdot (\boldsymbol{F}(\boldsymbol{q})) = \frac{\boldsymbol{R}(\boldsymbol{q})}{\epsilon}. \tag{1.5}$$

Such source terms are called *relaxation* source terms as they tend to drive the state $\boldsymbol{q}$ relax towards an equilibrium manifold defined by $\boldsymbol{R}(\boldsymbol{q}) = \boldsymbol{0}$. The smaller ϵ is, the stiffer the dynamics. Formally, we can consider that in the *instantaneous relaxation* limit where $\epsilon \to 0$, one obtain the equilibrium models

$$\begin{cases} \partial_t \boldsymbol{q}^* + \boldsymbol{\nabla} \cdot (\boldsymbol{F}^*(\boldsymbol{q}^*)) = \boldsymbol{0}, \\ \boldsymbol{R}(\boldsymbol{q}^*) = \boldsymbol{0}. \end{cases} \tag{1.6}$$

A theoretical framework for such models is provided in Chen et al. (1994); Bouchut (2004) for pairs of systems of the form (1.5) of dimension p and (1.6) of dimension q linked by a linear operator *i.e.* a matrix $\boldsymbol{L} : \mathbb{R}^p \to \mathbb{R}^q$ such that

$$\boldsymbol{L}\boldsymbol{R}(\boldsymbol{q}) = \boldsymbol{0}, \qquad \boldsymbol{q}^* = \boldsymbol{L}\boldsymbol{q}. \tag{1.7}$$

It is further assumed that, for all $\boldsymbol{q}^*$, one can define a unique equilibrium $\widetilde{\boldsymbol{L}}(\boldsymbol{q}^*)$ such that $\boldsymbol{R}(\widetilde{\boldsymbol{L}}(\boldsymbol{q}^*)) = 0$. It follows that the fluxes of (1.5) and (1.6) are related with $\boldsymbol{F}^*(\boldsymbol{q}^*) = \boldsymbol{L}\boldsymbol{F}(\widetilde{\boldsymbol{L}}(\boldsymbol{q}^*))$.

Then, in order to study the behaviour of the relaxing system (1.5) in the limit $\epsilon \to 0$, Chen et al. (1994) provided an *Entropy Extension Criterion* (see Definition 4) summarized in Bouchut (2004) which, when verified, shows that the relaxing system formally converges to the relaxed system with a first-order diffusion term.

Definition 4 (Entropy Extension Criterion (EEC))

There exists a convex mathematical entropy $\mathcal{H}$ for the relaxing system (1.5) such that $\mathcal{H} \circ \widetilde{\boldsymbol{L}}$ is a convex mathematical entropy for the relaxed system (1.6).
Moreover, the minimization principle holds, *i.e.*

$$\mathcal{H}(\widetilde{\boldsymbol{L}}(\boldsymbol{q}^*)) \leq \mathcal{H}(\boldsymbol{q}), \qquad \text{when} \quad \boldsymbol{L}\boldsymbol{q} = \boldsymbol{q}^*,$$

and the relaxation source term is dissipative

$$\boldsymbol{\nabla}(\mathcal{H}(\boldsymbol{q})) \cdot \boldsymbol{R}(\boldsymbol{q}) \leq 0.$$

Therefore, such EEC should be verified in further models when there are relaxing terms fitting this theoretical framework.

1.1.2 Averaging methods

We start the overview of the derivation technique with the averaging approach. Such approach is obtained through the averaging of single-fluid models coupled across an interface. We propose here to recover classic models of the literature starting from the works of Ishii and Hibiki (1975); Drew (1983).

1.1.2.1 Local instant formulation of fluid equations

Consider two fluid phases indexed by $k \in \{1, 2\}$, the continuity, momentum and energy equations read

$$\begin{cases} \partial_t \rho_k & + \boldsymbol{\nabla} \cdot (\rho_k \boldsymbol{u}_k) & = 0, \\ \partial_t (\rho_k \boldsymbol{u}_k) & + \boldsymbol{\nabla} \cdot (\rho_k \boldsymbol{u}_k \otimes \boldsymbol{u}_k + p_k \mathbf{I}) & = \boldsymbol{\nabla} \cdot \boldsymbol{D}_k + \boldsymbol{f}_k, \\ \partial_t (\rho_k E_k) & + \boldsymbol{\nabla} \cdot ((\rho_k E_k + p_k) \boldsymbol{u}_k) & = \boldsymbol{\nabla} \cdot (\boldsymbol{D}_k \cdot \boldsymbol{u}_k - \boldsymbol{q}_k) + \boldsymbol{f}_k \cdot \boldsymbol{u}_k + r_k, \end{cases} \tag{1.8}$$

with, for each fluid k, ρ_k the density, $\boldsymbol{u}_k$ the velocity, p_k the pressure, $\boldsymbol{D}_k$ the viscous tensor, $\boldsymbol{f}_k$ the body forces per unit of volume, $E_k = \frac{1}{2}\boldsymbol{u}_k^2 + e_k$ the total energy per unit of mass, e_k the internal energy per unit of mass, $\boldsymbol{q}_k$ the heat flux and r_k an energy source term per unit of volume.

These fluids are separated by a surface $\mathcal{S}$, and the equations (1.8) are supplemented with the following jump conditions across the interface

$$\begin{gathered} \sum_{k=1,2} (\rho_k (\boldsymbol{u}_k - \boldsymbol{u}_I)) \cdot \boldsymbol{n}_k = 0, \qquad \sum_{k=1,2} (\rho_k \boldsymbol{u}_k \otimes (\boldsymbol{u}_k - \boldsymbol{u}_I) + p_k \mathbf{I} - \mathbf{D}_k) \cdot \boldsymbol{n}_k = \sigma H \boldsymbol{n}, \\ \sum_{k=1,2} \left(\rho_k E_k (\boldsymbol{u}_k - \boldsymbol{u}_I) + (p_k \mathbf{I} - \mathbf{D}_k) \cdot \boldsymbol{u}_k + \boldsymbol{q}_k\right) \cdot \boldsymbol{n}_k = \sigma H \boldsymbol{n} \cdot \boldsymbol{u}_I, \end{gathered} \tag{1.9}$$

where $\boldsymbol{n}_k$ is the normal of the interface oriented from phase k to k', $\boldsymbol{u}_I$ is the local velocity of the interface, H is the local mean curvature and $\boldsymbol{n}$ the normal of the interface. These two latter quantities are not indexed by any phase as we choose the convention of defining them respectively with a positive sign for a locally convex surface from the liquid point of view and oriented from liquid to gaseous phase.

Example 1

With such convention, a static non-viscous liquid droplet of radius R at equilibrium $\boldsymbol{u}_k = \boldsymbol{u}_I = \mathbf{0}$ satisfies the following Laplace pressure jump with a positive mean curvature $H = 2/R$

$$p_1 - p_2 = \sigma H,$$

with 1 indexing the liquid phase and 2 the gaseous phase. This shows that the pressure within the droplet is superior to the surrounding gaseous pressure.

The set of equations (1.8) and (1.9) completed with constitutive laws and EOS for each phase is the starting point for DNS methods discussed in the introduction.

1.1.2.2 Averaging process

Before averaging the equations (1.8), we cast them in a single set of equation by introducing the characteristic function

$$X_k(\boldsymbol{x}, t) = \begin{cases} 0 & \text{if } \boldsymbol{x} \text{ is in phase } k \text{ at time } t, \\ 1 & \text{else,} \end{cases} \tag{1.10}$$

and its kinematics is given on the compact support of the interface surface through the *topological* equation

$$\partial_t X_k + \boldsymbol{u}_I \cdot \boldsymbol{\nabla} X_k = 0, \tag{1.11}$$

in the sense of generalized function. Then one can introduce an averaging process $\langle \cdot \rangle$ which can be either a time, a space or ensemble average depending on the desired nature of equations and available experimental data to close some averaged terms. For instance, space averaging can be useful over a cross area for a two-phase flow within a tube (Ransom and Hicks, 1984), while a volume average for disperse flow will help to capture the averaged behaviour of a collection of inclusions. However, time or ensemble averaging are the most common interpretations of such averaging process (Ishii and Hibiki, 1975).

Let us then define the volume fraction α_k as

$$\alpha_k := \langle X_k \rangle . \tag{1.12}$$

It corresponds to the average of presence probability of phase k. Remark also that in the separated regime, the transition of α_k from 0 to 1 provides an estimate of the "most probable location" of the interface. In the disperse regime, the volume fraction indicates the average volume occupation of the inclusions, but the interface location is assumed to be embedded within the carrier phase at a scale much below the averaging scale.

Regardless of this distinction, the equations (1.8) are multiplied by X_k then averaged with the operator $\langle \cdot \rangle$. Neglecting second-order fluctuations, we obtain

$$\begin{cases} \partial_t \left(\alpha_k \bar{\rho}_k\right) & + \boldsymbol{\nabla} \cdot \left(\alpha_k \bar{\rho}_k \widetilde{\boldsymbol{u}}_k\right) & = \Gamma_k, \\ \partial_t \left(\alpha_k \bar{\rho}_k \widetilde{\boldsymbol{u}}_k\right) & + \boldsymbol{\nabla} \cdot \left[\alpha_k \bar{\rho}_k \widetilde{\boldsymbol{u}}_k \otimes \widetilde{\boldsymbol{u}}_k + \alpha_k \left(\widetilde{p}_k \boldsymbol{I} - \widetilde{\mathbf{T}}_k\right)\right] & = \boldsymbol{M}_k, \\ \partial_t \left(\alpha_k \bar{\rho}_k \widetilde{E}_k\right) & + \boldsymbol{\nabla} \cdot \left[\alpha_k \left(\bar{\rho}_k \widetilde{E}_k + \widetilde{p}_k - \widetilde{\mathbf{T}}_k\right) \widetilde{\boldsymbol{u}}_k\right] & = P_{\mathrm{I},k}, \end{cases} \tag{1.13}$$

where the phase average and the mass-weighted average of a variable φ are defined by

$$\bar{\varphi} = \frac{\langle X_k \varphi \rangle}{\alpha_k}, \quad \tilde{\varphi} = \frac{\langle X_k \rho_k \varphi \rangle}{\alpha_k \bar{\rho}_k}, \tag{1.14}$$

where $\boldsymbol{T}_k := -p_k \mathbf{I} + \boldsymbol{D}_k$ is the stress tensor. The quantities $\Gamma_k, \boldsymbol{M}_k$ and $P_{I,k}$ are the interfacial source terms defined by

$$\begin{gathered} \Gamma_k = \langle \rho_k \left(\boldsymbol{u}_k - \boldsymbol{u}_I\right) \cdot \boldsymbol{\nabla} X_k \rangle , \qquad \boldsymbol{M}_k = \langle \rho_k \left(\boldsymbol{u}_k - \boldsymbol{u}_I\right) \otimes \boldsymbol{u}_k \cdot \boldsymbol{\nabla} X_k \rangle + \langle p_k \boldsymbol{\nabla} X_k \rangle - \langle \mathbf{D}_k \cdot \boldsymbol{\nabla} X_k \rangle , \\ P_{\mathrm{I},k} = \langle \rho_k E_k \left(\boldsymbol{u}_k - \boldsymbol{u}_I\right) \cdot \boldsymbol{\nabla} X_k \rangle + \langle p_k \boldsymbol{u}_k \cdot \boldsymbol{\nabla} X_k \rangle - \langle \mathbf{D}_k \boldsymbol{u}_k \cdot \boldsymbol{\nabla} X_k \rangle , \end{gathered} \tag{1.15}$$

with the jump conditions

$$\sum_{k=1,2} \Gamma_k = 0, \qquad \sum_{k=1,2} \boldsymbol{M}_k = \langle \sigma H \boldsymbol{\nabla} X_1 \rangle , \qquad \sum_{k=1,2} P_{\mathrm{I},k} = \langle \sigma H \boldsymbol{u}_I \cdot \boldsymbol{\nabla} X_1 \rangle . \tag{1.16}$$

The averaged equations then boil down to a set of conservation laws with unclosed interface source terms. These source terms are naturally split into mass transfer terms, pressure forces and viscous forces at the interface. Remark that all these terms involve averages of $\boldsymbol{\nabla} X_k = -\boldsymbol{n}_k \delta_I$, following the notations of Morel (2015), which supports and orientates the interface source terms. Therefore, the presence of either the interface velocity $\boldsymbol{u}_I$ or the weak gradient of the indicator function $\boldsymbol{\nabla} X_k$ in all the unclosed terms shows that the geometry of the interface encompassed by the averaging scale has a critical influence on the closure of those terms.

1.1.2.3 Definition of interfacial terms

Following the works of Drew (1983); Saurel and Abgrall (1999), one can further simplify equations (1.13) by defining interface velocities $\boldsymbol{u}_{I,k}$, pressures $p_{I,k}$ and energies, $E_{I,k}$ such that

$$\boldsymbol{u}_{I,k} := \frac{\langle \rho_k (\boldsymbol{u}_k - \boldsymbol{u}_I) \otimes \boldsymbol{u}_k \cdot \boldsymbol{\nabla} X_k \rangle}{\Gamma_k}, \quad p_{I,k} := \frac{\langle p_k \boldsymbol{\nabla} X_k \rangle \cdot \boldsymbol{\nabla} \alpha_k}{\| \boldsymbol{\nabla} \alpha_k \|^2}, \quad E_{I,k} := \frac{\langle \rho_k E_k (\boldsymbol{u}_k - \boldsymbol{u}_I) \cdot \boldsymbol{\nabla} X_k \rangle}{\Gamma_k}. \tag{1.17}$$

Moreover, as suggest in Perrier and Gutiérrez (2021), the term $\langle p_k \boldsymbol{u}_k \cdot \boldsymbol{\nabla} X_k \rangle$ should not necessarily be closed with $p_{I,k}$ and $\boldsymbol{u}_{I,k}$. Thus, we propose to define

$$(p\boldsymbol{u})_{I,k} := \frac{\langle p_k \boldsymbol{u}_k \cdot \boldsymbol{\nabla} X_k \rangle \boldsymbol{\nabla} \alpha_k}{\| \boldsymbol{\nabla} \alpha_k \|^2}, \tag{1.18}$$

such that the averaged set of equations (1.13) becomes

$$\begin{cases} \partial_t (\alpha_k \bar{\rho}_k) & + \boldsymbol{\nabla} \cdot (\alpha_k \bar{\rho}_k \widetilde{\boldsymbol{u}}_k) & = \Gamma_k, \\ \partial_t (\alpha_k \bar{\rho}_k \widetilde{\boldsymbol{u}}_k) & + \boldsymbol{\nabla} \cdot \left[\alpha_k \bar{\rho}_k \widetilde{\boldsymbol{u}}_k \otimes \widetilde{\boldsymbol{u}}_k + \alpha_k \left(\widetilde{p}_k \boldsymbol{I} - \widetilde{\mathbf{T}}_k \right) \right] & = \boldsymbol{u}_{I,k} \Gamma_k + p_{I,k} \boldsymbol{\nabla} \alpha_k + \boldsymbol{F}_k, \\ \partial_t \left(\alpha_k \bar{\rho}_k \widetilde{E}_k \right) & + \boldsymbol{\nabla} \cdot \left[\alpha_k \left(\bar{\rho}_k \widetilde{E}_k + \widetilde{p}_k - \widetilde{\mathbf{T}}_k \right) \widetilde{\boldsymbol{u}}_k \right] & = E_{I,k} \Gamma_k + (p\boldsymbol{u})_{I,k} \boldsymbol{\nabla} \alpha_k + P'_k, \end{cases} \tag{1.19}$$

with

$$\boldsymbol{F}_k = \left\langle (p_k - p_{I,k}) \boldsymbol{\nabla} X_k \right\rangle - \langle \mathbf{D}_k \cdot \boldsymbol{\nabla} X_k \rangle , \quad P'_k = - \langle \mathbf{D}_k \boldsymbol{u}_k \cdot \boldsymbol{\nabla} X_k \rangle . \tag{1.20}$$

The final modelling step now consists in closing the interface terms and providing an evolution equation for the volume fraction. In the model of Saurel and Abgrall (1999), the proposed closure is

$$p_{I,k} = p_I = \sum_{k=1,2} \alpha_k \tilde{p}_k, \qquad \boldsymbol{u}_{I,k} = \boldsymbol{u}_I = \sum_{k=1,2} \frac{\alpha_k \bar{\rho}_k \widetilde{\boldsymbol{u}}_k}{\alpha_k \bar{\rho}_k}, \qquad (p_k \boldsymbol{u}_k)_I = p_I \boldsymbol{u}_I, \qquad \boldsymbol{F}_k = \lambda (\widetilde{\boldsymbol{u}}_{k'} - \widetilde{\boldsymbol{u}}_k), \qquad P'_k = \boldsymbol{u}_I \cdot \boldsymbol{F}_k, \tag{1.21}$$

and, for the volume fraction,

$$\partial_t \alpha_k + \boldsymbol{u}_I \cdot \boldsymbol{\nabla} \alpha_k = 0. \tag{1.22}$$

From now on, we drop the notations attached to averaged quantities for clarity purposes (tildes and bars). The closure of $E_{I,k}$ is not provided under the further assumption of no mass transfer *i.e.* $\Gamma_k = 0$. Given the rotational invariance of the system, hyperbolicity is studied in an arbitrary direction $\boldsymbol{\omega}$. Except for a finite set of resonance conditions (Andrianov, 2003), the system is showed to be hyperbolic with the following eigenvalues

$$\boldsymbol{u}_I \cdot \boldsymbol{\omega} \quad \boldsymbol{u}_1 \cdot \boldsymbol{\omega}, \quad \boldsymbol{u}_1 \cdot \boldsymbol{\omega} \pm c_1, \quad \boldsymbol{u}_2 \cdot \boldsymbol{\omega}, \quad \boldsymbol{u}_2 \cdot \boldsymbol{\omega} \pm c_2, \tag{1.23}$$

where $c_k = ((\partial_{p_k} e_k)^{-1} (\rho_k^{-2} p_k - \partial_{\rho_k} e_k))^{1/2}$ is the sound velocity of phase k, and the eigenvalues $\boldsymbol{u}_k \cdot \boldsymbol{\omega}$ have a multiplicity of 3. Another closure was later proposed in Saurel et al. (2003) by considering the limit of discretized equations involving the solution of a linearized Riemann problem at the interfaces. For each direction, here along the x-axis,

$$p_I = \frac{Z_1 p_2 + Z_2 p_1}{Z_1 + Z_2} + \mathrm{sign}\,(\partial_x \alpha_1) \frac{(u_2 - u_1) Z_1 Z_2}{Z_1 + Z_2}, \quad u_I = \frac{Z_1 u_1 + Z_2 u_2}{Z_1 + Z_2} + \mathrm{sign}\,(\partial_x \alpha_1) \frac{p_2 - p_1}{Z_1 + Z_2}, \quad (pu)_I = p_I u_I. \tag{1.24}$$

Other closures are proposed in the work of Perrier and Gutiérrez (2021), based on a separation of length-scales in the averaging process, and take advantage of the interfacial term $(p_k \boldsymbol{u}_k)_I$. For instance, following similar ideas as Saurel et al. (2003), the averaging of the solution of a Riemann problem between two Euler systems in the acoustic approximation is considered, and the following closure is obtained

$$p_{I,k} = p_I = \frac{Z_{k'}\tilde{p}_k + Z_k\tilde{p}_{k'}}{Z_k + Z_{k'}}, \quad \boldsymbol{u}_{I,k} = \boldsymbol{u}_I = \frac{Z_k\boldsymbol{u}_k + Z_{k'}\boldsymbol{u}_{k'}}{Z_k + Z_{k'}}, \quad (p_k\boldsymbol{u}_k)_I = p_{I,k}\boldsymbol{u}_{I,k} + \frac{Z_k Z_{k'}(\tilde{p}_{k'} - \tilde{p}_k)(\boldsymbol{u}_{k'} - \boldsymbol{u}_k)}{(Z_k + Z_{k'})^2}, \tag{1.25}$$

and, for the volume fraction,

$$\partial_t \alpha_k + \boldsymbol{u}_I \cdot \boldsymbol{\nabla}\alpha_k = R_k, \tag{1.26}$$

where $Z_k = \bar{\rho}_k c_k$, and $\boldsymbol{F}_k$, P'_k and R_k are relaxation terms which are not detailed here. The system is showed to be hyperbolic with the same eigenvalues as listed in (1.23) with the use of the new closure for the definition of $\boldsymbol{u}_I$.

Beyond these examples, other closure relations have been found such that it yields both a hyperbolic system and associate the interface velocity with a discontinuity wave which translates the physical material advection of the interface location Coquel et al. (2002); Hérard and Mathis (2019); Jomée (2023).

1.1.2.4 Evolution of averaged geometry

Remark that the closures proposed for the averaging models in (1.21) or (1.25) are symmetric. Such closure assumes a role symmetry in the model regardless of the interface geometry. However, such an approach seems limited if one considers capillarity forces or mass transfer between the two-phases. Indeed, capillarity is related to the local mean curvature while mass transfer is known to be proportional to the area of the interface, and the process is expected to be faster in a disperse regime than in the separated regime. Then, the general closure problem for equations (1.13) strongly depends on the underlying geometry of the interface. Consequently, any additional knowledge about the interface geometry could help to find better closures for the averaged set of equations.

Averaging of geometric characteristics of the interface has been proposed in Drew (1990) or Lhuillier (2004) with, for instance, the interface area density Σ. While Drew proposed to investigate geometric scalars such as curvatures, Lhuillier introduced a tensorial point of view with the anisotropic tensor $\boldsymbol{q}_{ani}$ (Lhuillier, 2003). We propose to briefly present here the work of Lhuillier, while the results of Drew are detailed in Chapter 2 where geometric variables are introduced more carefully. Given the generalized function δ_I locating the interface and the interface orientation tensor $\boldsymbol{Q} = \langle \boldsymbol{n} \otimes \boldsymbol{n}\delta_I \rangle$, the IAD and the anisotropic tensor are defined by

$$\Sigma = \langle \delta_I \rangle, \qquad \boldsymbol{q}_{ani} = \left\langle \left(\boldsymbol{n} \otimes \boldsymbol{n} - \tfrac{1}{3}\boldsymbol{I}\right)\delta_I \right\rangle. \tag{1.27}$$

The kinematics of such quantities is obtained thanks to the topological equation (1.11) (Drew, 1990; Morel, 2015). First, the kinematics of δ_I and $\boldsymbol{n}$ read

$$\begin{cases} \partial_t \delta_I + \boldsymbol{\nabla}\cdot(\delta_I(\boldsymbol{u}_I\cdot\boldsymbol{n})\boldsymbol{n}) = \delta_I(\boldsymbol{u}_I\cdot\boldsymbol{n})\boldsymbol{\nabla}\cdot\boldsymbol{n}, \\ \partial_t \boldsymbol{n} + (\boldsymbol{u}_I\cdot\boldsymbol{\nabla})\boldsymbol{n} = -(\boldsymbol{I} - \boldsymbol{n}\otimes\boldsymbol{n})\cdot(\boldsymbol{n}\boldsymbol{\nabla}\boldsymbol{u}_I). \end{cases} \tag{1.28}$$

From the kinematics of δ_I and $\boldsymbol{n}$, the evolution of the orientation tensor is deduced, and the IAD is then obtained in Lhuillier (2003, 2004) from the relation $\Sigma = Tr(\boldsymbol{Q})$

$$\partial_t \Sigma + \boldsymbol{\nabla}\cdot\langle \boldsymbol{u}_I\delta_I\rangle = \left\langle \boldsymbol{q}_{ani} : \boldsymbol{\nabla}\boldsymbol{u}_I \right\rangle. \tag{1.29}$$

Remark that in the case of a model with a deterministic single velocity *i.e.* $\langle \boldsymbol{u}_I\rangle = \langle \boldsymbol{u}\rangle = vel$, the isotropic part can be extracted to provide

$$\partial_t \Sigma + \boldsymbol{\nabla}\cdot(\Sigma\boldsymbol{u}) = \frac{2}{3}\boldsymbol{\nabla}\cdot\boldsymbol{u} - \left\langle \left(\boldsymbol{q}_{ani} - \frac{1}{3}\boldsymbol{I}\right) : \boldsymbol{\nabla}\boldsymbol{u} \right\rangle. \tag{1.30}$$

Moreover, for a general probabilistic interface velocity $\boldsymbol{u}_I$, we can denote the scalar velocity $\tilde{\boldsymbol{u}}_{I,k} = \langle \boldsymbol{u}_I\cdot\boldsymbol{n}\delta_I\rangle / \Sigma$ such that the averaging of the topological equation gives the following kinematics for the volume fraction,

$$\partial_t \alpha_k = \tilde{\boldsymbol{u}}_{I,k}\Sigma. \tag{1.31}$$

In the end, the equations (1.29) and (1.31) push the averaging modelling a step further by introducing two unclosed equations on geometric quantities α_k and Σ. Augmenting the state vector of averaged variables with these two quantities allows the introduction of geometric information into the model. For instance, in the dilute disperse regime *i.e.* a collection of inclusions with a small volume fraction, a closure of $\langle \boldsymbol{u}_I \delta_I \rangle$ and $\left\langle \boldsymbol{q}_{ani} : \boldsymbol{\nabla} \boldsymbol{u}_I \right\rangle$ is proposed in Lhuillier (2004), partly through dimensional considerations. A general closure for such terms is not known by the author and seems out of reach for any flow regime. Nevertheless, an additional averaging step is proposed in Lhuillier (2003) where an unclosed equation is proposed for $\boldsymbol{q}_{ani}$, but such modelling strategies lead to many unclosed terms which are difficult to close without any *a priori* knowledge on the interface dynamics.

Let us conclude this overview on averaging process by underlining that many closures of these models exist and are not listed here. The closure of the averaged terms is mainly motivated by the obtained mathematical structure, such as hyperbolicity and the nature of the wave structure of the linearized model, rather than geometric considerations. Nevertheless, the averaging models provide insights to suggest adequate multi-fluid models depending on the interface flow regime.

1.1.3 Landau derivation approach

The *Landau* derivation approach is introduced in Khalatnikov (1965); Landau and Lifshitz (1986) (see English translations in Landau and Lifshitz (1987); Khalatnikov (1989)) for the derivation of superfluid models. It assumes balance equation with Galilean invariance along with a Gibbs thermodynamic identity.

This approach has notably been used for the derivation of the two-phase flow model of Baer and Nunziato (1986) describing gas-particle flows where conservation equations for mass, momentum and specific internal energies are assumed for each phase following Truesdell (1969). Consider first a Galilean invariant form of the system of fluid equations

$$\begin{cases} \partial_t(\alpha_k\rho_k) \quad + \boldsymbol{u}_k \cdot \boldsymbol{\nabla}(\alpha_k\rho_k) \quad = -\alpha_k\rho_k \boldsymbol{\nabla}\cdot\boldsymbol{u}_k + \Gamma_k, \\ \partial_t(\alpha_k\rho_k\boldsymbol{u}_k) + \boldsymbol{u}_k \cdot \boldsymbol{\nabla}(\alpha_k\rho_k\boldsymbol{u}_k) = -\boldsymbol{\nabla}\cdot\boldsymbol{T}_k + \alpha_k\rho_k\boldsymbol{f}_k + \boldsymbol{M}_k - \Gamma_k\boldsymbol{u}_k, \\ \partial_t(\alpha_k\rho_k e_k) + \boldsymbol{u}_k \cdot \boldsymbol{\nabla}(\alpha_k\rho_k e_k) = -\boldsymbol{T_k} : \boldsymbol{\nabla}\boldsymbol{u}_k - \boldsymbol{\nabla}\cdot\boldsymbol{q}_k + \alpha_k\rho_k r_k + P_k, \end{cases} \tag{1.32}$$

where $\boldsymbol{T}_k$ is the surface stress tensor, $\boldsymbol{f}_k$ the external body forces, $\boldsymbol{q}_k$ the heat conduction flux, r_k the external energy source terms and Γ_k, $\boldsymbol{M}_k$, P_k the mass, momentum and energy transfer source terms. Then, Gibbs thermodynamic relations are assumed for both phases and dissipative relaxation processes are added to the model preserving a second principle for the mixture where the mixture's entropy is the mass-weighted sum of the specific entropies of both phases. The resulting model is unclosed and the dynamics of the volume fraction needs to be specified so that it is compatible with the second principle. The final model reads

$$\begin{cases} \partial_t\alpha_2 \quad\quad + \boldsymbol{u}_2 \cdot \boldsymbol{\nabla}\alpha_2 \quad\quad = (p_2-\beta_2)\frac{\alpha_1\alpha_2}{\mu}(p_2-\beta_2-p_1) + \frac{\Gamma}{\rho_2}, \\ \partial_t(\alpha_k\rho_k) + \boldsymbol{\nabla}\cdot(\alpha_k\rho_k\boldsymbol{u}_k) = (-1)^k\Gamma, \\ \partial_t(\alpha_k\rho_k\boldsymbol{u}_k) + \boldsymbol{\nabla}\cdot[\alpha_k\rho_k\boldsymbol{u}_k\otimes\boldsymbol{u}_k + \alpha_k p_k] \quad = p_1\boldsymbol{\nabla}\alpha_k - \lambda(\boldsymbol{u}_k-\boldsymbol{u}_{k'}) + \Gamma(\boldsymbol{u}_k-\boldsymbol{u}_{k'}), \\ \partial_t(\alpha_k\rho_k E_k) + \boldsymbol{\nabla}\cdot\left[\alpha_k(\rho_k E_k + p_k)\boldsymbol{u}_k + \boldsymbol{q}_k\right] = p_1(\boldsymbol{u}_k-\boldsymbol{u}_{k'})\cdot\boldsymbol{\nabla}\alpha_k - (-1)^k\lambda(\boldsymbol{u}_k-\boldsymbol{u}_{k'})^2 + (-1)^k h(T_k-T_{k'}) \\ \qquad\qquad -(-1)^k(p_2-\beta_2)\frac{\alpha_1\alpha_2}{\mu}(p_2-\beta_2-p_1) - (-1)^k\Gamma(E_k-E_{k'}), \end{cases} \tag{1.33}$$

where quantities with index 1 relate to the gas and 2 with particles, T_k is the temperatures of phase k, β_2 is the contact pressure for particles, λ is a drag coefficient, h is a heat transfer coefficient, and μ_c is a compaction viscosity. It is also showed to be hyperbolic in any direction $\boldsymbol{\omega}$ with the following eigenvalues

$$\boldsymbol{u}_1\cdot\boldsymbol{\omega}, \quad \boldsymbol{u}_1\cdot\boldsymbol{\omega}\pm c_1, \quad \boldsymbol{u}_2\cdot\boldsymbol{\omega}, \quad \boldsymbol{u}_2\cdot\boldsymbol{\omega}\pm c_2, \tag{1.34}$$

with $\boldsymbol{u}_1\cdot\boldsymbol{\omega}$ of multiplicity 3 and $\boldsymbol{u}_2$ of multiplicity 4.

This model is well-known among two-phase flow models, and is also known as *seven-equation model* as it allows to describe a two-phase flow in full disequilibrium with relaxation source terms for: 1-mass transfer through the definition of Γ, 2-velocities with a drag force, 3-pressures with the compaction dynamics of viscosity μ, 4-temperature with heat transfer of coefficient h.

Other models have also been considered by taking the limit of these relaxation processes in the Baer-Nunziato model. For instance, the pressure and velocity equilibrium are assumed for the five-equation model (Kapila et al., 2001; Murrone and Guillard, 2005; Petitpas et al., 2007; Saurel et al., 2008). A six-equation model has also been proposed in Saurel et al. (2009) to build a numerical method to solve the five-equation model. Moreover, a compatibility exist with the seven-equation model obtained in Saurel and Abgrall (1999) via the averaging approach by selecting the closure

$$p_I = p_1, \qquad \boldsymbol{u}_I = \boldsymbol{u}_2. \tag{1.35}$$

This asymmetric closure for the averaging equations particularly suggest that the Baer-Nunziato model is more adapted to a specific gas-solid flow regime. Nevertheless, with specific closures, such a seven-equation model has also been used to model liquid-vapour flows Guillemaud (2007a,b).

Conclusion of Section 1.1

Let us conclude this overview by underlining some advantages of the averaging process, and consequently the Landau approach thanks to Saurel and Abgrall (1999) :

- A simple averaging process from the local instantaneous equation;
- A single set of fluid equations on averaged variables;
- Clear definitions of the unclosed averaged terms which bring insight on the interaction between the fluids and the interface dynamics;
- A set of equations on the geometric quantities associated with the interface;

However, we can observe that the dynamics of the flow is rarely coupled with the quantities describing interface geometry despite their intimately related dynamics. This observation can be explained by some drawbacks of the averaging strategy :

- The averaged terms that appear in the equations for fluid dynamics can be grouped in a non-unique way and their general closure seems out of reach for any flow;
- The choice of geometric quantities is non-unique and the most common ones (volume fraction, IAD, q_{ani}) are insufficient to tackle complex interface regime;
- The usual strategy for the closing of the averaged terms mostly relies on the mathematical structure of the resulting set of equations rather than experimental closures or physical knowledge of the underlying mechanisms.

Therefore, we propose now to focus on another model derivation strategy, the Hamilton's Stationary Action Principle, which offers another perspective where both the energies related to the two-phase mechanisms and the quantities of interest must be identified *a priori*. Such methodology addresses simpler flow regimes but provides a closed dynamical system.

1.2 Hamilton's Stationary Action Principle

We propose here to introduce the derivation methodology of the Hamilton's SAP through discrete mechanics and the Euler-Lagrange equations for discrete systems in Section 1.2.1. The extension to continuum mechanics is proposed in Section 1.2.2 with essential calculations and notations used throughout this manuscript for the derivation of each model. Finally, the addition of dissipation source terms is discussed in Section 1.2.3 through the relation between physical and mathematical entropies.

1.2.1 Euler-Lagrange equations for mechanics of point particles

We propose to introduce Hamilton's SAP by first recovering the equations of classic mechanics dealing with the motion of a set of punctual particles as a first step towards continuum mechanics. More particularly, we present here the derivation of the Euler-Lagrange equations. For a comprehensive introduction to variational mechanics, the reader is referred to Bourguignon (2007).

Consider a set of particles indexed by $i \in \mathcal{I}$. For a particle i denote its mass m_i, its position at time t $\boldsymbol{X}_i(t)$ and its velocity $\dot{\boldsymbol{X}}_i(t)$. When no explicit time dependency is retained, the Lagrangian $\mathcal{L}$ of the system is defined as the difference between the kinetic and potential energy $W(\boldsymbol{X}_i)$

$$\mathcal{L}(\boldsymbol{X}_i, \dot{\boldsymbol{X}}_i) = \sum_{i\in\mathcal{I}} \frac{1}{2} m_i \dot{\boldsymbol{X}}_i^2 - W((\boldsymbol{X}_i)_{i\in\mathcal{I}}). \tag{1.36}$$

The associated action $\mathcal{A}$ is defined as the time integral over $\Omega = (t_1, t_2)$,

$$\mathcal{A} = \int_\Omega \mathcal{L}(\boldsymbol{X}, \boldsymbol{X}_i, \dot{\boldsymbol{X}}_i)\, dt. \tag{1.37}$$

Then, Hamilton's SAP states that the motion of particles minimizes the action. Therefore, we introduce families of perturbed trajectories to provide a functional space over which the action is minimized. We introduce the families of trajectory variations $\widetilde{\boldsymbol{X}}_i(t, \epsilon)$ smoothly depending on ϵ a small-parameter in the vicinity of 0. This family satisfies two conditions:

- The family defines a perturbation of the minimizing trajectory, *i.e.* for all $i \in \mathcal{I}$ and $t \in (t_1, t_2)$

$$\widetilde{\boldsymbol{X}}_i(t, 0) = \boldsymbol{X}_i(t). \tag{1.38}$$

- The families do not introduce perturbation on the boundaries, *i.e.* for all $i \in \mathcal{I}$ and ϵ

$$\widetilde{\boldsymbol{X}}_i(t_1, \epsilon) = \boldsymbol{X}_i(t_1), \qquad \widetilde{\boldsymbol{X}}_i(t_2, \epsilon) = \boldsymbol{X}_i(t_2), \tag{1.39}$$

Then, we introduce the variational operator

$$\delta(\cdot) = \partial_\epsilon \widetilde{(\cdot)}|_{\epsilon=0}. \tag{1.40}$$

Then, Hamilton's SAP states that the motion of particles minimizes the action for any variation $\delta\boldsymbol{X}_i$ *i.e.*

$$\delta\mathcal{A} = 0. \tag{1.41}$$

As the boundaries are independent of time, we can develop the variation of the action as

$$\delta\mathcal{A} = \int_\Omega \sum_{i\in\mathcal{I}} \left((\partial_{\boldsymbol{X}_i}\mathcal{L})\delta\boldsymbol{X}_i + (\partial_{\dot{\boldsymbol{X}}_i}\mathcal{L})\delta\dot{\boldsymbol{X}}_i \right). \tag{1.42}$$

Then integrating by part leads to

$$\delta\mathcal{A} = \int_\Omega \sum_{i\in\mathcal{I}} \left(\partial_{\boldsymbol{X}_i}\mathcal{L} - d_t(\partial_{\dot{\boldsymbol{X}}_i}\mathcal{L}) \right) \delta\boldsymbol{X}_i. \tag{1.43}$$

Then, as the Hamilton's SAP gives $\delta\mathcal{A} = 0$ for any set of variations $\delta\boldsymbol{X}_i$, we have for all $i \in \mathcal{I}$, the set of Euler-Lagrange equations

$$\partial_{\boldsymbol{X}_i}\mathcal{L} - d_t(\partial_{\dot{\boldsymbol{X}}_i}\mathcal{L}) = 0. \tag{1.44}$$

Evaluating the derivatives of the Lagrangian with (1.36) gives Newton's fundamental principle of dynamics for each particle $i \in \mathcal{I}$ undergoing conservative forces of potential W,

$$m_i\ddot{\boldsymbol{X}}_i = -\partial_{\boldsymbol{X}_i}W. \tag{1.45}$$

Remark that the Lagrangian is non-unique for a system as one could have obtained the same dynamics by considering $\mathcal{L}' = \mathcal{L} + d_t F(\boldsymbol{X}_i, t)$. Moreover, we have not discussed here the cases where the Lagrangian explicitly depends on time or how boundary – here initial – conditions can be enforced with this formalism.

1.2.2 Application to single-phase fluid mechanics

Hamilton's SAP for continuum mechanics has been introduced with Herivel (1955) and the derivation of the Euler equations, and it can also be found in Serrin (1959) From the perspective of Hamilton's SAP, the main differences between continuum mechanics and the mechanics of point particles are: 1-the existence of a smooth path-function $\boldsymbol{\phi}$ which associates for any position $\boldsymbol{X}$ of a reference space domain Ω a position $\boldsymbol{x}$ in the transformed space domain $\Omega(t)$ at time t, 2-the mass conservation of the fluid particle, 3-the choice between the Eulerian and Lagrangian coordinates.

We define the path-function as a space-time function $\boldsymbol{\phi} : \Omega \times \mathbb{R}^+$ smooth in time and for any $t > 0$

$$\boldsymbol{\phi}(\cdot, t) := \begin{cases} \Omega \to \Omega(t), \\ \boldsymbol{X} \mapsto \boldsymbol{x} = \boldsymbol{\phi}(\boldsymbol{X}, t). \end{cases} \tag{1.46}$$

This path-function $\boldsymbol{\phi}$ also admits a reciprocal with respect to its first variable

$$\boldsymbol{\phi}^{-1}(\cdot, t) := \begin{cases} \Omega(t) \to \Omega, \\ \boldsymbol{x} \mapsto \boldsymbol{X} = \boldsymbol{\phi}^{-1}(\boldsymbol{x}, t). \end{cases} \tag{1.47}$$

We call Lagrangian coordinates the coordinates $\boldsymbol{X}$ of the reference space Ω and Eulerian coordinates at time t the coordinates of the space Ω. The first system follows the position $\boldsymbol{x}$ of a unique fluid particle given its initial position $\boldsymbol{X}$, while the second gives the initial position $\boldsymbol{\phi}^{-1}(\boldsymbol{x}, t)$ of a particle located at $\boldsymbol{x}$ and instant t. For a given fluid property, we note $b^L(\boldsymbol{X}, t)$ its Lagrangian field and $b(\boldsymbol{x}, t)$ its Eulerian field which are related for all $(\boldsymbol{X}, t)$ by

$$b^L(\boldsymbol{X}, t) = b(\boldsymbol{\phi}(\boldsymbol{X}, t)). \tag{1.48}$$

This Eulerian coordinates system is particularly convenient when the space domain under consideration is constant, with inflow and outflow conditions if needed, as there is no need to follow fluid particles and their paths with time. Only an in-and-out balance of fluid properties is locally accounted in a geometric volume.

Finally, the Lagrangian velocity field of the fluid is defined in Lagrangian coordinates as

$$\boldsymbol{u}^L(\boldsymbol{X}, t) = d_t\boldsymbol{\phi}(\boldsymbol{X}, t), \tag{1.49}$$

and the time derivative of a Lagrangian field defines a material derivative for the Eulerian field

$$\partial_t b^L(\boldsymbol{X}, t) = \partial_t b + \boldsymbol{\nabla} b \cdot d_t\boldsymbol{\phi} = \partial_t b + \boldsymbol{u} \cdot \boldsymbol{\nabla} b =: D_t b. \tag{1.50}$$

1.2.2.1 Definition of a family of perturbation for Eulerian fields

Despite both Eulerian and Lagrangian coordinates allows the derivation of the equations of fluid, given the Eulerian nature of some constraints further investigated, the Eulerian coordinates are chosen. Nevertheless, due to the Lagrangian coordinates are used to define the perturbation of the path-function and the variations of the Eulerian fields in order to apply Hamilton's SAP.

Let us emphasize that we will further make a special difference between the perturbations associated with the path-function $\boldsymbol{\phi}$, the velocity $\boldsymbol{u}$, the advected Eulerian fields b_a satisfying

$$\partial_t b_a + \boldsymbol{u} \cdot \boldsymbol{\nabla} b_a = 0, \tag{1.51}$$

describe constant quantities for a given fluid particle, and conserved Eulerian fields b_c satisfying

$$\partial_t b_c + \boldsymbol{\nabla} \cdot (b_c \boldsymbol{u}) = 0, \tag{1.52}$$

which corresponds to the conservation in time of mass-related extensive quantities.

First, let us introduce the family of perturbed trajectories $\widetilde{\boldsymbol{\phi}}(\boldsymbol{X}, t, \epsilon)$, indexed by ϵ, that maps the position $\boldsymbol{X}$ in a referential domain $\Omega = \Omega(0)$ to the Eulerian position $\boldsymbol{x}$ in $\Omega(t)$ at time $t \in (t_1, t_2)$. ϵ is a small parameter in a vicinity of 0. We similarly introduce families of perturbed Lagrangian fields $\widetilde{b}^L(\boldsymbol{X}, t, \epsilon)$ and Eulerian fields $\widetilde{b}(\widetilde{\boldsymbol{\phi}}(\boldsymbol{X}, t, \epsilon), t, \epsilon)$ such that for any ϵ,

$$\widetilde{b}^L(\boldsymbol{X}, t, \epsilon) = \widetilde{b}(\widetilde{\boldsymbol{\phi}}(\boldsymbol{X}, t, \epsilon), t, \epsilon). \tag{1.53}$$

We assume that these families of Lagrangian mappings and Eulerian fields satisfy the following properties:

- The mapping $\boldsymbol{\phi}$ and Eulerian fields b of the solution are included in the families for $\epsilon = 0$ *i.e.* for all $\boldsymbol{X} \in \Omega(0)$ and $(\boldsymbol{x}, t) \in \Omega$,
$$\begin{cases} \widetilde{\boldsymbol{\phi}}(\boldsymbol{X}, t, \epsilon = 0) = \boldsymbol{\phi}(\boldsymbol{X}, t), \\ \widetilde{b}(\boldsymbol{x}, t, \epsilon = 0) = b(\boldsymbol{x}, t). \end{cases} \tag{1.54}$$
- All the mappings and Eulerian fields preserve the constraints. Denote the conserved Eulerian field b_c, and the advected Eulerian fields b_a, then for all $(\boldsymbol{x}, t) \in \Omega$,
$$\begin{cases} \partial_t \widetilde{b}_c + \boldsymbol{\nabla} \cdot (\widetilde{b}_c \boldsymbol{u}) = 0, \\ \partial_t \widetilde{b}_a + \boldsymbol{u} \cdot \boldsymbol{\nabla} \widetilde{b}_a = 0. \end{cases} \tag{1.55}$$
- All the mappings and families of Eulerian fields b preserve the values at the boundaries of the space-time domain *i.e.* for all $(\boldsymbol{x}, t) \in \partial\Omega$,
$$\widetilde{b}(\boldsymbol{x}, t, \epsilon) = b(\boldsymbol{x}, t). \tag{1.56}$$

1.2.2.2 Eulerian variations

Then, we use the same variational operator as in (1.40)

$$\delta(\cdot) = \partial_\epsilon \widetilde{(\cdot)}|_{\epsilon=0}. \tag{1.57}$$

Then, we introduce is the infinitesimal Eulerian displacement in Eulerian coordinates,

$$\boldsymbol{\eta}(\boldsymbol{x}, t) := \delta \boldsymbol{x} = \left(\partial_\epsilon \widetilde{\boldsymbol{\phi}}\right)_{\boldsymbol{X}, t} ((\boldsymbol{\phi})^{-1}(\boldsymbol{x}, t), t, \epsilon = 0), \tag{1.58}$$

and the variation of Eulerian fields b

$$\delta b(\boldsymbol{x}, t) := \left(\partial_\epsilon \widetilde{b}\right)_{\boldsymbol{x}, t} (\boldsymbol{x}, t, \epsilon = 0). \tag{1.59}$$

Remark now that the velocity field $\boldsymbol{u}$, the advected fields b_a and the conserved fields b_c are linked to the variations of the trajectories through either their definitions or constraints. Two approaches are then possible to include this link into the minimization of the action either by adding the constraints within the Lagrangian energy with Lagrangian multipliers or by expressing the variation of the fields with the infinitesimal Eulerian displacement $\boldsymbol{\eta}$. One can find the first approach in Herivel (1955); Eckart (1960); Lin (1963); Gouin and Debieve (1986); Berdichevsky (2009) and the second in Serrin (1959); Berdichevsky (2009); Gavrilyuk (2011). Note that, in the first approach, the constraints mainly deal with: 1-for compressible fluids, enforcing conservation as all advected can be expressed as conserved quantities if multiplied by a conserved quantity, 2-for incompressible fluids, enforcing a divergence-free flow (Eckart,

1960; Berdichevsky, 2009), 3-enforcing the advection of particle labels to express the velocity field's dependency on the trajectories (Lin, 1963; Gouin and Debieve, 1986).

We propose here to pursue the second approach and derive, in Eulerian coordinates, the expression of the variation of the velocity field $\boldsymbol{u}$, a conserved variable b_c and an advected variable b_a. These computations can also be found in Gavrilyuk (2011).

1.2.2.2.a Variation of an Eulerian field

Let us remark first that the variation of an Eulerian field f is related to its associated Lagrangian field f^L by applying the variational operator on (1.53)

$$\delta b^L = \delta b + \boldsymbol{\nabla} b \cdot \boldsymbol{\eta}. \tag{1.60}$$

1.2.2.2.b Variation of the velocity field

From the definition of the Lagrangian velocity field $\boldsymbol{u}^L$ in Eulerian coordinates

$$\delta \boldsymbol{u}^L = D_t \boldsymbol{\eta}, \qquad \delta \boldsymbol{u}^L = \delta \boldsymbol{u} + \boldsymbol{\nabla}_{\boldsymbol{x}} \boldsymbol{u} \cdot \boldsymbol{\eta}. \tag{1.61}$$

Combining these two relations gives

$$\delta \boldsymbol{u} = \partial_t \boldsymbol{\eta} + \boldsymbol{u} \cdot \boldsymbol{\nabla} \boldsymbol{\eta} - (\boldsymbol{\eta} \cdot \boldsymbol{\nabla}) \boldsymbol{u}. \tag{1.62}$$

1.2.2.2.c Variation of a conserved field

The conservation of a Lagrangian field can be expressed by

$$b_c^L(\boldsymbol{X}, t) \det(\boldsymbol{F}(\boldsymbol{X}, t)) = b_c^L(\boldsymbol{X}, 0), \qquad \boldsymbol{F}(\boldsymbol{X}, t) = \frac{\partial \boldsymbol{\phi}}{\partial \boldsymbol{X}}. \tag{1.63}$$

Applying the variational operator δ then leads to

$$\delta b_c^L = -(\det \boldsymbol{F})^{-1} (b_c^L \delta \det \boldsymbol{F}). \tag{1.64}$$

From Jacobi's formula, we have that

$$\delta \det \boldsymbol{F} = (\det \boldsymbol{F}) Tr(\boldsymbol{F}^{-1} \delta \boldsymbol{F}) = (\det \boldsymbol{F}) \boldsymbol{\nabla} \cdot \boldsymbol{\eta}. \tag{1.65}$$

Combining these two relations gives

$$\delta b_c^L = -b_c^L \boldsymbol{\nabla} \cdot \boldsymbol{\eta}, \qquad \delta b_c = -\boldsymbol{\nabla} \cdot (b_c \boldsymbol{\eta}). \tag{1.66}$$

1.2.2.2.d Variation of an advected field

The advection of an Eulerian field just translates a constant Lagrangian field

$$b_a^L(\boldsymbol{X}, t) = b_a^L(\boldsymbol{X}, 0), \tag{1.67}$$

the variation of which is trivial

$$\delta b_a^L(\boldsymbol{X}, t) = 0. \tag{1.68}$$

Then, from the relation between Lagrangian and Eulerian fields (1.53), we have

$$\delta b_a = -\boldsymbol{\eta} \cdot \boldsymbol{\nabla} b_a. \tag{1.69}$$

1.2.2.3 Derivation of the isentropic Euler model with Hamilton's SAP

Let us now derive the isentropic Euler model with Hamilton's SAP. We first define the Lagrangian of the system in Eulerian coordinates with

$$\mathcal{L} = \frac{1}{2}\rho \boldsymbol{u}^2 - \rho e(\rho, s), \tag{1.70}$$

where ρ it the fluid density, $\boldsymbol{u}$ the fluid velocity and e the specific internal energy depending on the fluid density and the specific entropy s. The Action of the fluid on a space-time domain $\bar{\Omega} = \Omega \times (t_1, t_2)$ is defined by

$$\mathcal{A} = \int_{\Omega\times(t_1,t_2)} \mathcal{L}\, d\boldsymbol{x}dt. \tag{1.71}$$

The fluid density is assumed to be conserved while the specific entropy is advected,

$$\partial_t \rho + \boldsymbol{\nabla}\cdot(\rho\boldsymbol{u}) = 0, \qquad D_t s = 0, \tag{1.72}$$

and we have the Gibbs relation

$$TD_t s = D_t e + pD_t\left(\frac{1}{\rho}\right), \tag{1.73}$$

with $T = (\partial_s e)|_\rho$ the temperature and $p = \rho^2(\partial_\rho e)|_s$ the pressure.

With the variational operator δ, Hamilton's SAP reads

$$\delta\mathcal{A} = 0, \tag{1.74}$$

Denoting $(\partial_{\boldsymbol{u}}\mathcal{L} = \boldsymbol{K})^T$, we decompose the variation of the Action into

$$\delta\mathcal{A} = \int_{\bar{\Omega}} \partial_\rho\mathcal{L}\delta\rho + \partial_s\mathcal{L}\delta s + \boldsymbol{K}\cdot\delta\boldsymbol{u} = \int_{\bar{\Omega}} \partial_\rho\mathcal{L}(-\boldsymbol{\nabla}\cdot(\rho\boldsymbol{\eta})) + \partial_s\mathcal{L}(-\boldsymbol{\eta}\cdot s) + \boldsymbol{K}\cdot(\partial_t\boldsymbol{\eta} + \boldsymbol{u}\cdot\boldsymbol{\nabla}\boldsymbol{\eta} - (\boldsymbol{\eta}\cdot\boldsymbol{\nabla})\boldsymbol{u}). \tag{1.75}$$

Then, integrating by parts gives

$$\delta\mathcal{A} = \int_{\bar{\Omega}} \left[\rho\boldsymbol{\nabla}\partial_\rho\mathcal{L} - \partial_s\mathcal{L}\boldsymbol{\nabla}s - \partial_t\boldsymbol{K} - \boldsymbol{\nabla}\cdot(\boldsymbol{K}\boldsymbol{u}) - \boldsymbol{K}\boldsymbol{\nabla}\boldsymbol{u}\right]\cdot\boldsymbol{\eta}. \tag{1.76}$$

As the variation of the Action is minimized for any variation $\boldsymbol{\eta}$, it yields

$$\partial_t\boldsymbol{K} + \boldsymbol{\nabla}\cdot(\boldsymbol{K}\boldsymbol{u}) + \boldsymbol{K}\boldsymbol{\nabla}\boldsymbol{u} - \rho\boldsymbol{\nabla}\partial_\rho\mathcal{L} + \partial_s\mathcal{L}\boldsymbol{\nabla}s = \boldsymbol{0}. \tag{1.77}$$

Introducing $\mathcal{L}^* = \rho\partial_\rho\mathcal{L} - \mathcal{L}$, it also writes as the conservation law

$$\partial_t\boldsymbol{K} + \boldsymbol{\nabla}\cdot(\boldsymbol{K}\boldsymbol{u} - \mathcal{L}^*\boldsymbol{I}) = \boldsymbol{0}, \tag{1.78}$$

where $\boldsymbol{I}$ is the identity matrix. Then, evaluating the derivatives gives

$$\boldsymbol{K} = \rho\boldsymbol{u}, \qquad \mathcal{L}^* = -p, \tag{1.79}$$

and, from (1.78), we obtain the momentum equation

$$\partial_t(\rho\boldsymbol{u}) + \boldsymbol{\nabla}\cdot(\rho\boldsymbol{u}\otimes\boldsymbol{u} + p\boldsymbol{I}) = \boldsymbol{0}. \tag{1.80}$$

A supplementary equation can be obtained for the total energy $\rho E = \frac{1}{2}\rho\boldsymbol{u}^2 + \rho e$ by multiplying (1.80) by $\boldsymbol{u}$, and use the Gibbs relation (1.73) and the transport of specific entropy (1.72),

$$\partial_t(\rho E) + \boldsymbol{\nabla}\cdot((\rho E + p)\boldsymbol{u}) = 0. \tag{1.81}$$

The mass conservation equation (1.72) together with the momentum equation (1.80), and either the isentropic advection constraint (1.72) or the energy equation (1.81) form the *isentropic Euler model* 1.

Model 1 (Isentropic Euler equations)

Denoting ρ the density, $\boldsymbol{u}$ the velocity, $e(\rho, s)$ the specific internal energy, s the specific entropy, p the pressure and E the specific total energy, the Euler equations read

$$\begin{cases} \partial_t \rho & + \boldsymbol{\nabla} \cdot (\rho \boldsymbol{u}) & = 0, \\ \partial_t (\rho \boldsymbol{u}) & + \boldsymbol{\nabla} \cdot (\rho \boldsymbol{u} \otimes \boldsymbol{u} + p \boldsymbol{I}) & = \boldsymbol{0}, \\ \partial_t (\rho E) & + \boldsymbol{\nabla} \cdot ((\rho E + p(\rho, s)) \boldsymbol{u}) & = 0. \end{cases}$$

Let us assess now some properties given in Section 1.1.1 for the Euler equations. The study for an arbitrary direction $\boldsymbol{\omega}$ of the fluxes Jacobian gives us three eigenvalues

$$\boldsymbol{u} \cdot \boldsymbol{\omega} - c, \qquad \boldsymbol{u} \cdot \boldsymbol{\omega}, \qquad \boldsymbol{u} \cdot \boldsymbol{\omega} + c, \tag{1.82}$$

with $c = \sqrt{(\partial_\rho p)|_s}$, and $\boldsymbol{u} \cdot \boldsymbol{\omega}$ of multiplicity 3. Given a single space dimension, the system is strictly hyperbolic. Moreover, from the Gibbs relation and the Euler equations, one can show using the following supplementary conservation equation

$$\partial_t (-\rho f(s)) + \boldsymbol{\nabla} \cdot (-\rho f(s) \boldsymbol{u}) = 0, \tag{1.83}$$

with f a smooth function of s. It is then showed in Harten et al. (1998) that for any region where the Euler equations are hyperbolic, there exists a function f such that $-\rho f(s)$ is strictly convex and, consequently is a mathematical entropy. For an ideal gas of adiabatic index γ, it is showed in Godlewski and Raviart (1991) that choosing

$$f := (\rho, \boldsymbol{u}, \rho E) \mapsto \ln \left(\rho E - \frac{1}{2\rho} \boldsymbol{u}^2 \right) - \gamma \ln \rho, \tag{1.84}$$

makes $-\rho f(s)$ a mathematical entropy.

1.2.2.4 Derivation of the isothermal Euler mode with Hamilton's SAP

Let us consider now an isothermal flow such that the temperature is advected with the flow in the time-space domain, and a barotropic EOS defined by the function $e(\rho)$.

For the isothermal case, we introduce the *Helmholtz free energy* defined by

$$\varepsilon(\rho, T) = e(\rho, s) - Ts, \tag{1.85}$$

which allows to use the Gibbs relation with the temperature constraint,

$$D_t \varepsilon + s D_t T + p D_t \left(\frac{1}{\rho} \right) = 0, \tag{1.86}$$

with $p = \rho^2 (\partial_\rho \varepsilon)|_T$ and $s = -(\partial_T \varepsilon)|_\rho$. Hamilton's SAP is then applied with the following Lagrangian,

$$\mathcal{L} = \frac{1}{2} \rho \boldsymbol{u}^2 - \rho \varepsilon(\rho, T), \tag{1.87}$$

and the constraints $D_t T = 0$. It yields the following momentum equation

$$\partial_t (\rho \boldsymbol{u}) + \boldsymbol{\nabla} \cdot (\rho \boldsymbol{u} \otimes \boldsymbol{u} + p \boldsymbol{I}) = \boldsymbol{0}. \tag{1.88}$$

Moreover, multiplying the momentum equation by velocity gives

$$\partial_t (\rho \mathcal{E}) + \boldsymbol{\nabla} \cdot ((\rho \mathcal{E} + p) \boldsymbol{u}) = 0, \tag{1.89}$$

with $\rho\mathcal{E} = \frac{1}{2}\rho\boldsymbol{u}^2 + \rho\varepsilon(\rho)$, the total Helmholtz free energy. It is showed to be a mathematical entropy as the reduced mathematical entropy of the full Euler equations in the viscous limit of the Euler-Fourier system (Euler equations with thermal diffusion) (Serre, 2010).

Similarly to the isentropic case, the conservation of mass together with the momentum equation, and either the temperature advection constraint or the total Helmholtz free energy equation, forms the closed model of isothermal Euler equations 2.

Model 2 (Isothermal Euler equations)

Denoting ρ the density, $\boldsymbol{u}$ the velocity, $\varepsilon(\rho)$ the specific free energy, $p = \rho^2(\partial_\rho\varepsilon)|_T$ the pressure, T the temperature, the isothermal Euler equations read

$$\begin{cases} \partial_t\rho + \boldsymbol{\nabla}\cdot(\rho\boldsymbol{u}) = 0, \\ \partial_t T + \boldsymbol{u}\cdot\boldsymbol{\nabla}T = 0, \\ \partial_t(\rho\boldsymbol{u}) + \boldsymbol{\nabla}\cdot(\rho\boldsymbol{u}\otimes\boldsymbol{u} + p\boldsymbol{I}) = \boldsymbol{0}. \end{cases}$$

The isothermal Euler equations are similarly showed hyperbolic in an arbitrary direction $\boldsymbol{\omega}$ with the eigenvalues

$$\boldsymbol{u}\cdot\boldsymbol{\omega} - c, \qquad \boldsymbol{u}\cdot\boldsymbol{\omega}, \qquad \boldsymbol{u}\cdot\boldsymbol{\omega} + c, \tag{1.90}$$

with $c = \sqrt{(\partial_\rho p)|_T}$, and with $\boldsymbol{u}\cdot\boldsymbol{\omega}$ of multiplicity 2. Given a single space dimension, it is showed strictly hyperbolic.

In the end, the isentropic and isothermal models are very similar, and we refer to both of them as the barotropic Euler models as the temperature or the entropy have only a passive role.

With such mathematical properties, the models are also showed to admit a local-in-time unique smooth solution (Gårding, 1963; Serre, 1999). However, the global well-posedness of the Initial Boundary Value problem for Euler models 1 and 2 is not assessed yet. The reader is referred to Serre (2001); Markfelder (2021) for reviews of the available results.

1.2.3 Dissipative source terms

Hamilton's SAP has been used to derive conservative equations in Section 1.2.2, but we would like now to add some dissipative processes to these systems in a coherent way with both the mathematical structure of the model and the physical one associated with the second principle of thermodynamics. These two structures are related through the mathematical entropy and the physical entropy. The source of dissipation are various such as discontinuities of entropic weak solutions (Tadmor, 1986), viscous terms such as fluid viscosity or heat transfer (Courant and Friedrichs, 1948; Tadmor, 1986; Serre, 2010), or relaxation terms (Chen et al., 1994; Serre, 2008) which are not here at stake for classic Euler equations but will be later considered for two-phase flow models. We propose to illustrate here such relation by considering the addition of Stokes viscous terms to the Euler Models 1 and 2. Only elementary results and observations are provided here, and the interested reader is referred to the references aforementioned for a comprehensive introduction to viscous dissipation in conservation laws.

1.2.3.1 Mathematical entropy and physical entropy of the Euler equations

With the Euler equations, both the physical and mathematical entropies are conserved

$$\partial_t(\rho s) + \boldsymbol{\nabla}\cdot(\rho s\boldsymbol{u}) = 0, \qquad \partial_t(-\rho f(s)) + \boldsymbol{\nabla}\cdot(-\rho f(s)\boldsymbol{u}) = 0, \tag{1.91}$$

for some smooth increasing functions f.

Now let us add the classic Navier-Stokes viscous terms in the momentum and energy equations of the Euler equations

$$\begin{cases} \partial_t \rho & +\boldsymbol{\nabla}\cdot(\rho \boldsymbol{u}) & = 0, \\ \partial_t(\rho \boldsymbol{u}) & +\boldsymbol{\nabla}\cdot(\rho \boldsymbol{u}\otimes\boldsymbol{u} + p\boldsymbol{I}) & = \boldsymbol{\nabla}\cdot(\boldsymbol{T}_{stokes}), \\ \partial_t(\rho E) & +\boldsymbol{\nabla}\cdot((\rho E + p)\boldsymbol{u}) & = \boldsymbol{\nabla}\cdot(\boldsymbol{T}_{stokes}\cdot\boldsymbol{u}), \end{cases} \tag{1.92}$$

with $\boldsymbol{T}_{stokes} = \mu(\boldsymbol{\nabla u} + (\boldsymbol{\nabla u})^T) + \lambda(\boldsymbol{\nabla}\cdot\boldsymbol{u})\boldsymbol{I}$ and $\lambda + \frac{2}{3}\mu \geq 0$. We compute now the conservation of entropy density thanks to the Gibbs equation, and, after some calculations, we obtain

$$\begin{aligned} \partial_t(\rho s) + \boldsymbol{\nabla}\cdot(\rho s\boldsymbol{u}) &= \frac{1}{T}\boldsymbol{T}_{stokes} : \boldsymbol{\nabla u} \\ &= \frac{1}{T}\left(2\mu\left(\frac{\boldsymbol{\nabla u} + (\boldsymbol{\nabla u})^T}{2}\right)^2 + \lambda(\boldsymbol{\nabla}\cdot\boldsymbol{u})^2\right) \\ &= \frac{1}{T}\left(2\mu\left(\frac{\boldsymbol{\nabla u} + (\boldsymbol{\nabla u})^T}{2} - \frac{1}{3}(\boldsymbol{\nabla}\cdot\boldsymbol{u})\right)^2 + \left(\lambda + \frac{2}{3}\mu\right)(\boldsymbol{\nabla}\cdot\boldsymbol{u})^2\right) \geq 0. \end{aligned} \tag{1.93}$$

The right-hand side is also named the viscous dissipation rate ϵ_{diss}, and its positiveness shows that the entropy of the fluid increases. Furthermore, multiplying the above equation by the derivative $f(s)$ of an increasing smooth function defined for the mathematical entropy of the Euler equation leads to

$$\partial_t(-\rho f(s)) + \boldsymbol{\nabla}\cdot(-\rho f(s)\boldsymbol{u}) = -f'(s)\epsilon_{diss} \leq 0. \tag{1.94}$$

Then, this illustrates that the physical and mathematical entropy are here related, and they show opposite signs for their respective entropy production rate.

1.2.3.2 Mathematical entropy and physical entropy of the isothermal Euler equations

Let us now illustrate the same procedure on the isothermal Euler equation by adding the Stokes viscous tensor to the momentum equation

$$\begin{cases} \partial_t \rho & +\boldsymbol{\nabla}\cdot(\rho \boldsymbol{u}) & = 0, \\ \partial_t(\rho \boldsymbol{u}) & +\boldsymbol{\nabla}\cdot(\rho \boldsymbol{u}\otimes\boldsymbol{u} + p\boldsymbol{I}) & = \boldsymbol{\nabla}\cdot(\boldsymbol{T}_{stokes}). \end{cases} \tag{1.95}$$

Recalling the free energy definition $\varepsilon = e - Ts$, the Gibbs relation (1.73) becomes

$$D_t\varepsilon + sD_tT + pD_t\left(\frac{1}{\rho}\right) = 0. \tag{1.96}$$

Then, multiplying the momentum equation by $\boldsymbol{u}$ leads

$$\partial_t(\rho\mathcal{E}) + \boldsymbol{\nabla}\cdot((\rho\mathcal{E} + p)\boldsymbol{u} + \boldsymbol{T}_{stokes}\cdot\boldsymbol{u}) = -\epsilon_{diss} \leq 0. \tag{1.97}$$

We observe that, for isothermal barotropic flow, the free energy production is negatively signed when dissipative processes are added, and it is also coherent with the physical entropy nature of $\rho\mathcal{E}$.

Indeed, for an isothermal flow, the variation of the entropy of the fluid is not relevant to illustrate the second principle of thermodynamics as the temperature is maintained by an external system whose entropy is not described in the model. However, an isothermal second principle is verified through a decrease of the free energy (Chanteperdrix, 2004; Caro et al., 2006).

1.3 Multi-fluid modelling of the separate flow regime

In this section, we focus on the separated regime where the multi-fluid DIM gives a diffuse interface, *i.e.* a region where the volume fraction transitions from 0 to 1 and where the interface is thus located. Note that the length defined by such transition is not comparable with the physical thickness of the interface, which is orders of magnitude smaller in ambient conditions. Provided that no arbitrarily small dynamics are present in the described physics, it allows a good representation of the interface dynamics while ensuring physical conservation laws despite the numerical spreading of the interface. Note that some methods include supplementary terms to control the interface thickness by modifying the capillarity thermodynamics in liquid-vapour flows (Jamet et al., 2001), but discards the interface dynamics below the preset interface thickness. Eventually, the location of the interface can be defined using any level-set of the volume fraction. These models are very appreciated but are of limited validity when the interface dynamics becomes complex as discussed in Section 1.1.2 or when thermodynamic disequilibria are considered (Saurel and Abgrall, 1999; Coquel et al., 2002). Simpler configurations can then be considered with for instance thermal equilibrium (Allaire et al., 2002) or barotropic EOS (Chanteperdrix et al., 2002). However, such thermodynamics does not rely on the same physical grounds and mathematical developments as single-phase fluid particle do because of the diffuse interface represented by the volume fraction. Some efforts have been put towards the modelling of such thermodynamics involving a parameter order variable such as the volume fraction, mass fraction or other (Caro et al., 2005; Helluy and Seguin, 2006; Gaillard, 2015; Cordesse, 2020) for the proper modelling of phase transition or capillarity.

In this section, we place ourselves at a *large-scale* level where only a separated regime is accounted with a diffuse interface model. Moreover, we assume a simple configuration for clarity and illustrative purposes to further extend the models towards more complexity. We particularly propose to derive barotropic two-fluid models of the literature, first without capillarity in Section 1.3.1 and with capillarity in Section 1.3.2.

1.3.1 Barotropic multi-fluid model with one velocity

The purpose of this section is to derive a first two-fluid model under simplifying assumptions to both: assess the ability of Hamilton's SAP of recovering multi-fluid models from the literature, and to propose a building block model which will be successively extended throughout this manuscript.

1.3.1.1 Derivation of a conservative model with Hamilton's Stationary Action Principle

Let us consider the same physical assumptions as the three-equation model of Chanteperdrix et al. (2002):

- liquid and gaseous phases have the same velocity $\boldsymbol{u}$; (H1a)
- the fluids are equipped with a barotropic EOS; (H1b)
- there is no mass exchanges between the phases. (H1c)

The need of a velocity for each phase is here questionable as the two velocities would interact only in the mixture at the location of the diffuse interface where the physics is not well determined. Consequently, we assume the kinematic equilibrium (H1a) such that the velocity in the diffuse interface is defined unambiguously. A two-velocity framework is proposed in Section 1.4.2, but it is dedicated to a disperse multi-fluid model for advected inclusions at the small-scale. Moreover, we assume here (H1b) to focus the discussion on the study of the interface regime apart from the discussion on thermodynamics. In the light of the discussion proposed for the barotropic Euler equations in both isentropic and isothermal cases, we propose here, and for the rest of this manuscript, to consider an agnostic barotropic EOS for each fluid. The impact of the two-phase modelling on the temperature repartition between the fluids is therefore not discussed.

Finally, (H1c) is assumed as it would unnecessarily add complexity to the thermodynamics, the reader is referred to the references cited previously for a better overview of the topic.

Let us denote the quantities related to the liquid and gaseous phases by respectively the indexes 1 and 2. For a phase k, we write its volume fraction α_k and its density ρ_k. Then, the barotropic EOS is modelled by a specific barotropic internal energy $e_k(\rho_k)$. The pressure is defined by $p_k := \rho_k^2 e_k'(\rho_k)$ and the sound velocity by $c_k := (p_k')^{1/2}$.

The reader is referred to Sections 1.2.2.4 and 1.2.2.3 for case-specific definitions. Denoting $m_k := \alpha_k \rho_k$ the effective density for each phase $k = 1, 2$, the mass of each phase is then conserved following (H1a) and (H1c),

$$\partial_t m_k + \boldsymbol{\nabla} \cdot (m_k \boldsymbol{u}) = 0. \tag{1.98}$$

If we define $\rho := m_1 + m_2$ the density of the medium, summing the equation above for $k = 1, 2$ enables to retrieve the total mass conservation equation $\partial_t \rho + \boldsymbol{\nabla} \cdot (\rho \boldsymbol{u}) = 0$. The total volume occupancy of the phases in the mixture also enforces

$$\alpha_1 + \alpha_2 = 1. \tag{1.99}$$

We set the kinetic and potential energies of the phase k as

$$E_k^{kin} := \frac{1}{2} m_k \boldsymbol{u}^2, \quad E_k^{pot} := m_k e_k \left(\frac{m_k}{\alpha_k} \right), \tag{1.100}$$

and the mixture kinetic and potential energies are $\sum_k E_k^{kin}$ and $\sum_k E_k^{pot}$. This enables the definition of the Lagrangian energy $\mathcal{L}_k = E_k^{kin} - E_k^{pot}$ of the phase k and a mixture Lagrangian energy $\mathcal{L} = \sum_k \mathcal{L}_k$. Following the lines of Section 1.2.2.3, we use Hamilton's SAP by minimizing the Lagrangian's action over a space-time domain $\bar{\Omega} = \Omega \times (t_1, t_2)$. The volume fraction is here chosen as a free variable which is expected to lead to an additional equilibrium. Remark that other models assume the volume fraction to be advected (Allaire et al., 2002) and lead to a different equilibrium, but they are not considered here. Without developing the partial derivatives of the Lagrangian, the variation of the action $\mathcal{A} = \int_{\bar{\Omega}} \mathcal{L}$ reads

$$\delta \mathcal{A} = \int_{\bar{\Omega}} - \Big\{ \partial_t \boldsymbol{K} + \boldsymbol{\nabla} \cdot \Big[\boldsymbol{K} \otimes \boldsymbol{u} - (\mathcal{L}_1^* + \mathcal{L}_2^*) \boldsymbol{I} \Big] - (\partial_{\alpha_1} \mathcal{L}_1 - \partial_{\alpha_2} \mathcal{L}_2) \boldsymbol{\nabla} \alpha_1 \Big\} \cdot \boldsymbol{\eta} + \Big(\partial_{\alpha_1} \mathcal{L}_1 - \partial_{\alpha_2} \mathcal{L}_2 \Big) \delta \alpha_1. \tag{1.101}$$

Then, Hamilton's SAP $\delta \mathcal{A} = 0$ leads to the following two equations

$$\begin{cases} \partial_t \boldsymbol{K} + \boldsymbol{\nabla} \cdot (\boldsymbol{K} \otimes \boldsymbol{u}) - \boldsymbol{\nabla} (\mathcal{L}^* + \mathcal{L}_2^*) = \boldsymbol{0}, \\ \partial_{\alpha_1} \mathcal{L}_1 - \partial_{\alpha_2} \mathcal{L}_2 = 0, \end{cases} \tag{1.102}$$

where $\boldsymbol{K}^T = \partial_{\boldsymbol{u}} \mathcal{L}$, $\mathcal{L}_k^* = m_k (\partial_{m_k} \mathcal{L}_k) - \mathcal{L}_k$ and $\mathcal{L}^* = \sum_k \mathcal{L}_k^*$. The choice of energies (1.100) yields

$$\boldsymbol{K} = \rho \boldsymbol{u}, \quad \mathcal{L}_1^* = -\alpha_1 p_1, \quad \partial_{\alpha_1} \mathcal{L}_1 = p_1, \quad \mathcal{L}_2^* = -\alpha_2 p_2, \quad \partial_{\alpha_2} \mathcal{L}_2 = p_2. \tag{1.103}$$

Including the constraints (1.98) and evaluating the equations of (1.102) leads to Model 3.

Model 3 (Three-equation model)

With $m_k = \alpha_k \rho_k$ the phase effective densities, $\rho = m_1 + m_2$ the mixture density, p_k the phase pressures, $\boldsymbol{u}$ the mixture velocity, the *three-equation model* reads

$$\begin{cases} \partial_t m_1 & + \boldsymbol{\nabla} \cdot (m_1 \boldsymbol{u}) & = 0, \\ \partial_t m_2 & + \boldsymbol{\nabla} \cdot (m_2 \boldsymbol{u}) & = 0, \\ \partial_t (\rho \boldsymbol{u}) & + \boldsymbol{\nabla} \cdot (\rho \boldsymbol{u} \otimes \boldsymbol{u} + p \mathbf{I}) & = \boldsymbol{0}, \end{cases}$$

with $p(m_1, m_2) := p_1(m_1, \alpha^*) = p_2(m_2, \alpha^*)$ and α^* solution of $p_1(m_1, \alpha) = p_2(m_2, \alpha)$.

The pressure p is defined by the pressure equilibrium in the mixture thermodynamic closure $p := p_1 = p_2$ given by the second line of (1.102). This algebraic equation gives α_1 and p respectively as the solution and the value of the equilibrium for given m_1, m_2. Model 3 also admits a supplementary conservation equation

$$\partial_t \mathcal{H} + \boldsymbol{\nabla} \cdot ((\mathcal{H} + p) \boldsymbol{u}) = 0, \tag{1.104}$$

where $\mathcal{H} = \frac{1}{2}\rho\|\boldsymbol{u}\|^2 + \rho e$ with $\rho e = m_1 e_1 + m_2 e_2$ is showed in Chanteperdrix (2004) to be a mathematical entropy for (1.3.1.1). Moreover, the system is hyperbolic for any direction $\boldsymbol{\omega}$, with eigenvalues

$$\boldsymbol{u}\cdot\boldsymbol{\omega} - c_W, \qquad \boldsymbol{u}\cdot\boldsymbol{\omega}, \qquad \boldsymbol{u}\cdot\boldsymbol{\omega} + c_W, \tag{1.105}$$

where $\boldsymbol{u}\cdot\boldsymbol{\omega}$ of multiplicity 3 and c_W the Wood – or Wallis – velocity (Wood, 1930; Wallis, 1969),

$$c_W = \left(\rho\left(\frac{\alpha_1}{\rho_1 c_1^2} + \frac{\alpha_2}{\rho_2 c_2^2}\right)\right)^{-1/2}. \tag{1.106}$$

Despite accounting for only the coexistence of the two phases and no other phenomena, such a multi-fluid model presents all the good mathematical properties for a multi-fluid model. It offers a minimal building block upon which we will add a hierarchy of other phenomena. Remark that we could have obtained a similar set of equations in the isothermal limit rather than using barotropic EOS similarly to Euler equations in Section 1.2.2.4. Then, gathering mass conservation, momentum and total energy equations rather than the temperature advection constraint would have lead to the four-equation model given in Le Touze (2015).

1.3.1.2 Adding a dissipative pressure relaxation

Following the work of Chanteperdrix (2004), let us start by investigating the existence of a two-pressure multi-fluid model by relaxing the pressure equilibrium of (1.3.1.1) into

$$D_t\alpha_1 = \frac{1}{\mu}(p_1 - p_2), \tag{1.107}$$

where $\mu > 0$ has the dimension of a dynamic viscosity. For linearized barotropic EOS, the function $\alpha_1 \mapsto p_1(m_1, \alpha_1) - p_2(\alpha_1)$ is strictly decreasing from $+\infty$ to $-\infty$ as α_1 goes from 0 to 1. Therefore, there exists a unique equilibrium $\alpha_1^* \in (0,1)$ and (1.107) makes the volume fraction relax towards such equilibrium. Since the pressure equilibrium no longer provides a pressure definition, we postulate that the momentum equation reads

$$\partial_t(\rho\boldsymbol{u}) + \boldsymbol{\nabla}\cdot(\rho\boldsymbol{u}\otimes\boldsymbol{u} + \tilde{p}\boldsymbol{I}) = \boldsymbol{0}, \tag{1.108}$$

where $\tilde{p}$ is chosen to provide a signed dissipation of the mathematical entropy $\mathcal{H}$ similarly defined as the one of the three-equation model. Multiplying the momentum equation by $\boldsymbol{u}$ yields the following mathematical entropy production rate

$$\partial_t\mathcal{H} + \boldsymbol{\nabla}\cdot((\mathcal{H} + \tilde{p})\boldsymbol{u}) = (\tilde{p} - \alpha_1 p_1 - \alpha_2 p_2)\boldsymbol{\nabla}\cdot\boldsymbol{u} - \mu(1-\alpha_1^d)(D_t\alpha_1)^2. \tag{1.109}$$

Therefore, choosing $\tilde{p} := \alpha_1 p_1 + \alpha_2 p_2$ gives a signed mathematical entropy production $\varsigma \leq 0$ and the following four-equation Model 4.

Model 4 (Four-equation model)

With $m_k = \alpha_k\rho_k$ the phase effective densities, ρ the mixture density such that $\rho = m_1 + m_2$, p_k the phase pressures, α_k the volume fractions, $\boldsymbol{u}$ the mixture velocity, the *four-equation model* reads

$$\begin{cases} \partial_t m_1 + \boldsymbol{\nabla}\cdot(m_1\boldsymbol{u}) = 0, \\ \partial_t m_2 + \boldsymbol{\nabla}\cdot(m_2\boldsymbol{u}) = 0, \\ \partial_t(\rho\boldsymbol{u}) + \boldsymbol{\nabla}\cdot(\rho\boldsymbol{u}\otimes\boldsymbol{u} + p\boldsymbol{I}) = \boldsymbol{0}, \\ D_t\alpha_1 = \mu^{-1}(p_1 - p_2), \end{cases}$$

with $p = \alpha_1 p_1 + \alpha_2 p_2$.

The Model 4 is also showed to be hyperbolic for any direction $\boldsymbol{\omega}$ with eigenvalues

$$\boldsymbol{u}\cdot\boldsymbol{\omega} - c_F, \qquad \boldsymbol{u}\cdot\boldsymbol{\omega}, \qquad \boldsymbol{u}\cdot\boldsymbol{\omega} + c_F, \tag{1.110}$$

where $\boldsymbol{u}\cdot\boldsymbol{\omega}$ of multiplicity 4 and

$$c_F = \sqrt{\frac{m_1 c_1^2 + m_2 c_2^2}{\rho}}. \tag{1.111}$$

Remark that the pair of models 3 and 4 satisfies the criterion *EEC* of Definition 4. Therefore, one can consider that the four-equation model formally relaxes towards the three-equation model in the limit where $\mu \to 0$.

One could further discuss the nature of the viscous relaxation term introduced in (1.107) by considering a finite value for μ. This would correspond to an actual physical process that should be modelled with a physical closure of the parameter μ. One would also expect such a closure to depend on the interface geometry at all scales and consequently on the flow regime. Such closures have been proposed for disperse bubbly flows which requires a minimal amount of variables to describe its geometry, as a statistical average of a pressure equilibrium process in Perrier and Gutiérrez (2021) and a viscous damping of bubble pulsation in Drui et al. (2019). This discussion will be pursued in Chapter 2 dealing with the interface geometric modelling at small scales.

1.3.2 Adding a Brackbill-like capillarity model

We are now interested in proposing a multi-fluid model with capillarity. As previously discussed, such a task does not aim at proposing a sound thermodynamic and mathematical model as the multi-fluid modelling approach does not model the smallest scales where the capillarity phenomena originates, in contrast to phase-field models (Korteweg, 1901; Cahn and Hilliard, 1958; Anderson et al., 1998). Nevertheless, the CSF approach proposed by Brackbill et al. (1992) offers to describe the macroscopic effects of capillarity *via* a force density relying on a colour function. Note that a similar approach involves an equivalent flux form also referred to as the Continuum Surface Stress (CSS) model (Lafaurie et al., 1994; Gueyffier et al., 1999; Perigaud and Saurel, 2005; Grenier et al., 2013; Schmidmayer et al., 2017). Such models have been showed to be compatible with barotropic two-phase flow model in Chanteperdrix (2004) by using the volume fraction as the colour function and integrating it in the internal energy *via* a capillarity energy contribution

$$\rho e = m_1 e_1 + m_2 e_2 + \sigma\|\boldsymbol{\nabla}\alpha_1\|, \tag{1.112}$$

where σ is the capillarity coefficient. Remark that $\|\boldsymbol{\nabla}\alpha_1\|$ has the dimension of a surface density and is here used as an IAD estimator as (Perigaud and Saurel, 2005). Remark that one can further use this colour function that implicitly describes the large-scale interface to estimate geometric quantities such as mean curvature (Osher and Fedkiw, 2003; Goldman, 2005)

$$H(\boldsymbol{\nabla}\alpha_1) := -\boldsymbol{\nabla}\cdot\left(\frac{\boldsymbol{\nabla}\alpha_1}{\|\boldsymbol{\nabla}\alpha_1\|}\right). \tag{1.113}$$

Similarly to Schmidmayer et al. (2017), we consider then the following Lagrangian for our multi-fluid model

$$\mathcal{L} = \underbrace{\frac{1}{2}m_1\boldsymbol{u}^2 - m_1 e_1\left(\frac{m_1}{\alpha_1}\right)}_{\mathcal{L}_1} + \underbrace{\frac{1}{2}m_2\boldsymbol{u}^2 - m_2 e_2\left(\frac{m_2}{\alpha_2}\right)}_{\mathcal{L}_2} \underbrace{-\sigma\|\boldsymbol{\nabla}\alpha_1\|}_{\mathcal{L}_{cap}}. \tag{1.114}$$

Let us denote $\mathcal{L}_k^* := m_k\partial_{m_k}\mathcal{L}_k - \mathcal{L}_k$, for $k = 1, 2$, $\boldsymbol{D}^T := \partial_{\boldsymbol{\nabla}\alpha_1}\mathcal{L}_{cap}$, and $\boldsymbol{K}^T := \partial_{\boldsymbol{u}}\mathcal{L}$. Using integration by parts, the variation of the action associated with the Lagrangian boils down to

$$\begin{aligned}\delta\mathcal{A} = \int_\Omega &-\Big(\partial_t\boldsymbol{K} + \boldsymbol{\nabla}\cdot\Big[\boldsymbol{K}\otimes\boldsymbol{u} - (\mathcal{L}_1^* + \mathcal{L}_2^* - \mathcal{L}_{cap})\boldsymbol{I} - \boldsymbol{\nabla}\alpha_1\otimes\boldsymbol{D}\Big] - (\partial_{\alpha_1}\mathcal{L}_1 - \partial_{\alpha_2}\mathcal{L}_2 - \boldsymbol{\nabla}\cdot\boldsymbol{D})\boldsymbol{\nabla}\alpha_1\Big)\cdot\boldsymbol{\eta} \\ &+ \Big(\partial_{\alpha_1}\mathcal{L}_1 - \partial_{\alpha_2}\mathcal{L}_2 - \boldsymbol{\nabla}\cdot\boldsymbol{D}\Big)\delta\alpha_1,\end{aligned} \tag{1.115}$$

where $\boldsymbol{I}$ is the identity matrix. Then, Hamilton's SAP, *i.e.* $\delta\mathcal{A} = 0$ for any variation of the trajectories $\boldsymbol{\eta}$ and the volume fraction $\delta\alpha_1$, yields

$$\begin{cases} \partial_t \boldsymbol{K} + \boldsymbol{\nabla}\cdot\left[\boldsymbol{K}\otimes\boldsymbol{u} - (\mathcal{L}_1^* + \mathcal{L}_2^* - \mathcal{L}_{cap})\boldsymbol{I} - \boldsymbol{\nabla}\alpha_1 \otimes \boldsymbol{D}\right] = \boldsymbol{0}, \\ \partial_{\alpha_1}\mathcal{L}_1 - \partial_{\alpha_2}\mathcal{L}_2 - \boldsymbol{\nabla}\cdot\boldsymbol{D} = 0. \end{cases} \tag{1.116}$$

Evaluating the derivatives of the Lagrangian gives

$$\boldsymbol{K} = \rho\boldsymbol{u}, \quad \boldsymbol{D} = -\sigma\frac{\boldsymbol{\nabla}\alpha_1}{\|\boldsymbol{\nabla}\alpha_1\|}, \quad \mathcal{L}_1^* = -\alpha_1 p_1, \quad \mathcal{L}_2^* = -\alpha_2 p_2, \tag{1.117}$$

and for $k = 1, 2$,

$$\partial_{\alpha_1^d}\mathcal{L}_k = -\alpha_k p_k, \quad \partial_{\alpha_k}\mathcal{L}_k = (1-\alpha_1^d)p_k. \tag{1.118}$$

Using the conservative variables $(m_1, m_2, \rho\boldsymbol{u})$, the full system including constraints (1.98) reads as follows

Model 5 (Barotropic capillarity model)

With $m_k = \alpha_k\rho_k$ the phase effective densities, $\rho = m_1 + m_2$ the mixture density, p_k the phase pressures, α_k the volume fractions, $\boldsymbol{u}$ the mixture velocity, and σ the coefficient of capillarity, we have

$$\begin{cases} \partial_t m_1 + \boldsymbol{\nabla}\cdot(m_1\boldsymbol{u}) = 0, \\ \partial_t m_2 + \boldsymbol{\nabla}\cdot(m_2\boldsymbol{u}) = 0, \\ \partial_t(\rho\boldsymbol{u}) + \boldsymbol{\nabla}\cdot\left(\rho\boldsymbol{u}\otimes\boldsymbol{u} + (p - \sigma\|\boldsymbol{\nabla}\alpha_1\|)\boldsymbol{I} + \sigma\frac{\boldsymbol{\nabla}\alpha_1\otimes\boldsymbol{\nabla}\alpha_1}{\|\boldsymbol{\nabla}\alpha_1\|}\right) = \boldsymbol{0}, \end{cases}$$

with

$$p := \alpha_1 p_1\left(\frac{m_1}{\alpha_1}\right) + \alpha_2 p_2\left(\frac{m_2}{1-\alpha_1}\right),$$

and α_1 defined by the implicit Laplace equilibrium

$$p_1\left(\frac{m_1}{\alpha_1}\right) - p_2\left(\frac{m_2}{1-\alpha_1}\right) = \sigma H(\boldsymbol{\nabla}\alpha_1), \tag{1.119}$$

where $H(\boldsymbol{\nabla}\alpha_1)$ is defined by (1.113).

This system admits a supplementary equation of conservation for $\mathcal{H} := \frac{1}{2}\rho\boldsymbol{u}^2 + \rho e + \sigma\|\boldsymbol{\nabla}\|$ that reads

$$\partial_t\mathcal{H} + \boldsymbol{\nabla}\cdot\left(\mathcal{H}\boldsymbol{u} + (p - \sigma\|\boldsymbol{\nabla}\alpha_1\|)\boldsymbol{u} - \sigma\frac{\boldsymbol{\nabla}\alpha_1}{\|\boldsymbol{\nabla}\alpha_1\|}D_t\alpha_1\right) = 0, \tag{1.120}$$

where the material time derivative $D_t\alpha_1$ in the flux is implicitly obtained by taking the time material of the Laplace equilibrium (1.119). Remark then that Model 5 and the equation (1.120) are conservation equations with fluxes depending on the gradient of α_1. Consequently, the mathematical theory of conservation laws presented in Section 1.1.1 does not apply anymore. Nevertheless, we still refer to $\mathcal{H}$ as a "mathematical entropy" as it naturally extends the mathematical entropies without capillarity, and we still aim at verifying the same properties such as hyperbolicity, and a negatively signed mathematical entropy production. Regarding the hyperbolicity, it cannot be assessed for Model 5 as it involves second-order space derivatives and an implicit definition of pressure equilibrium also involving space derivatives.

One can similarly propose a relaxation model of Model 5 by introducing the following dynamic for α_1

$$\partial_t\alpha_1 + \boldsymbol{u}\cdot\boldsymbol{\nabla}\alpha_1 = \frac{1}{\mu}\left(p_1 - p_2 - \sigma H\right). \tag{1.121}$$

This yields the Model 6.

Model 6 (Barotropic capillarity model with relaxation)

With $m_k = \alpha_k \rho_k$ the phase effective densities, ρ the mixture density such that $\rho = m_1 + m_2$, p_k the phase pressures, α_k the volume fractions, $\boldsymbol{u}$ the mixture velocity, and σ the coefficient of capillarity, the model reads

$$\begin{cases} \partial_t m_1 & +\boldsymbol{\nabla}\cdot(m_1\boldsymbol{u}) & = 0, \\ \partial_t m_2 & +\boldsymbol{\nabla}\cdot(m_2\boldsymbol{u}) & = 0, \\ \partial_t \alpha_1 & +\boldsymbol{u}\cdot\boldsymbol{\nabla}\alpha_1 & = \frac{1}{\mu}(p_1 - p_2 - \sigma H) \\ \partial_t(\rho\boldsymbol{u}) + \boldsymbol{\nabla}\cdot\left(\rho\boldsymbol{u}\otimes\boldsymbol{u} + (p - \sigma\|\boldsymbol{\nabla}\alpha_1\|)\mathbf{I} + \sigma\frac{\boldsymbol{\nabla}\alpha_1\otimes\boldsymbol{\nabla}\alpha_1}{\|\boldsymbol{\nabla}\alpha_1\|}\right) = \mathbf{0}, \end{cases}$$

with

$$p := \alpha_1 p_1\left(\frac{m_1}{\alpha_1}\right) + \alpha_2 p_2\left(\frac{m_2}{1-\alpha_1}\right),$$

where $H(\boldsymbol{\nabla}\alpha_1)$ is defined by (1.113).

This model also admits a mathematical entropy inequality similar to the four-equation Model 4,

$$\partial_t \mathcal{H} + \boldsymbol{\nabla}\cdot\left(\mathcal{H}\boldsymbol{u} + (p - \sigma\|\boldsymbol{\nabla}\alpha_1\|)\boldsymbol{u} - \sigma\frac{\boldsymbol{\nabla}\alpha_1}{\|\boldsymbol{\nabla}\alpha_1\|}D_t\alpha_1\right) = -\epsilon^{-1}(1-\alpha_1^d)\left(p_1 - p_2 - \frac{\sigma}{1-\alpha_1^d}H\right)^2 \leq 0. \tag{1.122}$$

Moreover, thanks to the relaxed structure of the Model 6, one can propose an alternative way of studying hyperbolicity of the homogeneous form of Model 6. Indeed, by introducing $\boldsymbol{w} = \boldsymbol{\nabla}\alpha_1$ as a new variable, one can introduce the following homogeneous augmented model using similar lines as Schmidmayer et al. (2017).

Model 7 (Homogeneous augmented barotropic capillarity model)

With $m_k = \alpha_k\rho_k$ the phase effective densities, $\rho = m_1 + m_2$ the mixture density, p_k the phase pressures, α_k the volume fractions, $\boldsymbol{w}$ the gradient of the volume fraction α_1, $\boldsymbol{u}$ the mixture velocity, and σ the coefficient of capillarity, we have

$$\begin{cases} \partial_t m_k & +\boldsymbol{\nabla}\cdot(m_k\boldsymbol{u}) & =0, & k = 1,2, \\ \partial_t \alpha_1 & +\boldsymbol{u}\cdot\boldsymbol{\nabla}\alpha_1 & =0, & \\ \partial_t \boldsymbol{w} & +\boldsymbol{\nabla}(\boldsymbol{u}\cdot\boldsymbol{w}) & =\mathbf{0}, & \\ \partial_t(\rho\boldsymbol{u}) + \boldsymbol{\nabla}\cdot\left(\rho\boldsymbol{u}\otimes\boldsymbol{u} + (p - \sigma\|\boldsymbol{w}\|)\mathbf{I} + \sigma\frac{\boldsymbol{w}\otimes\boldsymbol{w}}{\|\boldsymbol{w}\|}\right) = \mathbf{0}, & & \end{cases}$$

with

$$p := \alpha_1 p_1\left(\frac{m_1}{\alpha_1}\right) + \alpha_2 p_2\left(\frac{m_2}{1-\alpha_1}\right).$$

Note that this augmented model is showed not to be rotational invariant, and one must study the hyperbolicity in every direction ω. The details of this study can be found in Appendix 1.A and the results are summarized here. Let us now note $u_\omega := \boldsymbol{u}\cdot\boldsymbol{\omega}$, $\boldsymbol{n} := \boldsymbol{\nabla}\alpha_1/\|\boldsymbol{\nabla}\alpha_1\|$, $\psi = \sigma\|\boldsymbol{\nabla}\overline{\alpha}_1\|/(\rho c_F^2)$, c_F, the velocity, a geometrical-physical parameter and the two-scale frozen sound speed as established in (1.111). In the diffuse interface with moderate capillarity effects in comparison with acoustics, *i.e.* $\psi \ll 1$, we have the following eigenvalues in the direction ω,

$$u_\omega, \qquad u_\omega \pm c_F(1 - (\boldsymbol{\omega}\cdot\boldsymbol{n})^2)\sqrt{\psi}, \qquad u_\omega \pm c_F\left(1 + \frac{1}{2}\psi(\boldsymbol{\omega}\cdot\boldsymbol{n})^2(1 - (\boldsymbol{\omega}\cdot\boldsymbol{n})^2)\right). \tag{1.123}$$

Remark that when the capillarity effects are negligible with respect to acoustics ones $\psi \gg 1$ or when we are oriented towards the surface normal $(\boldsymbol{\omega} \cdot \boldsymbol{n})^2 = 1$, we recover at the zeroth order the frozen speed of sound. Indeed, in such conditions the capillarity plays no role, and we recover the properties of Model 4. Otherwise, these velocities are *a priori* distinct but, as showed in the Appendix 1.A, the system is only weakly hyperbolic. Remark that strongly hyperbolic extensions of this augmented model are proposed in Chiocchetti et al. (2021) with a special care dedicated on the development of curl-free schemes for the evolution of $\boldsymbol{w}$, notably with divergence-cleaning techniques introduced by Munz et al. (2000) in the context of magneto-hydrodynamics.

1.4 Multi-fluid modelling of the disperse flow regime

We continue the flexibility assessment of the framework proposed by Hamilton's SAP by considering now the modelling of disperse multi-fluid models. Let us recall that modelling of disperse regimes deals with a collection of inclusions, liquid, gaseous or solid, embedded in a carrier phase. This regime encompasses itself another wide spectrum of regimes (*e.g.* bubbly, cap, slug or annular flows), which depends, among other parameters, on the volume occupation of the inclusions – dilute or dense –, the density ratio between the inclusion and the carrier phase, the size and velocity polydispersion, *etc* (Crowe et al., 2012). In order to propose a simpler description of the interface, these models need to translate at a macroscopic scale the numerous phenomena occurring at the small scale such as drag, added-mass, turbulence, segregation, collisions, or small-scale dynamics such as oscillation or pulsation of the inclusion.

One possibility to describe such regime is using a kinetic-based model to capture these phenomena from the dynamics of a single inclusion (Williams, 1958; O'Rourke and Amsden, 1987). Multi-fluid models can potentially be obtained by taking the statistical averages, but it requires a particular method which is later detailed in Chapter 2.

Actually, the derivation of disperse multi-fluid model has revealed to be challenging as many attempts provide ill-posed non-hyperbolic models as reviewed in Lhuillier et al. (2013). This difficulty notably arises when considering the buoyant forces in two-velocity models and correction terms need to be added to recover hyperbolicity (Raviart and Sainsaulieu, 1995; Fox et al., 2020). Another issue comes from the unphysical sound propagation at the inclusion's sound velocity as in Baer and Nunziato (1986); Saurel and Abgrall (1999). Such a modification of the Baer-Nunziato system is proposed in Saurel et al. (2017) by introducing an ad-hoc conservation equation for compressible and relaxing droplets at the small-scale. As pointed out by Lhuillier et al. (2013), a key feature to overcome this difficulty would lie in the proper modelling of the added-mass effects and pseudo-turbulence as recently proposed in the hyperbolic model of Fox et al. (2022) for a specific stiffened gas EOS.

In order to reach a better understanding of such modelling difficulty, a derivation of such models with Hamilton's SAP would help identify the key mechanisms restoring hyperbolicity of the model. The derivation of two-phase flow models with Hamilton's SAP in the disperse regime has first been proposed by Bedford and Drumheller (1978) where a micro-inertia term is added to describe the small-scale pulsation of a bubbly flow. The hyperbolicity of such model has not been assessed as it was not closed. This idea remained in the works of Gavrilyuk and Saurel (2002); Drui et al. (2019), but respectively include a propagation speed related to the inclusion or a single-velocity model. Following the ideas of Lhuillier, added-mass contributions have been accounted for in the derivation with Hamilton's SAP (Burtea et al., 2021) but hyperbolicity was not recovered.

In this section we propose to both recover some simple disperse models of the literature with Hamilton's SAP and investigate the derivation of two-velocity models. In Section 1.4.1, a single-velocity model disperse multi-fluid model is derived. Then, a naive derivation of a two-velocity model is proposed in Section 1.4.2 without adding added-mass effects. Finally, a novel approach to include added-mass effects in Hamilton's SAP is detailed in Section 1.4.3 and hyperbolicity is recovered for an original and simple model.

This last results is associated with the following contribution :

- Loison, Arthur, Teddy Pichard, Samuel Kokh, and Marc Massot. "Derivation of a disperse two-velocity model accounting for added-mass through the Stationary Action Principle", *In preparation.*

1.4.1 A disperse model with incompressible droplets

Let us first consider a collection of incompressible inclusions, either droplets or solid particles, embedded in a compressible gas. The only parameters used to describe these inclusions are their velocity and volume occupancy. As a consequence, the sole energy involved in the SAP will be the inclusions kinetic energy. The fine description of the small-scale is proposed in the dedicated Chapter 2. For consistency, we index with 2 the quantities related to the gaseous phase and with both an index 1 and an exponent d – or sometimes 1^d – the quantities related to the

disperse phase. We first assume

- liquid and gaseous phases have the same velocity $\boldsymbol{u}$; (H1d)
- the fluids are equipped with a barotropic EOS; (H1e)
- the inclusions are incompressible. (H1f)

Such one-velocity assumption is made to avoid any difficulty associated with hyperbolicity, and is further relaxed in Sections 1.4.2 and 1.4.3. The barotropic equations of state are assumed similarly as models for the separated regime derived in Section 1.3. Finally, the incompressibility of inclusions discards any non-physical sound propagation at their associated sound speed as remarked in Saurel et al. (2017).

We have the following occupation constraint,

$$\alpha_2 + \alpha_1^d = 1, \tag{1.124}$$

the conservation of phase densities for $k = 2, 1^d$ and the incompressibility properties of the inclusions,

$$\partial_t m_k + \boldsymbol{\nabla} \cdot (m_k \boldsymbol{u}) = 0, \qquad \partial_t \alpha_1^d + \boldsymbol{\nabla}(\alpha_1^d \boldsymbol{u}) = 0, \qquad D_t \rho_1^d = 0. \tag{1.125}$$

The Lagrangian associated with this system then reads

$$\mathcal{L} = \underbrace{\frac{1}{2} m_2 \boldsymbol{u}^2 - m_2 e_2 \left(\frac{m_2}{1 - \alpha_1^d} \right)}_{\mathcal{L}_2} + \underbrace{\frac{1}{2} m_1^d \boldsymbol{u}^2 - m_1^d e_1^d(\rho_1^d)}_{\mathcal{L}_1^d}. \tag{1.126}$$

As mentioned before, the internal energy of the inclusions has no impact on the derived model, and one could also have added similarly capillarity energy thanks to additional geometric parameters. The internal energy is unnecessarily kept here to highlight the absence of any contribution in the final model. Let us now write the variation of the action $\mathcal{A}$ associated with the Lagrangian defined by (1.126)

$$\delta \mathcal{A} = \int_{\bar{\Omega}} - \left\{ \partial_t \boldsymbol{K} + \boldsymbol{\nabla} \cdot \left[\boldsymbol{K} \otimes \boldsymbol{u} - \left(\mathcal{L}_2^* + \mathcal{L}_1^{d,*} + \alpha_1^d \partial_{\alpha_1^d} \mathcal{L}_2 \right) \boldsymbol{I} \right] \right\} \cdot \boldsymbol{\eta}. \tag{1.127}$$

Hamilton's SAP $\delta \mathcal{A} = 0$ yields

$$\partial_t \boldsymbol{K} + \boldsymbol{\nabla} \cdot \left[\boldsymbol{K} \otimes \boldsymbol{u} - \left(\mathcal{L}_2^* + \mathcal{L}_1^{d,*} + \alpha_1^d \partial_{\alpha_1^d} \mathcal{L}_2 \right) \boldsymbol{I} \right] = \boldsymbol{0}. \tag{1.128}$$

Then, evaluating the derivatives of the Lagrangian,

$$\boldsymbol{K} = \rho \boldsymbol{u}, \qquad \mathcal{L}_2^* = -(1 - \alpha_1^d) p_2, \qquad \mathcal{L}_1^{d,*} = 0, \qquad \partial_{\alpha_1^d} \mathcal{L}_2 = p_2. \tag{1.129}$$

Hence, the final momentum equation reads

$$\partial_t (\rho \boldsymbol{u}) + \boldsymbol{\nabla} \cdot (\rho \boldsymbol{u} \otimes \boldsymbol{u} + p_2 \boldsymbol{I}) = 0. \tag{1.130}$$

The final system is gathered in the Model 8.

Model 8 (Single-velocity disperse model)

With $m_k = \alpha_k \rho_k$ and α_k the phase densities and volume fractions of phases $k = 2, 1^d$, $\rho = m_1^d + m_2$ the mixture's density, $\boldsymbol{u}$ the velocity and $p_2(\rho_2)$ the pressure of the gaseous phase 2, the single-velocity disperse model reads

$$\begin{cases} \partial_t m_2 + \boldsymbol{\nabla} \cdot (m_2 \boldsymbol{u}) = 0, \\ \partial_t m_1^d + \boldsymbol{\nabla} \cdot (m_1^d \boldsymbol{u}) = 0, \\ \partial_t \alpha_1^d + \boldsymbol{\nabla} \cdot (\alpha_1^d \boldsymbol{u}) = 0, \\ \partial_t (\rho \boldsymbol{u}) + \boldsymbol{\nabla} \cdot (\rho \boldsymbol{u} \otimes \boldsymbol{u} + p_2 \boldsymbol{I}) = \boldsymbol{0}. \end{cases}$$

This model is showed to be hyperbolic in any direction $\boldsymbol{\omega}$ with the following eigenvalues

$$\boldsymbol{u}\cdot\boldsymbol{\omega} - c, \qquad \boldsymbol{u}\cdot\boldsymbol{\omega}, \qquad \boldsymbol{u}\cdot\boldsymbol{\omega} + c, \tag{1.131}$$

with

$$c = \frac{c_2}{(1-\alpha_1^d)\sqrt{1+\frac{\alpha_1^d}{1-\alpha_1^d}\frac{\rho_1^d}{\rho_2}}}, \tag{1.132}$$

and where $\boldsymbol{u}\cdot\boldsymbol{\omega}$ has multiplicity 4. We recover the same formula as the one derived in Urick and Ament (1949) where it is presented under the following equivalent form

$$\left(\frac{c_2}{c}\right)^2 = \left(1-\alpha_1^d\right)\left(1+\alpha_1^d\frac{\rho_1^d-\rho_2}{\rho_2}\right). \tag{1.133}$$

In the work of Urick and Ament, sound velocity measures show a good agreement with this model up to a volume fraction of 25%, which is remarkable for such a minimal model. Remark also that in the limit $\alpha_1^d \to 0$ the sound velocity of the barotropic Euler gaseous model is recovered and that, for any $\alpha_1^d > 0$, the sound velocities are decreasing for admissible values of α_1^d.

Finally, the Model 8 admits the following conservation equation for $\mathcal{H} = \frac{1}{2}\rho\boldsymbol{u}^2 + m_2 e_2$

$$\partial_t\mathcal{H} + \boldsymbol{\nabla}\cdot((\mathcal{H}+p_2)\boldsymbol{u}) = 0. \tag{1.134}$$

Moreover, we can show that $\mathcal{H}$ is a convex function of $(m_2, m_1^d, \alpha_1^d, \boldsymbol{u})$ by considering its Hessian $\mathbb{H}$ and verifying that $\boldsymbol{y}^T\mathbb{H}\boldsymbol{y} \geq 0$ for any vector $\boldsymbol{y}$. Writing $\boldsymbol{y} = (\tilde{\boldsymbol{y}}, \bar{\boldsymbol{y}})$ with $\tilde{\boldsymbol{y}} = (\tilde{y}_a, \tilde{y}_b, \tilde{y}_c)$ and $\bar{\boldsymbol{y}} = (\bar{y}_1, \bar{y}_2, \bar{y}_3)$, we indeed have that

$$\boldsymbol{y}^T\mathbb{H}\boldsymbol{y} = \frac{\|\bar{\boldsymbol{y}} - (\tilde{y}_a+\tilde{y}_b)\boldsymbol{u}\|^2}{\rho} + \frac{m_2^3((1-\alpha_1^d)\tilde{y}_a + m_2\tilde{y}_c)^2c_2^2}{(1-\alpha_1^d)^6} + \frac{4m_2^2((1-\alpha_1^d)\tilde{y}_a + m_2\tilde{y}_c)^2p_2}{(1-\alpha_1^d)^5} \geq 0. \tag{1.135}$$

Hence, $\mathcal{H}$ is then a mathematical entropy for the Model 8.

1.4.2 Towards two-velocity models

The derivation of two-velocity models is necessary for the proper modelling of critical phenomena arising in gas-liquid atomization such as drag, added mass, particle turbulence, etc. Let us consider first a simple extension of the previous one-velocity two-scale model in a disperse regime. Consider a naive first model where the kinetic energy is simply split in two contributions. We propose then the following Lagrangian

$$\mathcal{L} = \underbrace{\frac{1}{2}m_2\boldsymbol{u}^2 - m_2e_2(\rho_2)}_{\mathcal{L}_2} + \underbrace{\frac{1}{2}m_1^d(\boldsymbol{u}^d)^2 - m_1^de_1(\rho_1^d)}_{\mathcal{L}_1^d}, \tag{1.136}$$

and the mass conservation constraints assuming that the small-scale liquid phase is incompressible,

$$\partial_t m_2 + \boldsymbol{\nabla}\cdot(m_2\boldsymbol{u}) = 0, \quad \partial_t m_1^d + \boldsymbol{\nabla}\cdot(m_1^d\boldsymbol{u}^d) = 0, \qquad D_t\rho_1^d = 0, \quad \partial_t\alpha_1^d + \boldsymbol{\nabla}\cdot(\alpha_1^d\boldsymbol{u}^d) = 0. \tag{1.137}$$

For computational convenience, we express the Lagrangian was a function of $(m_1^d, m_2, \alpha_1^d, \boldsymbol{u}, \boldsymbol{u}^d)$,

$$\mathcal{L}(m_1^d, m_2, \alpha_1^d, \boldsymbol{u}, \boldsymbol{u}^d) = \frac{1}{2}m_2\boldsymbol{u}^2 - m_2e_2\left(\frac{m_2}{1-\alpha_1^d}\right) + \frac{1}{2}m_1^d(\boldsymbol{u}^d)^2 - m_1^de_1(\rho_1^d), \tag{1.138}$$

Remark now that we introduce two families of trajectories for the variation of the action $\mathcal{A}$ associated with the above Lagrangian. Note also that the Eulerian formulation is particularly convenient to use the Eulerian constraint

of volume occupancy $\alpha_1^d + \alpha_2 = 1$ *i.e.* $\delta\alpha_1^d + \delta\alpha_2 = 0$. Therefore, we introduce two Eulerian displacement variations $\boldsymbol{\eta}$ and $\boldsymbol{\eta}^d$, and we use the formula for the constraints variations accordingly

$$\begin{gathered}\delta m_2 = -\boldsymbol{\nabla}\cdot(m_2\boldsymbol{\eta}), \quad \delta m_1^d = -\boldsymbol{\nabla}\cdot(m_1^d\boldsymbol{\eta}^d), \quad \delta\alpha_1^d = -\boldsymbol{\nabla}\cdot(\alpha_1^d\boldsymbol{\eta}^d), \quad \delta\rho_1^d = -(\boldsymbol{\eta}^d\cdot\boldsymbol{\nabla})\rho_1^d, \\ \delta\boldsymbol{u} = \partial_t\boldsymbol{\eta} + (\boldsymbol{u}\cdot\boldsymbol{\nabla})\boldsymbol{u} - (\boldsymbol{\eta}\cdot\boldsymbol{\nabla})\boldsymbol{u}, \quad \delta\boldsymbol{u}^d = \partial_t\boldsymbol{\eta}^d + (\boldsymbol{u}^d\cdot\boldsymbol{\nabla})\boldsymbol{u}^d - (\boldsymbol{\eta}^d\cdot\boldsymbol{\nabla})\boldsymbol{u}^d.\end{gathered} \tag{1.139}$$

Defining $\boldsymbol{K}^T = \partial_{\boldsymbol{u}}\mathcal{L}$, $(\boldsymbol{K}^d)^T = \partial_{\boldsymbol{u}^d}\mathcal{L}$,$\mathcal{L}_2^* = m_2\partial_{m_2}\mathcal{L}_2 - \mathcal{L}_2$, and $\mathcal{L}_1^{d,*} = m_1^d\partial_{m_1^d}\mathcal{L}_1^d - \mathcal{L}_1^d$, the variation of the action reads

$$\delta\mathcal{A} = \int_{\bar{\Omega}} -\left\{\partial_t\boldsymbol{K} + \boldsymbol{\nabla}\cdot(\boldsymbol{K}\otimes\boldsymbol{u} - \mathcal{L}_2^*\boldsymbol{I}) - \partial_{\alpha_1^d}\mathcal{L}_2\boldsymbol{\nabla}(\alpha_1^d)\right\}\cdot\boldsymbol{\eta} - \left\{\partial_t\boldsymbol{K}^d + \boldsymbol{\nabla}\cdot(\boldsymbol{K}^d\otimes\boldsymbol{u}^d - \mathcal{L}_1^{*,d}\boldsymbol{I}) - \alpha_1^d\boldsymbol{\nabla}(\partial_{\alpha_1^d}\mathcal{L}_2)\right\}\cdot\boldsymbol{\eta}^d, \tag{1.140}$$

and Hamilton's SAP $\delta\mathcal{A} = 0$ provide for any variation $\boldsymbol{\eta}$ and $\boldsymbol{\eta}^d$ that

$$\begin{cases}\partial_t\boldsymbol{K} + \boldsymbol{\nabla}\cdot(\boldsymbol{K}\otimes\boldsymbol{u} - \mathcal{L}_2^*\boldsymbol{I}) - \partial_{\alpha_1^d}\mathcal{L}_2\boldsymbol{\nabla}\alpha_1^d = \boldsymbol{0}, \\ \partial_t\boldsymbol{K}^d + \boldsymbol{\nabla}\cdot(\boldsymbol{K}^d\otimes\boldsymbol{u}^d - \mathcal{L}_1^{*,d}\boldsymbol{I}) - \alpha_1^d\boldsymbol{\nabla}(\partial_{\alpha_1^d}\mathcal{L}_2) = \boldsymbol{0}.\end{cases} \tag{1.141}$$

Evaluating the derivatives yields,

$$\boldsymbol{K} = m_2\boldsymbol{u}, \quad \boldsymbol{K}^d = m_1^d\boldsymbol{u}^d, \quad \mathcal{L}_2^* = -(1-\alpha_1^d)p_2, \quad \partial_{\alpha_1^d}\mathcal{L}_2 = -p_2 \quad \mathcal{L}^{*,d} = 0. \tag{1.142}$$

The final momentum equations are then

$$\begin{cases}\partial_t(m_2\boldsymbol{u}) + \boldsymbol{\nabla}\cdot(m_2\boldsymbol{u}\otimes\boldsymbol{u} + p_2\boldsymbol{I}) - \alpha_1^d\boldsymbol{\nabla}p_2 = \boldsymbol{0}, \\ \partial_t(m_1^d\boldsymbol{u}^d) + \boldsymbol{\nabla}\cdot(m_1^d\boldsymbol{u}^d\otimes\boldsymbol{u}^d) + \alpha_1^d\boldsymbol{\nabla}p_2 = \boldsymbol{0}.\end{cases} \tag{1.143}$$

And the final two-velocity model is gathered in Model 9.

Model 9 (Two-velocity model without added-mass)

With $m_k = \alpha_k\rho_k$ and α_k the phase densities and volume fractions of phases $k = 2, 1^d$, $\rho = m_1 + m_2$ the mixture's density, $\boldsymbol{u}$ the velocity of the carrier phase, $\boldsymbol{u}^d$ the velocity of the inclusions and $p_2(\rho_2)$ the pressure of the gaseous phase 2,

$$\begin{cases}\partial_t m_2 + \boldsymbol{\nabla}\cdot(m_2\boldsymbol{u}) = 0, \\ \partial_t m_1^d + \boldsymbol{\nabla}\cdot(m_1^d\boldsymbol{u}^d) = 0, \\ \partial_t\alpha_1^d + \boldsymbol{\nabla}\cdot(\alpha_1^d\boldsymbol{u}^d) = 0, \\ \partial_t(m_2\boldsymbol{u}) + \boldsymbol{\nabla}\cdot(m_2\boldsymbol{u}\otimes\boldsymbol{u} + p_2\boldsymbol{I}) - \alpha_1^d\boldsymbol{\nabla}p_2 = \boldsymbol{0}, \\ \partial_t(m_1^d\boldsymbol{u}^d) + \boldsymbol{\nabla}\cdot(m_1^d\boldsymbol{u}^d\otimes\boldsymbol{u}^d) + \alpha_1^d\boldsymbol{\nabla}p_2 = \boldsymbol{0}.\end{cases}$$

Remark also that this model is very similar to the one of Raviart and Sainsaulieu (1995) except for an additional pressure term in the momentum equation of the inclusion. However, the hyperbolicity study of this system reveals that the model is not hyperbolic for velocity differential smaller than the mixture sound speed as remarked in Burtea et al. (2021). Indeed, the characteristic polynomial $\mathcal{P}$ of the linearized flux, denoting $u = \boldsymbol{u}\cdot\omega$ and $u^d = \boldsymbol{u}^d\cdot\omega$ for any direction $\boldsymbol{\omega}$, reads

$$\mathcal{P}(X) = (X - u^d)\mathcal{Q}(X), \tag{1.144}$$

with $\mathcal{Q}$ a fourth-order polynomial not reported explicitly here that we compute with the symbolic computational software Mathematica (Wolfram Research, 2023). The nature of the roots of a fourth-order polynomial can be accessed *via* the sign of its discriminant $\Delta_{\mathcal{Q}}$. To simplify this study, we focus on a neighbourhood of 0 for both α_1^d and $(u - u^d)$ which correspond to a dilute regime at small Stokes number. At first order in α_1^d and second order in $(u - u^d)$, the discriminant reads

$$\Delta_{\mathcal{Q}} = -\frac{16c_2^{10}\rho_2}{\rho_1^d}\alpha_1^d(u-u^d)^2 + o(\alpha_1^d(u-u^d)^2). \tag{1.145}$$

A negative discriminant in a fourth-order polynomial implies that two roots are complex and the other two are reals. Therefore, in a neighbourhood of 0 for both α_1^d and $(u - u^d)$, the model admits two complex eigenvalues and is not hyperbolic. Non-hyperbolicity property is not compatible with the well-posedness of the model (Métivier, 2005) if no other terms are added to the system to stabilize the solution, see for instance Ramshaw and Trapp (1978). Nonetheless, we choose here to restore hyperbolicity by considering additional physics.

1.4.3 Added mass effects for dilute disperse regime

Let us now account for a correction term in the kinetic energies of the Lagrangian in order to model added mass phenomena. These phenomena are accounted by adding correcting the assumption that the kinetic energy of the mixture is the sum of the kinetic energy of each flow as if they do not see each other. As we attempt to restore hyperbolicity, at least for a dilute regime of particles and small velocity differential, one can assume that the flow at small scale is a *d'Alembert* flow around a spherical rigid particle. Such assumption has already been considered in Biesheuvel and Wijngaarden (1984) where an averaging method is used to obtain a hyperbolic model. A model similar to the one proposed by Fox et al. (2020) is obtained therein where hyperbolicity is also achieved.

Inspired by these models, we include an energetic contribution related to added-mass with Hamilton's SAP. In order to do so, we need first to express the kinetic energy correction associated with the local *d'Alembert* flow. In order to get explicit expressions of these corrective terms, we make the following assumptions:

- The disperse phase is dilute such that the flow around an inclusion does not affect the flow around the others; (H1g)
- The flow is incompressible and irrotational at small scale; (H1h)
- The inclusion is a sphere and its centre of mass has exactly the velocity $\boldsymbol{u}^d$, and it is not rotating; (H1i)
- The small-scale flow tends to the velocity of the large scale $\boldsymbol{u}$ far from the inclusion. (H1j)

Under these assumptions, we place ourselves in the referential frame of the carrier phase such that the inclusion can be considered as moving at velocity $\boldsymbol{u} - \boldsymbol{u}^d$ and the velocity far from the inclusion vanishes. The kinetic energy of such flow is well known and can be found for instance in Lamb (1916, §92) for a sphere of radius R,

$$\frac{2}{3}\pi\rho_2^a R^3(\boldsymbol{u} - \boldsymbol{u}^d)^2, \tag{1.146}$$

where ρ_2^a is the density of the locally incompressible fluid. It is comparable to $\rho_2 := m_2/\alpha_2$ in terms of order of magnitude, however it does not follow the same dynamics. For a local volume fraction of α_1^d, the associated correction term is

$$e^a := \frac{1}{2}\rho_2^a\alpha_1^d(\boldsymbol{u} - \boldsymbol{u}^d)^2. \tag{1.147}$$

1.4.3.1 Hamilton's SAP

The following Lagrangian is then introduced,

$$\mathcal{L} = \underbrace{\frac{1}{2}m_2\boldsymbol{u}^2 - m_2 e_2(\rho_2)}_{\mathcal{L}_2} + \underbrace{\frac{1}{2}m_1^d(\boldsymbol{u}^d)^2 - m_1^d e_1(\rho_1^d) - \frac{1}{2}\rho_2^a\alpha_1^d(\boldsymbol{u} - \boldsymbol{u}^d)^2}_{\mathcal{L}_1^d}, \tag{1.148}$$

with $\alpha_1^d + \alpha_2 = 1$, and with two components identified within the Lagrangian: $\mathcal{L}_2$, $\mathcal{L}_1^d$. We also make the usual assumptions of mass conservation and incompressible small-scale liquid phase

$$\partial_t m_2 + \boldsymbol{\nabla}\cdot(m_2\boldsymbol{u}) = 0, \quad \partial_t m_1^d + \boldsymbol{\nabla}\cdot(m_1^d\boldsymbol{u}^d) = 0, \quad D_t\rho_1^d = 0, \quad \partial_t\alpha_1^d + \boldsymbol{\nabla}\cdot(\alpha_1^d\boldsymbol{u}^d) = 0. \tag{1.149}$$

However, the variable ρ_2^a is still non-constraint at this point, and we consequently assume that the added-mass kinetic energy is conserved with the flow of the inclusions,

$$\partial_t e^a + \boldsymbol{\nabla}\cdot(e^a \boldsymbol{u}^d) = 0. \tag{1.150}$$

Given these constraints, we choose to express the Lagrangian with the following dependencies

$$\mathcal{L}(m_1^d, m_2, \alpha_1^d, \rho_1^d, e^a, \boldsymbol{u}, \boldsymbol{u}^d) = \frac{1}{2} m_2 \boldsymbol{u}^2 - m_2 e_2\left(\frac{m_2}{1-\alpha_1^d}\right) + \frac{1}{2} m_1^d (\boldsymbol{u}^d)^2 - m_1^d e_1(\rho_1^d) - e^a, \tag{1.151}$$

where the added-mass kinetic energy correction is added with a negative sign as it is not a usual quadratic form. Denoting $(\boldsymbol{K})^T = \partial_{\boldsymbol{u}}\mathcal{L}$, $(\boldsymbol{K}^d)^T = \partial_{\boldsymbol{u}^d}\mathcal{L}$, $\mathcal{L}_2^* = m_2\partial_{m_2}\mathcal{L}_2 - \mathcal{L}_2$, and $\mathcal{L}^{*,d} = m_1^d\partial_{m_1^d}\mathcal{L}_1^d - \mathcal{L}_1^d$, the variation of the action associated the Lagrangian above reads

$$\begin{aligned}\delta\mathcal{A} = \int_{\bar{\Omega}} &- \left\{\partial_t \boldsymbol{K} + \boldsymbol{\nabla}\cdot(\boldsymbol{K}\otimes\boldsymbol{u} - \mathcal{L}_2^*\boldsymbol{I}) - \partial_{\alpha_1^d}\mathcal{L}_2\boldsymbol{\nabla}\alpha_1^d\right\}\cdot\boldsymbol{\eta} \\ &- \left\{\partial_t \boldsymbol{K}^d + \boldsymbol{\nabla}\cdot(\boldsymbol{K}^d\otimes\boldsymbol{u}^d - (\mathcal{L}^{*,d} + e^a\partial_{e^a}\mathcal{L}_1^d)\boldsymbol{I}) - \alpha_1^d\boldsymbol{\nabla}(\partial_{\alpha_1^d}\mathcal{L}_2)\right\}\cdot\boldsymbol{\eta}^d.\end{aligned} \tag{1.152}$$

Applying Hamilton's SAP to the action $\delta\mathcal{A} = 0$ boils down to nullifying the expressions factoring $\boldsymbol{\eta}$ and $\boldsymbol{\eta}^d$. It yields

$$\begin{cases}\partial_t \boldsymbol{K} + \boldsymbol{\nabla}\cdot(\boldsymbol{K}\otimes\boldsymbol{u} - \mathcal{L}_2^*\boldsymbol{I}) - \partial_{\alpha_1^d}\mathcal{L}_2\boldsymbol{\nabla}\alpha_1^d = \boldsymbol{0}, \\ \partial_t \boldsymbol{K}^d + \boldsymbol{\nabla}\cdot(\boldsymbol{K}^d\otimes\boldsymbol{u}^d - (\mathcal{L}^{*,d} + e^a\partial_{e^a}\mathcal{L}_1^d)\boldsymbol{I}) - \alpha_1^d\boldsymbol{\nabla}(\partial_{\alpha_1^d}\mathcal{L}_2) = \boldsymbol{0}.\end{cases} \tag{1.153}$$

Then, evaluating the partial derivatives gives

$$\boldsymbol{K} = m_2\boldsymbol{u}, \quad \mathcal{L}_2^* = -(1-\alpha_1^d)p_2, \quad \boldsymbol{K}^d = m_1^d\boldsymbol{u}^d, \quad \partial_{\alpha_1^d}\mathcal{L}_2 = -p_2 \quad \mathcal{L}^{*,d} = 0, \quad \partial_{e^a}\mathcal{L}_1^d = -1. \tag{1.154}$$

We report the final system in Model 10.

Model 10 (Two-velocity model with added-mass)

With $m_k = \alpha_k\rho_k$ and α_k the phase densities and volume fractions of phases $k = 2, 1^d$, ρ_2^a the density of the incompressible *d'Alembert* flow, $\boldsymbol{u}$, the velocity of the carrier phase, $\boldsymbol{u}^d$ the velocity of the inclusions and $p_2(\rho_2)$ the pressure of the gaseous phase 2,

$$\begin{cases}\partial_t m_2 + \boldsymbol{\nabla}\cdot(m_2\boldsymbol{u}) = 0, \\ \partial_t m_1^d + \boldsymbol{\nabla}\cdot(m_1^d\boldsymbol{u}^d) = 0, \\ \partial_t \alpha_1^d + \boldsymbol{\nabla}\cdot(\alpha_1^d\boldsymbol{u}^d) = 0, \\ \partial_t e^a + \boldsymbol{\nabla}\cdot(e^a\boldsymbol{u}^d) = 0, \\ \partial_t(m_2\boldsymbol{u}) + \boldsymbol{\nabla}\cdot(m_2\boldsymbol{u}\otimes\boldsymbol{u} + (1-\alpha_1^d)p_2\boldsymbol{I}) + p_2\boldsymbol{\nabla}\alpha_1^d = \boldsymbol{0}, \\ \partial_t(m_1^d\boldsymbol{u}^d) + \boldsymbol{\nabla}\cdot(m_1^d\boldsymbol{u}^d\otimes\boldsymbol{u}^d + \frac{1}{2}\rho_2^a\alpha_1^d(\boldsymbol{u}-\boldsymbol{u}^d)^2\boldsymbol{I}) + \alpha_1^d\boldsymbol{\nabla}p_2 = \boldsymbol{0},\end{cases}$$

with $e^a = \frac{1}{2}\rho_2^a\alpha_1^d(\boldsymbol{u}-\boldsymbol{u}^d)^2$.

Denoting $\mathcal{H} = \mathcal{H}_2 + \mathcal{H}_1^d$ with

$$\mathcal{H}_2 = \frac{1}{2}m_2\boldsymbol{u}^2 + m_2 e_2, \qquad \mathcal{H}_1^d = \frac{1}{2}m_1^d(\boldsymbol{u}^d)^2 + m_1^d e_1^d + e^a, \tag{1.155}$$

we have the following additional conservation equation

$$\partial_t\mathcal{H} + \boldsymbol{\nabla}\cdot\left[\left(\mathcal{H}_2 + (1-\alpha_1^d)p_2\right)\boldsymbol{u} + \left(\mathcal{H}_1^d + e^a + \alpha_1^d p_2\right)\boldsymbol{u}^d\right] = 0. \tag{1.156}$$

Moreover, $\mathcal{H}$ is showed to be convex function of $m_2, m_1^d, \alpha_1^d, e^a, \boldsymbol{u}, \boldsymbol{u}^d$. With its Hessian denoted $\mathbb{H}$, and given a vector $\boldsymbol{y} = (y_a, y_b, y_c, y_d, \bar{\boldsymbol{y}}, \tilde{\boldsymbol{y}})$, we have

$$\boldsymbol{y}^T \mathbb{H} \boldsymbol{y} = \frac{\|\bar{\boldsymbol{y}} - y_a \boldsymbol{u}\|^2}{m_2} + \frac{\|\tilde{\boldsymbol{y}} - y_b \boldsymbol{u}^d\|^2}{m_2} + \frac{(m_1^d)^2(\alpha_1^d y_b - m_1^d y_c)^2}{(\alpha_1^d)^5}\left(\frac{m_1^d c_1^2}{\alpha_1^d} + 4p_1\right) + \frac{m_2^2((1-\alpha_1^d)y_a + m_2 y_c)^2}{(\alpha_1^d)^5}\left(\frac{m_2 c_2^2}{1-\alpha_1^d} + 4p_2\right) \geq 0. \tag{1.157}$$

$\mathcal{H}$ is then a mathematical entropy for the Model 10.

1.4.3.2 Hyperbolicity

As the model is rotational invariant, we consider only a one-dimensional model for the hyperbolicity study, and we choose the primitive set of variables

$$\boldsymbol{q} = (\alpha_1^d, m_2, u, u_d, \rho_2^a). \tag{1.158}$$

The characteristic polynomial of the Jacobian shares a similar structure to the one of the model in Raviart and Sainsaulieu (1995) and writes

$$\mathcal{P}(X) = (X - u_d)\mathcal{Q}(X), \qquad \mathcal{Q}(X) = \left((X-u)^2 - c_2^2\right)\left(\frac{\rho_2^a}{2\rho_1^d}(u-u_d)^2 - (X-u_d)^2\right) + (X-u)^2 \frac{\rho_2 \alpha_1^d c_2^2}{(1-\alpha_1^d)\rho_1^d}. \tag{1.159}$$

We pursue a similar study considering the fourth-order polynomial $\mathcal{Q} =: aX^4 + bX^3 + cX^2 + dX + e$. The existence of four distinct real roots is given by the positivity of the determinant $\Delta_{\mathcal{Q}}$ along with the negativity of

$$P := 8ac - 3b^2, \qquad D := 64a^3 e - 16a^2 c^2 + 16ab^2 c - 16a^2 bd - 3b^4. \tag{1.160}$$

At first-order in both $(u-u_d)^2$ and α_1^d, we have

$$\Delta_{\tilde{\mathcal{Q}}} \sim \frac{8(u-u_d)^2 c_2^{10}}{(\rho_1^d)^2}\left(4\rho_2 \rho_2^a \alpha_1^d + \rho_1^d(\rho_2^a - 2\rho_2 \alpha_1^d)\right) \qquad P \sim -8c_2^2, \qquad D \sim -16 c_2^4. \tag{1.161}$$

Then, the hyperbolicity conditions $(\Delta_{\tilde{\mathcal{Q}}} > 0) \cap (P < 0) \cap (D < 0)$ are fulfilled in such neighbourhood under the sufficient condition

$$\alpha_1^d < \frac{\rho_1^d \rho_2^a}{2\rho_2(\rho_1^d - 2\rho_2^a)}. \tag{1.162}$$

For gaseous and liquid densities classically ordered such that $\rho_2^a \approx \rho_2 \ll \rho_1^d$, the hyperbolicity condition boils down to

$$\alpha_1^d < \frac{1}{2}, \tag{1.163}$$

which is reasonable for many disperse flows. Remark that the condition $\rho_2^a \approx \rho_2$ could be similarly expressed using the conservative set of variables of Model 10 as

$$e^a \approx \frac{1}{2}\frac{m_2 \alpha_1^d}{1-\alpha_1^d}(\boldsymbol{u} - \boldsymbol{u}^d)^2. \tag{1.164}$$

Such model demonstrates that hyperbolicity of a two-velocity model can be achieved with added-mass solely at least for a certain disperse flow regime.

1.4.3.3 Dissipation

From the non-dissipative Model 10 and the condition (1.164), we propose to add a relaxation process of e^a towards $\frac{1}{2}\frac{m_2 \alpha_1^d}{1-\alpha_1^d}(\boldsymbol{u} - \boldsymbol{u}^d)^2$. This corresponds to an exchange of kinetic energy between the bulk kinetic energies and the

corrective term e^a. Hence, we consider the following system with a scalar source term R_a and a vector-valued source term $\boldsymbol{R}$ for the following equations

$$\begin{cases} \partial_t e^a + \boldsymbol{\nabla}\cdot(e^a\boldsymbol{u}^d) = R_a, \\ \partial_t(m_2\boldsymbol{u}) \ +\boldsymbol{\nabla}\cdot(m_2\boldsymbol{u}\otimes\boldsymbol{u} + (1-\alpha_1^d)p_2\boldsymbol{I}) \qquad +p_2\boldsymbol{\nabla}\alpha_1^d = \boldsymbol{R}, \\ \partial_t(m_1^d\boldsymbol{u}^d)+\boldsymbol{\nabla}\cdot(m_1^d\boldsymbol{u}^d\otimes\boldsymbol{u}^d + \frac{1}{2}\rho_2^a\alpha_1^d(\boldsymbol{u}-\boldsymbol{u}^d)^2\boldsymbol{I})+\alpha_1^d\boldsymbol{\nabla}p_2 = -\boldsymbol{R}, \end{cases} \tag{1.165}$$

such that the total momentum is still conserved. The mathematical entropy production rate associated with $\mathcal{H}$ for this system reads

$$\partial_t\mathcal{H} + \boldsymbol{\nabla}\cdot\left[\left(\mathcal{H}_2 + (1-\alpha_1^d)p_2\right)\boldsymbol{u} + \left(\mathcal{H}_1^d + e^a + \alpha_1^d p_2\right)\boldsymbol{u}^d\right] = \boldsymbol{R}(\boldsymbol{u}-\boldsymbol{u}^d) + R_a. \tag{1.166}$$

We would like now to enforce the relaxation while having a negatively signed mathematical entropy production rate. We propose the following choice for $\mu > 0$

$$R_a = -\frac{1}{\mu}e^a(1-\alpha_1^d)\left(e^a - \frac{1}{2}\frac{m_2\alpha_1^d}{1-\alpha_1^d}(\boldsymbol{u}-\boldsymbol{u}^d)^2\right), \qquad \boldsymbol{R} = -\frac{1}{\mu}\frac{\alpha_1^d m_2}{2}\left(e^a - \frac{1}{2}\frac{m_2\alpha_1^d}{1-\alpha_1^d}(\boldsymbol{u}-\boldsymbol{u}^d)^2\right)(\boldsymbol{u}-\boldsymbol{u}^d). \tag{1.167}$$

These source terms yield

$$\partial_t\mathcal{H} + \boldsymbol{\nabla}\cdot\left[\left(\mathcal{H}_2 + (1-\alpha_1^d)p_2\right)\boldsymbol{u} + \left(\mathcal{H}_1^d + e^a + \alpha_1^d p_2\right)\boldsymbol{u}^d\right] = -\frac{1}{\mu}(1-\alpha_1^d)\left(e^a - \frac{1}{2}\frac{m_2\alpha_1^d}{1-\alpha_1^d}(\boldsymbol{u}-\boldsymbol{u}^d)^2\right)^2 \leq 0, \tag{1.168}$$

and the final set of equations is gathered in Model 11.

Model 11 (Two-velocity disperse model with added mass and relaxation)

With $m_k = \alpha_k\rho_k$ and α_k the phase densities and volume fractions of phases $k = 2, 1^d$, ρ_2^a the density of the incompressible *d'Alembert* flow, $\boldsymbol{u}$, the velocity of the carrier phase, $\boldsymbol{u}^d$ the velocity of the inclusions and $p_2(\rho_2)$ the pressure of the gaseous phase 2,

$$\begin{cases} \partial_t m_2 + \boldsymbol{\nabla}\cdot(m_2\boldsymbol{u}) \ = 0, \\ \partial_t m_1^d + \boldsymbol{\nabla}\cdot(m_1^d\boldsymbol{u}^d) = 0, \\ \partial_t \alpha_1^d + \boldsymbol{\nabla}\cdot(\alpha_1^d\boldsymbol{u}^d) = 0, \\ \partial_t e^a \ +\boldsymbol{\nabla}\cdot(e^a\boldsymbol{u}^d) = R_a, \\ \partial_t(m_2\boldsymbol{u}) \ +\boldsymbol{\nabla}\cdot(m_2\boldsymbol{u}\otimes\boldsymbol{u} + (1-\alpha_1^d)p_2\boldsymbol{I}) \qquad +p_2\boldsymbol{\nabla}\alpha_1^d = \boldsymbol{R}, \\ \partial_t(m_1^d\boldsymbol{u}^d)+\boldsymbol{\nabla}\cdot(m_1^d\boldsymbol{u}^d\otimes\boldsymbol{u}^d + \frac{1}{2}\rho_2^a\alpha_1^d(\boldsymbol{u}-\boldsymbol{u}^d)^2\boldsymbol{I})+\alpha_1^d\boldsymbol{\nabla}p_2 = -\boldsymbol{R}, \end{cases}$$

with

$$R_a = -\frac{1}{\mu}e^a(1-\alpha_1^d)\left(e^a - \frac{1}{2}\frac{m_2\alpha_1^d}{1-\alpha_1^d}(\boldsymbol{u}-\boldsymbol{u}^d)^2\right),$$

and

$$\boldsymbol{R} = -\frac{1}{\mu}\frac{\alpha_1^d m_2}{2}\left(e^a - \frac{1}{2}\frac{m_2\alpha_1^d}{1-\alpha_1^d}(\boldsymbol{u}-\boldsymbol{u}^d)^2\right)(\boldsymbol{u}-\boldsymbol{u}^d).$$

However, there is no linear operator nullifying the relaxation source terms while keeping a two-velocity model as considered in (1.7) in the theoretical framework of Chen et al. (1994); Bouchut (2004). Then, we cannot conclude regarding the convergence of the model towards its formal limit when $\mu \to 0$. Besides, despite being hyperbolic, the formal limit of Model 11 with two velocities is showed not to admit any entropy flux associated with the mathematical entropy of Model 11.

Therefore, one should rather interpret these source terms for a finite value of μ as a drag interaction between the bulk flow and the *d'Alembert* flow around the particle. One could also add a second and independent drag contribution with $\lambda > 0$ such that

$$\begin{cases} \partial_t(m_2\boldsymbol{u}) \ +\boldsymbol{\nabla}\cdot(m_2\boldsymbol{u}\otimes\boldsymbol{u}+(1-\alpha_1^d)p_2\boldsymbol{I}) & +p_2\boldsymbol{\nabla}\alpha_1^d = \boldsymbol{R} \ -\lambda(\boldsymbol{u}-\boldsymbol{u}^d), \\ \partial_t(m_1^d\boldsymbol{u}^d)+\boldsymbol{\nabla}\cdot(m_1^d\boldsymbol{u}^d\otimes\boldsymbol{u}^d+\frac{1}{2}\rho_2^a\alpha_1^d(\boldsymbol{u}-\boldsymbol{u}^d)^2\boldsymbol{I})+\alpha_1^d\boldsymbol{\nabla}p_2 = -\boldsymbol{R}+\lambda(\boldsymbol{u}-\boldsymbol{u}^d), \end{cases} \tag{1.169}$$

and the associated mathematical entropy production

$$\partial_t\mathcal{H}+\boldsymbol{\nabla}\cdot\left[\left(\mathcal{H}_2+(1-\alpha_1^d)p_2\right)\boldsymbol{u}+\left(\mathcal{H}_1^d+e^a+\alpha_1^d p_2\right)\boldsymbol{u}^d\right] = -\frac{1}{\mu}(1-\alpha_1^d)\left(e^a-\frac{1}{2}\frac{m_2\alpha_1^d}{1-\alpha_1^d}(\boldsymbol{u}-\boldsymbol{u}^d)^2\right)^2-\lambda(\boldsymbol{u}-\boldsymbol{u}^d)^2\leq 0. \tag{1.170}$$

In the end, these models provide us with hyperbolic two-velocity models for a disperse regime with incompressible and rigid inclusion, particularly for small velocity differentials and volume fraction of the disperse phase. This has been possible thanks to an original accounting of added-mass effect in the derivation of the model with Hamilton's SAP. Moreover, the proposed dissipation processes bring to light a particular exchange of kinetic energy between the phases, that can be interpreted as a drag phenomenon. One can consider these drag terms as which complementary with the classic form of drag forces. However, these models have not provided a non-dissipative two-velocity model showcasing both hyperbolicity and a mathematical entropy.

Conclusion of chapter 1

We proposed in this chapter an overview of multi-fluid modelling with a specific emphasis on the models dedicated either the separated or the disperse regime as they are used in the upcoming chapter. We introduced well-known but key elements that are used in the remaining of this manuscript :

- Mathematical properties regarding the mathematical properties of systems of conservation laws;
- The derivation of multi-fluid models with Hamilton's Stationary Action Principle in both the separated and disperse regime.

Moreover, we also proposed original contributions with :

- The accounting of added-mass for hyperbolic disperse multi-fluid models with two velocities.

This chapter particularly highlights the main challenges associated with the modelling of two-phase flow with the local description of the interfaces or the thermodynamics. We particularly address separately the multi-fluid models whether they correspond to a separated flow regime or a disperse flow regime. Indeed, Hamilton's SAP addresses these two classes of models by requiring *a priori* the modelling of both the interface regime and the thermodynamics of the mixture rather than the *a posteriori* interpretation or modelling occurring for averaged models or models via the *Landau* approach. Furthermore, the combination of Hamilton's SAP with the analysis of dissipation processes ensures the second principle of thermodynamics along with a better identification of the dissipative source terms. This last topic is fundamental for both the physics and mathematical consistency of the models and the upcoming numerical schemes. Finally, we showed that the Hamilton's SAP proposes an intuitive modelling approach through the definition of the Lagrangian, a scalar quantity gathering all the physics of the two-phase mixture. It allows to both recover existing models of the literature, notably in the separated regime, and propose new models in the disperse regime to account for the added mass effects of inclusions with their own mean velocity.

We have demonstrated here the modelling flexibility of Hamilton's SAP for the derivation of multi-fluid models by including the energies associated with the desired physical phenomena. It helps us to build a hierarchy of reduced-order models by successively adding these energies, particularly for the modelling of the small-scale dynamics as for the *d'Alembert* flow of Section 1.4.3 or the dynamics of the interface as studied in Chapter 2. Moreover, it offers the potential to combine the different multi-fluid models together as investigated in Chapter 3.

Appendix

1.A Hyperbolicity of augmented model with capillarity

The system of conservation equations modelling our two-phase flow with capillarity (see Model 6) involves fluxes, which not only depend on the set of conserved variables, but also on their gradients, in particular for α_1. A possible mean to study the mathematical properties of the system consists in considering an augmented system of equation including a new conserved variable $\boldsymbol{w} := \boldsymbol{\nabla}\alpha_1$. Depending on capillarity fluxes model, the system may still involve derivative of the conservative variables, and it is possible to resort to a symmetrization of the system using entropy variables in order to study the structure of the resulting system of Partial Differential Equations (PDEs) (Gavrilyuk and Gouin, 1999; Giovangigli et al., 2023).

Nevertheless, within the framework of our model, a study of hyperbolicity for Model 6 can be led under the following assumptions along the same lines as Schmidmayer et al. (2017): 1- we consider an augmented system of conservation equations, where the new variable $\boldsymbol{w}$ is introduced and satisfies an independent conservation equation. The link between $\boldsymbol{\nabla}\alpha_1$ and $\boldsymbol{w}$ is then a result of initial conditions and of the dynamics of the system of PDEs. 2- Even if we rely on this augmented variable, we are still in the presence of gradients of the conserved variables in the sources terms, where the mean curvature involves the derivative of $\boldsymbol{w}$. These terms are still considered as source terms and are supposed to be local fields, in the sense that they are not taken into account in the convective part of the system.

We then consider an augmented model with $\boldsymbol{w}$ as an independent variable. Taking the gradient of the equation on α_1 leads to

$$\partial_t \boldsymbol{w} + \boldsymbol{\nabla}(\boldsymbol{u} \cdot \boldsymbol{w}) = \boldsymbol{S}, \tag{1.171}$$

where $\boldsymbol{S}$ is a source term which does not impact the hyperbolicity study. We then consider the following first-order homogeneous system

$$\begin{cases} \partial_t m_k + \boldsymbol{\nabla} \cdot (m_k \boldsymbol{u}) = 0, \qquad k = 1, 2, \\ \partial_t \alpha_1 + \boldsymbol{u} \cdot \boldsymbol{\nabla}\alpha_1 = 0, \\ \partial_t \boldsymbol{w} + \boldsymbol{\nabla}(\boldsymbol{u} \cdot \boldsymbol{w}) = 0, \\ \partial_t(\rho \boldsymbol{u}) + \boldsymbol{\nabla} \cdot \left[\rho \boldsymbol{u} \otimes \boldsymbol{u} + (p - \sigma \|\boldsymbol{w}\|)\mathbf{I} + \sigma \frac{\boldsymbol{w} \otimes \boldsymbol{w}}{\|\boldsymbol{w}\|} \right] = 0. \end{cases} \tag{1.172}$$

Remark that the above system is not rotational invariant as the equation on $\boldsymbol{w}$ is not an equation of conservation and that hyperbolicity must be studied for each direction $\boldsymbol{\omega}$ with $\|\boldsymbol{\omega}\| = 1$. Denote the primitive set of variables $\boldsymbol{q} = (m_1, m_2, \alpha_1, w_x, w_y, w_z, u_x, u_y, u_z)$. We consider a smooth solution such that we look for a quasi-linear form

$$\partial_t \boldsymbol{q} + \mathbf{A}_x(\boldsymbol{q})\partial_x \boldsymbol{q} + \mathbf{A}_y(\boldsymbol{q})\partial_y \boldsymbol{q} + \mathbf{A}_z(\boldsymbol{q})\partial_z \boldsymbol{q} = \mathbf{0}, \tag{1.173}$$

with $\mathbf{A}_i$ are the Jacobian matrices in the direction i. Denote $\boldsymbol{n} := \boldsymbol{w}/\|\boldsymbol{w}\|$ and $\Delta p := p_1 - p_2$, then (1.172) admits a linearized form with, for each direction i the Jacobian matrices $\mathbf{A}_i$. As the system is not rotational invariant, consider

then the direction $\boldsymbol{\omega}$ with $\|\boldsymbol{\omega}\| = 1$. Let us study then the eigenvalues of the Jacobian matrix $\mathbf{A}_{\boldsymbol{\omega}} := \omega_x \mathbf{A}_x + \omega_y \mathbf{A}_y + \omega_z \mathbf{A}_z$ associated with this direction. The characteristic polynomial $P_{\boldsymbol{\omega}}$ of $\mathbf{A}_{\boldsymbol{\omega}}$ reads

$$P_{\boldsymbol{\omega}}(\lambda) = (\lambda - u_{\boldsymbol{\omega}})^8 \left[(\lambda - u_{\boldsymbol{\omega}})^4 + (\lambda - u_{\boldsymbol{\omega}})^2 (-c_F^2 - \frac{\sigma}{\rho}\|\boldsymbol{w}\|(1 - (\boldsymbol{\omega}\cdot\boldsymbol{n})^2)) + c_F^2 \frac{\sigma}{\rho}\|\boldsymbol{w}\|(1 - (\boldsymbol{\omega}\cdot\boldsymbol{n})^2) \right], \tag{1.174}$$

with $u_{\boldsymbol{\omega}} = \boldsymbol{u}\cdot\boldsymbol{\omega}$. Denote $u_{\boldsymbol{\omega}} := \boldsymbol{u}\cdot\boldsymbol{\omega}$, $\boldsymbol{n} := \boldsymbol{\nabla}\alpha_1/\|\boldsymbol{\nabla}\alpha_1\|$, $\psi = \sigma\|\boldsymbol{\nabla}\alpha_1\|/(\rho c_F^2)$, c_F, the velocity, a geometrical-physical parameter and the two-scale frozen sound speed as established in (1.111), the roots of $P_{\boldsymbol{\omega}}$ gives the following eigenvalues

$$\lambda_{1,2,3,4,5} = u_{\boldsymbol{\omega}}, \tag{1.175}$$

$$\lambda_{6,7} = u_{\boldsymbol{\omega}} \pm c_F \sqrt{\frac{1}{2}\left[1 + \psi(1 - (\boldsymbol{\omega}\cdot\boldsymbol{n})^2)\right] + \frac{1}{2}\sqrt{\left[1 - \psi(1 - (\boldsymbol{\omega}\cdot\boldsymbol{n})^2)\right]^2 + 4\psi(1 - (\boldsymbol{\omega}\cdot\boldsymbol{n})^2)(\boldsymbol{\omega}\cdot\boldsymbol{n})^2}}, \tag{1.176}$$

$$\lambda_{8,9} = u_{\boldsymbol{\omega}} \pm c_F \sqrt{\frac{1}{2}\left[1 + \psi(1 - (\boldsymbol{\omega}\cdot\boldsymbol{n})^2)\right] - \frac{1}{2}\sqrt{\left[1 - \psi(1 - (\boldsymbol{\omega}\cdot\boldsymbol{n})^2)\right]^2 + 4\psi(1 - (\boldsymbol{\omega}\cdot\boldsymbol{n})^2)(\boldsymbol{\omega}\cdot\boldsymbol{n})^2}}. \tag{1.177}$$

As $u_{\boldsymbol{\omega}}$ is a multiple eigenvalue, we are particularly interested in whether there are as many independent eigenvectors associated with $u_{\boldsymbol{\omega}}$ as the degree of multiplicity which is here 5. Remark that the eigenvectors are independent and span a subspace of dimension 3 when $\boldsymbol{n}$ and $\boldsymbol{\omega}$ are not collinear, and a subspace of dimension 4 when they are collinear. In either case, the Model 6 is weakly hyperbolic.

CHAPTER 2

Small-scale modelling

Let us now address one of the challenges of multi-fluid modelling: the lack of information about the small-scale dynamics of the interface. This geometric information is indeed at the heart of the averaged multi-fluid models (see discussion in Section 1.1.2). However, such dynamics can be very complex, and we propose here an efficient description of the small-scale such that the essential physical phenomena are represented with a minimal amount of variables. This complexity reduction is often named *reduced-order modelling*. In the context of the averaging approach, such enrichment of the usual models is proposed with the dynamics of geometric variables such as the interface area density (Vallet and Borghi, 1999; Chesnel et al., 2011), the mean curvature or the Gauss curvature (Drew, 1990; Pope, 1988). Their evolutions are obtained from the averaged kinematics of a deformed interface. Their dynamics, *i.e.* the cause of their of evolution, is then prescribed by closing the remaining averaged terms. Most of the time, these additional geometric variables account for all the scales of the interface *i.e.* the large-scale ones, which can be accessed from the volume fraction field, and the small-scale ones that are below the resolution length-scale. The closure of their dynamics is tractable only for certain regimes. For instance, in the disperse regime, such closures are reachable thanks to, either the isotropic assumption or the simplified dynamics of the closed interfaces of inclusions (Lhuillier, 2004). Multi-fluid models based on small-scale geometric variables have started to be proposed in the works of Devassy et al. (2015); Essadki et al. (2016); Drui et al. (2019); Cordesse et al. (2020); Di Battista (2021); Granger (2023), but are both restricted to the disperse regime and do not provide a general framework to include any kind of dynamics of the interface, associated with an identified mechanism (pulsation, oscillation, ...) for the inclusions.

In this chapter, we introduce an efficient framework to build small-scale reduced-order model by combining kinematic relations from differential geometry, a statistical description with a Geometric Method of Moments, and the Hamilton's SAP to derive the associate dynamics. Following the lines of the works aforementioned, the small-scale models are assumed to be in a disperse regime with a set of closed interface representing the inclusions (droplets or bubbles). Despite having their dynamics based on the disperse regime, the small-scale models should be expressed in terms of geometric quantities defined for any regime and accounting for a dynamical interface and not just static geometric quantities as previously considered in Essadki et al. (2019). Such a feature is essential for the extension to generic interface in movement which cannot rely on variables only defined for static disperse inclusions. Nevertheless, the disperse regime allows using efficient kinematic relations between the geometric variables, which can be used to describe the dynamics of the inclusions such as compressible pulsation or incompressible oscillation. The disperse regime assumption also gives the opportunity to rely on kinetic models, benefiting from a large existing literature (Williams, 1958; O'Rourke and Amsden, 1987; Laurent and Massot, 2001; Laurent et al., 2004; Essadki et al., 2018). The reduced-order models are then derived with a method of moments which reduces the multidimensional kinetic equation to a finite set of scalar equations. Following the lines of Essadki (2018); Essadki et al. (2019), we introduce the Geometric Method of Moments which extends the statistical definition of moments to an interpretation in terms of surface averages of geometric quantities. Such a property provides an interpretation of the small-scale models in the disperse regime with closed inclusions, but also in the mixed regime where the small scales correspond to a portion of an open interface. We particularly extend here this method to account for the dynamics of the inclusions

for droplet oscillation and bubble pulsation, and this extension has lead to the following contribution :

- For the two-scale modelling approach: Loison, Arthur, Teddy Pichard, Samuel Kokh, and Marc Massot. " Two-scale modelling of two-phase flows based on the Stationary Action Principle and a Geometric Method Of Moments". arXiv, 2023. https://doi.org/10.48550/arXiv.2308.15641.

We start with the introductory Section 2.1 on differential geometry with definition and properties related to the geometric quantities, firstly defined for a local point of any smooth interface, and secondly integrated over a closed interface or a set of closed interfaces as it occurs in the disperse regime. We discuss the equations of evolution of such variables starting from kinematics with only geometric considerations, and we introduce the associated equations for the modelling of dynamics. The Section 2.2 is dedicated to the detailed steps of the derivation technique for models in the disperse regime with the new framework combining Hamilton's SAP and GeoMOM. We then apply the method for the derivation of the new small-scale models including either a spray of droplets, with or without oscillation motion, or a pulsating bubbly flow like the one considered in Drui et al. (2019).

2.1 Introducing geometric variables

The aim of this section is to define the geometric quantities which we want to use to characterize the interface dynamics in the multi-fluid models. We propose the following guideline: 1- Defining some geometric quantities of interest to characterize the local geometry; 2- Extend their definitions to surface-averaged quantities to build quantities interpretable in both the separated and disperse regimes, 3- Determine the kinematic relations between them to assess potential redundancies of information, 4- Give them a probabilistic framework to define ensemble-averaged geometric quantities compatible with multi-fluid models. We particularly want to identify quantities that can describe the small-scale dynamics be it in the separated regime or the disperse regime.

We start in Section 2.1.1 with elementary definitions of local and surface-averaged quantities. In Section 2.1.2, we propose a probabilistic definition of the geometric variables to describe either a complex and fluctuating geometry in the mixed regime or the fluctuations within a large collection of inclusions as in the disperse regime. Along with these definitions, we recall and derive essential formulas in Section 2.1.3 describing the kinematics of these quantities under the deformation of the surface, regardless of the underlying cause of this deformation. After discussing how these descriptions relate to each other, we provide in Section 2.1.4 the means for the derivation of a system of PDEs involving the dynamics of the interface for the different regimes.

2.1.1 Elements of differential geometry for deterministic surfaces

The purpose of this section is to provide the definitions of the quantities and operators that are later used to define the dynamics of the inclusions, the geometry of which is impacted by the dynamics. There is no contribution contained in the following section 2.1.1.1, and the reader familiar with the concepts of differential geometry can skip it. However, we underline the presence of key definitions namely: the surface Laplace operator or *Laplace-Beltrami* operator (see Definition 8), the mean and Gauss curvatures (see Definition 10).

2.1.1.1 Local geometric quantities

The definition of the geometric quantities of interest relies on differential geometry which is reduced here to its most elementary elements. For a more exhaustive introduction to this mathematical domain, the reader is referred to Kreyszig (1991) or the introduction notes of Deserno (2015). To help the non-experienced reader and for the following application, we will systematically illustrate the definitions and properties with the simple example of the sphere. From now, we use the Einstein summation rule on repeated indices.

We follow here an explicit formalism where we consider a surface $\mathcal{S}$ defined by mapping a set $\mathcal{U} \subset \mathbb{R}^2$ onto $\mathcal{S} \subset \mathbb{R}^3$

$$\mathcal{S} := \left\{ \boldsymbol{r}(u^1, u^2) \in \mathbb{R}^3, \quad (u^1, u^2) \in \mathbb{R}^2 \right\}. \tag{2.1}$$

Example 2

The sphere of radius R can be defined with the colatitude-longitude $(\theta, \phi) \in \mathcal{U} = [0, \pi] \times [0, 2\pi]$ convention, which reads in the Cartesian coordinates of $\mathbb{R}^3$,

$$\boldsymbol{r}(\theta, \phi) = \begin{pmatrix} R \sin\theta \cos\phi \\ R \sin\theta \sin\phi \\ R \cos\theta \end{pmatrix}.$$

2.1.1.1.a Local orthogonal basis

We assume the function $\boldsymbol{r}$ to be sufficiently smooth, at least twice differentiable with respect to u and v, to locally define around a point of coordinate (u_0, v_0), a local orthonormal basis, composed of two tangential vectors and a normal one.

Definition 5 (Tangent vectors)

For an explicit definition of the surface (2.1), the tangent vectors are defined by

$$\boldsymbol{e}_{u^1} := \partial_{u^1} \boldsymbol{r}, \qquad \boldsymbol{e}_{u^2} := \partial_{u^2} \boldsymbol{r},$$

where we purposely omit the dependencies on (u_0, v_0) for readability purposes.

Using the convention of an outward normal unit vector, we define $\boldsymbol{n}$ with

$$\boldsymbol{n} := \frac{\boldsymbol{e}_{u^1} \times \boldsymbol{e}_{u^2}}{|\boldsymbol{e}_{u^1} \times \boldsymbol{e}_{u^2}|}, \tag{2.2}$$

such that $(\boldsymbol{e}_{u^1}, \boldsymbol{e}_{u^2}, \boldsymbol{n})$ locally define a direct orthogonal basis.

Example 3

With the chosen parametrization of the sphere, the orthogonal basis simply reads

$$\boldsymbol{e}_\theta = \begin{pmatrix} R \cos\theta \cos\phi \\ R \cos\theta \sin\phi \\ -R \sin\theta \end{pmatrix}, \quad \boldsymbol{e}_\phi = \begin{pmatrix} -R \sin\theta \sin\phi \\ R \sin\theta \cos\phi \\ 0 \end{pmatrix}, \quad \boldsymbol{n} = \begin{pmatrix} \sin\theta \cos\phi \\ \sin\theta \sin\phi \\ \cos\theta \end{pmatrix}.$$

2.1.1.1.b Metric - First fundamental form

One of the first important quantities arising in differential geometry is the metric, or first fundamental form, $\mathbf{g}$ or (g_{ij}) with $i, j \in 1, 2$.

Definition 6 (Metric - First fundamental form)

The metric matrix defined by the local tensor product of tangential vectors

$$g_{ij} := \boldsymbol{e}_i \cdot \boldsymbol{e}_j. \tag{2.3}$$

We particularly denote g the determinant of $\mathbf{g}$.

Remark that the metric is symmetric and invertible, we note on purpose its inverse g^{ij} such that

$$(g^{ij}) = \frac{1}{g}\begin{pmatrix} g_{22} & -g_{21} \\ -g_{12} & g_{11} \end{pmatrix}. \tag{2.4}$$

Example 4

For the sphere, we have

$$\mathbf{g} = \begin{pmatrix} R^2 & 0 \\ 0 & R^2 \sin^2\theta \end{pmatrix}.$$

The purpose of this quantity is to represent the change of basis between the tangent space, *i.e.* the linear approximation of the surface around $\boldsymbol{r}(u_0, v_0)$, and the cotangent space, *i.e.* its dual basis of real-valued functions derivatives defined on $\mathcal{S}$ around $\boldsymbol{r}(u_0, v_0)$.

Example 5

For the sphere, the tangent space around the top point $\boldsymbol{x}_T = (0,0,1)^T$, is

$$\mathcal{T}_{\boldsymbol{x}_T} = \boldsymbol{x}_T + Vect\left(\boldsymbol{e}_\theta(\boldsymbol{x}_T), \boldsymbol{e}_\phi(\boldsymbol{x}_T)\right).$$

The cotangent space $\widetilde{\mathcal{T}}$ is the dual space of linear forms which can be represented by the basis

$$\widetilde{\mathcal{T}} = Vect\left(v^\theta, v^\phi\right), \quad v^j(e_i) = \delta_i^j,$$

v^θ and v^ϕ can be chosen as the scalar products against vectors $\boldsymbol{e}_\theta/\|\boldsymbol{e}_\theta\|$ and $\boldsymbol{e}_\phi/\|\boldsymbol{e}_\phi\|$.

Consider a valid change of basis from (u^1, u^2) to $(\overline{u}^1, \overline{u}^2)$ with $\partial u^j/\partial \overline{u}^i$ invertible. Then, we qualify as a co-variant transformation, the relation between quantities a_i in basis (u^1, u^2) and $\overline{a}_i$ in basis $(\overline{u}^1, \overline{u}^2)$ behaving as

$$\overline{a}_i = a_j \frac{\partial u^j}{\partial \overline{u}^i}, \quad \text{or equivalently,} \quad a_j = \overline{a}_i \frac{\partial \overline{u}^i}{\partial u^j}, \tag{2.5}$$

and contra-variant the relations between b^i and $\overline{b}^i$ such that

$$\overline{b}^i = b^j \frac{\partial \overline{u}^i}{\partial u^j}, \quad \text{or equivalently,} \quad b^j = \overline{b}^i \frac{\partial u^j}{\partial \overline{u}^i}. \tag{2.6}$$

Example 6

Basis vectors $(\boldsymbol{e}_\theta, \boldsymbol{e}_\phi)$ *are co-variant quantities into* $(\overline{\boldsymbol{e}}_{\overline{\theta}}, \overline{\boldsymbol{e}}_{\overline{\phi}})$ *with the change of basis* $(\overline{\theta}, \overline{\phi}) := (\pi - \theta, \phi + 2\theta)$ *gives*

$$\overline{\boldsymbol{e}}_{\overline{\theta}} = \begin{pmatrix} -R(2\sin\theta\sin\phi + \cos\theta\cos\phi) \\ R(2\sin\theta\cos\phi - \cos\theta\sin\phi) \\ R\sin\theta \end{pmatrix}, \quad \overline{\boldsymbol{e}}_{\overline{\phi}} = \begin{pmatrix} -R\sin\theta\sin\phi \\ R\sin\theta\cos\phi \\ 0 \end{pmatrix},$$

$$\frac{\partial\theta}{\partial\overline{\theta}} = -1, \quad \frac{\partial\theta}{\partial\overline{\phi}} = 0, \quad \frac{\partial\phi}{\partial\overline{\theta}} = 2, \quad \frac{\partial\phi}{\partial\overline{\phi}} = 1.$$

We verify the co-variant property with $\overline{\boldsymbol{e}}_{\overline{\theta}} = -\boldsymbol{e}_\theta + 2\boldsymbol{e}_\phi$ *and* $\overline{\boldsymbol{e}}_{\overline{\phi}} = \boldsymbol{e}_\phi$. *The contra-variant property is however not verified as*

$$\frac{\partial\overline{\theta}}{\partial\theta} = -1, \quad \frac{\partial\overline{\theta}}{\partial\phi} = 0, \quad \frac{\partial\overline{\phi}}{\partial\theta} = 2, \quad \frac{\partial\overline{\phi}}{\partial\phi} = 1,$$

with $\overline{\boldsymbol{e}}_{\overline{\theta}} \neq -\boldsymbol{e}_\theta$ *and* $\overline{\boldsymbol{e}}_{\overline{\phi}} \neq 2\boldsymbol{e}_\theta + \boldsymbol{e}_\phi$.

Example 7

Conversely, one can show that the components λ^i *of a vector of a tangent space is contravariant, say* $\boldsymbol{w} = \lambda^\theta \boldsymbol{e}_\theta + \lambda^\phi \boldsymbol{e}_\phi$. *Writing the vector* $\boldsymbol{w}$ *in any other basis* $(\overline{\boldsymbol{e}}_{\overline{\theta}}, \overline{\boldsymbol{e}}_{\overline{\phi}})$ *gives*

$$\boldsymbol{w} = \overline{\lambda}^i \overline{\boldsymbol{e}}_i = \overline{\lambda}^i \overline{\boldsymbol{e}}_j \frac{\partial u^j}{\partial \overline{u}^i},$$

by unicity of the decomposition, we have then

$$\overline{\lambda}^j = \overline{\lambda}^i \frac{\partial u^j}{\partial \overline{u}^i}.$$

Remark also that the differentials are contravariant,

$$d\overline{u}^i = \frac{\partial \overline{u}^i}{\partial u^j} du^j. \tag{2.7}$$

Both covariant and contravariant quantities vary under a change of basis, but the contraction of co-variant and contra-variant quantities $a_i b^i$ are invariant under a change of basis as

$$\overline{a}_i \overline{b}^i = a_j \frac{\partial u^j}{\partial \overline{u}^i} b^j \frac{\partial \overline{u}^i}{\partial u^j} = a_j b^j. \tag{2.8}$$

With the definition of the metric and the differentials, we can now define the element of surface.

Definition 7 (Element of surface)

The local element of surface dA is defined by the local metric determinant g and differentials of the basis (u^1, u^2) with

$$dA = \sqrt{g} du^1 du^2,$$

We call $\sqrt{g}$ the stretching factor.

It is also demonstrated in Kreyszig (1991) that the element of surface is a contracted quantity and, thus, is independent of the coordinate system.

Example 8

For the sphere, we have that for both respectively (θ, ϕ) *and* $(\overline{\theta}, \overline{\phi})$ *(as defined in Example 6) that*

$$dA = R^2 \sin\theta d\theta d\phi = R^2 \sin\overline{\theta} d\overline{\theta} d\overline{\phi}.$$

Note that the metric tensor and its inverse have the ability to respectively raise or lower an index, *i.e.* it can change a co-variant quantity into a contra-variant one and *vice-versa*, following

$$b^i = g^{ik} b_k, \qquad \text{and} \qquad a_i = g_{ik} b^k. \tag{2.9}$$

2.1.1.1.c Covariant derivation

We introduce and note the covariant derivative of a quantity f as

$$f_{,i} = \nabla_i f = \frac{\partial f}{\partial u^i}. \tag{2.10}$$

The covariant derivative ∇_i of covariant and contravariant quantities is a derivative operator which extends the notion of derivative to curved space. Its definition uses Christoffel symbols,

$$\nabla_a X^b := \partial_a X^b + X^c \Gamma^b_{ac}, \qquad \nabla_a X_b := \partial_a X_b - X_c \Gamma^c_{ab}, \tag{2.11}$$

with

$$\Gamma^c_{ab} = g^{cd} \Gamma_{abd}, \qquad \Gamma_{abd} = \frac{1}{2} \left(\partial_a g_{bd} + \partial_b g_{da} - \partial_d g_{ab} \right). \tag{2.12}$$

If X is a scalar, then there is no Christoffel symbols and $\nabla_i X = \partial_i X$.

Example 9

The Christoffel symbols for the sphere read

$$\begin{array}{llll} \Gamma^\vartheta_{\vartheta\vartheta} = 0, & \Gamma^\vartheta_{\vartheta\phi} = 0, & \Gamma^\phi_{\vartheta\vartheta} = 0, & \Gamma^\phi_{\vartheta\phi} = \cot\vartheta, \\ \Gamma^\vartheta_{\phi\vartheta} = 0, & \Gamma^\vartheta_{\phi\phi} = -\sin\vartheta\cos\vartheta, & \Gamma^\phi_{\phi\vartheta} = \cot\vartheta, & \Gamma^\phi_{\phi\phi} = 0. \end{array}$$

In the case of the sphere, these expressions simplify considerably, and we obtain

$$\begin{array}{ll} \nabla_\vartheta X^\vartheta = \partial_\vartheta X^\vartheta, & \nabla_\vartheta X^\phi = \partial_\vartheta X^\phi + X^\phi \cot\vartheta, \\ \nabla_\phi X^\vartheta = \partial_\phi X^\vartheta - X^\phi \sin\vartheta\cos\vartheta, & \nabla_\phi X^\phi = \partial_\phi X^\phi + X^\vartheta \cot\vartheta, \\ \nabla_\vartheta X_\vartheta = \partial_\vartheta X_\vartheta, & \nabla_\vartheta X_\phi = \partial_\vartheta X_\phi - X_\phi \cot\vartheta, \\ \nabla_\phi X_\vartheta = \partial_\phi X_\vartheta - X_\phi \cot\vartheta, & \nabla_\phi X_\phi = \partial_\phi X_\phi + X_\vartheta \sin\vartheta\cos\vartheta. \end{array}$$

Then, we can define the surface Laplacian or Laplace-Beltrami operator which extends the definition of the Laplace operator to a surface.

Definition 8 (Laplace-Beltrami operator)

For any scalar field X, the Laplace-Beltrami operator reads

$$\Delta X := \nabla_i \nabla^i X = \frac{1}{\sqrt{g}} \frac{\partial}{\partial u^i} \left(\sqrt{g} g^{ij} \frac{\partial X}{\partial u^j} \right).$$

Example 10

Let us develop the expression of the Laplace-Beltrami operator for the sphere,

$$\begin{aligned}\Delta X &= \nabla_\vartheta \nabla^\vartheta X + \nabla_\phi \nabla^\phi X = \partial_\vartheta \nabla^\vartheta X + \partial_\phi \nabla^\phi X + \cot\vartheta \nabla^\vartheta X \\ &= \partial_\vartheta (g^{\vartheta\vartheta} \partial_\vartheta X) + \partial_\phi g^{\phi\phi} \partial_\phi X + \cot\vartheta g^{\vartheta\vartheta} \partial_\vartheta X \\ &= \frac{1}{R^2} \partial_{\vartheta\vartheta} X + \frac{1}{R^2 \sin^2\vartheta} \partial_{\phi\phi} X + \frac{\cot\vartheta}{R^2} \partial_\vartheta X.\end{aligned}$$

We retrieve the surface Laplacian over a sphere in spherical coordinates (r, θ, ϕ) for a surface-based quantity with no dependence on r.

Moreover, on a closed surface S, we have the useful integration-by-part formula,

$$\int_S Y \nabla_i X^i dS = -\int X^i \nabla_i Y dS. \tag{2.13}$$

2.1.1.1.d Second fundamental form and curvatures

We define now the second fundamental form which expresses the deformation of curves on surfaces (see Deserno (2004) for details).

Definition 9 (Second fundamental form)

The second fundamental form is defined by the following matrix,

$$b_{ij} := -\boldsymbol{\nabla}_j \boldsymbol{e}_i \cdot \boldsymbol{n} = \boldsymbol{e}_i \cdot \boldsymbol{\nabla}_j \boldsymbol{n},$$

The two expressions in the definition of $\mathbf{b} = (b_{ij})$ are equivalent and are linked to each other by the derivation of $\boldsymbol{e}_i \cdot \boldsymbol{n} = 0$.

Example 11

For the sphere,

$$\mathbf{b} = \begin{pmatrix} R & 0 \\ 0 & R\sin\theta \end{pmatrix}.$$

Remark that we have the specific property for the sphere that $b_{ij} = \frac{g_{ij}}{R}$.

Then, from this second fundamental form, we define the mean curvature and the Gauss curvature G.

Definition 10 (Mean and Gauss curvatures)

The mean curvature H and the Gauss curvature G are contracted quantities defined from the first and second fundamental forms,

$$H := \frac{1}{2} b_i^i = \frac{1}{2} g^{ij} b_{ij}, \qquad G := \frac{b}{g},$$

with $b = \det(\mathbf{b})$.

The geometric definitions of these curvatures can also be defined from the principal curvatures κ_1, κ_2 with $H = \frac{1}{2}(\kappa_1 + \kappa_2)$ and $G = \kappa_1 \kappa_2$. The principal curvatures are the local extremal curvatures.

Example 12

For the sphere, we recover the classic result

$$H = \frac{1}{R}, \quad \text{and} \quad G = \frac{1}{R^2}.$$

Let us conclude this section by recalling in Table 2.1.1 the contracted quantities that will be of interest for the following as they provide local information about the interface independently of the basis considered. Indeed, these geometric quantities provide independent information about the local geometry, as showed by their respective definitions involving different combination of covariant derivatives. Additional independent contracted geometric quantities could have been considered but involve more complex dependencies on covariant derivatives, see their derivation in Capovilla et al. (2003) and their ordering in Deserno (2015). However, such quantities are not adapted for the scale of description in the disperse regime. We propose in the next section to define surface averages of these quantities to recover extensive quantities which can be added in order to easily extend the description of one inclusion to a collection of inclusions.

Contracted quantity	Definition
A	$\sqrt{\det(\mathbf{g})}du^1du^2$
H	$\frac{1}{2}g^{ij}b_{ij}$
G	$\frac{b}{g}$.

Table 2.1.1: Local geometric quantities as contracted quantities.

2.1.1.2 Surface-averaged geometric quantities over closed surfaces

With the geometric defined in the previous section, we can characterize the geometry of the interface with two-dimensional fields all over the surface developed by the interface. To reduce such information in the case of multiple sets of closed interface, as it occurs in the disperse regime, we propose now to study integrated quantities over closed interfaces. We consider a single closed surface $\mathcal{S}$, enclosing a volume $\mathcal{V}$, defined by mapping a set $\mathcal{U} \subset \mathbb{R}^2$ onto $\mathcal{S} \subset \mathbb{R}^3$ such that we denote $A(u^1, u^2) = \sqrt{g}$ the local infinitesimal surface element defined in 2.1.1.1. Then, the surface area reads

$$S := \int_{\mathcal{U}} A(u^1, u^2)\, du^1 du^2, \tag{2.14}$$

and we can define a surface-average operator.

Definition 11 (Surface-average operator on a closed surface)

Given an interface defined on a two-dimensional smooth manifold $\mathcal{U}$ of surface area S and stretching factor A, the surface-average of a quantity X is defined by

$$\widetilde{(\cdot)} := \frac{1}{S}\int_{\mathcal{U}} (\cdot)\, A(u^1, u^2)\, du^1 du^2,$$

With the contracted quantities listed in Table 2.1.1, we obtain the total surface area $S = S\widetilde{1}$, the surface-averaged mean curvature $S\widetilde{H}$ and the surface-averaged Gauss curvature $S\widetilde{G}$. We prefer to multiply the averaged geometric with the surface area S to include the case of a null interface. With the divergence theorem, one can also access the

volume $V = \int_{\mathcal{V}} dV$ of a closed inclusion using

$$\widetilde{S\left(\frac{1}{3}\cdot r\right)} = \int_{\mathcal{U}} \frac{1}{3}\boldsymbol{n}\cdot\boldsymbol{r}\, A du^1 du^2 = \int_{\mathcal{V}} \boldsymbol{\nabla}\cdot\left(\frac{1}{3}\boldsymbol{r}\right) dV = V. \tag{2.15}$$

With this surface-averaging operator, we introduce the Gauss-Bonnet theorem 3 (Bonnet, 1848; Kreyszig, 1991).

> **Theorem 3 (Gauss-Bonnet theorem)**
>
> $$S\widetilde{G} = 2\pi\chi,$$
>
> where G is the Gauss curvature and χ the Euler characteristic (2 for a sphere).

This theorem gives us an invariant for inclusions sharing the same Euler characteristic. The Euler characteristic describes the topological nature of the volume. It varies when the number of holes increase (Essadki, 2018), *e.g.* between the sphere and the torus. However, it stays the same if two volumes are related to each other through a smooth deformation *e.g.* a sphere into an ellipsoid. Even if inclusions with holes can temporarily occur in gas-liquid flows, they naturally tend to recover a shape that can be obtained from a deformed sphere. Consequently, this theorem allows us to count the number of inclusions within a collection of inclusions with same Euler characteristic through the integral of a geometric property.

Note however that we have lost the independency of A, G, H through the surface-averaged process to get S, $S\widetilde{G}$, $S\widetilde{H}$ the independency of which is *a priori* unknown.

Furthermore, we now wish to extend these definitions to a probabilistic framework to define ensemble-averages of these quantities, and make them compatible with multi-fluid models both in the mixed and the disperse regimes.

2.1.2 Probabilistic definition of geometric quantities: Number Density Function *vs.* Surface Density Function

We propose now to make the geometric quantities, defined in the previous section, compatible with the ensemble-averaging interpretation of multi-fluid models in both the disperse regime and for an arbitrary open interface as it occurs in the description of the mixed or separated regimes. Such a definition is possible for each regime with a NDF in the disperse regime and a Surface Density Function (SDF) (Pope, 1988) in the separated regime. Quantities compatible with both regimes are identified by Essadki (2018) and a compatibility criterion is established. We show here that such criterion can encompass our geometric quantities of interest. We split the discussion in three stages : 1- The description of the interface in the disperse regime where its definition is reduced to a NDF evaluating geometrically as integrated values over a distribution; 2- The description of an interface in any regime with the introduction of an SDF evaluating the local geometry of an arbitrary interface; 3- The assessment of the compatibility between the two descriptions in the disperse regime through an original identification of geometric quantities, notably for the time derivatives of geometric quantities.

2.1.2.1 Definition of the NDF in the disperse regime

In the disperse regime, we assume a general framework where we have inclusions moving in a carrier fluid, and that can be deformed with their own dynamics. For the probabilistic description of such regime, let us introduce for a statistic outcome λ, a set of N barycentre locations $(\boldsymbol{x_{i,\lambda}}(t))_{i=1,\dots,N}$ with corresponding characteristics indexed by $k = 1,..,P$ gathered in a vector $\boldsymbol{\xi}_i = (\xi_{i,k}(t))$ which can include the volume, the surface, the average interface velocity, the temperature. We then define the associated NDF representing the statistical distribution of inclusions in Definition 12 with the ensemble average of Drew and Passman (1999).

Definition 12 (Number density function)

The NDF f that counts the average number of inclusions around a position $\boldsymbol{x}$ at time t with velocity $\boldsymbol{v}$ and characteristics $\hat{\boldsymbol{\xi}}$ is defined by the following ensemble average,

$$f(t,\boldsymbol{x},\boldsymbol{v},\hat{\boldsymbol{\xi}}) := \left\langle \sum_i \delta(\boldsymbol{x}-\boldsymbol{x}_{i,\lambda})\delta(\boldsymbol{v}-\dot{\boldsymbol{x}}_{i,\lambda})\delta(\hat{\boldsymbol{\xi}}-\boldsymbol{\xi}_{i,\lambda}) \right\rangle_E , \tag{2.16}$$

where $\delta(\cdot)$ is the Dirac function.

Note that the ensemble-average operator $\langle\cdot\rangle_E$ is only defined under certain conditions (Letournel, 2022) about the disperse regime that we assume to meet here. Note also that the ensemble-average operator $\langle\cdot\rangle_E$ differs from the surface-average operator $\langle\cdot\rangle$. The former averages over statistical realizations, while the latter integrate a quantity over a given surface. One can then evaluate an interface area density by integrating the NDF against the surface of the inclusions

$$\Sigma = \int_{\hat{\boldsymbol{\xi}}} S(\hat{\boldsymbol{\xi}}) f d\hat{\boldsymbol{\xi}}, \tag{2.17}$$

provided that the surface S of any inclusion can be expressed as a function of the phase-space variables $\hat{\boldsymbol{\xi}}$. We then define a moment $M_{(\beta_k)_{k=1,\dots,P+3}}$ as the integral over the phase-space of the NDF against the polynomial of $v_1, v_2, v_3, \hat{\xi}_1, \dots \hat{\xi}_P$ defined by the multi-index β_k

$$M_{\beta_k}(t,\boldsymbol{x}) = \int_{(\boldsymbol{v},\hat{\boldsymbol{\xi}})\in\mathbb{R}^3\times\hat{\Omega}} v_1^{\beta_1} v_2^{\beta_2} v_3^{\beta_3} \prod_{k=1}^{P} \hat{\xi}_k^{\beta_{k+3}} f(t,\boldsymbol{x},\boldsymbol{v},\hat{\boldsymbol{\xi}})\, d\boldsymbol{v} d\hat{\boldsymbol{\xi}}. \tag{2.18}$$

Note that if $\hat{\boldsymbol{\xi}}$ includes the surface as a variable, Σ would be a first-order moment of f. Remark also that surface-averaged quantities such as $\tilde{H}$ or $\tilde{G}$ can be included in the characteristics $\hat{\boldsymbol{\xi}}$ such that we can define averaging operators for the local population of inclusions. Such an operator can be non-weighted, but for further compatibility properties, we prefer to introduce it as a surface-weighted averaging operator as it is well-defined when there is no inclusion

$$\Sigma\langle\cdot\rangle := \int_{\boldsymbol{v},\hat{\boldsymbol{\xi}}} \widetilde{(\cdot)} S(\boldsymbol{\xi}) f d\boldsymbol{v} d\hat{\boldsymbol{\xi}}. \tag{2.19}$$

One can particularly define the surface average of mean and Gauss curvatures $\Sigma\langle H\rangle$ and $\Sigma\langle G\rangle$. Finally, let us underline that the Gauss-Bonnet theorem provides for inclusions of same genus χ that

$$\Sigma\langle G\rangle = \int_{\boldsymbol{v},\hat{\boldsymbol{\xi}}} \tilde{G} S(\hat{\boldsymbol{\xi}}) f d\boldsymbol{v} d\hat{\boldsymbol{\xi}} = \int_{\boldsymbol{v},\hat{\boldsymbol{\xi}}} 2\pi\chi f d\boldsymbol{v} d\hat{\boldsymbol{\xi}} = 2\pi\chi n, \tag{2.20}$$

where n is the number density of inclusions. This section has showed us how to extend the definition of surface-averaged quantities from one inclusion to a collection of inclusions thanks to the NDF, but such approach is restricted to the disperse regime. We discuss next the definition of geometric quantities for arbitrary surfaces.

2.1.2.2 Definition of the SDF for an arbitrary interface

Let us now tackle the probabilistic description of an interface in any kind of regime. Following the works of Pope (1988); Essadki et al. (2019), for a given outcome denoted λ of a random function $\boldsymbol{r}_\lambda : \mathbb{R}^+ \times \mathbb{R}^2 \to \mathbb{R}^3$, we define the following surface with an explicit formalism (see Section 2.1.1.1)

$$\mathcal{S}_\lambda(t) := \left\{ \boldsymbol{r}_\lambda(t,u^1,u^2) \in \mathbb{R}^3, \quad (u^1,u^2)\in\mathbb{R}^2 \right\}.$$

Note that the surface both evolves in time t and changes over the different outcomes λ. For a given outcome, we introduce surface-defined time functions $\boldsymbol{W}_\lambda : \mathbb{R}^+ \times \mathbb{R}^2 \to \mathbb{R}^P$ which provide P geometric quantities related to the

interface. These quantities stored $\boldsymbol{W}_\lambda$ account for at least for the local interface area A_λ. We introduce a single-layer generalized function F_λ, defined through its action against smooth test-functions ϕ, that locates additional geometric properties, denoted as the phase-space variables $\hat{\boldsymbol{w}}$, on the interface around the position $\boldsymbol{x}$,

$$F_\lambda(\boldsymbol{x}, t, \hat{\boldsymbol{w}}) := \phi \mapsto \int_{\mathcal{U}} \delta(\hat{\boldsymbol{w}} - \boldsymbol{W}_\lambda(t))\phi(\boldsymbol{r}_\lambda(t), \boldsymbol{W}_\lambda(t), t)A_\lambda(t)du^1du^2,$$

where the dependencies of $\boldsymbol{W}_\lambda$, $\boldsymbol{r}_\lambda$ and A_λ on u^1, u^2 were purposely dropped for the sake of readability. This definition allows defining and evaluating quantities integrated over the interface if there is some interface at $\boldsymbol{x}$ at time t and for outcome λ. If not, function F_λ is still defined but evaluates to nil.

Now, we access the probabilistic average of these surface-integrated quantities over all the outcomes to define our probabilistic geometric quantities with the SDF defined in Definition 13.

Definition 13 (Surface Density Function)

The SDF is defined as the ensemble average of F_λ,

$$F(\boldsymbol{x}, t, \hat{\boldsymbol{w}}) :=< F_\lambda(\boldsymbol{x}, t, \hat{\boldsymbol{w}}) >_E . \tag{2.21}$$

Then, one can define the probabilistic interface area density Σ as the 0^{th}-order moment of F,

$$\Sigma = \int_{\hat{\boldsymbol{w}}} F d\hat{\boldsymbol{w}}, \tag{2.22}$$

and the probabilistic surface-averaging operator as defined in Section 2.1.1.2 satisfies

$$\Sigma \langle \cdot \rangle = \int_{\hat{\boldsymbol{w}}} (\cdot) F d\hat{\boldsymbol{w}}. \tag{2.23}$$

Remark that choosing $\boldsymbol{W}_\lambda = (A_\lambda, H_\lambda, G_\lambda)$ provides Σ, $\Sigma \langle H \rangle$ and $\Sigma \langle G \rangle$ respectively as a zeroth-order moment and two first-order moments of F.

2.1.2.3 Multi-regime compatibility between the two approaches

While the definition of the NDF and the SDF has allowed us to define geometric quantities in the disperse regime and for an arbitrary interface respectively. We remark that some geometric quantities, the IAD and the surface-averaged geometric quantities can be defined with both NDF and SDF. These definitions actually provides a more general result obtained by Essadki et al. (2019) and that we tackle here.

In order to demonstrate such a result, let us first remark that the definitions of the NDF and the SDF share similarities especially when considering surface averaged characteristics for the NDF. Following Essadki et al. (2019), we introduce the Discrete SDF (DSDF) as the following generalized function

$$F^d(\boldsymbol{x}, t, \hat{\boldsymbol{w}}) := \phi(\cdot, t, \hat{\hat{\boldsymbol{w}}}) \mapsto \left\langle \sum_{i=1}^{N} \delta(\hat{\hat{\boldsymbol{w}}} - \overline{\boldsymbol{W}}_{i,\lambda}(t))\phi(\boldsymbol{x}_{i,\lambda}(t), t, \overline{\boldsymbol{W}}_{i,\lambda}(t))S_{i,\lambda}(t) \right\rangle_E ,$$

where $\overline{\boldsymbol{W}}$ only accounts for surface-averaged characteristics located at the barycentres of each inclusion. Then, the following Property 2 stands.

Property 2 (Shared moments between SDF and DSDF)

Given the SDF F depending on local interface characteristics $\boldsymbol{W}$ and the DSDF F^d defined using the same averaged characteristics $\overline{\boldsymbol{W}}$, the SDF and the DSDF share the same 0^{th}- and 1^{st}-order moments in these variables:

$$\int_{\boldsymbol{x}}\int_{\hat{\boldsymbol{w}}} F(\boldsymbol{x},t,\hat{\boldsymbol{w}})d\boldsymbol{x}d\hat{\boldsymbol{w}} = \int_{\boldsymbol{x}}\int_{\hat{\hat{\boldsymbol{w}}}} F^d(\boldsymbol{x},t,\hat{\hat{\boldsymbol{w}}})d\boldsymbol{x}d\hat{\hat{\boldsymbol{w}}},$$
$$\int_{\boldsymbol{x}}\int_{\hat{\boldsymbol{w}}} \hat{w}_k F(\boldsymbol{x},t,\hat{\boldsymbol{w}})d\boldsymbol{x}d\hat{\boldsymbol{w}} = \int_{\boldsymbol{x}}\int_{\hat{\hat{\boldsymbol{w}}}} \hat{w}_k F^d(\boldsymbol{x},t,\hat{\hat{\boldsymbol{w}}})d\boldsymbol{x}d\hat{\hat{\boldsymbol{w}}}.$$

The proof of this property can be found in Essadki et al. (2019). Remark that the phase-space variables $\hat{\hat{\boldsymbol{w}}}$ of the DSDF are obtained from the surface averages of the phase-space variables $\hat{\boldsymbol{w}}$ of the SDF. These shows that the probabilistic description for any regime with an SDF only shares zeroth- and first-order moments with the DSDF which is only defined in the disperse regime. Moreover, one has the following property,

$$f(\boldsymbol{x},t,\hat{\boldsymbol{\xi}}) = \int_{\hat{\hat{\boldsymbol{w}}}} \frac{G(\hat{\boldsymbol{\xi}})}{4\pi} F^d(\boldsymbol{x},t,\hat{\hat{\boldsymbol{w}}})\delta(\bar{\boldsymbol{w}}(\hat{\boldsymbol{\xi}}) - \hat{\hat{\boldsymbol{w}}})\, d\hat{\hat{\boldsymbol{w}}}, \tag{2.24}$$

that links the DSDF and the NDF provided that the surface-average Gauss curvature $\tilde{G}$ can be accessed through the characteristics variables $\hat{\boldsymbol{\xi}}$. The combination of these two results indicates that *all surface-averaged characteristics that can be reconstructed via* the phase-space of the NDF correspond to some zeroth-order and first-order moments of the all regime SDF. Thus, these pieces of information *may be chosen to describe the interface* is a requirement to build models that can be interpreted *in both disperse and mixed regimes*. Both the IAD and the surface averaged quantities are showed to satisfy this property Let us then state some variables equivalent to surface average characteristics that one can use for the NDF while satisfying Property 2.

(i) If the phase-space characteristics allow the reconstruction of surface average of contracted quantities such as $\widetilde{H}$, $\widetilde{G}$, or equivalently S thanks to the Gauss-Bonnet theorem, then the IAD and the surface-averaged quantities $\Sigma\langle H\rangle$ and $\Sigma\langle G\rangle$ satisfy Property 2.

(ii) As previously mentioned, the volume can also be cast as a surface average for a closed inclusion. Indeed, we have from the divergence theorem,

$$V = \int_{\mathcal{V}} dV = \int_{\mathcal{V}} \boldsymbol{\nabla}\cdot\left(\frac{1}{3}\boldsymbol{r}\right) dV = \int_{\mathcal{U}} \left(\frac{1}{3}\boldsymbol{r}\right)\cdot\boldsymbol{n} A du^1 du^2 = S\widetilde{\frac{\boldsymbol{r}\cdot\boldsymbol{n}}{3}}. \tag{2.25}$$

Then, if the volume can be reconstructed from the characteristics of the NDF, we conclude from (i) that $\Sigma\left\langle\frac{1}{3}\boldsymbol{r}\cdot\boldsymbol{n}\right\rangle$, which corresponds to the volume fraction α_1^d of the collection of inclusions in the disperse regime, satisfies Property 2.

(iii) We now propose the original accounting of time derivatives of surface-averaged quantities $\widetilde{X}$ *via* the underlying surface average $\widetilde{\dot{X} + \dot{A}/A}$. Indeed,

$$\partial_t(S\widetilde{X}) = \int_{\mathcal{U}} \partial_t((XA)) = \int_{\mathcal{U}} \left(X\frac{\dot{A}}{A} + \dot{X}\right) A = S\left(\widetilde{\dot{X} + X\frac{\dot{A}}{A}}\right), \tag{2.26}$$

which results in a first-order moment for the DSDF and the SDF. Remark that $\partial_t(S\widetilde{X}) \neq S\widetilde{\dot{X}}$. Then, it follows that $\partial_t\Sigma$, $\partial_t\alpha_1^d$, $\partial_t(\Sigma\langle H\rangle)$, and similar time derivatives satisfy Property 2. This last quantities allow us to endow the description of the interface with quantities related to its dynamics.

Conclusion of Section 2.1.2

This section provides guideline to identify geometric quantities of interest interpretable in different regimes from the description the more common NDF used in the disperse regime. Indeed, for a given model of the disperse regime described by a NDF f, one can build a DSDF F^d which transforms the counting of objects to an integration over surfaces, which is a more general approach but still defined in the disperse regime only. Then, the jump from the DSDF defined for disperse regime to the SDF defined for generic surface is only possible for a class of quantities satisfying the Property 2. This class is particularly showed to include the IAD and the mean and Gauss surface-averaged quantities, along with some non-classic time derivatives of these geometric quantities which are critical for the upcoming dynamics. This last result enables the description of interface dynamics rather than just a static description, such as polydisperse sprays in Essadki et al. (2018). Let us see a simple example of this multi-regime interpretation: the interpretability of the number density of inclusions n is restricted to the disperse regime while $\Sigma\langle G\rangle$, evaluating to $4\pi n$ in the disperse regime, has an extended interpretability out of the disperse regime. Then, using these variables enables to propose models with interpretability domains in both regimes.

2.1.3 Kinematics of the geometric quantities

Now that we have defined the geometric quantities we want to work with, we propose to investigate their equations of evolution, first in a kinematic framework where a deformation of the interface is assumed without discussing the underlying cause of the motion. The study of the origin of the underlying movement, *i.e. the dynamics* of the interface, is not provided here, and it will be discussed at the modelling stage in Section 2.1.4. The study of kinematics allows the potential identification of underlying quantities on which the geometric quantities are based. We split the discussion on the kinematics between a first part dedicated to the distortion of open surfaces and a second one to closed inclusions in the disperse regime.

2.1.3.1 For local geometric quantities over open surfaces

In Drew (1990); Essadki et al. (2019), one can find the derivation of the evolution equations for geometric quantities, namely the surface element stretch factor A, the mean curvature H, the Gauss curvature G, related to a same material point where the normal interface velocity is $v_n = \boldsymbol{v}_I \cdot \boldsymbol{n}$. The velocity $\boldsymbol{v}_I$ is here defined as the time derivative of the interface distortion rather than the actual velocity of a material point. With Δ the Laplace-Beltrami operator (see Definition 8), ∇_{u^i} the covariant derivative with respect to the i-th surface coordinate, the local instantaneous kinematics reads

$$\begin{cases} \partial_t A = 2Hv_n, \\ \partial_t H = \frac{1}{2}\Delta v_n - (2H^2 - G)v_n, \\ \partial_t G = -H\Delta v_n + \sqrt{H^2 - G}(\nabla_{u^1}\nabla^{u^1} v_n - \nabla_{u^2}\nabla^{u^2} v_n) - 2HGv_n. \end{cases} \tag{2.27}$$

Remark that only the normal interface velocity impacts the kinematics, as a tangential displacement only acts like a change of variables with no influence on the interface shape. Elementary examples of these equations for closed interfaces are provided in Drew (1990). A, H and G have been showed independent, and their respective dynamics confirm such property as each right-hand side show independent operators.

Let us now see what these equations become in a multi-fluid framework obtained after averaging. Drew suggests averaging these equations together with the topological equation (1.11) over a small volume. Following the same line as the averaging of the fluid equations in Section 1.1.2, we define the IAD with

$$\Sigma = \langle \|\boldsymbol{\nabla} X\| \rangle_E \,. \tag{2.28}$$

Then, assuming $\langle v_n \rangle_E = v_n$, the following equations are obtained from the averaging of (2.27),

$$\begin{cases} \partial_t \alpha + \Sigma \tilde{v} = 0, \\ \partial_t \Sigma + \boldsymbol{\nabla} \cdot (\Sigma \bar{\boldsymbol{v}}) = \tilde{v}\Sigma\langle H\rangle + \Sigma\Phi_\Sigma, \\ \partial_t (\Sigma\langle H\rangle) + \boldsymbol{\nabla} \cdot (\Sigma\langle H\rangle \bar{\boldsymbol{v}}) = -\boldsymbol{\nabla} \cdot (\Sigma \boldsymbol{q}_H) - \Sigma(\langle H\rangle^2 - \langle G\rangle)\tilde{v} + \Sigma\Phi_H, \\ \partial_t (\Sigma\langle G\rangle) + \boldsymbol{\nabla} \cdot (\Sigma\langle G\rangle \bar{\boldsymbol{v}}) = -\boldsymbol{\nabla} \cdot (\Sigma \boldsymbol{q}_G) - \Sigma\langle H\rangle\langle G\rangle\tilde{v} + \Sigma\Phi_G, \end{cases} \tag{2.29}$$

with

$$\tilde{v} = \langle v_n \|\boldsymbol{\nabla} X\| \rangle_E , \qquad \bar{\boldsymbol{v}} = \langle \boldsymbol{v}_I \|\boldsymbol{\nabla} X\| \rangle_E , \qquad \boldsymbol{q}_H = \langle \boldsymbol{v}_I - \bar{v} H \rangle_E , \qquad \boldsymbol{q}_G = \langle \boldsymbol{v}_I - \bar{v} G \rangle_E , \qquad \Phi_\Sigma = \left\langle (H - \langle H \rangle) \boldsymbol{u}_{I,n} \right\rangle_E ,$$
$$\Phi_H = -\frac{1}{2} \left\langle (\nabla_{u^1} \nabla^{u^1} v_n + \nabla_{u^2} \nabla^{u^2} v_n) \right\rangle_E - \left\langle (H^2 - \langle H \rangle^2) \boldsymbol{u}_{I,n} \right\rangle_E - \left\langle (G - \langle G \rangle) \boldsymbol{u}_{I,n} \right\rangle_E ,$$
$$\Phi_G = -\left\langle H (\nabla_{u^1} \nabla^{u^1} v_n + \nabla_{u^2} \nabla^{u^2} v_n) \right\rangle_E - \left\langle \sqrt{H^2 - K} (\nabla_{u^1} \nabla^{u^1} v_n + \nabla_{u^2} \nabla^{u^2} v_n) \right\rangle_E - \left\langle (HG - \langle G \rangle \langle H \rangle) \boldsymbol{u}_{I,n} \right\rangle_E . \tag{2.30}$$

These equations involve many averaged terms, the closure of which is far from trivial. Therefore, in a general case, the geometric quantities α, Σ, $\Sigma \langle H \rangle$ and $\Sigma \langle G \rangle$ contain independent information, and are therefore relevant for the description of the local interface geometry. However, the complexity of the right-hand side denotes that the finding of a closure with the geometric quantities under consideration seems unlikely in a general case.

2.1.3.2 For surface-averaged geometric quantities over closed surfaces

For disperse regimes, the deterministic kinematics can be detailed with more precision as the kinematics of the interface is the sum of the kinematics of all inclusions, Therefore, we propose now to start with the kinematics of one inclusion. From now on, we drop the dependencies on (u^1, u^2) to lighten the formulas. For convex and closed inclusions, we write a small deformation of length ψ in the direction of the non-deformed surface normal,

$$\boldsymbol{r} = \boldsymbol{r}_0 + \psi \boldsymbol{n}. \tag{2.31}$$

No tangential deformation need to be considered as any deformation of a closed interface can be written with a normal deformation.

With the deformation considered, we derive the perturbation δX of a quantity X as $\delta X = X(\boldsymbol{r}) - X(\boldsymbol{r}_0)$ for all the relevant geometric contracted quantities A, H, G and the perturbation of their corresponding integrated quantities S, $S\tilde{H}$ and $\tilde{G}$. We report here the results up to second order in ψ for any closed interface while the third order is only provided for the sphere in Appendix 2.A.

2.1.3.2.a First and second order perturbation of a closed inclusion

We provide here the results for the perturbation of closed inclusions at first and second order following the notes of Deserno (2004). In the following, we assume smooth perturbations ψ such that its covariant derivatives have an equivalent magnitude as ψ. First, we have the perturbation of the basis vectors and the metric, which follow

$$\begin{aligned} \delta \boldsymbol{e}_i &= (\nabla_i \psi)\, \boldsymbol{n} + \psi b_i^j \boldsymbol{e}_j, \\ \delta g_{ij} &= \psi b_{ij} + \psi b_{ji} + (\nabla_i \delta\psi) \left(\nabla_j \delta\psi\right) + \psi^2 b_i^k b_{jk}. \end{aligned} \tag{2.32}$$

Then, the following variations are obtained Deserno (2004) for the local surface element factor $A = \sqrt{g}$

$$\delta A = -2H\psi A + G\psi^2 + \frac{1}{2} (\nabla_i \psi) \left(\nabla^i \psi\right) A + O(\psi^3). \tag{2.33}$$

We denote $dS = A du^1 du^2$. For a closed inclusion, we integrate by part following 2.13 to obtain the variation of the surface

$$\delta S = \int_{\mathcal{U}} (-2H\psi + G\psi^2 - \frac{1}{2}\psi\Delta\psi) dS + O(\psi^4). \tag{2.34}$$

From the divergence theorem applied to $\boldsymbol{r} \cdot \boldsymbol{n}$, only a few calculation steps lead to

$$\delta V = \int_{\mathcal{U}} (\psi - H\psi^2) dS + O(\psi^3). \tag{2.35}$$

The variation of the local mean curvature is

$$\delta H = -(2H^2 - G)\psi - \frac{1}{2}\Delta\psi + H(4H^2 - 3G)\psi^2 + \psi(\nabla_k\psi)(\nabla^k H) + \psi b_{ij}\nabla^i\nabla^j\psi - \frac{1}{2}(H\nabla_i\psi\nabla^i\psi - b_{ij}\nabla^i\psi\nabla^j\psi) + O(\psi^3), \tag{2.36}$$

such that

$$\delta(H\,A) = \left[G\psi - \frac{1}{2}\Delta\psi + H(4H^2 - 2G)\psi^2 + \psi(\nabla_k\psi)(\nabla^k H) + \psi b_{ij}\nabla^i\nabla^j\psi + \frac{1}{2}b_{ij}\nabla^i\psi\nabla^j\psi\right] A + O(\psi^3). \tag{2.37}$$

Integrating over $\mathcal{U}$ and using integration by parts, we obtain

$$\delta(S\tilde{H}) = \int_{\mathcal{U}} \left[G\psi + H(4H^2 - 2G)\psi^2 - H\psi\Delta\psi - H(\nabla^k\psi)(\nabla_k\psi) + \psi b^k_j\nabla_k\nabla^j\psi + \frac{1}{2}b_{ij}\nabla^i\psi\nabla^j\psi\right] dS + O(\psi^3). \tag{2.38}$$

2.1.3.2.b Application: Second-order perturbation of the sphere inclusion

We provide here the second order perturbation applied to the geometry of a sphere for geometric quantities, the details of the calculation and the third-order variations are reported in Appendix 2.A. We are only interested here in the variation of the integrated surface S, volume V, and surface-weighted mean curvature $S\tilde{H}$. Given the metric of the sphere or radius R detailed in the examples of Section 2.1.1.1, we obtain

$$\begin{aligned}
\delta S &= 2R\int_{\mathbb{S}^2}\psi\, dS - \frac{1}{2}\int_{\mathbb{S}^2}\psi\Delta_{\mathbb{S}^2}\psi\, dS + \iint_{\mathbb{S}^2}\psi^2\, dS + o(\psi^3),\\
\delta(S\widetilde{H}) &= \int_{\mathbb{S}^2}\psi dS - \frac{1}{2R}\int_{\mathbb{S}^2}\psi\Delta_{\mathbb{S}^2}\psi dS + o(\psi^2),\\
\delta V &= R^2\int_{\mathbb{S}^2}\psi\, dS + R\int_{\mathbb{S}^2}\psi^2\, dS + o(\psi^2),
\end{aligned} \tag{2.39}$$

where $\mathbb{S}^2$ is the mapping of the unit sphere interface and dS the non-dimensional element of surface or stretching area factor. Remark that with first-order perturbation of the sphere, the perturbations of integrated geometric quantities S, $S\widetilde{H}$ and V all correspond to the same information about the underlying perturbation ψ, namely its integral over the surface. For higher orders, the relations between the different geometric quantities are not trivial.

However, thanks to the following Theorem 4, one can decompose the deformation field and select only the dominant modes in the manner of Fourier series for a time signal.

> **Theorem 4 (Spherical harmonics decomposition)**
>
> The continuous perturbation ψ of the sphere is uniquely decomposed on the spherical harmonics basis $(Y_{n,l})$
>
> $$\psi = \sum_l \sum_{|m|\le l} c_{l,m}Y_{l,m},$$
>
> with a unique sequence of real coefficients $(c_{l,m})$ and where $Y_{l,m}$ are orthonormal eigenvectors of the spherical Laplacian such that
>
> $$\Delta_{\mathbb{S}^2}Y_{l,m} = -l(l+1)Y_{l,m},$$
>
> and
>
> $$\int_{\mathbb{S}^2} Y_{l,m}Y_{l',m'} = \delta_{l,l'}\delta_{m,m'}.$$

The proof of this theorem can be found in (Müller, 1966). Such a decomposition allows to split the time and the space deformation of the interface with the coefficients $(c_{l,m})$ depending on time. Illustration of perturbation along these spherical harmonics in Figure 2.1.1. Injecting this form in the sphere perturbation of the integrated geometric

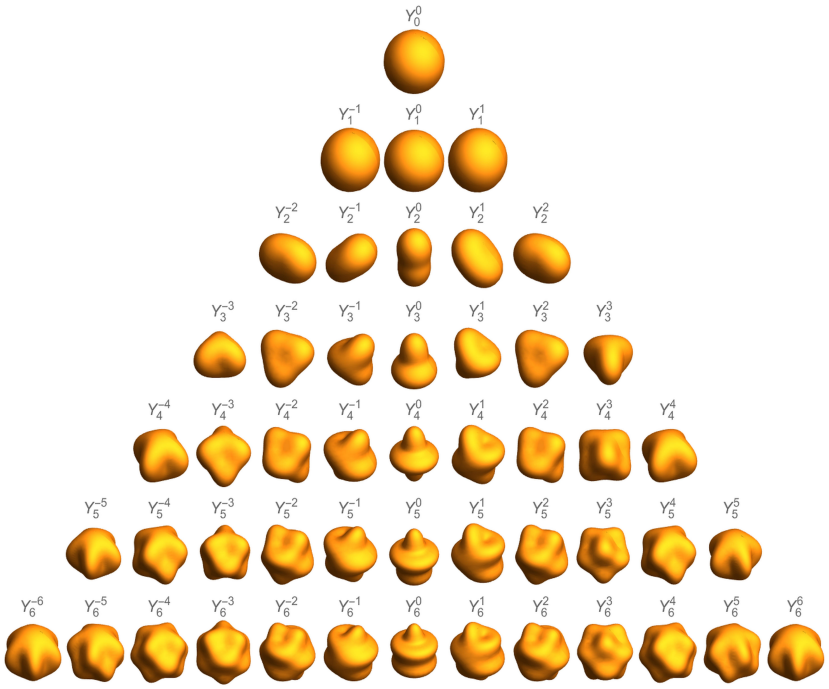

Figure 2.1.1: Spherical harmonics $Y_{l,m}$ for $l \in [\![0,6]\!]$ and $|m| \leq l$ computed with Mathematica (Wolfram Research, 2023).

quantities leads to

$$\begin{aligned} \delta S &= 2Rc_{0,0} + \sum_{l} \sum_{|m|\leq l} \left(1 + \frac{l(l+1)}{2}\right) c_{l,m}^2 + o(c_{l,m}^3), \\ \delta(S\widetilde{H}) &= c_{0,0} + \frac{1}{2R} \sum_{l} \sum_{|m|\leq l} l(l+1) c_{l,m}^2 + o(c_{l,m}^2), \\ \delta V &= R^2 c_{0,0} + R \sum_{l} \sum_{|m|\leq l} c_{l,m}^2 + o(c_{l,m}^2). \end{aligned} \tag{2.40}$$

This shows that we can drastically reduce the complexity of the kinematics of the interface to the data of only a few geometric quantities. However, one must be careful that if only specific deformation modes are considered, the geometric information can become redundant, for instance if only isotropic deformation is considered *i.e.* only $c_{0,0}$ is not null. Such an approach is proposed hereafter in Sections 2.2 for the incompressible oscillation of droplets and compressible pulsation of bubbles by respectively choosing modes $Y_{2,0}$ and $Y_{0,0}$.

2.1.3.2.c Application: Perturbation of the ellipsoid

The strength of differential geometry of closed surface not only apply to the spherical reference shapes, but also other shapes such an ellipsoidal shape of reference. Such inclusion shape can be relevant especially for rising bubbles (Moore, 1965; Risso, 2000). The discussion about the geometry of the ellipsoid relies on the results of Hobson (1931); Dassios (2012) and is proposed as illustrative purposes only as no two-phase flow disperse models relies on this geometry in this work. The mathematical details can be found in the references detailed aforementioned. An ellipsoid is classically described with the following implicit parametrization

$$\frac{x^2}{a_1^2} + \frac{y^2}{a_2^2} + \frac{z^2}{a_1^2} = 1, \tag{2.41}$$

with (x, y, z) the Cartesian coordinates and $a_1 > a_2 > a_3 > 0$ are the half-axes. Denoting $h_1^2 = a_2^2 - a_3^2$, $h_2^2 = a_1^2 - a_3^2$, $h_3^2 = a_1^2 - a_2^2$, each quadrant of the ellipsoid can then be classically described with the ellipsoidal coordinates $\rho = a_1$ and $(\mu, \nu) \in (h_3, h_2) \times (0, h_3)$ such that

$$x_1^2 = \frac{\rho^2\mu^2\nu^2}{h_2^2 h_3^2}, \qquad x_2^2 = \frac{\left(\rho^2 - h_3^2\right)\left(\mu^2 - h_3^2\right)\left(h_3^2 - \nu^2\right)}{h_1^2 h_3^2}, \qquad x_3^2 = \frac{\left(\rho^2 - h_2^2\right)\left(h_2^2 - \mu^2\right)\left(h_2^2 - \nu^2\right)}{h_1^2 h_2^2}. \tag{2.42}$$

Then, the surface ellipsoidal harmonics $S_{l,m}$ are eigenvectors of the ellipsoidal Laplace-Beltrami operator, as defined in Definition 8, and read

$$S_{l,m}(\mu, \nu) = E_l(\mu)E_m(\nu), \tag{2.43}$$

with E_k is a *Lamé* polynomial of order k and of any class K, L, M or N (see Dassios (2012) for the polynomials up to the third order). Similarly to the theorem 4 for the sphere, one can then uniquely decompose the perturbation of an ellipsoid along ellipsoidal harmonics (Dassios, 2012) which are represented in Figure 2.1.2. Again, this provides

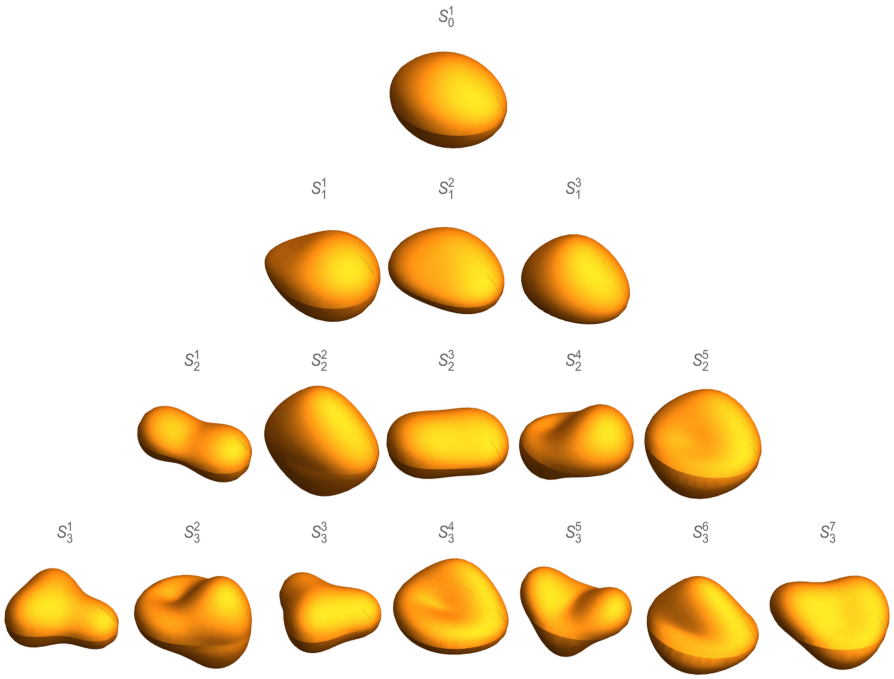

Figure 2.1.2: Ellipsoid harmonics $S_{l,m}$ for $l \in [[0, 3]]$ and $|m| \leq l$ computed with Mathematica (Wolfram Research, 2023).

us with an efficient way to decompose the kinematics of the interface of the inclusions and identify whether the geometric quantities represent redundant information or not.

Conclusion of Section 2.1.3

This section allowed us to better understand the information hold by the geometric quantities under an arbitrary distortion of the interface. Such knowledge is critical for the choice of the NDF phase-space where only an independent set of quantities must be chosen to unambiguously define the current state of the inclusion. We can conclude from this section that the geometric quantities under consideration are probably insufficient to have closed equation of evolution due to the arbitrary complexity of the interface motion in the general case. However, the decomposition of a closed interface deformation shows that the time evolution of the interface can be fully closed with only a small amount of information if specific modes are considered. Therefore, the derivation of models relying on the disperse

regime seems accessible with the geometric quantities at stake. We propose now to present the usual closure of dynamics before presenting a novel approach to close such dynamics with Hamilton's SAP in Section 2.2.

2.1.4 Dynamics of the geometric quantities

In this section, we discuss a straightforward approach to obtain the dynamics associated from the statistical distribution introduced in the previous section. This approach consists in providing the dynamics directly by closing the time evolution of the NDF and the SDF. While this approach works well in the disperse regime, it is not easy to account for the coupling with the carrier phase. Moreover, its application for an arbitrary interface is very challenging.

2.1.4.1 Dynamics in the disperse regime

Let us start with the disperse regime where the dynamics of the collection of inclusions is expressed as the transport in both the real-space associated with the space variable $\boldsymbol{x}$ and the phase-space associated with the velocity $\boldsymbol{v}$ and the phase-space variable $\boldsymbol{\xi}$. Differentiating in time the definition of the NDF yields,

$$\partial_t f + \boldsymbol{\nabla}_{\boldsymbol{x}} \cdot (\left\langle \boldsymbol{v}|\boldsymbol{x},\hat{\boldsymbol{\xi}}\right\rangle f) + \boldsymbol{\nabla}_{\boldsymbol{v}} \cdot (\left\langle \dot{\boldsymbol{v}}|\boldsymbol{x},\hat{\boldsymbol{\xi}}\right\rangle f) + \boldsymbol{\nabla}_{\hat{\boldsymbol{\xi}}} \cdot (\left\langle (\dot{\boldsymbol{\xi}}_\lambda)|\boldsymbol{x},\hat{\boldsymbol{\xi}}\right\rangle f) = \left(\left\langle \dot{S}|\boldsymbol{x},\hat{\boldsymbol{\xi}}\right\rangle + \left\langle \frac{\dot{\tilde{G}}}{\tilde{G}}|\boldsymbol{x},\hat{\boldsymbol{\xi}}\right\rangle\right) f, \tag{2.44}$$

with $\langle(\cdot)|\boldsymbol{x},\boldsymbol{\xi}\rangle$ is the conditional expectancy of $(\cdot)$ given $\boldsymbol{\xi}$ at position $\boldsymbol{x}$. It is remarked in Essadki et al. (2019) that assuming all the inclusions homeomorphic to spheres leads to

$$\left\langle \dot{S}|\boldsymbol{x},\hat{\boldsymbol{\xi}}\right\rangle + \left\langle \frac{\dot{\tilde{G}}}{\tilde{G}}|\boldsymbol{x},\hat{\boldsymbol{\xi}}\right\rangle = 0, \tag{2.45}$$

thanks to the Gauss-Bonnet theorem. Therefore, this term can be interpreted as a source term accounting for topological changes through, for instance, coalescence and break-up. Moreover, as the transport in the real-space is governed by the second Newton's law of dynamics, this equation is then usually interpreted as a population balance equation – or Williams-Boltzmann equation in the context of evaporating sprays (Shapiro and Erickson, 1957; Williams, 1958) – on a collection of objects written

$$\partial_t f + \boldsymbol{\nabla}_{\boldsymbol{x}} \cdot (\boldsymbol{v} f) + \boldsymbol{\nabla}_{\boldsymbol{v}} \cdot (\boldsymbol{F_{ext}} f) + \boldsymbol{\nabla}_{\hat{\boldsymbol{\xi}}} (R_{\boldsymbol{\xi}} f) = \Gamma, \tag{2.46}$$

where $\left\langle \dot{\boldsymbol{v}}|\boldsymbol{x},\hat{\boldsymbol{\xi}}\right\rangle = \boldsymbol{F}_{ext}$ are the external forces *i.e.* Stokes drag, gravity, $\left\langle (\dot{\boldsymbol{\xi}}_\lambda)|\boldsymbol{x},\hat{\boldsymbol{\xi}}\right\rangle = R_{\boldsymbol{w}}$ gathers the time rates of change of characteristics $\boldsymbol{w}$ and represents the *a priori* chosen phenomena *i.e.* evaporation, heat transfer, deformation, and we note Γ the right-hand side of (2.44) which accounts for source terms of phenomena such as break-up or coalescence. The closure of such dynamical system then comes from the knowledge of the dynamics for one inclusion (characteristics $\boldsymbol{\xi}$ and the associated $R_{\boldsymbol{\xi}}$) which is extended to the collection via the NDF.

2.1.4.2 Dynamics for an arbitrary regime

For the multi-regime offered by the SDF, we similarly get the unclosed dynamics equation by differentiating in time the definition of the SDF. It yields,

$$\partial_t F + \boldsymbol{\nabla}_{\boldsymbol{x}} \cdot (< \dot{\boldsymbol{X}}^o_\lambda|\boldsymbol{x},\hat{\boldsymbol{w}} > F) + \boldsymbol{\nabla}_{\hat{\boldsymbol{w}}} \cdot (< \dot{\boldsymbol{W}}^o_\lambda|\boldsymbol{x},\hat{\boldsymbol{w}} > F) = \left\langle \frac{\dot{A}^o_\lambda}{A^o_\lambda}|\boldsymbol{x},\hat{\boldsymbol{w}}\right\rangle F, \tag{2.47}$$

where $< \cdot|\boldsymbol{x},\hat{\boldsymbol{w}} >$ is the expectancy of $\cdot$ conditioned by $\boldsymbol{x},\hat{\boldsymbol{w}}$. Similarly, the dynamics is closed by choosing expressions for $< \dot{\boldsymbol{X}}^o_\lambda|\boldsymbol{x},\hat{\boldsymbol{w}} >$, $< \dot{\boldsymbol{W}}^o_\lambda|\boldsymbol{x},\hat{\boldsymbol{w}} >$ and $\left\langle \frac{\dot{A}^o_\lambda}{A^o_\lambda}|\boldsymbol{x},\hat{\boldsymbol{w}}\right\rangle$. However, the interpretation of the conditional expectancies is more delicate out of the disperse regime. In the disperse regime, we do not know the explicit closure of these conditional expectancies, but we can provide the dynamics of some specific moments of the SDF, which are related through Property 2 and the Gauss-Bonnet Theorem to some moments of the NDF, which are our geometric quantities of interest: the IAD, the surface-averaged curvatures, and their time derivatives if needed.

The details to include such a strategy in the modelling of two-phase flow are provided in the next section.

2.2 Extending the interpretation of the disperse regime with GeoMOM

In the previous sections, we have demonstrated that the geometric variables are good candidates to model the small-scale dynamics as they hold geometric information about the interface while being defined for any flow regime. However, the expression of their dynamic and their coupling with the flow appears very challenging without further assumptions. Conversely, we showed that the interface kinematics of closed inclusions in the disperse regime can be efficiently described with few quantities and then, the modelling of their dynamics is possible.

Therefore, we propose here an intermediate strategy where the identification of a dynamics in the disperse regime is used as a particular case of a more generic interface dynamics through the use of geometric variables interpretable in any regime.

Such a strategy would particularly allow the use of kinetic-based models which encompass a large variety of physical phenomena such as the evaporation of spherical droplets described through a size distribution (Williams, 1958; Dufour and Villedieu, 2005; Massot et al., 2010; Essadki et al., 2018), or the secondary break-up Taylor-Analogy Breakup (TAB) model with a vibrational oscillation of the droplets by adding a deformation parameter (O'Rourke and Amsden, 1987; Amsden et al., 1989). Once the PBE is closed, the resulting model has a large dimension, and the dimension of the model can be reduced with the Method of Moments (Schmüdgen, 2017) instead of discretizing both the physic and phase spaces. This method reduces the multidimensional model with the NDF to a set of conservation laws with unclosed source terms. Their closure then requires a reconstruction of the distribution with the moments at hand. This method has been widely applied to disperse models (Hulburt and Katz, 1964; Marchisio and Fox, 2005; Kah et al., 2012). While the reconstruction problem has a well-understood framework for one extra-dimension (size or velocity typically) and has led to numerous reconstruction techniques (McGraw, 1997; Laurent and Massot, 2001; Marchisio and Fox, 2005; Yuan et al., 2012; Essadki, 2016; Fox et al., 2022), the multidimensional one lacks a general theory and the reconstruction techniques depend both on the phase-space and the chosen moments (Fox, 2009; Yuan and Fox, 2011; Vié et al., 2012; Chalons et al., 2017).

For the strategy under consideration, we want to represent the small-scale dynamics with geometric quantities rather than statistical moments. In the case of spherical inclusions, the Geometric Method of Moments, as introduced in Essadki et al. (2016, 2018, 2019), has successfully identified geometric quantities through a method of moments applied to a NDF with a size distribution. However, more complex models with oscillation and secondary break such as TAB model are out of reach when using the geometric quantities used in Essadki et al. (2019).

We propose here a new contribution (Loison et al., 2023b) which extends the scope of GeoMOM to the description of inclusions endowed with their own interface kinematics and therefore kinematics.

In this section, we first detail the GeoMOM strategy and its coupling with the carrier flow through Hamilton's SAP. We illustrate this method with three examples: 1- the description of a polydisperse spray of spherical droplets, on which the model by Essadki for evaporating droplets is based, 2- a polydisperse spray of oscillating droplets based on a kinetic model inspired from O'Rourke and Amsden (1987), 3- a bubbly flow of pulsating bubbles, the dynamics of which follows the Rayleigh-Plesset equation.

These examples are of great interest in the modelling of a multiscale two-phase flow, say an atomization, as they correspond to elementary energy-conservative mechanisms which can temporarily store energy as the interface breaks up. Moreover, these models can also be considered on their own as building block models for the description of sprays or bubbly flows.

2.2.1 The Geometric Method of Moments

In this section, we detail the steps to build a two-phase model based on GeoMOM. Before that, in Section 2.2.1.1, we place ourselves in the simpler context of a unique velocity for both the inclusions and the carrier phase. Then, we split the strategy in three steps:

(A) Applying the method of moments on a closed kinetic-based model (Section 2.2.1.2);

(B) Linking the moments of the NDF to surface-averaged geometric variables, IAD, and their time derivatives if needed (Section 2.2.1.3);

(C) Construct the kinetic and potential energies associated with the small-scale dynamics, and include them in the Lagrangian used for the derivation of the two-phase model with Hamilton's SAP (Section 2.2.1.4).

2.2.1.1 The mono-kinetic assumption

In this section, we are mainly interested in the accounting for the geometry kinematics of the disperse phase. Therefore, we do not tackle the reconstruction of both velocities and geometric characteristics (see Vié et al. (2013) for an Eulerian model coupling the effects of size and velocity distributions).

We recall the generic PBE (2.46) of the NDF $f(t,\boldsymbol{x},\boldsymbol{v},\hat{\boldsymbol{\xi}})$,

$$\partial_t f + \boldsymbol{\nabla}_{\boldsymbol{x}} \cdot (\boldsymbol{v} f) + \boldsymbol{\nabla}_{\boldsymbol{v}} \cdot (\boldsymbol{F}_{ext} f) + \boldsymbol{\nabla}_{\hat{\boldsymbol{\xi}}} (R_{\boldsymbol{\xi}} f) = \Gamma, \tag{2.48}$$

Then, we discard the velocity dependency by considering the mono-kinetic assumption

$$f(t,\boldsymbol{x},\boldsymbol{v},\hat{\boldsymbol{\xi}}) = \delta(\boldsymbol{v} - \boldsymbol{U}(t,\boldsymbol{x},\hat{\boldsymbol{\xi}})) n_{\boldsymbol{\xi}}(t,\boldsymbol{x}), \tag{2.49}$$

with $n_{\boldsymbol{\xi}} = \int_{\boldsymbol{v}} f_{\boldsymbol{v},\widehat{\boldsymbol{\xi}}} d\boldsymbol{v}$ and $\boldsymbol{U} = \int_{\widehat{\boldsymbol{\xi}}} \boldsymbol{v} f$ is the averaged velocity conditioned by $\boldsymbol{\xi}$.

To further simplify and distinguish the geometric modelling and from the barycentre dynamics, we consider a Stokes force $\boldsymbol{F}$ in the limit of a vanishing Stokes number $St \to 0$, i.e. when the inertial timescale of inclusions is negligible compared to the timescale of the flow. The flow is then characterized by the carrier flow velocity $\boldsymbol{u}$ only. Following the works of Jabin (2002); Massot (2007), the dynamics of $n_{\boldsymbol{\xi}}$ reads

$$\partial_t n_{\boldsymbol{\xi}} + \boldsymbol{\nabla}_{\boldsymbol{x}} \cdot (n_{\boldsymbol{\xi}} \boldsymbol{u}) + \boldsymbol{\nabla}_{\hat{\boldsymbol{\xi}}} (R_{\boldsymbol{\xi}} n_{\boldsymbol{\xi}}) = 0, \tag{2.50}$$

where $\boldsymbol{u}$ is the unique velocity of both the inclusions and the carrier phase.

2.2.1.2 The method of moments

We reduce now the complexity of the inclusions' dynamics, modelled by the distribution $n_{\boldsymbol{\xi}}$ given in (2.50), by introducing a finite set of moments indexed by $\mathcal{I}$, $\boldsymbol{M}^{\boldsymbol{\xi}} = \left(M^{\boldsymbol{\xi}}_{(a_k)_i}\right)_{i\in\mathcal{I}}$ with

$$M^{\boldsymbol{\xi}}_{(a_k)_i} = \int_{\widehat{\boldsymbol{\xi}}} \prod_{k=1}^{P} \widehat{\boldsymbol{\xi}}^{a_{k,i}} \, n_{\boldsymbol{\xi}} \, d\widehat{\boldsymbol{\xi}}, \qquad i \in \mathcal{I} \text{ finite } \subset (\mathbb{N}^P)^{\mathbb{N}}, \tag{2.51}$$

where $(a_k)_i$ are P-multi-indices. These scalars retain statistical information about the NDF and their dynamics can be obtained by integrating (2.50) against the corresponding monomials,

$$\partial_t \boldsymbol{M}^{\boldsymbol{\xi}} + \boldsymbol{\nabla} \cdot (\boldsymbol{M}^{\boldsymbol{\xi}} \boldsymbol{u}) + \boldsymbol{\nabla}_{\hat{\boldsymbol{\xi}}} \cdot (\boldsymbol{\mathcal{R}}) = 0, \qquad \boldsymbol{\mathcal{R}} = \int_{\widehat{\boldsymbol{\xi}}} \prod_{k=1}^{P} \widehat{\boldsymbol{\xi}}^{a_{k,i}} \, R_{\boldsymbol{\xi}} n_{\boldsymbol{\xi}} \, d\widehat{\boldsymbol{\xi}}, \qquad i \in \mathcal{I}, \tag{2.52}$$

where the flux term $\boldsymbol{\mathcal{R}} = (\mathcal{R})_{i\in\mathcal{I}}$ is *a priori* not closed *i.e.* whether it can be expressed with the moments of $\boldsymbol{M}^{\boldsymbol{\xi}}$. The method of moments then gives a reduced-order model for the small-scale spray in comparison with (2.50). In general, the equations are unclosed, and a reconstruction of the NDF based on the selected moments must be provided such as Entropy-Maximization techniques (Mead and Papanicolaou, 1984), quadratures (McGraw, 1997) or multi-gaussian distributions (Vié et al., 2012). The selection of these moments is not obvious and is usually motivated on the basis of mathematical properties of the resulting moment model.

2.2.1.3 Linking moments to surface-averaged geometric variables

The specificity of GeoMOM consists in the selection of moments related to geometric quantities defined with (2.14) and (2.19) to construct a model interpretable even out of the disperse regime. The finite family of multi-indices $(a_k)_{\mathcal{I}}$ is chosen such that there exists geometric quantities gathered in vector $\boldsymbol{X}$ satisfying component-wise

$$\Sigma \langle \boldsymbol{X} \rangle = \mathcal{F}(\boldsymbol{M}^{\boldsymbol{\xi}}), \tag{2.53}$$

with $\mathcal{F}$ an invertible function. Such a property then provides both moments to close the fluxes $\boldsymbol{F}$ and $\Sigma\langle\boldsymbol{\xi}\rangle$ for their geometric interpretations. Then from the dynamics of $\boldsymbol{M}^{\boldsymbol{\xi}}$ obtained in (2.52), the dynamics of the geometric quantities $\Sigma\langle\boldsymbol{X}\rangle$ are obtained from (2.53).

2.2.1.4 Multi-fluid dynamics with Hamilton's SAP

The dynamics of the disperse model can be derived by combining the energies of the carrier fluid and the inclusions through the Lagrangian

$$\mathcal{L} = \frac{1}{2}m_k\boldsymbol{u}^2 - m_2 e_2\left(\frac{m_k}{\alpha_k}\right) + \frac{1}{2}m_{k'}\boldsymbol{u}^2 - m_{k'}e_{k'}\left(\frac{m_{k'}}{1-\alpha_{k'}}\right) + \mathcal{L}_{ss}(\boldsymbol{M}^{\boldsymbol{\xi}}), \tag{2.54}$$

with $(k,k') = (2,1^d)$ for disperse liquid inclusions or $(k,k') = (1,2^d)$ for a bubbly flow, and $\mathcal{L}_{ss}$ is the additional Lagrangian associated with the chosen small-scale dynamics. This latter contribution can account for small-scale kinetic energy of the fluid within the inclusion and its immediate surrounding, and potential energy accounting for capillarity energy.

Our contribution is materialized here in the small-scale kinetic energies added in $\mathcal{L}_{ss}$ which can only be accounted with time derivatives of geometric quantities. This will be illustrated in the upcoming examples of oscillating droplets in Section 2.2.4 and the pulsating bubbles in Section 2.2.3. Finally, the moments $\boldsymbol{M}^{\boldsymbol{\xi}}$ are constrained by (2.52), *e.g.* a conservation constraint if the associated flux $\mathcal{R}$ is nil, or unconstrained if they are associated with a dynamics. Another consequence of the addition of new time derivatives of geometric quantities in the phase space lies in the apparition of kinematic constraints. Indeed, consider the phase-space $\boldsymbol{\xi} = (\chi, \dot{\chi})$ and its homogeneous PBE,

$$\partial_t n + \boldsymbol{\nabla}\cdot(n\boldsymbol{u}) + \partial_\chi(\dot{\chi}n) + \partial_{\dot{\chi}}(\ddot{\chi}n) = 0. \tag{2.55}$$

Then, integrating against χ yields

$$\partial_t M^{\xi}_{1,0} + \boldsymbol{\nabla}\cdot(M^{\xi}_{1,0}\boldsymbol{u}) = M^{\xi}_{0,1}. \tag{2.56}$$

Assuming these moments to have a geometric nature, this latter relation translates into a kinematic relation between χ and $\dot{\chi}$. This concludes the main steps to build small-scale two-phase flow models with GeoMOM and Hamilton's SAP. We propose now different examples relying on this derivation technique.

2.2.2 Application 1: Polydispersion of a collection of inclusions

Let us first consider a simple example, treated in Loison et al. (2023a), to illustrate GeoMOM where we assume no individual dynamics associated with the inclusions, but they are compressible and equilibrates with the surrounding pressure. Therefore, we describe a spray of either spherical droplets or bubbles which are only characterized by their mass. Indeed, for a compressible inclusion, the size can variate from the surrounding pressure forces while its mass is constant when no evaporation is accounted. Then, we define the mass-based NDF $n_m(\widehat{m})$, with $\boldsymbol{\xi} = (\widehat{m})$ the mass of the inclusion, satisfying the following PBE

$$\partial_t n_m + \boldsymbol{\nabla}\cdot(n_m\boldsymbol{u}) = 0. \tag{2.57}$$

2.2.2.1 GeoMOM

We follow then the hierarchy of moments introduced by Essadki et al. (2018) to identify the averaged geometric quantities related to the moments $\boldsymbol{M}^m$ of n_m. For the spherical inclusions described by n_m, the local Gauss and mean curvatures G, H on the sphere are constant and equal respectively to R^{-1} and R^{-2} where $R = (3m/(4\pi\rho_k^d))^{1/3}$ is the radius of the sphere of density ρ_k^d and mass m. Therefore, considering a population of spherical inclusions, we

express the geometric quantities Σ, $\Sigma\langle G\rangle$ and $\Sigma\langle H\rangle$ as moments of the distribution n_m

$$\begin{aligned}
\Sigma\langle G\rangle &= \int_{\widehat{m}} 4\pi && n_m\, d\widehat{m} && = 4\pi && M_0^m,\\
\Sigma\langle H\rangle &= \int_{\widehat{m}} 4\pi \left(\frac{3}{4\pi\rho_k^d}\right)^{1/3} && \widehat{m}^{1/3}\, n_m\, d\widehat{m} && = 4\pi \left(\frac{3}{4\pi\rho_k^d}\right)^{1/3} && M_{1/3}^m,\\
\Sigma &= \int_{\widehat{m}} 4\pi \left(\frac{3}{4\pi\rho_k^d}\right)^{2/3} && \widehat{m}^{2/3}\, n_m\, d\widehat{m} && = 4\pi \left(\frac{3}{4\pi\rho_k^d}\right)^{2/3} && M_{2/3}^m.
\end{aligned} \tag{2.58}$$

Remark the special role of $\Sigma\langle G\rangle$ proportional to the zeroth-order moment of n_m. This results from the Gauss-Bonnet theorem 3, which indicates a geometric invariant $S\widetilde{G} = 4\pi$ for any continuous deformations of the sphere. Furthermore, the small-scale volume fraction is not surface-related in general, but in the specific case of spherical droplets, it is also linked to a moment of $n_{\boldsymbol{w}}$ via the surface averaged of $\frac{1}{3}\boldsymbol{r}\cdot\boldsymbol{r}$ (see (2.25)) with

$$\alpha_k^d = \int_{\widehat{m}} \frac{1}{\rho_k^d}\widehat{m}\, n_m\, d\widehat{m} = \frac{1}{\rho_k^d} M_1^m. \tag{2.59}$$

From (2.58) and (2.59), we select $\mathcal{I} = \{0,\ 1/3,\ 2/3,\ 1\}$ in (2.52) to get the dynamics of the geometric quantities

$$\begin{cases}
\partial_t(\Sigma\langle G\rangle) + \boldsymbol{\nabla}\cdot(\Sigma\langle G\rangle\boldsymbol{u}) = 0,\\
\partial_t((\rho_k^d)^{1/3}\Sigma\langle H\rangle) + \boldsymbol{\nabla}\cdot((\rho_k^d)^{1/3}\Sigma\langle H\rangle\boldsymbol{u}) = 0,\\
\partial_t((\rho_k^d)^{2/3}\Sigma) + \boldsymbol{\nabla}\cdot((\rho_k^d)^{2/3}\Sigma\boldsymbol{u}) = 0,\\
\partial_t m_k^d + \boldsymbol{\nabla}\cdot(m_k^d\boldsymbol{u}) = 0.
\end{cases} \tag{2.60}$$

Up to here, the model has been derived for compressible spherical inclusions. We can further assume a spray of liquid droplets ($k^d = 1^d$) by assuming the classic incompressibility of the small scale (Raviart and Sainsaulieu, 1995) thanks to the constraint $D_t\rho_1^d = 0$. Then, the geometric variables are governed by

$$\begin{cases}
\partial_t(\Sigma\langle G\rangle) + \boldsymbol{\nabla}\cdot(\Sigma\langle G\rangle\boldsymbol{u}) = 0,\\
\partial_t(\Sigma\langle H\rangle) + \boldsymbol{\nabla}\cdot(\Sigma\langle H\rangle\boldsymbol{u}) = 0,\\
\partial_t\Sigma + \boldsymbol{\nabla}\cdot(\Sigma\boldsymbol{u}) = 0,\\
\partial_t\alpha_k^d + \boldsymbol{\nabla}\cdot(\alpha_k^d\boldsymbol{u}) = 0.
\end{cases} \tag{2.61}$$

2.2.2.2 Geometrical constraints

System (2.61) corresponds to the system with surface-based moments of Essadki et al. (2018) when no evaporation nor condensation is accounted for. Indeed, when the droplets are incompressible, the mass-based NDF $n_{\boldsymbol{w}}$ relates to the surface-based NDF n_S defined by

$$n_S(\boldsymbol{x},t,\widehat{S}) := \int_{\widehat{m}} n_{\boldsymbol{w}}(\boldsymbol{x},t,\widehat{m})\delta(\widehat{m}-m(\widehat{S}))\, d\widehat{m}, \qquad m(\widehat{S}) = \rho_1^d\frac{\widehat{S}}{3\sqrt{4\pi}}. \tag{2.62}$$

As ρ_1^d is a constant along the streamlines, there is no variation of surface area for the droplets and the dynamics is then driven by

$$\partial_t n_S + \boldsymbol{\nabla}_{\boldsymbol{x}}\cdot(n_S\boldsymbol{u}) = 0. \tag{2.63}$$

Again, when the droplets have the same density, the geometric quantities are also expressed through the moments M_i^S of n_S,

$$\Sigma\langle G\rangle = 4\pi M_0^S, \quad \Sigma\langle H\rangle = \sqrt{4\pi}M_{1/2}^S, \quad \Sigma = M_1^S, \quad \alpha_1^d = \frac{1}{3\sqrt{4\pi}}M_{3/2}^S. \tag{2.64}$$

The change of variables (2.62) only modifies the dimensions and orders of the moments gathered in (2.58)-(2.59), and the half-integer moments (2.64) can be recovered as in Essadki et al. (2018). Remark that, in both the cases of (2.58)-(2.59) and (2.64), the moments are of ascending orders. With this special choice of moments, one can reconstruct a NDF by solving the *truncated Hausdorff problem* detailed in Theorem 5.

> **Theorem 5 (Hausdorff (1921) problem)**
>
> Given a finite set of scalars $\boldsymbol{M} = M_k$ $k = 0, ..., N$, one can find unidimensional representation distribution $n_{\boldsymbol{M}}$ supported on the segment $(0, 1)$ such that
>
> $$M_k = \int_0^1 x^k n_{\boldsymbol{M}}(x)\, dx, \qquad k = 0, ..., N,$$
>
> if and only if the Hankel matrices $\underline{\boldsymbol{H}}$ and $\overline{\boldsymbol{H}}$ are positive semi-definite. If $N = 2k$, they read
>
> $$\underline{\boldsymbol{H}} = (m_{i+j})_{i,j=0,...,k}, \qquad \overline{\boldsymbol{H}} = (m_{i+j+1} - m_{i+j+2})_{i,j=0,...,k-1},$$
>
> and, if $N = 2k + 1$, they read
>
> $$\underline{\boldsymbol{H}} = (m_{i+j+1})_{i,j=0,...,k}, \qquad \overline{\boldsymbol{H}} = (m_{i+j} - m_{i+j+1})_{i,j=0,...,k}.$$

Theorem 5 applies to our set of half-integer moments (2.64) *via* a change of variable and leads to the constraints

$$M_0^S > 0, \qquad M_{1/2}^S > 0, \qquad M_{1/2}^S M_{3/2}^S - (M_1^S)^2 > 0, \qquad M_0^S M_1^S - (M_{1/2}^S)^2 > 0, \tag{2.65}$$

and defines a moment-space which indicates a convex subset of $\mathbb{R}^{n+1}$ where the moments are properly defined.

This also implies constraints on the geometric variables α_1^d, Σ, $\Sigma\langle H\rangle$ and $\Sigma\langle G\rangle$ linked to these moments which read

$$\alpha_1^d > 0, \qquad \Sigma > 0, \qquad \Sigma\langle H\rangle > 0, \qquad \Sigma\langle G\rangle > 0, \qquad 3\langle H\rangle \alpha_1^d > \Sigma, \qquad \langle G\rangle - \langle H\rangle^2 > 0. \tag{2.66}$$

These constraints are not an issue at the modelling stage as they are all passively advected by the flow. However, they will raise issues at the numerical level as further discussed in Section 4.2.2.

2.2.2.3 Polydisperse multi-fluid models with Hamilton's SAP

2.2.2.3.a Incompressible inclusions – droplets

The derivation of the dynamics is very similar to the one-velocity disperse Model 8 as it does not modify its Lagrangian (except the capillarity term $\sigma\Sigma$, but it acts as a constant in Hamilton's SAP),

$$\mathcal{L} = \frac{1}{2} m_2 \boldsymbol{u}^2 - m_2 e_2\left(\frac{m_2}{1-\alpha_1^d}\right) + \frac{1}{2} m_1^d \boldsymbol{u}^2 - m_1^d e_1^d(\rho_1^d) + \sigma\Sigma. \tag{2.67}$$

Regarding the constraints, we assume conservation of effective densities and geometric quantities like (2.61), we particularly underline that α_1^d is conserved. Applying Hamilton's SAP leads to Model 12.

Model 12 (Polydisperse model of incompressible droplets)

We denote the carrier gaseous phase with index 2 and the liquid droplets with index 1^d. With $m_k = \alpha_k \rho_k$ and α_k the phase densities and volume fractions of phases $k = 2, 1^d$, $\rho = m_1^d + m_2$ the mixture's density, $\boldsymbol{u}$ the velocity and $p_2(\rho_2)$ the pressure of the gaseous phase 2, Σ the IAD, $\Sigma\langle H\rangle$, $\Sigma\langle G\rangle$ the surface-weighted mean curvature densities, the flow is governed by

$$\begin{cases} \partial_t m_2 & +\boldsymbol{\nabla}\cdot(m_2\boldsymbol{u}) & = 0, \\ \partial_t m_1^d & +\boldsymbol{\nabla}\cdot(m_1^d\boldsymbol{u}) & = 0, \\ \partial_t \alpha_1^d & +\boldsymbol{\nabla}\cdot(\alpha_1^d\boldsymbol{u}) & = 0, \\ \partial_t \Sigma & +\boldsymbol{\nabla}\cdot(\Sigma\boldsymbol{u}) & = 0, \\ \partial_t(\Sigma\langle H\rangle) & +\boldsymbol{\nabla}\cdot(\Sigma\langle H\rangle\boldsymbol{u}) & = 0, \\ \partial_t(\Sigma\langle G\rangle) & +\boldsymbol{\nabla}\cdot(\Sigma\langle G\rangle\boldsymbol{u}) & = 0, \\ \partial_t(\rho\boldsymbol{u}) & +\boldsymbol{\nabla}\cdot(\rho\boldsymbol{u}\otimes\boldsymbol{u} + p_2\boldsymbol{I}) & = \boldsymbol{0}. \end{cases}$$

Remark here that there is no interaction between the flow geometric quantities and the flow. From the averaging perspective, such a model also provides a trivial closure for the averaged equations (2.29) as there is no small-scale dynamics of the inclusions' interface.

2.2.2.3.b Compressible inclusions – bubbles

Now considering compressible inclusions (case $(k, k') = (1, 2^d)$), one can introduce the variables $z_a = (\rho_2^d)^{2/3}\Sigma/m_1^d$ and $z_b = (\rho_2^d)^{1/3}\Sigma\langle H\rangle/m_1^d$ which are constrained by $D_t z_a = 0$ and $D_t z_b = 0$ or equivalently

$$\begin{cases} \partial_t\Sigma + \boldsymbol{\nabla}\cdot(\Sigma\boldsymbol{u}) = \dfrac{2}{3}\Sigma\boldsymbol{\nabla}\cdot\boldsymbol{u} + \dfrac{2}{3}\Sigma\dfrac{D_t\alpha_2^d}{\alpha_2^d}, \\ \partial_t(\Sigma\langle H\rangle) + \boldsymbol{\nabla}\cdot(\Sigma\langle H\rangle\boldsymbol{u}) = \dfrac{2}{3}\Sigma\langle H\rangle\boldsymbol{\nabla}\cdot\boldsymbol{u} + \dfrac{2}{3}\Sigma\langle H\rangle\dfrac{D_t\alpha_2^d}{\alpha_2^d}. \end{cases} \tag{2.68}$$

This structure of equation for the IAD is similar to the one derived by Lhuillier (2004) for a single-velocity model recalled in (1.30). Similarly, the Hamilton's SAP is not affected by the additional capillarity energy. However, we consider here α_2^d as unconstrained for Hamilton's SAP such that we obtain similar models as the separated multi-fluid Model 3 and Model 4. Then, Hamilton's SAP provides the momentum equation

$$\partial_t(\rho\boldsymbol{u}) + \boldsymbol{\nabla}\cdot(\rho\boldsymbol{u}\otimes\boldsymbol{u} + p\mathbf{I}) = \boldsymbol{0}, \tag{2.69}$$

with $p := p_1 = p_2^d$, which for barotropic EOS and smooth solution gives the following dynamics for α_2^d,

$$D_t\alpha_2^d = \alpha_2^d\alpha_1\frac{\rho_1 c_1^2 - \rho_2^d(c_2^d)^2}{\alpha_2^d\rho_1 c_1^2 + \alpha_1\rho_2(c_2^d)^2}\boldsymbol{\nabla}\cdot\boldsymbol{u} =: \alpha_2^d\tilde{K}\boldsymbol{\nabla}\cdot\boldsymbol{u}.$$

Together with the constraints, this yields Model 13.

Model 13 (Polydisperse model of compressible bubbles)

We denote the carrier liquid phase with index 1 and the gaseous bubbles with index 2^d. With $m_k = \alpha_k \rho_k$ and α_k the phase densities and volume fractions of phases $k = 1, 2^d$, $\rho = m_1 + m_2^d$ the mixture's density, $\boldsymbol{u}$ the velocity and $p_2^d(\rho_2^d)$ the pressure of the gaseous phase 2, Σ the IAD, $\Sigma\langle H\rangle$, $\Sigma\langle G\rangle$ the surface-weighted mean curvature densities, the flow is governed by

$$\begin{cases} \partial_t m_1 & +\boldsymbol{\nabla}\cdot(m_1\boldsymbol{u}) & = 0, \\ \partial_t m_2^d & +\boldsymbol{\nabla}\cdot(m_2^d\boldsymbol{u}) & = 0, \\ \partial_t \Sigma & +\boldsymbol{\nabla}\cdot(\Sigma\boldsymbol{u}) & = \frac{2}{3}\Sigma \quad \boldsymbol{\nabla}\cdot\boldsymbol{u} + \frac{2}{3}\Sigma\tilde{K}\boldsymbol{\nabla}\cdot\boldsymbol{u}, \\ \partial_t(\Sigma\langle H\rangle) & +\boldsymbol{\nabla}\cdot(\Sigma\langle H\rangle\boldsymbol{u}) & = \frac{2}{3}\Sigma\langle H\rangle\boldsymbol{\nabla}\cdot\boldsymbol{u} + \frac{2}{3}\Sigma\langle H\rangle\tilde{K}\boldsymbol{\nabla}\cdot\boldsymbol{u}, \\ \partial_t(\Sigma\langle G\rangle) & +\boldsymbol{\nabla}\cdot(\Sigma\langle G\rangle\boldsymbol{u}) & = 0, \\ \partial_t(\rho\boldsymbol{u}) & +\boldsymbol{\nabla}\cdot(\rho\boldsymbol{u}\otimes\boldsymbol{u} + p\boldsymbol{I}) & = \boldsymbol{0}, \end{cases}$$

with $p := p_1 = p_2^d$, and $\tilde{K} = \alpha_1 \dfrac{\rho_1 c_1^2 - \rho_2^d (c_2^d)^2}{\alpha_2^d \rho_1 c_1^2 + \alpha_1 \rho_2 (c_2^d)^2}$.

We have now a complete set of closed equations for the small-scale geometric quantities, thus providing a closure for both the averaged equation of Drew and Lhuillier. The source terms in the equation of evolution of the geometric quantity dynamics translates the pressure adjustment of the bubbles with the carrier fluid when this latter undergoes compressibility phenomena. Finally, we can introduce the same dissipative relaxation as Model 4 such that we obtain the Model 14.

Model 14 (Polydisperse model of compressible bubbles with relaxation)

We denote the carrier liquid phase with index 1 and the gaseous bubbles with index 2^d. With $m_k = \alpha_k \rho_k$, α_k p_k the phase densities, volume fractions and pressures of phases $k = 1, 2^d$, $\rho = m_1 + m_2^d$ the mixture's density, $\boldsymbol{u}$ the velocity, Σ the IAD, $\Sigma\langle H\rangle$, $\Sigma\langle G\rangle$ the surface-weighted mean curvature densities, the flow is governed by

$$\begin{cases} \partial_t m_1 & +\boldsymbol{\nabla}\cdot(m_1\boldsymbol{u}) & = 0, \\ \partial_t m_2^d & +\boldsymbol{\nabla}\cdot(m_2^d\boldsymbol{u}) & = 0, \\ \partial_t \alpha_2^d & +\boldsymbol{u}\cdot\boldsymbol{\nabla}\alpha_2^d & = \frac{1}{\mu}(p_2^d - p_1), \\ \partial_t \Sigma & +\boldsymbol{\nabla}\cdot(\Sigma\boldsymbol{u}) & = \frac{2}{3}\Sigma\boldsymbol{\nabla}\cdot\boldsymbol{u} \quad +\frac{2}{3}\frac{\Sigma}{\alpha_2^d}\frac{1}{\mu}(p_2^d - p_1), \\ \partial_t(\Sigma\langle H\rangle) & +\boldsymbol{\nabla}\cdot(\Sigma\langle H\rangle\boldsymbol{u}) & = \frac{2}{3}\Sigma\langle H\rangle\boldsymbol{\nabla}\cdot\boldsymbol{u} + \frac{2}{3}\frac{\Sigma\langle H\rangle}{\alpha_2^d}\frac{1}{\mu}(p_2^d - p_1), \\ \partial_t(\Sigma\langle G\rangle) & +\boldsymbol{\nabla}\cdot(\Sigma\langle G\rangle\boldsymbol{u}) & = 0, \\ \partial_t(\rho\boldsymbol{u}) & +\boldsymbol{\nabla}\cdot(\rho\boldsymbol{u}\otimes\boldsymbol{u} + p\boldsymbol{I}) & = \boldsymbol{0}, \end{cases}$$

with $p = \alpha_1 p_1 + \alpha_2^d p_2^d$.

The source terms in the equation of evolution of the geometric quantity dynamics also shows that the inclusions see their pressure to be balanced with the pressure of the carrier fluid. In these last two models, the bubbles instantaneously react to the pressure variations of the carrier phase to maintain the pressure equilibrium. A more physical behaviour would be to account for the Laplace pressure jump and that the bubbles have their own dynamics

at small-scale resulting from the small-scale flow around the bubble and introduce inertial and damping terms. However, that would require enlarging the NDF phase-space and add non-trivial time-rate of change in the PBE (2.57). This modelling approach is tackled in the next section.

2.2.3 Application 2: Pulsating bubbly flow

We now propose a small-scale model of compressible inclusions, say bubbles in a liquid, with an independent small-scale dynamics. The modelling of pulsating bubble is well-known under the Rayleigh-Plesset model (Plesset and Prosperetti, 1977; Prosperetti, 1982), and accounts for the dynamics of spherical bubble embedded in a locally incompressible fluid, undergoing both internal and external pressure forces and capillarity surface tension. The resulting dynamics read

$$R\ddot{R} + \frac{3}{2}\dot{R}^2 = \frac{1}{\rho_1}\left(p_2 - p_1 - \frac{2\sigma}{R}\right). \tag{2.70}$$

Many multiphase models have already been proposed with related approaches to account for such pulsation of the bubbles, particularly using Hamilton's SAP and a *micro-inertia* term $\frac{1}{2}\nu(D_t\alpha)^2$ in the Lagrangian (Bedford and Drumheller, 1978; Gavrilyuk and Teshukov, 2001; Teshukov and Gavrilyuk, 2002; Gavrilyuk and Saurel, 2002; Drui et al., 2019). However, these model often postulates the expression of the micro-inertia or the compressibility of the carrier flow is not fully accounted for. Therefore, we propose here another derivation of such model addressing these two limits in a one-velocity model taking advantage of the GeoMOM framework.

2.2.3.1 Energetic derivation of the Rayleigh-Plesset equation

We propose first to derive the Rayleigh-Plesset equation as in Prosperetti (1982) by considering a small-scale incompressible flow of velocity $\tilde{\boldsymbol{u}}$ around the bubble of radius $R(t)$ such that. The dynamics is obtained by the time derivation of the total energy of the system made of the bubble and the surrounding flow such that the dominant added-mass kinetic energy is properly accounted.

First, let us determine the surrounding flow through the incompressibility condition with the spherical referential of the bubble (r, θ, ϕ),

$$\boldsymbol{\nabla} \cdot \tilde{\boldsymbol{u}} = 0. \tag{2.71}$$

From the spherical symmetry, it boils down to

$$\partial_r(r^2\tilde{u}_r) = 0, \tag{2.72}$$

that we integrate into

$$\tilde{u}_r(t, r) = \frac{C(t)}{r^2}, \tag{2.73}$$

where $C(t)$ is a quantity depending on time only. We determine this constant as the component normal to the interface is continuous at the interface of the bubble *i.e.* $\tilde{u}_r(t, R(t)) = \dot{R}(t)$, and then we obtain

$$\tilde{u}_r = \frac{R^2}{r^2}\dot{R}. \tag{2.74}$$

We neglect the kinetic energy brought by the fluid inside the bubble, and we obtain the following kinematic energy for one bubble with its liquid surrounding,

$$E_k = \int_{\theta=0}^{\pi}\int_{\phi=0}^{2\pi}\int_{r=R(t)}^{\infty} \frac{1}{2}\rho_1\tilde{u}_r^2 r^2 \sin\theta dr d\theta d\phi = \frac{1}{2}\dot{R}^2R^3\rho_1 4\pi. \tag{2.75}$$

The potential energy comes from the internal energy $e(\rho_2)$, the capillarity and the pressure work of the surrounding fluid with an energy constant set such that $E_k + E_p = 0$ at equilibrium when $R = R_0$ and $\dot{R} = 0$,

$$\begin{aligned} E_p &= \sigma(S - S_0(R_0)) + e(\rho_2) - e(\rho_2(m_b, R_0)) + p_{1,\infty}(V(R) - V_0(R_0)) \\ &= \sigma 4\pi(R^2 - R_0^2) + m_b e\left(\frac{m_b}{\frac{4}{3}\pi R^3}\right) - m_b e\left(\frac{m_b}{\frac{4}{3}\pi R_0^3}\right) + p_{1,\infty}\frac{4\pi}{3}(R^3 - R_0^3). \end{aligned} \tag{2.76}$$

Then, the equilibrium radius R_0 is a minimizer of E_p, *i.e.*

$$(\partial_R E_p)|_{R_0} = 4\pi\sigma 2R_0 - 4\pi R_0^2 \left[p_2\left(\frac{m_b}{\frac{4}{3}\pi R_0^3}\right) - p_{1,\infty} \right] = 0 \quad \Rightarrow \quad p_2\left(\frac{m_b}{\frac{4}{3}\pi R_0^3}\right) - p_{1,\infty} = \sigma\frac{2}{R_0}. \tag{2.77}$$

As expected, we recover the Laplace pressure jump at the equilibrium. For the dynamics, we derive in time the total energy $E_m = E_k + E_p$ which yields the Rayleigh-Plesset equation,

$$R\ddot{R} + \frac{3}{2}\dot{R}^2 = \frac{1}{\rho_1}\left[p_2\left(\frac{m_b}{\frac{4}{3}\pi R^3}\right) - p_{1,\infty} - \sigma\frac{2}{R} \right]. \tag{2.78}$$

In the limit of small oscillations, one can introduce $R = R_0 + \delta R$ with $\dot{R} = \delta\dot{R}$ and $\ddot{R} = \delta\ddot{R}$ such that the linearized Rayleigh-Plesset equation is obtained

$$\delta\ddot{R} + \frac{1}{\rho_1}\left[\frac{3\rho_2}{R_0^2}c_{2,0}^2 - \sigma\frac{2}{R_0^3} \right]\delta R = 0. \tag{2.79}$$

The coefficient of the zero order term is positive if $R_0 > \frac{2\sigma}{3\rho_2 c_{2,0}^2}$ which is very small (*e.g.* 10^{-8} m for an air bubble in water). We define then the pulsation $\omega_0^{RP} = \sqrt{\frac{3}{R_0^2}c_2^2 - \sigma\frac{2}{R_0^3}}$ of the oscillating dynamics.

2.2.3.2 GeoMOM with a monodisperse synchronous bubbly flow

Given the dynamics of a unique bubble, we are now interested in the dynamics of a bubbly flow that we derive with GeoMOM and Hamilton's SAP. We proceed by first describing the kinetic model at the small-scale, and we identify the variables we want to work with in the two-scale model. The assumptions are the following

- The local dynamics of one bubble follows a Rayleigh-Plesset equation with a surrounding incompressible flow at small-scale;
- The small-scale flow around the bubbles is potential;
- The bubbles locally are pulsating synchronously.

We first tackle the case where we have a monodisperse collection of bubbles following the non-linear Rayleigh-Plesset equation (2.78), and second a polydisperse collection of bubbles following the linear case (2.79).

2.2.3.2.a The monodisperse non-linear model

We describe the bubbly flow with a NDF f of phase space accounting for both the radius and the radius velocity $(\widehat{m}, \widehat{R}, \widehat{\dot{R}})$. The NDF is governed by the following PBE

$$\partial_t n_b + \boldsymbol{\nabla}\cdot(n_b\boldsymbol{u}) + \partial_{\widehat{R}}(\widehat{\dot{R}}n_b) + \partial_{\widehat{\dot{R}}}(\ddot{R}(\widehat{R},\widehat{\dot{R}})n_b) = 0, \tag{2.80}$$

where the relation $\ddot{R}(\widehat{R},\widehat{\dot{R}})$ is given by the Rayleigh-Plesset equation (2.78). Considering a monodisperse spray and the synchronous pulsation of the droplets, the NDF has the following form

$$n_b(\widehat{m},\widehat{R},\widehat{\dot{R}}) = n\delta(\widehat{m} - m_b)\delta(\widehat{R} - R)\delta(\widehat{\dot{R}} - \dot{R}), \tag{2.81}$$

where m_b, R and $\dot{R}$ are the abscissa of the bubble distribution n_b. It is then required to identify at least three geometric quantities following the GeoMOM approach. We choose them to be α_2^d the volume fraction of the gaseous

phase (denoted α in Drui et al. (2019)), $\Sigma\langle G\rangle$ and the time derivative $\partial_t\alpha_2^d$ as allowed by GeoMOM (see (2.26)). Integrating the NDF f against m, 4π, $\frac{4}{3}\pi\widehat{R}^3$ and the PBE (2.80) against $\frac{4}{3}\pi\widehat{R}^3$ yields,

$$m_2^d = m_b M_{0,0}, \quad \Sigma\langle G\rangle = 4\pi M_{0,0} = 4\pi n, \quad \alpha_2^d = \frac{4}{3}\pi M_{3,0} = n\frac{4}{3}\pi R^3, \quad w := \partial_t\alpha_2^d + \boldsymbol{u}\cdot\boldsymbol{\nabla}\alpha_2^d + \alpha_2^d\boldsymbol{\nabla}\cdot\boldsymbol{u} = n4\pi R^2\dot{R}, \tag{2.82}$$

which allows to identify the weight n and the abscissa m_b, R, $\dot{R}$. For the sake of readability and following comparable notation as in Drui et al. (2019), we note $w := D_t\alpha_2^d + \alpha_2^d\boldsymbol{\nabla}\cdot\boldsymbol{u}$. Remark that this definition translate a kinematic relation, as identified in (2.56) associated with the variation of the inclusions' volume. With w, relations (2.82) become

$$n = \frac{\Sigma\langle G\rangle}{4\pi}, \qquad m_b = \frac{m_2^d}{n} = \frac{\alpha_2^d\rho_2^d}{n}, \qquad R = \left(\frac{3\alpha_2^d}{\Sigma\langle G\rangle}\right)^{1/3}, \dot{R} = \frac{w}{\Sigma\langle G\rangle}\left(\frac{3\alpha_2^d}{\Sigma\langle G\rangle}\right)^{-2/3}. \tag{2.83}$$

The Lagrangian of the system is then evaluated using these variables by integrating the kinetic and potential energies against the NDF. However, in the context of multi-fluid models, the pressure work does not need to be added as it comes from the equilibrium of the internal energies of both phases. Using the abscissa, the Lagrangian reads

$$\mathcal{L} = \frac{1}{2}\rho\boldsymbol{u}^2 - \rho Y_1 e_1\left(\frac{\rho Y_1}{1-\alpha_2^d}\right) + n\left(\frac{1}{2}\dot{R}^2R^3\rho_1 4\pi\right) - m_2 e_2\left(\frac{\rho Y_2}{\alpha_2^d}\right) - \sigma\left(n4\pi R^2\right). \tag{2.84}$$

Then, for calculation purposes, we use relations (2.82) to express the Lagrangian notably with m_b, Y_2, and α_2^d,

$$\mathcal{L}(\boldsymbol{u},\rho,\alpha_2^d,w,m_b,Y_2,Y_1) = \frac{1}{2}\rho\boldsymbol{u}^2 - \rho Y_1 e_1\left(\frac{\rho Y_1}{1-\alpha_2^d}\right) - \rho Y_2 e_2\left(\frac{\rho Y_2}{\alpha_2^d}\right) + \frac{1}{2}\nu(m_b,Y_2,\rho,\alpha_2^d)w^2 - \sigma(4\pi)^{1/3}3^{2/3}(\alpha_2^d)^{2/3}\left(\frac{\rho Y_2}{m_b}\right)^{1/3}, \tag{2.85}$$

with

$$\nu(m_b,Y_2,\rho,\alpha_2^d) = \frac{1}{(4\pi)^{2/3}3^{1/3}}\left(\frac{(1-Y_2)m_b^{2/3}}{Y_2^{2/3}}\right)\frac{\rho^{1/3}}{(\alpha_2^d)^{1/3}(1-\alpha_2^d)}. \tag{2.86}$$

Remark that this Lagrangian extends the one proposed by Gavrilyuk and Teshukov (2001), and additionally accounts for the carrier liquid phase compressibility and capillarity of the bubbles. Also note that a Lagrangian for a bubbly potential flow accounting for two velocities and added-mass has been proposed in Teshukov and Gavrilyuk (2002). We further consider the following constraints,

$$D_tY_1 = 0, \qquad D_tY_2 = 0, \qquad D_tm_b = 0, \qquad \partial_t\rho + \boldsymbol{\nabla}\cdot(\rho\boldsymbol{u}) = 0. \tag{2.87}$$

For an Eulerian variation of the trajectories $\boldsymbol{\eta}$, we have the following variations,

$$\begin{aligned} \delta b_a &= -(\boldsymbol{\eta}\cdot\boldsymbol{\nabla})b_a, \qquad \text{for} \quad b_a \in \{Y_1, Y_2, m_b\}, \\ \delta\rho &= -\boldsymbol{\nabla}\cdot(\rho\boldsymbol{\eta}), \qquad \delta\boldsymbol{u} = D_t\boldsymbol{\eta} - (\boldsymbol{\eta}\cdot\boldsymbol{\nabla})\boldsymbol{u}, \\ \delta w = \delta(D_t\alpha_2^d + \alpha_2^d\boldsymbol{\nabla}\cdot\boldsymbol{u}) &= \partial_t\delta\alpha_2^d + \delta\boldsymbol{u}\cdot\boldsymbol{\nabla}\alpha_2^d + \boldsymbol{u}\cdot\boldsymbol{\nabla}\delta\alpha_2^d + \alpha_2^d\boldsymbol{\nabla}\cdot\delta\boldsymbol{u} + (\boldsymbol{\nabla}\cdot\boldsymbol{u})\delta\alpha_2^d, \end{aligned} \tag{2.88}$$

and the following variation for the action,

$$\begin{aligned} \delta\mathcal{A} = \int_{\bar{\Omega}} - \Big\{ & \partial_t\boldsymbol{K} + \boldsymbol{\nabla}\cdot(\boldsymbol{K}\otimes\boldsymbol{u}) + \boldsymbol{K}\cdot\boldsymbol{\nabla}\boldsymbol{u} - \rho\boldsymbol{\nabla}(\partial_\rho\mathcal{L}) + \partial_{m_b}\mathcal{L}\boldsymbol{\nabla}m_b + \partial_{Y_1}\mathcal{L}\boldsymbol{\nabla}Y_1 + \partial_{Y_2}\mathcal{L}\boldsymbol{\nabla}Y_2 \\ & + M\boldsymbol{\nabla}(D_t\alpha_2^d) + (\partial_tM + \boldsymbol{\nabla}\cdot(M\boldsymbol{u}))\boldsymbol{\nabla}\alpha_2^d \\ & - \boldsymbol{\nabla}\left(\alpha_2^d(\partial_tM + \boldsymbol{\nabla}\cdot(M\boldsymbol{u})) + M(D_t\alpha_2^d + \alpha_2^d(\boldsymbol{\nabla}\cdot\boldsymbol{u}))\right) - \alpha_2^d\boldsymbol{\nabla}(M(\boldsymbol{\nabla}\cdot\boldsymbol{u})) - M\boldsymbol{\nabla}(\alpha_2^d(\boldsymbol{\nabla}\cdot\boldsymbol{u}))\Big\}\cdot\boldsymbol{\eta} \\ & - \Big\{\partial_tM + \boldsymbol{\nabla}\cdot(M\boldsymbol{u}) - M(\boldsymbol{\nabla}\cdot\boldsymbol{u}) - \partial_{\alpha_2^d}\mathcal{L}\Big\}. \end{aligned} \tag{2.89}$$

Hamilton's SAP then implies

$$\begin{cases} \partial_t \boldsymbol{K} + \boldsymbol{\nabla}\cdot(\boldsymbol{K}\otimes\boldsymbol{u}) + \boldsymbol{K}\cdot\boldsymbol{\nabla}\boldsymbol{u} + \partial_{Y_1}\mathcal{L}\boldsymbol{\nabla}Y_1 + \partial_{Y_2}\mathcal{L}\boldsymbol{\nabla}Y_2 + \partial_{m_b}\mathcal{L}\boldsymbol{\nabla}m_b - \rho\boldsymbol{\nabla}(\partial_\rho\mathcal{L}) \\ \qquad -\left[(D_t\alpha_2^d + \alpha_2^d\boldsymbol{\nabla}\cdot\boldsymbol{u})\boldsymbol{\nabla}M + \alpha_2^d\boldsymbol{\nabla}(\partial_{\alpha_2^d}\mathcal{L})\right] = \boldsymbol{0}, \\ \partial_t M + \boldsymbol{\nabla}\cdot(M\boldsymbol{u}) = \partial_{\alpha_2^d}\mathcal{L} + M(\boldsymbol{\nabla}\cdot\boldsymbol{u}). \end{cases} \tag{2.90}$$

Introducing $\mathcal{L}^* = \rho\partial_\rho\mathcal{L} - \mathcal{L}$, we have

$$\begin{cases} \partial_t \boldsymbol{K} + \boldsymbol{\nabla}\cdot(\boldsymbol{K}\otimes\boldsymbol{u} - (\mathcal{L}^* + M(D_t\alpha_2^d + \alpha_2^d(\boldsymbol{\nabla}\cdot\boldsymbol{u})) + \alpha_2^d\partial_{\alpha_2^d}\mathcal{L})\boldsymbol{I}) = \boldsymbol{0}, \\ \partial_t M + \boldsymbol{u}\cdot\boldsymbol{\nabla}M = \partial_{\alpha_2^d}\mathcal{L}. \end{cases} \tag{2.91}$$

Evaluating the partial derivatives of the Lagrangian gives

$$\begin{aligned} \boldsymbol{K} = \rho\boldsymbol{u}, \qquad M = \nu(D_t\alpha_2^d + \alpha_2^d\boldsymbol{\nabla}\cdot\boldsymbol{u}), \qquad \mathcal{L}^* &= -(1-\alpha_2^d)p_1 - \alpha_2^d p_2 - \frac{1}{3}\nu(D_t\alpha_2^d + \alpha_2^d(\boldsymbol{\nabla}\cdot\boldsymbol{u}))^2 + \frac{2}{3}\sigma\Sigma, \\ \partial_{\alpha_2^d}\mathcal{L} &= p_2 - p_1 + \frac{1}{2}\nu\left(\frac{1}{1-\alpha_2^d} - \frac{1}{3\alpha_2^d}\right)w^2 - \frac{2}{3\alpha_2^d}\sigma\Sigma, \\ \mathcal{L}^* + M(D_t\alpha_2^d + \alpha_2^d(\boldsymbol{\nabla}\cdot\boldsymbol{u})) + \alpha\partial_{\alpha_2^d}\mathcal{L} &= -p_1 + \frac{1}{2}\frac{\nu}{1-\alpha_2^d}w^2. \end{aligned} \tag{2.92}$$

The dynamics of the pulsation is simplified remarking that

$$D_t\nu = \nu\left(\left(\frac{1}{(1-\alpha_2^d)} - \frac{1}{3(\alpha_2^d)}\right)(w - \alpha_2^d(\boldsymbol{\nabla}\cdot\boldsymbol{u})) - \frac{(\boldsymbol{\nabla}\cdot\boldsymbol{u})}{3}\right), \tag{2.93}$$

and the final model is gathered in Model 15.

Model 15 (Monodisperse model of pulsating bubbles)

With $m_k = \alpha_k\rho_k$ the phase densities for $k = 1, 2^d$, ρ the mixture density, $\boldsymbol{u}$ the mixture velocity, $\Sigma\langle G\rangle$ the surface-average density of Gauss curvature (linked to the number density of bubbles), p_k the pressure of phase k, the flow is governed by

$$\begin{cases} \partial_t m_1 + \boldsymbol{\nabla}\cdot(m_1\boldsymbol{u}) = 0, \\ \partial_t m_2^d + \boldsymbol{\nabla}\cdot(m_2^d\boldsymbol{u}) = 0, \\ \partial_t(\Sigma\langle G\rangle) + \boldsymbol{\nabla}\cdot(\Sigma\langle G\rangle\boldsymbol{u}) = 0, \\ \partial_t(\rho\boldsymbol{u}) + \boldsymbol{\nabla}\cdot\left(\rho\boldsymbol{u}\otimes\boldsymbol{u} + (p_1 - \frac{1}{2}\frac{1}{1-\alpha_2^d}\nu w^2)\boldsymbol{I}\right) = \boldsymbol{0}, \\ \partial_t w + \boldsymbol{u}\cdot\boldsymbol{\nabla}w + \frac{\alpha_2^d}{1-\alpha_2^d}\boldsymbol{\nabla}\cdot\boldsymbol{u} = \frac{1}{2}\left(\frac{1}{3\alpha_2^d} - \frac{1}{1-\alpha_2^d}\right)w^2 + \frac{1}{\nu}\left(p_2 - p_1 - \sigma\frac{2}{R}\right), \end{cases}$$

with $w = D_t\alpha_2^d + \alpha_2^d\boldsymbol{\nabla}\cdot\boldsymbol{u}$, ν defined by (2.86) and $R(\alpha_2^d, \Sigma\langle G\rangle)$ the radius defined using (2.82).

Let us first remark that the pressure of the mixture in the mixture momentum equation is the one of the carrier fluid perturbed with a term corresponding to the pulsating dynamics, notably the time derivative of α. This corresponds to a dispersive system, and we refer the reader to Gavrilyuk and Teshukov (2001), where some properties of such systems are studied. The absence of pressure contribution p_2 in the mixture momentum is reminiscent of what is observed for the modelling of disperse particle flow, and comes from the introduction of the pulsation *via* a "conservative" derivative $w = D_t\alpha + \alpha\boldsymbol{\nabla}\cdot\boldsymbol{u}$. The additional equation for the dynamics of the pulsating bubbles is quite complex and results from the non-linear Rayleigh-Plesset equation governing the pulsation of each bubble. In the limit with no velocity, it yields

$$\partial_{tt}\alpha_2^d = \frac{1}{2}\left(\frac{1}{3\alpha_2^d} - \frac{1}{1-\alpha_2^d}\right)(\partial_t\alpha_2^d)^2 + \frac{1}{\nu}\left(p_2\left(\frac{m_2^d}{\alpha_2^d}\right) - p_1\left(\frac{m_1}{1-\alpha_2^d}\right) - \sigma\frac{2}{R}\right). \tag{2.94}$$

As expected, in the equilibrium state when there is no more pulsation, *i.e.* $w = 0$, simply gives the Laplace pressure jump relation where the quantity R is implicitly defined by the pressure equilibrium depending on the carrier fluid pressure p_1 as in (2.77).

For the hyperbolicity study, we consider the augmented model corresponding with Model 15 by decoupling w and α_2^d and introducing the former definition of w as an additional equation. For an arbitrary direction ω, denote $u = \boldsymbol{u} \cdot \omega$, then the augmented model is hyperbolic with, after some calculations, the following eigenvalues

$$u, \quad u - c, \quad u + c, \qquad \text{with} \quad c = \frac{1}{1-\alpha_2^d}\sqrt{\frac{(1-\alpha_2^d)\rho_1 c_1^2 - \alpha_2 \nu w(1+w)}{\rho}}, \tag{2.95}$$

with u of multiplicity 5 and 5 independent eigenvectors. Remark that there is no sound propagation associated with the sound velocity of the gaseous phase conversely to the modified frozen sound velocity found in Drui et al. (2019). This property is physically more acceptable as the sound propagation within the gaseous bubbles is not relevant at the scale of the bubbly flow mixture (see the remark in Saurel et al. (2017, Sec. II-A, infra)).

Finally, the dynamics of the geometric quantities Σ or $\Sigma\langle H\rangle$ is not required to close the dynamical system. Nevertheless, one can have their equations of evolution the PBE (2.80) against the right monomials, *e.g.*

$$\partial_t \Sigma + \boldsymbol{\nabla} \cdot (\Sigma \boldsymbol{u}) = 2\left(\frac{\Sigma\langle G\rangle}{3\alpha_2^d}\right)^{1/3} w, \tag{2.96}$$

which translates the relation $\partial_t(4\pi R^2) = 2(\partial_t V)/R$ for a sphere.

2.2.3.3 The monodisperse linearized model

Given the equilibrium state around the Laplace equilibrium, we propose now to investigate the linearized problem around this very state. For the linearized Rayleigh-Plesset equation, the dynamics of each droplet is determined by $(\delta R, \delta\dot{R})$ which defines the new phase-space of the NDF n_b describing the bubbles. The PBE governing the dynamics of n_b is then

$$\partial_t n_b + \boldsymbol{\nabla} \cdot (n_b \boldsymbol{u}) + \partial_{\widehat{\delta R}}(\widehat{\delta\dot{R}} n_b) + \partial_{\widehat{\delta\dot{R}}}(\delta\ddot{R}(\widehat{\delta R}, \widehat{\delta\dot{R}}) n_b) = 0, \tag{2.97}$$

For this model, we account for mass polydispersion, but the need of explicit reconstruction for Hamilton's SAP energies makes us choose a distribution of Dirac,

$$n_b(\widehat{m}, \widehat{\delta R}, \widehat{\delta\dot{R}}) = n\delta(\widehat{m} - m)\delta(\widehat{\delta R} - \delta R)\delta(\widehat{\delta\dot{R}} - \delta\dot{R}). \tag{2.98}$$

This form, similarly assume the synchronicity of the bubbles' pulsation. However, for simpler calculations, we change the mass dependency into a dependency on the radius equilibrium through the implicit function defined by the Laplace equilibrium

$$p_2\left(\frac{m}{\frac{4}{3}\pi R_0}\right) - p_1\left(\frac{m_1}{1 - n\frac{4}{3}\pi R_0^3}\right) = \sigma\frac{2}{R_0}, \tag{2.99}$$

that we assume invertible. Thus, we consider now

$$n_b(\widehat{R_0}, \widehat{\delta R}, \widehat{\delta\dot{R}}) = n\delta(\widehat{R_0} - R_0)\delta(\widehat{\delta R} - \delta R)\delta(\widehat{\delta\dot{R}} - \delta\dot{R}). \tag{2.100}$$

For consistency with the non-linear model, we write the relations between the geometric variables α_2^d and $\Sigma\langle G\rangle$ and the moments of n_b

$$\alpha_2^d = \frac{4}{3}\pi M_{3,0,0} + 4\pi M_{2,1,0}, \qquad D_t\alpha_2^d + \alpha_2^d \boldsymbol{\nabla}\cdot\boldsymbol{u} = 4\pi M_{2,0,1}, \qquad \Sigma\langle G\rangle = 4\pi M_{0,0,0}. \tag{2.101}$$

We propose then to decompose the volume fraction α_2^d in its static contribution α_0 and $\tilde{\alpha}$ associated with the pulsation. We can then link them to the abscissa n, R_0, δR, $\delta\dot{R}$ with

$$n = \frac{\Sigma\langle G\rangle}{4\pi}, \qquad R_0 = \left(\frac{3\alpha_0}{\Sigma\langle G\rangle}\right)^{1/3}, \qquad \delta R = \frac{\tilde{\alpha}}{\Sigma\langle G\rangle}\left(\frac{3\alpha_0}{\Sigma\langle G\rangle}\right)^{-2/3}, \qquad \delta\dot{R} = \frac{D_t\tilde{\alpha} + \tilde{\alpha}\boldsymbol{\nabla}\cdot\boldsymbol{u}}{\Sigma\langle G\rangle}\left(\frac{3\alpha_0}{\Sigma\langle G\rangle}\right)^{-2/3}. \tag{2.102}$$

Using both geometric quantities and abscissa, we write the potential energy

$$E_p = m_1 e_1\left(\frac{m_1}{1-\alpha_0-\tilde{\alpha}}\right) + \sigma n 4\pi (R_0+\delta R)^2 + m_2^d e_2\left(\frac{m_2^d}{\alpha_0+\tilde{\alpha}}\right), \tag{2.103}$$

and differentiating this equation around its equilibrium gives the potential energy in the limit of small pulsation

$$\mathcal{E}_p = \underbrace{m_1 e_1\left(\frac{m_1}{1-\alpha_0}\right) + m_2^d e_2\left(\frac{m_2^d}{\alpha_0}\right)}_{\mathcal{E}_0} + \frac{1}{2}\underbrace{\left[c_2^2\left(\frac{m_1}{(1-\alpha_0)^2}+\frac{m_2^d}{\alpha_0^2}\right)+\frac{2\sigma}{R_0^4\Sigma\langle G\rangle}\right]}_{\gamma}\tilde{\alpha}^2. \tag{2.104}$$

The kinetic energy reads for small pulsations

$$E_k = \frac{1}{2}\nu(m_b, Y_2, \rho, \alpha_0)(D_t\tilde{\alpha} + \tilde{\alpha}\boldsymbol{\nabla}\cdot\boldsymbol{u})^2, \tag{2.105}$$

with ν defined by (2.86). Let us gather the terms of the Lagrangian following

$$\mathcal{L} = \frac{1}{2}\rho\boldsymbol{u}^2 + \frac{1}{2}\nu(m_b, Y_2, \rho, \alpha)(D_t\alpha + \alpha\boldsymbol{\nabla}\cdot\boldsymbol{u})^2 - \mathcal{E}_p(m_b, Y_2, \rho, \alpha), \tag{2.106}$$

where $\mathcal{E}_p$ is the potential energies gathering both specific internal energies and capillarity energy.

We now express the linearized Lagrangian around the equilibrium volume fraction α_0 defined as the minimizer of $\mathcal{E}_p$. It yields

$$\mathcal{L} = \frac{1}{2}\rho\boldsymbol{u}^2 - \mathcal{E}_p(m_b, Y_2, \rho, \alpha_0) + \frac{1}{2}\nu(m_b, Y_2, \rho, \alpha_0)(D_t\tilde{\alpha} + \tilde{\alpha}(\boldsymbol{\nabla}\cdot\boldsymbol{u}))^2 - \frac{1}{2}\gamma(m_b, Y_2, \rho, \alpha_0)\tilde{\alpha}^2, \tag{2.107}$$

with ν defined as in (2.86), and

$$\gamma(m_b, Y_2, \rho, \alpha_0) = (\partial_\alpha^2\mathcal{E}_p)|_{\alpha_0} = \frac{\rho(1-Y_2)c_1^2}{(1-\alpha_0)^2} + \frac{\rho Y_2 c_2^2}{\alpha_0^2} - \frac{2(4\pi)^{1/3}}{(3\alpha_0)^{4/3}}\sigma\left(\frac{\rho Y_2}{m_b}\right)^{1/3}. \tag{2.108}$$

We assume the same constraints as considered previously, except for α_0 which varies under the constraint of the equilibrium $\partial_\alpha\mathcal{E}_p(\alpha_0, \rho, Y_2, m_b) = 0$. It follows that

$$\gamma\,\delta\alpha_0 + (\partial_\rho\partial_\alpha\mathcal{E}_p)|_{\alpha_0}\,\delta\rho + (\partial_{Y_2}\partial_\alpha\mathcal{E}_p)|_{\alpha_0}\,\delta Y_2 + (\partial_{m_b}\partial_\alpha\mathcal{E}_p)|_{\alpha_0}\,\delta m_b = 0. \tag{2.109}$$

Decomposition the variation of the action along each variable gives

$$\begin{aligned}
\delta\mathcal{A}_{b_a} = -\int \partial_{b_a}\mathcal{L}\boldsymbol{\nabla}b_a\cdot\boldsymbol{\eta}, \qquad \delta\mathcal{A}_{b_a} = -\int \partial_{b_a}\mathcal{L}\boldsymbol{\nabla}b_a\cdot\boldsymbol{\eta}, \qquad \delta\mathcal{A}_\rho = \int_\Omega \rho\boldsymbol{\nabla}(\partial_\rho\mathcal{L})\cdot\boldsymbol{\eta}, \qquad \delta\mathcal{A}_{\tilde{\alpha}} = \int_\Omega \partial_{\tilde{\alpha}}\mathcal{L}\delta\tilde{\alpha},\\
\delta\mathcal{A}_{\boldsymbol{u}} &= \int_\Omega -(\partial_t\boldsymbol{K} + \boldsymbol{\nabla}\cdot(\boldsymbol{K}\otimes\boldsymbol{u}) + \boldsymbol{K}\cdot\boldsymbol{\nabla}\boldsymbol{u})\cdot\boldsymbol{\eta},\\
\delta\mathcal{A}_{\alpha_0} &= \int_\Omega \left\{\rho\boldsymbol{\nabla}\left[\gamma^{-1}(\partial_{\alpha_0}\mathcal{L})(\partial_\rho\partial_\alpha\mathcal{E}_p)|_{\alpha_0}\right] + \gamma^{-1}(\partial_{\alpha_0}\mathcal{L})(\partial_{Y_2}\partial_\alpha\mathcal{E}_p)|_{\alpha_0}\boldsymbol{\nabla}Y_2 + \gamma^{-1}(\partial_{\alpha_0}\mathcal{L})(\partial_{m_b}\partial_\alpha\mathcal{E}_p)|_{\alpha_0}\boldsymbol{\nabla}m_b\right\}\cdot\boldsymbol{\eta},\\
\delta\mathcal{A}_{(D_t\tilde{\alpha}+\tilde{\alpha}\boldsymbol{\nabla}\cdot\boldsymbol{u})} &= \int_\Omega (-\partial_t M - \boldsymbol{\nabla}\cdot(M\boldsymbol{u}) + M(\boldsymbol{\nabla}\cdot\boldsymbol{u}))\delta\tilde{\alpha}\\
&\quad - \int_\Omega (M\boldsymbol{\nabla}(D_t\tilde{\alpha}) + (\partial_t M + \boldsymbol{\nabla}\cdot(M\boldsymbol{u}))\boldsymbol{\nabla}\tilde{\alpha})\cdot\boldsymbol{\eta}\\
&\quad + \int_\Omega [\boldsymbol{\nabla}(\tilde{\alpha}(\partial_t M + \boldsymbol{\nabla}\cdot(M\boldsymbol{u})) + M(D_t\tilde{\alpha} + \tilde{\alpha}(\boldsymbol{\nabla}\cdot\boldsymbol{u}))) - \tilde{\alpha}\boldsymbol{\nabla}(M(\boldsymbol{\nabla}\cdot\boldsymbol{u})) - M\boldsymbol{\nabla}(\tilde{\alpha}(\boldsymbol{\nabla}\cdot\boldsymbol{u}))]\cdot\boldsymbol{\eta}.
\end{aligned} \tag{2.110}$$

It yields the following system

$$\begin{cases} \partial_t \boldsymbol{K} + \boldsymbol{\nabla}\cdot(\boldsymbol{K}\otimes\boldsymbol{u} - (\mathcal{L}^* + M(D_t\tilde{\alpha} + \tilde{\alpha}\boldsymbol{\nabla}\cdot\boldsymbol{u}) + \tilde{\alpha}(\partial_{\tilde{\alpha}}\mathcal{L}) + \rho(\partial_{\alpha_0}\mathcal{L})\gamma^{-1}(\partial_\rho\partial_\alpha\mathcal{E}_p)|_{\alpha_0})\mathbf{I}) = \mathbf{0}, \\ \partial_t M + \boldsymbol{u}\cdot\boldsymbol{\nabla}M = \partial_{\tilde{\alpha}}\mathcal{L}, \end{cases} \tag{2.111}$$

Evaluating the derivatives of the Lagrangian gives

$$\begin{gathered} \boldsymbol{K} = \rho\boldsymbol{u}, \qquad \mathcal{L}^* = -\left((1-\alpha_0)p_1 + \alpha_0 p_2 - \frac{2}{3}\sigma(4\pi)^{1/3}(3\alpha)^{2/3}\left(\frac{\rho Y_2}{m_b}\right)\right) - \frac{1}{3}\nu(D_t\tilde{\alpha} + \tilde{\alpha}\boldsymbol{\nabla}\cdot\boldsymbol{u})^2 - \frac{1}{2}(\rho\partial_\rho\gamma - \gamma)\tilde{\alpha}^2, \\ M = \nu(D_t\tilde{\alpha} + \tilde{\alpha}\boldsymbol{\nabla}\cdot\boldsymbol{u}), \qquad \partial_{\tilde{\alpha}}\mathcal{L} = -\gamma\tilde{\alpha}, \qquad \partial_{\alpha_0}\mathcal{L} = \frac{1}{2}\left(\frac{1}{3\alpha_0} - \frac{1}{1-\alpha_0}\right)(D_t\tilde{\alpha} + \tilde{\alpha}\boldsymbol{\nabla}\cdot\boldsymbol{u})^2 - \frac{1}{2}\partial_{\alpha_0}\gamma\tilde{\alpha}^2, \end{gathered} \tag{2.112}$$

and

$$\begin{aligned} &\mathcal{L}^* + M(D_t\tilde{\alpha} + \tilde{\alpha}\boldsymbol{\nabla}\cdot\boldsymbol{u}) + \tilde{\alpha}(\partial_{\tilde{\alpha}}\mathcal{L}) + \rho(\partial_{\alpha_0}\mathcal{L})\gamma^{-1}(\partial_\rho\partial_\alpha\mathcal{E}_p)|_{\alpha_0} \\ =& -p_1 + \frac{1}{2}(\frac{4}{3} + \rho\frac{1}{\gamma}(\frac{1}{3\alpha_0} - \frac{1}{1-\alpha_0})(\partial_\rho\partial_\alpha\mathcal{E}_p)|_{\alpha_0})\nu(D_t\tilde{\alpha} + \tilde{\alpha}\boldsymbol{\nabla}\cdot\boldsymbol{u})^2 - \frac{1}{2}(\rho\partial_\rho\gamma + \rho\frac{\partial_{\alpha_0}\gamma}{\gamma}(\partial_\rho\partial_\alpha\mathcal{E}_p)|_{\alpha_0} + \gamma)\tilde{\alpha}^2. \end{aligned} \tag{2.113}$$

We further simplify the expressions by assuming a linearized EOS and a dilute bubbly flow $\alpha_0 \ll 1$. The expressions above simplify particularly for

$$\begin{gathered} \nu = \frac{1}{(4\pi)^{2/3}3^{1/3}}\left(\frac{(1-Y_2)m_b^{2/3}}{Y_2^{2/3}}\right)\frac{\rho^{1/3}}{\alpha_0^{1/3}}, \qquad \gamma = \frac{\rho Y_2 c_2^2}{\alpha_0^2}, \\ \mathcal{L}^* + M(D_t\tilde{\alpha} + \tilde{\alpha}\boldsymbol{\nabla}\cdot\boldsymbol{u}) + \tilde{\alpha}(\partial_{\tilde{\alpha}}\mathcal{L}) + \rho(\partial_{\alpha_0}\mathcal{L})\gamma^{-1}(\partial_\rho\partial_\alpha\mathcal{E}_p)|_{\alpha_0} = -p_1 + \frac{1}{2}\nu(D_t\tilde{\alpha} + \tilde{\alpha}\boldsymbol{\nabla}\cdot\boldsymbol{u})^2 + \frac{\gamma}{\alpha_0}\tilde{\alpha}^2. \end{gathered} \tag{2.114}$$

Under these assumptions, and using the notation $w = D_t\tilde{\alpha} + \tilde{\alpha}\boldsymbol{\nabla}\cdot\boldsymbol{u}$, we obtain Model 16.

Model 16 (Dilute monodisperse model of linearly pulsating bubbles)

With $m_k = \alpha_k\rho_k$ the phase densities for $k = 1, 2^d$, $\alpha_2^d = \alpha_0 + \tilde{\alpha}$ the bubbles volumes fraction decomposed in an equilibrium part and a pulsating part, ρ the mixture density, $\boldsymbol{u}$ the mixture velocity, $\Sigma\langle G\rangle$ the surface-average density of Gauss curvature, p_1 the liquid pressure, the flow is governed by

$$\begin{cases} \partial_t m_1 & +\boldsymbol{\nabla}\cdot(m_1\boldsymbol{u}) & = 0, \\ \partial_t m_2^d & +\boldsymbol{\nabla}\cdot(m_2^d\boldsymbol{u}) & = 0, \\ \partial_t(\Sigma\langle G\rangle) & +\boldsymbol{\nabla}\cdot(\Sigma\langle G\rangle\boldsymbol{u}) & = 0, \\ \partial_t(\rho\boldsymbol{u}) & +\boldsymbol{\nabla}\cdot(\rho\boldsymbol{u}\otimes\boldsymbol{u} + (p_1 - \frac{1}{2}\nu w^2 - \frac{\gamma}{\alpha_0}\tilde{\alpha}^2)\boldsymbol{I}) & = \mathbf{0}, \\ \partial_t w + \boldsymbol{u}\cdot\boldsymbol{\nabla}w = -\frac{\gamma}{\nu}\tilde{\alpha}, \end{cases}$$

with α_0 defined by the Laplace equilibrium

$$p_2\left(\frac{m_2^d}{\alpha_0}\right) - p_1\left(\frac{m_1}{1-\alpha_0}\right) = \sigma\frac{2}{R_0},$$

and $w = D_t\tilde{\alpha} + \tilde{\alpha}\boldsymbol{\nabla}\cdot\boldsymbol{u}$, ν, γ defined by (2.114) and $R_0 = \left(\frac{3\alpha_0}{\Sigma\langle G\rangle}\right)^{1/3}$.

The obtained Laplace equilibrium is reminiscent of Models 3 and 5 with pressure equilibria. Then, similarly to the separated Model 3 at pressure and the relaxed separated Model 4, we relax the Laplace pressure jump of the Model 16 above to obtain the relaxed Model 17 below.

Model 17 (Dilute monodisperse model of linearly pulsating bubbles with relaxation)

With $m_k = \alpha_k \rho_k$ the phase densities for $k = 1, 2^d$, $\alpha_2^d = \alpha_0 + \tilde{\alpha}$ the bubbles volumes fraction decomposed in an equilibrium part and a pulsating part, ρ the mixture density, $\boldsymbol{u}$ the mixture velocity, $\Sigma \langle G \rangle$ the surface-average density of Gauss curvature, p_1 the liquid pressure, the flow is governed by

$$\begin{cases} \partial_t m_1 + \boldsymbol{\nabla} \cdot (m_1 \boldsymbol{u}) = 0, \\ \partial_t m_2^d + \boldsymbol{\nabla} \cdot (m_2^d \boldsymbol{u}) = 0, \\ \partial_t (\Sigma \langle G \rangle) + \boldsymbol{\nabla} \cdot (\Sigma \langle G \rangle \boldsymbol{u}) = 0, \\ \partial_t \alpha_0 + \boldsymbol{u} \cdot \boldsymbol{\nabla} \alpha_0 = \frac{1}{\mu} \left(p_2 \left(\frac{m_2^d}{\alpha_0} \right) - p_1 \left(\frac{m_1}{1-\alpha_0} \right) - \sigma 2 \left(\frac{\Sigma \langle G \rangle}{\alpha_0} \right)^{1/3} \right), \\ \partial_t w + \boldsymbol{u} \cdot \boldsymbol{\nabla} w = -\frac{\gamma}{\nu} \tilde{\alpha}, \\ \partial_t (\rho \boldsymbol{u}) + \boldsymbol{\nabla} \cdot \left(\rho \boldsymbol{u} \otimes \boldsymbol{u} + (p_1 - \frac{1}{2} \nu w^2 - \frac{\gamma}{\alpha_0} \tilde{\alpha}^2) \boldsymbol{I} \right) = \boldsymbol{0}, \end{cases}$$

with $w = D_t \tilde{\alpha} + \tilde{\alpha} \boldsymbol{\nabla} \cdot \boldsymbol{u}$, ν, γ defined by (2.114).

The hyperbolicity of the augmented model where w is independent of $\tilde{\alpha}$, with $D_t \tilde{\alpha} + \tilde{\alpha} \boldsymbol{\nabla} \cdot \boldsymbol{u} = w$. The following eigenvalues are obtained

$$u, \quad u - c, \quad u + c, \qquad \text{with} \quad c = \sqrt{c_1^2 - \frac{\nu w^2}{6\rho} + \frac{3 Y_2^d c_2^2}{\alpha_0^3} \tilde{\alpha}^2}, \tag{2.115}$$

with u of multiplicity 6 and 6 corresponding independent eigenvectors. The pulsation motion of the bubbles still affects the propagation of sound in the medium, but weakly as we assumed a dilute regime. Moreover, in the limit where the volume fraction of bubbles vanishes,

$$w \to 0, \qquad \frac{3 Y_2^d c_2^2}{\alpha_0^3} \tilde{\alpha}^2 = \frac{3 c_2^2}{\rho} \frac{\tilde{\alpha}^2}{\alpha_0^2} \left(1 + \frac{\tilde{\alpha}}{\alpha_0} \right) \to 0,$$

such that the velocity of the carrier fluid is recovered $c \to c_1$.

2.2.3.4 Conclusion of Section 2.2

Finally, these models for monodisperse pulsating bubbles have illustrated how the compressible effects of both the carrier liquid phase and the gaseous bubbles act on each other. At the level of the bubble, the compressibility allows the bubble oscillation around an equilibrium volume defined by the Laplace law. At the level of the carrier phase, the variations of pressure p_1 modifies this Laplace equilibrium. In the non-linear model, these two effects are fully coupled whereas they have been split between two different contributions for the linear model, either through the change of volume of equilibrium of the bubbles with α_0, or the pulsation motion at the small-scale with the dynamics of $\tilde{\alpha}$. One can extend this approach to the bi-disperse regime, but it adds a significant step of complexity as the model would involve two Laplace laws, one for each size of bubbles, coupled together through the influence of volume occupation in the pressure of the carrier phase.

2.2.4 Application 3: Spray of oscillating droplets

Let us model the spray of oscillating droplets by first considering the following hypotheses :

- the droplets' internal flow is irrotational; (H2a)
- the amplitude of the interface deformation is small; (H2b)
- the droplets' interface is deformed along the second axisymmetric spherical harmonic. (H2c)

2.2.4.1 The oscillation model

The dynamics of a droplet satisfying (H2a) and (H2b) has been studied thoroughly (John W. Strutt (3rd Baron Rayleigh), 1879; Prosperetti, 1977; Plümacher et al., 2020). Denote $\boldsymbol{r}$ the position of the droplet interface in spherical coordinates (r, θ, ϕ) and $(\boldsymbol{e}_r, \boldsymbol{e}_\theta, \boldsymbol{e}_\phi)$ the spherical orthonormalized basis. Following (H2c), we denote $Y_2(\theta) = \sqrt{5}/(4\sqrt{\pi})(3\cos^2\theta - 1)$ the second axisymmetric spherical harmonic (see Figure 2.1.1), and R_0 the radius of the non-deformed spherical droplet, such that the position writes

$$\boldsymbol{r} = (R_0 + x_2 Y_2)\boldsymbol{e}_r, \tag{2.116}$$

where x_2 denotes the amplitude of the deformation. The dynamics of this motion follows the harmonic oscillation

$$\ddot{x}_2 + \omega^2 x_2 = 0, \qquad \omega^2 = 8\frac{\sigma}{\rho_1^d R_0^3} = \tilde{\omega}^2 S_0^{-3/2}, \tag{2.117}$$

where $\tilde{\omega}^2 = (8(4\pi)^{3/2}\sigma/\rho_1^d)$ is a constant along the streamlines. The dynamics of the droplets is then characterized by $(S_0, x_2, \dot{x}_2)$. For computational reasons, we introduce $\chi = (2/S_0)^{1/2} x_2$ which satisfies the same dynamics (2.117) as x_2. The balance equation for the NDF n_ξ in the phase-space $\widehat{\boldsymbol{\xi}} = (\widehat{S}_0, \widehat{\chi}, \widehat{\dot{\chi}})$ yields

$$\partial_t n_\xi + \boldsymbol{\nabla}_{\boldsymbol{x}} \cdot (n_\xi \boldsymbol{u}) + \partial_{\widehat{\chi}}(R_\chi n_\xi) + \partial_{\widehat{\dot{\chi}}}(R_{\dot{\chi}} n_\xi) = 0, \tag{2.118}$$

where R_χ and $R_{\dot{\chi}}$ are rates of change that remain to be closed. With the oscillator model (2.117), we close (2.118) by fixing $R_\chi = \widehat{\dot{\chi}}$ and $R_{\widehat{\dot{\chi}}} = -\tilde{\omega}^2 \widehat{S}_0^{-3/2}\widehat{\chi}$,

$$\partial_t n_\xi + \boldsymbol{\nabla}_{\boldsymbol{x}} \cdot (n_\xi \boldsymbol{u}) + \partial_{\widehat{\chi}}(\widehat{\dot{\chi}} n_\xi) + \partial_{\widehat{\dot{\chi}}}(-\tilde{\omega}^2 \widehat{S}_0^{-3/2}\widehat{\chi} n_\xi) = 0. \tag{2.119}$$

This model can be seen as a particular case of the kinetic model considered by O'Rourke and Amsden (1987); Amsden et al. (1989) where only the oscillation motion is retained.

2.2.4.2 Modelling a spray of asynchronously oscillating droplets

With the new PBE (2.119), GeoMOM leads to a non-trivial closure problem and the geometric quantities chosen in (2.58) and (2.59) cannot model an arbitrary distribution. With such a choice, we propose in this section to approximate the distribution with

$$n_\xi(\boldsymbol{x}, t, \widehat{S}_0, \widehat{\chi}, \widehat{\dot{\chi}}) = n_{S_0}(\boldsymbol{x}, t, \widehat{S}_0)\frac{1}{|\mathcal{E}(\widehat{S}_0)|}\mathbb{1}_{\mathcal{E}(\widehat{S}_0)}(\widehat{\chi}, \widehat{\dot{\chi}}), \tag{2.120}$$

where the amplitudes and their rates of change $(\widehat{\chi}, \widehat{\dot{\chi}})$ are uniformly distributed on a compact space $\mathcal{E} \subset \mathbb{R}^2$ of area $|\mathcal{E}(\widehat{S}_0)|$ that allows a maximal energy for a given droplet size $\widehat{S}_0$. It is later identified in (2.131). This approximation of the NDF discards situations where droplets oscillate synchronously, and consequently a macroscopic oscillation motion of the spray. However, it could be more adapted to the mixed regime where the droplets resulting from primary breakups are very agitated by coalescence and drag phenomena.

2.2.4.2.a GeoMOM based on the classic surface-average operator

We apply GeoMOM with the same surface-average operators $\langle\cdot\rangle$ and $\widetilde{(\cdot)}$ defined in Section 2.1, and geometric quantities $\Sigma\langle G\rangle$, $\Sigma\langle H\rangle$, Σ, α_1^d. We establish then the relations between these geometric quantities and moments of the NDF in the context of a disperse regime,

$$\Sigma\langle G\rangle = \int_{\widehat{\xi}} S\widetilde{G}\, n_\xi \, d\widehat{\boldsymbol{\xi}}, \quad \Sigma\langle H\rangle = \int_{\widehat{\xi}} S\widetilde{H}\, n_\xi \, d\widehat{\boldsymbol{\xi}}, \quad \Sigma = \int_{\widehat{\xi}} S\, n_\xi \, d\widehat{\boldsymbol{\xi}}, \quad \alpha_1^d = \int_{\widehat{\xi}} V\, n_\xi \, d\widehat{\boldsymbol{\xi}}. \tag{2.121}$$

When the oscillations are small and considering only a perturbation along mode Y_2, (2.40) shows that

$$\delta V = R_0^2 x_0 + R_0 x_0^2 + R_0 x_2^2 + o(x_0^2 + x_2^2), \qquad \delta S = 2R_0 x_0 + x_0^2 + 4x_2^2 + o(x_0^2 + x_2^2), \qquad \delta(S\tilde{H}) = x_0 + 3R_0^{-1}x_2^2 + o(x_0^2 + x_2^2). \tag{2.122}$$

Then enforcing incompressibility at the kinematics level *i.e.* $\delta V = 0$ yields

$$x_0 = -R_0^{-1} x_2^2 + o(x_2^2), \tag{2.123}$$

and the geometric variations read

$$\delta V = 0, \quad \delta S = 2x_2^2 + o(x_2^2), \quad \delta(S\tilde{H}) = 2R_0^{-1} x_2^2 + o(x_2^2). \tag{2.124}$$

Equivalently, with the variable χ, it reads

$$S\tilde{G} = 4\pi, \quad S\tilde{H} - S_0\tilde{H}_0 = \sqrt{4\pi} S_0^{1/2} \chi^2, \quad V = \frac{1}{3\sqrt{4\pi}} S_0^{3/2}, \quad S - S_0 = S_0 \chi^2, \tag{2.125}$$

where $\tilde{H}_0 = \sqrt{4\pi} S_0^{-1/2}$ is the surface averaged mean curvature when the droplet is a sphere *i.e.* $\chi = 0$. Remark that $S\tilde{G}$ and α_1^d are constant despite the oscillation thanks to the Gauss-Bonnet Theorem 3 and the incompressibility assumption. Finally, relations between geometric quantities and moments $M^{\xi}_{i,j,k} := \int_{\widehat{\boldsymbol{\xi}}} \widehat{S}^i \widehat{\chi}^j \widehat{\chi}^k \, n_\xi \, d\widehat{\boldsymbol{\xi}}$ of n_ξ are obtained

$$\begin{aligned} \Sigma \langle G \rangle &= 4\pi M^{\xi}_{0,0,0}, & \Sigma \langle H \rangle &= \sqrt{4\pi}(M^{\xi}_{1/2,0,0} + M^{\xi}_{1/2,2,0}), \\ \Sigma &= M^{\xi}_{1,0,0} + M^{\xi}_{1,2,0}, & \alpha_1^d &= \frac{1}{3\sqrt{4\pi}} M^{\xi}_{3/2,0,0}. \end{aligned} \tag{2.126}$$

These relations extend the ones of (2.64) with moments dedicated to the oscillatory dynamics. Such decomposition leads us to define and choose the following geometric quantities and moments for our model

$$\begin{aligned} \Sigma \langle H \rangle_0 &:= \sqrt{4\pi} M^{\xi}_{1/2,0,0}, & \Delta(\Sigma \langle H \rangle) &:= \sqrt{4\pi} M^{\xi}_{1/2,2,0}, \\ \Sigma_0 &:= M^{\xi}_{1,0,0}, & \Delta\Sigma &:= M^{\xi}_{1,2,0}, \end{aligned} \tag{2.127}$$

instead of just Σ and $\Sigma \langle H \rangle$ which can be reconstructed with (2.126). Integrating (2.119) against $1, \widehat{S}_0^{1/2}, \widehat{S}_0, \widehat{S}_0^{3/2}, \widehat{S}_0^{1/2}\widehat{\chi}^2, \widehat{S}_0\widehat{\chi}^2$ provides

$$\begin{cases} \partial_t(\Sigma \langle G \rangle) & + \boldsymbol{\nabla} \cdot (\Sigma \langle G \rangle \boldsymbol{u}) & = 0, \\ \partial_t(\Sigma \langle H \rangle_0) & + \boldsymbol{\nabla} \cdot (\Sigma \langle H \rangle_0 \boldsymbol{u}) & = 0, \\ \partial_t \Sigma_0 & + \boldsymbol{\nabla} \cdot (\Sigma_0 \boldsymbol{u}) & = 0, \\ \partial_t \alpha_1^d & + \boldsymbol{\nabla} \cdot (\alpha_1^d \boldsymbol{u}) & = 0, \\ \partial_t(\Delta(\Sigma \langle H \rangle)) & + \boldsymbol{\nabla} \cdot (\Delta(\Sigma \langle H \rangle) \boldsymbol{u}) & = 2\sqrt{4\pi} M^{\xi}_{1/2,1,1}, \\ \partial_t(\Delta\Sigma) & + \boldsymbol{\nabla} \cdot (\Delta\Sigma \boldsymbol{u}) & = 2M^{\xi}_{1,1,1}. \end{cases} \tag{2.128}$$

We obtained that $\Sigma \langle G \rangle$, $\Sigma \langle H \rangle_0$, Σ_0 and α_1^d are conserved similarly as (2.61) with two additional equations for the oscillatory components $\Delta(\Sigma \langle H \rangle)$ and $\Delta\Sigma$.

2.2.4.2.b Energies of the spray

In the context of two-scale modelling with Hamilton's SAP, we are specifically interested in defining the energies of the spray with the geometric quantities. For the oscillatory motion described by (2.117), the kinetic and potential energies of a droplet can be expressed as function of $\boldsymbol{\xi}$ (John W. Strutt (3rd Baron Rayleigh), 1879, appendix II)

$$E^{kin,1d} = \frac{1}{2} \frac{\rho_1^d}{4(4\pi)^{3/2}} S_0^{5/2} \dot{\chi}^2, \qquad E^{pot,1d} = \sigma S = \sigma S_0 + \sigma S_0 \chi^2. \tag{2.129}$$

It is then straightforward to obtain the energies of the spray $E^{kin,d}$ and $E^{pot,d}$ from moments of n_ξ by integrating the expressions above,

$$E^{kin,d} = \frac{1}{2} \frac{\rho_1^d}{4(4\pi)^{3/2}} M^{\xi}_{5/2,0,2}, \qquad E^{pot,d} = \sigma\Sigma = \sigma M^{\xi}_{1,0,0} + \sigma M^{\xi}_{1,2,0}. \tag{2.130}$$

Remark that the moment $M^{\xi}_{5/2,0,2}$ is not linked to any of the selected geometric quantities of the model. We can find a closure for this moment using the approximation of n^{ξ} given in (2.120). It requires to provide a definition for $\mathcal{E}$ which is chosen following the break-up criterion of O'Rourke and Amsden (1987). Therefore, we authorize the droplets to oscillate with an energy lower than a fraction $c \in [0,1]$ of the maximal energy E_{max} before break-up,

$$\mathcal{E}(\widehat{S}_0) := \left\{ (\widehat{\chi}, \widehat{\dot{\chi}}) \in \mathbb{R}^2 \text{ s.t. } E^{kin,1d}(\widehat{S}_0, \widehat{\chi}, \widehat{\dot{\chi}}) + E^{pot,1d}(\widehat{S}_0, \widehat{\chi}, \widehat{\dot{\chi}}) \leq c E_{max}(\widehat{S}_0) \right\}. \tag{2.131}$$

The break-up energy $E_{max}(S_0)$ corresponds to a deformation up to an equatorial radius reaching half the value of the spherical radius

$$R_{eq} := \|\boldsymbol{r}(\pi/2)\| = \frac{R_0}{2}. \tag{2.132}$$

Then, the subset $\mathcal{E}$ boils down to $\mathcal{E} = \{\chi^2 + (\dot{\chi}/\omega)^2 \leq 2c/5\}$ whose area is $|\mathcal{E}| = \frac{2}{5}\pi\omega c$. We can now close the expression of $E^{kin,d}$, $E^{pot,d}$ in (2.130) and find the dynamics of the parameter c using (2.128) and the approximation of the NDF (2.120). It yields

$$E^{kin,d} = \frac{1}{10} c\sigma\Sigma_0, \quad E^{pot,d} = \sigma\Sigma_0 + \frac{1}{10} c\sigma\Sigma_0, \quad D_t c = 0. \tag{2.133}$$

Remark that, as $(\chi, \dot{\chi})$ are uniformly distributed in $\mathcal{E}$, the mechanical energy is evenly distributed between kinetic and potential energies. Regarding the dynamics of c, it means that the energy of the oscillation is advected along the streamline. Moreover, using the relation $\Delta\Sigma = M^{\xi}_{1,2,0}$, one can replace c by geometric quantities with $c = 10\Delta\Sigma/\Sigma_0$. Remark also that we chose $\Delta\Sigma$ to define the energies over $\Delta(\Sigma\langle H\rangle)$ which is now omitted in the following models, but it can be reconstructed with the relations (2.127).

Now, the energies of the small-scale have been defined, and we can proceed to the derivation of the two-phase model dynamics with Hamilton's SAP.

2.2.4.2.c Two-scale model with the small-scale spray model of asynchronous droplets

Energies related to the small-scale oscillation are negatively signed in Hamilton's SAP as the kinetic energy is not a quadratic form of any kind of velocity. Indeed, the energy of the droplets is here considered as a whole energetic contribution without following their specific dynamics. The expression of the Lagrangian corresponds then to

$$\mathcal{L} = \frac{1}{2}\rho\|\boldsymbol{u}\|^2 - m_2 e_2\left(\frac{m_2}{1-\alpha_1^d}\right) - m_1^d e_1(\rho_1^d) - \sigma\Sigma_0\left(1 + \frac{c}{5}\right). \tag{2.134}$$

The constraints are the same as in Section 1.4.1 with the additional advection constraint $D_t c = 0$. The derivation of the two-scale mixture's dynamics with Hamilton's SAP is very similar (only advected or conserved variables are added) and yields Model 18.

Model 18 (Polydisperse spray model of asynchronously oscillating droplets)

With $m_k = \alpha_k \rho_k$ and α_k the phase densities and volume fractions of phases $k = 2, 1^d$, $\rho = m_1 + m_2$ the mixture's density, $\boldsymbol{u}$ the velocity and $p_2(\rho_2)$ the pressure of the gaseous phase 2, $\Sigma = \Sigma_0 + \Delta\Sigma$ the IAD decomposed in a static part and an oscillation-related part, the static-related parts of the surface-averaged density of the mean and Gauss curvatures $\Sigma \langle H \rangle_0$ and $\Sigma \langle G \rangle$, the flow is governed by

$$\begin{cases} \partial_t m_2 & + \boldsymbol{\nabla} \cdot (m_2 \boldsymbol{u}) & = 0, \\ \partial_t m_1^d & + \boldsymbol{\nabla} \cdot (m_1^d \boldsymbol{u}) & = 0, \\ \partial_t \alpha_1^d & + \boldsymbol{\nabla} \cdot (\alpha_1^d \boldsymbol{u}) & = 0, \\ \partial_t \Sigma_0 & + \boldsymbol{\nabla} \cdot (\Sigma_0 \boldsymbol{u}) & = 0, \\ \partial_t (\Delta\Sigma) & + \boldsymbol{\nabla} \cdot (\Delta\Sigma \boldsymbol{u}) & = 0, \\ \partial_t (\Sigma \langle G \rangle) & + \boldsymbol{\nabla} \cdot (\Sigma \langle G \rangle \boldsymbol{u}) & = 0, \\ \partial_t (\Sigma \langle H \rangle_0) & + \boldsymbol{\nabla} \cdot (\Sigma \langle H \rangle_0 \boldsymbol{u}) & = 0, \\ \partial_t (\rho \boldsymbol{u}) & + \boldsymbol{\nabla} \cdot (\rho \boldsymbol{u} \otimes \boldsymbol{u} + p_2 \boldsymbol{I}) & = \boldsymbol{0}. \end{cases}$$

The model also admits an additional equation for the mathematical entropy for Model 18,

$$\partial_t \mathcal{H} + \boldsymbol{\nabla} \cdot ((\mathcal{H} + p_2)\boldsymbol{u}) = 0, \qquad \mathcal{H} = \frac{1}{2}\rho \|\boldsymbol{u}\|^2 + m_2 e_2 \left(\frac{m_2}{1 - \alpha_1^d} \right) + m_1^d e_1(\rho_1^d) + \sigma \Sigma_0 \left(1 + \frac{c}{5} \right). \tag{2.135}$$

Now considering dissipation processes, we could also add the pressure relaxation as in the previous two-scale models. We propose here to focus on the dissipation associated with the small-scale oscillatory dynamics. Indeed, the oscillation motion eventually decreases and the associated energy dissipates into thermal energy or small-scale kinetic energy of the gas phase. Each of these last two energies are not modelled here, so the system loses this energy, and we only consider the following source term R_c on the dynamics of c,

$$D_t c = R_c. \tag{2.136}$$

The mathematical entropy production writes

$$\partial_t \mathcal{H} + \boldsymbol{\nabla} \cdot ((\mathcal{H} + p_2)\boldsymbol{u}) = -(\partial_c \mathcal{L}) R_c. \tag{2.137}$$

As $\partial_c \mathcal{L} = -\sigma \Sigma_0 / 5$, we choose $R_c = -c/\tau$ in Model 19 to sign the mathematical entropy production $\varsigma \leq 0$ and model the dissipation with an exponential decrease of characteristic time $\tau > 0$.

Model 19 (Dissipative polydisperse spray model of asynchronously oscillating droplets)

With $m_k = \alpha_k \rho_k$ and α_k the phase densities and volume fractions of phases $k = 2, 1^d$, $\rho = m_1 + m_2$ the mixture's density, $\boldsymbol{u}$ the velocity and $p_2(\rho_2)$ the pressure of the gaseous phase 2, $\Sigma = \Sigma_0 + \Delta\Sigma$ the IAD decomposed in a static part and an oscillation-related part, the static-related parts of the surface-averaged density of the mean and Gauss curvatures $\Sigma \langle H \rangle_0$ and $\Sigma \langle G \rangle$, the flow is governed by

$$\begin{cases} \partial_t m_2 & + \boldsymbol{\nabla} \cdot (m_2 \boldsymbol{u}) & = 0, \\ \partial_t m_1^d & + \boldsymbol{\nabla} \cdot (m_1^d \boldsymbol{u}) & = 0, \\ \partial_t \alpha_1^d & + \boldsymbol{\nabla} \cdot (\alpha_1^d \boldsymbol{u}) & = 0, \\ \partial_t \Sigma_0 & + \boldsymbol{\nabla} \cdot (\Sigma_0 \boldsymbol{u}) & = 0, \\ \partial_t (\Delta\Sigma) & + \boldsymbol{\nabla} \cdot (\Delta\Sigma \boldsymbol{u}) & = -\tau^{-1} \Delta\Sigma, \\ \partial_t (\Sigma \langle G \rangle) & + \boldsymbol{\nabla} \cdot (\Sigma \langle G \rangle \boldsymbol{u}) & = 0, \\ \partial_t (\Sigma \langle H \rangle_0) & + \boldsymbol{\nabla} \cdot (\Sigma \langle H \rangle_0 \boldsymbol{u}) & = 0, \\ \partial_t (\rho \boldsymbol{u}) & + \boldsymbol{\nabla} \cdot (\rho \boldsymbol{u} \otimes \boldsymbol{u} + p_2 \boldsymbol{I}) & = \boldsymbol{0}. \end{cases}$$

One can see that the component of the interface area density modelling the droplets' dynamics have now its own dynamics with an additional source term that makes it dissipate over time. We proposed, with this first model, a precise derivation framework to recover some essential dynamical mechanisms in the evolution of volume fraction, namely a conservative structure and a dissipation rate. This model is further extended in Section 3.2.3 with a creation term such that a model with comparable dynamics as Vallet et al. (2001) is obtained. Then, in the context of droplets all resulting from a same mechanism, say the synchronous break up of multiple filaments, we would be interested in capturing a global oscillation motion. Such a situation is discussed in the next section.

2.2.4.3 Modelling a spray of synchronously oscillating droplets

With the choice of geometric quantities of the previous section, the moments are not suited to obtain a macroscopic oscillation of the spray. Therefore, we introduce now new geometric quantities with GeoMOM based on another surface-average operator, and the following NDF approximation

$$n_{\xi}(\widehat{S}_0, \widehat{\chi}, \widehat{\dot{\chi}}) = \sum_i n_i \delta(\widehat{S}_0 - (S_0)_i) \delta(\widehat{\chi} - \chi_i) \delta(\widehat{\dot{\chi}} - \dot{\chi}_i). \tag{2.138}$$

This corresponds to several populations of droplets which share the same size and oscillate synchronously.

2.2.4.3.a GeoMOM based on an oriented surface-average operator

Similarly to Section 2.1, we consider a surface $\mathcal{S}$ and its mapping $\mathcal{U} \subset \mathbb{R}^2$ onto $\mathcal{S} \subset \mathbb{R}^3$ such that $A(u,v)\, dudv$ is the infinitesimal surface element over $\mathcal{S}$. We decompose the surface local area into two contributions, one related to a preferred direction $\boldsymbol{N}$, say the one given by the large-scale dynamics. In this sense, we decompose this infinitesimal surface element $A(u,v)\, dudv$ using its definition using tangential vectors $\boldsymbol{e}_u$ and $\boldsymbol{e}_v$ (see Figure 2.2.1),

$$A = \|\boldsymbol{e}_u \times \boldsymbol{e}_v\|, \qquad A_{\parallel} = |(\boldsymbol{e}_u \times \boldsymbol{e}_v) \cdot \boldsymbol{N}|, \qquad A_{\perp} = A - A_{\parallel}. \tag{2.139}$$

From them, we decompose the surface into parallel and perpendicular components $S_{\parallel}$ and $S_{\perp}$ such that

$$S = \int_{\mathcal{U}} A(u,v)\, dudv = \int_{\mathcal{U}} A_{\parallel}(u,v)\, dudv + \int_{\mathcal{U}} A_{\perp}(u,v)\, dudv = S_{\parallel} + S_{\perp}. \tag{2.140}$$

We also define new surface-average operators similarly to (2.14)

$$\langle \cdot \rangle_{\parallel} := \frac{1}{S_{\parallel}} \int_{\mathcal{U}} (\cdot)\, A_{\parallel}(u,v)\, dudv, \qquad \langle \cdot \rangle_{\perp} := \frac{1}{S_{\perp}} \int_{\mathcal{U}} (\cdot)\, A_{\perp}(u,v)\, dudv, \tag{2.141}$$

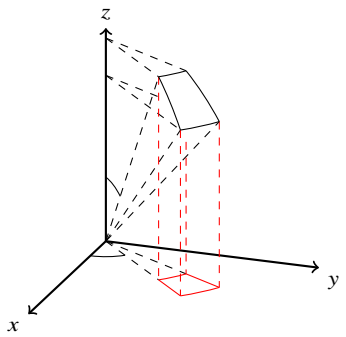

Figure 2.2.1: Decomposition of the element of surface.

and the surface-average operators $\widetilde{(\cdot)}^{\parallel}$, $\widetilde{(\cdot)}^{\perp}$ for one closed inclusion. Considering now the oscillatory motion (2.117), we have the following dynamics for the geometric quantities of one droplet (see details in appendix 2.B)

$$\begin{aligned} S_{\parallel} &= \frac{1}{2}S_0 - \frac{1}{\sqrt{4\pi}}\sqrt{\frac{5\pi}{2}}S_0\chi, \qquad S_{\parallel}\widetilde{H}^{\parallel} = \frac{1}{2}\sqrt{4\pi}\sqrt{S_0} - \frac{1}{2}\sqrt{\frac{5\pi}{2}}\sqrt{S_0}\chi, \\ S_{\perp} &= \frac{1}{2}S_0 + \frac{1}{\sqrt{4\pi}}\sqrt{\frac{5\pi}{2}}S_0\chi, \qquad S_{\perp}\widetilde{H}^{\perp} = \frac{1}{2}\sqrt{4\pi}\sqrt{S_0} + \frac{1}{2}\sqrt{\frac{5\pi}{2}}\sqrt{S_0}\chi. \end{aligned} \tag{2.142}$$

Defining the oriented interface area densities $\Sigma_{\perp}$ and $\Sigma_{\parallel}$ within the mixture, we remark that $\Sigma = \Sigma_{\perp} + \Sigma_{\parallel}$ and $\Sigma\langle\cdot\rangle = \Sigma_{\perp}\langle\cdot\rangle_{\perp} + \Sigma_{\parallel}\langle\cdot\rangle_{\parallel}$. Integrating (2.142) against n_{ξ} provides

$$\begin{aligned} \Sigma_{\parallel} &= \frac{1}{2}M^{\xi}_{1,0,0} - \frac{1}{\sqrt{4\pi}}\sqrt{\frac{5\pi}{2}}M^{\xi}_{1,1,0}, \quad (\Sigma\langle H\rangle)_{\parallel} = \frac{1}{2}\sqrt{4\pi}M^{\xi}_{1/2,0,0} - \frac{1}{2}\sqrt{\frac{5\pi}{2}}M^{\xi}_{1/2,1,0}, \\ \Sigma_{\perp} &= \frac{1}{2}M^{\xi}_{1,0,0} + \frac{1}{\sqrt{4\pi}}\sqrt{\frac{5\pi}{2}}M^{\xi}_{1,1,0}, \quad (\Sigma\langle H\rangle)_{\perp} = \frac{1}{2}\sqrt{4\pi}M^{\xi}_{1/2,0,0} + \frac{1}{2}\sqrt{\frac{5\pi}{2}}M^{\xi}_{1/2,1,0}. \end{aligned} \tag{2.143}$$

Remark that both the parallel and perpendicular geometric variables represent the same information for the spray as they are related to the same moments of the NDF. Consequently, we here retain the perpendicular components only, and we extract the part dedicated to the dynamics by defining

$$\begin{aligned} \Sigma_{\perp,0} &:= \tfrac{1}{2}M^{\xi}_{1,0,0}, & (\Delta\Sigma_{\perp}) &:= \frac{1}{\sqrt{4\pi}}\sqrt{\frac{5\pi}{2}}M^{\xi}_{1,1,0}, \\ (\Sigma\langle H\rangle)_{\perp,0} &:= \tfrac{1}{2}\sqrt{4\pi}M^{\xi}_{1/2,0,0}, & (\Delta(\Sigma\langle H\rangle))_{\perp} &:= \frac{1}{2}\sqrt{\frac{5\pi}{2}}M^{\xi}_{1/2,1,0}. \end{aligned} \tag{2.144}$$

We intentionally factored some indexes in the two last geometric quantities to lighten the notations. This splitting allows us to retain more information on the NDF in our model by including two moments rather than the sum of two moments. We know from (2.128) that $\Sigma_{\perp,0}$ and $(\Sigma\langle H\rangle)_{\perp,0}$ are conserved, while we integrate (2.119) to obtain the dynamics of the two other geometric quantities

$$\begin{cases} \partial_t(\Delta\Sigma_{\perp}) + \boldsymbol{\nabla}\cdot((\Delta\Sigma_{\perp})\boldsymbol{u}) = \dfrac{1}{\sqrt{4\pi}}\sqrt{\dfrac{5\pi}{2}}M^{\xi}_{1,0,1}, \\ \partial_t(\Delta(\Sigma\langle H\rangle))_{\perp} + \boldsymbol{\nabla}\cdot((\Delta(\Sigma\langle H\rangle))_{\perp}\boldsymbol{u}) = \dfrac{1}{2}\sqrt{\dfrac{5\pi}{2}}M^{\xi}_{1/2,0,1}. \end{cases} \tag{2.145}$$

With the moments considered up to now, we cannot model a macroscopic oscillatory spray as we lack some information regarding the distribution of $\widehat{\chi}$ in our model. We propose then to add two new geometric quantities that correspond

to the unclosed moments of (2.145)

$$\begin{aligned}(\Delta_t\Sigma_\perp) &:= \Sigma_\perp\left\langle\frac{\partial_t A_\perp}{A_\perp}\right\rangle_\perp &&= \frac{1}{\sqrt{4\pi}}\sqrt{\frac{5\pi}{2}}M^\xi_{1,0,1},\\ (\Delta_t(\Sigma\langle H\rangle))_\perp &:= \Sigma_\perp\left\langle\partial_t H + H\frac{\partial_t A_\perp}{A_\perp}\right\rangle_\perp &&= \frac{1}{2}\sqrt{\frac{5\pi}{2}}M^\xi_{1/2,0,1}.\end{aligned} \tag{2.146}$$

The above definitions with the oriented surface-average operators show that these quantities are also well-defined regardless of the flow regime. Finally, we consider the following eight geometric quantities to describe the spray of oscillating droplets: α_1^d, $\Sigma_{\perp,0}$, $(\Delta\Sigma_\perp)$, $(\Delta_t\Sigma_\perp)$, $(\Sigma\langle H\rangle)_{\perp,0}$, $(\Delta(\Sigma\langle H\rangle))_\perp$, $(\Delta_t(\Sigma\langle H\rangle))_\perp$, $\Sigma\langle G\rangle$.

2.2.4.3.b Synchronous closure

With the eight moments given by the eight corresponding geometric quantities, we propose to look for a two-point quadrature which corresponds to two population of droplets as defined in (2.138),

$$n_\xi(\widehat{S}_0,\widehat{\chi},\widehat{\dot{\chi}}) = \sum_{i=1,2} n_i\delta(\widehat{S}_0-(S_0)_i)\delta(\widehat{\chi}-\chi_i)\delta(\widehat{\dot{\chi}}-\dot{\chi}_i), \tag{2.147}$$

where n_i are the weights or numbers of droplets that share the same abscissas χ_i and $\dot{\chi}_i$. The quadrature above admits a unique solution (excluding symmetry) under some realizability conditions that ensure that $\Sigma\langle G\rangle$, $(\Sigma\langle H\rangle)_{\perp,0}$, $\Sigma_{\perp,0}$ and α_1^d are positive with additional geometric constraints (see appendix 2.C). Remark that n_i and $(S_0)_i$ depend only on $\Sigma\langle G\rangle$, $(\Sigma\langle H\rangle)_{\perp,0}$, $\Sigma_{\perp,0}$, α_1^d and, for $(i,j)\in\{(1,2),(2,1)\}$,

$$\chi_i = \sqrt{\frac{2}{5\pi}}\frac{\sqrt{4\pi}(\Delta\Sigma_\perp)-2\sqrt{(S_0)_j}(\Delta(\Sigma\langle H\rangle))_\perp}{n_i\left((S_0)_i-\sqrt{(S_0)_i(S_0)_j}\right)},\quad \dot{\chi}_i = \sqrt{\frac{2}{5\pi}}\frac{\sqrt{4\pi}(\Delta_t\Sigma_\perp)-2\sqrt{(S_0)_j}(\Delta_t(\Sigma\langle H\rangle))_\perp}{n_i\left((S_0)_i-\sqrt{(S_0)_i(S_0)_j}\right)}. \tag{2.148}$$

We easily obtain that α_1^d, $\Sigma\langle G\rangle$, $(\Sigma\langle H\rangle)_{\perp,0}$ and $\Sigma_{\perp,0}$ are conserved such that, together with (2.145), it implies

$$\partial_t n_i + \boldsymbol{\nabla}\cdot(n_i\boldsymbol{u}) = 0,\quad D_t(S_0)_i = 0,\quad D_t\chi_i = \dot{\chi}_i,\quad i=1,2. \tag{2.149}$$

A synchronous oscillatory dynamics of two droplet size population is then expected while being advected by the flow at velocity $\boldsymbol{u}$.

2.2.4.3.c Two-scale model with the small-scale spray model of synchronous droplets

Denote $\nu := \rho_1^d/(4(4\pi)^{3/2})$ and $\gamma := 2\sigma$ such the kinetic and potential energies of the spray of oscillating droplets given in (2.130) write

$$E^{kin,d} = \frac{1}{2}\nu M^\xi_{5/2,0,2},\qquad E^{pot,d} = \sigma M^\xi_{1,0,0}+\frac{1}{2}\gamma M^\xi_{1,2,0}, \tag{2.150}$$

and $\tilde{\omega}^2 = \gamma/\nu$. The closure (2.147) then yields

$$E^{kin,d} = \sum_{i=1,2}\frac{1}{2}\nu n_i(S_0)_i^{5/2}\dot{\chi}_i^2,\qquad E^{pot,d} = \sum_{i=1,2}\sigma n_i(S_0)_i+\frac{1}{2}\gamma n_i(S_0)_i\chi_i^2. \tag{2.151}$$

We extend the two-scale Lagrangian of the one-velocity disperse model given in (3.10) by adding the energies above to account for the small-scale oscillation

$$\mathcal{L} = \mathcal{L}_1(\alpha_1,m_1,\boldsymbol{u})+\mathcal{L}_2(\alpha_2,m_2,\boldsymbol{u})+\mathcal{L}_1^d\left(m_1^d,\rho_1^d,\boldsymbol{u}\right)+\mathcal{L}_1^{vib}(n_1,(S_0)_1,\chi_1,\dot{\chi}_1)+\mathcal{L}_2^{vib}(n_2,(S_0)_2,\chi_2,\dot{\chi}_1), \tag{2.152}$$

where $\mathcal{L}_i^{vib}$ is defined using vibrating energies of (2.151)

$$\mathcal{L}_i^{vib} = \frac{1}{2}\nu n_i(S_0)_i^{5/2}\dot{\chi}_i^2-\sigma n_i(S_0)_i-\frac{1}{2}\gamma n_i(S_0)_i\chi_i^2. \tag{2.153}$$

Remark that the kinetic energy is here positively signed as it is a quadratic form of $\dot{\chi}_1$ and $\dot{\chi}_2$ with their associated momentum equations after Hamilton's SAP. We provided an expression using the quadrature's abscissas rather than the geometric quantities for computational convenience, but the dynamics of the geometric quantities is equivalently obtained using the quadrature expression of appendix 2.C. The quantities χ_1 and χ_2 are here free variables which results in the following system with two additional momentum equations for each population of droplets of same size in the spray (see appendix 2.D)

Model 20 (Polydisperse spray model of synchronously oscillating droplets)

With $m_k = \alpha_k \rho_k$ and α_k the phase densities and volume fractions of phases $k = 2, 1^d$, $\rho = m_1 + m_2$ the mixture's density, $\boldsymbol{u}$ the velocity and $p_2(\rho_2)$ the pressure of the gaseous phase 2, and n_i, (S_0), χ_i, $\dot{\chi}_i$ respectively the number density, the equilibrium surface area, the amplitude parameters of droplets of population i, the flow is governed by

$$\begin{cases} \partial_t m_2 & +\boldsymbol{\nabla}\cdot(m_2\boldsymbol{u}) & = 0, & \\ \partial_t m_1^d & +\boldsymbol{\nabla}\cdot(m_1^d\boldsymbol{u}) & = 0, & \\ \partial_t n_i & +\boldsymbol{\nabla}\cdot(n_i\boldsymbol{u}) & = 0, & i=1,2, \\ \partial_t (n_i(S_0)_i) & +\boldsymbol{\nabla}\cdot(n_i(S_0)_i\boldsymbol{u}) & = 0, & i=1,2, \\ \partial_t (n_i\dot{\chi}_i) & +\boldsymbol{\nabla}\cdot(n_i\dot{\chi}_i\boldsymbol{u}) & = -\omega_i^2 n_i\chi_i, & i=1,2, \\ \partial_t (n_i\chi_i) & +\boldsymbol{\nabla}\cdot(n_i\chi_i\boldsymbol{u}) & = n_i\dot{\chi}_i, & i=1,2, \\ \partial_t (\rho\boldsymbol{u}) & +\boldsymbol{\nabla}\cdot(\rho\boldsymbol{u}\otimes\boldsymbol{u}+p_2) & = \boldsymbol{0}, & \end{cases}$$

with $\omega_i^2 = \tilde{\omega}^2 (S_0)_i^{-3/2}$.

Combining the equations at the fifth and sixth lines of the system above, one can recognize the equations of harmonic oscillators advected along the streamlines

$$D_t(D_t\chi_i) + \omega_i^2\chi_i = 0, \qquad i = 1,2. \tag{2.154}$$

Similarly to the previous models, this system admits an additional conservation equation for mathematical entropy $\mathcal{H}$ defined hereafter

$$\partial_t\mathcal{H} + \boldsymbol{\nabla}\cdot((\mathcal{H}+p_2)\boldsymbol{u}) = 0, \qquad \mathcal{H} = \frac{1}{2}\rho|\boldsymbol{u}|^2 + m_2 e_2 + m_1^d e_1^d + \sum_{i=1,2}\frac{1}{2}\nu n_i (S_0)_i^{5/2}\dot{\chi}_i^2 + \sigma n_i (S_0)_i + \frac{1}{2}\gamma n_i (S_0)_i \chi_i^2. \tag{2.155}$$

Once again, we could consider a pressure relaxation model, but we would like to focus again on the dissipation associated with the oscillation process, and we introduce source terms R_{χ_i} in the new momentum equations

$$\partial_t(n_i\dot{\chi}_i) + \boldsymbol{\nabla}\cdot(n_i\dot{\chi}_i\boldsymbol{u}) = -\omega_i^2 n_i\chi_i + R_{\chi_i}, \qquad i = 1,2. \tag{2.156}$$

This source term provides the following mathematical entropy production

$$\partial_t\mathcal{H} + \boldsymbol{\nabla}\cdot((\mathcal{H}+p_2)\boldsymbol{u}) = \sum_{i=1,2}\nu(S_0)_i^{5/2} R_{\chi_i} D_t\chi_i. \tag{2.157}$$

As the closure (2.147) groups droplets by size, we can now model the first-order size-dependent damping term of the viscous droplet in a light carrier phase (Prosperetti, 1977; Plümacher et al., 2020). Then, we expect each population of oscillators to be damped following

$$D_t(D_t(\chi_i)) + \omega_i^2\chi_i = -\beta_i D_t\chi_i \quad \Longleftrightarrow \quad D_t\dot{\chi}_i + \omega_i^2\chi_i = -\beta_i\dot{\chi}_i, \tag{2.158}$$

with $\beta_i = 4\pi\nu_{vis}/(S_0)_i > 0$ with ν_{vis} the liquid kinematic viscosity. One can then choose $R_{\chi_i} = -n_i\beta_i\dot{\chi}_i$ and recover both the above dissipation process for both populations of droplets and a signed production of mathematical entropy

$$\partial_t\mathcal{H} + \boldsymbol{\nabla}\cdot((\mathcal{H}+p_2)\boldsymbol{u}) = -\beta_1 n_1 \nu (S_0)_1^{5/2}\dot{\chi}_1^2 - \beta_2 n_2 \nu (S_0)_2^{5/2}\dot{\chi}_2^2 \leq 0. \tag{2.159}$$

It leads to the dissipative Model 21.

Model 21 (Dissipative polydisperse spray model of synchronously oscillating droplets)

With $m_k = \alpha_k \rho_k$ and α_k the phase densities and volume fractions of phases $k = 2, 1^d$, $\rho = m_1 + m_2$ the mixture's density, $\boldsymbol{u}$ the velocity and $p_2(\rho_2)$ the pressure of the gaseous phase 2, and n_i, (S_0), χ_i, $\dot{\chi}_i$ respectively the number density, the equilibrium surface area, the amplitude parameters of droplets of population i, the flow is governed by

$$\begin{cases} \partial_t m_2 & +\boldsymbol{\nabla}\cdot(m_2\boldsymbol{u}) & = 0, & \\ \partial_t m_1^d & +\boldsymbol{\nabla}\cdot(m_1^d\boldsymbol{u}) & = 0, & \\ \partial_t n_i & +\boldsymbol{\nabla}\cdot(n_i\boldsymbol{u}) & = 0, & i=1,2, \\ \partial_t (n_i(S_0)_i) & +\boldsymbol{\nabla}\cdot(n_i(S_0)_i\boldsymbol{u}) & = 0, & i=1,2, \\ \partial_t (n_i\dot{\chi}_i) & +\boldsymbol{\nabla}\cdot(n_i\dot{\chi}_i\boldsymbol{u}) & = -\omega_i^2 n_i\chi_i - \beta_i n_i\dot{\chi}_i, & i=1,2, \\ \partial_t (n_i\chi_i) & +\boldsymbol{\nabla}\cdot(n_i\chi_i\boldsymbol{u}) & = n_i\dot{\chi}_i, & i=1,2, \\ \partial_t (\rho\boldsymbol{u}) & +\boldsymbol{\nabla}\cdot(\rho\boldsymbol{u}\otimes\boldsymbol{u} + p_2\boldsymbol{I}) & = \boldsymbol{0}, & \end{cases}$$

with $\omega_i^2 = \tilde{\omega}^2 (S_0)_i^{-3/2}$ and $\beta_i = 4\pi\nu_{vis}/(S_0)_i$.

This model shows a macroscopic synchronous oscillation through the two momentum equations on $\dot{\chi}_1$ and $\dot{\chi}_2$ and includes a physics-based dissipation rate. The system is here written using the weights and abscissas, but it can also be written using the geometric quantities of the model. This last models show that the dynamics of geometric cannot be simply expressed relying on the usual quantities α_1^d and Σ, but sometimes must require other geometric quantities, both related to curvatures to capture size polydispersion or geometry dynamics to capture the small-scale dynamics.

Conclusion of chapter 2

Small-scale multi-fluid models are inherently very complex as they aim at representing the phenomena below the scale of the volume fraction variations. In the disperse regime, they correspond to the dynamics of inclusions with closed interfaces while, in the separated regime, they describe the dynamics of the small-scale geometric quantities below the scale of computational resolution. This chapter has proposed a flexible modelling framework to efficiently describe the small-scale interface with geometric quantities through GeoMOM and Hamilton's SAP. An original contribution is also proposed to account for the small-scale dynamics with key mechanisms such as incompressible oscillation and compressible pulsation of small-scale inclusions. These new dynamical systems, based on GeoMOM and kinetic-models, pave the way to the modelling in the mixed regime where the interface undergoes break-ups and deformations. We summarize here the key contributions of this chapter :

- Definition of geometric quantities either locally or integrated over a closed interface, and either for a deterministic or averaged interface location;
- A proper separation between kinematics and dynamics of geometric quantities;
- The extended GeoMOM framework with both statistic information of the disperse small-scale model and information about the small-sale geometry and its dynamics;
- Several new reduced-order models for a collection of oscillating droplets or pulsating bubbles;

With such geometric information and the new small-scale dynamics models of this chapter, the next critical step lies in the interaction of the large-scale model with the small-scale model. Indeed, the regime transition from separated regime to disperse regime, physically happening through strong deformations of the interface, pinching,

filament break-ups and other topology changes, is modelled in the next Chapter 3 as a user-defined mass transfer. As this strategy bypasses the complex dynamics of the mixed regime, the upcoming inter-scale mass transfer must contain enough parameters about the small-scale geometry to model the resulting distribution of droplets. The variety of small-scale models proposed in this chapter are then critical for such modelling strategy.

Appendix

2.A Third order variations of local and surface-average geometric quantities

Greatly based on the working notes Deserno (2004), we compute third-order variation in ϕ around the sphere of radius R for geometric quantities of interest.

Tangential vectors

From the definition (2.1.1.1.a) and the Weingarten formula $\boldsymbol{n}_{,i} = b_i^j \boldsymbol{e}_j$, we obtain

$$\boxed{\delta \boldsymbol{e}_i} = (\psi \boldsymbol{n})_{,i} = \psi_{,i} \boldsymbol{n} + \psi \boldsymbol{n}_{,i} = (\nabla_i \delta\psi)\, \boldsymbol{n} + \psi b_i^j \boldsymbol{e}_j = (\nabla_i \delta\psi)\, \boldsymbol{n} + \psi g^{jk} b_{ik} \boldsymbol{e}_j \boxed{= (\nabla_i \delta\psi)\, \boldsymbol{n} + \frac{\psi}{R} \boldsymbol{e}_i.} \tag{2.160}$$

The metric

As the metric coefficients are dot product of the tangential vectors, the perturbation is of order 2 and reads

$$g_{ij} + \delta^1 g_{ij} + \delta^2 g_{ij} = (\boldsymbol{e}_i + \delta \boldsymbol{e}_i) \cdot (\boldsymbol{e}_j + \delta \boldsymbol{e}_j), \tag{2.161}$$

$$\text{and} \qquad \boxed{\delta^1 g_{ij}} = 2\delta \boldsymbol{e}_i \cdot \boldsymbol{e}_j = \boxed{\frac{2\psi}{R} g_{ij}}, \qquad \boxed{\delta^2 g_{ij}} = \delta \boldsymbol{e}_i \cdot \delta \boldsymbol{e}_j \boxed{= (\nabla_i \delta\psi)\left(\nabla_j \delta\psi\right) + \frac{\psi^2}{R^2} g_{ij}.} \tag{2.162}$$

Metric determinant

As we are considering a 2D surface, it is easy to work with the explicit formula (without Einstein summation) of the determinant $g = g_{\vartheta\vartheta} g_{\phi\phi} - g_{\vartheta\phi}^2$. We limit ourselves to the 3rd order. Moreover, the metric of the sphere is diagonal, hence

$$g + \delta^1 g + \delta^2 g + \delta^3 g = (g_{\vartheta\vartheta} + \delta^1 g_{\vartheta\vartheta} + \delta^2 g_{\vartheta\vartheta})(g_{\phi\phi} + \delta^1 g_{\phi\phi} + \delta^2 g_{\phi\phi}) - (0 + 0 + \delta^2 g_{\phi\vartheta})^2, \tag{2.163}$$

Then

$$\boxed{\delta^1 g} = g_{\vartheta\vartheta} \delta^1 g_{\phi\phi} + g_{\phi\phi} \delta^1 g_{\vartheta\vartheta} = g_{\vartheta\vartheta} \frac{2\psi}{R} g_{\phi\phi} + g_{\phi\phi} \frac{2\psi}{R} g_{\vartheta\vartheta} \boxed{= \frac{4\psi}{R} g,} \tag{2.164}$$

$$\begin{aligned}
\boxed{\delta^2 g} &= g_{\vartheta\vartheta}\delta^2 g_{\phi\phi} + g_{\phi\phi}\delta^2 g_{\vartheta\vartheta} + \delta^1 g_{\phi\phi}\delta^1 g_{\vartheta\vartheta} \\
&= g_{\vartheta\vartheta}\left(\left(\nabla_\phi\delta\psi\right)\left(\nabla_\phi\delta\psi\right) + \frac{\psi^2}{R^2}g_{\phi\phi}\right) + \left(\left(\nabla_\vartheta\delta\psi\right)\left(\nabla_\vartheta\delta\psi\right) + \frac{\psi^2}{R^2}g_{\vartheta\vartheta}\right)g_{\phi\phi} + \frac{4\psi^2}{R^2}g \\
&= g\left(\left(\nabla^\phi\delta\psi\right)\left(\nabla_\phi\delta\psi\right) + \frac{\psi^2}{R^2}\right) + g\left(\left(\nabla^\vartheta\delta\psi\right)\left(\nabla_\vartheta\delta\psi\right) + \frac{\psi^2}{R^2}\right) + \frac{4\psi^2}{R^2}g \\
&\boxed{= g\left(\left(\nabla^k\delta\psi\right)\left(\nabla_k\delta\psi\right) + \frac{6\psi^2}{R^2}\right).}
\end{aligned} \tag{2.165}$$

$$\begin{aligned}
\boxed{\delta^3 g} &= \delta^1 g_{\vartheta\vartheta}\delta^2 g_{\phi\phi} + \delta^1 g_{\phi\phi}\delta^2 g_{\vartheta\vartheta} \\
&= \frac{2\psi}{R}g_{\vartheta\vartheta}\left(\left(\nabla_\phi\delta\psi\right)\left(\nabla_\phi\delta\psi\right) + \frac{\psi^2}{R^2}g_{\phi\phi}\right) + \frac{2\psi}{R}g_{\phi\phi}\left(\left(\nabla_\vartheta\delta\psi\right)\left(\nabla_\vartheta\delta\psi\right) + \frac{\psi^2}{R^2}g_{\vartheta\vartheta}\right) \\
&\boxed{= g\left(\frac{2\psi}{R}\left(\nabla^k\delta\psi\right)\left(\nabla_k\delta\psi\right) + \frac{4\psi^3}{R^3}\right).}
\end{aligned} \tag{2.166}$$

Element of surface and total surface

The local element of surface is necessary for the surface integration and is given by $dS = \sqrt{g}d\vartheta d\phi$. Let's write its Taylor series with only the contributive variations up to the 3rd order.

$$\sqrt{g} + \delta^1(\sqrt{g}) + \delta^2(\sqrt{g}) + \delta^3(\sqrt{g}) = \sqrt{g}\left(1 + \frac{1}{2}\frac{\delta^1 g + \delta^2 g + \delta^3 g}{g} - \frac{1}{8}\left(\frac{\delta^1 g + \delta^2 g}{g}\right)^2 + \frac{1}{16}\left(\frac{\delta^1 g}{g}\right)^3\right). \tag{2.167}$$

Then

$$\boxed{\delta^1(\sqrt{g})} = \frac{1}{2}\frac{\delta^1 g}{g}\sqrt{g}\boxed{= \frac{2\psi}{R}\sqrt{g}.} \tag{2.168}$$

$$\begin{aligned}
\boxed{\delta^2(\sqrt{g})} &= \frac{1}{2}\frac{\delta^2 g}{g}\sqrt{g} - \frac{1}{8}\left(\frac{\delta^1 g}{g}\right)^2\sqrt{g} = \frac{1}{2}\left(\left(\nabla^k\delta\psi\right)\left(\nabla_k\delta\psi\right) + \frac{6\psi^2}{R^2}\right)\sqrt{g} - \frac{1}{8}\frac{16\psi^2}{R^2}\sqrt{g} \\
&\boxed{= \left(\frac{1}{2}\left(\nabla^k\delta\psi\right)\left(\nabla_k\delta\psi\right) + \frac{\psi^2}{R^2}\right)\sqrt{g}.}
\end{aligned} \tag{2.169}$$

$$\begin{aligned}
\boxed{\delta^3(\sqrt{g})} &= \frac{1}{2}\frac{\delta^3 g}{g}\sqrt{g} - \frac{1}{8}2\left(\frac{\delta^1 g}{g}\right)\left(\frac{\delta^2 g}{g}\right)\sqrt{g} + \frac{1}{16}\left(\frac{\delta^1 g}{g}\right)^3\sqrt{g} \\
&= \frac{1}{2}\left(\frac{2\psi}{R}\left(\nabla^k\delta\psi\right)\left(\nabla_k\delta\psi\right) + \frac{4\psi^3}{R^3}\right)\sqrt{g} - \frac{1}{4}\frac{4\psi}{R}\left(\left(\nabla^k\delta\psi\right)\left(\nabla_k\delta\psi\right) + \frac{6\psi^2}{R^2}\right)\sqrt{g} + \frac{1}{16}\frac{64\psi}{R^3} \\
&\boxed{= 0.}
\end{aligned} \tag{2.170}$$

Using the integration-by-part relation of (2.13), the variation of the surface is then

$$\boxed{\delta S = 2R\iint_{\mathbb{S}^2}\psi\, dS - \frac{1}{2}\iint_{\mathbb{S}^2}\psi\Delta_{\mathbb{S}^2}\psi\, dS + \iint_{\mathbb{S}^2}\psi^2\, dS.} \tag{2.171}$$

Remark that, for a sphere, the second-order approximation variation of the surface is valid up to third order. One can further show that there is a non-trivial fourth-order term.

Inverse metric

The inverse of the metric is needed to compute the mean curvature through $H = \frac{1}{2} g^{ij} b_{ij}$. We use the explicit formula for 2×2 matrices and the specific metric of the sphere such that $g^{\vartheta\vartheta} = \frac{g_{\phi\phi}}{g}$, $g^{\vartheta\phi} = -\frac{g_{\vartheta\phi}}{g}$, and

$$g^{\vartheta\vartheta} + \delta^1 g^{\vartheta\vartheta} + \delta^2 g^{\vartheta\vartheta} + \delta^3 g^{\vartheta\vartheta} = \frac{1}{g}\left(g_{\phi\phi} + \delta^1 g_{\phi\phi} + \delta^2 g_{\phi\phi}\right)\left(1 - \frac{\delta^1 g + \delta^2 g + \delta^3 g}{g} + \left(\frac{\delta^1 g + \delta^2 g}{g}\right)^2 - \left(\frac{\delta^1 g}{g}\right)^3\right), \quad (2.172)$$

and

$$\boxed{\delta^1 g^{\vartheta\vartheta}} = \frac{1}{g}\left(\delta^1 g_{\phi\phi} + g_{\phi\phi}\left(-\frac{\delta^1 g}{g}\right)\right) = \frac{1}{g}\left(\frac{2\psi}{R} g_{\phi\phi} - \frac{4\psi}{R} g_{\phi\phi}\right) \boxed{= -\frac{2\psi}{R} g^{\vartheta\vartheta},} \quad (2.173)$$

$$\begin{aligned}\boxed{\delta^2 g^{\vartheta\vartheta}} &= \frac{1}{g}\left(\delta^2 g_{\phi\phi} + g_{\phi\phi}\left(-\frac{\delta^2 g}{g} + \left(\frac{\delta^1 g}{g}\right)^2\right) + \delta^1 g_{\phi\phi}\left(-\frac{\delta^1 g}{g}\right)\right) \\ &= \frac{1}{g}\left(\left(\nabla_\phi \delta\psi\right)\left(\nabla_\phi \delta\psi\right) + \frac{\psi^2}{R^2} g_{\phi\phi} + g_{\phi\phi}\left(-\left(\nabla^k \delta\psi\right)\left(\nabla_k \delta\psi\right) - \frac{6\psi^2}{R^2} + \frac{16\psi^2}{R^2}\right) + \frac{2\psi}{R} g_{\phi\phi}\left(-\frac{4\psi}{R}\right)\right) \quad (2.174) \\ &\boxed{= \left(-\left(\nabla^\vartheta \delta\psi\right)\left(\nabla_\vartheta \delta\psi\right) + \frac{3\psi^2}{R^2}\right) g^{\vartheta\vartheta},}\end{aligned}$$

$$\begin{aligned}\boxed{\delta^3 g^{\vartheta\vartheta}} &= \frac{1}{g}\left(\delta^2 g_{\phi\phi}\left(-\frac{\delta^1 g}{g}\right) + \delta^1 g_{\phi\phi}\left(-\frac{\delta^2 g}{g} + \left(\frac{\delta^1 g}{g}\right)^2\right) + g_{\phi\phi}\left(-\frac{\delta^3 g}{g} + 2\left(\frac{\delta^1 g}{g}\right)\left(\frac{\delta^2 g}{g}\right) - \left(\frac{\delta^1 g}{g}\right)^3\right)\right) \\ &= \frac{1}{g}\left[\left(\left(\nabla^\phi \delta\psi\right)\left(\nabla_\phi \delta\psi\right) + \frac{\psi^2}{R^2}\right) g_{\phi\phi}\left(-\frac{4\psi}{R}\right) + \frac{2\psi}{R} g_{\phi\phi}\left(-\left(\nabla^i \delta\psi\right)\left(\nabla_i \delta\psi\right) - \frac{6\psi^2}{R^2} + \frac{16\psi^2}{R^2}\right)\right. \\ &\qquad \left. + g_{\phi\phi}\left(-\frac{2\psi}{R}\left(\nabla^i \delta\psi\right)\left(\nabla_i \delta\psi\right) - \frac{4\psi^3}{R^3} + 2\frac{4\psi}{R}\left(\left(\nabla^i \delta\psi\right)\left(\nabla_i \delta\psi\right) + \frac{6\psi^2}{R^2}\right) - \frac{64\psi^3}{R^3}\right)\right] \quad (2.175) \\ &= g^{\vartheta\vartheta}\left(-\frac{4\psi}{R}\left(\nabla^\phi \delta\psi\right)\left(\nabla_\phi \delta\psi\right) + \frac{4\psi}{R}\left(\nabla^i \delta\psi\right)\left(\nabla_i \delta\psi\right)\right) \\ &\boxed{= g^{\vartheta\vartheta}\left(-\frac{4\psi^3}{R^3} + \frac{4\psi}{R}\left(\nabla^\vartheta \delta\psi\right)\left(\nabla_\vartheta \delta\psi\right)\right).}\end{aligned}$$

We obtain the same expression for $\delta g^{\phi\phi}$.

Now let's develop the first orders of $\delta g^{\vartheta\phi} = \delta\left(-\frac{g_{\vartheta\phi}}{g}\right)$ with

$$g^{\vartheta\phi} + \delta^1 g^{\vartheta\phi} + \delta^2 g^{\vartheta\phi} + \delta^3 g^{\vartheta\phi} = -\frac{1}{g}\left(0 + 0 + \delta^2 g_{\vartheta\phi}\right)\left(1 - \frac{\delta^1 g + \delta^2 g + \delta^3 g}{g} + \left(\frac{\delta^1 g + \delta^2 g}{g}\right)^2 - \left(\frac{\delta^1 g}{g}\right)^3\right). \quad (2.176)$$

Then

$$\boxed{\delta^1 g^{\vartheta\phi} = 0,} \qquad \boxed{\delta^2 g^{\vartheta\phi}} = -\frac{\delta^2 g_{\vartheta\phi}}{g} \boxed{= -\frac{1}{g}\left(\nabla_\vartheta \delta\psi\right)\left(\nabla_\phi \delta\psi\right),} \qquad \boxed{\delta^3 g^{\vartheta\phi}} = -\frac{\delta^2 g_{\vartheta\phi}}{g}\left(-\frac{\delta^1 g}{g}\right) \boxed{= \frac{1}{g}\frac{4\psi}{R}\left(\nabla_\vartheta \delta\psi\right)\left(\nabla_\phi \delta\psi\right).} \quad (2.177)$$

We can now generalize these relations to

$$\boxed{\delta^1 g^{ij} = -\frac{2\psi}{R} g^{ij},} \qquad \boxed{\delta^2 g^{ij} = -\left(\nabla^i \delta\psi\right)\left(\nabla^j \delta\psi\right) + \frac{3\psi^2}{R^2} g^{ij},} \qquad \boxed{\delta^3 g^{ij} = \frac{4\psi}{R}\left(\nabla^i \delta\psi\right)\left(\nabla^j \delta\psi\right) - \frac{4\psi^3}{R^3} g^{ij}.} \quad (2.178)$$

Normal unit vector

As $\boldsymbol{n} = \frac{\boldsymbol{e}_\theta \times \boldsymbol{e}_\phi}{\sqrt{g}}$, let's start by the perturbation of $\boldsymbol{e}_\theta \times \boldsymbol{e}_\phi$. As it is a product of first orders, we have at most a second order. Hence,

$$\begin{aligned}\boxed{\delta^1\left(\boldsymbol{e}_\theta \times \boldsymbol{e}_\phi\right)} &= \boldsymbol{e}_\theta \times \delta\boldsymbol{e}_\phi + \delta\boldsymbol{e}_\theta \times \boldsymbol{e}_\phi = -\sqrt{\frac{g_{\vartheta\vartheta}}{g_{\phi\phi}}}\left(\nabla_\phi\psi\right)\boldsymbol{e}_\phi + \sqrt{g}\frac{\psi}{R}\boldsymbol{n} - \sqrt{\frac{g_{\phi\phi}}{g_{\vartheta\vartheta}}}\left(\nabla_\vartheta\psi\right)\boldsymbol{e}_\theta + \sqrt{g}\frac{\psi}{R}\boldsymbol{n} \\ &\boxed{= \sqrt{g}\left(\frac{2\psi}{R}\boldsymbol{n} - \left(\nabla^i\psi\right)\boldsymbol{e}_i\right),}\end{aligned} \tag{2.179}$$

$$\begin{aligned}\boxed{\delta^2\left(\boldsymbol{e}_\theta \times \boldsymbol{e}_\phi\right)} &= \delta\boldsymbol{e}_\theta \times \delta\boldsymbol{e}_\phi \\ &= \left(\left(\nabla_\vartheta\delta\psi\right)\boldsymbol{n} + \frac{\psi}{R}\boldsymbol{e}_\theta\right) \times \left(\left(\nabla_\phi\delta\psi\right)\boldsymbol{n} + \frac{\psi}{R}\boldsymbol{e}_\phi\right) \\ &= -\sqrt{\frac{g_{\vartheta\vartheta}}{g_{\phi\phi}}}\left(\nabla_\phi\delta\psi\right)\frac{\psi}{R}\boldsymbol{e}_\phi - \sqrt{\frac{g_{\phi\phi}}{g_{\vartheta\vartheta}}}\left(\nabla_\vartheta\delta\psi\right)\frac{\psi}{R}\boldsymbol{e}_\theta + \sqrt{g}\frac{\psi^2}{R^2}\boldsymbol{n} \\ &\boxed{= \sqrt{g}\left(\frac{\psi^2}{R^2}\boldsymbol{n} - \frac{\psi}{R}\left(\nabla^k\psi\right)\boldsymbol{e}_k\right).}\end{aligned} \tag{2.180}$$

Then,

$$\begin{aligned}\boldsymbol{n} + \delta^1\boldsymbol{n} + \delta^2\boldsymbol{n} + \delta^3\boldsymbol{n} = &\left(\boldsymbol{e}_\theta \times \boldsymbol{e}_\phi + \delta^1\left(\boldsymbol{e}_\theta \times \boldsymbol{e}_\phi\right) + \delta^2\left(\boldsymbol{e}_\theta \times \boldsymbol{e}_\phi\right)\right)\frac{1}{\sqrt{g}} \\ &\times\left(1 - \frac{\delta^1(\sqrt{g}) + \delta^2(\sqrt{g})}{\sqrt{g}} + \left(\frac{\delta^1(\sqrt{g}) + \delta^2(\sqrt{g})}{\sqrt{g}}\right)^2 - \left(\frac{\delta^1(\sqrt{g})}{\sqrt{g}}\right)^3\right),\end{aligned} \tag{2.181}$$

and

$$\boxed{\delta^1\boldsymbol{n}} = \frac{1}{\sqrt{g}}\delta^1\left(\boldsymbol{e}_\theta \times \boldsymbol{e}_\phi\right) - \frac{\delta^1(\sqrt{g})}{\sqrt{g}}\boldsymbol{n} = \frac{2\psi}{R}\boldsymbol{n} - \left(\nabla^k\psi\right)\boldsymbol{e}_k - \frac{2\psi}{R}\boldsymbol{n}\boxed{= -\left(\nabla^k\psi\right)\boldsymbol{e}_k,} \tag{2.182}$$

$$\begin{aligned}\boxed{\delta^2\boldsymbol{n}} &= \frac{1}{\sqrt{g}}\delta^2\left(\boldsymbol{e}_\theta \times \boldsymbol{e}_\phi\right) + \left(-\frac{\delta^2(\sqrt{g})}{\sqrt{g}} + \left(\frac{\delta^1(\sqrt{g})}{\sqrt{g}}\right)^2\right)\boldsymbol{n} + \frac{1}{\sqrt{g}}\delta^1\left(\boldsymbol{e}_\theta \times \boldsymbol{e}_\phi\right)\left(-\frac{\delta^1(\sqrt{g})}{\sqrt{g}}\right) \\ &= \frac{\psi^2}{R^2}\boldsymbol{n} - \frac{\psi}{R}\left(\nabla^i\psi\right)\boldsymbol{e}_i + \left(-\left(\frac{1}{2}\left(\nabla^k\delta\psi\right)\left(\nabla_k\delta\psi\right) + \frac{\psi^2}{R^2}\right) + \frac{4\psi^2}{R^2}\right)\boldsymbol{n} - \frac{2\psi}{R}\left(\frac{2\psi}{R}\boldsymbol{n} - \left(\nabla^l\psi\right)\boldsymbol{e}_l\right) \\ &\boxed{= \frac{\psi}{R}\left(\nabla^i\psi\right)\boldsymbol{e}_i - \frac{1}{2}\left(\nabla^k\delta\psi\right)\left(\nabla_k\delta\psi\right)\boldsymbol{n},}\end{aligned} \tag{2.183}$$

$$
\begin{aligned}
\boxed{\delta^3 \boldsymbol{n}} &= \frac{1}{\sqrt{g}}\delta^2\left(\boldsymbol{e}_\theta \times \boldsymbol{e}_\phi\right)\left(-\frac{\delta^1(\sqrt{g})}{\sqrt{g}}\right) + \frac{1}{\sqrt{g}}\delta^1\left(\boldsymbol{e}_\theta \times \boldsymbol{e}_\phi\right)\left(-\frac{\delta^2(\sqrt{g})}{\sqrt{g}} + \left(\frac{\delta^1(\sqrt{g})}{\sqrt{g}}\right)^2\right) \\
&\quad + \left(2\left(\frac{\delta^1(\sqrt{g})}{\sqrt{g}}\right)\left(\frac{\delta^2(\sqrt{g})}{\sqrt{g}}\right) - \left(\frac{\delta^1(\sqrt{g})}{\sqrt{g}}\right)^3\right)\boldsymbol{n} \\
&= -\frac{2\psi}{R}\left(\frac{\psi^2}{R^2}\boldsymbol{n} - \frac{\psi}{R}\left(\nabla^i\psi\right)\boldsymbol{e}_i\right) + \left(\frac{2\psi}{R}\boldsymbol{n} - \left(\nabla^k\psi\right)\boldsymbol{e}_k\right)\left(-\left(\frac{1}{2}\left(\nabla^l\delta\psi\right)\left(\nabla_l\delta\psi\right) + \frac{\psi^2}{R^2}\right) + \frac{4\psi^2}{R^2}\right) \\
&\quad + \left(2\frac{2\psi}{R}\left(\frac{1}{2}\left(\nabla^m\delta\psi\right)\left(\nabla_m\delta\psi\right) + \frac{\psi^2}{R^2}\right) - \frac{8\psi^3}{R^3}\right)\boldsymbol{n} \\
&\boxed{= -\frac{\psi^2}{R^2}\left(\nabla^i\psi\right)\boldsymbol{e}_i + \frac{\psi}{R}\left(\nabla^j\delta\psi\right)\left(\nabla_j\delta\psi\right)\boldsymbol{n} + \frac{1}{2}\left(\nabla^k\delta\psi\right)\left(\nabla_k\delta\psi\right)\left(\nabla^l\psi\right)\boldsymbol{e}_l.}
\end{aligned}
\tag{2.184}
$$

Second fundamental form

We consider the definition $b_{ij} = -\nabla_j \boldsymbol{e}_i \cdot \boldsymbol{n}$. We recall the Weingarten formula, and we assume the Gauss formula :

$$
\boxed{\nabla_i \boldsymbol{n}} = b_i^j \boldsymbol{e}_j = g^{jk} b_{ik} \boldsymbol{e}_j \boxed{= g^{ii} b_{ii} \boldsymbol{e}_i,} \qquad \boxed{\nabla_k \boldsymbol{e}_i = -b_{ik}\boldsymbol{n}.}
\tag{2.185}
$$

Therefore,

$$
b_{ij} + \delta^1 b_{ij} + \delta^2 b_{ijj} + \delta^3 b_{ij} = -\nabla_j(\boldsymbol{e}_i + \delta\boldsymbol{e}_i) \cdot \left(\boldsymbol{n} + \delta^1\boldsymbol{n} + \delta^2\boldsymbol{n} + \delta^3\boldsymbol{n}\right),
\tag{2.186}
$$

and

$$
\begin{aligned}
\boxed{\delta^1 b_{ij}} &= -\nabla_j \boldsymbol{e}_i \cdot \delta^1\boldsymbol{n} - \nabla_j \delta\boldsymbol{e}_i \cdot \boldsymbol{n} = -b_{ij}\boldsymbol{n} \cdot \left(\nabla^k\psi\right)\boldsymbol{e}_k - \nabla_j\left(\left(\nabla_i\delta\psi\right)\boldsymbol{n} + \frac{\psi}{R}\boldsymbol{e}_i\right) \cdot \boldsymbol{n} = -\nabla_j\left(\nabla_i\psi\right) - \frac{\psi}{R}\left(\nabla_j\boldsymbol{e}_i\right) \cdot \boldsymbol{n} \\
&\boxed{= -\nabla_j\left(\nabla_i\psi\right) + \frac{\psi}{R}b_{ij},}
\end{aligned}
\tag{2.187}
$$

$$
\begin{aligned}
\boxed{\delta^2 b_{ij}} &= -\nabla_j \boldsymbol{e}_i \cdot \delta^2\boldsymbol{n} - \nabla_j \delta^1\boldsymbol{e}_i \cdot \delta^1\boldsymbol{n} \\
&= b_{ij}\boldsymbol{n} \cdot \left(\frac{\psi}{R}\left(\nabla^k\psi\right)\boldsymbol{e}_k - \frac{1}{2}\left(\nabla^l\delta\psi\right)\left(\nabla_l\delta\psi\right)\boldsymbol{n}\right) - \nabla_j\left(\left(\nabla_i\delta\psi\right)\boldsymbol{n} + \frac{\psi}{R}\boldsymbol{e}_i\right) \cdot \left(-\left(\nabla^m\psi\right)\boldsymbol{e}_m\right) \\
&= -\frac{1}{2}b_{ij}\left(\nabla^l\delta\psi\right)\left(\nabla_l\delta\psi\right) + \left(\left(\nabla_j\nabla_i\psi\right)\boldsymbol{n} + \left(\nabla_i\psi\right)\left(\nabla_j\boldsymbol{n}\right) + \frac{\nabla_j\psi}{R}\boldsymbol{e}_i + \frac{\psi}{R}\left(\nabla_j\boldsymbol{e}_i\right)\right) \cdot \left(\nabla^m\psi\right)\boldsymbol{e}_m \\
&= -\frac{1}{2}b_{ij}\left(\nabla^l\delta\psi\right)\left(\nabla_l\delta\psi\right) + \left(\left(\nabla_i\psi\right)g^{jj}b_{jj}\boldsymbol{e}_j + \frac{\nabla_j\psi}{R}\boldsymbol{e}_i\right) \cdot \left(\nabla^m\psi\right)\boldsymbol{e}_m \\
&= -\frac{1}{2}b_{ij}\left(\nabla^l\delta\psi\right)\left(\nabla_l\delta\psi\right) + \left(\nabla^j\psi\right)\left(\nabla_i\psi\right)b_{jj} + \frac{1}{R}\left(\nabla^i\psi\right)\left(\nabla_j\psi\right)g_{ii} \\
&\boxed{= -\frac{1}{2}b_{ij}\left(\nabla^l\delta\psi\right)\left(\nabla_l\delta\psi\right) + \frac{2}{R}\left(\nabla_i\psi\right)\left(\nabla_j\psi\right),}
\end{aligned}
\tag{2.188}
$$

$$
\begin{aligned}
\boxed{\delta^3 b_{ij}} &= -\nabla_j \boldsymbol{e}_i \cdot \delta^3 \boldsymbol{n} - \nabla_j \delta^1 \boldsymbol{e}_i \cdot \delta^2 \boldsymbol{n} \\
&= b_{ij} \boldsymbol{n} \cdot \left(-\frac{\psi^2}{R^2} \left(\nabla^k \psi \right) \boldsymbol{e}_k + \frac{\psi}{R} \left(\nabla^l \delta\psi \right) \left(\nabla_l \delta\psi \right) \boldsymbol{n} + \frac{1}{2} \left(\nabla^m \delta\psi \right) \left(\nabla_m \delta\psi \right) \left(\nabla^n \psi \right) \boldsymbol{e}_n \right) \\
&\quad - \nabla_j \left(\left(\nabla_i \delta\psi \right) \boldsymbol{n} + \frac{\psi}{R} \boldsymbol{e}_i \right) \cdot \left(\frac{\psi}{R} \left(\nabla^p \psi \right) \boldsymbol{e}_p - \frac{1}{2} \left(\nabla^q \delta\psi \right) \left(\nabla_q \delta\psi \right) \boldsymbol{n} \right) \\
&= b_{ij} \frac{\psi}{R} \left(\nabla^l \delta\psi \right) \left(\nabla_l \delta\psi \right) - \left(\nabla_j \nabla_i \psi \boldsymbol{n} + \left(\nabla_i \psi \right) \left(\nabla_j \boldsymbol{n} \right) + \frac{\nabla_j \psi}{R} \boldsymbol{e}_i + \frac{\psi}{R} \left(\nabla_j \boldsymbol{e}_i \right) \right) \cdot \left(\frac{\psi}{R} \left(\nabla^p \psi \right) \boldsymbol{e}_p - \frac{1}{2} \left(\nabla^q \delta\psi \right) \left(\nabla_q \delta\psi \right) \boldsymbol{n} \right) \\
&= b_{ij} \frac{\psi}{R} \left(\nabla^l \delta\psi \right) \left(\nabla_l \delta\psi \right) - \left(\nabla_j \nabla_i \psi \boldsymbol{n} + \left(\nabla_i \psi \right) g^{jj} b_{jj} \boldsymbol{e}_j + \frac{\nabla_j \psi}{R} \boldsymbol{e}_i - b_{ij} \frac{\psi}{R} \boldsymbol{n} \right) \cdot \left(\frac{\psi}{R} \left(\nabla^p \psi \right) \boldsymbol{e}_p - \frac{1}{2} \left(\nabla^q \delta\psi \right) \left(\nabla_q \delta\psi \right) \boldsymbol{n} \right) \\
&= b_{ij} \frac{\psi}{R} \left(\nabla^l \delta\psi \right) \left(\nabla_l \delta\psi \right) + \frac{1}{2} \left(\nabla^q \delta\psi \right) \left(\nabla_q \delta\psi \right) \nabla_j \nabla_i \psi - \frac{\psi}{R} \left(\nabla^j \psi \right) \left(\nabla_i \psi \right) b_{jj} - \frac{\nabla_j \psi}{R} \frac{\psi}{R} \left(\nabla^i \psi \right) g_{ii} \\
&\quad - \frac{1}{2} b_{ij} \frac{\psi}{R} \left(\nabla^q \delta\psi \right) \left(\nabla_q \delta\psi \right) \\
&\boxed{= \frac{1}{2} b_{ij} \frac{\psi}{R} \left(\nabla^l \delta\psi \right) \left(\nabla_l \delta\psi \right) + \frac{1}{2} \left(\nabla^q \delta\psi \right) \left(\nabla_q \delta\psi \right) \nabla_j \nabla_i \psi - \frac{2\psi}{R^2} \left(\nabla_i \psi \right) \left(\nabla_j \psi \right).}
\end{aligned}
\tag{2.189}
$$

Mean curvature

We use the definition $H = \frac{1}{2}(g^{ij} b_{ij})$ such that

$$
H + \delta^1 H + \delta^2 H + \delta^3 H = \frac{1}{2} \left(g^{ij} + \delta^1 g^{ij} + \delta^2 g^{ij} + \delta^3 g^{ij} \right) \left(b_{ij} + \delta^1 b_{ij} + \delta^2 b_{ij} + \delta^3 b_{ij} \right), \tag{2.190}
$$

and

$$
\begin{aligned}
\boxed{\delta^1 H} &= \frac{1}{2} \left(g^{ij} \delta^1 b_{ij} + \delta^1 g^{ij} b_{ij} \right) = \frac{1}{2} \left(g^{ij} \left(-\nabla_j \left(\nabla_i \psi \right) + \frac{\psi}{R} b_{ij} \right) + \left(-\frac{2\psi}{R} g^{ij} \right) b_{ij} \right) = \frac{1}{2} \left(-\nabla^i \left(\nabla_i \psi \right) - \frac{\psi}{R} g^{ij} b_{ij} \right) \\
&\boxed{= -\frac{\psi}{R^2} - \frac{1}{2} \Delta\psi,}
\end{aligned}
\tag{2.191}
$$

$$
\begin{aligned}
\boxed{\delta^2 H} &= \frac{1}{2} \left(g^{ij} \delta^2 b_{ij} + \delta^1 g^{ij} \delta^1 b_{ij} + \delta^2 g^{ij} b_{ij} \right) \\
&= \frac{1}{2} \left(g^{ij} \left(-\frac{1}{2} b_{ij} \left(\nabla^l \delta\psi \right) \left(\nabla_l \delta\psi \right) + \frac{2}{R} (\nabla_i \psi)(\nabla_j \psi) \right) + \left(-\frac{2\psi}{R} g^{ij} \right) \left(-\nabla_j \left(\nabla_i \psi \right) + \frac{\psi}{R} b_{ij} \right) \right. \\
&\quad \left. + \left(- \left(\nabla^i \delta\psi \right) \left(\nabla^j \delta\psi \right) + \frac{3\psi^2}{R^2} g^{ij} \right) b_{ij} \right) \\
&= \frac{1}{2} \left(-\frac{1}{R} \left(\nabla^l \delta\psi \right) \left(\nabla_l \delta\psi \right) + \frac{2}{R} (\nabla^i \psi)(\nabla_i \psi) + \left(\frac{2\psi}{R} \Delta\psi - \frac{4\psi^2}{R^3} \right) - \frac{1}{R} \left(\nabla^j \delta\psi \right) \left(\nabla_j \delta\psi \right) + \frac{6\psi^2}{R^3} \right) \\
&\boxed{= \frac{\psi^2}{R^3} + \frac{\psi}{R} \Delta\psi,}
\end{aligned}
\tag{2.192}
$$

$$
\begin{aligned}
\boxed{\delta^3 H} &= \frac{1}{2}\left(g^{ij}\delta^3 b_{ij} + \delta^1 g^{ij}\delta^2 b_{ij} + \delta^2 g^{ij}\delta^1 b_{ij} + \delta^3 g^{ij} b_{ij}\right) \\
&= \frac{1}{2}\left[g^{ij}\left(\frac{1}{2}b_{ij}\frac{\psi}{R}\left(\nabla^l\delta\psi\right)\left(\nabla_l\delta\psi\right) + \frac{1}{2}\left(\nabla^q\delta\psi\right)\left(\nabla_q\delta\psi\right)\nabla_j\nabla_i\psi - \frac{2\psi}{R^2}\left(\nabla_i\psi\right)\left(\nabla_j\psi\right)\right)\right. \\
&\quad + \left(-\frac{2\psi}{R}g^{ij}\right)\left(-\frac{1}{2}b_{ij}\left(\nabla^l\delta\psi\right)\left(\nabla_l\delta\psi\right) + \frac{2}{R}(\nabla_i\psi)(\nabla_j\psi)\right) + \left(-\left(\nabla^i\delta\psi\right)\left(\nabla^j\delta\psi\right) + \frac{3\psi^2}{R^2}g^{ij}\right)\left(-\nabla_j\left(\nabla_i\psi\right) + \frac{\psi}{R}b_{ij}\right) \\
&\quad \left. + \left(\frac{4\psi}{R}\left(\nabla^i\delta\psi\right)\left(\nabla^j\delta\psi\right) - \frac{4\psi^3}{R^3}g^{ij}\right)b_{ij}\right] \\
&= \frac{1}{2}\left[\frac{\psi}{R^2}\left(\nabla^l\delta\psi\right)\left(\nabla_l\delta\psi\right) + \frac{1}{2}\left(\nabla^q\delta\psi\right)\left(\nabla_q\delta\psi\right)\Delta\psi - \frac{2\psi}{R^2}\left(\nabla^j\psi\right)\left(\nabla_j\psi\right) + \frac{2\psi}{R^2}\left(\nabla^l\delta\psi\right)\left(\nabla_l\delta\psi\right) - \frac{4\psi}{R^2}(\nabla^i\psi)(\nabla_i\psi)\right. \\
&\quad \left. + \left(\nabla^i\delta\psi\right)\left(\nabla^j\delta\psi\right)\nabla_j\left(\nabla_i\psi\right) - \frac{3\psi^2}{R^2}\Delta\psi - \frac{\psi}{R^2}\left(\nabla^i\delta\psi\right)\left(\nabla_i\delta\psi\right) + \frac{6\psi^3}{R^4} + \frac{4\psi}{R^2}\left(\nabla^i\delta\psi\right)\left(\nabla_i\delta\psi\right) - \frac{8\psi^3}{R^4}\right] \\
&\boxed{= -\frac{\psi^3}{R^4} - \frac{3\psi^2}{2R^2}\Delta\psi + \frac{1}{4}\left(\nabla^q\delta\psi\right)\left(\nabla_q\delta\psi\right)\Delta\psi + \frac{1}{2}\left(\nabla^i\delta\psi\right)\left(\nabla^j\delta\psi\right)\nabla_j\left(\nabla_i\psi\right).}
\end{aligned}
\tag{2.193}
$$

Integrated mean curvature

In order to integrate the mean curvature over the surface, we need the perturbation of $H\sqrt{g}$, that reads

$$
H\sqrt{g} + \delta^1\left(H\sqrt{g}\right) + \delta^2\left(H\sqrt{g}\right) + \delta^3\left(H\sqrt{g}\right) = \left(H + \delta^1 H + \delta^2 H + \delta^3 H\right)\left(\sqrt{g} + \delta^1(\sqrt{g}) + \delta^2(\sqrt{g}) + \delta^3(\sqrt{g})\right). \tag{2.194}
$$

Then

$$
\begin{aligned}
\boxed{\delta^1\left(H\sqrt{g}\right)} &= H\delta^1(\sqrt{g}) + \delta^1 H\sqrt{g} = \frac{1}{R}\left(\frac{2\psi}{R}\sqrt{g}\right) + \left(-\frac{\psi}{R^2} - \frac{1}{2}\Delta\psi\right)\sqrt{g} \\
&\boxed{= \left(\frac{\psi}{R^2} - \frac{1}{2}\Delta\psi\right)\sqrt{g},}
\end{aligned}
\tag{2.195}
$$

$$
\begin{aligned}
\boxed{\delta^2\left(H\sqrt{g}\right)} &= H\delta^2(\sqrt{g}) + \delta^1 H\delta^1(\sqrt{g}) + \delta^2 H\sqrt{g} \\
&= \left(\frac{1}{R}\left(\frac{1}{2}\left(\nabla^k\delta\psi\right)\left(\nabla_k\delta\psi\right) + \frac{\psi^2}{R^2}\right)\sqrt{g} + \left(-\frac{\psi}{R^2} - \frac{1}{2}\Delta\psi\right)\left(\frac{2\psi}{R}\sqrt{g}\right) + \left(\frac{\psi^2}{R^3} + \frac{\psi}{R}\Delta\psi\right)\sqrt{g}\right) \\
&= \left(\frac{1}{2R}\left(\nabla^k\delta\psi\right)\left(\nabla_k\delta\psi\right) + \frac{\psi^2}{R^3} - \frac{2\psi^2}{R^3} - \frac{\psi}{R}\Delta\psi + \frac{\psi^2}{R^3} + \frac{\psi}{R}\Delta\psi\right)\sqrt{g} \\
&\boxed{= \frac{1}{2R}\left(\nabla^k\delta\psi\right)\left(\nabla_k\delta\psi\right)\sqrt{g}.}
\end{aligned}
\tag{2.196}
$$

$$
\begin{aligned}
\boxed{\delta^3\left(H\sqrt{g}\right)} &= H\delta^3(\sqrt{g}) + \delta^1 H\delta^2(\sqrt{g}) + \delta^2 H\delta^1(\sqrt{g}) + \delta^3 H\sqrt{g} \\
&= \frac{1}{R}\times 0 + \left(-\frac{\psi}{R^2} - \frac{1}{2}\Delta\psi\right)\left(\frac{1}{2}\left(\nabla^k\delta\psi\right)\left(\nabla_k\delta\psi\right) + \frac{\psi^2}{R^2}\right)\sqrt{g} + \left(\frac{\psi^2}{R^3} + \frac{\psi}{R}\Delta\psi\right)\frac{2\psi}{R}\sqrt{g} \\
&\quad + \left(-\frac{\psi^3}{R^4} - \frac{3\psi^2}{2R^2}\Delta\psi + \frac{1}{4}\left(\nabla^q\delta\psi\right)\left(\nabla_q\delta\psi\right)\Delta\psi + \frac{1}{2}\left(\nabla^i\delta\psi\right)\left(\nabla^j\delta\psi\right)\nabla_j\left(\nabla_i\psi\right)\right)\sqrt{g} \\
&= \left[-\frac{\psi}{2R^2}\left(\nabla^k\delta\psi\right)\left(\nabla_k\delta\psi\right) - \frac{1}{4}\left(\nabla^k\delta\psi\right)\left(\nabla_k\delta\psi\right)\Delta\psi - \frac{\psi^3}{R^4} - \frac{\psi^2}{2R^2}\Delta\psi + \frac{2\psi^3}{R^4} + \frac{2\psi^2}{R^2}\Delta\psi\right. \\
&\quad \left. -\frac{\psi^3}{R^4} - \frac{3\psi^2}{2R^2}\Delta\psi + \frac{1}{4}\left(\nabla^q\delta\psi\right)\left(\nabla_q\delta\psi\right)\Delta\psi + \frac{1}{2}\left(\nabla^i\delta\psi\right)\left(\nabla^j\delta\psi\right)\nabla_j\left(\nabla_i\psi\right)\right]\sqrt{g} \\
&\boxed{= \left(-\frac{\psi}{2R^2}\left(\nabla^k\delta\psi\right)\left(\nabla_k\delta\psi\right) + \frac{1}{2}\left(\nabla_i\delta\psi\right)\left(\nabla^j\delta\psi\right)\nabla_j\left(\nabla^i\psi\right)\right)\sqrt{g}.}
\end{aligned}
\tag{2.197}
$$

From $\delta\left(\Sigma\langle H\rangle\right) = \int_{\mathcal{U}}\delta\left(H\sqrt{g}\right)du^1du^2$ and using integration by part (2.13), we obtain

$$
\boxed{
\begin{aligned}
\delta\left(\Sigma\langle H\rangle\right) = &\int_{\mathbb{S}^2}\psi dS - \frac{1}{2R}\int_{\mathbb{S}^2}\psi\Delta_{\mathbb{S}^2}\psi dS \\
&+ \frac{1}{4R^2}\int_{\mathbb{S}^2}\psi^2\Delta_{\mathbb{S}^2}\delta\psi dS + \frac{1}{4}\int_{\mathbb{S}^2}\psi\left(\Delta_{\mathbb{S}^2}\delta\psi\right)^2 dS - \frac{1}{8}\int_{\mathbb{S}^2}\psi^2\Delta_{\mathbb{S}^2}^2\delta\psi dS.
\end{aligned}
}
\tag{2.198}
$$

Volume

From the Gauss theorem, one can write :

$$
V = \int_V dV = \int_V \frac{\nabla\cdot\boldsymbol{r}}{3}\,dV = \frac{1}{3}\int_S \boldsymbol{n}\cdot\boldsymbol{r}\,dS = \frac{1}{3}\int_{\mathcal{U}}\boldsymbol{n}\cdot\boldsymbol{r}\sqrt{g}du^1du^2. \tag{2.199}
$$

Knowing that $\boldsymbol{n}\sqrt{g}\cdot\boldsymbol{r} = \left(\boldsymbol{e}_\theta\times\boldsymbol{e}_\phi\right)\cdot\boldsymbol{r}$ and that these three quantities admit at most first-order variations, the perturbation of the volume is at most of third-order

$$
\begin{aligned}
\boxed{\delta^1\left(\sqrt{g}\boldsymbol{n}\cdot\boldsymbol{r}\right)} &= \left(\delta^{(1)}\boldsymbol{e}_\theta\times\boldsymbol{e}_\phi\right)\cdot\boldsymbol{r} + \left(\boldsymbol{e}_\theta\times\delta^{(1)}\boldsymbol{e}_\phi\right)\cdot\boldsymbol{r} + \left(\boldsymbol{e}_\theta\times\boldsymbol{e}_\phi\right)\cdot\delta^{(1)}\boldsymbol{r} \\
&= \left(\left(\left(\nabla_\vartheta\delta\psi\right)\boldsymbol{n} + \frac{\psi}{R}\boldsymbol{e}_\theta\right)\times\boldsymbol{e}_\phi\right)\cdot\boldsymbol{r} + \left(\boldsymbol{e}_\theta\times\left(\left(\nabla_\phi\delta\psi\right)\boldsymbol{n} + \frac{\psi}{R}\boldsymbol{e}_\phi\right)\right)\cdot\boldsymbol{r} + \left(\boldsymbol{e}_\theta\times\boldsymbol{e}_\phi\right)\cdot\delta\psi\boldsymbol{n} \\
&= \frac{\psi}{R}\sqrt{g}\boldsymbol{n}\cdot\boldsymbol{r} + \frac{\psi}{R}\sqrt{g}\boldsymbol{n}\cdot\boldsymbol{r} + \frac{\psi}{R}\sqrt{g}\boldsymbol{n}\cdot\boldsymbol{r} \\
&\boxed{= 3\psi\sqrt{g},}
\end{aligned}
\tag{2.200}
$$

$$
\begin{aligned}
\boxed{\delta^2\left(\sqrt{g}\boldsymbol{n}\cdot\boldsymbol{r}\right)} &= \left(\delta^{(1)}\boldsymbol{e}_\theta\times\delta^{(1)}\boldsymbol{e}_\phi\right)\cdot\boldsymbol{r} + \left(\boldsymbol{e}_\theta\times\delta^{(1)}\boldsymbol{e}_\phi\right)\cdot\delta^{(1)}\boldsymbol{r} + \left(\delta^{(1)}\boldsymbol{e}_\theta\times\boldsymbol{e}_\phi\right)\cdot\delta^{(1)}\boldsymbol{r} \\
&= \left(\left(\left(\nabla_\vartheta\delta\psi\right)\boldsymbol{n} + \frac{\psi}{R}\boldsymbol{e}_\theta\right)\times\left(\left(\nabla_\phi\delta\psi\right)\boldsymbol{n} + \frac{\psi}{R}\boldsymbol{e}_\phi\right)\right)\cdot\boldsymbol{r} + \left(\boldsymbol{e}_\theta\times\left(\left(\nabla_\phi\delta\psi\right)\boldsymbol{n} + \frac{\psi}{R}\boldsymbol{e}_\phi\right)\right)\cdot\delta\psi\boldsymbol{n} \\
&\quad + \left(\left(\left(\nabla_\vartheta\delta\psi\right)\boldsymbol{n} + \frac{\psi}{R}\boldsymbol{e}_\theta\right)\times\boldsymbol{e}_\phi\right)\cdot\delta\psi\boldsymbol{n} \\
&= \frac{\psi^2}{R^2}\left(\boldsymbol{e}_\theta\times\boldsymbol{e}_\phi\right)\cdot\boldsymbol{r} + \frac{\psi^2}{R^2}\left(\boldsymbol{e}_\theta\times\boldsymbol{e}_\phi\right)\cdot\boldsymbol{r} + \frac{\psi^2}{R^2}\left(\boldsymbol{e}_\theta\times\boldsymbol{e}_\phi\right)\cdot\boldsymbol{r} \\
&\boxed{= 3\frac{\psi^2}{R}\sqrt{g}.}
\end{aligned}
\tag{2.201}
$$

$$\boxed{\delta^3\left(\sqrt{g}\boldsymbol{n}\cdot\boldsymbol{r}\right)} = \left(\delta^{(1)}\boldsymbol{e}_\theta \times \delta^{(1)}\boldsymbol{e}_\phi\right)\cdot\delta^{(1)}\boldsymbol{r} = \left(\left(\left(\nabla_\vartheta\delta\psi\right)\boldsymbol{n} + \frac{\psi}{R}\boldsymbol{e}_\theta\right)\times\left(\left(\nabla_\phi\delta\psi\right)\boldsymbol{n} + \frac{\psi}{R}\boldsymbol{e}_\phi\right)\right)\cdot\delta\psi\boldsymbol{n} = \frac{\psi^3}{R^3}\left(\boldsymbol{e}_\theta\times\boldsymbol{e}_\phi\right)\cdot\boldsymbol{r}$$
$$\boxed{= \frac{\psi^3}{R^2}\sqrt{g}.} \tag{2.202}$$

The variation of the volume is then

$$\boxed{\delta V = R^2\iint_{\mathbb{S}^2}\psi\,dS + R\iint_{\mathbb{S}^2}\psi^2\,dS + \frac{1}{3}\iint_{\mathbb{S}^2}\psi^3\,dS.} \tag{2.203}$$

2.B Variations of the oriented geometric quantities

In Section 2.2.4.3, new geometric quantities $S_\parallel$, $S_\perp$, $S_\parallel\widetilde{H}^\parallel$ and $S_\perp\widetilde{H}^\perp$ are defined to recover first order variations in x_2 using the decomposition of the local surface element into

$$A = \|\boldsymbol{e}_\theta\times\boldsymbol{e}_\phi\| = \left|(\boldsymbol{e}_\theta\times\boldsymbol{e}_\phi)\cdot\boldsymbol{N}\right| + \left(\|\boldsymbol{e}_\theta\times\boldsymbol{e}_\phi\| - \left|(\boldsymbol{e}_\theta\times\boldsymbol{e}_\phi)\cdot\boldsymbol{N}\right|\right) =: A_\parallel + A_\perp, \tag{2.204}$$

where $\boldsymbol{e}_a := \partial_a\boldsymbol{r}$ for $a = \theta,\phi$, and $\boldsymbol{e}_v := \partial_v\boldsymbol{r}(u,v)$ are the tangential vectors and $\boldsymbol{N} = (0,0,1)$ is a constant vector chosen along the axisymmetric axis. Then for any local geometric quantity $X(u,v)$, we split the variation of the surface-averaged geometric quantity into

$$\delta(S\widetilde{X}) = \delta(S_\parallel\widetilde{X}^\parallel) + \delta(S_\perp\widetilde{X}^\perp), \tag{2.205}$$

such that we can focus on the variation $\delta(S_\parallel\widetilde{X}^\parallel)$, and $\delta(S_\perp\widetilde{X}^\perp)$ follows from (2.122). The variation of $S_\parallel\widetilde{X}^\parallel$ reads

$$\delta(S_\parallel\widetilde{X}^\parallel) = \int_{\mathcal{U}}\delta(XA_\parallel) = \int_{\mathcal{U}}\delta\left(X\left|(\boldsymbol{e}_\theta\times\boldsymbol{e}_\phi)\cdot\boldsymbol{N}\right|\right), \tag{2.206}$$

We get rid of the absolute value by remarking that the perturbations along harmonics Y_0 and Y_2 are symmetric with respect to the equatorial plane of the droplet. We split $\mathcal{U}$ into two hemispheres using the half unit sphere mapping $\frac{1}{2}\mathcal{U} = (0,\pi/2)\times(0,2\pi)$ where $(\boldsymbol{e}_\theta\times\boldsymbol{e}_\phi)\cdot\boldsymbol{N} > 0$ and perform a change of variables leading to

$$\begin{aligned}\delta(S_\parallel\widetilde{X}^\parallel) &= \int_{\frac{1}{2}\mathcal{U}}\delta(X(\boldsymbol{e}_\theta\times\boldsymbol{e}_\phi)\cdot\boldsymbol{N}) - \int_{\mathcal{U}\setminus\frac{1}{2}\mathcal{U}}\delta(X(\boldsymbol{e}_\theta\times\boldsymbol{e}_\phi)\cdot\boldsymbol{N})\\ &= 2\int_{\frac{1}{2}\mathcal{U}}\delta(X(\boldsymbol{e}_\theta\times\boldsymbol{e}_\phi))\cdot\boldsymbol{N}.\end{aligned} \tag{2.207}$$

Then, the variation is decomposed following

$$\delta(S_\parallel\widetilde{X}^\parallel) = 2\int_{\frac{1}{2}\mathcal{U}}\delta(XA)(\boldsymbol{n}\cdot\boldsymbol{N}) + 2\int_{\frac{1}{2}\mathcal{U}}X_0A_0\delta\boldsymbol{n}\cdot\boldsymbol{N}, \tag{2.208}$$

with $A_0\delta\boldsymbol{n} = \delta(\boldsymbol{e}_\theta\times\boldsymbol{e}_\phi) - \boldsymbol{n}\delta A$. The first-order variation in x_2 is non-trivial here, and we retain only the first-order terms in ψ for $\delta(HA)$ and δA in (2.39). Only the first-order variation of $\delta(\boldsymbol{e}_\theta\times\boldsymbol{e}_\phi)$ is still undetermined. For the first-order deformation $\psi = x_2Y_2 + o(x_2)$, it yields

$$\begin{aligned}\delta(\boldsymbol{e}_\theta\times\boldsymbol{e}_\phi) &= \partial_\theta\boldsymbol{r}\times\partial_\phi\boldsymbol{r} - \partial_\theta\boldsymbol{r}_0\times\partial_\phi\boldsymbol{r}_0\\ &= x_2R_0Y_2(\partial_\theta\boldsymbol{n}\times\partial_\phi\boldsymbol{n}) + x_2R_0(\partial_\theta Y_2)(\boldsymbol{n}\times\partial_\phi\boldsymbol{n}) + R_0x_2Y_2(\partial_\theta\boldsymbol{n}\times\partial_\phi\boldsymbol{n}) + o(x_2^2).\end{aligned} \tag{2.209}$$

For the sphere, we recall that

$$\begin{aligned}&\partial_\theta\boldsymbol{n} = R_0^{-1}\boldsymbol{e}_\theta, \quad \partial_\phi\boldsymbol{n} = R_0^{-1}\boldsymbol{e}_\phi, \quad \boldsymbol{e}_\theta\times\boldsymbol{e}_\phi = A_0\boldsymbol{n},\\ &A_0 = R_0^2\sin\theta, \quad \boldsymbol{N}\cdot\boldsymbol{n} = \cos\theta, \quad \boldsymbol{N}\cdot\boldsymbol{e}_\theta = -R_0\sin\theta.\end{aligned} \tag{2.210}$$

The first-order variation $\delta(\boldsymbol{e}_\theta \times \boldsymbol{e}_\phi)$ then reads

$$\begin{aligned}\delta(\boldsymbol{e}_\theta \times \boldsymbol{e}_\phi) &= x_2 R_0^{-1} Y_2(\boldsymbol{e}_\theta \times \boldsymbol{e}_\phi) + x_2(\partial_\theta Y_2)(\boldsymbol{n} \times \boldsymbol{e}_\phi) + R_0^{-1} x_2 Y_2(\boldsymbol{e}_\theta \times \boldsymbol{e}_\phi) + o(x_2^2)\\ &= x_2 R_0^{-1} Y_2 A_0 \boldsymbol{n} - x_2(\partial_\theta Y_2) A_0 R_0^{-2} \boldsymbol{e}_\theta + R_0^{-1} x_2 Y_2 A_0 \boldsymbol{n} + o(x_2^2)\\ &= 2x_2 R_0^{-1} Y_2 A_0 \boldsymbol{n} - x_2(\partial_\theta Y_2)\boldsymbol{e}_\theta + o(x_2^2).\end{aligned} \tag{2.211}$$

Now, taking $X = 1$ in (2.208) gives

$$\begin{aligned}\delta S_\parallel &= 2\int_{\frac{1}{2}\mathcal{U}} \delta(\boldsymbol{e}_u \times \boldsymbol{e}_v)\cdot \boldsymbol{N}\\ &= 2\int_{\frac{1}{2}\mathcal{U}} 2x_2 R_0^{-1} Y_2 A_0(\boldsymbol{n}\cdot\boldsymbol{N}) - x_2 A_0 R_0^{-2}(\partial_\theta Y_2)(\boldsymbol{e}_\theta\cdot\boldsymbol{N}) + o(x_2^2)\\ &= 4x_2 R_0 \int_{\frac{1}{2}\mathcal{U}} Y_2 \sin\theta\cos\theta + 2x_2 R_0 \int_{\frac{1}{2}\mathcal{U}} (\partial_\theta Y_2)\sin^2\theta + o(x_2^2)\\ &= 4x_2 R_0 \frac{\sqrt{5\pi}}{8} + 2x_2 R_0\left(-\frac{3\sqrt{5\pi}}{4}\right) + o(x_2^2)\\ &= -x_2 R_0\sqrt{5\pi} + o(x_2^2).\end{aligned} \tag{2.212}$$

For $X = H$, there is an extra term in the first-order variation $\delta(HA) = (G_0 - \frac{1}{2}\Delta)\psi A_0$ (Capovilla et al., 2003) which has been nullified in (2.39) as the inclusion is closed. Here, it is taken into account as we integrate twice over a half inclusion. It yields

$$\begin{aligned}\delta S_\parallel \tilde{H}^\parallel &= 2\int_{\frac{1}{2}\mathcal{U}} \delta(HA)(\boldsymbol{n}\cdot\boldsymbol{N}) + 2\int_{\frac{1}{2}\mathcal{U}} H_0(\delta(\boldsymbol{e}_\theta\times\boldsymbol{e}_\phi) - \boldsymbol{n}\delta A)\cdot\boldsymbol{N},\\ &= 2\int_{\frac{1}{2}\mathcal{U}} (G_0 - 2H_0^2)\psi A_0(\boldsymbol{n}\cdot\boldsymbol{N}) + \int_{\frac{1}{2}\mathcal{U}} \Delta\psi A_0(\boldsymbol{n}\cdot\boldsymbol{N}) + 2\int_{\frac{1}{2}\mathcal{U}} H_0\delta(\boldsymbol{e}_\theta\times\boldsymbol{e}_\phi)\cdot\boldsymbol{N},\\ &= -2x_2\int_{\frac{1}{2}\mathcal{U}} Y_2\sin\theta\cos\theta + -x_2\int_{\frac{1}{2}\mathcal{U}} (\Delta_{\mathbb{S}^2}Y_2)\sin\theta\cos\theta + 2R_0^{-1}\int_{\frac{1}{2}\mathcal{U}} \delta(\boldsymbol{e}_\theta\times\boldsymbol{e}_\phi)\cdot\boldsymbol{N},\\ &= -x_2\frac{1}{2}\sqrt{5\pi}.\end{aligned} \tag{2.213}$$

Replacing x_2 with its expression in χ and S_0 yields geometric relations (2.142).

2.C Weights and quadrature points of the bi-disperse quadrature

The bi-disperse closure for $n_1, n_2, (S_0)_1, (S_0)_2$ in terms of the moment in size only $M_k = M^\xi_{k,0,0}$ with $k = 0, 1/2, 1, 3/2$ is obtained by solving the truncated moment problem with Mathematica (Wolfram Research, 2023) and reads

$$\begin{aligned}n_i &= \frac{1}{2}\left(M_0 + (-1)^{i+1}\frac{3M_0M_1M_{1/2} - 2M_{1/2}^3 - M_0^2M_{3/2}}{\sqrt{\Delta}}\right),\\ (S_0)_i &= (2(M_{1/2}^2 - M_0M_1)^2)^{-1}\Big(M_0^2M_{3/2}^2 - M_1^2M_{1/2}^2 + 2(M_0M_1^3 + M_{1/2}^3M_{3/2})\\ &\qquad -4M_0M_{1/2}M_1M_{3/2} + (-1)^{i+1}(M_0M_{3/2} - M_1M_{1/2})\sqrt{\Delta}\Big),\\ \text{with}\quad \Delta &= 4M_0M_1^3 - 3M_1^2M_{1/2}^2 - 6M_0M_{1/2}M_1M_{3/2} + 4M_{1/2}^3M_{3/2} + M_0^2M_{3/2}^2.\end{aligned} \tag{2.214}$$

It can be written with the geometric variables using either relations (2.64), (2.126)-(2.127) or (2.143)-(2.144). Mathematica also shows that these relations yield positive values of n_i and $(S_0)_i$ provided that the moments M_k are positive

and

$$M_{1/2}M_{3/2} - M_1^2 > 0, \qquad M_0 M_1 - M_{1/2}^2 > 0. \tag{2.215}$$

These last two conditions ensure the positivity of Hankel matrices involved in the realizability conditions of the Hausdorff truncated moment problem (Schmüdgen, 2017).

2.D Hamilton's SAP for the polydisperse spray of oscillating droplets

This model is built on the basis of the one velocity disperse Model 8 where additional energies are added to take into account capillarity at the small-scale along with the internal flow of the droplets. We recall the Lagrangian given in (2.152) for the two-scale mixture

$$\mathcal{L} = \mathcal{L}_1(\alpha_1, m_1, \boldsymbol{u}) + \mathcal{L}_2(\alpha_2, m_2, \boldsymbol{u}) + \mathcal{L}_1^d\left(m_1^d, \rho_1^d, \boldsymbol{u}\right) + \mathcal{L}_1^{vib}(n_1, (S_0)_1, \chi_1, \dot{\chi}_1) + \mathcal{L}_2^{vib}(n_2, (S_0)_2, \chi_2, \dot{\chi}_1), \tag{2.216}$$

where $\mathcal{L}_i^{vib} = \frac{1}{2}\nu n_i (S_0)_i^{5/2}\chi_i^2 - \sigma n_i (S_0)_i - \frac{1}{2}\gamma n_i (S_0)_i \chi_i^2$. We define the action $\mathcal{A} = \int_\Omega$. As same as previous models, α_1 is a free variable in the minimization process, while effective densities m_k are conserved, ρ_1^d is advected. For the additional variables, the number densities of droplets n_i are conserved, the surfaces $(S_0)_i$ are advected, χ_i are free variables describing the oscillatory motion of the droplets, and $\dot{\chi}_i$ are linked to time derivatives of χ_i with $D_t\chi_i = \dot{\chi}_i$. This last constraint translates in terms of variations

$$\delta(\dot{\chi}_i) = \delta(D_t\chi_i) = \partial_t(\delta\chi_i) + \boldsymbol{u}\cdot\boldsymbol{\nabla}(\delta\chi_i) + \delta\boldsymbol{u}\cdot\boldsymbol{\nabla}\chi_i. \tag{2.217}$$

Denoting $K_{\dot{\chi}_i} = \partial_{\dot{\chi}_i}\mathcal{L}_i^{vib}$ and $\boldsymbol{u} = \partial_{\boldsymbol{u}}\mathcal{L}$, we decompose then the variation of the action according to each dependency

$$\delta\mathcal{A}_{\alpha_1} = \int_\Omega \partial_{\alpha_1}\mathcal{L}_1\,\delta\alpha_1, \tag{2.218}$$

$$\delta\mathcal{A}_{\alpha_2} = \int_\Omega \partial_{\alpha_2}\mathcal{L}_2\,\delta\alpha_2 = -\int_\Omega \alpha_1^d \boldsymbol{\nabla}(\partial_{\alpha_2}\mathcal{L}_2)\cdot\boldsymbol{\eta} - \int_\Omega \partial_{\alpha_2}\mathcal{L}_2\,\delta\alpha_1, \tag{2.219}$$

$$\delta\mathcal{A}_{m_k} = \int_\Omega \partial_{m_k}\mathcal{L}_k\,\delta m_k = \int_\Omega m_k\boldsymbol{\nabla}(\partial_{m_k}\mathcal{L}_k)\cdot\boldsymbol{\eta}, \tag{2.220}$$

$$\delta\mathcal{A}_{\rho_1^d} = \int_\Omega -\partial_{\rho_1^d}(\mathcal{L}_1^d + \mathcal{L}_1^{vib} + \mathcal{L}_2^{vib})\,\boldsymbol{\nabla}\rho_1^d\cdot\boldsymbol{\eta}, \tag{2.221}$$

$$\delta\mathcal{A}_{(S_0)_i} = \int_\Omega -\partial_{(S_0)_i}\mathcal{L}_i^{vib}\,\boldsymbol{\nabla}(S_0)_i\cdot\boldsymbol{\eta}, \tag{2.222}$$

$$\delta\mathcal{A}_{n_i} = \int_\Omega \partial_{n_i}\mathcal{L}_i^{vib}\,\delta n_i = \int_\Omega n_i\boldsymbol{\nabla}(\partial_{n_i}\mathcal{L}_i^{vib})\cdot\boldsymbol{\eta}, \tag{2.223}$$

$$\delta\mathcal{A}_{\chi_i} = \int_\Omega \partial_{\chi_i}\mathcal{L}_i^{vib}\,\delta\chi_i, \tag{2.224}$$

$$\delta\mathcal{A}_{\dot{\chi}_i} = \int_\Omega K_{\dot{\chi}_i}\,\delta\dot{\chi}_i = \int_\Omega K_{\dot{\chi}_i}(\partial_t(\delta\chi_i) + \boldsymbol{u}\cdot\boldsymbol{\nabla}(\delta\chi_i) + \delta\boldsymbol{u}\cdot\boldsymbol{\nabla}\chi_i), \tag{2.225}$$

$$= -\int_\Omega (\partial_t K_{\dot{\chi}_i} + \boldsymbol{\nabla}\cdot(K_{\dot{\chi}_i}\boldsymbol{u}))\delta\chi_i \tag{2.226}$$

$$-\int_\Omega (\partial_t(K_{\dot{\chi}_i}\boldsymbol{\nabla}\chi_i) + \boldsymbol{\nabla}\cdot((K_{\dot{\chi}_i}\boldsymbol{\nabla}\chi_i)\boldsymbol{u}) + K_{\dot{\chi}_i}\boldsymbol{\nabla}\chi_i\cdot\boldsymbol{\nabla}\boldsymbol{u})\cdot\boldsymbol{\eta}, \tag{2.227}$$

$$\delta\mathcal{A}_{\boldsymbol{u}} = \int_\Omega -(\partial_t\boldsymbol{K} + \boldsymbol{\nabla}\cdot(\boldsymbol{K}\otimes\boldsymbol{u}) + \boldsymbol{K}\cdot\boldsymbol{\nabla}\boldsymbol{u})\cdot\boldsymbol{\eta}. \tag{2.228}$$

We denote $\mathcal{L}_k^* = m_k\partial_{m_k}\mathcal{L}_k - \mathcal{L}_k$, $\mathcal{L}_i^{vib,*} = n_i\partial_{n_i}\mathcal{L}_i^{vib} - \mathcal{L}_i^{vib}$ and $\mathcal{L}^* = \mathcal{L}_1^* + \mathcal{L}_2^* + \mathcal{L}_1^{d,*}$ such that the variation of the action related to the mixture Lagrangian reads

$$\delta\mathcal{A} = \int \boldsymbol{A}_{\boldsymbol{\eta}}\cdot\boldsymbol{\eta} + \boldsymbol{A}_{\alpha_1}\delta\alpha_1 + \boldsymbol{A}_{\chi_1}\delta\chi_1 + \boldsymbol{A}_{\chi_2}\delta\chi_2, \tag{2.229}$$

with

$$\begin{aligned}
\boldsymbol{A}_{\alpha_1} &= \partial_{\alpha_1}\mathcal{L}_1 - \partial_{\alpha_2}\mathcal{L}_2,\\
\boldsymbol{A}_{\chi_i} &= \partial_{\chi_i}\mathcal{L}_k^{vib} - \partial_t K_{\dot{\chi}_i} - \boldsymbol{\nabla}\cdot(K_{\dot{\chi}_i}\boldsymbol{u}),\\
\boldsymbol{A}_{\boldsymbol{\eta}} &= -\Big(\partial_t \boldsymbol{K} + \boldsymbol{\nabla}\cdot(\boldsymbol{K}\otimes\boldsymbol{u}) - \boldsymbol{\nabla}(\mathcal{L}^* - \alpha_1^d\partial_{\alpha_2}\mathcal{L}_2) - \boldsymbol{A}_{\alpha_1}\boldsymbol{\nabla}\alpha_1 - \boldsymbol{A}_{\chi_1}\boldsymbol{\nabla}\chi_1 - \boldsymbol{A}_{\chi_2}\boldsymbol{\nabla}\chi_2\Big),
\end{aligned} \tag{2.230}$$

and $\mathcal{L}_i^{vib,*} := n_i\partial_{n_i}\mathcal{L}_i^{vib} - \mathcal{L}_i^{vib}$. Nullifying the variations gives the following system

$$\begin{cases}
\partial_t \boldsymbol{K} + \boldsymbol{\nabla}\cdot(\boldsymbol{K}\otimes\boldsymbol{u}) - \boldsymbol{\nabla}(\mathcal{L}^* - \alpha_1^d\partial_{\alpha_2}\mathcal{L}_2) = \boldsymbol{0},\\
\partial_{\chi_1}\mathcal{L}_1^{vib} - \partial_t K_{\dot{\chi}_1} - \boldsymbol{\nabla}\cdot(K_{\dot{\chi}_1}\boldsymbol{u}) = 0,\\
\partial_{\chi_2}\mathcal{L}_2^{vib} - \partial_t K_{\dot{\chi}_2} - \boldsymbol{\nabla}\cdot(K_{\dot{\chi}_2}\boldsymbol{u}) = 0,\\
\partial_{\alpha_1}\mathcal{L}_1 - \partial_{\alpha_2}\mathcal{L}_2 = 0.
\end{cases} \tag{2.231}$$

Evaluating the derivatives of the Lagrangian as defined in (2.153) yields

$$\begin{gathered}
\boldsymbol{K}_{\boldsymbol{u}} = \partial_{\boldsymbol{u}}\mathcal{L} = \rho\boldsymbol{u}, \qquad \mathcal{L}^* = -\alpha_1 p_1 - \alpha_2 p_2, \qquad \partial_{\alpha_2}\mathcal{L}_2 = p_2, \qquad \partial_{\alpha_1}\mathcal{L}_1 = p_1,\\
\partial_{\chi_i}\mathcal{L}_i^{vib} = -\gamma n_i (S_0)_i\chi_i, \qquad K_{\dot{\chi}_i} = \partial_{\dot{\chi}_i}\mathcal{L}_i^{vib} = \nu n_i (S_0)_i^{5/2}\dot{\chi}_i.
\end{gathered} \tag{2.232}$$

Finally, with the constraints and the relation $D_t\chi_i = \dot{\chi}_i$, we write the final system in its conservative form

$$\begin{cases}
\partial_t m_k & +\boldsymbol{\nabla}\cdot(m_k\boldsymbol{u}) & = 0, & k = 1,2,1^d,\\
\partial_t n_i & +\boldsymbol{\nabla}\cdot(n_i\boldsymbol{u}) & = 0, & i = 1,2,\\
\partial_t(n_i(S_0)_i) & +\boldsymbol{\nabla}\cdot(n_i(S_0)_i\boldsymbol{u}) & = 0, & i = 1,2,\\
\partial_t(n_i\dot{\chi}_i) & +\boldsymbol{\nabla}\cdot(n_i\dot{\chi}_i\boldsymbol{u}) & = -\omega_i^2 n_i\chi_i, & i = 1,2,\\
\partial_t(n_i\chi_i) & +\boldsymbol{\nabla}\cdot(n_i\chi_i\boldsymbol{u}) & = n_i\dot{\chi}_i, & i = 1,2,\\
\partial_t(\rho\boldsymbol{u}) & +\boldsymbol{\nabla}\cdot(\rho\boldsymbol{u}\otimes\boldsymbol{u} + p\boldsymbol{I}) & = \boldsymbol{0}, &
\end{cases} \tag{2.233}$$

where $p := p_1 = p_2$ and $\omega_i^2 = \gamma/\nu(S_0)_i^{-3/2}$.

2.E The monodisperse case

We consider a monodisperse closer of the synchronous oscillating droplet kinetic model. In this case, only four geometric quantities are required, two related to statics and two related to dynamics. We choose $(\Sigma\langle G\rangle, \alpha_1^d, (\Delta\Sigma_\perp), (\Delta_t\Sigma_\perp))$ or equivalently $(n_1^d, \alpha_1^d, (\Delta\Sigma_\perp), (\Delta_t\Sigma_\perp))$. We then obtain the following quadrature in terms of the geometric quantities,

$$\begin{gathered}
n(\boldsymbol{x}, t, \widehat{S}_0, \widehat{\chi}, \widehat{\dot{\chi}}) = n_1^d\delta(\widehat{S}_0 - S_0)\delta(\widehat{\chi} - \chi)\delta(\widehat{\dot{\chi}} - \dot{\chi}),\\
S_0 = \frac{(6\sqrt{\pi}\alpha_1^d)^{2/3}}{(n_1^d)^{2/3}}, \quad \chi = 2\sqrt{\frac{2}{5}}\frac{(\Delta\Sigma_\perp)}{(n_1^d)^{1/3}(6\sqrt{\pi}\alpha_1^d)^{2/3}}, \quad \dot{\chi} = 2\sqrt{\frac{2}{5}}\frac{(\Delta_t\Sigma_\perp)}{(n_1^d)^{1/3}(6\sqrt{\pi}\alpha_1^d)^{2/3}}.
\end{gathered} \tag{2.234}$$

It can also be written in terms of moments with

$$n_1^d = M^\xi_{0,0,0}, \quad S_0 = \left(\frac{M^\xi_{3/2,0,0}}{M^\xi_{0,0,0}}\right)^{2/3}, \quad \chi = \frac{M^\xi_{1,1,0}}{(M^\xi_{0,0,0})^{1/3}(M^\xi_{3/2,0,0})^{2/3}}, \quad \dot{\chi} = \frac{M^\xi_{1,0,1}}{(M^\xi_{0,0,0})^{1/3}(M^\xi_{3/2,0,0})^{2/3}}. \tag{2.235}$$

CHAPTER 3

Two-scale modelling

In complex multi-scale flows, typically when the regime transitions from a separated regime to a disperse regime, the interface goes through a mixed regime, where several length-scales coexist. Such flows are observed in atomization (Marmottant and Villermaux, 2004; Fuster et al., 2009; Shinjo and Umemura, 2010; Chesnel et al., 2011; Hoarau et al., 2023), dam breaks (Koshizuka and Oka, 1996) or gaseous jets impacts on liquid surfaces (Banks and Chandrasekhara, 1963; Haegeman et al., 2024). The mixed regime is inherently difficult to model as it involves a wide spectrum of length-scales and a variety of phenomena. A more common approach consists in bypassing the modelling of this regime through the transition of a separated model to a disperse model as those presented in Chapters 1 and 2. With such an approach, the interface is resolved in the separated regime that we call *large-scale*, and it is modelled in a *small-scale* regime is the disperse regime.

A first approach to model such transitions would be to couple two different models, each adapted to one of the two regimes. The two models then exchange mass, momentum and energy *via* Eulerian-Lagrangian coupling (Vallet et al., 2001; Zuzio et al., 2013) or Eulerian-Eulerian coupling (Le Touze et al., 2020), either through a virtual interface or everywhere in the domain. In both cases, the coupling is challenging as it requires transferring seamlessly mass from one model to another. Indeed, such transfer is intrinsically difficult as it requires an unphysical appearance, or disappearance, of one of the two phases. Furthermore, the mathematical properties associated with such coupling are rarely studied and must be compatible with the second principle of thermodynamics.

The main idea of this chapter is to pursue a second approach through the derivation of a unified model which is able to describe the two regimes within the same set of equations. Some preliminary ideas of such approach have been proposed in Devassy et al. (2015) to account for primary atomization, but the model was mainly proposed through heuristics, and the dissipation of the coupling was not studied. First steps towards the derivation of such a unified model with Hamilton's SAP were proposed in Cordesse (2020); Di Battista (2021) with the addition of geometric quantities representing the small-scale dynamics. Here, we introduce a two-scale mixture model where two models coexist with independent volume fractions: large-scale volume fractions for a multi-fluid DIM in the separated regime and a small-scale volume fraction for a multi-fluid disperse model. We take here full advantage of the flexibility of Hamilton's SAP as the physics of both models are combined in a unified model by combining their energies into a unique Lagrangian energy. Remark that this approach sets a particular disperse regime for the small-scale and thus differs from the statistical approach of Cordesse et al. (2019) where the small scale is defined using a length-scale threshold in the statistical distribution of the interface length-scales. However, such a threshold is recovered as a regularizing parameter of the large-scale interface in a mass transfer between the two scales. This mass transfer proposes here an original coupling between the models of each scale by both regularizing the large-scale interface and preserving the energy of the flow. It has led to the two following contributions :

- For the two-scale modelling approach: Loison, Arthur, Teddy Pichard, Samuel Kokh, and Marc Massot. " Two-scale modelling of two-phase flows based on the Stationary Action Principle and a Geometric Method Of Moments". arXiv, 2023. https://doi.org/10.48550/arXiv.2308.15641.
- For the regularization process: Loison, Arthur, Samuel Kokh, Teddy Pichard, and Marc Massot. "A unified

two-scale gas-liquid multi-fluid model with capillarity and interface regularization through a mass transfer between scales ". arXiv, 2024. https://doi.org/10.48550/arXiv.2401.09169.

The two-scale mixture is presented in Section 3.1 where an atomization process is assumed. Thus, both a separated gas-liquid large-scale model and a disperse small-scale model of liquid inclusions are combined in a single set of conservation laws using Hamilton's SAP. Then, in Section 3.2, mass exchange is defined between the two scales while ensuring both good mathematical properties of the model (supplementary conservation equation and hyperbolicity) and its compliance with the second principle of thermodynamics. The parameters characterizing the mass transfer between the separated and the disperse regime are identified. They are showed to model some physical mechanisms comparable to the primary break-up process. Finally, in order to keep the large-scale model in a separated regime, we introduce, in Section 3.3, a regularization process which detects the location where the curvature of the large-scale interface is considered too high to be accurately represented with a multi-fluid DIM. A length-scale is then introduced at the modelling stage to split the length-scales of the large-scale separated regime from the ones of the small-scale disperse regime. Such a regularization is enabled by a modification of the local Laplace equilibrium which triggers an energy-conservative mass transfer from the liquid large-scale phase to the small-scale while being energy-conservative.

Such approach shares a similar goal as two-phase Large-Eddy Simulations (Herrmann, 2015; Fleau, 2017) where the small length-scales are gathered in a small-scale model. However, the two-scale approach presented in this chapter relies on the *a priori* modelling of the small scales whereas LES small-scale models are obtained *a posteriori* when closing the filtered terms of the dynamics. This technique is usually more suited for turbulence modelling.

3.1 Derivation of two-scale unified models

In this section, we introduce two-scale unified models by combining the models derived in both the separated regime (see Chapter 1) and the disperse regime (see Chapters 1 and 2). In order to do so, the energies introduced in their respective Lagrangian are here combined in a single one.

We start by introducing in Section 3.1.1 the notion of a *two-scale mixture* along with some assumptions retained in this chapter. Then, we continue in Section 3.1.2 with the derivation of a first two-scale model without capillarity

based on separated Models 3 and 4 and disperse Model 8. We finish by the derivation of two-scale models with capillarity accounted at both scales in Section 3.1.3, thus extending the separated-regime capillarity Models 5 and 6 and the polydisperse Model 12.

3.1.1 Definition of the two-scale mixture

The unified modelling approach relies on the definition of a two-scale two-phase mixture where we account for the presence of both large-scale and small-scale phases at the same location. This artificial mixture follows the same philosophy of the two-fluid mixture of immiscible fluids. This allows a smooth and gradual transition from the separated model to the disperse model. Let us recall that this multi-fluid diffuse interface approach does not involve here any preset length-scale for the interface thickness which is not comparable to the physical thickness introduced in second-gradient DIM.

To fix the ideas, from now on, we will focus on an atomization process where a gas-liquid large-scale mixture in the separated regime evolves towards a disperse regime with a spray of liquid droplets (see Figure 3.1.1). Therefore,

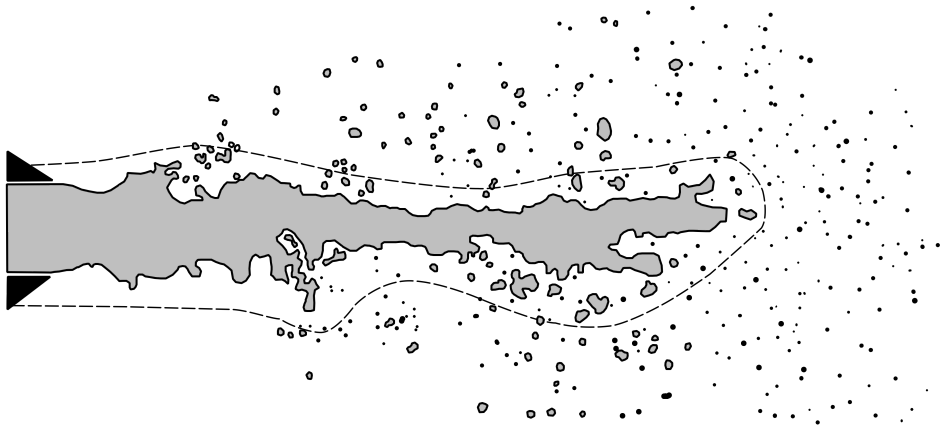

Figure 3.1.1: Schematic view of an atomization process. The liquid is injected from the nozzle on the left in a separated regime. The liquid core then destabilizes to form a mixed regime. Finally, a disperse regime is observed away from the liquid core. The dashed line delimits the zone where the one-velocity assumption can be considered adequate.

we also make the following assumptions :

- all phases have the same mean velocity; (H3a)
- the small-scale liquid phase is incompressible; (H3b)
- each phase is isothermal with barotropic equations of state. (H3c)

These assumptions correspond to the ones of the separated Models 3 and 4 and the disperse Model 8. The one-velocity assumption is here retained for clarity purposes and is acceptable in the immediate surrounding of the liquid core (see Figure 3.1.1). It would however be possible to add a second velocity as proposed in Models 10 and 11.

Following Section 1.3.1, we denote with the subscript $k = 1$ the liquid and $k = 2$ the gaseous phase of the separated large-scale model. Similarly to Section 1.4.1, an additional superscript d identifies the small-scale disperse liquid phase as a third phase. Following (H3c), each large-scale fluid $k = 1, 2$ is equipped with a barotropic equation of state of the form $\rho_k \mapsto e_k(\rho_k)$, where ρ_k and e_k are the density and the internal energy of the phase $k = 1, 2$. The pressure p_k of the large scale phase $k = 1, 2$ is then defined by $p_k = \rho_k^2 e_k'(\rho_k)$. We assume that $p_k'(\rho_k) > 0$ so that the sound speed c_k associated with the phase $k = 1, 2$ is $c_k = \sqrt{p_k'(\rho_k)}$. With α_k the volume fraction of the phase

$k = 1, 2, 1^d$, we consider a two-scale mixture such that it obeys the volume constraint,

$$\alpha_1 + \alpha_2 + \alpha_1^d = 1, \tag{3.1}$$

and its density ρ is obtained from the effective phase densities $m_k := \alpha_k \rho_k$,

$$m_1 + m_2 + m_1^d = \rho. \tag{3.2}$$

Moreover, we introduce the large-scale volume fractions for $k = 1, 2$

$$\overline{\alpha}_k = \frac{\alpha_k}{1 - \alpha_1^d}. \tag{3.3}$$

The large-scale volume fractions allow to symmetrize the roles of the large-scale phases regarding the modelling of the interface (see Figure 3.1.2). Thus, the presence of the small scale is not particularly associated with any of the two phase preferably but to the large-scale mixture symmetrically. Eventually, the small scale is here carried by the gaseous phase, but this symmetric construction of the large-scale volume fraction allows the large-scale model interface not to be impacted. Let us underline here that the coexistence of both the separated regime and disperse regime is confined to the immediate surrounding of the interface and serves as a modelling framework to allow the transition from the separated regime to the disperse one (see Figure 3.1.2). This approach notably differs from the previous works of Cordesse (2020); Di Battista (2021) where the small-scale model was defined as the scales present below a filtered threshold with additional geometric quantities but not an independent volume fraction as we propose here following also some ideas of Devassy et al. (2015). However, we propose in the following sections an original variational derivation of such a system along with the assertion of the mathematical properties of the set of equations, including when inter-scale transfer terms are added (cf. Section 3.2).

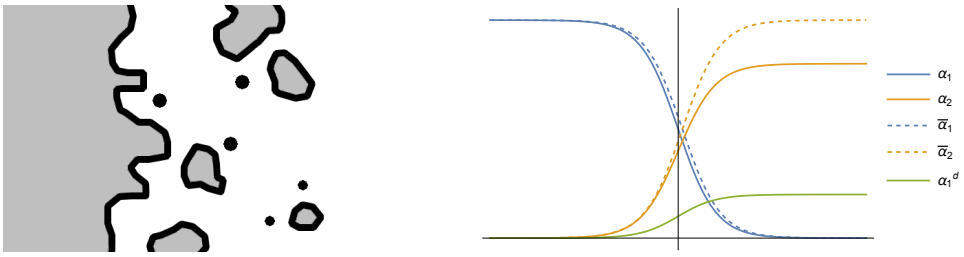

Figure 3.1.2: Left: Schematic view of the transition within the mixed regime from a liquid core in a separated regime and to disperse liquid inclusions. Right: Diffuse schematic representation of the transition showed on the left. The diffuse interface is represented through the evolution of the volume fractions of the two-scale mixture. Note the symmetrized role of the large-scale volume fractions and the absence of explicit interface width in the model.

3.1.2 The minimal two-scale model without capillarity

For the derivation of the first two-scale model, we make the simplifying assumption :

- capillarity effects are negligible. (H3d)

3.1.2.1 Energies and constraints

Let us then define the energies and constraints associated with the mixture. Denoting Y_k the mass fraction, the specific internal energy e of the two-phase material is defined by

$$e = Y_1 e_1(\rho_1) + Y_2 e_2(\rho_2) + Y_1^d e_1(\rho_1^d). \tag{3.4}$$

As we considered here a unique velocity $\boldsymbol{u}$ describing the mixture

$$\boldsymbol{u} := \boldsymbol{u}_1 = \boldsymbol{u}_2 = \boldsymbol{u}_1^d, \tag{3.5}$$

such that the mass conservation property of each phase reads

$$\partial_t m_k + \boldsymbol{\nabla} \cdot (m_k \boldsymbol{u}) = 0, \quad \text{for} \quad k = 1, 2, 1^d. \tag{3.6}$$

Summing these equations provides the total mass conservation equation

$$\partial_t \rho + \boldsymbol{\nabla}_{\boldsymbol{x}} \cdot (\rho \boldsymbol{u}) = 0. \tag{3.7}$$

Moreover, the incompressibility of the small-scale liquid phase yields

$$D_t \rho_1^d = 0, \qquad \partial_t \alpha_1^d + \boldsymbol{\nabla} \cdot (\alpha_1^d \boldsymbol{u}) = 0. \tag{3.8}$$

We set the kinetic and potential energies of the phase k as follows

$$E_k^{kin} := \frac{1}{2} m_k \boldsymbol{u}^2, \quad E_k^{pot} := m_k e_k \left(\frac{m_k}{\alpha_k} \right), \tag{3.9}$$

and the mixture kinetic and potential energies are $\sum_k E_k^{kin}$ and $\sum_k E_k^{pot}$.

3.1.2.2 Hamilton's Stationary Action Principle

Let us now use Hamilton's SAP for the derivation of the model. We define the Lagrangian energy $\mathcal{L}_k = E_k^{kin} - E_k^{pot}$ of each phase k and a mixture Lagrangian energy $\mathcal{L} = \sum_k \mathcal{L}_k$.

Thereby, the Lagrangian associated with our system reads

$$\mathcal{L}(\alpha_1, m_1, \alpha_2, m_2, m_1^d, \rho_1^d, \boldsymbol{u}) = \underbrace{\frac{1}{2} m_1 \boldsymbol{u}^2 - m_1 e_1 \left(\frac{m_1}{\alpha_1} \right)}_{\mathcal{L}_1(\alpha_1, m_1, \boldsymbol{u})} + \underbrace{\frac{1}{2} m_2 \boldsymbol{u}^2 - m_2 e_2 \left(\frac{m_2}{\alpha_2} \right)}_{\mathcal{L}_2(\alpha_2, m_2, \boldsymbol{u})} + \underbrace{\tfrac{1}{2} m_1^d \boldsymbol{u}^2 - m_1^d e_1(\rho_1^d)}_{\mathcal{L}_1^d(m_1^d, \rho_1^d, \boldsymbol{u})}. \tag{3.10}$$

The dependency on $\rho_1^d = m_1^d / \alpha_1^d$ was added to take advantage of the constraint $D_t \rho_1^d = 0$ in the derivation with Hamilton's SAP. Hamilton's SAP provides the momentum equation by minimizing the Lagrangian's action, i.e. the integral of the Lagrangian over a space domain $\boldsymbol{\Omega_x}$ and a time interval $[0, T]$. We also note $\bar{\Omega} = \boldsymbol{\Omega_x} \times [0, T]$. This minimization takes place under the mass conservation and incompressibility constraints. Regarding the volume fraction, either α_1 or α_1^d can be considered as a free variable. This choice is equivalent here, and, for comparison purposes with the derivation of the barotropic model in the separated regime in Section 1.3.1, we choose α_1 as the free variable. The choice between the two quantities will however have its significance in the next section where capillarity is accounted for. Then, we compute the variation of the action $\mathcal{A}$ associated with the mixture's Lagrangian. It yields

$$\delta \mathcal{A} = -\int_{\bar{\Omega}} (\partial_t \boldsymbol{K} + \boldsymbol{\nabla} \cdot (\boldsymbol{K} \otimes \boldsymbol{u}) - \boldsymbol{\nabla}(\mathcal{L}^* - \alpha_1^d \partial_{\alpha_2} \mathcal{L}_2) - (\partial_{\alpha_1} \mathcal{L}_1 - \partial_{\alpha_2} \mathcal{L}_2) \boldsymbol{\nabla} \alpha_1) \cdot \boldsymbol{\eta} + \int_{\bar{\Omega}} (\partial_{\alpha_1} \mathcal{L}_1 - \partial_{\alpha_2} \mathcal{L}_2)\, \delta \alpha_1. \tag{3.11}$$

Hamilton's SAP then requires that $\delta \mathcal{A} = 0$ which leads to the following two equations

$$\begin{cases} \partial_t \boldsymbol{K} + \boldsymbol{\nabla} \cdot (\boldsymbol{K} \otimes \boldsymbol{u}) - \boldsymbol{\nabla}(\mathcal{L}_1^* + \mathcal{L}_2^* + \mathcal{L}_1^{d*} - \alpha_1^d \partial_{\alpha_2} \mathcal{L}_2) = \boldsymbol{0}, \\ \partial_{\alpha_1} \mathcal{L}_1 - \partial_{\alpha_2} \mathcal{L}_2 = 0, \end{cases} \tag{3.12}$$

where $\boldsymbol{K} = \partial_{\boldsymbol{u}} \mathcal{L}$, $\mathcal{L}_k^* = m_k (\partial_{m_k} \mathcal{L}_k) - \mathcal{L}_k$. Evaluating the partial derivatives of the mixture's Lagrangian then gives

$$\boldsymbol{K} = \rho \boldsymbol{u}, \quad \mathcal{L}_1^* = -\alpha_1 p_1, \quad \partial_{\alpha_1} \mathcal{L}_1 = p_1, \quad \mathcal{L}_1^{d,*} = 0, \quad \mathcal{L}_2^* = -\alpha_2 p_2, \quad \partial_{\alpha_2} \mathcal{L}_2 = p_2. \tag{3.13}$$

Including the mass conservation and incompressibility constraints, we obtain the two-scale Model 22.

Model 22 (Two-scale model with incompressible small-scale and at pressure equilibrium)

With $m_k = \alpha_k \rho_k$ the phase effective densities of the large-scale liquid phase $k = 1$, gaseous phase $k = 2$ and small-scale liquid phase $k = 1^d$, the mixture density $\rho = m_1 + m_2 + m_1^d$, p_k the large-scale phase pressures, α_k the volume fractions, $\boldsymbol{u}$ the mixture velocity, the flow is governed by

$$\begin{cases} \partial_t m_1 + \boldsymbol{\nabla} \cdot (m_1 \boldsymbol{u}) = 0, \\ \partial_t m_2 + \boldsymbol{\nabla} \cdot (m_2 \boldsymbol{u}) = 0, \\ \partial_t m_1^d + \boldsymbol{\nabla} \cdot (m_1^d \boldsymbol{u}) = 0, \\ \partial_t \alpha_1^d + \boldsymbol{\nabla} \cdot (\alpha_1^d \boldsymbol{u}) = 0, \\ \partial_t (\rho \boldsymbol{u}) + \boldsymbol{\nabla} \cdot (\rho \boldsymbol{u} \otimes \boldsymbol{u} + p \boldsymbol{I}) = \boldsymbol{0}, \end{cases}$$

with $p := p_1\left(\frac{m_1}{\alpha_1}\right) = p_2\left(\frac{m_1}{1-\alpha_1-1\alpha_1^d}\right)$.

Model 22 admits a supplementary conservation equation,

$$\partial_t \mathcal{H} + \boldsymbol{\nabla} \cdot ((\mathcal{H} + p)\boldsymbol{u}) = 0, \tag{3.14}$$

where the total energy $\mathcal{H} = \rho \|\boldsymbol{u}\|^2 + m_1 e_1 + m_2 e_2 + m_1^d e_1^d$ is convex with respect to $(m_1, m_2, m_1^d, \alpha_1^d, \rho\boldsymbol{u})$ and thus is a mathematical entropy. The model is also showed hyperbolic for an arbitrary direction ω, with the following eigenvalues,

$$\boldsymbol{u} \cdot \omega, \qquad \boldsymbol{u} \cdot \omega - c_W^d, \qquad \boldsymbol{u} \cdot \omega + c_W^d, \tag{3.15}$$

with the modified Wallis sound velocity,

$$(c_W^d)^2 = \frac{c_W^2}{(1-\alpha_1^d)^2}, \quad (c_W^2)^{-1} = \rho\left(\frac{\alpha_1}{\rho_1 c_1^2} + \frac{\alpha_2}{\rho_2 c_2^2}\right), \tag{3.16}$$

and $\boldsymbol{u} \cdot \omega$ of multiplicity 5.

Then, let us derive the associated model with pressure relaxation similarly to Models 3 and 4 in the separated regime. We would like to reproduce the symmetric roles of the large-scale phases with respect to the definition of the interface. Therefore, such relaxation associated with the large-scale process of pressure balancing through the large-scale interface is expected to be similarly symmetric. Therefore, we consider the large-scale volume fractions defined in (3.3) to parameter the pressure relaxation,

$$D_t \overline{\alpha}_1 = \frac{1}{\mu}(p_1 - p_2), \tag{3.17}$$

where $\mu > 0$ has the dimension of a dynamic viscosity. Remark that another relaxation process $D_t \alpha_1 = \mu^{-1}(p_1 - p_2)$ is also showed to be dissipative but does not preserve the symmetric roles of the large-scale phases with respect to the pressure balancing process. Introducing these two pressures prevents the use of the equilibrium pressure in the momentum flux. Consequently, we look for a new momentum equation that we choose to express as follows,

$$\partial_t (\rho \boldsymbol{u}) + \boldsymbol{\nabla} \cdot (\rho \boldsymbol{u} \otimes \boldsymbol{u} + \overline{p} \boldsymbol{I}) = \boldsymbol{0}, \tag{3.18}$$

where $\overline{p}$ is chosen to provide a mathematical entropy extension of Model 22 as defined by Definition 4, and such that it yields signed dissipation of the mathematical $\mathcal{H}$ which reads

$$\partial_t \mathcal{H} + \boldsymbol{\nabla} \cdot ((\mathcal{H} + \overline{p})\boldsymbol{u}) = (\overline{p} - \overline{\alpha}_1 p_1 - \overline{\alpha}_2 p_2)\boldsymbol{\nabla} \cdot \boldsymbol{u} - \mu(1-\alpha_1^d)(D_t \overline{\alpha}_1)^2. \tag{3.19}$$

Therefore, choosing $\overline{p} := \overline{\alpha}_1 p_1 + \overline{\alpha}_2 p_2$ satisfies the two conditions we stated above, and we obtain the Model 23.

Model 23 (Two-scale model with incompressible small-scale and pressure relaxation)

With $m_k = \alpha_k \rho_k$ the phase effective densities of the large-scale liquid phase $k = 1$, gaseous phase $k = 2$ and small-scale liquid phase $k = 1^d$, the mixture density $\rho = m_1 + m_2 + m_1^d$, p_k the large-scale phase pressures, α_k the volume fractions, $\overline{\alpha}_k$ the large-scale volume fractions, $\boldsymbol{u}$ the mixture velocity, the flow is governed by

$$\begin{cases} \partial_t m_k + \boldsymbol{\nabla} \cdot (m_k \boldsymbol{u}) = 0, \quad \text{for} \quad k = 1, 2, 1^d, \\ \partial_t \alpha_1^d + \boldsymbol{\nabla} \cdot (\alpha_1^d \boldsymbol{u}) = 0, \\ \partial_t (\rho \boldsymbol{u}) + \boldsymbol{\nabla} \cdot (\rho \boldsymbol{u} \otimes \boldsymbol{u} + \overline{p} \boldsymbol{I}) = \boldsymbol{0}, \\ D_t \overline{\alpha}_1 = \mu^{-1} (p_1 - p_2), \end{cases}$$

with $\overline{p} = \overline{\alpha}_1 p_1 + \overline{\alpha}_2 p_2$.

This latter model is also showed hyperbolic with, for an arbitrary direction ω, the following eigenvalues,

$$\boldsymbol{u} \cdot \omega, \qquad \boldsymbol{u} \cdot \omega - c_F^d, \qquad \boldsymbol{u} \cdot \omega + c_F^d, \qquad \text{with} \quad (c_F^d)^2 = \frac{c_F^2}{(1 - \alpha_1^d)^2}, \quad c_F^2 = Y_1 c_1^2 + Y_2 c_2^2, \tag{3.20}$$

with $\boldsymbol{u} \cdot \omega$ of multiplicity 6.

3.1.2.3 Discussion of the two-scale models

The Models 22 and 23 fulfil our first goal of proposing models that describe simultaneously separated and disperse regimes, and consequently allows a transition between these two regimes. This mixture couples the different phases with a dissipative pressure relaxation at the large scale while the large-scale phases are coupled with the small-scale one through the incompressibility constraint on its volume occupancy. Let us discuss now the consequences of such a coupling on the mathematical and physical properties of these systems, with a particular interest in their separated regime limit, when $\alpha_1^d \to 0$, and disperse regime limit, when $\alpha_1 \to 0$.

In the region where both the separated and the disperse model coexist, we assess the model hyperbolicity along with a supplementary equation of conservation for a mathematical entropy. From the hyperbolicity study, we notably observe that the presence of the small-scale increases the sound speed by a factor $(1 - \alpha_1^d)^{-1}$ in the transition region between the separated and disperse regime. This phenomenon is confined to a very thin region of the flow and only impacts the acoustics in the neighbourhood of the interface.

In the separated regime limit $\alpha_1^d \to 0$, the Models 22 and 23 formally tend towards separated Models 3 and 4 derived in Section 1.3. In the disperse limit $\alpha_1 \to 0$, both models reduce the one-velocity disperse Model 8. Note that this latter disperse regime limit is however very limited to the surrounding of the interface as the modelling of the disperse regime requires at least two independent velocities: one for the carrier phase and one for the inclusions as proposed in the Section 1.4.3

3.1.3 Two-scale modelling with capillarity

In this section, we introduce the capillarity phenomena at both scales. The objective here is twofold: first, we study how the small-scale phase impacts the large-scale capillarity modelling proposed in Section 1.3.2, second, we underline the difference of interface modelling between each scale, whether it models a separated or a disperse regime.

3.1.3.1 Interfacial area density modelling at both scales

In order to write the capillarity energies for the subsequent derivation with Hamilton's SAP, we need first to estimate the IAD at both scales.

At the large scale, the IAD estimator defined by (1.112) has lost its symmetry with respect to each of the large-scale phases because of the presence of the small-scale as depicted in Figure 3.1.2. Thus, we now use the norm of

the gradient of the large-scale fraction $\|\boldsymbol{\nabla}\overline{\alpha}_1\|$ which is showed to be a volume-based estimator of the IAD (Sethian, 1999). We end up with the mixture's internal energy ρe

$$\rho e = m_1 e_1(\rho_1) + m_2 e_2(\rho_2) + m_1^d e_1(\rho_1^d) + \sigma\|\boldsymbol{\nabla}\overline{\alpha}_1\|, \tag{3.21}$$

where σ is the capillarity coefficient.

At small-scale, we place ourselves in the same context of a polydisperse spray of incompressible liquid droplets as Model 12 and the following conservation constraints are obtained for the following small-scale geometric quantities,

$$\begin{cases} \partial_t \alpha_1^d + \boldsymbol{\nabla}\cdot(\alpha_1^d \boldsymbol{u}) = 0, \\ \partial_t \Sigma + \boldsymbol{\nabla}\cdot(\Sigma \boldsymbol{u}) = 0, \\ \partial_t(\Sigma\langle H\rangle) + \boldsymbol{\nabla}\cdot(\Sigma\langle H\rangle \boldsymbol{u}) = 0, \\ \partial_t(\Sigma\langle G\rangle) + \boldsymbol{\nabla}\cdot(\Sigma\langle G\rangle \boldsymbol{u}) = 0, \end{cases} \tag{3.22}$$

with Σ the small-scale IAD, $\Sigma\langle H\rangle$, $\Sigma\langle G\rangle$ the small-scale surface-weighted mean curvature densities. The capillarity density of energy associated with the small-scale is then $\sigma\Sigma$.

We have illustrated here the fundamental difference between the large-scale separated model and the small-scale disperse model. The interface geometry of the former is described through the field of its colour function and its derivatives, *e.g.* $\|\boldsymbol{\nabla}\overline{\alpha}_1\|$ to estimate the IAD or

$$\overline{H} := -\boldsymbol{\nabla}\cdot\left(\frac{\boldsymbol{\nabla}\overline{\alpha}_1}{\|\boldsymbol{\nabla}\overline{\alpha}_1\|}\right), \tag{3.23}$$

to estimate the large-scale mean curvature (Sethian, 1999). The geometry of the latter disperse model is locally described *via* a handful of statistical moments as showed in Chapter 2.

3.1.3.2 Derivation of the model with Hamilton's SAP

The energy of the two-scale mixture is gathered into the following Lagrangian

$$\mathcal{L} := \underbrace{\frac{1}{2}m_1\boldsymbol{u}^2 - m_1 e_1\left(\frac{m_1}{\alpha_1}\right)}_{\mathcal{L}_1} + \underbrace{\frac{1}{2}m_2\boldsymbol{u}^2 - m_2 e_2\left(\frac{m_2}{\alpha_2}\right)}_{\mathcal{L}_2} \underbrace{-\sigma\|\boldsymbol{\nabla}\overline{\alpha}_1\|}_{\mathcal{L}_{cap}} + \underbrace{\frac{1}{2}m_1^d\boldsymbol{u}^2 - m_1^d e_1\left(\rho_1^d\right) - \sigma\Sigma}_{\mathcal{L}_1^d}. \tag{3.24}$$

Then, using $\alpha_k = \overline{\alpha}_k(1-\alpha_1^d)$ for $k = 1, 2$ and $z = \Sigma/m_1^d$, we make the Lagrangian (3.24) depend only on the conserved quantities $b_c \in \{m_1, m_2, m_1^d, \alpha_1^d\}$, the advected quantities $b_a \in \{z, \rho_1^d\}$, and $\boldsymbol{u}$, $\overline{\alpha}_1$, $\overline{\alpha}_2$, $\boldsymbol{\nabla}\overline{\alpha}_1$,

$$\mathcal{L} = \mathcal{L}_1(m_1, \overline{\alpha}_1, \alpha_1^d, \boldsymbol{u}) + \mathcal{L}_2(m_2, \overline{\alpha}_1, \alpha_1^d, \boldsymbol{u}) + \mathcal{L}_{cap}(\|\boldsymbol{\nabla}\overline{\alpha}_1\|) + \mathcal{L}_1^d(m_1^d, \rho_1^d, z, \boldsymbol{u}). \tag{3.25}$$

Let us denote $\mathcal{L}_k^* := m_k\partial_{m_k}\mathcal{L}_k - \mathcal{L}_k$, for $k = 1, 2, 1^d$, $\boldsymbol{D}^T := \partial_{\boldsymbol{\nabla}\overline{\alpha}_1}\mathcal{L}_{cap}$, and $\boldsymbol{K}^T := \partial_{\boldsymbol{u}}\mathcal{L}$. The derivation of the model is very similar to the one of Model 5 Using the variation formula for constrained variables given in Section 1.2.2.2, the variation of the action reads

$$\begin{aligned} \delta\mathcal{A} = \int_\Omega - \Big\{ & \partial_t \boldsymbol{K} + \boldsymbol{\nabla}\cdot\Big[\boldsymbol{K}\otimes\boldsymbol{u} - (\mathcal{L}_1^* + \mathcal{L}_2^* + \mathcal{L}_1^{d,*} - \mathcal{L}_{cap} + \alpha_1^d\partial_{\alpha_1^d}(\mathcal{L}_1 + \mathcal{L}_2))\boldsymbol{I} - \boldsymbol{\nabla}\overline{\alpha}_1\otimes\boldsymbol{D}\Big] \\ & - (\partial_{\overline{\alpha}_1}\mathcal{L}_1 - \partial_{\overline{\alpha}_2}\mathcal{L}_2 - \boldsymbol{\nabla}\cdot\boldsymbol{D})\boldsymbol{\nabla}\overline{\alpha}_1\Big\}\cdot\boldsymbol{\eta} + \Big(\partial_{\overline{\alpha}_1}\mathcal{L}_1 - \partial_{\overline{\alpha}_2}\mathcal{L}_2 - \boldsymbol{\nabla}\cdot\boldsymbol{D}\Big)\delta\overline{\alpha}_1, \end{aligned} \tag{3.26}$$

where $\boldsymbol{I}$ is the identity matrix. Then, Hamilton's SAP, *i.e.* $\delta\mathcal{A} = 0$ for any variation of the trajectories $\boldsymbol{\eta}$ and the large-scale volume fraction $\delta\overline{\alpha}_1$, yields

$$\begin{cases} \partial_t \boldsymbol{K} + \boldsymbol{\nabla}\cdot\Big[\boldsymbol{K}\otimes\boldsymbol{u} - (\mathcal{L}_1^* + \mathcal{L}_2^* + \mathcal{L}_1^{d,*} - \mathcal{L}_{cap} + \alpha_1^d\partial_{\alpha_1^d}(\mathcal{L}_1 + \mathcal{L}_2))\boldsymbol{I} - \boldsymbol{\nabla}\overline{\alpha}_1\otimes\boldsymbol{D}\Big] = \boldsymbol{0}, \\ \partial_{\overline{\alpha}_1}\mathcal{L}_1 - \partial_{\overline{\alpha}_2}\mathcal{L}_2 - \boldsymbol{\nabla}\cdot\boldsymbol{D} = 0. \end{cases} \tag{3.27}$$

Evaluating the derivatives of Lagrangian gives

$$\begin{gathered}\boldsymbol{K}=\rho\boldsymbol{u},\quad \boldsymbol{D}=-\sigma\frac{\boldsymbol{\nabla}\overline{\alpha}_1}{\|\boldsymbol{\nabla}\overline{\alpha}_1\|},\quad \mathcal{L}_1^*=-\alpha_1 p_1,\quad \mathcal{L}_2^*=-\alpha_2 p_2,\quad \mathcal{L}_1^{d,*}=0,\\ \partial_{\alpha_1^d}\mathcal{L}_k=-\overline{\alpha}_k p_k,\quad \partial_{\overline{\alpha}_k}\mathcal{L}_k=(1-\alpha_1^d)p_k,\quad \text{for } k=1,2.\end{gathered}\tag{3.28}$$

The full model is reported in Model 24.

Model 24 (Two-scale model with capillarity and a small-scale polydisperse spray)

With $m_k=\alpha_k\rho_k$ the phase effective densities of the large-scale liquid phase $k=1$, gaseous phase $k=2$ and small-scale liquid phase $k=1^d$, $\rho=m_1+m_2+m_1^d$ the mixture density, p_k the large-scale phase pressures, $\overline{\alpha}_k$ the large-scale volume fractions, $\boldsymbol{u}$ the mixture velocity, Σ the small-scale IAD, $\Sigma\langle H\rangle$, $\Sigma\langle G\rangle$, the small-scale mean and Gauss curvatures, the flow is governed by

$$\begin{cases}\partial_t m_k & +\boldsymbol{\nabla}\cdot(m_k\boldsymbol{u}) & =0, & k=1,2,1^d,\\ \partial_t\alpha_1^d & +\boldsymbol{\nabla}\cdot(\alpha_1^d\boldsymbol{u}) & =0,\\ \partial_t\Sigma\langle X\rangle & +\boldsymbol{\nabla}\cdot(\Sigma\langle X\rangle\boldsymbol{u}) & =0, & X=1,H,G,\\ \partial_t(\rho\boldsymbol{u})+\boldsymbol{\nabla}\cdot\left(\rho\boldsymbol{u}\otimes\boldsymbol{u}+(\overline{p}-\sigma\|\boldsymbol{\nabla}\overline{\alpha}_1\|)\mathbf{I}+\sigma\frac{\boldsymbol{\nabla}\overline{\alpha}_1\otimes\boldsymbol{\nabla}\overline{\alpha}_1}{\|\boldsymbol{\nabla}\overline{\alpha}_1\|}\right)=\mathbf{0},\end{cases}$$

with $\overline{p}:=\overline{\alpha}_1 p_1\left(\frac{m_1}{\overline{\alpha}_1(1-\alpha_1^d)}\right)+\overline{\alpha}_2 p_2\left(\frac{m_2}{(1-\overline{\alpha}_1)(1-\alpha_1^d)}\right)$, and $\overline{\alpha}_1$ defined by the implicit Laplace equilibrium

$$p_1\left(\frac{m_1}{\overline{\alpha}_1(1-\alpha_1^d)}\right)-p_2\left(\frac{m_2}{(1-\overline{\alpha}_1)(1-\alpha_1^d)}\right)=\frac{\sigma}{1-\alpha_1^d}\overline{H},$$

where $\overline{H}(\boldsymbol{\nabla}\overline{\alpha}_1):=-\boldsymbol{\nabla}\cdot\left(\frac{\boldsymbol{\nabla}\overline{\alpha}_1}{\|\boldsymbol{\nabla}\overline{\alpha}_1\|}\right)$ estimates the large-scale mean curvature.

Moreover, this system admits a supplementary equation of conservation for

$$\mathcal{H}=\frac{1}{2}\rho\boldsymbol{u}^2+m_1e_1+m_2e_2+\sigma\|\boldsymbol{\nabla}\overline{\alpha}_1\|+m_1^de_1^d+\sigma\Sigma,\tag{3.29}$$

that reads

$$\partial_t\mathcal{H}+\boldsymbol{\nabla}\cdot\left(\mathcal{H}\boldsymbol{u}+(\overline{p}-\sigma\|\boldsymbol{\nabla}\overline{\alpha}_1\|)\boldsymbol{u}-\sigma\frac{\boldsymbol{\nabla}\overline{\alpha}_1}{\|\boldsymbol{\nabla}\overline{\alpha}_1\|}D_t\overline{\alpha}_1\right)=0,\tag{3.30}$$

where the material time derivative $D_t\overline{\alpha}_1$ in the flux is implicitly obtained for smooth solutions by taking the time material of the Laplace equilibrium (1.119) similarly to the capillarity Model 5 obtained for the separated regime. A similar supplementary equation as (3.30) has been obtained in Cordesse (2020) and is compatible with the ones of Perigaud and Saurel (2005); Schmidmayer et al. (2017) where a constraint $D_tc=0$ was considered on the colour function c (here $c=\overline{\alpha}_1$ is not constrained).

We similarly introduce a relaxation dynamics using the large-scale volume fraction,

$$\partial_t\overline{\alpha}_1+\boldsymbol{u}\cdot\boldsymbol{\nabla}\overline{\alpha}_1=R_{\overline{\alpha}_1},\tag{3.31}$$

where $R_{\overline{\alpha}_1}$ is an unclosed source term. Considering this dynamics for $\overline{\alpha}_1$ along with the Model 24, we write the mathematical entropy production rate ς associated with $\mathcal{H}$ (see details in Appendix 3.A)

$$\varsigma:=\partial_t\mathcal{H}+\boldsymbol{\nabla}\cdot\mathcal{G}=\left[(1-\alpha_1^d)(p_1-p_2)-\sigma\overline{H}\right]R_{\overline{\alpha}_1},\tag{3.32}$$

with the flux $\mathcal{G}=\mathcal{H}\boldsymbol{u}+\mathbf{P}\boldsymbol{u}-\sigma\frac{\boldsymbol{\nabla}\overline{\alpha}_1}{\|\boldsymbol{\nabla}\overline{\alpha}_1\|}R_{\overline{\alpha}_1}$ and $\mathbf{P}=(\overline{\alpha}_1p_1+\overline{\alpha}_2p_2-\sigma\|\boldsymbol{\nabla}\overline{\alpha}_1\|)\mathbf{I}+\sigma\frac{\boldsymbol{\nabla}\overline{\alpha}_1\otimes\boldsymbol{\nabla}\overline{\alpha}_1}{\|\boldsymbol{\nabla}\overline{\alpha}_1\|}$. The dissipation of the system is then ensured when $\varsigma\leq 0$. We propose now to consider a dissipative process with a pressure relaxation

source term that relaxes towards the Laplace equilibrium

$$\partial_t \overline{\alpha}_1 + \boldsymbol{u} \cdot \boldsymbol{\nabla} \overline{\alpha}_1 = \mu^{-1} \left(p_1 - p_2 - \frac{\sigma}{1-\alpha_1^d} \overline{H} \right), \tag{3.33}$$

where μ has the dimension of a viscosity. The equilibrium (1.119) is formally recovered for the instantaneous limit case when $\mu \to 0$. With such dynamics for $\overline{\alpha}_1$, we obtain the Model 25.

Model 25 (Two-scale model with capillarity, pressure relaxation and a small-scale polydisperse spray)

With $m_k = \alpha_k \rho_k$ the phase effective densities of the large-scale liquid phase $k = 1$, gaseous phase $k = 2$ and small-scale liquid phase $k = 1^d$, the mixture density $\rho = m_1 + m_2 + m_1^d$, p_k the large-scale phase pressures, α_k the volume fractions, $\boldsymbol{u}$ the mixture velocity, Σ the small-scale IAD, $\Sigma \langle H \rangle$, $\Sigma \langle G \rangle$, the small-scale mean and Gauss curvatures, the fluid flow is governed by

$$\begin{cases} \partial_t m_k & + \boldsymbol{\nabla} \cdot (m_k \boldsymbol{u}) & = 0, & k = 1, 2, 1^d, \\ \partial_t \alpha_1^d & + \boldsymbol{\nabla} \cdot (\alpha_1^d \boldsymbol{u}) & = 0, & \\ \partial_t \Sigma \langle X \rangle & + \boldsymbol{\nabla} \cdot (\Sigma \langle X \rangle \boldsymbol{u}) & = 0, & X = 1, H, G, \\ \partial_t \overline{\alpha}_1 + \boldsymbol{u} \cdot \boldsymbol{\nabla} \overline{\alpha}_1 = \mu^{-1} \left(p_1 - p_2 - \frac{\sigma}{1-\alpha_1^d} \overline{H} \right), & & & \\ \partial_t (\rho \boldsymbol{u}) + \boldsymbol{\nabla} \cdot \left(\rho \boldsymbol{u} \otimes \boldsymbol{u} + (\overline{p} - \sigma \| \boldsymbol{\nabla} \overline{\alpha}_1 \|) \mathbf{I} + \sigma \frac{\boldsymbol{\nabla} \overline{\alpha}_1 \otimes \boldsymbol{\nabla} \overline{\alpha}_1}{\| \boldsymbol{\nabla} \overline{\alpha}_1 \|} \right) = \mathbf{0}. & & & \end{cases}$$

Model 25 is dissipative in the sense that, following (3.32), we have a negative mathematical entropy production rate

$$\varsigma = -\mu^{-1} (1 - \alpha_1^d) \left(p_1 - p_2 - \frac{\sigma}{1-\alpha_1^d} \overline{H} \right)^2 \leq 0. \tag{3.34}$$

Remark that, with the relaxation (3.33), the entropy flux $\mathcal{G}$ in (3.32) is now explicit.

3.1.3.3 Discussion of the two-scale models with capillarity

The equilibrium Model 24 and the relaxation Model 25 both formally extend the two-scale models derived in Section 3.1.2 by including capillarity energies. The reader is referred to the discussion therein about the behaviour of these systems in the disperse limit $\overline{\alpha}_1 \to 0$ and the separated regime limit $\alpha_1^d \to 0$. Regarding capillarity modelling, both models show that the addition of capillarity at the large-scale impacts the flow dynamics through the addition of a capillarity flux. Normalizing the large-scale volume gradients shows that this flux is proportional with the IAD estimator $\| \boldsymbol{\nabla} \overline{\alpha}_1 \|$ and consequently impacts the flow at the location of the large-scale diffuse interface. However, the capillarity at small-scale does not impact the flow as it is passively advected by the flow. The coupling with the flow will be described in the following section.

Regarding the hyperbolicity of Model 25, it is studied through an augmented system, where $\overline{w} = \boldsymbol{\nabla} \overline{\alpha}_1$ is added as an independent quantity following the same line as Appendix 1.A. Let us now note $u_\omega := \boldsymbol{u} \cdot \boldsymbol{\omega}$, $\boldsymbol{n} := \boldsymbol{\nabla} \overline{\alpha}_1 / \| \boldsymbol{\nabla} \overline{\alpha}_1 \|$, $\psi = \sigma \| \boldsymbol{\nabla} \overline{\alpha}_1 \| / (\rho (c_F^d)^2)$, c_F^d, the velocity, a geometrical-physical parameter and the two-scale frozen sound speed as established in (3.20). By replacing α_1 with $\overline{\alpha}_1$ in Model 5, the properties of such a system are then identical. In the diffuse interface with moderate capillarity effects in comparison with acoustics, *i.e.* $\psi \ll 1$, we have the following eigenvalues in the direction ω,

$$u_\omega, \qquad u_\omega \pm c_F^d (1 - (\boldsymbol{\omega} \cdot \boldsymbol{n})^2) \sqrt{\psi}, \qquad u_\omega \pm c_F^d \left(1 + \frac{1}{2} \psi (\boldsymbol{\omega} \cdot \boldsymbol{n})^2 (1 - (\boldsymbol{\omega} \cdot \boldsymbol{n})^2) \right). \tag{3.35}$$

These eigenvalues illustrate the impact of the small-scale on the model which modifies the eigenvalues at two levels : by increasing the Frozen velocities, and through the estimation of large-scale interface normal and IAD with the colour function $\overline{\alpha}_1$. Let us note that the system is weakly hyperbolic as the separated Model 5.

Conclusion of Section 3.1

We have constructed in this section a framework for the unified modelling approach through the splitting of the liquid volume fraction into a large-scale volume fraction $\overline{\alpha}_1$ and a small-scale volume fraction α_1^d. Moreover, we have added the modelling of capillarity at both scales of modelling using different IAD estimators: $\|\boldsymbol{\nabla}\overline{\alpha}_1\|$ at large scale and $\boldsymbol{\Sigma}$ at small scale. While the first estimator is based on the implicit representation of surfaces with level-set (Sethian, 1999), the second is obtained from GeoMOM (see Section 2.2) where the IAD is a statistical moment of the spray distribution. All these two-scale models are showed hyperbolic and admit supplementary equations on energy.

With this framework, we propose in the next Section 3.2 to further couple each scales through the addition of inter-scale source terms. Moreover, some more advanced small-scale models of Chapter 2 are introduced in the two-scale unified approach to use the inter-scale transfer as a primary break-up model. Then, in Section 3.3 a length-scale threshold will be introduced to define an interface scale separation.

3.2 Two-scale coupling via inter-scale mass exchanges

In the previous section, two-scale models have been proposed with good properties when the two regimes are coexisting, thus allowing a progressive transition from the separated regime to the disperse regime.

In this section, we focus on the modelling of this transition through the addition of source terms allowing a transfer of mass and momentum between the scales. Note that this inter-scale mass transfer considered here is manually introduced and does not result from a thermodynamic equilibrium. A geometric criterion is however introduced later in Section 3.3 to trigger the mass transfer through the introduction of a disequilibrium. We propose here an intermediary modelling step to emphasize the various parametrizations possible of the inter-scale transfer in a simpler framework. We notably illustrate how it can be used to model the primary break-up similarly to Devassy et al. (2015) based on experimental correlations (Pilch and Erdman, 1987; Marmottant and Villermaux, 2004). Moreover, a specific attention is dedicated to the sign study of the mathematical entropy to ensure dissipation properties and thus ensuring the fulfilment of the second principle of thermodynamics. Remark also that we consider a momentum exchange in single-velocity two-scale models, not to accelerate the small-scale inclusions as they have here the same velocity as the large scale, but to balance the energy transfer between the scales, notably when capillarity is accounted.

In this section, we gradually introduce the inter-scale mass transfer with models of increasing complexity. We start in Section 3.2.1 by adding source terms without accounting for polydispersion or capillarity to extend Model 23. Then, these exchanges terms are added with a polydisperse spray model in Section 3.2.2, extending 25. Finally, we aim at describing primary break-up with the inter-scale transfer towards small-scale model with oscillating droplets in Section 3.2.3.

3.2.1 Mass and momentum exchanges for a disperse small-scale model without capillarity

Consider again the assumptions of Models 22 and 23, namely an incompressible disperse small-scale, but we neglect the capillarity energies. We add unclosed source terms on each quantity, say of Model 23, involved in the transfer between scales

$$\begin{cases} \partial_t m_1 + \boldsymbol{\nabla}\cdot(m_1\boldsymbol{u}) = R_{m_1}, \\ \partial_t m_2 + \boldsymbol{\nabla}\cdot(m_2\boldsymbol{u}) = 0, \\ \partial_t m_1^d + \boldsymbol{\nabla}\cdot(m_1^d\boldsymbol{u}) = R_{m_1^d}, \\ \partial_t \alpha_1^d + \boldsymbol{\nabla}\cdot(\alpha_1^d\boldsymbol{u}) = R_{\alpha_1^d}, \\ \partial_t(\rho\boldsymbol{u}) + \boldsymbol{\nabla}\cdot(\rho\boldsymbol{u}\otimes\boldsymbol{u} + \overline{p}\boldsymbol{I}) = \boldsymbol{R_u}, \\ D_t\overline{\alpha}_1 = R_{\overline{\alpha}_1}, \end{cases} \tag{3.36}$$

with $\overline{p} = \overline{\alpha}_1 p_1 + \overline{\alpha}_2 p_2$. Remark immediately that liquid mass conservation and small-scale incompressibility gives us that

$$R_{m_1^d} = -R_{m_1}, \qquad R_{\alpha_1^d} = -\frac{R_{m_1}}{\rho_1^d}. \tag{3.37}$$

Then, writing the equation of evolution for the associated mathematical entropy $\mathcal{H}$ defined by (3.19) (see Appendix 3.A) yields

$$\partial_t\mathcal{H} + \boldsymbol{\nabla}\cdot((\mathcal{H}+\overline{p})\boldsymbol{u}) = -(1-\alpha_1^d)(p_1-p_2)R_{\overline{\alpha}_1} - \left(e_1^d + \frac{\overline{p}}{\rho_1^d} - e_1 - \frac{p_1}{\rho_1}\right)R_{m_1} + \boldsymbol{R_u}\cdot\boldsymbol{u}. \tag{3.38}$$

We recognize in the right-hand side the mathematical entropy production associated with a potential pressure relaxation, a mass transfer and a momentum transfer. The dissipation of the model requires a negative right-hand sign. Remark first that we can split the source term on $\overline{\alpha}_1$ into a term related to the instantaneous pressure relaxation and another source term $R^m_{\overline{\alpha}_1}$ related to the mass transfer at finite timescale and at pressure equilibrium,

$$D_t\overline{\alpha}_1 = \frac{1}{\mu}(p_1-p_2) + R^m_{\overline{\alpha}_1}. \tag{3.39}$$

The source term $R^m_{\overline{\alpha}_1}$ is then obtained by differentiating the pressure equilibrium $p_1(m_1, \overline{\alpha}_1, \alpha_1^d) = p_2(m_2, \overline{\alpha}_1, \alpha_1^d)$. After some calculations, it yields

$$R^m_{\overline{\alpha}_1} = (1-\overline{\alpha}_1)\overline{\alpha}_1 \frac{m_2\overline{\alpha}_1 c_2^2 + (1-\overline{\alpha}_1)((1-\alpha_1^d)\rho_1^d - m_1)}{\rho_1^d(1-\alpha_1^d)\left((1-\overline{\alpha}_1)^2 m_1 c_1^2 + \overline{\alpha}_1^2 m_2 c_2^2\right)} R_{m_1} =: \mathcal{K} R_{m_1}. \tag{3.40}$$

With the pressure equilibrium satisfied during the mass transfer, this yields the following mathematical entropy production

$$\partial_t \mathcal{H} + \boldsymbol{\nabla}\cdot((\mathcal{H}+\overline{p})\boldsymbol{u}) = -\mu^{-1}(1-\alpha_1^d)(p_1-p_2)^2 - \left(e_1^d + \frac{\overline{p}}{\rho_1^d} - e_1 - \frac{p_1}{\rho_1}\right) R_{m_1} + \boldsymbol{R_u}\cdot\boldsymbol{u}. \tag{3.41}$$

Then, the term in factor of the mass source term can be identified as a chemical potential difference and accounts for the thermodynamic disequilibrium between the large-scale and small-scale liquid phase. In the context of liquid phases, this disequilibrium is expected to be small and can be compensated by choosing an appropriate momentum source term such that

$$\boldsymbol{R_u}\cdot\boldsymbol{u} = \left(e_1^d + \frac{\overline{p}}{\rho_1^d} - e_1 - \frac{p_1}{\rho_1}\right) R_{m_1}. \tag{3.42}$$

Remark that such a relation cannot be satisfied if there is both a thermodynamic disequilibrium and a null velocity amplitude. Moreover, this compensation process is only required to ensure the dissipation of the system when

$$-\left(e_1^d + \frac{\overline{p}}{\rho_1^d} - e_1 - \frac{p_1}{\rho_1}\right) R_{m_1} > 0, \qquad \Longleftrightarrow \qquad e_1^d + \frac{\overline{p}}{\rho_1^d} > e_1 + \frac{p_1}{\rho_1}. \tag{3.43}$$

We denote this conditions as

$$C_1 : \left(e_1^d + \frac{\overline{p}}{\rho_1^d} > e_1 + \frac{p_1}{\rho_1}\right). \tag{3.44}$$

Then, the source terms must satisfy

$$R_{m_1} = R_{m_1,1}(1 - \mathbb{1}_{C_1}) + R_{m_1,2}\|\boldsymbol{u}\|^2 \mathbb{1}_{C_1}, \qquad \boldsymbol{R_u} = R_{m_1,2}\left(e_1^d + \frac{\overline{p}}{\rho_1^d} - e_1 - \frac{p_1}{\rho_1}\right)\boldsymbol{u}\,\mathbb{1}_{C_1}, \tag{3.45}$$

with the mass transfer rates $R_{m_1,1}$ and $R_{m_1,2}$ are yet to be determined, but must keep $m_1 > 0$. They may include experimental heuristics or geometric criteria to provide the right timescale for the transfer process or locate the transfer given supplementary conditions such as a high large-scale curvature to detect the growth of filaments. A simple heuristic closure would be $R_{m_1,1} = -\tau^{-1} m_1$ and $R_{m_1,2} = -l^{-1} m_1$ where τ and l are characteristic time and length which provide an exponential decay of the large-scale phase density and can be chosen to mimic an actual primary break-up process. Remark that the momentum transfer does not represent a clear physical mechanism, but compensates the small disequilibrium between the large-scale and small-scale liquid densities. We summarize the overall system in Model 26.

Model 26 (Two-scale model with incompressible small-scale and inter-scale transfer)

With $m_k = \alpha_k \rho_k$ the phase effective densities of the large-scale liquid phase $k = 1$, gaseous phase $k = 2$ and small-scale liquid phase $k = 1^d$, the mixture density $\rho = m_1 + m_2 + m_1^d$, p_k the large-scale phase pressures, α_k the volume fractions, $\boldsymbol{u}$ the mixture velocity, the flow is governed by

$$\begin{cases} \partial_t m_2 + \boldsymbol{\nabla} \cdot (m_2 \boldsymbol{u}) = 0, \\ \partial_t m_1 + \boldsymbol{\nabla} \cdot (m_1 \boldsymbol{u}) = R_{m_1}, \\ \partial_t m_1^d + \boldsymbol{\nabla} \cdot (m_1^d \boldsymbol{u}) = -R_{m_1}, \\ \partial_t \alpha_1^d + \boldsymbol{\nabla} \cdot (\alpha_1^d \boldsymbol{u}) = -\frac{R_{m_1}}{\rho_1^d}, \\ \partial_t (\rho \boldsymbol{u}) + \boldsymbol{\nabla} \cdot (\rho \boldsymbol{u} \otimes \boldsymbol{u} + \overline{p} \boldsymbol{I}) = \boldsymbol{R_u}, \\ D_t \overline{\alpha}_1 = \mu^{-1}(p_1 - p_2) + \mathcal{K} R_{m_1}, \end{cases}$$

with

$$R_{m_1} = R_{m_1,1}(1 - \mathbb{1}_{C_1}) + R_{m_1,2} \|\boldsymbol{u}\|^2 \mathbb{1}_{C_1}, \qquad \boldsymbol{R_u} = R_{m_1,2} \left(e_1^d + \frac{\overline{p}}{\rho_1^d} - e_1 - \frac{p_1}{\rho_1} \right) \boldsymbol{u} \mathbb{1}_{C_1},$$

$$\overline{p} = \overline{\alpha}_1 p_1 + \overline{\alpha}_2 p_2,$$

and C_1 defined by (3.44), $\mathcal{K}$ defined in (3.40).

With such choice of source terms, (3.38) ensures the second principle of thermodynamics. The hyperbolicity properties are not affected by the source terms, therefore, Model 26 is hyperbolic as Model 23.

3.2.2 Mass and momentum exchange accounting for small-scale capillarity and polydispersion

Let us now account for the small-scale capillarity. The combination of inter-scale transfer and capillarity modelling at both scale is treated in the next Section 3.3. We consider the same set of equation but add source terms for all quantities at stake for the inter-scale mass transfer, namely Σ, $\Sigma \langle H \rangle$, $\Sigma \langle G \rangle$,

$$\begin{cases} \partial_t m_2 + \boldsymbol{\nabla} \cdot (m_2 \boldsymbol{u}) = 0, \\ \partial_t m_1 + \boldsymbol{\nabla} \cdot (m_1 \boldsymbol{u}) = R_{m_1}, \\ \partial_t m_1^d + \boldsymbol{\nabla} \cdot (m_1^d \boldsymbol{u}) = R_{m_1^d}, \\ \partial_t \alpha_1^d + \boldsymbol{\nabla} \cdot (\alpha_1^d \boldsymbol{u}) = R_{\alpha_1^d}, \\ \partial_t \Sigma \langle X \rangle + \boldsymbol{\nabla} \cdot (\Sigma \langle X \rangle \boldsymbol{u}) = R_X, \qquad X = 1, H, G, \\ \partial_t \overline{\alpha}_1 + \boldsymbol{u} \cdot \boldsymbol{\nabla} \overline{\alpha}_1 = \mu^{-1} (p_1 - p_2), \\ \partial_t (\rho \boldsymbol{u}) + \boldsymbol{\nabla} \cdot (\rho \boldsymbol{u} \otimes \boldsymbol{u} + \overline{p} \mathbf{I}) = \boldsymbol{R_u}, \end{cases} \tag{3.46}$$

with $\mu > 0$ and $\overline{p} = \overline{\alpha}_1 p_1 + \overline{\alpha}_2 p_2$. First, the liquid mass conservation similarly gives $R_{m_1^d} = -R_{m_1}$. For all the other quantities related to the spray, we reconsider the underlying kinetic equation with a source term $R_n(S)$,

$$\partial_t n_S(\widehat{S}) + \boldsymbol{\nabla} \cdot (n_S(\widehat{S}) \boldsymbol{u}) = R_n(\widehat{S}), \tag{3.47}$$

such that the source terms on the surface-averaged geometry of the spray is obtained by integrating the equation above,

$$R_{\Sigma\langle X \rangle} = \int_{\widehat{S}} \widehat{S}\widetilde{X}(\widehat{S}) R_n(\widehat{S}) \, d\widehat{S} =: (S\widetilde{X})_{avg} \int_{\widehat{S}} R_n(\widehat{S}) \, d\widehat{S}, \tag{3.48}$$

with $\widetilde{(\cdot)}$ the surface averaging operator defined in Definition 11. For the sphere, we have $\widetilde{H}(\widehat{S}) = (4\pi/\widehat{S})^{1/2}$ and $\widetilde{G}(\widehat{S}) = 4\pi/\widehat{S}$ and S_{avg}, $(S\widetilde{H})_{avg}$ and $(S\widetilde{G})_{avg} = 4\pi$ which characterize the averaged geometric characteristics of the

droplets created at small-scale. Similarly, from small-scale incompressibility, we have that

$$R_{m_1^d} = \int_{\widehat{S}} m(\widehat{S}) R_n(\widehat{S}) =: m_{avg} \int_{\widehat{S}} R_n(\widehat{S})\, d\widehat{S}. \tag{3.49}$$

It yields the following relations,

$$R_\Sigma = -\frac{S_{avg}}{m_{avg}} R_{m_1}, \quad R_{\Sigma\langle H\rangle} = -\frac{(S\widetilde{H})_{avg}}{m_{avg}} R_{m_1}, \quad R_{\Sigma\langle G\rangle} = -\frac{4\pi}{m_{avg}} R_{m_1}, \quad R_{\alpha_1^d} = -\frac{R_{m_1}}{\rho_1^d}. \tag{3.50}$$

Only the source term related to the IAD impacts the mathematical entropy production. Indeed, we show in Appendix 3.A that the mathematical entropy production rate ς associated with the supplementary equation obtained in (3.30) for the total energy $\mathcal{H}$ now reads

$$\varsigma := -((1-\alpha_1^d)(p_1-p_2) - \sigma\overline{H})(R^{relax}_{\overline{\alpha}_1} + R^{mass}_{\overline{\alpha}_1}) - \left(e_1(\rho_1^d) + \frac{\overline{p}}{\rho_1^d} - \left(e_1(\rho_1) + \frac{p_1}{\rho_1}\right) + \sigma\frac{S_{avg}}{m_{avg}}\right) R_{m_1} + \boldsymbol{u}\cdot\boldsymbol{R_u}, \tag{3.51}$$

where we split the source term on large-scale volume fraction between the instantaneous relaxation process and the inter-scale mass transfer. The large-scale pressure relaxation now accounts for the local Laplace pressure jump, and we choose

$$R^{relax}_{\overline{\alpha}_1} = \frac{1}{\mu}(p_1 - p_2). \tag{3.52}$$

The inter-scale source term accounting for large-scale volume fraction is chosen similarly as (3.40) in order to preserve $p_1 - p_2$ constant. The mathematical entropy production is negatively in the same way such that we obtain the following Model 27.

Model 27 (Two-scale capillarity model with incompressible small-scale and inter-scale transfer)

With $m_k = \alpha_k\rho_k$ the phase effective densities of the large-scale liquid phase $k=1$, gaseous phase $k=2$ and small-scale liquid phase $k=1^d$, the mixture density $\rho = m_1 + m_2 + m_1^d$, p_k the large-scale phase pressures, α_k the volume fractions, $\boldsymbol{u}$ the mixture velocity, σ the capillarity coefficient, Σ the IAD, $\Sigma\langle H\rangle$, $\Sigma\langle G\rangle$ the surface-weighted mean curvature densities, the flow is governed by

$$\begin{cases}
\partial_t m_2 + \boldsymbol{\nabla}\cdot(m_2\boldsymbol{u}) = 0,\\
\partial_t m_1 + \boldsymbol{\nabla}\cdot(m_1\boldsymbol{u}) = R_{m_1},\\
\partial_t m_1^d + \boldsymbol{\nabla}\cdot(m_1^d\boldsymbol{u}) = -R_{m_1},\\
\partial_t \alpha_1^d + \boldsymbol{\nabla}\cdot(\alpha_1^d\boldsymbol{u}) = -\frac{R_{m_1}}{\rho_1^d},\\
\partial_t \Sigma\langle X\rangle + \boldsymbol{\nabla}\cdot(\Sigma\langle X\rangle\boldsymbol{u}) = -\frac{(S\widetilde{X})_{avg}}{m_{avg}} R_{m_1}, \qquad X = 1, H, G,\\
\partial_t\overline{\alpha}_1 + \boldsymbol{u}\boldsymbol{\nabla}\overline{\alpha}_1 = \mu^{-1}(p_1 - p_2) + \mathcal{K}R_{m_1},\\
\partial_t(\rho\boldsymbol{u}) + \boldsymbol{\nabla}\cdot(\rho\boldsymbol{u}\otimes\boldsymbol{u} + \overline{p}\mathbf{I}) = \boldsymbol{R_u},
\end{cases}$$

with $\mu > 0$, $\overline{p} = \overline{\alpha}_1 p_1 + \overline{\alpha}_2 p_2$, $\mathcal{K}$ defined by (3.40), and the source terms read

$$R_{m_1} = R_{m_1,1}(1 - \mathbb{1}_{C_1}) + R_{m_1,2}\|\boldsymbol{u}\|^2\mathbb{1}_{C_1}, \qquad \boldsymbol{R_u} = R_{m_1,2}\left(e_1^d + \frac{\overline{p}}{\rho_1^d} + \sigma\frac{S_{avg}}{m_{avg}} - e_1 - \frac{p_1}{\rho_1}\right)\boldsymbol{u},$$

with $R_{m_1,1}$ and $R_{m_1,2}$ unclosed and

$$C_1 : \left(e_1^d + \frac{\overline{p}}{\rho_1^d} + \sigma\frac{S_{avg}}{m_{avg}} > e_1 + \frac{p_1}{\rho_1}\right).$$

Remark here that the additional geometric quantities used to characterize the underlying spray do not interact with the transfer process except for Σ, which is associated with the capillarity energy. Such a polydisperse structure offers more possibilities to use experimental or heuristics (see for instance Marmottant and Villermaux (2004)) in the inter-scale transfer as a model of primary break-up. For instance, the three parameters of the source terms m_{avg}, S_{avg} and $(S\widetilde{H})_{avg}$ can be specifically chosen to create two sizes of droplets S_1 and S_2 with a given proportion p associated with a kinetic source term,

$$R_n(\widehat{S}) = p\delta(\widehat{S} - S_1) + (1-p)\delta(\widehat{S} - S_2). \tag{3.53}$$

These parameters are related through

$$m_{avg} = pm(S_1) + (1-p)m(S_2), \qquad S_{avg} = \frac{pS_1 + (1-p)S_2}{pm(S_1) + (1-p)m(S_2)}, \qquad (S\widetilde{H})_{avg} = \frac{pS_1\widetilde{H}(S_1) + (1-p)S_2\widetilde{H}(S_2)}{pm(S_1) + (1-p)m(S_2)},$$

with $\widetilde{H}(\widehat{S}) = (4\pi/\widehat{S})^{1/2}$ and $m(\widehat{S}) = \rho_1^d(4\pi/3)(\widehat{S}/(4\pi))^{3/2}$. Then the sizes S_1 and S_2 of the droplets produced by the inter-scale transfer can be chosen either using the flow parameters or large-scale interface geometry such as its local mean-curvature $\overline{H}(\boldsymbol{\nabla}\overline{\alpha}_1)$. Remark that any distribution characterized by at most three parameters can be used in this modelling approach.

3.2.3 Inter-scale transfer with a polydisperse spray of oscillating droplets

In this section, we provide an additional example of inter-scale transfer that takes advantage of an enhanced description of the small scale with more geometric quantities and demonstrates the modelling capabilities of the primary break-up. We particularly consider the context of a two-scale model where capillarity is only accounted for at the small-scale with an oscillating spray. Such a model is physically relevant for atomization setup with regions dominated by inertial forces, and other regions, particularly for interface small scales, where capillarity forces are not negligible any more.

Such models are derived by combining the Lagrangian of the two-scale Model 23 with the asynchronous oscillation Model 19. We get the Model 28.

Model 28 (Two-scale model with a small-scale polydisperse spray of oscillating droplets)

With $m_k = \alpha_k\rho_k$ and α_k the phase densities and volume fractions of phases $k = 2, 1^d$, $\rho = m_1 + m_2$ the mixture's density, $\boldsymbol{u}$ the velocity and $p_2(\rho_2)$ the pressure of the gaseous phase 2, $\Sigma = \Sigma_0 + \Delta\Sigma$, the IAD decomposed in a static part and an oscillation-related part, the static-related parts of the surface-averaged density of the mean and Gauss curvatures $\Sigma\langle H\rangle_0$ and $\Sigma\langle G\rangle$,

$$\begin{cases} \partial_t m_k + \boldsymbol{\nabla}\cdot(m_k\boldsymbol{u}) = 0, & k = 1, 2, 1^d, \\ \partial_t \alpha_1^d + \boldsymbol{\nabla}\cdot(\alpha_1^d\boldsymbol{u}) = 0, \\ \partial_t \Sigma_0 + \boldsymbol{\nabla}\cdot(\Sigma_0\boldsymbol{u}) = 0, \\ \partial_t(\Delta\Sigma) + \boldsymbol{\nabla}\cdot(\Delta\Sigma\boldsymbol{u}) = 0, \\ \partial_t(\Sigma\langle G\rangle) + \boldsymbol{\nabla}\cdot(\Sigma\langle G\rangle\boldsymbol{u}) = 0, \\ \partial_t(\Sigma\langle H\rangle_0) + \boldsymbol{\nabla}\cdot(\Sigma\langle H\rangle_0\boldsymbol{u}) = 0, \\ \partial_t\overline{\alpha}_1 + \boldsymbol{u}\cdot\boldsymbol{\nabla}\overline{\alpha} = -\frac{1}{\mu}(p_1 - p_2), \\ \partial_t(\rho\boldsymbol{u}) + \boldsymbol{\nabla}\cdot(\rho\boldsymbol{u}\otimes\boldsymbol{u} + \overline{p}\boldsymbol{I}) = \boldsymbol{0}. \end{cases}$$

This model admits a supplementary equation of conservation on the energy

$$\mathcal{H} = \frac{1}{2}\rho\|\boldsymbol{u}\|^2 + m_2 e_2\left(\frac{m_2}{1-\alpha_1^d}\right) + m_1^d e_1(\rho_1^d) + \sigma\Sigma_0\left(1 + \frac{c}{5}\right), \tag{3.54}$$

with $c = 10\Delta\Sigma/\Sigma_0$ introduced in Section 2.2.4.2 measuring the "intensity" of the oscillation motion. When $c = 1$ the droplets break up. Its equation simply reads $D_t c = 0$.

Let us now consider an inter-scale mass and energy transfer trough source terms for the oscillation motion of the droplets. We denote R_X the source terms of the equation on quantities $X \in \{m_1, m_1^d, \alpha_1^d, \Sigma_0, \Delta\Sigma, \Sigma\langle G\rangle, \Sigma\langle H\rangle_0, \rho\boldsymbol{u}\}$. Then the conservation of the liquid mass and the incompressibility still gives

$$R_{m_1^d} = -R_{m_1}, \qquad R_{\alpha_1^d} = -\frac{R_{m_1}}{\rho_1^d}.$$

Similarly to Section 3.2.1, we introduce a source term in the underlying PBE (2.119) that now reads

$$\partial_t n_\xi + \boldsymbol{\nabla}_{\boldsymbol{x}} \cdot (n_\xi \boldsymbol{u}) + \partial_{\widehat{\chi}}(\dot{\widehat{\chi}} n_\xi) + \partial_{\widehat{\dot{\chi}}}(-\tilde{\omega}^2 \widehat{S}_0^{-3/2} \widehat{\chi} n_\xi) = R_\xi(\widehat{S_0}, \widehat{\chi}, \widehat{\dot{\chi}}), \tag{3.55}$$

and the source terms for geometric quantities related to the surface S_0 are derived according to the relations between moments and geometric quantities (2.126) and (2.127), it yields

$$R_{\Sigma_0} = -\frac{S_{0,avg}}{m_{avg}} R_{m_1}, \quad R_{\Sigma\langle H\rangle_0} = -\frac{(S\widetilde{H})_{0,avg}}{m_{avg}} R_{m_1}, \quad R_{\Sigma\langle G\rangle} = -\frac{4\pi}{m_{avg}} R_{m_1}, \quad R_{\alpha_1^d} = -\frac{R_{m_1}}{\rho_1^d}. \tag{3.56}$$

The source term $R_{\Delta\Sigma}$ can be decomposed in two contributions: a creation term arising from the mass transfer $R_{\Delta\Sigma,m}$ and a viscous damping $R_{\Delta\Sigma,v}$ as in Model 19. As $\Delta\Sigma = 4\pi M_{1,2,0}$, the creation source term then read

$$R_{\Delta\Sigma,m} = \int_\xi \widetilde{S_0}\widetilde{\chi}^2 R_\xi(\widehat{S_0}, \widehat{\chi}, \widehat{\dot{\chi}}). \tag{3.57}$$

Let us then assume that :

- the droplets are created at a fraction q of their maximal amplitude. (H3e)

Given the definitions of Section 2.2.4.1, that $\chi_{max}(S_0) = 2/\sqrt{5}$, such that the assumption translates as

$$R_{\Delta\Sigma,m} = \frac{4}{5} q^2 R_{\Sigma_0} = -\frac{4}{5} q^2 \frac{S_{0,avg}}{m_{avg}} R_{m_1}. \tag{3.58}$$

The source terms $R_{\overline{\alpha}_1}$ $R_{\Delta\Sigma,v}$ R_{m_1} and $\boldsymbol{R_u}$ are left unconstrained for now. Now, the "mathematical entropy" dissipation rate ς associated with the energy $\mathcal{H}$ gives

$$\varsigma = -(1-\alpha_1^d)(p_1 - p_2) R_{\overline{\alpha}_1} + 2\sigma R_{\Delta\Sigma,v} - \left(e_1(\rho_1^d) + \frac{\overline{p}}{\rho_1^d} - \left(e_1(\rho_1) + \frac{p_1}{\rho_1} \right) + \sigma\left(1 + \frac{8}{5} q^2\right) \left(\frac{S_{avg}}{m_{avg}} \right) \right) R_{m_1} + \boldsymbol{u} \cdot \boldsymbol{R_u}. \tag{3.59}$$

We sign the two first terms, respectively the pressure relaxation and the viscous damping of the oscillation, with

$$R_{\overline{\alpha}_1} = -\frac{1}{\mu}(p_1 - p_2), \qquad R_{\Delta\Sigma,v} = -\tau^{-1}\Delta\Sigma, \tag{3.60}$$

and $\mu, \tau > 0$ a dynamic viscosity and a damping timescale. Finally, we obtain a dissipation rate similar to Model 27 that we close similarly to get Model 29.

Model 29 (Two-scale model with inter-scale transfer with a small-scale polydisperse spray of oscillating droplets)

With $m_k = \alpha_k \rho_k$ and α_k the phase densities and volume fractions of phases $k = 2, 1^d$, $\rho = m_1 + m_2$ the mixture's density, $\boldsymbol{u}$ the velocity and $p_2(\rho_2)$ the pressure of the gaseous phase 2, $\Sigma = \Sigma_0 + \Delta\Sigma$ the IAD decomposed in a static part and an oscillation-related part, the static-related parts of the surface-averaged density of the mean and Gauss curvatures $\Sigma \langle H \rangle_0$ and $\Sigma \langle G \rangle$, the flow is governed by

$$\begin{cases} \partial_t m_2 & +\boldsymbol{\nabla} \cdot (m_2 \boldsymbol{u}) & = 0, \\ \partial_t m_1 & +\boldsymbol{\nabla} \cdot (m_1 \boldsymbol{u}) & = R_{m_1}, \\ \partial_t m_1^d & +\boldsymbol{\nabla} \cdot (m_1^d \boldsymbol{u}) & = -R_{m_1}, \\ \partial_t \alpha_1^d & +\boldsymbol{\nabla} \cdot (\alpha_1^d \boldsymbol{u}) & = -\frac{R_{m_1}}{\rho_1^d}, \\ \partial_t \Sigma \langle X \rangle_0 & +\boldsymbol{\nabla} \cdot (\Sigma \langle X \rangle_0 \boldsymbol{u}) & = -\frac{(SX)_{0,avg}}{m_{avg}} R_{m_1}, \qquad X = 1, H, G \\ \partial_t (\Delta\Sigma) & + \boldsymbol{\nabla} \cdot (\Delta\Sigma \boldsymbol{u}) & = -\tau^{-1} \Delta\Sigma - \frac{4}{5} q^2 \frac{S_{0,avg}}{m_{avg}} R_{m_1}, \\ \partial_t \overline{\alpha}_1 & + \boldsymbol{u} \cdot \boldsymbol{\nabla} \overline{\alpha} & = -\frac{1}{\mu}(p_1 - p_2), \\ \partial_t (\rho \boldsymbol{u}) & + \boldsymbol{\nabla} \cdot (\rho \boldsymbol{u} \otimes \boldsymbol{u} + \overline{p} \boldsymbol{I}) & = \boldsymbol{R_u}, \end{cases}$$

with $\overline{p} = \overline{\alpha}_1 p_1 + \overline{\alpha}_2 p_2$, and the source terms

$$R_{m_1} = R_{m_1,1}(1 - \mathbb{1}_{C_1}) + R_{m_1,2} \|\boldsymbol{u}\| \mathbb{1}_{C_1}, \qquad \boldsymbol{R_u} = R_{m_1,2} \left(e_1^d + \frac{\overline{p}}{\rho_1^d} + \sigma(1 + \frac{8}{5} q^2) \frac{S_{avg}}{m_{avg}} - e_1 - \frac{p_1}{\rho_1} \right) \boldsymbol{u},$$

with $R_{m_1,1}$ and $R_{m_1,2}$ unclosed and

$$C_1 : \left(e_1^d + \frac{\overline{p}}{\rho_1^d} + \sigma(1 + \frac{8}{5} q^2) \frac{S_{avg}}{m_{avg}} > e_1 + \frac{p_1}{\rho_1} \right).$$

This model allows an extended modelling of the mechanism of the primary breakup with the additional parameter q. Depending on the flow conditions, one can either create static inclusions by setting $q = 0$ or deformed inclusion on the verge of breaking up a second time by choosing $q = 1$. This initial deformation influences the dynamics of the inclusions right after the break-up. Depending on the oscillation pulsation, the damping timescale and additional source terms such as velocity drag, the initial deformation can either lead to a secondary break-up or not. The combination with two-velocity models like the ones in Section 1.4.3 is not proposed in this work and is left for a further study.

This model shows a similar structure with the model of Vallet et al. (2001) with a conservative structure and both "creation and destruction" terms which have here rather the interpretation of a creation and a dissipation.

Conclusion of Section 3.2

In this section, we have demonstrated how we can couple the scales with each other through a mass transfer while preserving a dissipative structure.

Three models of inter-scale mass transfer of increasing complexity have been proposed to emphasize the parametrization possibilities. In the first Model 26, the small-scale model is only described through its volume fraction and no information on the size of the produced droplets can be set up. The second Model 27 then includes a model of polydisperse droplets such that three parameters are then added to the tuning of the inter-scale mass transfer. It typically allows choosing the production of droplets with two different sizes. Finally, Model 29 includes the oscillation dynamics of the small-scale spray of droplets. Thus, it enables the parametrization of additional information on the small-scale dynamics expressed in terms of geometric quantities during the inter-scale transfer. Such information

could correspond to the residual motion of detached ligaments after primary break-up.

Remark that all these models provide a framework to model an inter-scale transfer in the manner of a primary break-up, but it does not indicate how to choose these parameters. Local heuristics based on experimental observations should be included to make the models able to reproduce the mixed regime in the most generic way.

In the next section, we discuss the final key element for the setting a proper two-scale method: the definition of a length-scale separating the two scales of the flow.

3.3 Regularization of the large-scale interface through local inter-scale mass transfer

We have demonstrated how to proceed with mass transfers between scales within the unified models, letting the opportunity for the user to select where to activate it and on which criteria. We propose now another kind of inter-scale transfer following three simultaneous goals: 1- modelling the transition from the separated regime to the disperse regime, 2- introducing a length-scale threshold separating the two scales, 3- limiting locally the large-scale interface curvature through an energy redistribution between the scales while complying with the second principle of thermodynamics.

Such a regularizing process is represented in Fig. 3.3.1: mass transfer from the large scale to the small scale initiates at points where the mean curvature is the most pronounced, advancing until the mean curvature criterion is satisfied everywhere on the large-scale interface. This geometric criterion thus quantifies the amount of mass transferred from one scale to another at the difference with the inter-scale transfers of the previous section. Under the chosen convention, the local normal $\boldsymbol{\nabla}\overline{\alpha}_1/\|\boldsymbol{\nabla}\overline{\alpha}_1\|$ is oriented inward the liquid phase and the curvature $\overline{H}$ has a positive value in the red areas.

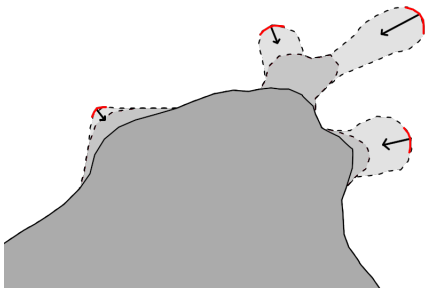

Figure 3.3.1: Schematic representation of the regularization of the large-scale interface. The grey region corresponds to the liquid $\overline{\alpha}_1 = 1$ and the white region is the gas $\overline{\alpha}_1 = 0$. The red zones represent the locations where the mean curvature $\overline{H}$ is higher than a prescribed maximal mean curvature H_{max}.

3.3.1 Mathematical entropy production of the inter-scale mass transfer

In order to introduce such process, we consider again the addition of source terms in Model 25,

$$\begin{cases} \partial_t m_1 + \boldsymbol{\nabla}\cdot(m_1\boldsymbol{u}) = R_{m_1}, \\ \partial_t m_1^d + \boldsymbol{\nabla}\cdot(m_1^d\boldsymbol{u}) = R_{m_1^d}, \\ \partial_t m_2 + \boldsymbol{\nabla}\cdot(m_2\boldsymbol{u}) = 0, \\ \partial_t \alpha_1^d + \boldsymbol{\nabla}\cdot(\alpha_1^d\boldsymbol{u}) = R_{\alpha_1^d}, \\ \partial_t \Sigma + \boldsymbol{\nabla}\cdot(\Sigma\boldsymbol{u}) = R_\Sigma, \\ \partial_t \overline{\alpha}_1 + \boldsymbol{u}\cdot\boldsymbol{\nabla}\overline{\alpha}_1 = R_{\overline{\alpha}_1}, \\ \partial_t(\rho\boldsymbol{u}) + \boldsymbol{\nabla}\cdot\left(\rho\boldsymbol{u}\otimes\boldsymbol{u} + (\overline{p} - \sigma\|\boldsymbol{\nabla}\overline{\alpha}_1\|)\mathbf{I} + \sigma\frac{\boldsymbol{\nabla}\overline{\alpha}_1\otimes\boldsymbol{\nabla}\overline{\alpha}_1}{\|\boldsymbol{\nabla}\overline{\alpha}_1\|}\right) = R_{\boldsymbol{u}}. \end{cases} \tag{3.61}$$

Here, the equation on total momentum has also a source term to balance the expected gain of capillarity energy at small scale with a loss of kinetic energy at large scale. Let us first relate $R_{m_1^d}$, $R_{\alpha_1^d}$, R_Σ to R_{m_1}. Given the total liquid mass conservation and the incompressibility of the small-scale,

$$R_{m_1^d} = -R_{m_1}, \qquad R_{\alpha_1^d} = -\frac{R_{m_1}}{\rho_1^d}. \tag{3.62}$$

For the source term R_Σ, we consider the underlying kinetic equation with an additional source term R_n accounting for the creation of droplets, *i.e.*

$$\partial_t n + \boldsymbol{\nabla}\cdot(n\boldsymbol{u}) = R_n. \tag{3.63}$$

As R_n depends on $\widehat{m}$, it produces droplets of average size and mass

$$S_{avg} := \frac{\int_{\widehat{m}} S(\widehat{m},\rho_1^d) R_n \, d\widehat{m}}{\int_{\widehat{m}} R_n \, d\widehat{m}}, \qquad m_{avg} := \frac{\int_{\widehat{m}} \widehat{m} R_n \, d\widehat{m}}{\int_{\widehat{m}} R_n \, d\widehat{m}}. \tag{3.64}$$

Integrating (3.63) against $S(\widehat{m},\rho_1^d)$ and $\widehat{m}$ provides the desired relation

$$\begin{cases} \partial_t \Sigma + \boldsymbol{\nabla}\cdot(\Sigma\boldsymbol{u}) = S_{avg}\int_{\widehat{m}} R_n \, d\widehat{m}, \\ \partial_t m_1^d + \boldsymbol{\nabla}\cdot(m_1^d\boldsymbol{u}) = m_{avg}\int_{\widehat{m}} R_n \, d\widehat{m}, \end{cases} \tag{3.65}$$

so that we have

$$R_\Sigma = -\frac{S_{avg}}{m_{avg}} R_{m_1}. \tag{3.66}$$

More information could be recovered about the polydispersity of the mass transfer as demonstrated in Section 3.2.1 and 3.2.3. This model can easily be extended to account for these geometric variables, but they are not relevant here as only the interface area density has an impact in the inter-scale mass transfer through capillarity. With the mass transfer process, the system yields

$$\begin{cases} \partial_t m_1 + \boldsymbol{\nabla}\cdot(m_1\boldsymbol{u}) = R_{m_1}, \\ \partial_t m_1^d + \boldsymbol{\nabla}\cdot(m_1^d\boldsymbol{u}) = -R_{m_1}, \\ \partial_t m_2 + \boldsymbol{\nabla}\cdot(m_2\boldsymbol{u}) = 0, \\ \partial_t \alpha_1^d + \boldsymbol{\nabla}\cdot(\alpha_1^d\boldsymbol{u}) = -(\rho_1^d)^{-1} R_{m_1}, \\ \partial_t \Sigma + \boldsymbol{\nabla}\cdot(\Sigma\boldsymbol{u}) = -\frac{S_{avg}}{m_{avg}} R_{m_1}, \\ \partial_t \overline{\alpha}_1 + \boldsymbol{u}\cdot\boldsymbol{\nabla}\overline{\alpha}_1 = R_{\overline{\alpha}_1}, \\ \partial_t(\rho\boldsymbol{u}) + \boldsymbol{\nabla}\cdot\left(\rho\boldsymbol{u}\otimes\boldsymbol{u} + (\overline{p} - \sigma\|\boldsymbol{\nabla}\overline{\alpha}_1\|)\mathbf{I} + \sigma\frac{\boldsymbol{\nabla}\overline{\alpha}_1\otimes\boldsymbol{\nabla}\overline{\alpha}_1}{\|\boldsymbol{\nabla}\overline{\alpha}_1\|}\right) = R_{\boldsymbol{u}}. \end{cases} \tag{3.67}$$

Concerning the dissipation of the model, the mathematical entropy production rate ς associated with the energy $\mathcal{H}$ defined in (3.29) is

$$\varsigma = -((1-\alpha_1^d)(p_1-p_2) - \sigma\overline{H})R_{\overline{\alpha}_1} - \left(e_1(\rho_1^d) + \frac{\overline{p}}{\rho_1^d} - \left(e_1(\rho_1) + \frac{p_1}{\rho_1}\right) + \sigma\frac{S_{avg}}{m_{avg}}\right) R_{m_1} + \boldsymbol{u}\cdot R_{\boldsymbol{u}}. \tag{3.68}$$

The reader is referred to Appendix 3.A for calculation details.

3.3.2 Large-scale mean curvature limitation *via* the pressure relaxation

In order to define the mass transfer between scales, we proceed as follows: we alter the large-scale Laplace equilibrium by introducing a different curvature H_{lim} instead of $\overline{H}$ in (1.119),

$$R_{\overline{\alpha}_1} = \frac{1}{\mu}\left(p_1 - p_2 - \frac{\sigma H_{lim}}{1-\alpha_1^d}\right), \tag{3.69}$$

and we further compensate the "mathematical entropy" production with the source term of the momentum equation. The regularization process is introduced by the definition of $H_{lim} := \min(\overline{H}, H_{max})$ where H_{max} is a positive curvature threshold to locally control the capillarity phenomena as suggested by the scheme in Figure 3.3.1.

Choosing such a different equilibrium leads to an unsigned term in the mathematical entropy production rate (3.68) when no mass transfer is accounted for, *i.e.* $R_{m_1} = 0$. Thus, we must determine the right mass and momentum

transfer to make the total process dissipative. With such dynamics, the mathematical entropy production rate is now

$$\varsigma = -((1-\alpha_1^d)(p_1-p_2)-\sigma\overline{H})\frac{1}{\mu}\left(p_1-p_2-\frac{\sigma H_{lim}}{1-\alpha_1^d}\right)-\left(e_1(\rho_1^d)+\frac{\overline{p}}{\rho_1^d}-\left(e_1(\rho_1)+\frac{p_1}{\rho_1}\right)+\sigma\frac{S_{avg}}{m_{avg}}\right)R_{m_1}+\boldsymbol{u}\cdot\boldsymbol{R_u}. \quad (3.70)$$

Then, considering that the large-scale and small-scale densities are close, we set $\Delta\rho_1 = \rho_1^d - \rho_1$ and we define a non-dimensional function h corresponding to the first-order integral remainder of $e_1(\rho_1^d)+\overline{p}/\rho_1^d-(e_1(\rho_1)+p_1/\rho_1)$ such that

$$e_1(\rho_1^d)+\frac{\overline{p}}{\rho_1^d}-\left(e_1(\rho_1)+\frac{p_1}{\rho_1}\right)=-\frac{\overline{\alpha}_2}{\rho_1}(p_1-p_2)(1+h), \quad (3.71)$$

with $h\to 0$ when $\Delta\rho_1/\rho_1\to 0$. Then, defining

$$\Delta H := \overline{H}-H_{lim}, \quad (3.72)$$

we reorganize the terms in (3.70) to obtain

$$\begin{aligned}\varsigma =& -\frac{1}{\mu}(1-\alpha_1^d)\left(p_1-p_2-\frac{\sigma H_{lim}}{1-\alpha_1^d}\right)^2+\left(\frac{\overline{\alpha}_2}{\rho_1}R_{m_1}+\frac{1}{\mu}\sigma\Delta H\right)(p_1-p_2)\\ &-\frac{1}{\mu}\sigma\Delta H\left(\frac{\sigma H_{lim}}{1-\alpha_1^d}\right)+\left(\frac{\overline{\alpha}_2}{\rho_1}(p_1-p_2)h-\sigma\frac{S_{avg}}{m_{avg}}\right)R_{m_1}+\boldsymbol{u}\cdot\boldsymbol{R_u}.\end{aligned} \quad (3.73)$$

This reorganization suggests nullifying the second unsigned term with the pressure difference by choosing

$$R_{m_1} = -\frac{1}{\mu}\frac{\rho_1\sigma\Delta H}{\overline{\alpha}_2}. \quad (3.74)$$

This choice seems coherent as it is only activated when $\Delta H > 0$ *i.e.* when the local curvature $\overline{H}$ is greater than the prescribed curvature H_{max}. Then, the mathematical entropy production rate becomes

$$\varsigma = -\frac{1}{\mu}(1-\alpha_1^d)\left(p_1-p_2-\frac{\sigma H_{lim}}{1-\alpha_1^d}\right)^2-\frac{1}{\mu}\sigma\Delta H\left(\frac{\sigma H_{lim}}{1-\alpha_1^d}+(p_1-p_2)\,h-\sigma\frac{S_{avg}}{m_{avg}}\frac{\rho_1}{\overline{\alpha}_2}\right)+\boldsymbol{u}\cdot\boldsymbol{R_u}. \quad (3.75)$$

The first term of the right-hand side is obviously negative for any $\mu\geq 0$. However, as h is expected to be small, the sign of the second term depends mainly on both the chosen limiting large-scale curvature H_{lim} and the ratio S_{avg}/m_{avg} pthat arametrizes the production of small-scale droplets. This second term has approximately the sign of

$$\frac{S_{avg}}{m_{avg}}\frac{\rho_1}{\overline{\alpha}_2}-\frac{H_{lim}}{1-\alpha_1^d}. \quad (3.76)$$

For a classic configuration and given a mixture-volume of typical length l with a small-scale of typical length l_{ss}, large-scale and small-scale density are almost the same so that $m_{avg}\sim\rho_1 l_{ss}^3$, and we also have $1-\alpha_1^d\sim 1$ and $\overline{\alpha}_2\sim 1$. However, the typical length-scale of the small-scale l_{ss} is much smaller than H_{lim}^{-1} that is comparable to l. Then, the quantity (3.76) behaves as

$$\frac{S_{avg}}{m_{avg}}\frac{\rho_1}{\overline{\alpha}_2}-\frac{H_{lim}}{1-\alpha_1^d}\sim\frac{1}{l_{ss}}-\frac{1}{l}, \quad (3.77)$$

which is consequently expected to be positive. Then, the dissipative nature of the inter-scale transfer must be enforced by choosing a momentum source term that provides a negative contribution through the third term of the mathematical entropy production rate (3.75).

3.3.3 Choice of the momentum source term to enforce a dissipative inter-scale transfer

We look for an expression of the momentum source term such that it provides a negative contribution in the mathematical entropy production rate that can be activated similarly as the other source terms R_{m_1}, $R_{m_1^d}$, R_Σ, $R_{\overline{\alpha}_1}$ of the inter-scale mass transfer. We propose a momentum source term of the following form

$$\boldsymbol{R_u} = -\mu^{-1}\sigma\Delta H\tilde{R}_{\boldsymbol{u}}\boldsymbol{u}, \tag{3.78}$$

with $\tilde{R}_{\boldsymbol{u}} > 0$. This choice enforces that the momentum source term is similarly activated when $\Delta H > 0$ and that both velocity amplitude and the kinetic energy decrease. Indeed, imposing the negative sign of the mathematical entropy production rate (3.75) is now possible by enforcing a last condition on $\tilde{R}_{\boldsymbol{u}}$,

$$\frac{\sigma H_{lim}}{1-\alpha_1^d} + (p_1 - p_2)\, h - \sigma\frac{S_{avg}}{m_{avg}}\frac{\rho_1}{\overline{\alpha}_2} + \boldsymbol{u}^2\tilde{R}_{\boldsymbol{u}} \geq 0. \tag{3.79}$$

Such a source term is only possible for non-zero velocity which is here assumed, but later discussed in Section 3.3.4. In order not to dissipate energy through the contributions related to the inter-scale transfer, we choose $\tilde{R}_{\boldsymbol{u}}$ so that it satisfies the equality case of the above inequality, that is to say

$$\tilde{R}_{\boldsymbol{u}} = \frac{1}{\boldsymbol{u}^2}\left(-\frac{\sigma H_{lim}}{1-\alpha_1^d} + (p_2 - p_1)\, h + \sigma\frac{S_{avg}}{m_{avg}}\frac{\rho_1}{\overline{\alpha}_2}\right), \tag{3.80}$$

with the assumption that

$$-\frac{\sigma H_{lim}}{1-\alpha_1^d} + (p_2 - p_1)\, h + \sigma\frac{S_{avg}}{m_{avg}}\frac{\rho_1}{\overline{\alpha}_2} > 0. \tag{3.81}$$

Despite its *a priori* satisfaction with the setting of a small value for S_{avg}, this latter condition is required to allow the inter-scale mass transfer as further discussed in Section 3.3.4. Such an energy transfer from large-scale momentum is necessary as the regularization process creates small-scale droplets involving more interface area and therefore more energy due to capillarity. The final set of equations is gathered in Model 30.

Model 30 (Two-scale model with large-cale curvature regularization)

With $m_k = \alpha_k\rho_k$ the phase effective densities of the large-scale liquid phase $k = 1$, gaseous phase $k = 2$ and small-scale liquid phase $k = 1^d$, ρ the mixture density such that $\rho = m_1 + m_2 + m_1^d$, p_k the large-scale phase pressures, α_k the volume fractions, $\boldsymbol{u}$ the mixture velocity, σ the capillarity coefficient, Σ the IAD,

$$\begin{cases}
\partial_t m_1 + \boldsymbol{\nabla}\cdot(m_1\boldsymbol{u}) = -\frac{1}{\mu}\frac{\rho_1\sigma}{\overline{\alpha}_2}\Delta H, \\
\partial_t m_1^d + \boldsymbol{\nabla}\cdot(m_1^d\boldsymbol{u}) = \frac{1}{\mu}\frac{\rho_1\sigma}{\overline{\alpha}_2}\Delta H, \\
\partial_t m_2 + \boldsymbol{\nabla}\cdot(m_2\boldsymbol{u}) = 0, \\
\partial_t \alpha_1^d + \boldsymbol{\nabla}\cdot(\alpha_1^d\boldsymbol{u}) = \frac{1}{\mu}\frac{\rho_1\sigma}{\overline{\alpha}_2\rho_1^d}\Delta H, \\
\partial_t \Sigma + \boldsymbol{\nabla}\cdot(\Sigma\boldsymbol{u}) = \frac{1}{\mu}\frac{S_{avg}}{m_{avg}}\frac{\rho_1\sigma\Delta H}{\overline{\alpha}_2}, \\
\partial_t \overline{\alpha}_1 + \boldsymbol{u}\cdot\boldsymbol{\nabla}\overline{\alpha}_1 = \frac{1}{\mu}(p_1 - p_2 - \frac{\sigma}{1-\alpha_1^d}H_{lim}), \\
\partial_t(\rho\boldsymbol{u}) + \boldsymbol{\nabla}\cdot\left(\rho\boldsymbol{u}\otimes\boldsymbol{u} + (\overline{p} - \sigma\|\boldsymbol{\nabla}\overline{\alpha}_1\|)\mathbf{I} + \sigma\frac{\boldsymbol{\nabla}\overline{\alpha}_1\otimes\boldsymbol{\nabla}\overline{\alpha}_1}{\|\boldsymbol{\nabla}\overline{\alpha}_1\|}\right) \\
\qquad = -\frac{1}{\mu}\sigma\Delta H\left(\frac{3}{\kappa\rho_1^d}\frac{\rho_1}{\overline{\alpha}_2} - \frac{1}{1-\alpha_1^d} + (p_2 - p_1)\,\frac{h}{\sigma H_{lim}}\right)\sigma H_{lim}\frac{\boldsymbol{u}}{\boldsymbol{u}^2},
\end{cases}$$

with $\overline{p} = \overline{\alpha}_1 p_1 + \overline{\alpha}_2 p_2$ and $\mu > 0$.

Remark that in the limit of an instantaneous relaxation, we have

$$p_1 - p_2 = \frac{\sigma H_{lim}}{1-\alpha_1^d}, \quad \text{and} \quad \overline{H} = H_{lim}. \tag{3.82}$$

It particularly enforces the local modified Laplace equilibrium and the limited curvature such that the large-scale interface regularized.

3.3.4 Mass transfer location

In Model 30, the mass transfer from large to small scale is *a priori* triggered everywhere in the domain provided that $\overline{H} \neq H_{lim}$. However, the discussion of the inter-scale model showed that it can only occur provided that

$$-\frac{\sigma H_{lim}}{1-\alpha_1^d} + (p_2 - p_1)\, h + \sigma \frac{S_{avg}}{m_{avg}} \frac{\rho_1}{\overline{\alpha}_2} > 0, \qquad \text{and} \qquad \|\boldsymbol{u}\| > 0. \tag{3.83}$$

Moreover, due to the interface thickness and the absence of proper accounting of small- to large-scale mass transfer model, we propose to locate the mass transfer at the most desirable location of the flow to avoid the limits of our model. Therefore, we modify the definition of H_{lim} into

$$H_{lim} = \mathbb{1}_{\mathcal{C}} \min(\overline{H}, H_{max}) + (1 - \mathbb{1}_{\mathcal{C}})\overline{H}, \tag{3.84}$$

where $\mathcal{C}$ is a condition or a set of conditions that enables the mass transfer *via* curvature limitation, only at the location where $\mathcal{C}$ is satisfied. Note that we have omitted here the space and time dependencies.

We propose to account for the following conditions, $\mathcal{C} := \mathcal{C}_1 \cap \mathcal{C}_2 \cap \mathcal{C}_3$ with

$$\mathcal{C}_1 := \left(\frac{3}{\kappa \rho_1^d} \frac{\rho_1}{\overline{\alpha}_2} - \frac{1}{1-\alpha_1^d} + (p_2 - p_1)\, \frac{h}{\sigma H_{lim}} \geq 0 \right), \qquad \mathcal{C}_2 := \left(\overline{\alpha}_{I,min} < \overline{\alpha}_1 < \overline{\alpha}_{I,max} \right), \qquad \mathcal{C}_3 := \left(\boldsymbol{\nabla} \overline{\alpha}_1 \cdot \boldsymbol{u} > 0 \right). \tag{3.85}$$

$\mathcal{C}_1$ corresponds to the decreasing condition of the kinetic energy that also ensures the dissipative nature of the mass transfer process as showed by the signed equation on the mathematical entropy (3.75). $\mathcal{C}_2$ ensures that the mass transfer occurs in the outer side of the numerically thickened interface. The lower bound $\overline{\alpha}_{I,min}$ ensures that we indeed are in or very near of the interface while the upper bound $\overline{\alpha}_{I,max}$ prevents that small-scale appear with almost no gaseous phase to contain it. $\mathcal{C}_3$ avoids re-impact of the small-scale into the large-scale liquid phase as it is not modelled here. Indeed, this criterion favours situations where the small-scale to be carried away from the large-scale interface. Remark also that this condition also requires the velocity amplitude to be positive as required by (3.83).

3.3.5 Closure of the two-scale model

We conclude the modelling part of this work by proposing a specific closure of the two-scale Model 30 that relies on a closure for S_{avg}/m_{avg} and the choice of EOS for h. For weakly compressible test-cases, and with the reduced information about the small-scale geometry α_1^d and Σ, we make the following assumptions:

- the small-scale and large-scale liquid phases have the same linearized barotropic EOS; (H3f)
- the inter-scale produces a spray of monodisperse droplets; (H3g)
- the radius of the droplets is smaller than the large-scale curvature threshold. (H3h)

With (H3f), we define p_0 and $\rho_{0,1}$ a pressure of reference and a density of reference for the liquid such that the EOS reads $p_1(\rho_1) = p_0 + c_1^2(\rho_1 - \rho_{0,1})$. Integrating the pressure law leads to

$$e_1(\rho_1) = \frac{(\rho_1 \log(\rho_1))c_1^2 - p_0}{\rho_1} + e_c, \tag{3.86}$$

where e_c is an energy constant. Then, from (3.71) and denoting $\delta_{\rho_1} = \Delta\rho_1/\rho_1$, we obtain

$$h = -\frac{-\delta_{\rho_1}}{1+\delta_{\rho_1}} + \frac{\rho_1 c_1^2}{(p_2 - p_1)\overline{\alpha}_2} \left(-\frac{\delta_{\rho_1}}{1+\delta_{\rho_1}} \log(1+\delta_{\rho_1}) \right) = -\delta_{\rho_1} + O(\delta_{\rho_1}^2). \tag{3.87}$$

Following (H3g), let us denote with r the radius of the droplets produced, then $S_{avg}/m_{avg} = 3/(r\rho_1^d)$. Then, according to (H3h), we have that $r = \kappa H_{lim}^{-1}$, with $\kappa < 1$ a scaling factor. Using this expression of S_{avg}/m_{avg} in (3.78) and (3.80), the source term on the momentum equation becomes

$$\boldsymbol{R_u} = -\frac{1}{\mu}\sigma\Delta H\left(\frac{3}{\kappa\rho_1^d}\frac{\rho_1}{\overline{\alpha}_2} - \frac{1}{1-\alpha_1^d} + (p_2-p_1)\,\frac{h}{\sigma H_{lim}}\right)\sigma H_{lim}\frac{\boldsymbol{u}}{\boldsymbol{u}^2}. \tag{3.88}$$

The final set of equations is gathered in Model 31.

Model 31 (Two-scale model with large-scale curvature regularization)

With $m_k = \alpha_k\rho_k$ the phase effective densities of the large-scale liquid phase $k=1$, gaseous phase $k=2$ and small-scale liquid phase $k=1^d$, ρ the mixture density such that $\rho = m_1+m_2+m_1^d$, p_k the large-scale phase pressures, α_k the volume fractions, $\boldsymbol{u}$ the mixture velocity, σ the capillarity coefficient, Σ the IAD, the flow is governed by

$$\begin{cases}
\partial_t m_1 + \boldsymbol{\nabla}\cdot(m_1\boldsymbol{u}) = -\frac{1}{\mu}\frac{\rho_1\sigma}{\overline{\alpha}_2}\Delta H,\\
\partial_t m_1^d + \boldsymbol{\nabla}\cdot(m_1^d\boldsymbol{u}) = \frac{1}{\mu}\frac{\rho_1\sigma}{\overline{\alpha}_2}\Delta H,\\
\partial_t m_2 + \boldsymbol{\nabla}\cdot(m_2\boldsymbol{u}) = 0,\\
\partial_t \alpha_1^d + \boldsymbol{\nabla}\cdot(\alpha_1^d\boldsymbol{u}) = \frac{1}{\mu}\frac{\rho_1\sigma}{\overline{\alpha}_2\rho_1^d}\Delta H,\\
\partial_t \Sigma + \boldsymbol{\nabla}\cdot(\Sigma\boldsymbol{u}) = \frac{1}{\mu}\frac{3H_{lim}}{\kappa\rho_1^d}\frac{\rho_1\sigma\Delta H}{\overline{\alpha}_2},\\
\partial_t \overline{\alpha}_1 + \boldsymbol{u}\cdot\boldsymbol{\nabla}\overline{\alpha}_1 = \frac{1}{\mu}(p_1 - p_2 - \frac{\sigma}{1-\alpha_1^d}H_{lim}),\\
\partial_t(\rho\boldsymbol{u}) + \boldsymbol{\nabla}\cdot\left(\rho\boldsymbol{u}\otimes\boldsymbol{u} + (\overline{p} - \sigma\|\boldsymbol{\nabla}\overline{\alpha}_1\|)\mathbf{I} + \sigma\frac{\boldsymbol{\nabla}\overline{\alpha}_1\otimes\boldsymbol{\nabla}\overline{\alpha}_1}{\|\boldsymbol{\nabla}\overline{\alpha}_1\|}\right)\\
\qquad = -\frac{1}{\mu}\sigma\Delta H\left(\frac{3}{\kappa\rho_1^d}\frac{\rho_1}{\overline{\alpha}_2} - \frac{1}{1-\alpha_1^d} + (p_2-p_1)\,\frac{h}{\sigma H_{lim}}\right)\sigma H_{lim}\frac{\boldsymbol{u}}{\boldsymbol{u}^2},
\end{cases} \tag{3.89}$$

with $\overline{p} = \overline{\alpha}_1 p_1 + \overline{\alpha}_2 p_2$, $\nu > 0$ and $0 < \kappa \leq 1$.

The remaining unclosed parameters are H_{max} and κ, and are meant to be parametrized for each setup. The parameter H_{max} is the inverse of the length-scale that splits the separated model from the disperse one and should be chosen such that the global shape of the bulk liquid phase is resolved. The parameter κ is used to tune the average size of the droplets created at small-scale. More parameters could be introduced by adding further information about the small scale to capture polydispersion in Model 27 or oscillatory dynamics of the inclusions in Model 29. Additional phenomena such as added-mass or drag could also be added with the two-velocity disperse models of Section 1.4.3.

Conclusion of chapter 3

This chapter provides key features for two-scale models to describe multi-scale two-phase flows with different regimes, including :

- the unified derivation of two-scale models with coexisting models for the separated and disperse regime in Section 3.1;
- the identification of mass, momentum and geometric source terms taking advantage of small-scale models to model phenomena of the mixed regime such as primary break-up in Section 3.2;
- a regularization process of the large-scale interface which indicates the transition from the separated to the disperse regime in Section 3.3.

More particularly, in Section 3.1, the unified derivation of the two-scale models with Hamilton's SAP is showed to provide unified models allowing a transition zone where the two regimes can interact while recovering the usual multi-fluid DIM and disperse models in the regions where the separated regime and disperse regime are respectively well identified. Then in Section 3.2, the main feature consists in authorizing local exchange source terms between both scales while ensuring the local conservation of energy and the dissipative structure of the model. Finally, in Section 3.3, we specifically introduce a regularizing process which modifies the large-scale Laplace pressure equilibrium while transferring liquid from the large scale to the small scale. It allows to manually introduce a length-scale separating the large and small scales without modifying the thermodynamics of the large-scale. It particularly limits the curvature of the large scale diffuse interface but not its thickness which is not prescribed here. Finally, we use the geometric information at both scales to build some source terms which allows to model the mixed regime, *e.g.* the polydispersity or deformations of the small-scale resulting from a primary atomization mechanism or the deformation, or the location of the inter-scale mass transfer.

Appendix

3.A Mathematical entropy production of the two-scale capillarity model

For calculation purposes, we consider a transport equation on the variable $z = (\rho_1^d)^{2/3}\Sigma/m_1^d$ similarly to Di Battista (2021) instead of the conservation equation on Σ. We introduce then the source term R_z such that $D_t z = R_z$, and $R_z = R_\Sigma(\rho_1^d)^{2/3}/m_1^d + zR_{m_1}/m_1^d$. We do not prescribe the dynamics of $\overline{\alpha}_1$, and we consider then the following system of equations,

$$\begin{cases} \partial_t m_1 & +\boldsymbol{\nabla}\cdot(m_1\boldsymbol{u}) & = R_{m_1}, \\ \partial_t m_2 & +\boldsymbol{\nabla}\cdot(m_2\boldsymbol{u}) & = 0, \\ \partial_t m_1^d & +\boldsymbol{\nabla}\cdot(m_1^d\boldsymbol{u}) & = -R_{m_1}, \\ \partial_t \alpha_1^d & +\boldsymbol{\nabla}\cdot(\alpha_1^d\boldsymbol{u}) & = -(\rho_1^d)^{-1}R_{m_1}, \\ \partial_t z & +\boldsymbol{u}\cdot\boldsymbol{\nabla} z & = R_z, \\ \partial_t(\rho\boldsymbol{u}) & +\boldsymbol{\nabla}\cdot(\rho\boldsymbol{u}\otimes\boldsymbol{u}+\mathbf{P}) & = \boldsymbol{R_u}, \end{cases} \tag{3.90}$$

where the dynamics of $\overline{\alpha}_1$ is not specified and $\mathbf{P}$ is a general pressure tensor. Remark also that the fourth and fifth equations are equivalent to $D_t\rho_1^d = 0$ and $D_t z = R_z$. We look for a supplementary conservation equation for an entropy-entropy flux pair $(\mathcal{H}, \mathcal{G})$ such that the entropy production rate ς is negatively signed,

$$\varsigma := \partial_t\mathcal{H} + \boldsymbol{\nabla}\cdot\boldsymbol{\mathcal{G}} \leq 0. \tag{3.91}$$

With $\mathcal{H} := \boldsymbol{K}\cdot\boldsymbol{u} - \mathcal{L}$, multiplying the momentum equation of (3.90) by $\boldsymbol{u}$ gives

$$\begin{aligned} 0 =& \boldsymbol{u}\cdot\partial_t\boldsymbol{K} + \boldsymbol{u}\cdot[\boldsymbol{\nabla}\cdot(\boldsymbol{K}\otimes\boldsymbol{u}+\boldsymbol{P})] - \boldsymbol{u}\cdot R_{\boldsymbol{u}} \\ =& \partial_t(\boldsymbol{K}\cdot\boldsymbol{u}) - \boldsymbol{K}\cdot\partial_t\boldsymbol{u} + \boldsymbol{\nabla}\cdot\left[(\boldsymbol{K}\cdot\boldsymbol{u})\otimes\boldsymbol{u} + \boldsymbol{P}^T\boldsymbol{u}\right] - (\boldsymbol{K}\otimes\boldsymbol{u}) : \boldsymbol{\nabla}\boldsymbol{u} - \boldsymbol{P} : \boldsymbol{\nabla}\boldsymbol{u} - \boldsymbol{u}\cdot R_{\boldsymbol{u}} \\ =& \partial_t\mathcal{H} + \boldsymbol{\nabla}\cdot(\mathcal{H}\boldsymbol{u} + \boldsymbol{P}^T\boldsymbol{u}) + \partial_t\mathcal{L} + \boldsymbol{\nabla}\cdot(\mathcal{L}\boldsymbol{u}) - \boldsymbol{K}\cdot\partial_t\boldsymbol{u} - (\boldsymbol{K}\otimes\boldsymbol{u}) : \boldsymbol{\nabla}\boldsymbol{u} - \boldsymbol{P} : \boldsymbol{\nabla}\boldsymbol{u} - \boldsymbol{u}\cdot R_{\boldsymbol{u}}. \end{aligned} \tag{3.92}$$

Developing the derivatives of the Lagrangian and accounting for the dynamics given by (3.90) yields

$$
\begin{aligned}
0 =& \partial_t \mathcal{H} + \boldsymbol{\nabla} \cdot \left[\mathcal{H}\boldsymbol{u} + \boldsymbol{P}^T \boldsymbol{u} \right] \\
&+ \partial_{m_1} \mathcal{L}_1 D_t m_1 + \partial_{\overline{\alpha}_1} \mathcal{L}_1 D_t \overline{\alpha}_1 + \partial_{\alpha_1^d} \mathcal{L}_1 D_t \alpha_1^d \\
&+ \partial_{m_2} \mathcal{L}_2 D_t m_2 + \partial_{\overline{\alpha}_2} \mathcal{L}_2 D_t \overline{\alpha}_2 + \partial_{\alpha_1^d} \mathcal{L}_2 D_t \alpha_1^d \\
&+ \partial_{m_1^d} \mathcal{L}_1^d D_t m_1^d + \partial_{\rho_1^d} \mathcal{L}_1^d D_t \rho_1^d + \partial_z \mathcal{L}_1^d D_t z \\
&+ \boldsymbol{D} \cdot D_t(\boldsymbol{\nabla}\overline{\alpha}_1) + \mathcal{L}\boldsymbol{\nabla} \cdot \boldsymbol{u} - \boldsymbol{P} : \boldsymbol{\nabla}\boldsymbol{u} - \boldsymbol{u} \cdot R_{\boldsymbol{u}} \\
=& \partial_t \mathcal{H} + \boldsymbol{\nabla} \cdot \left[\mathcal{H}\boldsymbol{u} + \boldsymbol{P}^T \boldsymbol{u} + (D_t \overline{\alpha}_1)\boldsymbol{D} \right] + (\partial_{\overline{\alpha}_1} \mathcal{L}_1 - \partial_{\overline{\alpha}_2} \mathcal{L}_2 - \boldsymbol{\nabla} \cdot \boldsymbol{D}) D_t \overline{\alpha}_1 \\
&+ \left[\partial_{m_1} \mathcal{L}_1 - \partial_{m_1^d} \mathcal{L}_1^d - \frac{1}{\rho_1^d} \left(\partial_{\alpha_1^d} \mathcal{L}_1 + \partial_{\alpha_1^d} \mathcal{L}_2 \right) \right] R_{m_1} + \partial_z \mathcal{L}_1^d R_z \\
&- \left\{ \boldsymbol{P} + \left[\mathcal{L}_1^* + \mathcal{L}_2^* + \mathcal{L}_1^{d,*} - \mathcal{L}_{cap} + \alpha_1^d \left(\partial_{\alpha_1^d} \mathcal{L}_1 + \partial_{\alpha_1^d} \mathcal{L}_2 \right) \right] \boldsymbol{I} + \boldsymbol{D} \otimes \boldsymbol{\nabla}\overline{\alpha}_1 \right\} : \boldsymbol{\nabla}\boldsymbol{u} - \boldsymbol{u} \cdot R_{\boldsymbol{u}}.
\end{aligned}
$$

Evaluating the Lagrangian leads to

$$
\begin{aligned}
0 =& \partial_t \mathcal{H} + \boldsymbol{\nabla} \cdot \left(\mathcal{H}\boldsymbol{u} + \mathbf{P}^T \boldsymbol{u} - \sigma \frac{\boldsymbol{\nabla}\overline{\alpha}_1}{\|\boldsymbol{\nabla}\overline{\alpha}_1\|} D_t \overline{\alpha}_1 \right) + \left[(1 - \alpha_1^d)(p_1 - p_2) - \sigma \overline{H} \right] D_t \overline{\alpha}_1 \\
&+ \left(e_1^d - e_1 - \frac{p_1}{\rho_1} + \sigma z (\rho_1^d)^{-2/3} + \frac{\overline{\alpha}_1 p_1 + \overline{\alpha}_2 p_2}{\rho_1^d} \right) R_{m_1} \\
&- \left(\mathbf{P} - \left((\overline{\alpha}_1 p_1 + \overline{\alpha}_2 p_2 - \sigma \|\boldsymbol{\nabla}\overline{\alpha}_1\|) \mathbf{I} + \sigma \frac{\boldsymbol{\nabla}\overline{\alpha}_1 \otimes \boldsymbol{\nabla}\overline{\alpha}_1}{\|\boldsymbol{\nabla}\overline{\alpha}_1\|} \right) \right) : \boldsymbol{\nabla}\boldsymbol{u} \\
&- \sigma m_1^d (\rho_1^d)^{-2/3} R_z - \boldsymbol{u} \cdot R_{\boldsymbol{u}},
\end{aligned}
$$

with $e_1^d := e_1(\rho_1^d)$ and $e_1 := e_1(\rho_1)$. We choose the entropy flux $\boldsymbol{\mathcal{G}}$ by setting

$$
\begin{aligned}
\mathbf{P} &:= (\overline{\alpha}_1 p_1 + \overline{\alpha}_2 p_2 - \sigma \|\boldsymbol{\nabla}\overline{\alpha}_1\|) \, \mathbf{I} + \sigma \frac{\boldsymbol{\nabla}\overline{\alpha}_1 \otimes \boldsymbol{\nabla}\overline{\alpha}_1}{\|\boldsymbol{\nabla}\overline{\alpha}_1\|}, \\
\boldsymbol{\mathcal{G}} &:= \mathcal{H}\boldsymbol{u} + \mathbf{P}^T \boldsymbol{u} - \sigma \frac{\boldsymbol{\nabla}\overline{\alpha}_1}{\|\boldsymbol{\nabla}\overline{\alpha}_1\|} D_t \overline{\alpha}_1.
\end{aligned}
\tag{3.93}
$$

With the expression of Lagrangian (3.24), the mathematical entropy production rate finally evaluates to

$$
\begin{aligned}
\varsigma =& - \left[(1 - \alpha_1^d)(p_1 - p_2) - \sigma \overline{H} \right] D_t \overline{\alpha}_1 - \left(e_1^d - e_1 - \frac{p_1}{\rho_1} + \sigma z (\rho_1^d)^{-2/3} + \frac{\overline{\alpha}_1 p_1 + \overline{\alpha}_2 p_2}{\rho_1^d} \right) R_{m_1} \\
&+ \sigma m_1^d (\rho_1^d)^{-2/3} R_z + \boldsymbol{u} \cdot R_{\boldsymbol{u}}.
\end{aligned}
\tag{3.94}
$$

Then, the sign of the mathematical entropy production rate ς depends on the assumptions on the dynamics of $\overline{\alpha}_1$ and the source terms R_{m_1} and R_z.

Part II

Numerics

CHAPTER 4

Numerical strategy and methods

In this work, we have derived several multi-fluid compressible models as systems of partial differential equations which outreach the classic theory of Lax (1957) for systems of conservation laws. Indeed, the models of Chapters 1-2-3 particularly feature additional equilibrium equations or relaxation source terms, dispersive terms and non-conservative terms. Nevertheless, such models are derived following specific guidelines ensuring necessary conditions for a possible well-posedness of the system, including supplementary conservation equations (Cordesse and Massot, 2020), the extension of dispersive system to hyperbolic systems (Tkachenko et al., 2023), the good definitions of jump conditions (Gallouët et al., 2004) or that the supplementary equilibria are reachable with relaxation processes (Jomée, 2023; Bussac, 2023).

Besides, the small-scale models that we have proposed in Chapter 2 mostly rely on a kinetic equation and a method of moments through GeoMOM and requires the satisfaction of supplementary constraints to ensure the existence of a positive distribution for the inclusions. These constraints on moments are called *realizability conditions* and define a convex moment space for the well-known *truncated moment problem* (Stieltjes, 1894; Akhiezer, 1965; Curto and Fialkow, 1991; Schmüdgen, 2017). Depending on the support of the distributions, the realizability conditions are different. In one dimension, the problems are known under the following names: the Hamburger moment problem for the open support $\mathbb{R}$, the Stieltjes moment problem for a support $(0, +\infty)$ and the Hausdorff moment problem for a bounded support $(0, 1)$. In the multidimensional case, no general solution is known. Nevertheless, some results are available for specific phase-spaces, *e.g.* (Curto and Fialkow, 2000, 2005; Kleiber and Stoyanov, 2013).

These specific features then require adequate numerical schemes which can be treated separately *via* a time-splitting procedure (Trotter, 1959; Strang, 1968; Hundsdorfer and Verwer, 2003) as in Schmidmayer et al. (2017). However, the issue of non-conservative terms is not treated here as the scope of this contribution has been purposely restricted to focus on the small-scale models of Chapter 2 and inter-scale mass transfers of 3.

Regarding the classic conservative model, we consider a classic Finite-Volume (FV) method (LeVeque, 1992; Smoller, 1994; Godlewski and Raviart, 1996; Serre, 1999; Toro, 2009) with second-order MUSCL schemes extending the Godunov scheme (Godunov and Bohachevsky, 1959; Van Leer, 1979) in order to minimize the numerical diffusion introduced by the scheme. The FV method relies on the evaluation of the fluxes on the faces of the cells of the mesh, *i.e.* the space discretization of the domain. In the context of Godunov-type schemes, the evaluation of the fluxes requires solving or approximating the solution of a Riemann problem, *i.e.* a local discontinuous problem between the numerical states of two adjacent mesh cells. Second, some models involve relaxation source terms which yield the definition an equilibrium manifold defined by algebraic relations and drive the variables of the system towards these manifolds. In the limit case of an infinite stiffness, this enables the definition of a new equilibrium system (Liu, 1987; Chen et al., 1994; Natalini, 1998; Bouchut, 1999, 2004). Its use in multiphase flow modelling translates into an instantaneous relaxation step (Saurel and Abgrall, 1999; Saurel et al., 2009; Pelanti, 2022) where the state vector of the model is projected on the equilibrium variety defined by a supplementary closure relation. Such relaxation usually adopts implicit methods. Thus, the Newton-Raphson method offers an efficient and locally implicit solve of the equilibrium relation. However, we derive new relaxation procedures, *e.g.* for the inter-scale regularization process of Model 30, that involves space derivatives in the modified pressure law (3.69), which induces a global

coupling during the Newton-Raphson process. Therefore, we propose here an innovative implicit-explicit (ImEx) procedure to efficiently solve the equilibrium. Finally, for the small-scale kinetic models, the realizability of the numerical scheme, *i.e.* its ability of preserving the realizability of moments, relies on the use of kinetic schemes (Perthame, 1990; Bouchut, 1994; Aregba-Driollet and Natalini, 2000; Bouchut et al., 2003), which provides realizable schemes at first-order.

In this chapter, we deal separately with the issues aforementioned, which are all present in a complete two-scale model with polydisperse dynamic small-scale model, by proposing, in Section 4.1, a numerical scheme for the two-scale Model 30 with the inter-scale regularizing mass transfer but a minimal small-scale model without realizability issues. Then, a specific numerical scheme is proposed in Section 4.2 for the numerical solution of the small-scale polydisperse Model 20 of oscillating droplets in the disperse regime.

This chapter has led to the following contributions :

- For the numerical procedure of the two-scale regularizing model: Loison, Arthur, Samuel Kokh, Teddy Pichard, and Marc Massot. "A unified two-scale gas-liquid multi-fluid model with capillarity and interface regularization through a mass transfer between scales ". arXiv, 2024. https://doi.org/10.48550/arXiv.2401.09169.
- For the numerical procedure of the small-scale kinetic model of oscillating droplets: Katia Ait-Ameur, Arthur Loison, Teddy Pichard, et Marc Massot. "Simulation of polydisperse oscillating droplets with kinetic schemes for geometric moment equations". *In preparation.*

4.1 Numerical strategy for the two-scale model with mass transfer

We now propose a numerical scheme to solve the two-scale Model 30 as it combines some key features of this work: a two-scale unified model, capillarity modelling at both scale, inter-scale mass transfer with regularization. The other key features, including polydispersion and small-scale oscillation dynamics are treated in the next Section 4.2. The numerical scheme proposed here relies on a first-order Lie splitting procedure such that numerical methods for the other models of Chapters 1-2-3 can be built by selecting the relevant sub-system solved in this section. Each of these sub-systems is then solved with a dedicated scheme: a Godunov method (Godunov and Bohachevsky, 1959) for the hyperbolic model to limit artificial viscosity, an arithmetic solver (Chanteperdrix et al., 2002; Schmidmayer et al., 2017) for the capillarity model, and a relaxation step to solve the pressure equilibrium. For the Model 30, the relaxation step includes the regularization procedure with an equilibrium relation involving space derivatives. As this extra relation is not an algebraic equation any more, we propose here a new numerical procedure to solve the equilibrium.

4.1.1 Splitting, relaxation and time integration

For the building of the numerical method, we propose to cast the system into a fully conservative form with a state vector $\boldsymbol{q}$, fluxes $\boldsymbol{F}$ and the source term $\mu^{-1}\boldsymbol{r}(\boldsymbol{q})$ that we will solve in the limit $\mu \to 0$. We obtain

$$\partial_t \boldsymbol{q} + \boldsymbol{\nabla} \cdot \boldsymbol{F}(\boldsymbol{q}) = \mu^{-1}\boldsymbol{r}(\boldsymbol{q}). \tag{4.1}$$

The chosen state variable is $\boldsymbol{q} := (\overline{\alpha}_1\rho, \alpha_1\rho_1, \alpha_2\rho_2, \alpha_1^d\rho_1^d, \alpha_1^d, \Sigma, \rho\boldsymbol{u})^T$, and the fluxes $\boldsymbol{F} = \boldsymbol{F}_{conv} + \boldsymbol{F}_{cap}$ are decomposed following a convective-related part $\boldsymbol{F}_{conv}$ and a capillarity-related part $\boldsymbol{F}_{cap}$,

$$\boldsymbol{F}^{conv} := \begin{pmatrix} \overline{\alpha}_1\rho \\ \alpha_1\rho_1 \\ \alpha_2\rho_2 \\ \alpha_1^d\rho_1^d \\ \alpha_1^d \\ \Sigma \\ \rho\boldsymbol{u}\otimes\boldsymbol{u} + \overline{p}\boldsymbol{I} \end{pmatrix}, \qquad \boldsymbol{F}^{cap} := \begin{pmatrix} 0 \\ 0 \\ 0 \\ 0 \\ 0 \\ 0 \\ \sigma\left(\dfrac{\boldsymbol{\nabla}\overline{\alpha}_1\otimes\boldsymbol{\nabla}\overline{\alpha}_1}{\|\boldsymbol{\nabla}\overline{\alpha}_1\|} - \|\boldsymbol{\nabla}\overline{\alpha}_1\|\boldsymbol{I}\right) \end{pmatrix}, \tag{4.2}$$

and the source term corresponding to the pressure relaxation and the inter-scale mass transfer process is

$$\boldsymbol{r}(\boldsymbol{q}) = \begin{pmatrix} -\dfrac{\sigma\rho_1}{\overline{\alpha}_2}\Delta H \\ \dfrac{\sigma\rho_1}{\overline{\alpha}_2}\Delta H \\ 0 \\ \dfrac{\sigma\rho_1}{\overline{\alpha}_2\rho_1^d}\Delta H \\ \dfrac{S_{avg}}{m_{avg}}\dfrac{\sigma\rho_1}{\overline{\alpha}_2}\Delta H \\ \rho\left(p_1 - p_2 - \dfrac{\sigma}{1-\alpha_1^d}H_{lim}\right) \\ \sigma\Delta H\left(\frac{3}{\kappa\rho_1^d}\frac{\rho_1}{\overline{\alpha}_2} - \frac{1}{1-\alpha_1^d} + (p_2-p_1)\frac{h}{\sigma H_{lim}}\right)\sigma H_{lim}\dfrac{\boldsymbol{u}}{\boldsymbol{u}^2} \end{pmatrix}. \tag{4.3}$$

Due to the different natures of each term of the system (hyperbolic flux, capillarity flux, source terms), we propose to introduce a splitting procedure in order to use different numerical schemes for each part of the system. We decompose the fluxes and introduce an instantaneous relaxation process for the source term (Bouchut, 1999). It results in solving successively the three following systems,

$$\begin{cases} \partial_t \boldsymbol{q} + \boldsymbol{\nabla}\cdot\boldsymbol{F}^{conv}(\boldsymbol{q}) = \boldsymbol{0}, \\ \partial_t \boldsymbol{q} + \boldsymbol{\nabla}\cdot\boldsymbol{F}^{cap}(\boldsymbol{q}) = \boldsymbol{0}, \\ \boldsymbol{r}(\boldsymbol{q}) = \boldsymbol{0}. \end{cases} \tag{4.4}$$

We formalize the procedure by introducing the discrete operators $\mathbf{L}^{conv}$, $\mathbf{L}^{cap}$, $\mathbf{L}^{relax}$ and $\mathbf{L}^F = \mathbf{L}^{cap} \circ \mathbf{L}^{conv}$ that are integrated in time with a Lie splitting procedure, *i.e.* successive first-order explicit Euler integrations in time. Regarding the building of high-order time integration scheme with relaxation methods requires special numerical schemes *e.g.* Jin (1995); Caflisch et al. (1997); Lafitte et al. (2017). In our case, the state $\boldsymbol{q}^n$ computed at the $n-$th time-step results from the asymptotic limit of the second-order scheme of Jin (1995) extending the second-order Total Variation Diminishing Runge-Kutta (Shu and Osher, 1988) for relaxation systems. It yields

$$\begin{cases} \boldsymbol{q}^{(1)} &= \mathbf{L}^F\left(\boldsymbol{q}^{n-1}\right), \\ \boldsymbol{q}^{(1)}_{rel} &= \mathbf{L}^{relax}\left(\boldsymbol{q}^{(1)}\right), \\ \boldsymbol{q}^{(2)} &= \mathbf{L}^F\left(\boldsymbol{q}^{(1)}_{rel}\right), \\ \boldsymbol{q}^{(3)} &= \dfrac{1}{2}\left(\boldsymbol{q}^{n-1} + \boldsymbol{q}^{(2)}\right), \\ \boldsymbol{q}^{n} &= \mathbf{L}^{relax}\left(\boldsymbol{q}^{(3)}\right). \end{cases} \tag{4.5}$$

Remark that if the intermediary relaxation steps are removed, we recover the *Heun*'s method. However, the stability of this time integration is not well established as the eigenvalues of Model 30 are not known. Therefore, we consider an upper-bound of the eigenvalues of the very similar augmented model obtained in (3.35), the eigenvalues of which are known. For any direction ω, with $\psi = \sigma\|\boldsymbol{\nabla}\overline{\alpha}_1\|/(\rho(c_F^d)^2)$, these eigenvalues are upper-bounded by

$$\lambda_{max} := \|\boldsymbol{u}\| + c_F^d\left(1 + \frac{1}{8}\psi\right), \tag{4.6}$$

so that we set

$$\Delta t = \mathrm{CFL} \times \lambda_{max}, \tag{4.7}$$

where CFL is the Courant-Friedrichs-Lewy number. Let us now detail the numerical procedure to solve each of these operators.

4.1.2 Hyperbolic fluxes

We focus here on the numerical method dedicated to the numerical approximation of operator $\boldsymbol{L}^{conv} : \boldsymbol{q}^0 \mapsto \boldsymbol{q}^{conv}$. We choose here a Godunov method (Godunov and Bohachevsky, 1959; Godlewski and Raviart, 1991; LeVeque, 1992; Toro, 2009) to solve this system of conservation laws. It particularly enables minimizing the numerical dissipation and allows a better capture of large-scale geometry which is of prime interest here. For the sake of readability, we now consider one-dimensional space problems, and we discretize the model into

$$\frac{\boldsymbol{q}_i^{conv} - \boldsymbol{q}_i^0}{\Delta t} = \frac{\mathcal{S}_i}{\mathcal{V}_i}\left(F_{i+1/2}^{conv} - F_{i-1/2}^{conv}\right), \tag{4.8}$$

where the subscript i indexes the $i-$th cell encompassing the space domain between $x_{i-1/2} = x_i - \Delta x/2$ and $x_{i+1/2} = x_i + \Delta x/2$, the superscript n indexes the discretized time t^n, $\boldsymbol{q}_i^n$ is the volume average of the state of the $i-$th cell at the discretized time t^n, $\mathcal{V}_i$ is the volume of the $i-$th cell, $\mathcal{S}_i$ the surface area with the neighbouring cells. $F_{i\pm1/2}^{conv}$ are the fluxes at the interface between the $i-$th cell and the $(i+1)-$th cell. Remark that for a one-dimensional regular mesh we have $\mathcal{S}_i/\mathcal{V}_i = 1/\Delta x$.

Following a Godunov scheme, we consider the following Riemann problem centred at $x_{i+1/2}$,

$$\begin{cases} \partial_t \boldsymbol{q} + \boldsymbol{\nabla} \cdot \boldsymbol{F}^{conv}(\boldsymbol{q}) = 0, \\ \boldsymbol{q}(x,0) = \begin{cases} \boldsymbol{q}_i & \text{if } x < 0, \\ \boldsymbol{q}_{i+1} & \text{if } x > 0. \end{cases} \end{cases} \tag{4.9}$$

The solution $\tilde{\boldsymbol{q}}$ of this problem is self-similar and for $t > 0$, and we note $\tilde{\boldsymbol{q}}(x/t) = \boldsymbol{q}(x,t)$. The flux at the interface $\boldsymbol{F}_{i+1/2}^{conv}$ is computed by evaluating $\boldsymbol{F}^{conv}(\tilde{\boldsymbol{q}}(0))$. Details of the procedure to solve the Riemann problem (4.9) is given in Appendix 4.A. It extends to the two-scale approach the resolution of the Riemann problem of the Model 3 as in Chanteperdrix (2004). We extend here this approach to a MUSCL scheme (Van Leer, 1979; Toro, 2009) that relies on the linear extrapolation of the conservative set of variables into $\boldsymbol{q}_{i\pm1/2}$ on the faces of cell $[x_{i-1/2}, x_{i+1/2}]$. The previous method is the same except that the initial conditions of the interface Riemann problem are now

$$\boldsymbol{q}(x,0) = \begin{cases} \boldsymbol{q}_{i+1/2}^-, & \text{if } x < 0, \\ \boldsymbol{q}_{i+1/2}^+, & \text{if } x > 0. \end{cases} \tag{4.10}$$

For a regular mesh the linear extrapolation within the $i-$th cell is defined by

$$\boldsymbol{q}^+ = \boldsymbol{q}_i + \frac{\Delta x}{2}\boldsymbol{s}_i, \qquad \boldsymbol{q}^- = \boldsymbol{q}_i - \frac{\Delta x}{2}\boldsymbol{s}_i, \qquad \boldsymbol{s}_i := \tfrac{1}{2}(\boldsymbol{s}_{i-1/2} + \boldsymbol{s}_{i+1/2}), \qquad \boldsymbol{s}_{i+1/2} := \tfrac{1}{2}(\boldsymbol{q}_{i+1}^n - \boldsymbol{q}_i^n). \tag{4.11}$$

Furthermore, the slopes are limited component-wise to avoid spurious oscillation using the MINMOD limiter (Sweby, 1984; Coquel and LeFloch, 1996; Toro, 2009) so that each component $(\boldsymbol{s}_i)_k$ of the slope $\boldsymbol{s}_i$ reads

$$(\boldsymbol{s}_i)_k = \begin{cases} \max(0, \min((\boldsymbol{s}_{i-1/2})_k (\boldsymbol{s}_{i+1/2})_k)) & \text{if} \quad (\boldsymbol{s}_{i+1/2})_k > 0, \\ \min(0, \max((\boldsymbol{s}_{i-1/2})_k (\boldsymbol{s}_{i+1/2})_k)) & \text{if} \quad (\boldsymbol{s}_{i+1/2})_k < 0. \end{cases} \tag{4.12}$$

The fluxes extend for multidimensional problems by adding fluxes for all the other faces in (4.8).

4.1.3 Capillarity fluxes

Let us focus now on the building of a numerical scheme for the capillarity fluxes, *i.e.* operator $\boldsymbol{L}^{cap} : \boldsymbol{q}^0 \mapsto \boldsymbol{q}^{cap}$, with an arithmetical-average approach as proposed in Chanteperdrix (2004); Schmidmayer et al. (2017). The numerical scheme is here written in two dimensions with $\boldsymbol{u} = (u_x, u_y)$, and the cells of a regular mesh space of step sizes Δx, Δy

are here indexed by the subscripts i and j. The update relations for the momentum read

$$
\begin{aligned}
\frac{(\rho u_x)_{i,j}^{cap} - (\rho u_x)_{i,j}^{0}}{\Delta t} &= \sigma \frac{1}{\Delta x}\left[\frac{(\partial_x \overline{\alpha}_1)_{i+1/2,j}\,(\partial_x \overline{\alpha}_1)_{i+1/2,j}}{\|\boldsymbol{\nabla}\overline{\alpha}_1\|_{i+1/2,j}} + \frac{(\partial_x \overline{\alpha}_1)_{i+1/2,j}\,(\partial_y \overline{\alpha}_1)_{i+1/2,j}}{\|\boldsymbol{\nabla}\overline{\alpha}_1\|_{i+1/2,j}} - \|\boldsymbol{\nabla}\overline{\alpha}_1\|_{i+1/2,j} \right. \\
&\quad \left. - \left(\frac{(\partial_x \overline{\alpha}_1)_{i-1/2,j}\,(\partial_x \overline{\alpha}_1)_{i-1/2,j}}{\|\boldsymbol{\nabla}\overline{\alpha}_1\|_{i-1/2,j}} + \frac{(\partial_x \overline{\alpha}_1)_{i-1/2,j}\,(\partial_y \overline{\alpha}_1)_{i-1/2,j}}{\|\boldsymbol{\nabla}\overline{\alpha}_1\|_{i-1/2,j}} - \|\boldsymbol{\nabla}\overline{\alpha}_1\|_{i-1/2,j} \right) \right] \\
&\quad + \sigma \frac{1}{\Delta y}\left[\frac{(\partial_x \overline{\alpha}_1)_{i,j+1/2}\,(\partial_x \overline{\alpha}_1)_{i,j+1/2}}{\|\boldsymbol{\nabla}\overline{\alpha}_1\|_{i,+1/2}} + \frac{(\partial_x \overline{\alpha}_1)_{i,j+1/2}\,(\partial_y \overline{\alpha}_1)_{i,j+1/2}}{\|\boldsymbol{\nabla}\overline{\alpha}_1\|_{i,j+1/2}} - \|\boldsymbol{\nabla}\overline{\alpha}_1\|_{i,j+1/2} \right. \\
&\quad \left. - \left(\frac{(\partial_x \overline{\alpha}_1)_{i,j-1/2}\,(\partial_x \overline{\alpha}_1)_{i,j-1/2}}{\|\boldsymbol{\nabla}\overline{\alpha}_1\|_{i,j-1/2}} + \frac{(\partial_x \overline{\alpha}_1)_{i,j-1/2}\,(\partial_y \overline{\alpha}_1)_{i,j-1/2}}{\|\boldsymbol{\nabla}\overline{\alpha}_1\|_{i,j-1/2}} - \|\boldsymbol{\nabla}\overline{\alpha}_1\|_{i,j-1/2} \right) \right], \\
\frac{(\rho u_y)_{i,j}^{cap} - (\rho u_y)_{i,j}^{0}}{\Delta t} &= \sigma \frac{1}{\Delta x}\left[\frac{(\partial_y \overline{\alpha}_1)_{i+1/2,j}\,(\partial_x \overline{\alpha}_1)_{i+1/2,j}}{\|\boldsymbol{\nabla}\overline{\alpha}_1\|_{i+1/2,j}} + \frac{(\partial_y \overline{\alpha}_1)_{i+1/2,j}\,(\partial_y \overline{\alpha}_1)_{i+1/2,j}}{\|\boldsymbol{\nabla}\overline{\alpha}_1\|_{i+1/2,j}} - \|\boldsymbol{\nabla}\overline{\alpha}_1\|_{i+1/2,j} \right. \\
&\quad \left. - \left(\frac{(\partial_y \overline{\alpha}_1)_{i-1/2,j}\,(\partial_x \overline{\alpha}_1)_{i-1/2,j}}{\|\boldsymbol{\nabla}\overline{\alpha}_1\|_{i-1/2,j}} + \frac{(\partial_y \overline{\alpha}_1)_{i-1/2,j}\,(\partial_y \overline{\alpha}_1)_{i-1/2,j}}{\|\boldsymbol{\nabla}\overline{\alpha}_1\|_{i-1/2,j}} - \|\boldsymbol{\nabla}\overline{\alpha}_1\|_{i-1/2,j} \right) \right] \\
&\quad + \sigma \frac{1}{\Delta y}\left[\frac{(\partial_y \overline{\alpha}_1)_{i,j+1/2}\,(\partial_x \overline{\alpha}_1)_{i,j+1/2}}{\|\boldsymbol{\nabla}\overline{\alpha}_1\|_{i,+1/2}} + \frac{(\partial_y \overline{\alpha}_1)_{i,j+1/2}\,(\partial_y \overline{\alpha}_1)_{i,j+1/2}}{\|\boldsymbol{\nabla}\overline{\alpha}_1\|_{i,j+1/2}} - \|\boldsymbol{\nabla}\overline{\alpha}_1\|_{i,j+1/2} \right. \\
&\quad \left. - \left(\frac{(\partial_y \overline{\alpha}_1)_{i,j-1/2}\,(\partial_x \overline{\alpha}_1)_{i,j-1/2}}{\|\boldsymbol{\nabla}\overline{\alpha}_1\|_{i,j-1/2}} + \frac{(\partial_y \overline{\alpha}_1)_{i,j-1/2}\,(\partial_y \overline{\alpha}_1)_{i,j-1/2}}{\|\boldsymbol{\nabla}\overline{\alpha}_1\|_{i,j-1/2}} - \|\boldsymbol{\nabla}\overline{\alpha}_1\|_{i,j-1/2} \right) \right],
\end{aligned}
\tag{4.13}
$$

where the gradients are discretized following

$$
(\partial_x \overline{\alpha}_1)_{i+1/2,j} = \frac{(\overline{\alpha}_1)_{i+1,j} - (\overline{\alpha}_1)_{i,j}}{\Delta x}, \qquad (\partial_y \overline{\alpha}_1)_{i+1/2,j} = \frac{1}{2}\left(\frac{(\overline{\alpha}_1)_{i,j+1} - (\overline{\alpha}_1)_{i,j-1}}{2\Delta x} + \frac{(\overline{\alpha}_1)_{i+1,j+1} - (\overline{\alpha}_1)_{i+1,j-1}}{2\Delta x} \right), \tag{4.14}
$$

and $(\partial_y \overline{\alpha}_1)_{i,j+1/2}$, $(\partial_x \overline{\alpha}_1)_{i,j+1/2}$ are obtained by symmetrically inverting the role of the x-axis and y-axis. Finally, the norm of the gradient is obtained with

$$
\|\boldsymbol{\nabla}\overline{\alpha}_1\|_{i+1/2,j} = \sqrt{(\partial_x \overline{\alpha}_1)_{i+1/2,j}^2 + (\partial_y \overline{\alpha}_1)_{i+1/2,j}^2}. \tag{4.15}
$$

As discussed in Section 1.3.2, other numerical schemes are possible for the capillarity fluxes, notably by using a strongly hyperbolic reformulation of the augmented model as in Chiocchetti et al. (2021). With such a numerical strategy, the quantity $\boldsymbol{w} = \boldsymbol{\nabla}\overline{\alpha}_1$ is solved independently in time, and an additional curl cleaning step is enforced to conserve the gradient nature of $\boldsymbol{w}$. The augmented formulations proposed in this work are notably showed to be more robust on some test cases like the oscillation of an ellipsoidal column.

4.1.4 Relaxation method

This section is now dedicated to the relaxation of the state $\boldsymbol{q}^{cap} = \boldsymbol{L}^{cap} \circ \boldsymbol{L}^{hyper}(\boldsymbol{q}^n)$ towards a state $\boldsymbol{q}^{n+1}$ such that $\boldsymbol{r}(\boldsymbol{q}^{n+1}) = \boldsymbol{0}$. Such step corresponds to a singular perturbation of the dynamical system (Hairer and Wanner, 1996), also called an instantaneous relaxation procedure, and is, in general, a very challenging task, notably when full EOS are involved (Saurel et al., 2007; Pelanti, 2022; Jomée, 2023; Bussac, 2023). Despite the consideration of the simpler barotropic EOS as Chanteperdrix et al. (2002) where an explicit solution of the equilibrium is available, the presence of the discretized mean curvature estimator keeps the relaxation challenging as the Newton-Raphson cannot be used straightforwardly.

In order to build an efficient solution to this problem, we start in Section 4.1.4.1 by recalling the classic Newton-Raphson method, assuming first a constant mean curvature estimator as a first development stage of the relaxation

scheme. Then, an alternative formulation of this method is proposed in Section 4.1.4.2 through the computation of the asymptotic solution of a dynamical ODE solved with a Rosenbrock scheme. Finally, an original implicit-explicit Rosenbrock scheme is introduced in Section 4.1.4.3 along with the proper account of a varying mean curvature during the relaxation.

4.1.4.1 Relaxation towards the equilibrium with a Newton-Raphson method

We consider first the case without regularization mass transfer $\Delta H = 0$ and neglect variations of the mean curvature $\overline{H}$. This corresponds to the two-scale capillarity Model 25, the problem boils down to solving, at the continuous level, the pressure equilibrium by finding the solution field $\overline{\alpha}_1^{relax}$ such that $\mathcal{F} = 0$ with,

$$\mathcal{F}(\overline{\alpha}_1) := (1-\alpha_1^d)\left(p_1\left(\frac{\alpha_1\rho_1}{(1-\alpha_1^d)\overline{\alpha}_1}\right) - p_2\left(\frac{\alpha_2\rho_2}{(1-\alpha_1^d)(1-\overline{\alpha}_1)}\right) - \sigma\overline{H}\right), \tag{4.16}$$

while all other components of $\boldsymbol{q}^{cap}$ are kept constant. The relaxation problem stated in Chanteperdrix (2004) is recovered when no small-scale is accounted for *i.e.* $\alpha_1^d = 0$ and, in the case of linearized barotropic EOS, an explicit solution is available. However, the Newton-Raphson method is used here as an introductory step in the building of a relaxation method when capillarity is accounted for. Remark that $\overline{H} = \boldsymbol{\nabla}\cdot(\boldsymbol{\nabla}\overline{\alpha}_1/\|\boldsymbol{\nabla}\overline{\alpha}_1\|)$ depends on $\overline{\alpha}_1$ through derivative operators such that the discretized problem in one cell depends on the neighbouring cells. In this first method, the mean curvature is assumed constant such that the equilibrium value of $\overline{\alpha}_1$ can be found with a Newton-Raphson method. Given an initial guess $\overline{\alpha}_1^0 = (\rho\overline{\alpha}_1)^{cap}/(\rho)^{cap}$, the $(k+1)$-th iteration is obtained from the k-th through a corrective term

$$(\Delta\overline{\alpha}_1)_{NR}^k = -\frac{\mathcal{F}(\overline{\alpha}_1^k)}{\mathcal{F}'(\overline{\alpha}_1^k)}. \tag{4.17}$$

Remark that $\mathcal{F}'(\overline{\alpha}_1^k)$ is always strictly negative

$$\mathcal{F}'(\overline{\alpha}_1^k) = -\left(\frac{(\alpha_1\rho_1)^{cap}c_{0,1}^2}{\overline{\alpha}_1^2} + \frac{(\alpha_2\rho_2)^{cap}c_{0,2}^2}{(1-\overline{\alpha}_1)^2}\right) < 0. \tag{4.18}$$

To avoid overshoots of the procedure where an iteration of the large-scale volume fraction could escape the admissibility range of $[0,1]$, we adopt a modified Newton-Raphson algorithm combined with an asymmetric bisection step when the root finding iterations are close to the boundaries of the interval. The next iteration is computed with the following modified corrective term

$$\widetilde{(\Delta\overline{\alpha}_1)}^k = \begin{cases} \min((\Delta\overline{\alpha}_1)_{NR}^k,\ \lambda(1-\overline{\alpha}_1^k)) & \text{if } (\Delta\overline{\alpha}_1)^k > 0, \\ \max((\Delta\overline{\alpha}_1)_{NR}^k,\ -\lambda\overline{\alpha}_1^k) & \text{if } (\Delta\overline{\alpha}_1)^k < 0, \end{cases} \tag{4.19}$$

with $0 < \lambda < 1$ close to 1 to ensure that the next iteration

$$\overline{\alpha}_1^{k+1} = \overline{\alpha}_1^k + \widetilde{(\Delta\overline{\alpha}_1)}^k \in (0,1), \tag{4.20}$$

does not get closer than a fraction λ of the distance that separated it from the boundary of $[0,1]$. In the simulations of Chapter 5 and 6, λ is set to 0.9.

We expect the relaxation process to end when the value $\mathcal{F}(\overline{\alpha}_1^k)$ either reaches a sufficiently small value or $\overline{\alpha}_1^k$ becomes too small to have a significant impact in the fluxes. Moreover, as a preparative stage for regularization mass transfer, we introduce a supplementary condition preventing the relaxation process when volume fraction is too small to be accurately stored. The stopping criterion is then fulfilled when

$$|\mathcal{F}(\overline{\alpha}_1^k)| < tol_{res}P_{ref}, \qquad \text{or} \qquad \overline{\alpha}_1^k < tol_{pure} \qquad \text{or} \qquad 1-\overline{\alpha}_1^k < tol_{pure}, \tag{4.21}$$

where P_{ref} is a reference pressure such as the reference pressure of the linearized EOS, the Laplace pressure jump at the beginning of the relaxation process, or a combination of both. The constants tol_{res} and tol_{pure} are tolerance

parameters that respectively indicate that the pressure equilibrium is reached *via* a low residual of $\mathcal{F}$ and that the phase is considered pure and the relaxation of pressures do not impact the mixture's pressure anymore. Furthermore, due to the difficulty of accurately solving the pressure equilibria at very different orders of magnitude, we introduce a final criterion to ensure robustness by ending the process if

$$|\widetilde{(\Delta\overline{\alpha}_1)}^k| < tol_{iter}, \tag{4.22}$$

with tol_{iter} a tolerance parameter to build a stopping criterion on the iteration step. The use of a tolerance parameter tol_{res} on pressure residual and tol_{iter} on iteration of the volume fraction is respectively adapted to the case where a mixture is present with a well conditioned problem, and the case of an almost pure phase where the finding of the equilibrium is a stiff problem (Deuflhard, 2011). In the following numerical setups, we choose the following values

$$tol_{res} = 10^{-10}, \qquad tol_{pure} = 10^{-14}, \qquad tol_{iter} = 10^{-14}. \tag{4.23}$$

Remark that, for values of volume fraction below these thresholds, the relaxation process does not take place any more. Indeed, the problem of finding the pressure equilibrium is so stiff that the iterative procedure requires change of volume fraction less than the machine precision. In this case, the two-phase model boils down to a single-phase model with a residual amount of the other phase which is passively advected. This case is illustrated in Section 5.2.1.3 and the pure phases are showed to have a similar behaviour as almost pure phases for material advection problems. Such particular treatment is of particular interest to avoid issues when the computation of mean curvature is involved in Section 4.1.4.3.

4.1.4.2 The Newton-Raphson method as a first-order Rosenbrock scheme

In this second subsection, we propose to interpret the Newton-Raphson procedure as an integration in fictitious time of the relaxation source term with a Rosenbrock scheme (Hairer and Wanner, 1996; Hundsdorfer and Verwer, 2003). Such schemes consist in the linearization of implicit Runge-Kutta methods and are showed to be both A-stable and L-stable. Moreover, in the limit of an instantaneous relaxation, the Rosenbrock scheme extension for Differential-Algebraic Equations (DAE) boils down to a Newton-Raphson step (Hairer and Wanner, 1996) for all the component concerned by the singular perturbation. We consider then the pressure relaxation dynamics with respect to a fictitious time τ

$$\partial_\tau \overline{\alpha}_1 = \frac{1}{\mu}\left(p_1 - p_2 - \frac{\sigma}{1-\alpha_1^d}\overline{H}(\overline{\alpha}_1^{cap})\right), \tag{4.24}$$

for $\mu > 0$. We consider then a first-order Rosenbrock scheme which corresponds to a linearized implicit Euler discretization of (4.24),

$$\frac{\overline{\alpha}_1^{k+1} - \overline{\alpha}_1^k}{\Delta\tau} = \frac{1}{\mu}\left(\mathcal{F}(\overline{\alpha}_1^k) + \mathcal{F}'(\overline{\alpha}_1^k)(\overline{\alpha}_1^{k+1} - \overline{\alpha}_1^k)\right), \tag{4.25}$$

so that

$$\overline{\alpha}_1^{k+1} = \overline{\alpha}_1^k + \frac{\frac{\Delta\tau}{\mu}\mathcal{F}(\overline{\alpha}_1^k)}{1 - \frac{\Delta\tau}{\mu}\mathcal{F}'(\overline{\alpha}_1^k)}. \tag{4.26}$$

One can then immediately see that the usual Newton-Raphson step (4.17) in the singular perturbation limit $\frac{\Delta\tau}{\mu} \to \infty$. The modified corrective term is also recovered through the introduction of a stability criterion on the ratio $\frac{\Delta\tau}{\mu}$ to ensure that $\overline{\alpha}_1^{k+1}$ stays in $[0,1]$. Using the same parameter λ, we look for the maximal step ratio $\left(\frac{\Delta\tau}{\mu}\right)_{max}$ such that

$$-\lambda\overline{\alpha}_1^k \leq \overline{\alpha}_1^{k+1} - \overline{\alpha}_1^k \leq \lambda(1 - \overline{\alpha}_1^k). \tag{4.27}$$

Considering the condition given by the left side of the above inequality and using the expression obtained in (4.26), we obtain

$$\frac{\Delta\tau}{\mu}\mathcal{F}'(\overline{\alpha}_1^k)\left(\lambda\overline{\alpha}_1^k + (\Delta\overline{\alpha}_1)_{NR}^k\right) \leq \lambda\overline{\alpha}_1^k. \tag{4.28}$$

Three cases arise depending on the sign of $(\Delta\overline{\alpha}_1)_{NR}^k$ and the comparison between $-\lambda\overline{\alpha}_1^k$ and $(\Delta\overline{\alpha}_1)_{NR}^k$:

- if $(\Delta\overline{\alpha}_1)^k_{NR} > 0$, then (4.28) is satisfied;
- if $(\Delta\overline{\alpha}_1)^k_{NR} < 0$ and $-\lambda\overline{\alpha}^k_1 < (\Delta\overline{\alpha}_1)^k_{NR}$, then (4.28) is also satisfied;
- if $(\Delta\overline{\alpha}_1)^k_{NR} < 0$ and $-\lambda\overline{\alpha}^k_1 > (\Delta\overline{\alpha}_1)^k_{NR}$, then (4.28) enforces the following condition

$$\frac{\Delta\tau}{\mu} \leq \frac{\lambda\overline{\alpha}^k_1}{\mathcal{F}'(\overline{\alpha}^k_1)\left(\lambda\overline{\alpha}^k_1 + (\Delta\overline{\alpha}_1)^k_{NR}\right)} =: \left(\frac{\Delta\tau}{\mu}\right)_{max}. \tag{4.29}$$

In the case under consideration, selecting the maximal step ratio defined above in the implicit Euler step (4.26) is equivalent to computing $\overline{\alpha}^{k+1}_1$ following (4.20).

A similar discussion stands for the right-side inequality of (4.27) such that the Newton-Raphson method with the modified update $(\widetilde{\overline{\alpha}_1})^k$ is equivalent to the implicit Euler integration of the relaxation with respect to a fictitious time with the stability condition (4.27).

4.1.4.3 ImEx integration of the instantaneous relaxation process for regularizing mass transfer

We consider now the full dynamical system of the relaxation with inter-scale mass transfer reads

$$\begin{cases} \partial_\tau(\alpha_1\rho_1) &= -\frac{1}{\mu}\frac{\rho_1\sigma}{\overline{\alpha}_2}\Delta H, \\ \partial_\tau(\alpha^d_1\rho^d_1) &= \frac{1}{\mu}\frac{\rho_1\sigma}{\overline{\alpha}_2}\Delta H, \\ \partial_\tau(\alpha_2\rho_2) &= 0, \\ \partial_\tau\alpha^d_1 &= \frac{1}{\mu}\frac{\rho_1\sigma}{\overline{\alpha}_2\rho^d_1}\Delta H, \\ \partial_\tau\Sigma &= \frac{1}{\mu}\frac{S_{avg}}{m_{avg}}\frac{\rho_1\sigma\Delta H}{\overline{\alpha}_2}, \\ \partial_\tau\overline{\alpha}_1 &= \frac{1}{\mu}(p_1 - p_2 - \frac{\sigma}{1-\alpha^d_1}H_{lim}), \\ \partial_\tau(\rho\boldsymbol{u}) &= -\frac{1}{\mu}\left(\frac{3}{\kappa\rho^d_1}\frac{\rho_1}{\overline{\alpha}_2} - \frac{1}{1-\alpha^d_1} + (p_2 - p_1)\frac{h}{\sigma H_{lim}}\right)\sigma H_{lim}\frac{\boldsymbol{u}}{\boldsymbol{u}^2}\sigma\Delta H. \end{cases} \tag{4.30}$$

Extending the numerical methods for the relaxation processes introduced in Section 4.1.4.1 and 4.1.4.2, we propose to use the Rosenbrock scheme for the whole dynamical system 4.30. As previously remarked, the discretization of the mean curvature $\overline{H}$ requires the neighbouring cells and an implicit treatment of the source terms would then result in an integration solver coupling the whole computational domain. To avoid such a computational expense, we propose to choose a Rosenbrock scheme where we integrate implicitly the source term on $\overline{\alpha_1}$, and explicitly all the other source terms including a discretized mean curvature. The relaxed state $\boldsymbol{q}^{rel}$ is then the asymptotic state for the fictitious time $\tau \to +\infty$ of (4.30) and initial state $\boldsymbol{q}^0$. Following the chosen implicit-explicit time integration, and defining the function of the Laplace pressure equilibrium at the continuous,

$$\mathcal{F}(\alpha_1\rho_1, \alpha_2\rho_2, \overline{\alpha}_1, \alpha^d_1) := (1-\alpha^d_1)\left(p_1\left(\frac{\alpha_1\rho_1}{\overline{\alpha}_1(1-\alpha^d_1)}\right) - p_2\left(\frac{\alpha_2\rho_2}{(1-\overline{\alpha}_1)(1-\alpha^d_1)}\right) - \sigma\overline{H}(\boldsymbol{\nabla}\overline{\alpha}_1)\right), \tag{4.31}$$

the discretization in fictitious time writes in all computational cells

$$\begin{cases} (\alpha_1\rho_1)^{k+1} - (\alpha_1\rho_1)^k = -\dfrac{\Delta\tau}{\mu}\dfrac{\rho_1^k\sigma}{\overline{\alpha}_2^k}(\Delta H)^k, \\ (\alpha_1^d\rho_1^d)^{k+1} - (\alpha_1^d\rho_1^d)^k = \dfrac{\Delta\tau}{\mu}\dfrac{\rho_1\sigma}{\overline{\alpha}_2}(\Delta H)^k, \\ (\alpha_2\rho_2)^k = (\alpha_2\rho_2)^0, \\ (\alpha_1^d)^{k+1} - (\alpha_1^d)^k = \dfrac{\Delta\tau}{\mu}\dfrac{\rho_1\sigma}{\overline{\alpha}_2\rho_1^d}(\Delta H)^k, \\ \Sigma^{k+1} - \Sigma^k = \dfrac{\Delta\tau}{\mu}\dfrac{S_{avg}}{m_{avg}}\dfrac{\rho_1\sigma}{\overline{\alpha}_2}(\Delta H)^k, \\ \overline{\alpha}_1^{k+1} - \overline{\alpha}_1^k = \dfrac{\Delta\tau}{\mu}\dfrac{1}{1-(\alpha_1^d)^k}\Big(\mathcal{F}^k + (\overline{\alpha}_1^{k+1} - \overline{\alpha}_1^k)(\partial_{\overline{\alpha}_1}\mathcal{F})^k \\ \qquad\qquad + ((\alpha_1\rho_1)^{k+1} - (\alpha_1\rho_1)^k)(\partial_{(\alpha_1\rho_1)}\mathcal{F})^k + ((\alpha_1^d)^{k+1} - (\alpha_1^d)^k)(\partial_{(\alpha_1^d)}\mathcal{F})^k\Big), \\ (\rho\boldsymbol{u})^{k+1} - (\rho\boldsymbol{u})^k = -\dfrac{\Delta\tau}{\mu}\left(\dfrac{3}{\kappa\rho_1^d}\dfrac{\rho_1^k}{\overline{\alpha}_2^k} - \dfrac{1}{1-(\alpha_1^d)^k} + \left(p_2^k - p_1^k\right)\dfrac{h^k}{\sigma H_{lim}^k}\right)\sigma H_{lim}^k\dfrac{(\boldsymbol{u}^k)}{(\boldsymbol{u}^k)^2}\sigma(\Delta H)^k, \end{cases} \tag{4.32}$$

where

$$\rho_1^k := \frac{(\alpha_1\rho_1)^k}{\overline{\alpha}_1^k(1-(\alpha_1^d)^k)}, \qquad \overline{\alpha}_2^k := 1 - \overline{\alpha}_1^k, \qquad \boldsymbol{u}^k := \frac{(\rho\boldsymbol{u})^k}{(\alpha_1\rho_1)^k + (\alpha_2\rho_2)^k + (\alpha_1^d\rho_1^d)^k}, \tag{4.33}$$

and with the initial condition $\boldsymbol{q}^0 = \boldsymbol{q}^{cap}$. Remark that all the terms in (4.32) are evaluated in the same computational cell except the mean curvature difference ΔH, which depends on the neighbouring cells. For readability purpose, we now omit to write the update formula of $(\alpha_1^d\rho_1^d)$ and Σ, which are expressed straightforwardly from $(\alpha_1^d)^{k+1}$. After some manipulations, the update for $\overline{\alpha}_1$ reads

$$\overline{\alpha}_1^{k+1} - \overline{\alpha}_1^k = \frac{\frac{\Delta\tau}{\mu}\frac{1}{1-(\alpha_1^d)^k}}{1 - \frac{\Delta\tau}{\mu}\frac{1}{1-(\alpha_1^d)^k}(\partial_{\overline{\alpha}_1}\mathcal{F})^k}\left(\mathcal{F}^k - \frac{\Delta\tau}{\mu}\frac{\rho_1^k\sigma}{\overline{\alpha}_2^k}(\Delta H)^k\left((\partial_{(\alpha_1\rho_1)}\mathcal{F})^k + \frac{\Delta\tau}{\mu}\frac{1}{\rho_1^d}(\partial_{(\alpha_1^d)}\mathcal{F})^k\right)\right). \tag{4.34}$$

4.1.4.4 Relaxation restricted to admissible states

Furthermore, we want to enforce stability conditions for $\rho\boldsymbol{u}$, $\alpha_1\rho_1$, α_1^d and $\overline{\alpha}_1$, by keeping the updated values in their respective admissible set during the relaxation process. These set are $(0,1)$ for $\overline{\alpha}_1$, α_1^d, $\mathbb{R}^+$ for $\alpha_1\rho_1$ and such that $\rho\boldsymbol{u}\cdot\boldsymbol{u} \geq 0$ for $\rho\boldsymbol{u}$.

We proceed by introducing $0 < \lambda < 1$ close to 1 to ensure that the next iteration $\overline{\alpha}_1^{k+1}$ does not get closer than a fraction λ of the distance that separated it from the boundaries of $[0,1]$.

For the constraint on $\rho\boldsymbol{u}$, this yields the two following conditions

$$\frac{3}{\kappa\rho_1^d}\frac{\rho_1^k}{\overline{\alpha}_2^k} - \frac{1}{1-(\alpha_1^d)^k} + (p_2 - p_1)\frac{h}{\sigma H_{lim}} \geq 0, \tag{4.35}$$

and

$$(\rho\boldsymbol{u})^{k+1}\cdot\boldsymbol{u}^k \geq 0 \iff \frac{\Delta\tau}{\mu} \leq \left(\sigma(\Delta H)^k\left(\frac{3}{\kappa\rho_1^d}\frac{\rho_1^k}{\overline{\alpha}_2^k} - \frac{1}{1-(\alpha_1^d)^k} + \left(p_2^k - p_1^k\right)\frac{h^k}{\sigma H_{lim}^k}\right)\sigma H_{lim}\right)^{-1}(\rho\boldsymbol{u})^k\cdot\boldsymbol{u}^k =: \left(\frac{\Delta\tau}{\mu}\right)_{\rho\boldsymbol{u},max}. \tag{4.36}$$

For the constraint on $\alpha_1\rho_1$, we have the following condition ensuring positivity

$$(\alpha_1\rho_1)^{k+1} \geq 0 \iff \frac{\Delta\tau}{\mu} \leq (\alpha_1\rho_1)^k\left(\frac{\rho_1^k\sigma}{\overline{\alpha}_2^k}(\Delta H)^k\right)^{-1} =: \left(\frac{\Delta\tau}{\mu}\right)_{\alpha_1\rho_1,max}. \tag{4.37}$$

For the constraint on α_1^d, we ensure that it does not go beyond 1 (in practice, we actually expect it to remain small compared to 1). It yields

$$(\alpha_1^d)^{k+1} - (\alpha_1^d)^k \leq \lambda(1-(\alpha_1^d)^k) \iff \frac{\Delta\tau}{\mu} \leq \lambda(1-(\alpha_1^d)^k)\left(\frac{\rho_1^k\sigma}{\overline{\alpha}_2^k\rho_1^d}(\Delta H)^k\right)^{-1} =: \left(\frac{\Delta\tau}{\mu}\right)_{\alpha_1^d,max}. \tag{4.38}$$

Finally, for the constraint of $\overline{\alpha}_1$, we have the following condition,

$$-\lambda\overline{\alpha}_1^k \leq \overline{\alpha}_1^{k+1} - \overline{\alpha}_1^k \leq \lambda(1-\overline{\alpha}_1^k) \iff \left(\mathcal{P}_1\left(\frac{\Delta\tau}{\mu}\right) \leq 0 \quad \text{and} \quad \mathcal{P}_2\left(\frac{\Delta\tau}{\mu}\right) \geq 0\right), \tag{4.39}$$

with

$$\mathcal{P}_1(X) := aX^2 + b_1X + c_1, \quad \mathcal{P}_2(X) := aX^2 + b_2X + c_2, \tag{4.40}$$

and

$$\begin{gathered} a := \frac{\rho_1^k\sigma}{\overline{\alpha}_2^k(1-(\alpha_1^d)^k)}(\Delta H)^k((\rho_1^d)^{-1}(\partial_{\alpha_1^d}\mathcal{F})^k - (\partial_{\alpha_1\rho_1}\mathcal{F})^k), \quad b_1 := (1-(\alpha_1^d)^k)^{-1}(\mathcal{F}^k + \lambda\overline{\alpha}_2^k(\partial_{\overline{\alpha}_1}\mathcal{F})^k), \\ b_2 := (1-(\alpha_1^d)^k)^{-1}(\mathcal{F}^k - \lambda\overline{\alpha}_1^k(\partial_{\overline{\alpha}_1}\mathcal{F})^k), \quad c_1 := -\lambda(1-\overline{\alpha}_1^k), \quad c_2 := \lambda\overline{\alpha}_1^k. \end{gathered} \tag{4.41}$$

For the first condition $\mathcal{P}_1(\Delta\tau/\mu) \leq 0$, its validity depends on the sign of the discriminant Δ_1 of the second-order polynomial $\mathcal{P}_1$.

- If $\Delta_1 < 0$, the condition is always satisfied as $c_1 < 0$ and the stability of $\overline{\alpha}_1$ does not introduce any restriction on $\Delta\tau/\mu$;
- If $\Delta_1 > 0$, $\Delta\tau/\mu$ is restricted by either the first root of $\mathcal{P}_1$ when $a < 0$ or the second root when $a > 0$.

A similar discussion can be conducted for the second condition $\mathcal{P}_2(\Delta\tau/\mu) \geq 0$ such that one can define a maximal step ratio $(\Delta\tau/\mu)_{\overline{\alpha}_1,max}$ defined by the minimal bound enforced on $\Delta\tau/\mu$ by the two conditions of (4.39).

Indeed, the final step ratio $\Delta\tau/\mu$ to be used for the integration with respect to fictitious time (4.34) is

$$\frac{\Delta\tau}{\mu} = \min\left(\left(\frac{\Delta\tau}{\mu}\right)_{\rho\boldsymbol{u},max}, \left(\frac{\Delta\tau}{\mu}\right)_{\alpha_1\rho_1,max}, \left(\frac{\Delta\tau}{\mu}\right)_{\alpha_1^d,max}, \left(\frac{\Delta\tau}{\mu}\right)_{\overline{\alpha}_1,max}\right), \tag{4.42}$$

such that the next iteration $\boldsymbol{q}^{k+1}$ stays an admissible state, and consequently the convergence of the method is improved.

Conclusion of Section 4.1.4

We have detailed in this section an original relaxation method to solve the local Laplace equilibrium

$$p_1\left(\frac{\alpha_1\rho_1}{\overline{\alpha}_1(1-\alpha_1^d)}\right) - p_2\left(\frac{\alpha_2\rho_2}{(1-\overline{\alpha}_1)(1-\alpha_1^d)}\right) - \frac{\sigma}{1-\alpha_1^d}\overline{H}(\boldsymbol{\nabla}\overline{\alpha}_1), \tag{4.43}$$

which involves space derivatives of $\boldsymbol{\nabla}\overline{\alpha}_1$. The method relies on three ingredients: 1- the interpretation of the Newton-Raphson method as the asymptotic state of a dynamical process; 2- the use of an ImEx Rosenbrock method for DAE to extend the Newton-Raphson method in the singular perturbation limit, *i.e.* $\mu \to 0$; 3- the combination of the Rosenbrock scheme with admissibility criteria to enhance the convergence of the method. While existence criteria of the solution are not assessed, we observe in Chapter 6 that the convergence is reached and indeed regularize the large-scale interface.

In the two-scale regularizing model discussed in this section, only a simple small-scale is accounted with a spray of droplets described with two geometric quantities α_1^d and Σ as the associated realizability constraints are simply their positivity. However, when more geometric quantities are accounted for, *e.g.* the surface-average densities of curvatures, additional constraints must be fulfilled. In order to satisfy these conditions at the numerical level, we discuss in the next section a special class of numerical schemes preserving the fulfilment of such constraints: the kinetic schemes.

4.2 Numerical strategy for the transport of geometric moments

Denoting $\widehat{\xi} = (\widehat{S_0}, \widehat{\chi}, \widehat{\dot{\chi}})$, we consider the kinetic small-scale model of oscillating droplets with the velocity-dependent NDF $f_\xi(t, \boldsymbol{x}, \boldsymbol{v}, \widehat{\xi})$ which counts the droplets by their velocity $\boldsymbol{v}$, by their surface area S_0 when they are spherical, and with amplitude and its time rate of change $\widehat{\chi}$ and $\widehat{\dot{\chi}}$ as defined in Section 2.2.4. Then, we consider the mono-kinetic assumption

$$f_\xi(t, \boldsymbol{x}, \boldsymbol{v}, \widehat{\xi}) = n_\xi(t, \boldsymbol{x}, \widehat{\xi})\delta(\boldsymbol{v} - \boldsymbol{U}), \tag{4.44}$$

with $\boldsymbol{U} = \int_\xi \boldsymbol{v} f_\xi$ and the NDF $n_\xi(t, \boldsymbol{x}, \widehat{\xi})$. Moreover, we assume the limit of a vanishing Stokes number such that the average velocity of the spray is the same as the one of the carrier gaseous phase $\boldsymbol{u} = \boldsymbol{U}$. Despite this modelling simplification, we introduce an artificial interaction with the carrier fluid with a force $\frac{F_{ext}}{S_0}$ sharing the same size dependence as drag forces (O'Rourke and Amsden, 1987). The geometry dynamics is then given by the PBE (2.118) with

$$\ddot{\chi}_2 + \omega^2 \chi_2 = \frac{F_{ext}}{S_0}, \qquad \omega^2 = 8\frac{\sigma}{\rho_1^d R_0^3} = \tilde{\omega}^2 S_0^{-3/2}. \tag{4.45}$$

he dynamics of the NDF f_ξ is then

$$\partial_t f_\xi + \boldsymbol{\nabla}_{\boldsymbol{x}} \cdot (f_\xi \boldsymbol{u}) + \partial_{\widehat{\chi}}(\widehat{\dot{\chi}} f_\xi) + \partial_{\widehat{\dot{\chi}}}((-\tilde{\omega}^2 \widehat{S}_0^{-3/2}\widehat{\chi} + \frac{F_{ext}}{S_0}) f_\xi) = 0. \tag{4.46}$$

Moreover, the disperse phase is one way coupled with the carrier phase by assuming a carrier flow velocity $\boldsymbol{u}$ and the dynamics of the disperse phase to be given by the second equation of (2.50),

$$\partial_t n_\xi + \boldsymbol{\nabla}_{\boldsymbol{x}} \cdot (n_\xi \boldsymbol{u}) + \partial_{\widehat{\chi}}(\widehat{\dot{\chi}} n_\xi) + \partial_{\widehat{\dot{\chi}}}\left((-\tilde{\omega}^2 \widehat{S}_0^{-3/2}\widehat{\chi} - \frac{F_{ext}}{S_0}) n_\xi\right) = 0. \tag{4.47}$$

Following Section 2.2.4.3, we assume either a monodisperse case where n_ξ has the form

$$n_\xi(t, \boldsymbol{x}, \widehat{S_0}, \widehat{\chi}, \widehat{\dot{\chi}}) = n_1(t, \boldsymbol{x})\delta(\widehat{S_0} - (S_0)_1)\delta(\widehat{\chi} - \chi_1)\delta(\widehat{\dot{\chi}_1} - \dot{\chi}_1), \tag{4.48}$$

or a bi-disperse form

$$n_\xi(t, \boldsymbol{x}, \widehat{S_0}, \widehat{\chi}, \widehat{\dot{\chi}}) = \sum_{k=1,2} n_k(t, \boldsymbol{x})\delta(\widehat{S_0} - (S_0)_k)\delta(\widehat{\chi} - \chi_k)\delta(\widehat{\dot{\chi}_1} - \dot{\chi}_k). \tag{4.49}$$

4.2.1 The small-scale moment model

The model is built upon up either four or eight geometric quantities corresponding for as many moments of the mono-kinetic NDF gathered respectively in moment vectors $\boldsymbol{M}_{mono}$ and $\boldsymbol{M}_{poly}$ with

$$\begin{aligned} \boldsymbol{M}_{mono} &= \left(M^\xi_{0,0,0}, M^\xi_{3/2,0,0}, M^\xi_{1,1,0}, M^\xi_{1,0,1}\right), \\ \boldsymbol{M}_{poly} &= \left(M^\xi_{0,0,0}, M^\xi_{1/2,0,0}, M^\xi_{1,0,0}, M^\xi_{3/2,0,0}, M^\xi_{1/2,1,0}, M^\xi_{1/2,0,1}, M^\xi_{1,1,0}, M^\xi_{1,0,1}\right), \end{aligned} \tag{4.50}$$

respectively in bijection with $\boldsymbol{b} = \boldsymbol{b}_{mono}, \boldsymbol{b}_{poly}$ (see (2.148) and Appendices 2.Cand 2.E), the monomial vectors corresponding to the moments of the monodisperse and bi-disperse cases

$$\boldsymbol{b}_{mono} = \left(1, \widehat{S_0}^{3/2}, \widehat{S_0}\widehat{\chi}, \widehat{S_0}\widehat{\dot{\chi}}\right)^T, \quad \boldsymbol{b}_{poly} = \left(1, \widehat{S_0}^{1/2}, \widehat{S_0}, \widehat{S_0}^{3/2}, \widehat{S_0}\widehat{\chi}, \widehat{S_0}\dot{\chi}, \widehat{S_0}^{1/2}\widehat{\chi}, \widehat{S_0}^{1/2}\dot{\chi}\right)^T. \tag{4.51}$$

Integrating the geometric dynamics of (4.47) with the monomial corresponding to $\boldsymbol{M}_{mono}$ and $\boldsymbol{M}_{poly}$, and the momentum dynamics against 1 yields for the monodisperse case

$$\begin{cases} \partial_t M^\xi_{i,0,0} + \boldsymbol{\nabla} \cdot (M^\xi_{i,0,0}\boldsymbol{u}) = 0, & i = 0, 3/2, \\ \partial_t M^\xi_{1,1,0} + \boldsymbol{\nabla} \cdot (M^\xi_{1,1,0}\boldsymbol{u}) = M^\xi_{1,0,1}, \\ \partial_t M^\xi_{1,0,1} + \boldsymbol{\nabla} \cdot (M^\xi_{1,0,1}\boldsymbol{u}) = M^\xi_{1,1,0} + F_{ext} M^\xi_{0,0,0}, \end{cases} \tag{4.52}$$

and the polydisperse case

$$\begin{cases} \partial_t M^{\xi}_{i,0,0} & +\boldsymbol{\nabla}\cdot(M^{\xi}_{i,0,0}\boldsymbol{u}) & = 0, & i = 0, 1/2, 1, 3/2, \\ \partial_t M^{\xi}_{1,1,0} & +\boldsymbol{\nabla}\cdot(M^{\xi}_{1,1,0}\boldsymbol{u}) & = M^{\xi}_{1,0,1}, & \\ \partial_t M^{\xi}_{1,0,1} & +\boldsymbol{\nabla}\cdot(M^{\xi}_{1,0,1}\boldsymbol{u}) & = M^{\xi}_{1,1,0} - F_{ext} M^{\xi}_{0,0,0}, & \\ \partial_t M^{\xi}_{1/2,1,0} & +\boldsymbol{\nabla}\cdot(M^{\xi}_{1/2,1,0}\boldsymbol{u}) & = M^{\xi}_{1/2,0,1}, & \\ \partial_t M^{\xi}_{1/2,0,1} & +\boldsymbol{\nabla}\cdot(M^{\xi}_{1/2,0,1}\boldsymbol{u}) & = M^{\xi}_{1,1,0} + F_{ext} M^{\xi}_{-1/2,0,0}. & \end{cases} \tag{4.53}$$

A direct discretization of the system of equations above would probably lead to a set of updated moments which is not realizable. The kinetic schemes then offer realizable numerical schemes by taking advantage of the underlying kinetic equation.

4.2.2 Kinetic schemes to preserve realizability

In order to preserve realizability of the set of moments *i.e.* the existence of a positive distribution associated with the moments, we write a numerical scheme for these moments where the fluxes are evaluated using the advected solution of the kinetic equation. We consider a uniform discretization in one direction of space. With no loss of generality, we consider a one-dimensional problem, and the averaged moment $(M^{\xi}_{j,k,l})^n_i$ over a cell $C_i = (x_{i-1/2}, x_{i+1/2})$ at time t_n is

$$(M^{\xi}_{j,k,l})^n_i = \frac{1}{\Delta x}\int_{C_i} M^{\xi}_{j,k,l}(t_n, x)dx = \frac{1}{\Delta x}\int_{C_i\times E} \widehat{S_0}^{j}\widehat{\chi}^{k}\widehat{\dot{\chi}}^{l} f(t_n, x, v, \widehat{S_0}, \widehat{\chi}, \widehat{\dot{\chi}})dv d\widehat{S_0} d\widehat{\chi} d\widehat{\dot{\chi}} dx, \tag{4.54}$$

with the phase space $E = E_{S_0}\times E_v \times E_\chi \times E_{\dot\chi} = (0,1)\times\mathbb{R}^3$. The momentum q^n_i attributed to cell i at time t_n is

$$q^n_i = (M^{\xi}_{0,0,0})^n_i U^n_i = \frac{1}{\Delta x}\int_{C_i} M^{\xi}_{0,0,0}(t_n, x)U(t_n, x)dx = \frac{1}{\Delta x}\int_{C_i\times\mathbb{R}} U f(t_n, x, v, \widehat{S_0}, \widehat{\chi}, \widehat{\dot{\chi}})dv dx. \tag{4.55}$$

We compute the transported solution with the characteristics of the kinetic equation (4.46) with $F_{ext} = 0$ for $t \in [t_n, t_{n+1}]$ in cell C_i. Let us note that equation (4.46) can be rewritten as follows

$$(\partial_t \cdot + v\partial_x \cdot) f(t, x, v, \widehat{S_0}, (X, \dot X)(t)) = 0, \tag{4.56}$$

where $(X, \dot X)$ are defined by the ordinary differential equation (ODE) $(\dot X, \ddot X) = (\dot X, -\tilde\omega^2 \widehat{S_0}^{-3/2} X)$. Solving the ODE between t^n and t^{n+1} yields

$$\begin{pmatrix} X(t^{n+1}) \\ \dot X(t^{n+1}) \end{pmatrix} = \begin{pmatrix} \cos\left(\tilde\omega\widehat{S_0}^{-3/4}\Delta t\right) & \dfrac{\sin\left(\tilde\omega\widehat{S_0}^{-3/4}\Delta t\right)}{\tilde\omega\widehat{S_0}^{-3/4}} \\ -\tilde\omega\widehat{S_0}^{-3/4}\sin\left(\tilde\omega\widehat{S_0}^{-3/4}\Delta t\right) & \cos\left(\tilde\omega\widehat{S_0}^{-3/4}\Delta t\right) \end{pmatrix} \begin{pmatrix} X(t^n) \\ \dot X(t^n) \end{pmatrix}. \tag{4.57}$$

We end up with the following updated solution of the kinetic equation (4.46) without source term

$$\begin{aligned} f(t, x, v, \widehat{S_0}, (X, \dot X)(t)) = f\Big(t^n, x + v(t-t^n), v, \widehat{S_0}, &\widehat{\chi}\cos\left(\tilde\omega\widehat{S_0}^{-3/4}(t-t^n)\right) + \widehat{\dot\chi}\frac{\sin\left(\tilde\omega\widehat{S_0}^{-3/4}(t-t^n)\right)}{\tilde\omega\widehat{S_0}^{-3/4}}, \\ &\widehat{\dot\chi}\cos\left(\tilde\omega\widehat{S_0}^{-3/4}(t-t^n)\right) - \tilde\omega\widehat{S_0}^{-3/4}\widehat{\chi}\sin\left(\tilde\omega\widehat{S_0}^{-3/4}(t-t^n)\right)\Big). \end{aligned} \tag{4.58}$$

Here we present briefly the main steps to derive the first-order kinetic schemes for the systems (4.52) and (4.53). We use the finite volume discretization by integrating over $[t^n, t^{n+1}]\times C_i$ the kinetic equation against $\boldsymbol{b} = \boldsymbol{b}_{mono}, \boldsymbol{b}_{poly}$,

$$\boldsymbol{M}^{n+1}_i = \boldsymbol{M}^n_i - \frac{\Delta t}{\Delta x}\left(\boldsymbol{F}_{i+1/2} - \boldsymbol{F}_{i-1/2}\right), \tag{4.59}$$

where $\boldsymbol{F}_{i\pm1/2}$ are the fluxes oriented outwards at the interfaces are obtained with

$$\boldsymbol{F}_{i+1/2} \quad = \quad \frac{1}{\Delta t}\int_{t_n}^{t_{n+1}}\int_E \boldsymbol{b}(v,\widehat{S_0},\widehat{\chi},\widehat{\dot{\chi}})f(t,x_{i+1/2},v,\widehat{S_0},\widehat{\chi},\widehat{\dot{\chi}})dv d\widehat{S_0}d\widehat{\chi}d\widehat{\dot{\chi}}dt. \tag{4.60}$$

We split the fluxes in two integral parts $\boldsymbol{F}_{i+1/2} = \boldsymbol{F}^{+}_{i+1/2} + \boldsymbol{F}^{-}_{i+1/2}$ where the first corresponds to the droplet of positive velocity in x-direction. Then we use the advected solution (4.58) of the kinetic system, to express the fluxes as function of the NDF at $t = t_n$. We obtain the following expressions

$$\boldsymbol{F}^{mono,\pm}_{i+1/2} = \frac{1}{\Delta t}\int_{x_{i-1/2}}^{x_{i+1/2}} \begin{pmatrix} M^{\xi}_{0,0,0}(t_n,x) \\ M^{\xi}_{3/2,0,0}(t_n,x) \\ R_1(t_n,x)S^1_0(t_n,x) \\ M^{\xi}_{0,0,0}u(t_n,x) \end{pmatrix} \mathbb{1}_{\Sigma^{\pm}}(x)dx, \qquad \boldsymbol{F}^{poly,\pm}_{i+1/2} = \frac{1}{\Delta t}\int_{x_{i-1/2}}^{x_{i+1/2}} \begin{pmatrix} M^{\xi}_{0,0,0}(t_n,x) \\ M^{\xi}_{1/2,0,0}(t_n,x) \\ M^{\xi}_{1,0,0}(t_n,x) \\ M^{\xi}_{3/2,0,0}(t_n,x) \\ \sum\limits_{k=1,2} R_k(t_n,x)S^k_0(t_n,x) \\ \sum\limits_{k=1,2} R_k(t_n,x)(S^k_0)^{1/2}(t_n,x) \\ M^{\xi}_{0,0,0}u(t_n,x) \end{pmatrix} \mathbb{1}_{\Sigma^{\pm}}(x)dx, \tag{4.61}$$

where $\Sigma^{\pm} = \left\{x', \pm(x_{i+1/2} - \Delta t u(t_n,x')) < \pm x'\right\}$ and R_k is the rotation defined by (4.57),

$$R_k(x) = n_k \begin{pmatrix} \cos(\tilde{\omega}(S^k_0)^{-3/4}\Delta t)\chi_k - \dfrac{\sin(\tilde{\omega}(S^k_0)^{-3/4}\Delta t)}{\tilde{\omega}(S^k_0)^{-3/4}}\dot{\chi}_k \\ \tilde{\omega}(S^k_0)^{-3/4}\sin(\tilde{\omega}(S^k_0)^{-3/4}\Delta t)\chi_k + \cos(\tilde{\omega}(S^k_0)^{-3/4}\Delta t)\dot{\chi}_k \end{pmatrix}, \tag{4.62}$$

where we have written $n_k = n_k(t_n,x)$, $S^k_0 = S^k_0(t_n,x)$, $\chi_k = \chi_k(t_n,x)$, $\dot{\chi}_k = \dot{\chi}_k(t_n,x)$ for concision. Hence, following the above strategy, we obtain two kinetic finite volume schemes of first order for the moment system with a monodisperse (4.48) and a polydisperse quadrature (4.49). The numerical fluxes are defined as follows,

$$\boldsymbol{F}^{mono}_{i+1/2} \quad = \quad \begin{pmatrix} (M^{\xi}_{0,0,0})^n_i \\ (M^{\xi}_{3/2,0,0})^n_i \\ \frac{1}{\Delta t}(R'_1)^n_i(S^1_0)^n_i \\ (M^{\xi}_{0,0,0})^n_i u^n_i \end{pmatrix} \max(u^n_i,0) + \begin{pmatrix} (M^{\xi}_{0,0,0})^n_{i+1} \\ (M^{\xi}_{3/2,0,0})^n_{i+1} \\ \frac{1}{\Delta t}(R'_1)^n_i(S^1_0)^n_{i+1} \\ (M^{\xi}_{0,0,0})^n_{i+1} u^n_{i+1} \end{pmatrix} \min(u^n_{i+1},0) \ , \tag{4.63}$$

and

$$\boldsymbol{F}^{poly}_{i+1/2} = \begin{pmatrix} (M^{\xi}_{0,0,0})^n_i \\ (M^{\xi}_{1/2,0,0})^n_i \\ (M^{\xi}_{1,0,0})^n_i \\ (M^{\xi}_{3/2,0,0})^n_i \\ \frac{1}{\Delta t}\left[(R'_1)^n_i(S^1_0)^n_i + (R'_2)^n_i(S^2_0)^n_i\right] \\ \frac{1}{\Delta t}\left[(R'_1)^n_i((S^1_0)^{1/2})^n_i + (R'_2)^n_i((S^2_0)^{1/2})^n_i\right] \\ (M^{\xi}_{0,0,0})^n_i u^n_i \end{pmatrix} \max(u^n_i,0) + \begin{pmatrix} (M^{\xi}_{0,0,0})^n_{i+1} \\ (M^{\xi}_{1/2,0,0})^n_{i+1} \\ (M^{\xi}_{1,0,0})^n_{i+1} \\ (M^{\xi}_{3/2,0,0})^n_{i+1} \\ \frac{1}{\Delta t}(R'_1)^n_{i+1}(S^1_0)^n_{i+1} + (R'_2)^n_{i+1}(S^2_0)^n_i \\ \frac{1}{\Delta t}(R'_1)^n_{i+1}((S^1_0)^{1/2})^n_{i+1} + (R'_2)^n_{i+1}((S^2_0)^{1/2})^n_{i+1} \\ (M^{\xi}_{0,0,0})^n_{i+1} u^n_{i+1} \end{pmatrix} \min(u^n_{i+1},0), \tag{4.64}$$

where the rotation R'_k is given by

$$(R'_k)^n_i = n_k \begin{pmatrix} \dfrac{\sin(\tilde{\omega}(S^k_0)^{-3/4}\Delta t)}{\tilde{\omega}(S^k_0)^{-3/4}}\chi_k + \dfrac{\cos(\tilde{\omega}(S^k_0)\Delta t) - 1}{\tilde{\omega}^2(S^k_0)^{-3/2}}\dot{\chi}_k \\ \dfrac{\sin(\tilde{\omega}(S^k_0)^{-3/4}\Delta t)}{\tilde{\omega}(S^k_0)^{-3/4}}\chi_k - \left(\cos(\tilde{\omega}(S^k_0)^{-3/4}\Delta t) - 1\right)\dot{\chi}_k \end{pmatrix}, \tag{4.65}$$

with the weights and abscissa evaluated at time t^n and cell C_i. The kinetic finite-volume schemes for respectively the monodisperse and bi-disperse model write

$$\boldsymbol{M}^n_{mono,i} = \begin{pmatrix} (M^{\xi}_{0,0,0})^n_i \\ (M^{\xi}_{3/2,0,0})^n_i \\ (R'_1)^n_i (S^1_0)^n_i \\ (M^{\xi}_{0,0,0})^n_i u^n_i \end{pmatrix} - \frac{\Delta t}{\Delta x}\left(\boldsymbol{F}^{mono}_{i+1/2} - \boldsymbol{F}^{mono}_{i-1/2}\right) + \Delta t \begin{pmatrix} 0 \\ 0 \\ 0 \\ F_{ext}(M^{\xi}_{0,0,0})^n_i \\ 0 \end{pmatrix}, \tag{4.66}$$

and

$$\boldsymbol{M}^n_{poly,i} = \begin{pmatrix} (M^{\xi}_{0,0,0})^n_i \\ (M^{\xi}_{1/2,0,0})^n_i \\ (M^{\xi}_{1,0,0})^n_i \\ (M^{\xi}_{3/2,0,0})^n_i \\ (R'_1)^n_i (S^1_0)^n_i + (R'_2)^n_i (S^2_0)^n_i \\ (R'_1)^n_i ((S^1_0)^{1/2})^n_i + (R'_2)^n_{i+1} ((S^2_0)^{1/2})^n_i \\ (M^{\xi}_{0,0,0})^n_i u^n_i \end{pmatrix} - \frac{\Delta t}{\Delta x}\left(\boldsymbol{F}^{poly}_{i+1/2} - \boldsymbol{F}^{poly}_{i-1/2}\right) + \Delta t \begin{pmatrix} 0 \\ 0 \\ 0 \\ F_{ext}(M^{\xi}_{0,0,0})^n_i \\ 0 \\ F_{ext}(M^{\xi}_{-1/2,0,0})^n_i \\ 0 \end{pmatrix}. \tag{4.67}$$

Remark that, except for the source term, these two updating formula results of rotations R'_1 and R'_1 and a convex combination of a set of moments of cells C_{i-1}, C_i and C_{i+1}. As the moment space associated with the size distribution is convex (Schmüdgen, 2017), the updating formulas keep the size moments in their corresponding convex moment space. Finally, the source terms act on the moments $M^{\xi}_{1,0,1}$ and $M^{\xi}_{1/2,0,1}$ but are not subject to any restriction if the ones on sizes are satisfied. Indeed, if the moments related to size only $M^{\xi}_{0,0,0}$, $M^{\xi}_{1/2,0,0}$, $M^{\xi}_{1,0,0}$, $M^{\xi}_{3/2,0,0}$ are realizable for the size distribution, one can reconstruct a quadrature distribution on the full distribution following the quadratures (2.148) and Appendix 2.C without any further restrictions. Thus, a realizable set of moments is obtained at time t^n and makes the schemes realizable under the CFL condition $\Delta t \leq \Delta x$. The numerical scheme can also be showed to preserve the oscillation energy if no source term is accounted for, this will be numerically assessed in Section 5.4. Note that a second-order extension of this scheme can be found in Ait-Ameur et al. (2024).

Remark also that the update of the moment vector at time t^{n+1} depends directly on the weights n_i and abscissas $(S_0)_i, \chi_i, \dot{\chi}_i, i = 1, 2$ defined by (4.49) at time t^n, and the moment $M^{\xi}_{-1/2,0,0}$ which is closed with the same weights and abscissas. The calculation of n_i and $(S_0)_i, i = 1, 2$ only depending on the monodisperse of polydisperse closure are respectively found in (2.148) and Appendix 2.C, and in Appendix 2.E.

Conclusion of chapter 4

We have detailed in this chapter numerical methods adapted to the specificities of the models derived in this manuscript, namely sets of conservation laws, additional equilibrium equations and dynamics of sets of moments. This chapter included the following contributions :

- A Godunov method for the hyperbolic fluxes of the two-scale model with small-scale liquid inclusions;
- A dynamical interpretation of the relaxation process;
- An efficient implicit-explicit procedure to solve the relaxation towards an equilibrium involving space derivatives;
- A realizability-preserving kinetic scheme for the small scale of polydisperse oscillating droplets.

We have proposed numerical schemes for two-scale models, with a time splitting procedure where sub-systems are successively integrated in time. This method allows dealing with systems with simpler structures, namely a convective-related sub-system, a capillarity-related sub-system and a relaxation sub-system. The hyperbolicity and the knowledge of the eigen-structure of the convection-related part of the two-scale model allows us to build a Godunov method

for the convective-related sub-system and an extension at second order. The evaluation of the capillarity flux is here approximated with arithmetic averages as in Schmidmayer et al. (2017); Cordesse (2020). Then, a new procedure has been introduced to solve the algebraic equation given by a local Laplace pressure equilibrium. For usual pressure relaxation, a simple Newton-Raphson procedure is sufficient to solve the pressure equilibrium. However, the presence of space derivatives in the Laplace pressure jump couple all the space domain at the discretized level with the same procedure. Therefore, we propose to interpret the Newton-Raphson procedure as the solution of a dynamical system integrated with a Rosenbrock method with respect to fictitious time. To avoid the growth of the computational cost, we specifically choose to integrate explicitly the source terms involving the discretization of space derivatives. We identify stability conditions, similarly as a Newton-Raphson combined with a bisection method, that keep the intermediary states in an admissible range during the relaxation procedure. Finally, we have derived a realizable kinetic scheme for the small-scale model with a spray of oscillating droplets. This integration approach relies on the exact solution of the kinetic equation and involves here both a material advection in space and a rotation in the phase space of the oscillation motions.

Appendix

4.A Solution of the Riemann problem

We detail here the computational method to evaluate the flux at the interface between two cells, arbitrarily called "left" and "right" and denoted with the indexes L and R. We consider the x-axis oriented in the direction of the interface. For the considered Godunov method, we recall that the fluxes at the interface are evaluated using the solution $\boldsymbol{q}$ of the Riemann problem

$$\begin{cases} \partial_t \boldsymbol{q} + \boldsymbol{\nabla} \cdot \boldsymbol{F}(\boldsymbol{q}) = 0, \\ \boldsymbol{q}(x,0) = \begin{cases} \boldsymbol{q}_L & \text{if } x < 0, \\ \boldsymbol{q}_R & \text{if } x > 0, \end{cases} \end{cases} \tag{4.68}$$

with $\boldsymbol{q} = (\rho\overline{\alpha}_1, \alpha_1\rho_1, \alpha_2\rho_2, \alpha_1^d\rho_1^d, \alpha_1^d, \rho u_x, \rho u_y)$. Given the self-similar nature of the solution, we denote $\tilde{\boldsymbol{q}}(x/t) = \boldsymbol{q}(x,t)$ for $t > 0$, and the interface flux is evaluated as $\boldsymbol{F}(\tilde{\boldsymbol{q}}(0))$. The solution of this Riemann problem with linearized barotropic EOS is an extension of the work proposed by (Chanteperdrix et al., 2002). Indeed, the model presented in their work is recovered when $\alpha_1^d \to 0$, and the structure of the eigenvalues is the same with two truly non-linear waves of velocity $u_x \pm c_F^d$, and additional linearly degenerate fields to the material velocity u_x.

Given the structure of the eigenvalues and eigenvectors, the solution of this problem is self-similar with three waves denoted from left to right in the usual $x-t$ plane as the 1-wave, the discontinuity wave, and the 3-wave. They separate the $x-t$ plane in four regions:

- the left state $\boldsymbol{q}_L$ at the left of the 1-wave,
- the left star-state $\boldsymbol{q}_L^*$ between the 1-wave and the discontinuity wave,
- the left star-state $\boldsymbol{q}_R^*$ between the discontinuity wave and the 3-wave,
- the right state $\boldsymbol{q}_R$ at the right of the 3-wave.

From the Rankine-Hugoniot conditions, one can demonstrate that the normal velocity u_x and the pressure $\overline{p}$ are constant across the discontinuity wave. For either shocks or rarefaction waves, left and right states are both linked to their respective star regions of same velocity u_x^* and $\overline{p}^*$. We express that relation with functions f_L and f_R giving respectively the velocity of the star region from the left/right state and the pressure of the star region. The common normal velocity within the star region gives

$$f_L(p^*, \boldsymbol{q}_L) = (u_x)^* = (u_x)_R^* = f_R(p^*, \boldsymbol{q}_R). \tag{4.69}$$

For concision purposes, only the main computational procedure along with the differences are highlighted here, and the reader is referred to their work for an exhaustive discussion. We propose here to establish the expression of f_L for the 1-wave only, as the expression of f_R is similarly obtained.

Expression of f_L for a 1-shock

Let us write the Rankine-Hugoniot conditions for a 1-shock of velocity s,

$$s\left(\boldsymbol{q}_L^* - \boldsymbol{q}_L\right) = \boldsymbol{F}^{conv}(\boldsymbol{q}_L^*) - \boldsymbol{F}^{conv}(\boldsymbol{q}_L). \tag{4.70}$$

Such a shock is only valid if the Lax inequality $(u_x)_L > s > (u_x)^*$ holds. We develop and reorganize this set of equation to obtain for $q \in (\rho\overline{\alpha}_1, \alpha_1\rho_1, \alpha_2\rho_2, \alpha_1^d\rho_1^d, \alpha_1^d, \rho u_y)$

$$\left\{\begin{array}{lcll} q_L^* & = & q_L & \frac{(u_x)_L - s}{(u_x)^* - s}, \\ (\rho u_x)_L^* & = & (\rho_L u_x)_L & \frac{(u_x)_L - s}{(u_x)^* - s} + \frac{\overline{p}_L - \overline{p}_L^*}{(u_x)^* - s}. \end{array}\right. \tag{4.71}$$

From these equations, we particularly obtain that

$$(\overline{\alpha}_1)_L^* = (\overline{\alpha}_1)_L, \qquad \rho_L^* = \rho_L \frac{(u_x)_L - s}{(u_x)^* - s}, \qquad s = (u_x)_L + \frac{\overline{p}_L - \overline{p}^*}{\rho_L\left[(u_x)_L - (u_x)^*\right]}. \tag{4.72}$$

In order to get the expression of f_L for a shock, we need to express s as a function of $\overline{p}^*$ and $(u_x)^*$. We do so by using the linearized barotropic EOS and the first relation of (4.71) in the last relation of (4.72) to express $\overline{p}^*$ with s and $(u_x)^*$. Then, isolating s yields

$$s = \frac{1 - (\alpha_1^d)_L \frac{(u_x)_L}{(u_x)^*}}{1 - (\alpha_1^d)_L}(u_x)^* + \rho_L (c_F^d)_L^2 \frac{(u_x)_L - (u_x)^*}{\overline{p}_L - \overline{p}^*}. \tag{4.73}$$

Using this relation with the last relation of (4.72) finally gives

$$(u_x)^* = (u_x)_L - \sqrt{1 - (\alpha_1^d)_L}\frac{\overline{p}^* - \overline{p}_L}{\sqrt{\rho_L(\overline{p}^* - \overline{p}_L + (1 - (\alpha_1^d)_L)\rho_L(c_F^d)_L^2)}} =: f_L^{shock}(\overline{p}^*, \boldsymbol{q}_L). \tag{4.74}$$

According to the Lax inequality, this last relation is only valid for $\overline{p}^* > \overline{p}_L$.

Expression of f_L for a 1-rarefaction

Consider now a rarefaction wave connecting the state $\boldsymbol{q}_L$ and $\boldsymbol{q}_L^*$. From the Riemann invariants associated with $u_x - c_F^d$ for the barotropic linearized EOS,

$$\overline{\alpha}_1, \quad \frac{\alpha_1\rho_1}{\alpha_2\rho_2}, \quad \frac{\alpha_1^d\rho_1^d}{\alpha_1\rho_1}, \quad \frac{\Sigma}{\alpha_1\rho_1}, \quad \rho_1^d, \quad c_F^d(1-\alpha_1^d), \quad u_x + \frac{1}{2}c_F^d(1-\alpha_1^d)\log\left(\frac{(\alpha_1\rho_1)(\alpha_2\rho_2)}{(1-\alpha_1^d)^2\overline{\alpha}_1(1-\overline{\alpha}_1 8)\rho_{0,1}\rho_{0,2}}\right). \tag{4.75}$$

As these invariants are equal in state $\boldsymbol{q}_L$ and $\boldsymbol{q}_L^*$, some calculations provide for $q \in (\rho\overline{\alpha}_1, \alpha_1\rho_1, \alpha_2\rho_2, \alpha_1^d\rho_1^d, \alpha_1^d, \rho u_y)$

$$\left\{\begin{array}{lcll} q_L^* & = & q_L & \frac{1-\alpha_{d,*}^1}{(1-\alpha_{d,g}^1)}\exp\left(\frac{u_g - u^*}{c_g(1-\alpha_{d,g}^1)}\right), \\ (u_x)_L^* & = & (u_x)_L & +(c_F^d)_L(1-(\alpha_1^d)_L)\log\left(\frac{\rho_L(c_F^d)_L^2(1-(\alpha_1^d)_L)}{\overline{p}^* - \overline{p}_L + \rho_L(c_F^d)_L^2(1-(\alpha_1^d)_L)}\right) =: f_L^{raref}(\overline{p}^*, \boldsymbol{q}_L), \end{array}\right. \tag{4.76}$$

where the last relation defines the function f_L for $\overline{p}^* < \overline{p}_L$ such that $(u_x)_L < (u_x)_L^*$ Remark that we start computing the state in the star region with the component $\alpha_{d,*}^1$ thanks to the first relation of (4.76) with $q = \alpha_1^d$ and a Newton-Raphson method.

We finally define the function f_L with

$$f_L(\overline{p}^*, \boldsymbol{q}_L) = \begin{cases} f_L^{raref}(\overline{p}^*, \boldsymbol{q}_L) & \text{if } \overline{p}^* < \overline{p}_L, \\ f_L^{shock}(\overline{p}^*, \boldsymbol{q}_L) & \text{if } \overline{p}^* > \overline{p}_L. \end{cases} \tag{4.77}$$

Solution algorithm

Given the definition of f_L and assuming that we have obtained f_R similarly, we obtain the solution of the Riemann problem (4.68) by proceeding as follows:

(i) Identifying the nature of the 1-wave and 3 wave by solving in $\overline{p}$ the invariance of velocity (u_x) in the star region with a Newton-Raphson method,

$$f_L(\overline{p}, \boldsymbol{q}_L) - f_R(\overline{p}, \boldsymbol{q}_R) = 0. \tag{4.78}$$

(ii) Identifying the region where the cell interface stationary wave $x/t = 0$ belong,

(iii) Computing the state $\tilde{\boldsymbol{q}}(0)$ and the flux $\boldsymbol{F}(\tilde{\boldsymbol{q}}(0))$ with the set of relations (4.71) or (4.76).

CHAPTER 5

Verification test-cases

We implement the numerical methods provided in chapter 4 in the code Josiepy (2023)[1], the development of which was initiated during the PhD thesis of Di Battista (2021). Following good software development practices and the development guidelines of `Josiepy`, some verification test-cases are required to ensure the correctness of both the implementation and the models before investigating more complex setups. This chapter and the following also illustrate the numerical development and software implementation proposed by the author including second-order MUSCL scheme, implementation of models, numerical solution of Riemann problems and relaxation schemes. The reader interested on details about the software architecture is referred to the PhD manuscript of R. Di Battista aforementioned, the documentation and the introductory Jupyter notebooks available on the GitHub repository. These verification test-cases are the topic of this chapter. By nature, such tests only rely on the existence of either an analytical solution for the model to test the numerical schemes, or a physical solution to test both the model and the numerical schemes. We sort these tests in four groups :

- convergence order assessment of the space-time numerical schemes with one-dimensional smooth solution;
- one-dimensional exact Riemann problems;
- two-dimensional capillarity setups;
- one-dimensional setup for the small-scale model of oscillating droplets.

In Section 5.1, we assess the convergence order of MUSCL-type and Runge-Kutta schemes on the advection of a smooth profile. We also test the order convergence of the proposed scheme for the two-phase barotropic Model 4 at pressure equilibrium and without capillarity. We ensure that the pressure relaxation, solved in its instantaneous limit, actually corresponds to the Model 3 at pressure equilibrium with the right sound propagation velocity. Then, we propose successive Riemann test-cases in Section 5.2 for the barotropic Model 4 without capillarity, also solved in the instantaneous relaxation limit and the corresponding two-scale extension with an incompressible small-scale as proposed in Model 22. Two-dimensional capillarity problems are then investigated in Section 5.3 to assess the capabilities and limits of the numerical scheme. The evolution two-dimensional liquid column with either a circular shape and a square shape are studied. We conclude on the assessment of the proposed numerical strategy for the various models at play.

[1] https://github.com/hpc-maths/josiepy

5.1 Smooth test-cases

5.1.1 Scalar advection

We assess the correct implementation of the numerical methods by checking that the expected order of convergence is obtained for two numerical strategies :

- a classic first-order finite-volume scheme with an upwind flux and explicit Euler integration scheme;
- a second-order MUSCL scheme as detailed in 4.1.2 with the upwind flux and second-order Runge-Kutta integration scheme.

We consider here the one-dimensional scalar advection model of the following smooth initial condition

$$\begin{cases} \partial_t q + U\partial_x q = 0, \\ q(0,x) = e^{-\beta x^2}, \qquad \beta = 8 \text{ m}^{-2}, \end{cases} \tag{5.1}$$

in the domain $x \in (-1,1)$ m with periodic boundary conditions. This advection problem is solved for $U = 1$ m.s^{-1} for $\Delta x = 0.01$ m and a CFL condition of $CFL = 0.8$ for $t \in [0,2]$ s. Consequently, the profile is expected to travel back to its original position. The numerical solutions are compared with the exact solution in Figure 5.1.1a. Then, the convergence order is assessed from the L^2-error E_{L^2} defined for the numerical solution $(q_i)_{i=1,\dots,N}$ for N cells located at $x_i = \left(i - \frac{1}{2}\right)\Delta x$ at final time T by

$$E_{L^2}((q_i)) = \sqrt{\sum_{i=1}^{N} (q^i - q_{exa}(x_i))^2 \Delta x}. \tag{5.2}$$

The L^2-error is plotted for different mesh sizes in Figure 5.1.1b and a first-order convergence is obtained for the classic finite-volume scheme and a second-order one for the MUSCL scheme.

5.1.2 Three-equation model

We propose here to solve the 3-eq. Model 3 using the relaxation 4-eq. Model 4. We assess here first- and second-order strategies on two test-cases: a material advection and a sound propagation.

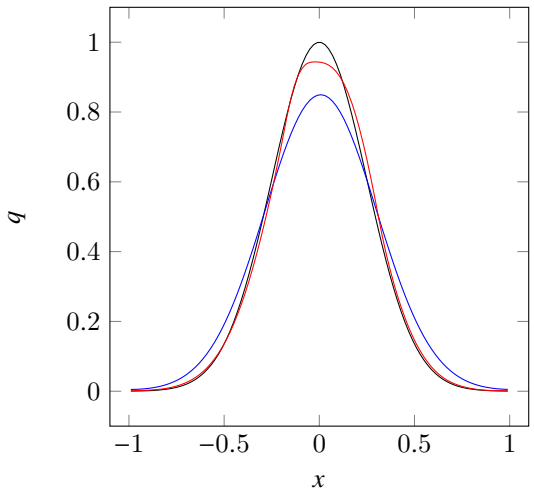

(a) Scalar advection at time $T = 2$ with a 100-cell mesh.

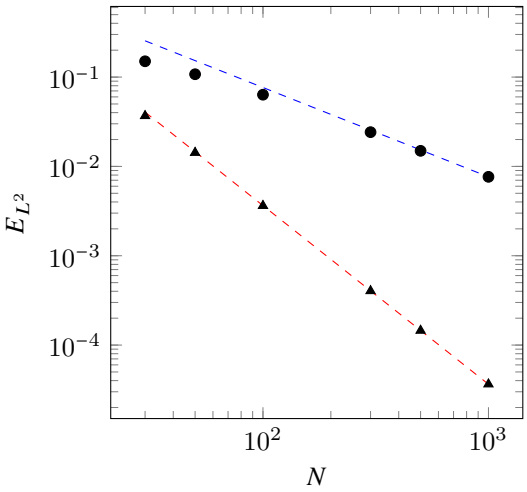

(b) L^2-error for different mesh sizes.

Figure 5.1.1: Advection problem solution with first-order upwind scheme and second-order MUSCL scheme. (a) The exact solution (——), and numerical solutions with the upwind scheme (——) and the (——). (b) Discrete L^2-error for the upwind scheme (●) and the MUSCL scheme (▲). Slopes of order 1 (- - -) and order 2 (- - -) are reported

5.1.2.1 Material advection

The multi-fluid modelling approach allows to represent the transition between two pure fluids as a smooth transition. Therefore, we consider an inclusion of fluid 1 in a fluid 2, all phases at pressure equilibrium and moving at the same velocity $U = 1$ m^{-1}. The EOS of each phase is a linearized barotropic equation of the form

$$p_k(\rho_k) = p_{0,k} + c_k^2(\rho_k - \rho_{0,k}), \tag{5.3}$$

the parameters of which are summarized in Table 5.1.1. Moreover, we follow the relaxation method detailed in Section 4.1.4, and we choose the same parameters as the one listed in (4.23). We particularly choose reference pressures and densities physically relatable with a gas-liquid density ratio at ambient pressure. However, unrealistically slow sound velocities are chosen to avoid the fast propagation of pressure perturbations in comparison with the material velocity. We consider an initial condition on the volume fraction α_1 such that it approximates a characteristic function of the

Phase	$p_{0,k}$	c_k	$\rho_{0,k}$
1	10^5 Pa	3 m.s^{-1}	10^3 kg.m^{-3}
2	10^5 Pa	1 m.s^{-1}	1 kg.m^{-3}

Table 5.1.1: Linearized EOS parameters.

interval $[-0.5, 0.5]$ in a one-dimensional periodic domain $(-1, 1)$ m with the following smooth function,

$$\alpha_1 = \begin{cases} \frac{1}{2} + \frac{1}{2}\tanh(k(x - x_L)), & \text{if} \quad x < 0, \\ \frac{1}{2} + \frac{1}{2}\tanh(-k(x - x_R)), & \text{if} \quad x \geq 0, \end{cases} \tag{5.4}$$

with $k = 20$ m^{-1}, $x_L = -0.5$ m and $x_R = 0.5$ m. The densities are initialized at equilibrium such that the pressure is p_0 everywhere. We evaluate then two numerical strategies :

- a first-order Godunov scheme based on the solution of the 4-eq. Riemann problem and an explicit Euler integration scheme followed by the relaxation step;

- a second-order MUSCL scheme based on the solution of the 4-eq. Riemann problem and second-order Runge-Kutta integration scheme with relaxation steps as described in Section 4.1.1.

We compare the two strategies with the exact solution in Figure 5.1.2.

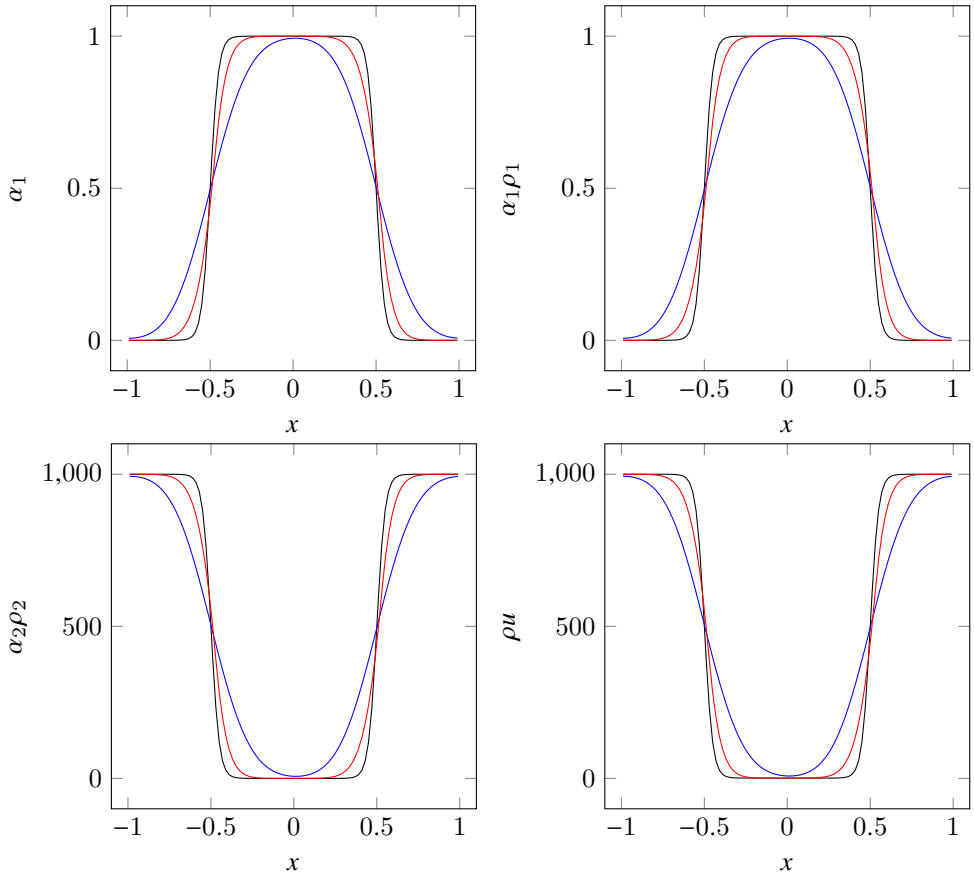

Figure 5.1.2: Material advection problem numerical solution at time $T = 2$ s and $\Delta x = 0.02$ m with first-order Godunov scheme (——) and second-order MUSCL scheme (——). The exact solution (——) is plotted for reference.

Convergence orders are measured in Figure 5.1.3 with the L^2-error defined by

$$E_{L^2}((\boldsymbol{q}_i)) = \sqrt{\sum_{i=1}^{N} (\boldsymbol{q}^i - \boldsymbol{q}_{exa}(x_i))^2 \Delta x}, \qquad \text{with} \quad \boldsymbol{q} = (\alpha_1\rho_1, \alpha_2\rho_2, \rho u). \tag{5.5}$$

5.1.2.2 Sound propagation

We consider in this test-case a homogeneous mixture of the two phases with $\alpha_1 = 0.12$ and linearized barotropic EOS (5.3), the properties of which are given in Table 5.1.2.

At initialization, there is no velocity but an initial pressure bump given by

$$p(x, 0) = p_0 + \delta p e^{-bx^2}, \qquad \delta p = 1\text{Pa}, \quad b = 80\text{m}^{-2}. \tag{5.6}$$

In Figure 5.1.4a, we compare the two strategies for $\Delta x = 0.02$ m with a quasi-exact solution obtained with the second-order strategy for $\Delta x = 0.001$ m and after a time integration of $T = 0.01$ s. Comparing the distance of the

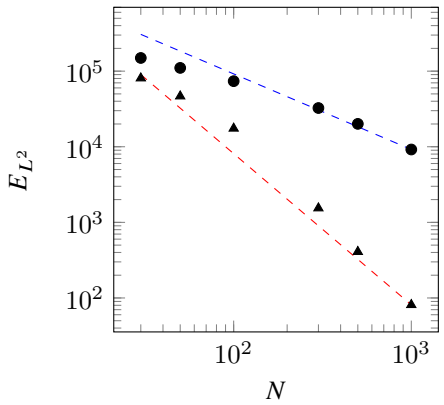

Figure 5.1.3: Order assessment, *via* L^2-error for different mesh sizes, of the Godunov scheme (●) and MUSCL scheme (▲) for a 3-eq advection problem. Slopes of order 1 (- - -) and order 2 (- - -) are plotted for comparison.

Phase	$p_{0,k}$	c_k	$\rho_{0,k}$
1	10^5 Pa	3 m.s^{-1}	1 kg.m^{-3}
2	10^5 Pa	15 m.s^{-1}	10^3 kg.m^{-3}

Table 5.1.2: Linearized EOS parameters.

local maxima from the initial maximum at $x = 0$, we observe that the initial pressure bump propagates in each direction as expected from the eigenvalues (1.105) with a measured sound velocity of 0.30 m.s^{-1}. The frozen and Wallis sound velocity for such mixture are respectively $c_F = 15$ m.s^{-1} and $c_W = 0.29$ m.s^{-1}. Thus, this measure confirms that the relaxation scheme based on the 4-eq. Model 4 indeed provides an approximation the 3-eq. Model 3. Then, the convergence order of these schemes towards the quasi-exact solution obtained with the second order scheme is assessed in Figure 5.1.4b. A first- and third-order convergence are respectively observed for the Godunov and MUSCL schemes. Such orders were expected as the quasi-exact solution is of second-order.

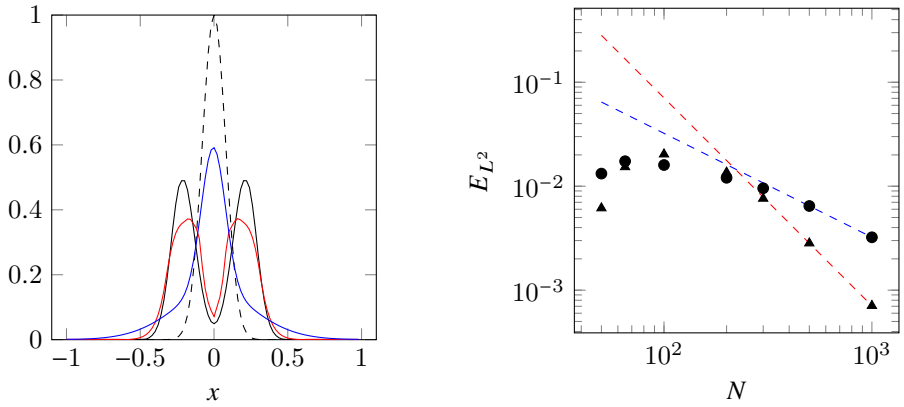

(a) Numerical solution at time $T = 0.7$s. (b) L^2-error for different mesh sizes.

Figure 5.1.4: (a) Sound propagation problem for the 3-eq. model. Pressure difference from the reference pressure p_0 for the initial pressure profile (- - -), the quasi exact one (——), the one obtained with the MUSCL scheme (——), the one obtained with the Godunov scheme (——). (b) Convergence plot of L^2-error for the Godunov scheme (●), the MUSCL scheme (▲) and reference slopes of order 1 (- - -) and 2 (- - -).

5.1.3 Two-scale three-equation model

Let us finish by assessing the properties of the two-scale Model 22 by considering a similar sound propagation test-case as one of Section 5.1.2.2. The relaxation method is set similarly as the previous section but with the pressure equilibrium of Model 22 We consider a homogeneous two-scale mixture with a large-scale volume fraction $\overline{\alpha}_1 = 0.12$ and a small-scale volume fraction $\alpha_1^d = 0.2$ with the same EOS as the ones of Table 5.1.2. The small-scale density is set to $\rho_1^d = \rho_1$. The same pressure bump as (5.6) is considered. We then compare the numerical solutions obtained with the second-order approach for $\Delta x = 0.01$m and at time $T = 0.7$s in Figure 5.1.5.

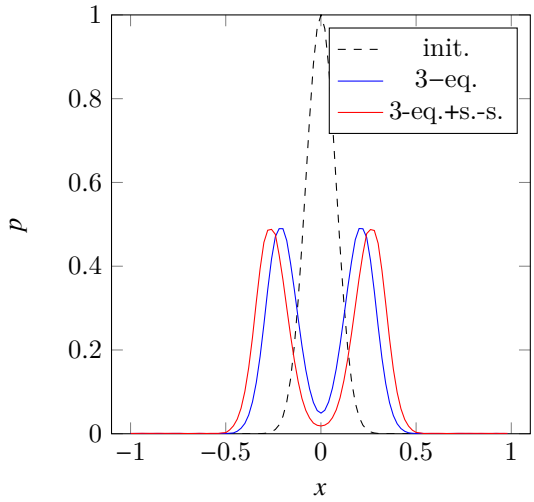

Figure 5.1.5: Sound propagation comparison at time $T = 0.7$s between the three-equation model with and without incompressible small-scale.

The theoretical sound propagation velocities are respectively $c_W = 0.29$ m.s^{-1} and $c_W^d = 0.36$ m.s^{-1} for the three-equation models without or with the small-scale phase. As expected, we graphically measure sound velocities using the position of the maxima, and we obtain sound velocities of 0.30 m.s^{-1} and 0.37 m.s^{-1}.

Conclusion of Section 5.1

In this first set of verification test-cases, we considered problems with initial smooth profiles and without apparition of discontinuities such that we can measure the convergence order of the numerical method. While the scalar advection test-case has only tested the second-order space discretization, the two following test-cases were performed on multi-fluid models with a pressure equilibrium such that the relaxation procedure is tested. We observe that the solution showcases both the expected propagation velocities of the model, including the modified velocity in the presence of a small-scale phase, and the correct convergence orders. Starting from these successful tests on smooth solutions, the next section focuses on some typical test-cases that are specific to systems of conservation laws: the Riemann problems.

5.2 Riemann test-cases

5.2.1 The three-equation model

We propose here to reproduce the Riemann problems proposed by Chanteperdrix (2004) for the Model 3. We solve these test-case with the same numerical strategy the numerical strategy which is recovered from the numerical methods for two-scale models detailed in Section 4.1 applied with α_1^d. These test-cases consist in a material discontinuity and a shock between almost pure phases. Then, for demonstrative purpose, we also propose the same test-cases for initially pure phases such that it is solved only where a mixture is locally present. This particular setup differs from the usual approach the pure phases contains a residual amount of the other phase at initialization, and a physically questionable pressure equilibrium is satisfied.

5.2.1.1 Material advection

We consider two phases endowed with barotropic linearized EOS, the parameteres of which are listed in Table 5.1.2. A Riemann problem on a domain $(0,1)$ m is then considered with respectively constant left and right states initially separated at $x_0 = 0.25$ m. The initial states are given through a primitive set of variables (α_1, ρ_1, U) given in Table 5.2.1. Remark that the density ρ_2 is necessarily equal to $\rho_{0,2}$ as pressure equilibrium is always satisfied.

Side	α_1	ρ_1	U
Left	$1-\epsilon$	1	0.15
Right	ϵ	1	0.15

Table 5.2.1: State characteristics with $\epsilon = 10^{-7}$ on each side of the material discontinuity $x_0 = 0.25$ m.

We compare the first-order and second-order approaches with the exact solution for $\Delta x = 0.02$m at integration time $T = 3.33$ s in Figure 5.2.1.

We observe that both schemes accurately solve the position of the discontinuity which moved from $x_0 = 0.25$ m to $x_F = x_0 + UT \approx 0.75$ m with a more precise profile for the second-order scheme.

5.2.1.2 Shock test

We consider now the shock test proposed in Chanteperdrix (2004) which consists in a Riemann problem on a domain $(0,1)$ m where the left and right states are separated at $x_0 = 0.3$ m and at a pressure disequilibrium of 891 Pa by considering the initial states reported in Table 5.2.2.

Side	α_1	ρ_1	U
Left	$1-\epsilon$	100	0
Right	ϵ	1	0

Table 5.2.2: State characteristics with $\epsilon = 10^{-7}$ on each side of $x_0 = 0.3$.

The numerical solution obtained with the second-order approach is compared with the exact solution in Figure 5.2.2 for $\Delta x = 0.02$ m and at integration time $T = 0.03$ s. The exact solution is computed thanks to the procedure detailed in 4.A.

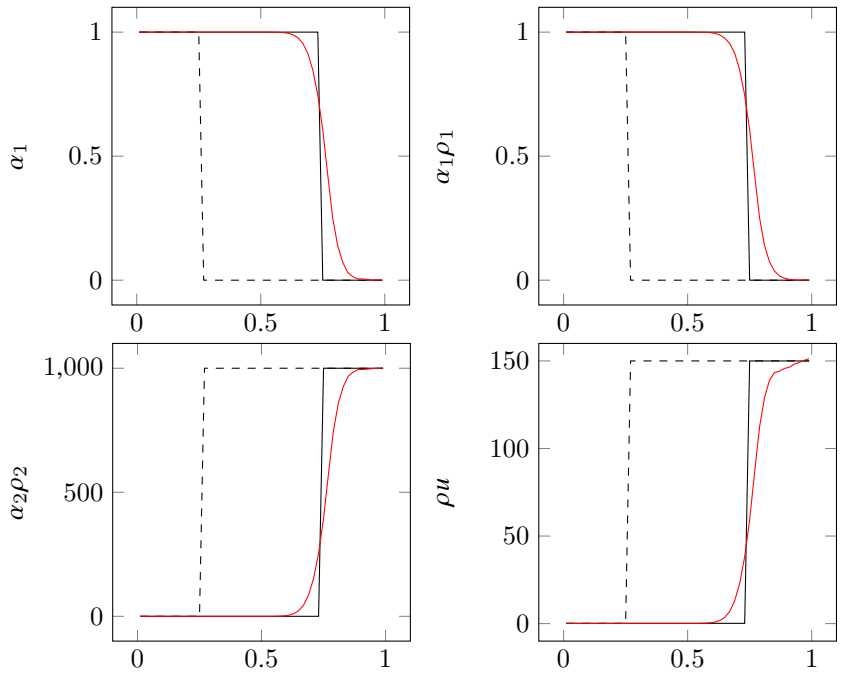

Figure 5.2.1: Material advection problem numerical solution at time $T = 3.33$ s and $\Delta x = 0.02$ m with second-order MUSCL scheme respectively for the initial condition (- - -), the exact solution (——) and the numerical solution computed with MUSCL (——).

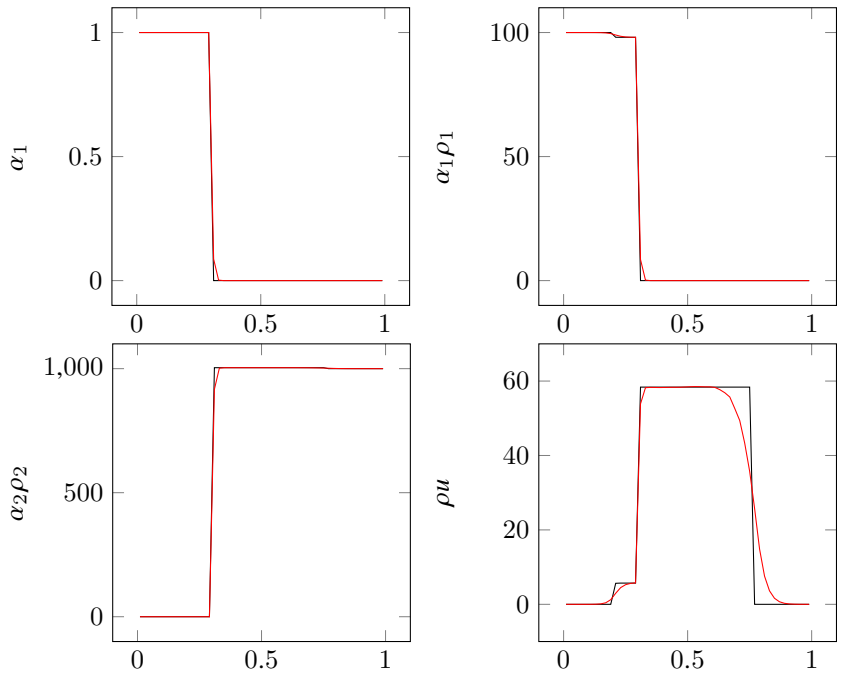

Figure 5.2.2: Shock problem numerical solution at time $T = 0.03$ s and $\Delta x = 0.02$ m with second-order MUSCL scheme respectively for the exact solution (——) and the numerical solution computed with MUSCL (——).

5.2.1.3 With pure phases

Let us now consider the same test-cases, but where the parameter ϵ is nil. Before any further discussion, let us clarify that this study only affects the initialization and the first time steps of the test-case as, with numerical diffusion, the pure phases rapidly acquire a vanishing amount of the other. Yet, this discussion is motivated by the upcoming test-cases on capillarity where the vanishing presence of volume fraction affects the computation of local mean curvature (see Section 5.3.2.2). Given that the current parameters of the discretization (4.23), the relaxation is performed for $\alpha_1 \in (10^{-14}, 1 - 10^{-14})$. With such low values, we expect the relaxation to rapidly extends to the whole domain. During this short period of time, this numerical setup can also be formally interpreted as a coupling between pure phase Euler models and a multi-fluid model at pressure equilibrium.

We respectively compare these two setups for the material advection of the discontinuity and the shock in Figures 5.2.3 and 5.2.4, by considering a residual volume fraction of $\epsilon = 10^{-7}$ as in the previous section or not. We observe no qualitative difference between the two approaches as the orders of magnitude for the volume fractions are locally the same everywhere in the domain at time T. This shows that the initialization at $\epsilon = 0$ or $\epsilon = 10^{-7}$ has no impact on these test-cases and can be considered at an initialization strategy in Section 5.3 where the delicate question of mean curvature initialization arises.

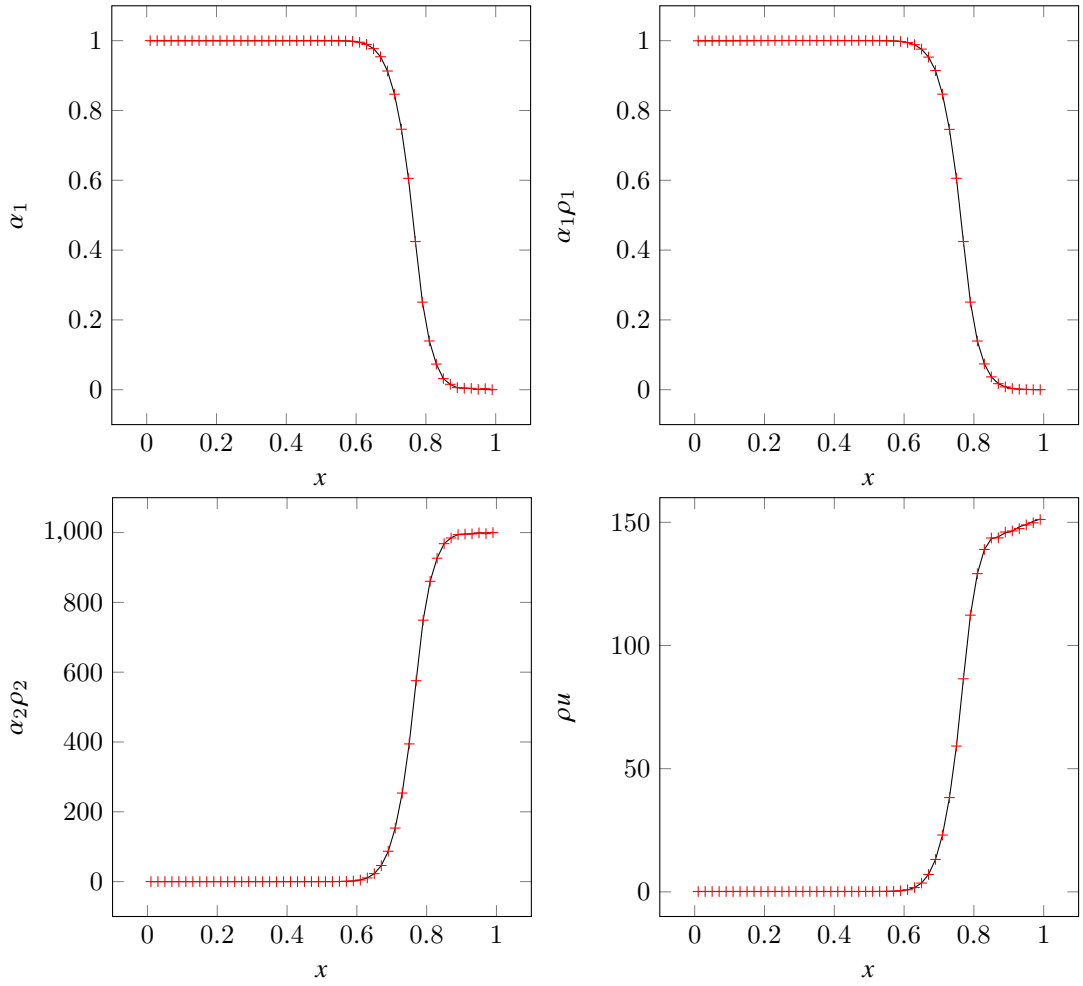

Figure 5.2.3: Material advection problem numerical solution at time $T = 3.33$ s and $\Delta x = 0.02$ m with second-order MUSCL scheme respectively for $\epsilon = 10^{-7}$ (——) and $\epsilon = 0$ (+).

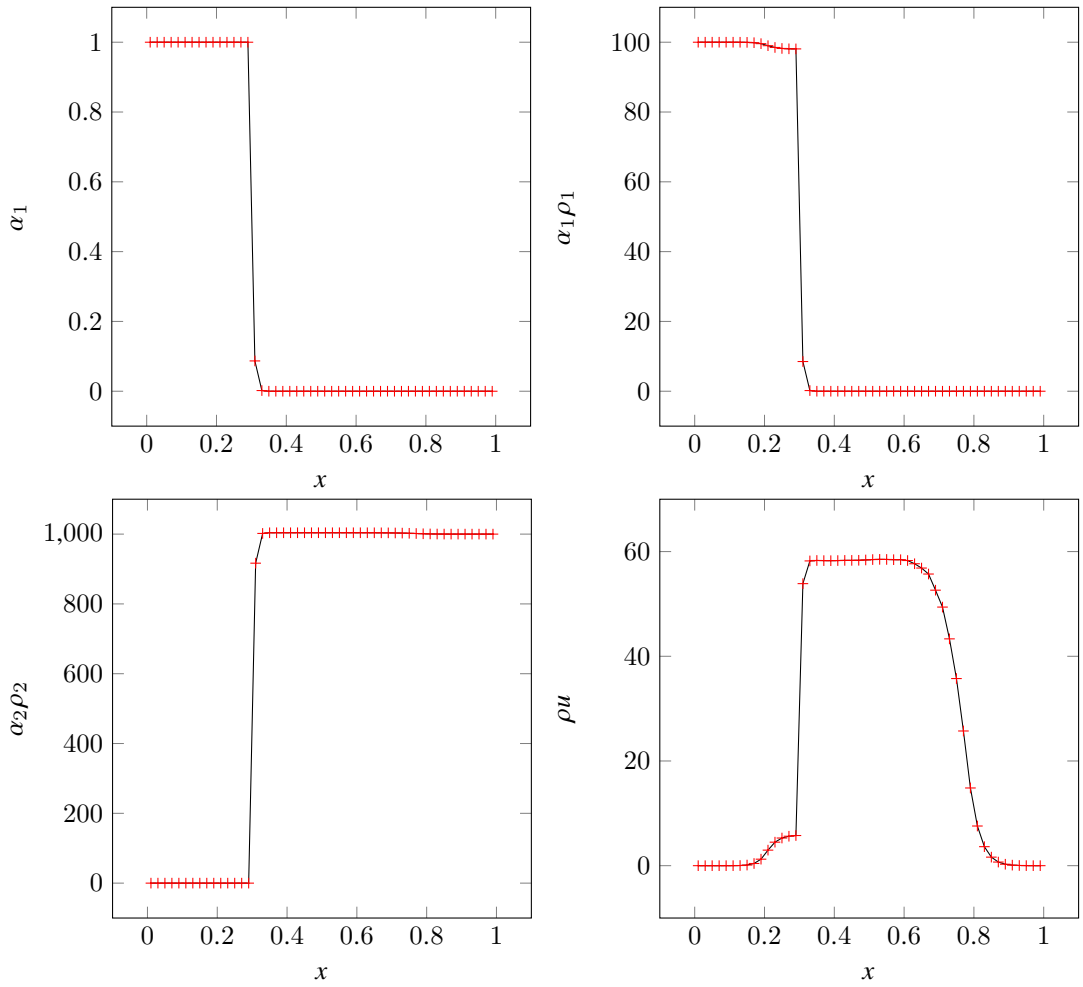

Figure 5.2.4: Shock problem numerical solution at time $T = 0.03$ s and $\Delta x = 0.02$ m with second-order MUSCL scheme respectively for $\epsilon = 10^{-7}$ (——) and $\epsilon = 0$ (+).

5.2.2 Two-scale three-equation model

We are now interested in the impact of the small-scale on the shock velocities. Therefore, we set up a similar shock test-case as the one described for the three-equation model but where the volume fraction α_1 are replaced by the large-scale volume fraction $\overline{\alpha}_1$ and with a small-scale volume fraction $\alpha_1^d = 0.2$ of density $\rho_1^d = \rho_1$. The numerical solutions for these two models are obtained following the methods of Section 4.1 and plotted in Figure 5.2.5 along with the exact solution of the two-scale model computed with the procedure provided in Appendix 4.A. We observe that the shock velocities are increased by a factor 1.25 which corresponds to the same increasing factor of $(1-\alpha_1^d)^{-1}$ obtained for sound propagation in Section 5.1.3.

Conclusion of Section 5.2

The numerical solutions of the Riemann problems presented in this section are showed very comparable to the ones obtained in Chanteperdrix (2004). This successful reproduction of the test-cases assess the correct implementation of the numerical method. Moreover, we also showed that the associated model and numerical methods extends consistently to the two-scale model with $\alpha_1^d = 0.2$ where the velocity of shocks is increased by a factor $(1-\alpha_1^d)$.

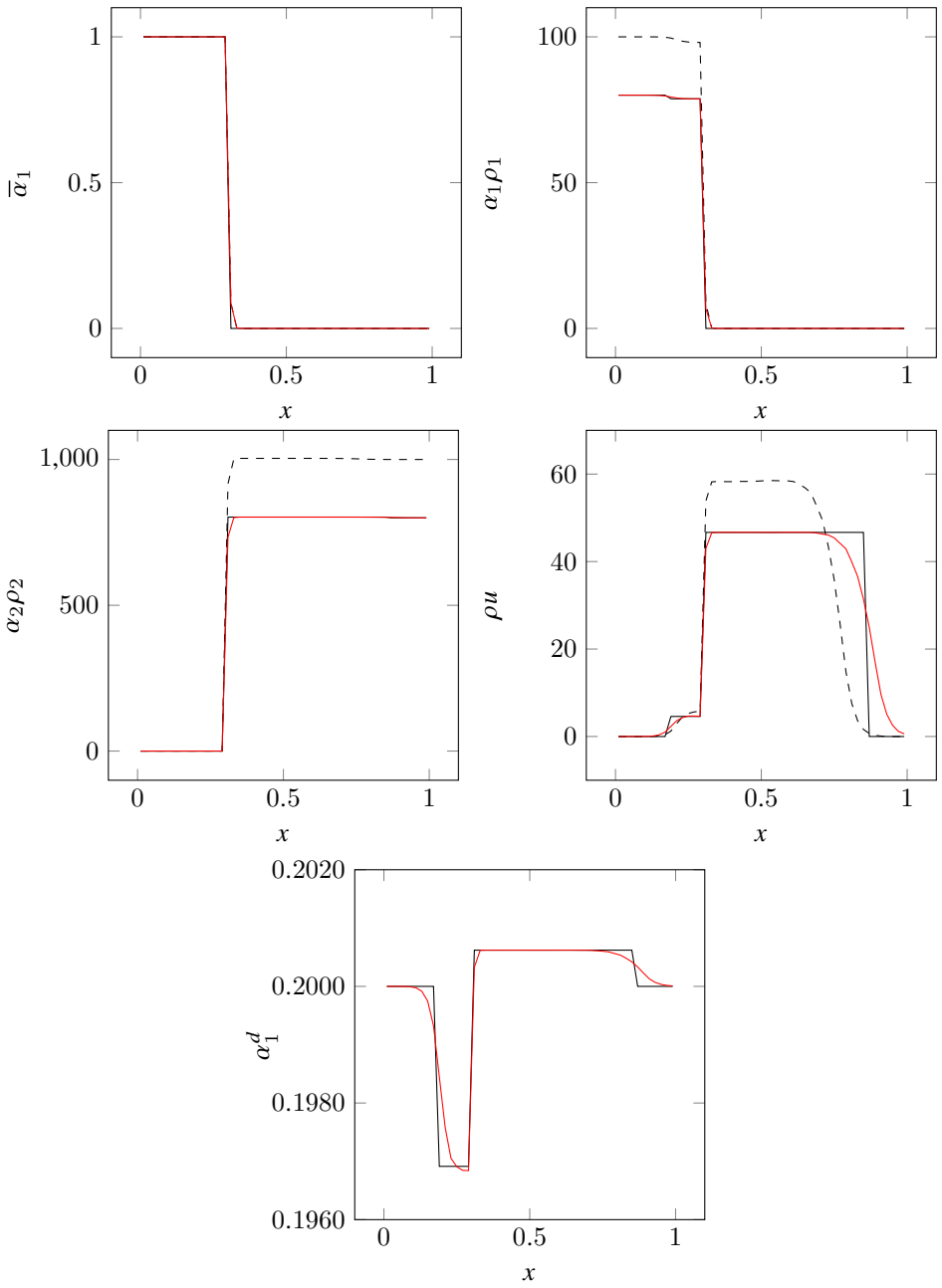

Figure 5.2.5: Comparison between the classic three-equation model (- - -) and the two-scale one on the Riemann shock problem at time $T = 0.03$ s and $\Delta x = 0.02$ m, respectively the exact solution (——) with second-order MUSCL scheme (——).

5.3 Capillarity test-cases

We consider now the numerical study of the capillarity effects as present in Models 5, 6 with gradients of the volume fraction α_1, and Models 24, 25, 30 with gradients of large-scale volume fraction $\overline{\alpha}_1$. The discretization of the capillarity fluxes is detailed in Section 4.1.3 and follows the numerical strategies proposed by Schmidmayer et al. (2017); Cordesse (2020). We assess here the general properties of capillarity trough two numerical test-cases: the global Laplace pressure jump of a two-dimensional spherical-shaped liquid column, the deformation of a square-shaped liquid column towards a spherical-shaped column.

Note that our model mainly differs from similar models of the literature (Chanteperdrix, 2004; Perigaud and Saurel, 2005; Schmidmayer et al., 2017; Cordesse, 2020) with the presence of a local Laplace law which is not neglected and solved numerically as it has a critical role in the regularization process detailed in Section 3.3. A particular emphasis is put on this particular point during the following study. In Section 5.3.1, we discuss the initialization of the first test-case with respect to the initial thickness of the diffuse interface. Then, we solve in Section 5.3.2 the oscillatory motion of the droplet pressure towards the global Laplace law following a similar setup as the one proposed in Schmidmayer et al. (2017). We pursue in Section 5.3.2.2 with a close up on the different pressure profiles when the droplet reaches the global Laplace pressure law. At the difference with the global Laplace law that is known, the local one, specific to this capillarity modelling, is not well understood at the analytical level. Indeed, the mean curvature does not degenerate well when one of the large-scale volume fraction becomes small. Finally, we consider in Section 5.3.3 the dynamics of a liquid column is initialized with a square shape, which progressively recovers a circular shape.

5.3.1 Initialization of the diffuse interface

The modelling of capillarity in Model 6 relies on the introduction of an interface area density estimator which is only defined for diffuse interface. However, no information about interface thickness can be obtained from the model. This consequently raises the question of initialization of the interface thickness at the numerical level. This question is also linked to the fact that our model differs from the one of Schmidmayer et al. (2017) through the definition of a local Laplace pressure jump

$$p_1 - p_2 = \sigma \boldsymbol{\nabla} \cdot \left(\frac{\boldsymbol{\nabla}\alpha_1}{\|\boldsymbol{\nabla}\alpha_1\|} \right) = \sigma H(\boldsymbol{\nabla}\alpha_1), \tag{5.7}$$

which requires the proper definition of $\boldsymbol{\nabla}\alpha_1$. In the regions where there are pure phases, a constant initialization of the volume fraction makes the mean curvature hardly defined as it requires to normalize the gradients of the volume fraction which is expected to be null. In order to avoid such an issue, the volume fraction in the pure phases is *initially* set to 0 or 1 respectively and the relaxation does not take place according to parameters given in 4.23 (see also the discussion in Section 5.2.1.3). Such a choice introduces an initial interface thickness which cannot be chosen arbitrary small as the mean curvature is not approximated well on a Cartesian mesh. For the test-case under consideration, we propose to initialize the volume fraction axisymmetrically using the distance r from the center of the liquid,

$$\alpha_1 = \begin{cases} 1 & \text{if} \quad r < R - \frac{\epsilon}{2}, \\ 0 & \text{if} \quad r < R + \frac{\epsilon}{2}, \\ g\left(\frac{r - R + \frac{\epsilon}{2}}{\epsilon}\right) & \text{else}, \end{cases} \qquad g(r) = \frac{1}{2} + \frac{1}{2}\tanh\left(-8\left(r - \frac{1}{2}\right)\right), \tag{5.8}$$

with ϵ the initial thickness of the interface. First, we assess the ability of the IAD estimator $\|\overline{\alpha}_1\|$ to capture the right amount of IAD depending on the mesh size and the initial thickness. We report the numerical integral of $\|\overline{\alpha}_1\|$ and compute the relative error in comparison with the IAD reference, *i.e.* the perimeter of the circle shape $2\pi R$ in two dimensions. The results are reported in Table 5.3.1.

The IAD estimator shows a very good agreement with the exact one even for coarse meshes and does not indicate a preferred initial choice o interface thickness. We propose then to study the impact of interface thickness on the mean curvature field.

In Figure 5.3.1, we plot the gradient norm of $\|\boldsymbol{\nabla}\alpha_1\|$ and $H(\boldsymbol{\nabla}\alpha_1)$ for different values of ϵ.

$\epsilon/R \setminus N$	60	80	100	120
0.6	5.1×10^{-4}	4.0×10^{-5}	6.7×10^{-5}	8.2×10^{-5}
1	6.2×10^{-4}	3.9×10^{-4}	2.5×10^{-4}	1.8×10^{-4}
1.4	7.9×10^{-4}	4.6×10^{-4}	2.9×10^{-4}	1.9×10^{-4}

Table 5.3.1: Relative errors between the estimated IAD and the exact IAD at initialization for different widths and mesh sizes $N \times N$.

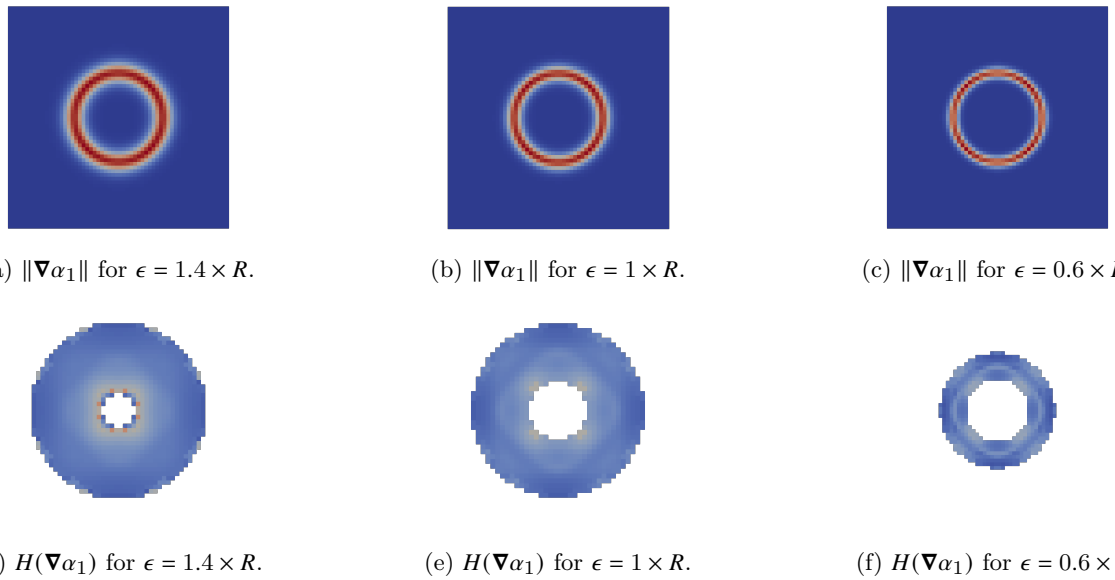

(a) $\|\boldsymbol{\nabla}\alpha_1\|$ for $\epsilon = 1.4 \times R$. (b) $\|\boldsymbol{\nabla}\alpha_1\|$ for $\epsilon = 1 \times R$. (c) $\|\boldsymbol{\nabla}\alpha_1\|$ for $\epsilon = 0.6 \times R$.

(d) $H(\boldsymbol{\nabla}\alpha_1)$ for $\epsilon = 1.4 \times R$. (e) $H(\boldsymbol{\nabla}\alpha_1)$ for $\epsilon = 1 \times R$. (f) $H(\boldsymbol{\nabla}\alpha_1)$ for $\epsilon = 0.6 \times R$.

Figure 5.3.1: Comparison of mean curvature field $H(\boldsymbol{\nabla}\alpha_1) \in (0, 30)$ m^{-1} and normalized field $\|\boldsymbol{\nabla}\alpha_1\| \in (0, 1)$ for different interface thickness ϵ on a 60×60 mesh.

We observe that the choice of a thin interface gives a non-homogeneous estimate of the mean curvature within the interface thickness. In addition to breaking the rotational invariance of the problem, it triggers unphysical pressure inhomogeneities due to the local Laplace pressure jump. Moreover, the light inhomogeneities in the field of $\|\boldsymbol{\nabla}\alpha_1\|$ also disturbs the capillarity fluxes, the intensity of which is proportional to $\|\boldsymbol{\nabla}\alpha_1\|$.

A compromise to choose the initial interface thickness is here chosen based on the following criterion : the initial width is the smaller length such that the initialization profile gives a sufficiently constant field for both $\|\boldsymbol{\nabla}\alpha_1\|$ and $H(\boldsymbol{\nabla}\alpha_1)$ in any direction. Hence, we chose the minimal initial width ϵ which provides an axisymmetric field for both $\|\boldsymbol{\nabla}\alpha_1\|$ and $H(\boldsymbol{\nabla}\alpha_1)$. In the simulations presented in the upcoming sections, we have chosen $\epsilon = 1.4 \times R$. The width of the interface could seem very large, but it has to be compared here with the chosen discretization space step. A more refine simulation would allow the use of a smaller interface initial width.

5.3.2 Relaxation of the liquid towards the Laplace pressure law

This two-dimensional test-case consists in a liquid pressure column embedded in a lighter fluid such as a gaseous phase. For comparison purposes, we implement the setup proposed by Schmidmayer et al. (2017) by considering two fluids with linearized barotropic EOS (5.3) as detailed in Table 5.3.2. However, a lower capillarity coefficient is chosen as $\sigma = 30$ N.m^{-1} due to the choice of linearized EOS and the two fluids are initially at the same pressure p_0. Considering a two-dimensional periodic domain $(0, 0.75)m \times (0, 0.75)m$, and the centered liquid column of radius $R = 0.15m$ we expect a global pressure jump of 200 Pa.

Phase k	p_0	c_0	ρ_0
1	10^5Pa	374 m.s^{-1}	1kg.m^{-3}
2	10^5Pa	48 m.s^{-1}	10^3kg.m^{-3}

Table 5.3.2: Parameters of the static column test-case.

With a space discretization of $N = 60$ cells in each direction and with a time integration of $T = 2$, the dynamics of the pressure is reported in Figure 5.3.2 at different times and goes through the following steps :

- The pressures of each phase quickly relax in the diffuse interface region to satisfy the local Laplace pressure jump $p_1 - p_2 = \sigma H(\nabla\alpha_1)$ with the mean curvature computed with the discretized gradients of α_1 (see Figure 5.3.2a);
- Pressure waves travel within the liquid column, thus generating pressure oscillations within the liquid (see Figures 5.3.2b-5.3.2c);
- The oscillatory motion stabilizes around a pressure profile corresponding to the global Laplace jump $p_{in} - p_{out} = 1/R$ for the 2D liquid column (see Figure 5.3.2d).

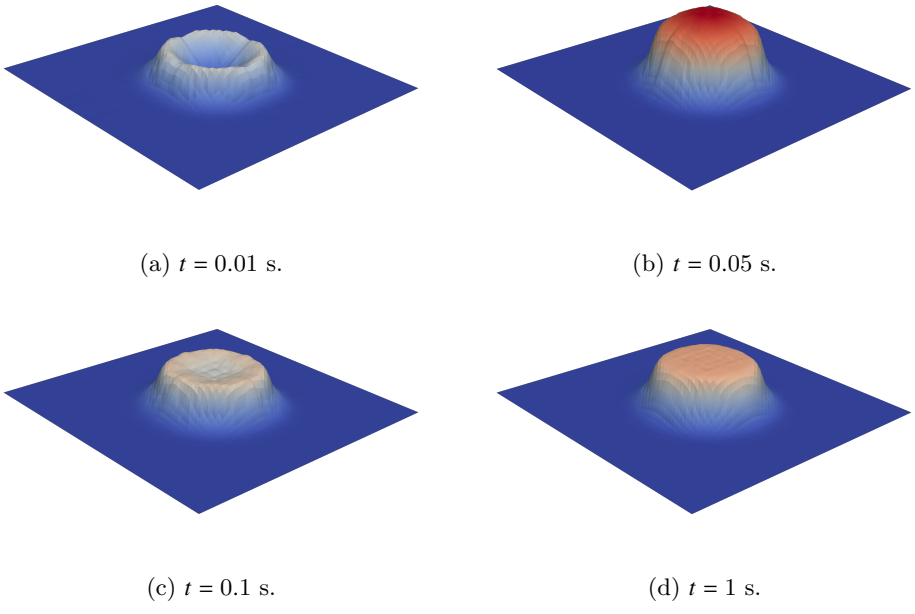

(a) $t = 0.01$ s. (b) $t = 0.05$ s.

(c) $t = 0.1$ s. (d) $t = 1$ s.

Figure 5.3.2: Pressure field $p - p_0 \in (0, 300)$ Pa (with proportional vertical deformation) during the transitional dynamics towards the global Laplace equilibrium of the liquid column.

5.3.2.1 Oscillating dynamics of the averaged pressure

Let us study the average pressure oscillatory dynamics and damping towards the global Laplace pressure jump. We define the average pressure within the droplet with

$$P_{in,avg} = \frac{\int_\Omega p \mathbb{1}_{\alpha_1 > \alpha_{int}}}{\int_\Omega \mathbb{1}_{\alpha_1 > \alpha_{int}}}, \qquad p = \alpha_1 p_1 + \alpha_2 p_2, \tag{5.9}$$

and we consider that the interior of the droplet delimited by the volume fraction threshold $\alpha_{int} = 0.99$. The outside pressure P_{ext} away from the droplet remains at the reference pressure $P_{ext} = p_0$ with rapidly damped pressure waves so that their propagation are negligible. We report in Figure 5.3.3a the evolution in time of the averaged interior pressure $P_{in,avg}$. It starts at p_0, as both pressures p_1 and p_2 are initialized at the reference pressure at the beginning. Then, it oscillates and progressively stabilizes to satisfy the expected pressure jump of 200 Pa. Denoting $P_{eq} = p_0 + \frac{\sigma}{R}$, we confirm this observation by plotting in Figure 5.3.3b the relative error towards the expected pressure jump against time. We observe that it converges to the right pressure jump with a relative error of 0.6%.

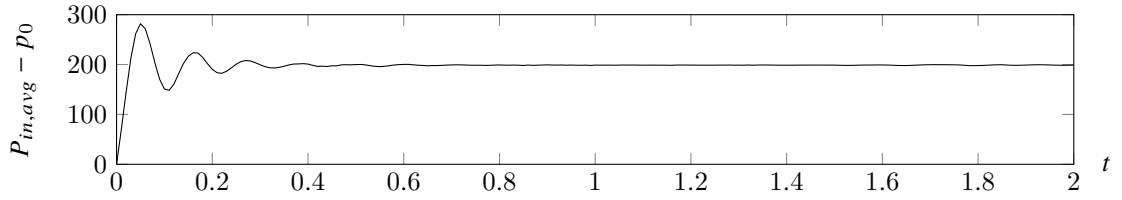

(a) Oscillatory motion of the averaged inside pressure $P_{in,avg}$.

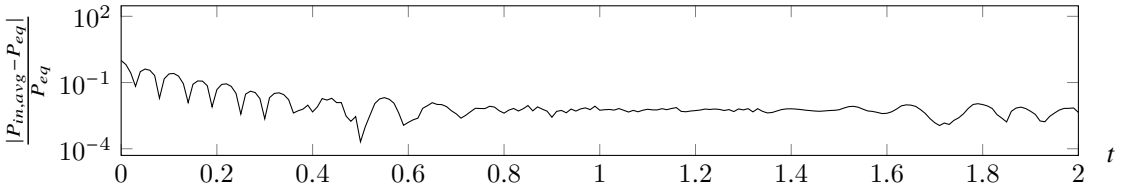

(b) Relative convergence of $P_{in,avg}$ towards the equilibrium pressure $P_{eq} = p_0 + \frac{\sigma}{R}$.

Figure 5.3.3: Pressure evolution in time towards the Laplace equilibrium.

After the equilibrium is reached, we observe that the averaged pressure becomes slightly unstable with the development of small oscillations after a longer integration time. Such behaviour has been similarly observed in Schmidmayer et al. (2017), but does not seem to be associated with spurious currents as the maximal magnitude of the velocity field is only decreasing with time (see Figure 5.3.4).

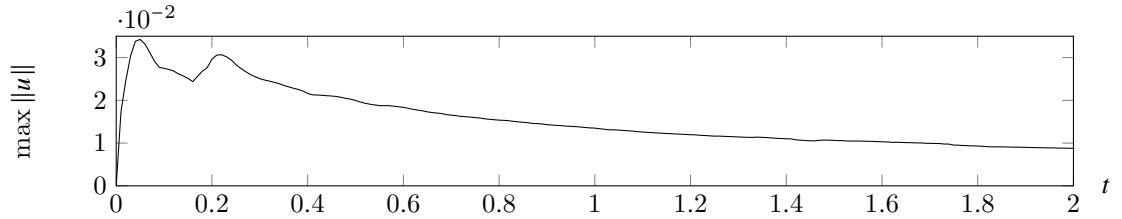

Figure 5.3.4: Evolution in time of the maximal velocity magnitude in the computational domain.

5.3.2.2 Pressure profiles and mean curvature

The capillarity model in this manuscript differs from the one of Schmidmayer et al. (2017) as it aims at satisfying two Laplace relations :

- a local one, explicitly present in the model which describes the partial pressure difference between the phases within the diffuse interface,
$$p_1 - p_2 = \sigma H(\boldsymbol{\nabla}\alpha_1); \tag{5.10}$$
- a global one which corresponds to the physical Laplace law describing the pressure jump across the interface that was numerically studied in Section 5.3.2.1,
$$P_{avg,in} - P_{ext} = \frac{\sigma}{R}. \tag{5.11}$$

While the target pressure equilibrium relation is le Laplace law (5.11), we do not know the partial pressure profiles at equilibrium for the phase pressures p_1, p_2 or the pressure of the mixture p. Such pressure profiles are plotted in Figure 5.3.5 and the corresponding mean curvature estimator is plotted in Figure 5.3.6 through the pressure-dimensioned term $\sigma H(\boldsymbol{\nabla}\alpha_1)$.

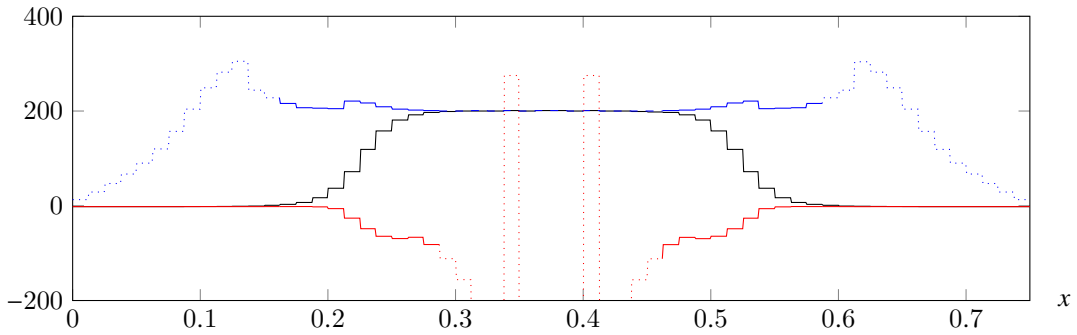

Figure 5.3.5: Profiles of pressure $p_1 - p_0$ (——/·····), $p_2 - p_0$(——/·····), $p - p_0$(——). The pressure profiles are dotted for the gaseous pressure when $\alpha_1 > 0.99$ and for the liquid phase when $\alpha < 0.01$.

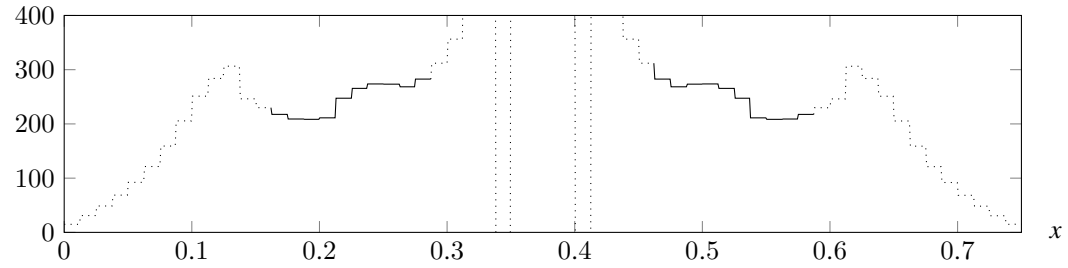

Figure 5.3.6: Profile of $\sigma H(\boldsymbol{\nabla}\alpha_1)$ in Pa. The profile is dashed when the phases are almost pure $\alpha_1 > 0.99$ and when $\alpha < 0.01$.

We observe that the local Laplace equilibrium is indeed satisfied within the interface (see the mean curvature in Figure 5.3.6 through the profile of $\sigma H(\boldsymbol{\nabla}\alpha_1)$), with a pressure difference between p_1 and p_2 that slightly decreases following the mean curvature profile when going from the inner side of the interface to the outer side. The behaviour of the partial pressure in a region where its respective phase has almost vanished cannot be considered as physically relevant as the mean curvature estimate is no longer reasonably accurate. Remark that the equilibrium profiles are rather complex to analyse and conjecturing its form is difficult.

5.3.3 Relaxation of a square column

In order to further confirm the validity of the capillarity model and numerical scheme, we propose to consider a modified version of the test presented in the previous section, but with an initial square shape. Then, we expect that our capillarity model to bring the liquid column back to a circular shape. With an initialization out of the circular shape equilibrium, the liquid column is expected to oscillate similarly to the oscillating droplet problem discussed in Section 2.2.4. However, with numerical diffusion, such oscillatory motion is damped and converge to the circular equilibrium shape. Snapshots of the pressure field with a three-dimensional deformation of the mesh illustrates such dynamics in Figure 5.3.7. Right after the beginning of the simulation, we observe that they are pressure peaks coming from the corners of the column. They result from the local Laplace law pressure equilibrium as the corners have very large mean curvatures despite the smoothing of the interface. As a consequence of the intensity of these initial peaks, the pressure waves travel for a longer time within the liquid column than for the circular-shaped column (see Figure 5.3.2) but a global pressure equilibrium is eventually reached within the liquid column. The volume fraction field is also provided in Figure 5.3.8. We indeed observe that the shape of liquid column slightly oscillates before reaching its equilibrium circular shape.

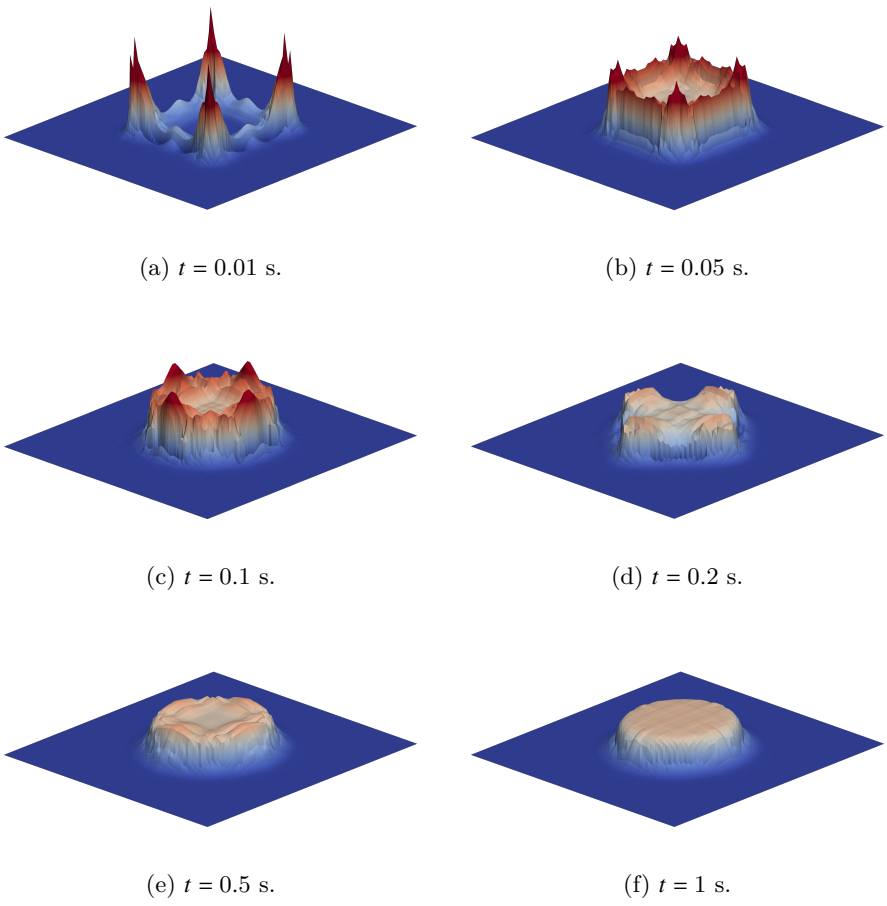

(a) $t = 0.01$ s. (b) $t = 0.05$ s.

(c) $t = 0.1$ s. (d) $t = 0.2$ s.

(e) $t = 0.5$ s. (f) $t = 1$ s.

Figure 5.3.7: Pressure field $p - p_0 \in (0, 300)$ Pa (with proportional vertical deformation) during the transitional dynamics towards the global Laplace equilibrium of the liquid column initialized with a square shape.

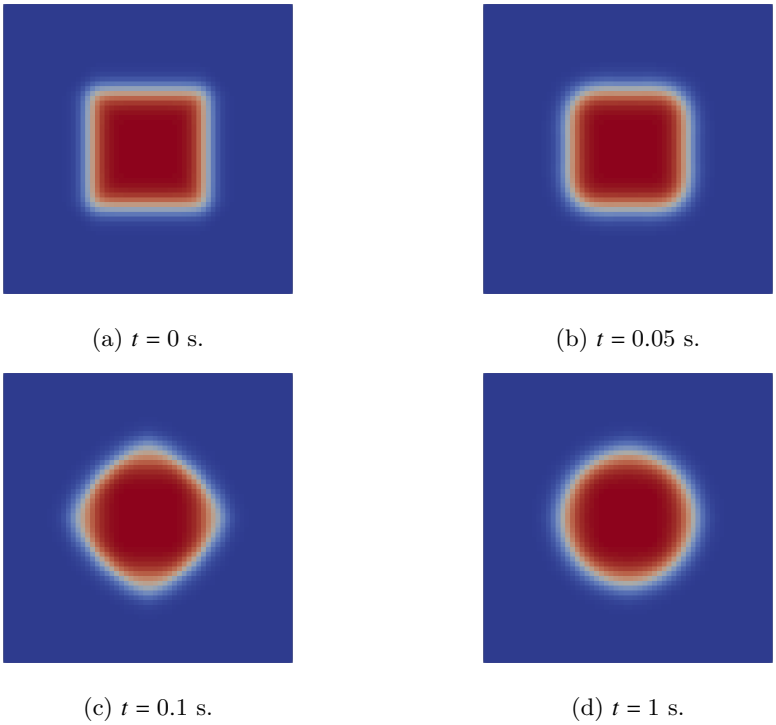

(a) $t = 0$ s. (b) $t = 0.05$ s.

(c) $t = 0.1$ s. (d) $t = 1$ s.

Figure 5.3.8: Volume fraction field $\alpha_1 \in (0, 1)$ during the transitional dynamics towards the global Laplace equilibrium of the liquid column.

Conclusion of Section 5.3

These simple test-cases have showed that the capillarity model has indeed the correct physical behaviour with both the capture of global Laplace pressure jump and the surface minimization of a given shape towards the circular shape, in two-dimension test-cases. We have also investigated the particular local Laplace pressure jump in this model within the diffuse interface. Remark that satisfying the local pressure jump between the pressures of the two phases requires a sufficiently good estimation of mean curvature and therefore a relatively thick initialization of the interface to recover the rotational invariance on a Cartesian mesh. We can then conclude that the modelling of capillarity will be accurate at the largest scales of the simulation, but not at the smallest scales. Such a property is not an issue for the two-scale simulation further presented in 6 as a regularization process purposely introduces a third scale, with the mean curvature threshold H_{max} between the large-scale of the bulk and the under-resolved small scale, such that it transfers these small scales to a small-scale model. In this small-scale model, the interface dynamics is no longer resolved at the bulk scale, but follows a dynamics described by handful scalar quantities that carry information about the subscale interface geometry. The simulation of such model is the subject of the following section.

5.4 Harmonic oscillation of the spray of droplets

In this section, we consider the small-scale model of oscillating droplet presented in Section 4.2. We consider here a simple test-case for verification purposes which consists in the advection at velocity $\boldsymbol{u} = 1$ m.s^{-1} of a spray of oscillating droplets without any forcing term. Each size of droplet in the spray defines a population of droplets whose dynamics follows the equation of a harmonic oscillator. We assess the correctness of the model and the numerical schemes with respect to the energy conservation property. Indeed, the proposed kinetic scheme is expected to preserve the oscillation energy as its construction is based on the method of characteristics. We consider here two subcases: a monodisperse one defined by the moments $\boldsymbol{M}_{mono}$ of (4.50) and a bi-disperse one defined by the moments $\boldsymbol{M}_{poly}$ of (4.50). The spray is localized in the region $\mathcal{D}_{init} := (0.25, 0.75)$ m of the one-dimensional computational domain $\mathcal{D} = (0, 2)$ m with the following initialization :

- for the monodisperse case, for $x \in \mathcal{D}$,

$$\begin{cases} M^{\xi}_{0,0,0}(x,0) & = \mathbb{1}_{\mathcal{D}_{init}}(x), \\ M^{\xi}_{3/2,0,0}(x,0) & = \mathbb{1}_{\mathcal{D}_{init}}(x), \\ M^{\xi}_{1,1,0}(x,0) & = 0, \\ M^{\xi}_{1,0,1}(x,0) & = \mathbb{1}_{\mathcal{D}_{init}}(x), \end{cases} \tag{5.12}$$

- for the polydisperse case, for $x \in \mathcal{D}$,

$$\begin{cases} M^{\xi}_{i,0,0}(x,0) & = (i+1)^{-1}\, \mathbb{1}_{\mathcal{D}_{init}}(x), \quad i = 0, 1/2, 1, 3/2 \\ M^{\xi}_{1/2,1,0}(x,0) & = 0, \\ M^{\xi}_{1/2,0,1}(x,0) & = \mathbb{1}_{\mathcal{D}_{init}}(x), \\ M^{\xi}_{1,1,0}(x,0) & = 0, \\ M^{\xi}_{1,0,1}(x,0) & = \mathbb{1}_{\mathcal{D}_{init}}(x). \end{cases} \tag{5.13}$$

The kinetic energy due to the oscillation is defined by setting $\tilde{\omega} = 4$ (respectively $\tilde{\omega} = 2$) for the mono-disperse (respectively poly-disperse) case. The domain $\mathcal{D}$ is discretized with 400 cells and the CFL is equal to 0.9 in all the simulations.

We assess the conservation of total energy over many periods by following in time an advected cell of the spray. The total energy of the monodisperse case and polydisperse case respectively reads

$$\begin{aligned} E^{mono} &= \underbrace{\frac{1}{2\tilde{\omega}^2} n_1 (S_0)_1^{5/2} \dot{\xi}_1^2}_{E^{mono}_{kin}} + \underbrace{\frac{1}{2} n_1 (S_0)_1 + \frac{1}{2} n_1 (S_0)_1 \xi_1^2}_{E^{mono}_{pot}}, \\ E^{poly} &= \underbrace{\sum_{k=1,2} \frac{1}{2\tilde{\omega}^2} n_k (S_0)_k^{5/2} \dot{\xi}_k^2}_{E^{poly}_{kin}} + \underbrace{\frac{1}{2} n_k (S_0)_k + \frac{1}{2} n_k (S_0)_k \xi_k^2}_{E^{poly}_{pot}}. \end{aligned} \tag{5.14}$$

In Figures 5.4.1-5.4.2, we plot the evolution in time of the kinetic, potential and total energies in one advected cell of the domain. We see that the first order kinetic scheme indeed preserves the total energy of the harmonic oscillator over many periods. For the bi-disperse quadrature, two droplets populations are considered where each population is expected to oscillate at a different frequency, that depends on size. Let us note that in the bi-disperse spray, the initial condition gives initial size ratio of 0.42 and an initial total energy ratio of 7.5×10^{-3} between the two populations of droplets. Therefore, we only see a single oscillatory dynamics for the bi-disperse test-case.

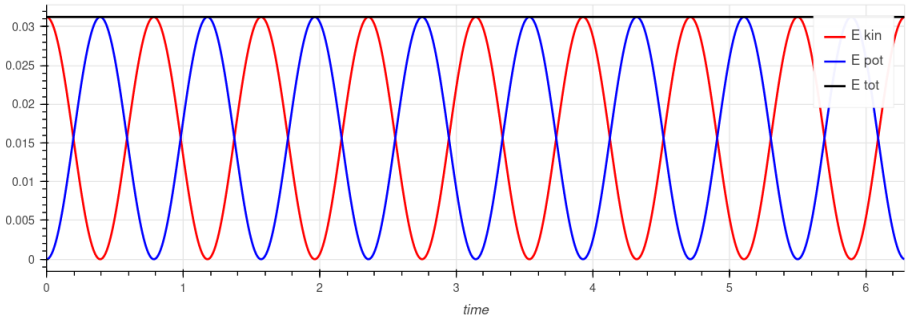

Figure 5.4.1: Evolution in time of the kinetic, potential and total energies in one advected cell of the domain: harmonic oscillator case, monodisperse quadrature. Mesh size $\Delta x = \Delta x = 5 \cdot 10^{-3}$ m. Final time $T = 2\pi$ s.

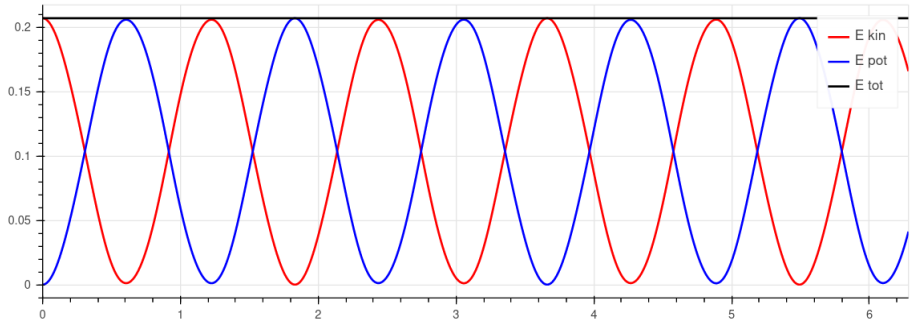

Figure 5.4.2: Evolution in time of the kinetic, potential and total energies E^{poly} of the two populations in one advected cell of the domain: harmonic oscillator, bi-disperse quadrature. Mesh size $\Delta x = 5 \cdot 10^{-3}$ m. Final time $T = 2\pi$ s.

Conclusion of chapter 5

In this chapter, we demonstrated the validity of the implementation of the numerical schemes presented in Chapter 4, namely :

- the MUSCL extrapolation method combined with the Runge-Kutta integrator are showed to provide a second-order method for smooth solutions of the convection-related systems;
- the sound propagation velocities are recovered for the systems at pressure equilibrium thanks to relaxation methods and the expected increasing of sound velocities is observed in the presence of incompressible small-scale;
- the Riemann problems are accurately solved for classic two-phase and two-phase two-scale models;
- the dynamics induced by capillarity is assessed while satisfying both a global and local Laplace pressure law;
- the total energy of oscillation is conserved thanks to a kinetic scheme for the advection of oscillating droplets.

The verification test-cases presented in this chapter both assess the correct implementation of the numerical methods and show the limits of what can be solved in the upcoming numerical experiments. For advection problems of smooth solutions, the implementation of the numerical scheme is tested by convergence tests and evaluating their convergence rate. The Riemann problems showed the right capture of exact entropy solutions for advection- and shock-type test

cases, with and without an incompressible small-scale. Then, the numerical scheme related to the capillarity effects is tested against the capillarity-driven evolution of a circular-shaped liquid column in two dimensions. Both the circular shape and the global pressure jump across the interface are showed to be recovered as an equilibrium setup. Moreover, the pressures within the diffuse interface layer are showed to satisfy a local Laplace pressure law that requires a relatively thick interface in comparison to the mesh discretization. Indeed, the local pressure law includes the local mean curvature estimator which requires a smooth transition of the volume fraction to correctly estimates the local mean curvature of the interface. Consequently, this study of capillarity unsurprisingly reveals that the proper capillarity behaviour are more accurate at the largest scales rather than the smallest. The simulation, involving a two-scale test-case, proposed in the next chapter is not strongly affected by this issue as the under-resolved interface is regularized.

CHAPTER 6

Simulations

In this final chapter, we propose to assess the properties of two models which encompass to the most original contributions of this work towards the simulation of a full atomization. A first demonstrative test-case is proposed to illustrate the inter-scale coupling, capillarity modelling and its regularization properties as presented in Chapter 3. It consists in an air-blasted liquid column at high Weber number and offers a simple test-case with multiscale interface behaviour similar to shear-stripping observed for droplets (see Figure 6.0.1). At the scale of a unique droplet, a transition from a separated phase towards a fully disperse one is observed and makes the use of a two-scale approach very relevant. A second demonstrative test-case illustrates the advection and dynamics of the geometric quantities associated with a spray of oscillating droplets undergoing size-dependent source terms.

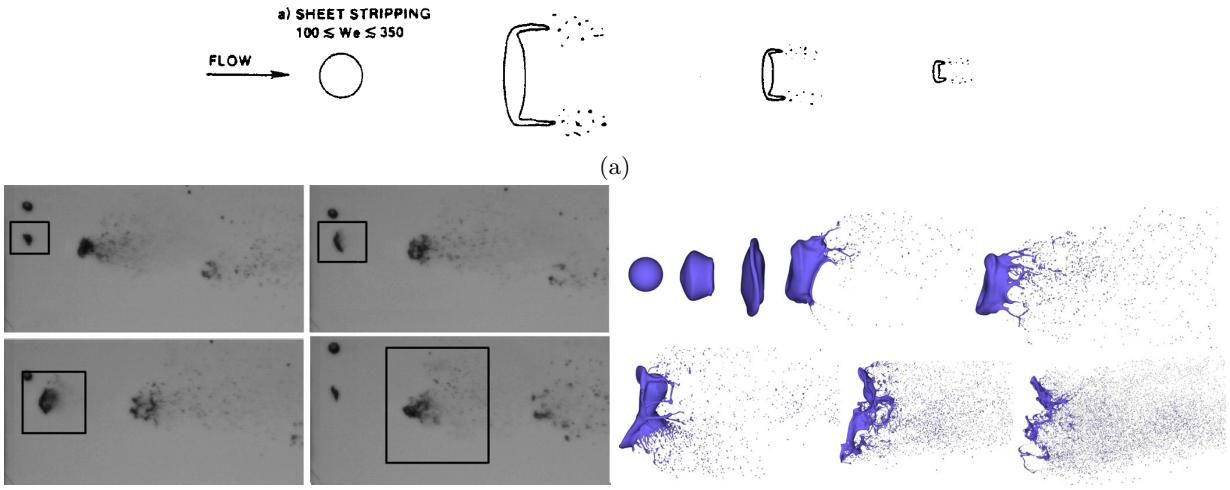

(a)

(b) (c)

Figure 6.0.1: (a) Schematic view of *sheet stripping* atomization of a droplet from Pilch and Erdman (1987). (b) Experimental pictures and (c) simulations (from left to right and top to bottom) of an air-blasted droplet (squared in the picture) with $We = 120$ (Jain et al., 2015) with the solver `Gerris` (Popinet, 2003).

These two test-cases demonstrate original key features to tackle a full atomization test-case: 1- the transition from the separated regime to the disperse regime while keeping track of key geometric quantities, and consequently capillarity energy, 2- the complex dynamics of geometric quantities of a spray of droplets deformed, for instance as a result of primary atomization or because of a velocity differential with the carrying phase.

The first test-case presented in Section 6.1 proposes a setup at a high Weber number where a liquid column is

embedded within a gaseous flow with a strong velocity differential. After a short period, the column deforms and is atomized after the apparition of filaments on each side of the column. It allows the apparition of small scales which are not well resolved by the multi-fluid DIM adapted to a separated regime. The test-case is therefore adequate to illustrate the regularization properties and inter-scale transfer to the small-scale disperse model of the two-scale model. Then, a second setup is investigated in Section 6.2 dealing with the advection and oscillation of a polydisperse spray of droplets within a carrier flow. Only a one-way coupled setup is investigated here by enforcing a specific velocity field for the carrier phase. Nevertheless, a size-dependent source term is added to mimic the size-dependent drag forces as modelled in O'Rourke and Amsden (1987) and enables to exhibit complex dynamics. Therefore, the model includes the main numerical challenges associated the realizability and opens the way to its use as a small scale-model in a full atomization setup.

These two contributions have addressed some critical modelling challenges associated with the global modelling of an atomization setup and a natural extension of this work would be to couple the two test-cases. Moreover, such a two-scale model would include several inter-scale parameters to model the primary break-up and this task is one of the perspective of this work.

6.1 Two-scale simulation of the deformation and atomization of a liquid column

We propose now to study the two-dimensional test-case of a liquid column deformed by an incident gaseous flow such that filaments appear on each side of the deformed column (see Figure 6.0.1) using either the separated regime Model 5 with capillarity or the two-scale Model 24. Such a test-case provides us with a curved interface involving a very large spectrum of scales: a large scale interface corresponding to the shape of the column core and a small scale for the filaments and droplets.

In Section 6.1.1 the physical and computational parameters of the test-case are detailed. A simulation without inter-scale mass transfer is proposed to underline the limits of a single-scale approach, and the different stages of the simulation are identified in terms of the large-scale interface regime and geometry. Section 6.1.2 then tackles the same test-case with the inter-scale transfer. The threshold length-scale is chosen to keep the large-scale dynamics, and both the mass and IAD transfers to small-scale are quantitatively discussed in comparison with the case without inter-scale transfer. Finally, a comparison with a simulation of higher fidelity is proposed in Section 6.1.3. It allows the illustration of how the parameters of the inter-scale mass transfer can be tuned to reproduce an experimental data, or in this case, a high fidelity simulation. Note that the simulations presented in this chapter, except the high fidelity simulation, rely on the numerical schemes detailed in Chapter 4 and implemented with the open-source finite-volume solver Josiepy (2023).

6.1.1 Description of the test-case and simulation without inter-scale transfer

We consider a two-dimensional 4×2 m^2 domain $\mathcal{D}$ filled with a gaseous phase (denoted by the subscript 2) and a liquid column of circular section of radius $R = 0.15$ m and located at the position $C = (1, 1)$ m. The fluids are given a linearized barotropic EOS: $p(\rho) = p_0 + c_0^2(\rho - \rho_0)$, the parameters of which are listed in Table 6.1.1. The capillarity coefficient is set at $1 \cdot 10^{-2}$ N.m^{-1}. With an impacting gas velocity of 6.66 m.s^{-1}, the Weber and Mach numbers are $We = 665$ and $Ma = 0.66$, thus the flow compressibility must not be neglected. The parameters of the model have been purposely chosen such that the time needed for the deformation of the column is comparable with the one of advection throughout the domain. A liquid water/air density ratio has been chosen to mimic the inertia effects of a liquid droplet in a gas, but the sound velocities involved in the barotropic EOS are strongly decreased to mitigate the computational cost of the fast propagation of shock waves. Nevertheless, this test-case presents all the ingredients to illustrate the inter-scale mass transfer and its curvature-limitation properties. We distinguish then

Phase	p_0	c_0	ρ_0
1	10^5 Pa	10 m.s^{-1}	10^3 kg.m^{-3}
2	10^5 Pa	10 m.s^{-1}	1 kg.m^{-3}

Table 6.1.1: Parameters of the fluids' barotropic linearized EOS.

three areas : the gaseous area (G), the liquid area (L) and the mixture area (M) resulting from a smoothening of the interface of thickness $R/5$. The location of these areas along with the initialization parameters are summarized in Table 6.1.2. An inlet boundary condition enforces the initial state of region (G) on the left side of the domain

Area	Location	$\overline{\alpha}_1$	p_1	p_2	u_x	u_y	α_1^d	Σ
(G)	$\mathcal{D} \setminus \mathcal{B}_C(R + R/5)$	0	NaN	p_0	6.66 m.s^{-1}	0 m.s^{-1}	0	0 m^{-1}
(L)	$\mathcal{B}_C(R)$	1	$p_0 + \sigma/R$	NaN	0 m.s^{-1}	0 m.s^{-1}	0	0 m^{-1}
(M)	$\mathcal{B}_C(R + R/5) \setminus \mathcal{B}_C(R)$	$h_{\overline{\alpha}_1}(\boldsymbol{x})$	$p_0 + \sigma\overline{H}$	p_0	$Y_1 u_{x,(\mathrm{L})} + Y_2 u_{x,(\mathrm{G})}$	0 m.s^{-1}	0	0 m^{-1}

Table 6.1.2: Initialization state for each area. $\mathcal{B}_C(r)$ denotes the ball of radius r centred in C, and $h_{\overline{\alpha}_1}$ is a smoothening function defined by $h_{\overline{\alpha}_1} : \boldsymbol{x} \mapsto \tilde{h}_{\overline{\alpha}_1}(\|\boldsymbol{x} - \boldsymbol{x}_C\|)$ with $\tilde{h}_{\overline{\alpha}_1} : \boldsymbol{x} \mapsto \exp(2x^2(x^2-3)/(x^2-1)^2)$, and the mass fractions are denoted $Y_k = \alpha_k \rho_k / \rho$.

with Dirichlet conditions on $\overline{\alpha}_1$, $\boldsymbol{u}$, α_1^d and Σ, while a homogeneous Neumann condition is set on phase pressures. An outlet boundary condition is set on the right side with a Neumann condition on all components. Top and bottom boundaries are periodic. The simulations are then performed over a time of 3 s on 400×200 cells with a CFL condition set on 0.4. The mesh is coarse, but only the large-scale dynamics has to be simulated at this stage, and further convergence in mesh refinement does not offer all the scales down to the spray as illustrated in 6.1.3. For the demonstrative purpose of this test-case, the numerical setup chosen here is sufficient to illustrate the two-scale modelling strategy. In this first test-case, the mass transfer is deactivated by choosing $H_{max} = 10^3$ m^{-1} which is an order of magnitude larger than the discretization length inverse $\Delta x^{-1} = 10^2$ m^{-1}.

The overall dynamics is showed in Fig. 6.1.1 and can be described in three successive stages:

- Stage 1: The liquid column deforms as it undergoes the upstream pressure of the incident flow between $t = 0$ s and $t = 0.25$ s. The interface is well resolved as the iso-line $\overline{\alpha}_1 = 0.5$ and the interface area estimator maxima are superposed.
- Stage 2: We observe the growth of two filaments on both the top and bottom sides of the liquid column between $t = 0.25$ s and $t = 1.25$ s. The interface is less and less well-located as we go further to the filament's extremity and the IAD estimator shows an opening at its end. This shows that the simulation is not converged enough in space discretization and the capillarity phenomena are lost at these small scales.
- Stage 3: The water column breaks in two and gets out of the simulation domain between $t = 1.25$ s and $t = 2$ s. The interface has numerically spread too much such that the liquid core of the column does not reach a volume fraction of 1.

These numerical difficulties can also be quantified through the evolution of $H_{lig} := \max(\overline{H}\mathbb{1}_C)$ defined with the criteria (3.85) that is almost always located at the end of the ligaments. Fig. 6.1.2 shows that H_{lig} quickly rises from $1/R$ as the ligaments start to grow, and it saturates at approximately 150 m^{-1} which corresponds to the scales of the space discretization length.

6.1.2 Comparison with the activated mass-transfer

In order to circumvent the challenging resolution of the filaments' growth at large-scale, we introduce now the inter-scale transfer to both regularize the large-scale interface, and model the primary atomization in the under-resolved mixed-regime region. We consider then the same initial setup as the one described in Section 6.1.1. However, we change the settings dedicated to the inter-scale mass transfer by choosing $H_{max} = 40$ m^{-1}, $\rho_1^d = 1000$ $\mathrm{kg.m}^{-3}$ and $\kappa = 1$. We expect that the curvature threshold limits the mean curvature H_{lig} while the latter pilots the amount of interface area density created when mass is transferred form large to small scales.

We propose to discuss the dynamics of this system by highlighting the impact of the two main effects of the inter-scale mass transfer: (i) the large-scale regularizing properties of the inter-scale process, (ii) the quantitative repartition of both the liquid mass and IAD between large and small scales. The following two sets of figures address each of these effects:

(i) In Figs. 6.1.4-6.1.5, we compare the dynamics at large-scale of the two cases by plotting respectively the large-scale volume fraction $\overline{\alpha}_1$ and the large-scale IAD estimator $\|\boldsymbol{\nabla}\overline{\alpha}_1\|$. In Fig. 6.1.3, we compare the evolution in time of the curvature H_{lig} to measure the regularizing impact of the inter-scale transfer.

(ii) In Fig. 6.1.7, effective densities at large scale $\alpha_1\rho_1$ and small scale $\alpha_1^d\rho_1^d$ are compared and their repartition between the two scales is plotted in time in Fig. 6.1.8. The same discussion is proposed for the IAD in Fig. 6.1.6 along with its evolution in time in Fig. 6.1.9.

6.1.2.1 Regularizing properties

Let us first observe from Figs. 6.1.4-6.1.5 that the dynamics is similar during stage 1 as the inter-scale transfer has not started yet. When the filaments begin to grow in stage 2, we see that the growth is stopped when the mass transfer is activated *via* a curvature threshold set to $H_{max} = 40$ m^{-1}. The interface is locally regularized in the sense that the under-resolved filaments, appearing when there is no mass transfer, have been transferred to the small-scale part of the model. As showed by the Fig. 6.1.3, the curvature H_{lig} is indeed limited starting from stage 2 and is almost always kept below the threshold H_{max}. We observe that the curvature goes over the limit for very few snapshots which correspond to situations where the condition C_1 is not satisfied, and then, mass transfer cannot occur despite the mean curvature higher than the threshold. This regularization also allows to "close" the interface through a non-negligible amount of interface area density $\|\boldsymbol{\nabla}\overline{\alpha}_1\|$ all around the level-set $\overline{\alpha}_1 = 0.5$ at large-scale which makes the intensity of capillarity fluxes stronger. This consequently impacts the overall dynamics, and we particularly observe that the core of the liquid column has a more compact shape.

Given the mesh resolution considered, we have a better resolution of the large-scale capillarity phenomena with the inter-scale transfer. The previously under-resolved small-scale interface dynamics is now purposely modelled with geometric quantities.

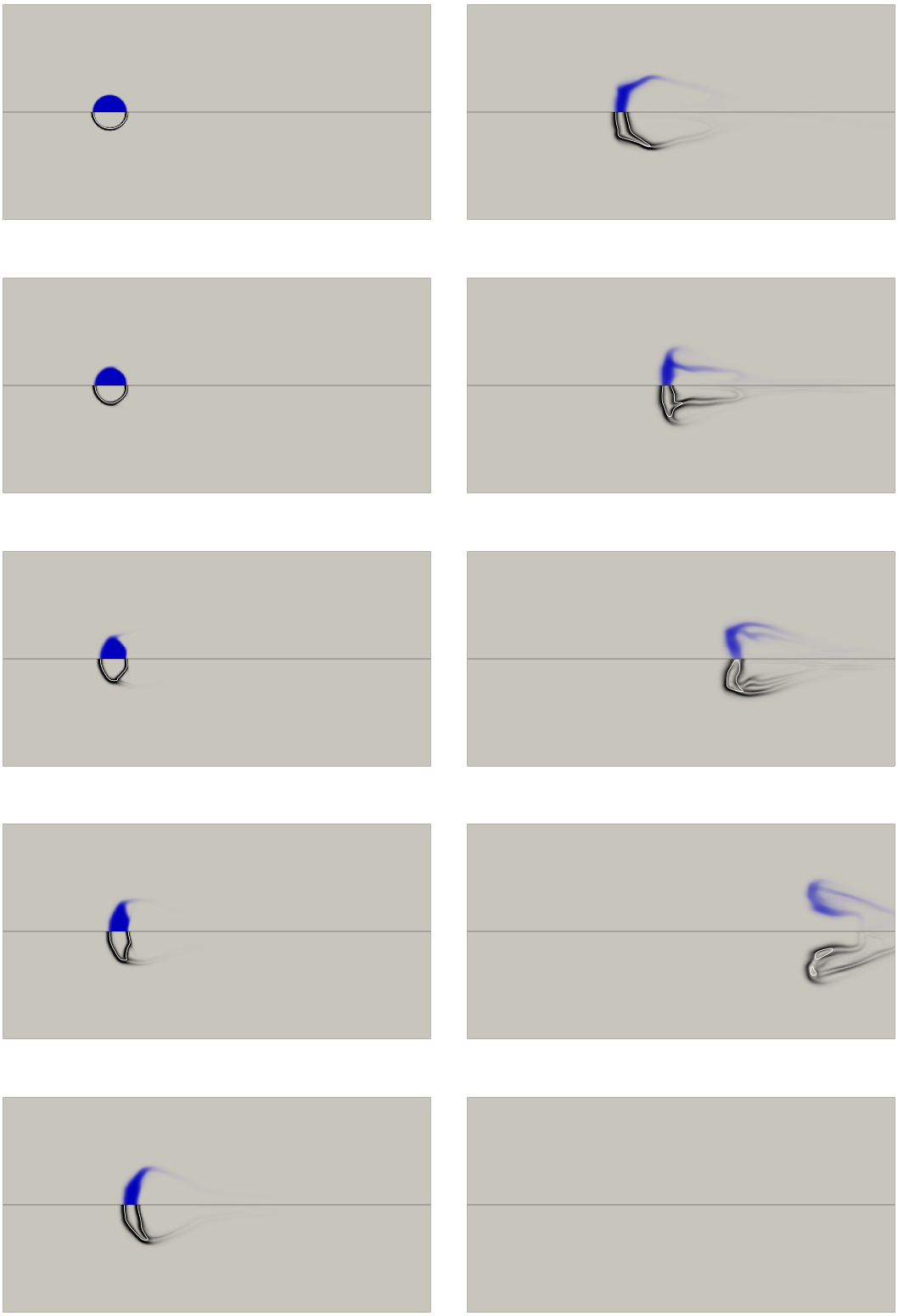

Figure 6.1.1: Liquid column deformation without inter-scale transfer. Liquid volume fraction $\overline{\alpha}_1 \in (0,1)$ (top) and estimator of the interface area density $\| \nabla \overline{\alpha}_1 \| \in (0,16)$ (bottom) with the iso-line $\overline{\alpha}_1 = 0.5$ (white, bottom). Snapshots are taken each 0.25 s from $t = 0$ s to $t = 2.5$ s from top to bottom and left to right.

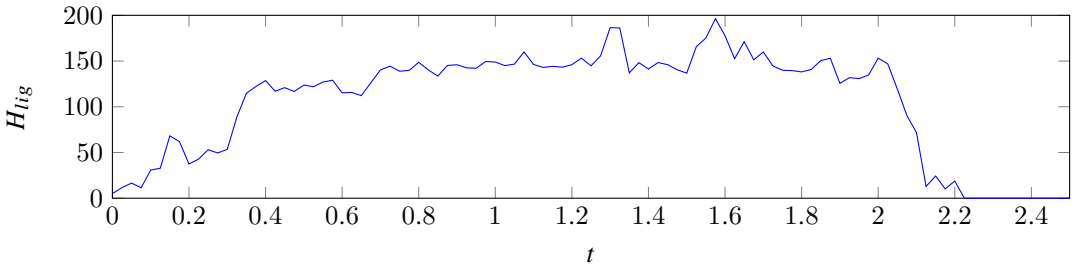

Figure 6.1.2: Evolution in time of the mean curvature H_{lig} when inter-scale transfer is deactivated.

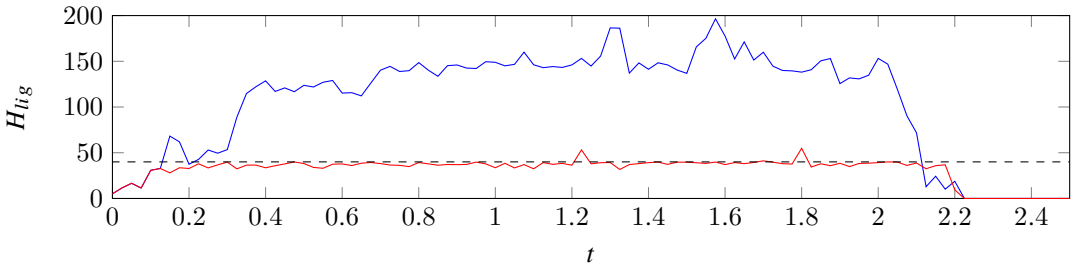

Figure 6.1.3: Evolution in time of the mean curvature H_{lig} when inter-scale transfer is either activated (——) or deactivated (——). Threshold $H_{max} = 40$ m^{-1} is represented with the black dashed line.

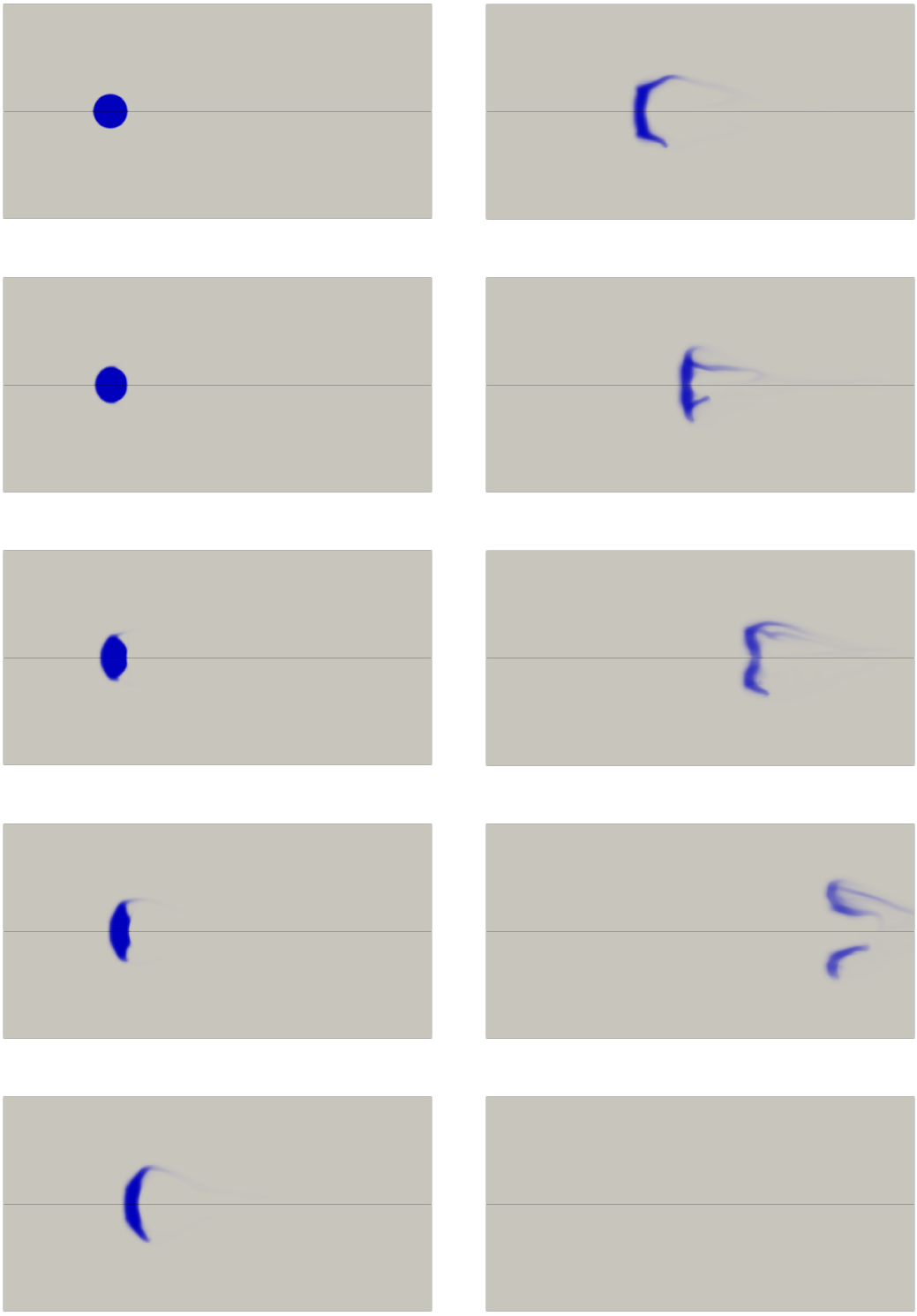

Figure 6.1.4: Large-scale liquid volume fraction $\overline{\alpha}_1 \in (0, 1)$ with mass transfer (top) and without mass transfer (bottom). Snapshots are taken each 0.25 s from $t = 0$ s to $t = 2.5$ s from top to bottom and left to right.

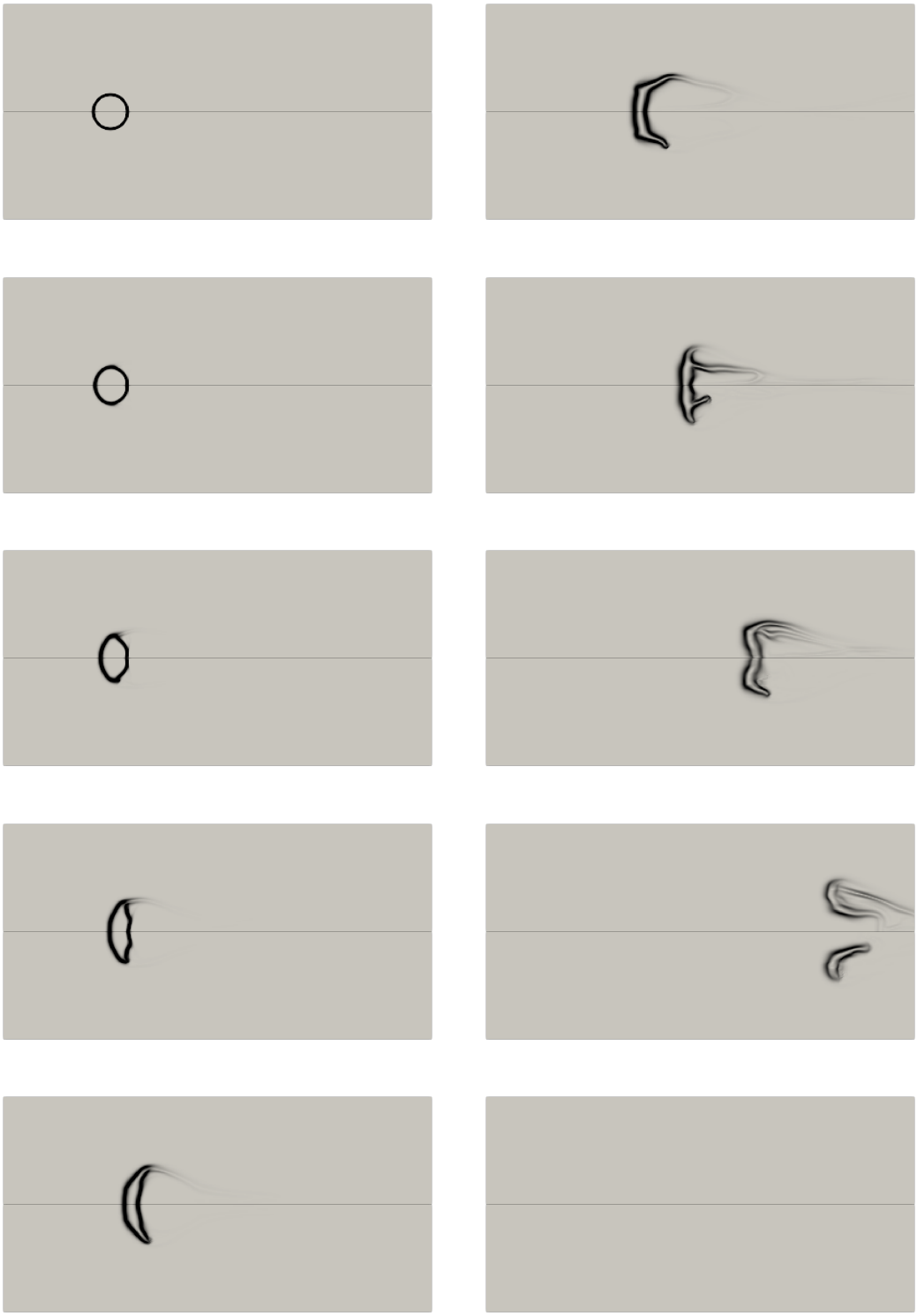

Figure 6.1.5: Large-scale IAD $\|\boldsymbol{\nabla}\overline{\alpha}_1\| \in (0, 16)$ with mass transfer (top) and without mass transfer (bottom). Snapshots are taken each 0.25 s from $t = 0$ s to $t = 2.5$ s from top to bottom and left to right.

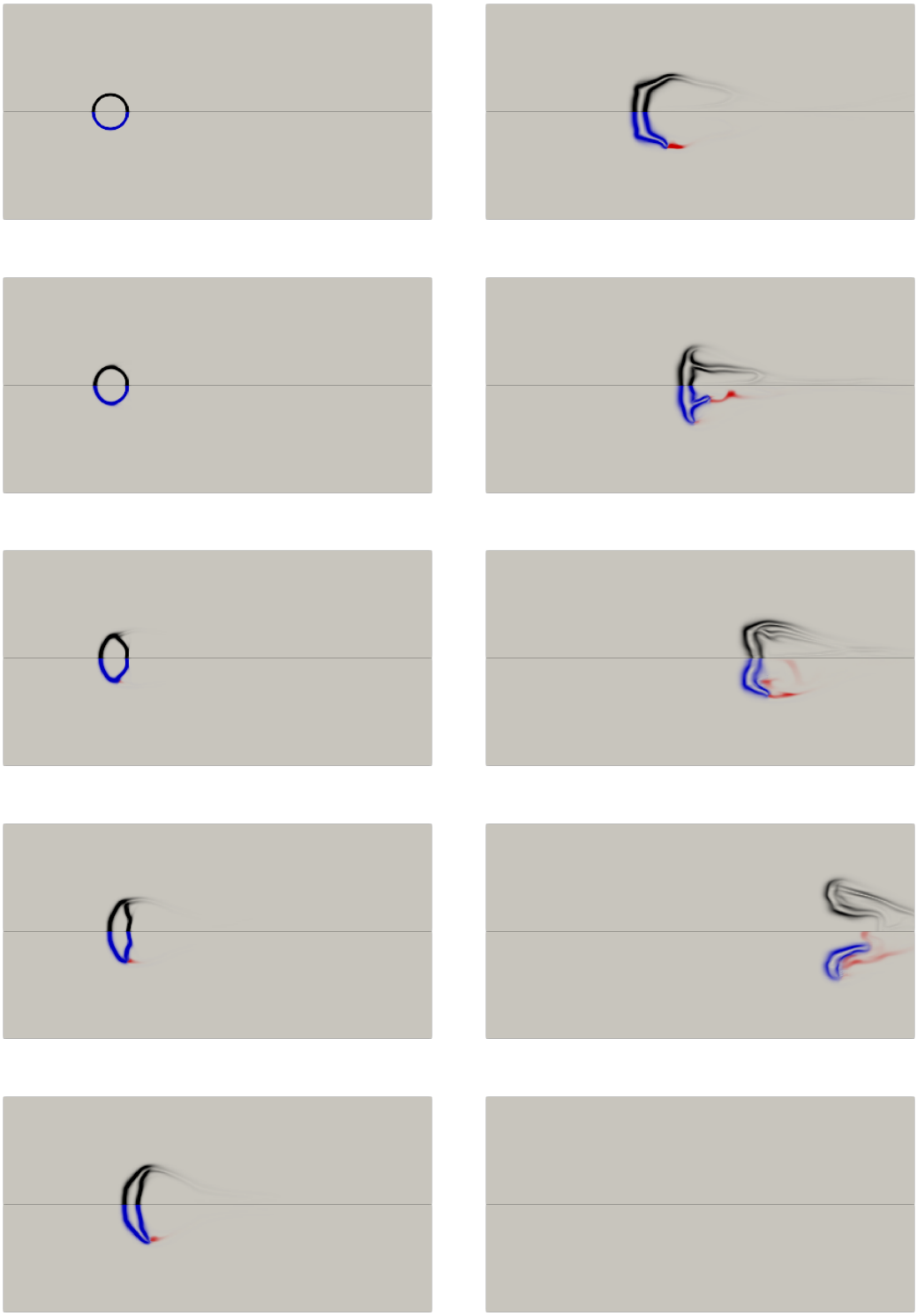

Figure 6.1.6: Large-scale IAD $\|\boldsymbol{\nabla}\overline{\alpha}_1\| \in (0, 16)$ m^{-1} without inter-scale transfer (top), with inter-scale transfer (bottom), and small-scale IAD $\Sigma \in (0, 3.4)$ m^{-1} with inter-scale transfer (bottom). Snapshots are taken each 0.25 s from $t = 0$ s to $t = 2.5$ s from top to bottom and left to right.

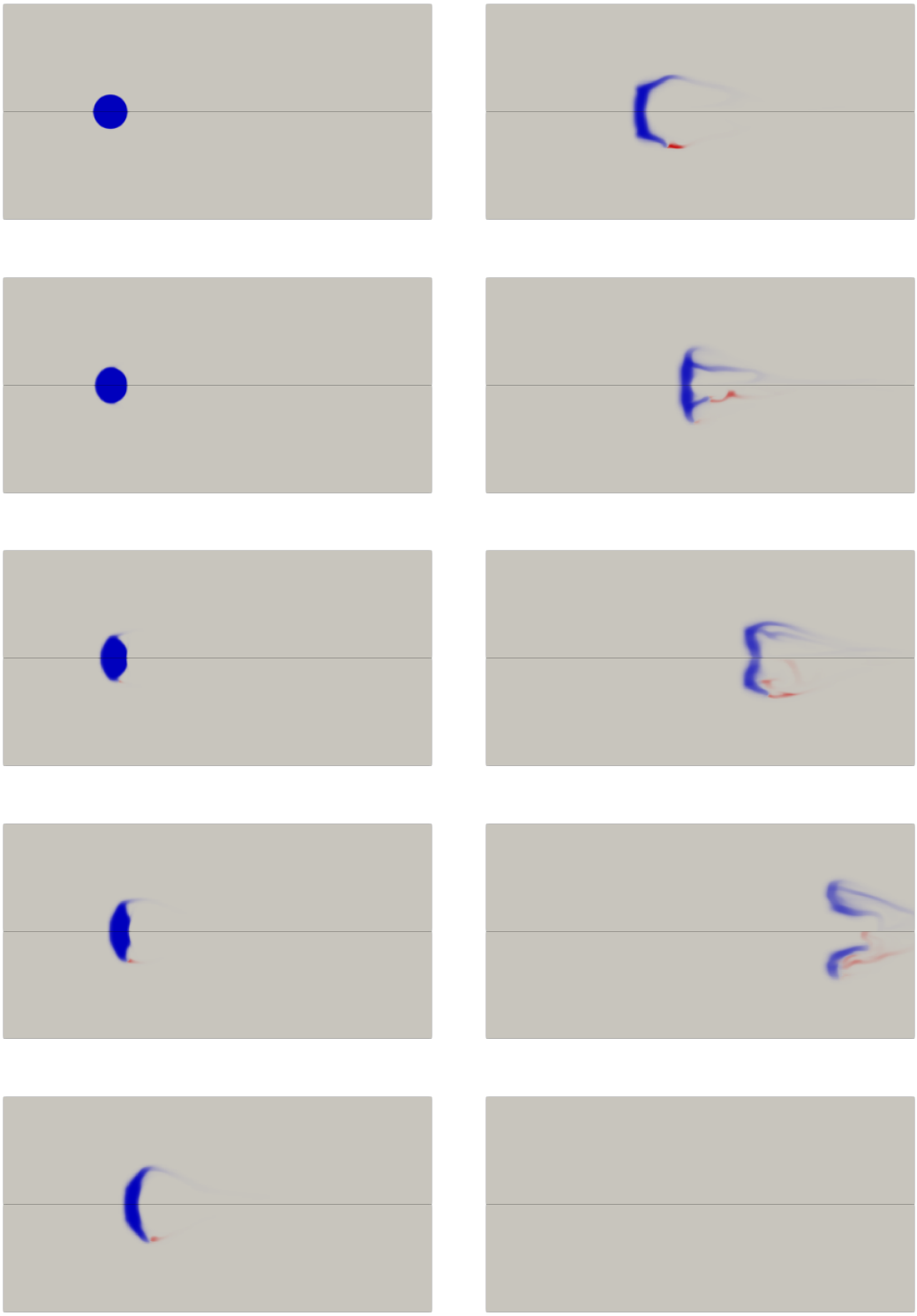

Figure 6.1.7: Large-scale liquid effective density $\alpha_1\rho_1 \in (0, 10^3)$ without inter-scale transfer (top), with inter-scale transfer (bottom), and small-scale liquid effective density $\alpha_1^d\rho_1^d \in (0, 3.8 \times 10^2)$ with inter-scale transfer (bottom). Snapshots are taken each 0.25 s from $t = 0$ s to $t = 2.5$ s from top to bottom and left to right.

6.1.2.2 Repartition of mass and IAD between scales

Now let us discuss the repartition of both the liquid mass and IAD transfer and production. As expected one can observe in Fig. 6.1.8 that the large-scale liquid effective density is transferred to the small-scale model while conserving the total liquid mass during stage 2. Remark that such a transfer does not generate any loss of mass or excess in comparison with the available volume for each scale as the two scales are gathered in a single set of equations, thus describing a two-scale mixture. This approach particularly differs from the coupling strategies (Lebas et al., 2009; Zuzio et al., 2013; Le Touze, 2015) between two solvers where the transferred mass is not compensated in terms of volume occupation and can produce pressure artefacts. The superposition of the effective densities at both scales shows that the mass transfer has happened at the extremities of the large-scale ligaments, and the small-scale liquid phase is then advected by the flow. We can again measure the impact on the dynamics as the liquid mass is not spatially distributed at the same location, whether the inter-scale transfer is activated or not, by summing the contributions of both the large- and small-scale components.

Regarding the IAD, one can see in Fig. 6.1.9 that the regularization tends to decrease the total large-scale IAD when mass transfer is activated, in accordance with the more compact shape of the liquid core. However, we observe for activated inter-scale transfer that the sum of the IAD from both scales largely exceed the large-scale IAD when the inter-scale transfer is deactivated. This follows from the greater amount of IAD generated by droplets than the one associated with a small bit of an under-resolved open interface for a given liquid mass. The choice of the parameter S_{avg}/m_{avg}, or in our case κ, strongly impacts the amount of small-scale IAD produced from the same amount of mass as the IAD source term is inversely proportional to κ in Model 31 The fitting of such a parameter is discussed in the next section thanks to the comparison with a high fidelity simulation.

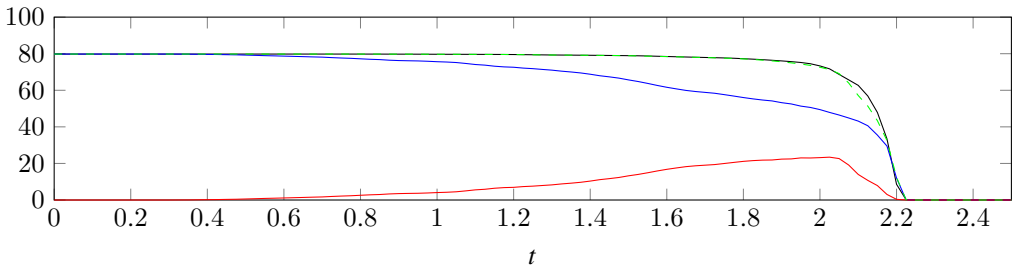

Figure 6.1.8: Evolution in time of liquid effective density for large-scale $\alpha_1\rho_1$ and no inter-scale transfer (——), for large-scale $\alpha_1\rho_1$ and inter-scale transfer (——), for small-scale $\alpha_1^d\rho_1^d$ and inter-scale transfer (——), for both scales $\alpha_1\rho_1 + \alpha_1^d\rho_1^d$ and inter-scale transfer (- - -).

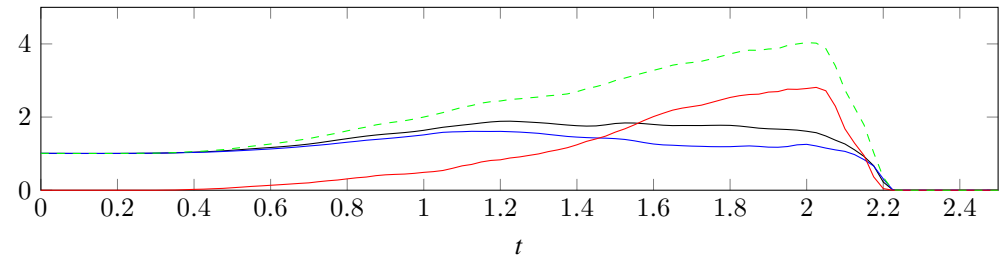

Figure 6.1.9: Evolution in time of IAD for large-scale $\|\boldsymbol{\nabla}\overline{\alpha}_1\|$ and no inter-scale transfer (——), for large-scale $\|\boldsymbol{\nabla}\overline{\alpha}_1\|$ and inter-scale transfer (——), for small-scale Σ and inter-scale transfer (——), for both scales $\|\boldsymbol{\nabla}\overline{\alpha}_1\| + \Sigma$ and inter-scale transfer (- - -).

6.1.3 Comparison with a high fidelity simulation

The previous section has demonstrated the ability of the two-scale model to describe the interface at two levels: a large-scale one where the interface is regularized and estimated *via* the gradient of the volume fraction, and a small-scale one where it is represented with the small-scale IAD, a moment of a spray distribution. However, the regularization process proposed in the two-scale model used in the previous section relies on two key size parameters which strongly influence the resulting amount of IAD in the whole simulation: the maximal mean curvature threshold H_{max} and the parameter κ which pilots the size of the produced droplets.

In this section, we compare, for demonstrating purpose, the results from the two-scale simulation with another simulation, now referred as *high fidelity* simulation, without two-scale transfer, performed on a refined mesh to qualitatively measure to what extent the two-scale model can model the small-scale dynamics. In Section 6.1.3.1, we discuss the differences between the models used for the two-scale simulation and the one used for the high-fidelity simulation along with the numerical parameters of the simulations. Due to the small differences at both modelling and numerical stages, we first assess in Section 6.1.3.2 that both simulations provide comparable large-scale dynamics. Finally, the total IAD obtained from each simulation is compared in Section 6.1.3.3.

6.1.3.1 High fidelity test-case comparison: model and numerical methods

The high fidelity simulation is obtained with another solver based on the same one-velocity model but with a different numerical method detailed in Grenier et al. (2013). When the regularization process is deactivated, this solver is then able to solve the same test-case, but more efficiently, on a parallel architecture. Therefore, it offers a size resolution which is out of reach with the current implementation of the two-scale model in `Josiepy`. However, the two implementations differ slightly as they do not precisely solve the same set of equations, and do not use the same numerical methods. Let us then detail their differences.

From the modelling perspective, let us recall that the large-scale sub-model of the two-scale model is based on the Model 5, which is adapted to separated regime and accounting for capillarity. The set of equations solved in the high fidelity simulation differs only on the local Laplace equilibrium where the capillarity pressure jump is neglected. Therefore, this second model consider a pressure equilibrium $p_1 = p_2$ and avoid the issues associated with the evaluation of the estimator of the local mean curvature $\overline{H}(\boldsymbol{\nabla}\overline{\alpha}_1)$.

From the numerical perspective, the implementation associated with the high-fidelity simulation differs on two main points from the one proposed in `Josiepy`:

- A low-Mach compressible scheme is used following Grenier et al. (2013);
- The compressive limiter of Blanchard (2014).

While the former scheme has *a priori* not a significant impact in the test-case at stake where we have an initial Mach number of $Ma = 0.66$, the latter limiter keeps the interface as thin as possible while keeping the consistencies of the numerical schemes. Such limitation procedure helps the development of the small-scale dynamics without the requirement of a very fine meshing of the domain. Finally, the high fidelity simulation proposes a much more refined mesh with a regular meshing of 3200×1600 cells distributed on 120 different regions (see Figure 6.1.10) while the two-scale simulation only has 400×200 cells.

This modelling and numerical frameworks particularly allows simulating smaller length-scales of the interface dynamics that we want to measure to calibrate the two-scale model. Before comparing the small-scale models, we assess in the following section that the two simulations provide similar dynamics at large scale.

6.1.3.2 Large-scale dynamics assessment

Before comparing the high fidelity simulation with the simulations obtained with `Josiepy`, we propose to first identify the interface regimes from the dynamics of the high fidelity simulation displayed in Figure 6.1.11. We identify three stages :

- A "two-scale regime" from $t = 0$ s to $t = 0.75$ s: two different scales are clearly visible to describe the interface dynamics, a large one corresponding to the contour of the core of the liquid column, and a small one associated with the creation of small and thin filaments on the top, left and bottom sides of the liquid column.

Figure 6.1.10: The decomposition of the 3200×1600-cell Cartesian mesh into 120 regions where the model is solved in parallel.

- A mixed regime from $t = 0.75$ s to 1.25 s: we can still identify a liquid core with filaments attached to it, but their respective length-scales are now comparable as the liquid core has become thinner and the filaments have grown.
- A disperse regime after $t = 1.25$ s: the liquid core is atomized into a disperse phase that quickly dissipates due to the numerical scheme.

This dynamics reveals that the time of the transition from the separated and two-scale regime to the disperse regime is shorter than the one suggested by the coarser two-scale simulation obtained with `Josiepy`, and that the very small length-scales appear all over the liquid surface rather than just at the extremities of the filaments. Furthermore, the quick numerical dissipation of the smallest scales associated with the final disperse regime illustrates the difficulty of such simulations which, despite the refined mesh and the compressive limiter, cannot resolve the dynamics of the interface of such inclusions. Moreover, the use of a compressive limiter at such small scales is questionable as no interface can be properly defined when the length-scales become comparable with the mesh size.

Then, we confirm the right setting of the test-cases by verifying that the dynamics of the two simulations, the high fidelity one and the two-scale one, present similar dynamics, at least for the two-scale regime where the interface dynamics has not influenced the whole flow yet. The comparison between the volume fraction, pressure and velocity fields of these two simulations are showed in Figures 6.1.12-6.1.13-6.1.14. We qualitatively observe a very good agreement between the two simulations up to the moment where the first filaments break up into small inclusions at the end of the two-scale regime timespan. However, the presence of such inclusions strongly perturbs the structure of the pressure waves and the velocity field downstream the liquid column. Nevertheless, the pressure and velocity fields upstream and the "averaged" shape of the liquid core are very comparable in the two simulations.

At the end of the "two-scale regime", the influence of the dispersed inclusions have a strong influence on the overall flow and the displacement of the liquid column starts to desynchronize between the two simulations (see Figure 6.1.16). The right simulation of the disperse phase then shows to be of great influence on the overall dynamics and further studies must be provided to better understand this phenomenon, notably to measure the influence of convergence which reveals more and more inclusions in the disperse phase.

Now that the large-scale dynamics have been studied and showed comparable during the two-scale regime, let us study the small-scale dynamics afterwards.

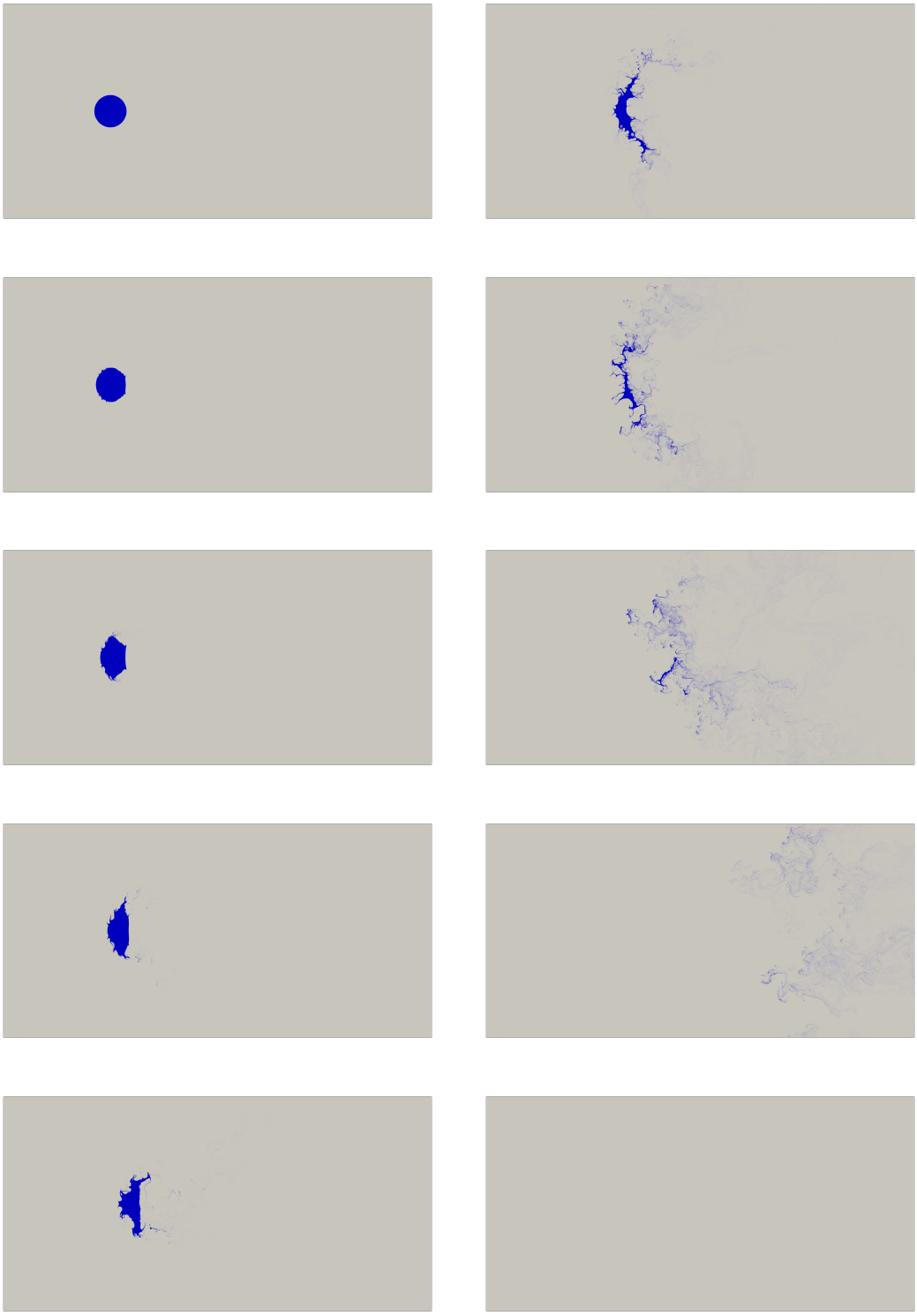

Figure 6.1.11: Liquid volume fraction $\alpha_1 \in (0, 1)$ of the high fidelity simulation. Snapshots are taken each 0.25 s from $t = 0$ s to $t = 2.25$ s from top to bottom and left to right.

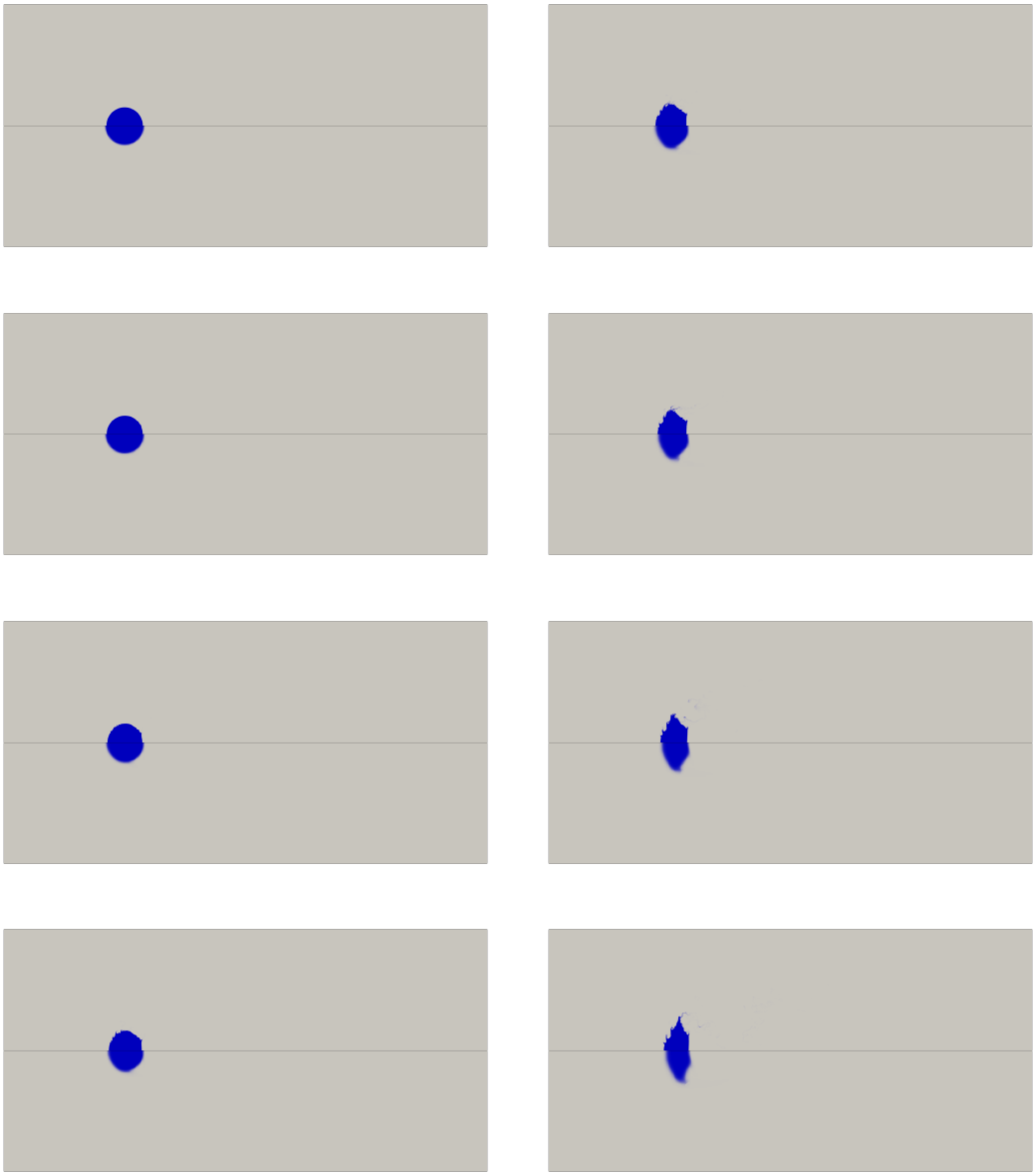

Figure 6.1.12: Volume fraction and large-scale volume fraction field $\alpha_1, \overline{\alpha}_1 \in (0, 1)$ respectively for the high fidelity simulation (top) and the two-scale simulation (bottom). Snapshots are taken each 0.1 s from $t = 0$ s to $t = 0.7$ s from top to bottom and left to right.

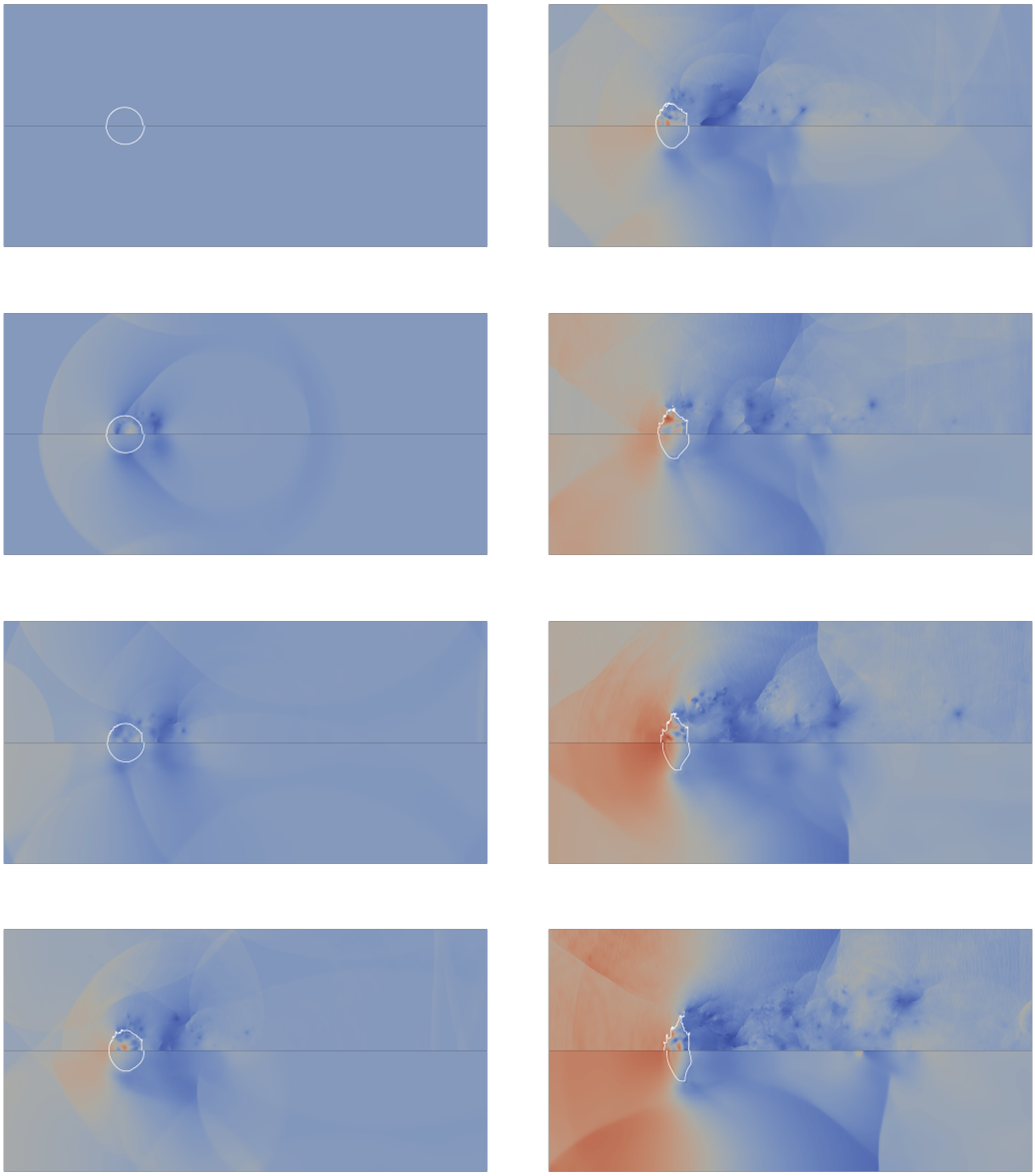

Figure 6.1.13: Pressure field $p, \overline{p} \in (99900, 100200)$ Pa respectively for the high fidelity simulation (top) and the two-scale simulation (bottom). The interface of the liquid column is located respectively for the high fidelity simulation and the two-scale one with the level set $\alpha_1 = 0.5$ and $\overline{\alpha}_1 = 0.5$. Snapshots are taken each 0.1 s from $t = 0$ s to $t = 0.7$ s from top to bottom and left to right.

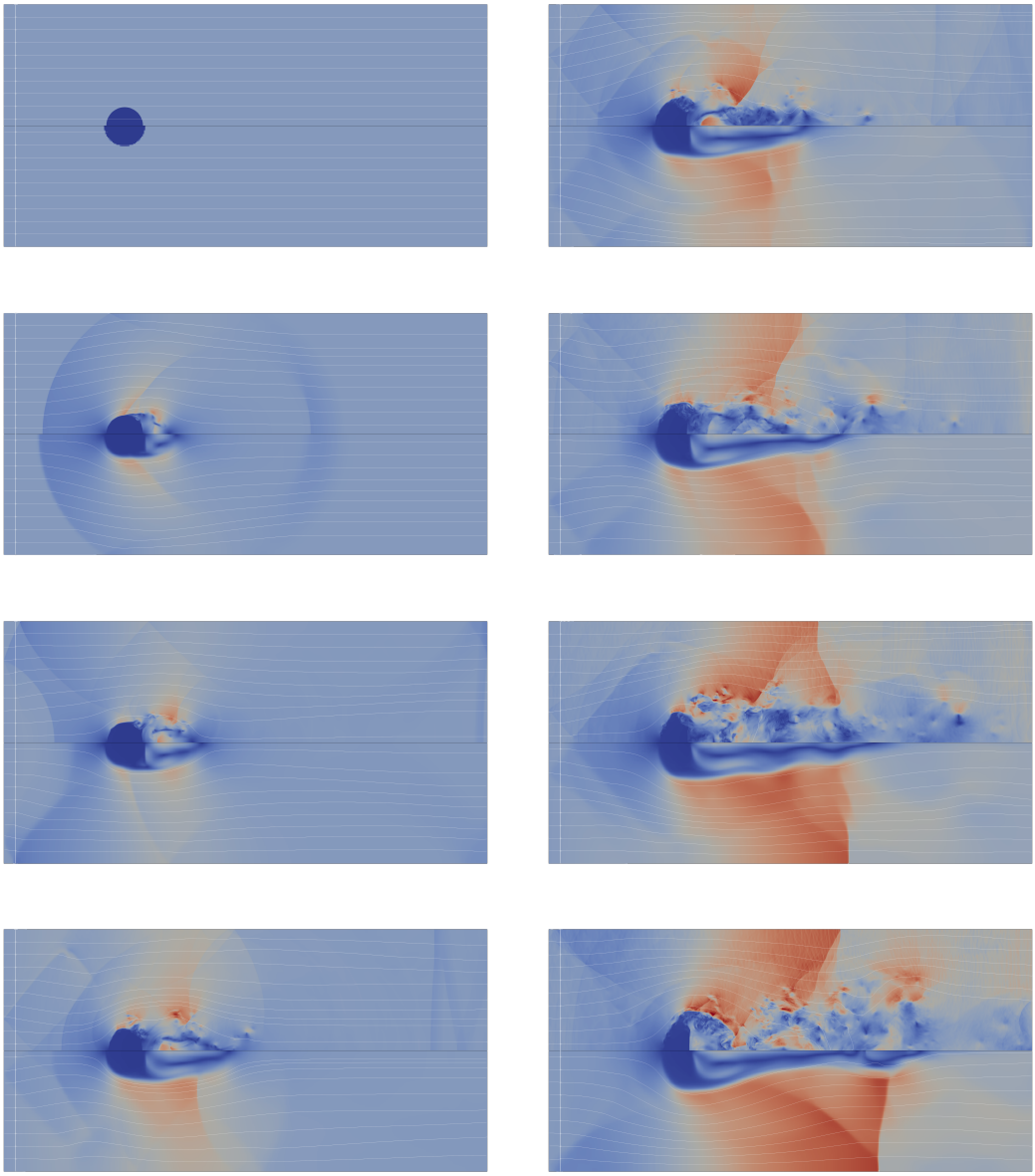

Figure 6.1.14: Velocity streamlines and magnitude field $\|\boldsymbol{u}\| \in (0, 20)$ m.s^{-1} respectively for the high fidelity simulation (top) and the two-scale simulation (bottom). Snapshots are taken each 0.1 s from $t = 0$ s to $t = 0.7$ s from top to bottom and left to right.

6.1.3.3 Comparison of the small-scale interface area density

From the previous study, we have identified three regimes: a two-scale one, a mixed one and a disperse one. Based on this distinction of regimes, we propose to compare both the amount and the location of the interface area density between the two simulations. For the high-fidelity simulation, we estimate the IAD with the gradient magnitude of the volume fraction $\|\boldsymbol{\nabla}\overline{\alpha}_1\|$ while, for the two-scale simulation, we combine both the large-scale IAD estimator $\|\boldsymbol{\nabla}\overline{\alpha}_1\|$ and the small-scale IAD $\boldsymbol{\Sigma}$. The location of the IAD and their evolution in time are plotted respectively in Figure 6.1.16 and in Figure 6.1.15.

Regarding the location of the IAD, the two simulations offers very different space repartition of the IAD as the dynamics of the liquid core is very different once the two-scale regime has ended. We particularly observe that the disperse inclusions are spread further from the liquid core in the high fidelity simulation while it is restricted to the neighbouring of the growing filaments in the other one.

In terms of evolution of the total IAD, we remark that the small-scale IAD in the two-scale simulation is mostly created from the end of the two-scale regime and mainly during the mixed and disperse regime. Indeed, the inter-scale regularization only acts on resolved filaments and the current resolution of the two-scale simulation does not allow the capture of the small filaments appearing during the two-scale regime. The accounting of this small-scale IAD would either require a refined simulation or a small-scale model representing the local growth of filaments.

Then, the amount of IAD generated in the high fidelity simulation indicates that the averaged size of the droplets of the two-scale simulation has been overestimated. Such an observation was expected as a very large size of droplets was chosen for the inter-scale transfer with $\kappa = 1$ *i.e.* a droplet radius of the same size as the inverse of the curvature threshold H_{max} (see Model 30). Assuming that the impact on the flow is negligible, a projection of the amount of IAD produced by selecting $\kappa = 0.2$ is sketched in Figure 6.1.9. Such a projection provides a very good match with the high fidelity simulation regarding the global evolution of IAD within the spray. This demonstrates that the inter-scale model is able to recover global quantity of interest with very few parameters despite the inexact location of the small-scale or beginning time of the primary atomization process.

More advanced modelling of the atomization process would require the include more phenomena such as a small-scale two-velocity model with drag, oscillation and secondary break-up with parameters chosen with experimental heuristics.

Conclusion of Section 6.1

We have presented in this section an original two-scale simulation which illustrates numerous contributions present in this manuscript and demonstrates the potential of the two-scale modelling strategy of Chapter 3 which combines the models for both the separated and disperse regimes derived in Chapter 1. Given a test-case with multiscale interface dynamics, we have introduced a relevant length-scale threshold which pilots the location of inter-scale transfer as a regularization of the large-scale interface. This successful regularization process, notably illustrated by the limitation of mean curvatures (see Figure 6.1.3), has also demonstrated the efficiency of the underlying numerical methods presented in Chapter 4 which are another contribution of this work. Many complementary studies could follow from this test-case with the assessment of the influence of inter-scale transfer parameters, here H_{max} and κ, the testing of different test-cases, or other numerical schemes to better capture the large-scale interface dynamics with compression limiters or adaptive mesh refinement. A critical extension of this setup also relies on an enhanced modelling of the small-scale dynamics with models of Chapter 2. Indeed, the two-scale model used for this simulation was intentionally deprived of non-required geometric quantities to focus this section on inter-scale mass transfer. We propose now to tackle separately a test-case related to the small-scale modelling with the advection of an agitated spray of oscillating droplets and thus conclude on one of the other main modelling contribution from this manuscript.

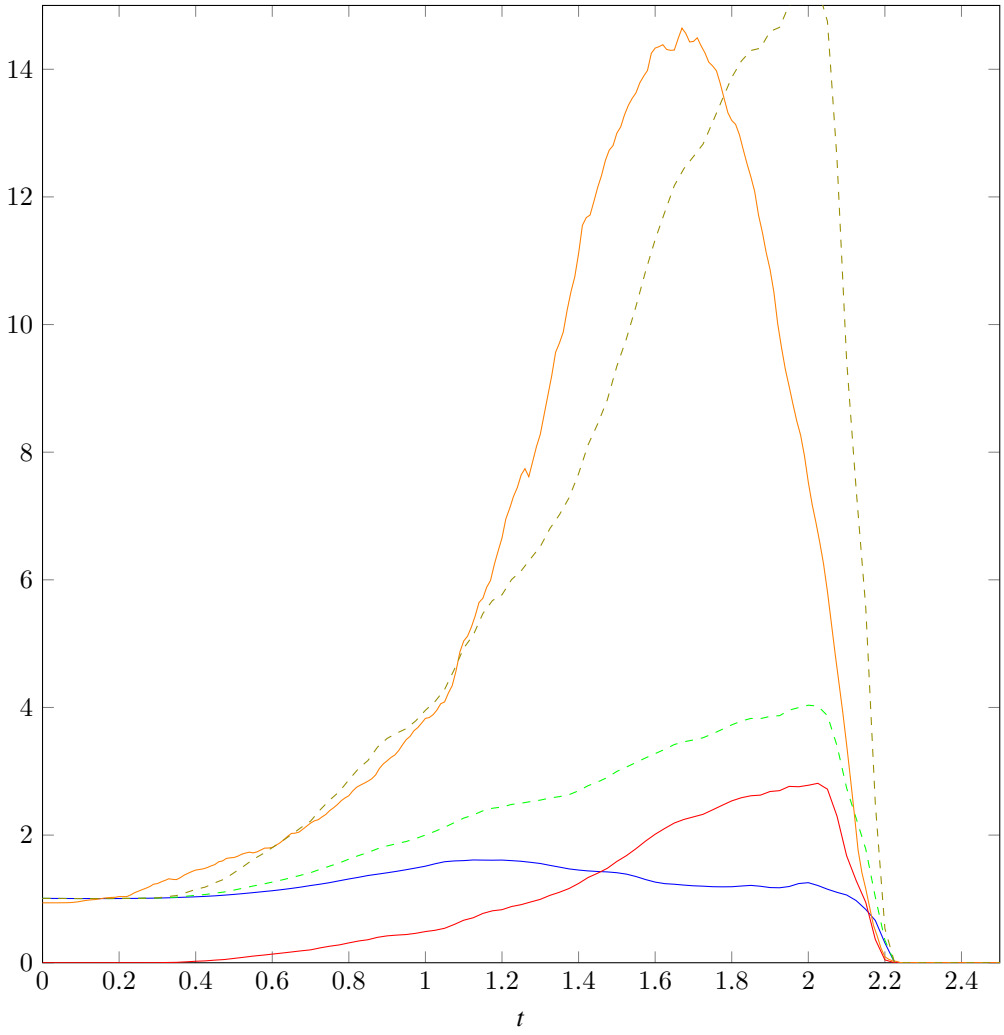

Figure 6.1.15: Evolution in time of IAD for the high fidelity simulation with $\|\boldsymbol{\nabla}\alpha_1\|$ (——), the two-scale simulation with $\kappa = 1$ for large-scale $\|\boldsymbol{\nabla}\overline{\alpha}_1\|$ (——), for small-scale Σ (——), for both scales $\|\boldsymbol{\nabla}\overline{\alpha}_1\| + \Sigma$ (- - -), and an approximate evolution for the two-scale simulation in a projected scenario with $\kappa = 0.2$, for both scales $\|\boldsymbol{\nabla}\overline{\alpha}_1\| + \Sigma$ (- - -).

Figure 6.1.16: IAD $\|\nabla\alpha_1\| \in (0, 400)$ m^{-1} (top) of the high-fidelity simulation, large-scale IAD $\|\nabla\alpha_1\| \in (0, 16)$ m^{-1} (bottom) and small-scale IAD $\Sigma \in (0, 34)$ m^{-1} (bottom) of the two-scale simulation. Snapshots are taken each 0.25 s from $t = 0$ s to $t = 2.5$ s from top to bottom and left to right.

6.2 Polydisperse spray of oscillating droplets

In this second simulation, we propose to illustrate the potential dynamics of the small-scale model of oscillating droplets detailed in Section 4.2 that we recall here for the polydisperse case,

$$\begin{cases} \partial_t M^{\xi}_{i,0,0} + \boldsymbol{\nabla}\cdot(M^{\xi}_{i,0,0}\boldsymbol{u}) = 0, & i = 0, 1/2, 1, 3/2, \\ \partial_t M^{\xi}_{1,1,0} + \boldsymbol{\nabla}\cdot(M^{\xi}_{1,1,0}\boldsymbol{u}) = M^{\xi}_{1,0,1}, & \\ \partial_t M^{\xi}_{1,0,1} + \boldsymbol{\nabla}\cdot(M^{\xi}_{1,0,1}\boldsymbol{u}) = M^{\xi}_{1,1,0} - F_{ext} M^{\xi}_{0,0,0}, & \\ \partial_t M^{\xi}_{1/2,1,0} + \boldsymbol{\nabla}\cdot(M^{\xi}_{1/2,1,0}\boldsymbol{u}) = M^{\xi}_{1/2,0,1}, & \\ \partial_t M^{\xi}_{1/2,0,1} + \boldsymbol{\nabla}\cdot(M^{\xi}_{1/2,0,1}\boldsymbol{u}) = M^{\xi}_{1,1,0} + F_{ext} M^{\xi}_{-1/2,0,0}. & \end{cases} \tag{6.1}$$

6.2.1 Test-case description

This test case aims at providing a more physical setup than the one provided as a verification test-case in Section 5.4 and illustrating the potential of the oscillatory model. To this end, we consider the advection of a spray of droplets which becomes agitated due to an external force as it goes across an "agitated region". We interpret here this external force as a drag force in a region with a velocity differential between the inclusions and the carrier flow that is strong enough to trigger a deformation of the droplet as in a jet crossflow (Herrmann, 2009; Sakano et al., 2022; Janodet et al., 2022). Following this interpretation, the external force is chosen to be size-dependent with the same dependency as the drag force proposed in the TAB model of O'Rourke and Amsden (1987). Such force has been introduced in the model of moments (4.52) and (4.53) defined in Section 4.2.

Then, we initialize the test-case with a bi-disperse spray of static droplets located in a domain $\mathcal{D}_{init} = (0.25, 0.75)$ of the total periodic domain $\mathcal{D} = (0, 3)$ which contains the agitated region $\mathcal{D}_{agit} = (1.75, 2.25)$ (see Figure 6.2.1). The droplets oscillations are further triggered by the external force as it goes across the agitated region where the intensity of the external force is defined for $x \in \mathcal{D}$,

$$F_{ext}(x) = F\mathbb{1}_{\mathcal{D}_{agit}}(x), \tag{6.2}$$

with $F = 5$ in the following simulations.

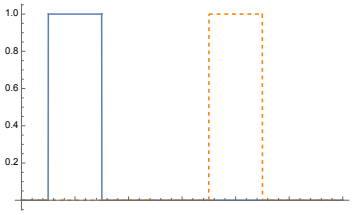

Figure 6.2.1: Schematic representation of the setup with the initial position of the spray and the location of the forcing term through the characteristic functions $\mathbb{1}_{\mathcal{D}_{init}}$ and $\mathbb{1}_{\mathcal{D}_{agit}}$.

Similarly to the verification test-case of Section 5.4, we set $\tilde{\omega} = 4$ for the monodisperse cases, $\tilde{\omega} = 2$ for the polydispere test-case. The CFL is chosen at 0.9 for all the simulations. In the following Figures 6.2.2, 6.2.3 and 6.2.4, we track the dynamic of an advected cell in the center of the spray and observe its dynamics as it goes across the agitated region several times.

6.2.2 One-dimensional simulation of the oscillating spray

In the polydisperse case, we initialize the simulation with the following set of moments,

$$\begin{cases} M^{\xi}_{i,0,0}(x,0) & = (i+1)^{-1}\, \mathbb{1}_{\mathcal{D}_{init}}(x), \quad i = 0, 1/2, 1, 3/2 \\ M^{\xi}_{1/2,1,0}(x,0) & = 0, \\ M^{\xi}_{1/2,0,1}(x,0) & = 0, \\ M^{\xi}_{1,1,0}(x,0) & = 0, \\ M^{\xi}_{1,0,1}(x,0) & = 0. \end{cases} \tag{6.3}$$

As the external force always increases the oscillation velocity parameter, it accelerates the dynamics and total energy builds up when the oscillation velocity is positive, and slows the dynamics when the oscillation velocity is negative. In Figures 6.2.2, 6.2.3 and 6.2.4, we plot the kinetic, potential and total energies for respectively the population of large droplets, small droplets and the whole spray. After reaching the forcing zone, the two droplets populations start to oscillate with different oscillation frequencies depending on their size. The kinetic energy is initially triggered by the forcing term since the source term arises in the moments equations $M^{\xi}_{1,0,1}$ and $M^{\xi}_{1/2,0,1}$ of the model (6.1). For the population of large droplets in Figure 6.2.2, the total energy increases to a first threshold and a second one when the droplets cross the forcing term area the first two times. However, the third crossing of the agitated zone happens at a moment where the oscillation velocity is negative. The oscillation motion is slowed down, and the droplets lose some energy. Besides, we can remark in Figure 6.2.2 that the energy of large droplets slightly dissipates between two agitated zones due to the numerical diffusion of the kinetic scheme, while the energy of small droplets in Figure 6.2.3 decreases faster. This phenomenon originates in the quadrature relation between moments and abscissa which affects more the small droplets due to the initial large ratio of 7.5×10^{-3} between the energy of the small droplets over the one of the large droplets. In Figure 6.2.3, the dynamics of the second droplet population is displayed. Due to the higher oscillation frequency associated with the smaller size of droplets, the oscillation dynamics is successively accelerated and slowed down as the velocity has the time to oscillate with both positive and negative values in the agitated area.

Finally, the energy associated with the small-sized droplets is negligible in comparison with the energy of the larger ones. Therefore, the energies of the spray plotted in Figure 6.2.4 are comparable to the ones of the larger droplets given in Figure 6.2.2.

This test-case illustrates that the small-scale model of oscillation droplet can provide a rich dynamics despite the simple oscillatory model underneath. The energy of the spray results from the subtle combination of the time of exposure to external source terms and size-dependent frequencies of the droplets within the spray. From this test-case, we can make the following conjectures : for some sizes where the period of oscillation is of the same order of magnitude as the advection time through an agitated zone, the oscillation energy of the droplets builds up, and an eventual break up has to be further considered as extension of this model. For some smaller sizes, the frequency of oscillation is too high to show a similar kind of resonance phenomenon and the energy remains stable asymptotically. Such an observation shows that the oscillation motion in polydisperse sprays can influence the resulting secondary break-up phenomenon as some sizes are more probable to break-up than the others. Indeed, break-up occurs more often for larger Weber numbers which scale here with the radius of the droplet.

Conclusion of Section 6.2

Let us conclude this second test-case on small-scale modelling by underlining that this dynamical model aims at being coupled with the previous test-case of inter-scale transfer to model a full atomization process. Moreover, a more comprehensive approach of the small-scale dynamics should also include a two-velocity modelling framework, secondary break-up, and potentially coalescence and re-impact if the spray is dense. The inclusion of these phenomena in a two-scale model is a natural perspective to this work which mainly offered an original framework to treat the dynamics of the interface resulting from the mixed regime.

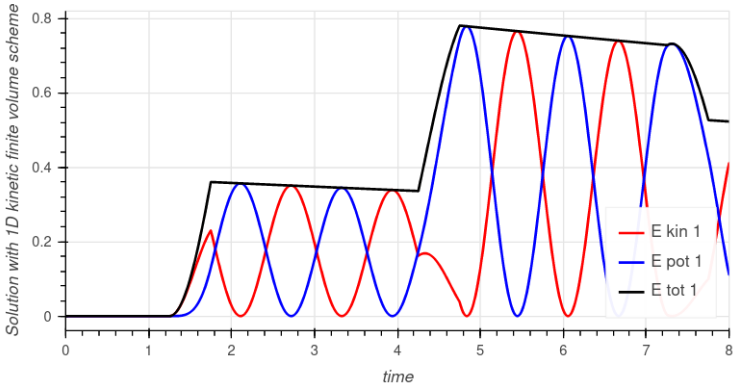

Figure 6.2.2: Evolution in time of the kinetic, potential and total energies of the population of larger droplets in the cell at the center of the spray. Mesh size $\Delta x = 0.003$ m . Final time $T = 8$.

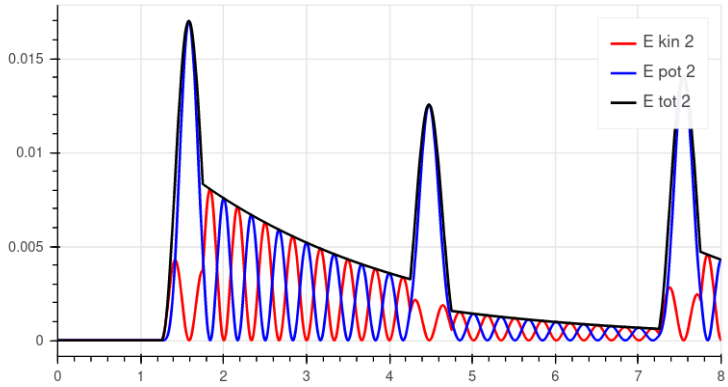

Figure 6.2.3: Evolution in time of the kinetic, potential and total energies of the population of smaller droplets in the cell at the center of the spray. Mesh size $\Delta x = 0.003$ m . Final time $T = 8$.

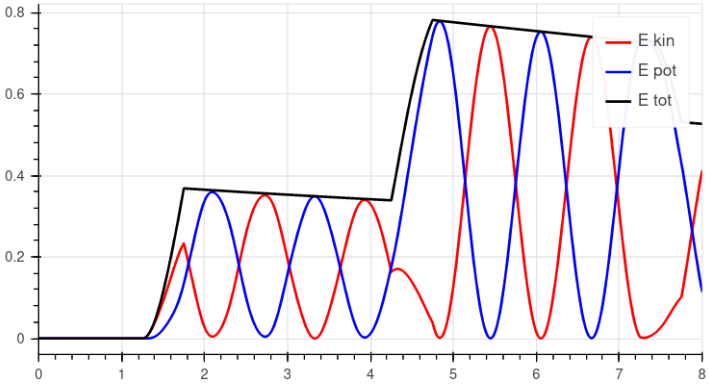

Figure 6.2.4: Evolution in time of the kinetic, potential and total energies E^{poly} of the spray in the cell at the center of the spray. Mesh size $\Delta x = 0.003$ m . Final time $T = 8$.

Conclusion of chapter 6

In this chapter, we have successfully demonstrated the innovative capabilities of the two-scale and polydisperse small-scale models :

- The coupling of multi-fluid models for both the separated and disperse regime within a unified model;
- The regularization of the large-scale interface through a local and dissipative coupling with the small-scale;
- The efficient modelling of the primary break-up process through the parametrization of the small-scale droplet sizes;
- The dynamics of a polydisperse spray of oscillating droplets.

The liquid column deformation test-cases has assessed the potential of two-scale modelling at multiple levels. Indeed, the inter-scale mass transfer successfully regularize the large-scale while offering tunable parameters to account for the production of a small-scale polydisperse spray. An example of such a tuning is proposed thanks to the comparison with a high-fidelity simulation on a refined mesh and with a compressive limiter providing a better resolution of the interface dynamics. Besides, the proposed regularization process is set at the modelling stage, does not involve an explicit dependency with the mesh size, and respects a dissipative principle. Such a framework aims at providing accessible mesh convergence for a given curvature threshold, which is usually out of reach when all scales of the interface dynamics are resolved. Finally, the test-case involving the polydisperse spray of oscillating droplets demonstrates that, once the liquid phase would be transferred from large to small scale, the reduced-order model still offers the modelling of complex behaviour such as droplet deformation resulting from either the primary atomization through the inter-scale transfer or possible secondary break-up in presence of velocity differential.

This chapter demonstrates the possibility of a more comprehensive modelling and simulation of the atomization process thanks to efficient reduced-order models for mechanism involved while offering a proper mathematical framework.

Conclusions and outlooks

Conclusive remarks

This thesis has proposed new contributions for the modelling of complex two-phase flows involving different flow regimes and multiscale interface dynamics by enabling the use of two-scale unified models. Indeed, the direct simulation of such flows with state-of-the-art numerical methods is out of reach due to the multiscale nature of the interface, and alternative, cheaper but predictive two-phase flow models have to be developed to lift this computational bottleneck. This work has pursued a long-term effort in developing such a solution through unified multi-fluid models (Drui, 2017; Essadki, 2018; Cordesse, 2020; Di Battista, 2021) able to tackle both the separated and disperse flow regimes occurring in liquid-gas atomization. The idea of this modelling approach lies in an efficient description of the different regimes in a single set of partial differential equations with desirable mathematical and physical properties such as energy conservation, hyperbolicity or entropy-dissipative structure. The work presented in this manuscript particularly offers new critical features for the applicability of such unified models: the two-scale approach with independent volume fractions for the large- and small-scale liquid phase, and the inter-scale interface-regularizing mass transfer to model the transition from the separated to the disperse regime. These two features are respectively found in the following contributions Loison et al. (2023a,b). However, an accurate modelling of the complex interface dynamics occurring in an atomization process requires the accounting of multiple mechanisms (break-up, polydispersion, added-mass) coupled together. Steps towards a more comprehensive description of these phenomena and their coupling have been proposed in this manuscript through both the use of Hamilton's Stationary Action Principle for the derivation of conservative mechanisms, and the addition of source terms complying with the second principle of thermodynamics for the modelling of dissipative mechanisms. We propose to summarize here the main results contributing to the development of unified multi-fluid models :

- The two-scale approach presented in Chapter 3 is one of the key ingredients of the unified models as it enable to make two models, a large-scale one describing a separated regime, and a small-scale one for the disperse regime, coexist locally, and thus let the opportunity of setting up a local transfer between each other. In our context of liquid atomization, two independent large- and small-scale liquid phases have been combined in a one-velocity two-scale model with Hamilton's SAP. With a compressible large scale and an incompressible small scale, this two-scale model particularly extends classic multi-fluid models in both the separated and disperse regime with a conservative hyperbolic structure. Moreover, the two-scale model offers a two-fold representation of the interface geometry and thus, of capillarity energy which is of prime interest for the inter-scale coupling.

- Another main feature of the unified models is the coupling between the models of each scale also presented in Chapter 3. Such a transfer must comply with the second principle of thermodynamics, which translates, in the context of barotropic EOS, as an energy redistribution from the large- to the small-scale models. Then, the location of such a transfer is chosen where it is both physically and numerically relevant: at the end of growing filaments, where the interface bends and pinches before breaking up and where the length-scales are the smallest in the computational domain. In order to do so, we take advantage of a modification of the local

Laplace equilibrium to both locate the mass transfer at the points of the highest curvatures, and regularize the interface to prevent the further apparition of small length-scales below of chosen mean curvature threshold. Such a transfer also interacts greatly with the modelling of capillarity energies at both scales. Indeed, the regularization of the large-scale interface creates a capillarity energy loss which is over-compensated by the production of small-scale droplets. Then, this imbalance is corrected by locally decreasing the flow momentum.

- The modelling of small-scale phenomena is also critical to describe and obtain the right spray properties in the disperse regime. In the inter-scale transfers discussed before, we showed that they rely on an energy redistribution where the capillarity pilots the average size of the produced droplets. In order to model more information about the small scale, enhanced reduced-order models of the small-scale with several geometric quantities are introduced in Chapter 2 with the Geometric Method of Moments GeoMOM. The proposed models allow the description of the spray polydispersion *i.e.* distribution in sizes a polydisperse description of the spray, but also the small-scale dynamics with incompressible pulsation, or compressible pulsation. Other energetic contributions such as added-mass can be accounted for as detailed in Chapter 1. All these mechanisms can then be put together in a more complex inter-scale transfer to better model the energy exchanges taking place in the mixed regime and during the primary break-up.

From the numerical perspectives, classic numerical methods are used with the unified models under consideration. They are recalled in Chapter 4 along with new methods dedicated to the specificities of the inter-scale transfer. Moreover, demonstrative simulations are provided to assess the specific properties of some key models presented in this manuscript. We summarize these contributions here :

- In two-scale models with regularizing mass transfer, the resolution of the modified local Laplace pressure law particularly relies on a new implicit-explicit integration method in fictitious time. This method, presented in Chapter 4, provides an alternative to the classic use of Newton-Raphson methods with an efficient and stable procedure to solve the pressure equilibrium despite the presence of spatial gradients through the estimator of mean curvature.

- A numerical simulation of a static liquid column in Chapter 5 also reveals the pressure profiles in the presence of the local and global Laplace pressure laws within the large-scale capillarity Model 5. Indeed, a local one pilots the pressure jump within the two-fluid mixture in the diffuse interface while the global one accounts for the usual pressure jump between the pressure in and out the liquid column. In the literature (Chanteperdrix, 2004), the global one is usually obtained without the resolution of local one, but its presence, here due to the multi-fluid framework, is at the center of the inter-scale transfer. Nevertheless, its proper solve is showed particularly challenging due to the complex evaluation of the mean curvature on a Cartesian grid.

- A final simulation of a liquid column deformation and atomization with either a regularizing inter-scale transfer model or a high-fidelity solver is presented in Chapter 6. It particularly shows the ability of the inter-scale transfer to regularize the large-scale interface and triggers the creation of droplets. Moreover, we also illustrate the potential tuning of the inter-scale transfer to match the same amount of interface area density as a high-fidelity simulation. This simple test-case then demonstrates the efficiency of the small-scale reduced-order modelling approach to capture relevant geometric information about the interface within a unified modelling framework.

These contributions have proved the potential of two-scale unified models for the simulation of multiscale two-phase flows and now pave the way to further extensions.

Outlooks of this manuscript

The modelling contributions proposed in this manuscript have opened a new spectrum of models which could not have been tackled entirely due to the numerous combinations of models and configurations to investigate. Nevertheless, we gather here some immediate applications and extensions of the modelling and numerical contributions to indicate some promising research directions. This first group of extensions is followed with longer-term outlooks requiring some in-depth investigation.

Starting with the immediate extensions in terms of modelling, we have:

- The derivation of a two-scale unified model with both the inter-scale transfer *via* the regularizing of the large-scale and the small-scale model of oscillating spray. Such model could then be used to simulate the test-case of the airblasted liquid column proposed in Section 6.1 and propose a similar comparison with a high fidelity simulation for different parameters of the inter-scale transfer.

- A natural symmetric extension of the two-scale modelling approach proposed in this work would be to account for a small-scale gaseous phase in the liquid with, for instance small bubbles. Such extension would require to include a supplementary set of variables to characterize this new phase, particularly with its own volume fraction.

- The rigid rotation of fluid inclusions, or the presence of Hill's vortices (Hill and Henrici, 1894) within the inclusions could also be added as another source of energy. Such rotating motion could notably influence the energy redistribution happening during the inter-scale transfer and add another parameter to fit the mechanisms of the primary break-up.

- The inter-scale transfer can be extended to include transfer from small to large scale with the modelling of the re-impact of inclusions into its respective large-scale phase similarly as the model proposed by Le Touze (2015). Such a transfer could also be considered for high volume occupation of the small scale where the inclusions coalesce to form a large-scale bulk phase.

- The primary break-up modelling can be enhanced with the proper choice of parameters in the inter-scale transfer. Similarly to Granger (2023), such choices can rely on either the use of experimental heuristics (Pilch and Erdman, 1987; Marmottant and Villermaux, 2004), or modelling heuristics (Vallet and Borghi, 1999).

Then, we list the following short-term numerical contributions and investigations:

- The introduction of compressive limiter in the resolution of the large-scale interface which could help to locate more accurately where the primary atomization occurs. Moreover, the use of such a limiter in a two-scale model also avoids applying it in the disperse regime where the compression of the interface does no make sense anymore. Indeed, the inclusions are smaller than the discretization length-scale and their interfaces cannot be properly described.

- A numerical study to measure the convergence of the two-scale simulations with respect to the curvature threshold. Indeed, the inter-scale mass transfer prevents the appearance of arbitrarily small-scale and the numerical convergence is expected happen, especially the mean curvature threshold is low, *i.e.* when the interface is intensively regularized.

Regarding the long-term outcomes of this manuscript, we have the following perspectives in terms of modelling:

- The development of a small-scale model adapted to the mixed regime where some additional information on the interface dynamics could enhance the inter-scale transfer, and thus help for the modelling of primary break-up. The modelling of dynamics in such model can notably take advantage of the dynamic modelling of geometrical quantities performed with GeoMOM which opened new perspective in this research area. Besides, such small-scale models could be derived from the geometric analysis of high-fidelity simulations resolving the interface with the geometric post-processing library `Mercur(v)e` (Di Battista, 2018). Some works in this direction are currently in progress in collaboration with Giuseppe Orlando, post-doctoral researcher at CMAP.

- The extension to non-barotropic/full equations of state in the two-scale unified modelling approach is also of primary interest for industrial test-case involving evaporation, cavitation of combustion, and is partly the subject of the PhD thesis of Haegeman (2025), PhD candidate at CMAP/ONERA. In this context, the modelling of heat or mass transfer (evaporation or condensation) should benefit from additional information about the local interface geometry.

- The accounting of the two-velocity Model 11 with a velocity for the large-scale model and a different velocity for the small-scale model would be another critical feature to model numerous phenomena such as drag, secondary

break-up and a more accurate space distribution of the spray in the domain. However, such phenomena would trigger the appearance of a continuous distribution in velocities, and its use with Hamilton's SAP should be further investigated, for instane through a method of moments involving size-velocity coupling in the manner of Vié et al. (2013).

- The modelling of turbulence *via* the addition of velocity dispersion in the framework of Hamilton's SAP is also investigated in the PhD thesis of W. Haegeman.

Finally, the numerical perspectives which could significantly impacts this work in the long run are:

- The development of numerical schemes for the two-velocity Model 11 adapted to the non-conservative and relaxation source terms. Following Gallouët et al. (2004), we could verify that the corresponding Riemann problem has well-defined non-conservative terms and Rankine-Hugoniot conditions.
- The use of Adaptive Mesh Refinement (AMR) techniques, as currently developed in the Samurai (2023) library by the HPC@Maths team, would also enable a better resolution of the large-scale dynamics. Indeed, as depicted in the simulation of the atomized liquid column, the complexity of the flow is concentrated in the neighbourhood of the large-scale interface and the inclusions. While the computational cost of such a technique is still high for complex multiscale flow, the combination of the regularizing inter-scale mass exchange with AMR should bring a determining execution speed up.

Bibliography

Abgrall, R. and Karni, S. A comment on the computation of non-conservative products. *Journal of Computational Physics*, 229(8):2759–2763, 2010. 10.1016/j.jcp.2009.12.015.

Ait-Ameur, K., Essadki, M., Massot, M., and Pichard, T. Limitation strategies for high-order discontinuous Galerkin schemes applied to an Eulerian model of polydisperse sprays. Preprint, 2024.

Akhiezer, N. The classical moment problem, Hafner Publ. *Co., New York*, pp. 299–2, 1965.

Aliseda, A. and Heindel, T. J. X-Ray Flow Visualization in Multiphase Flows. *Annual Review of Fluid Mechanics*, 53(1):543–567, 2021. 10.1146/annurev-fluid-010719-060201.

Allaire, G., Clerc, S., and Kokh, S. A Five-Equation Model for the Simulation of Interfaces between Compressible Fluids. *Journal of Computational Physics*, 181(2):577–616, 2002. 10.1006/jcph.2002.7143.

Amsden, A. A., O'Rourke, P. J., and Butler, T. D. KIVA-II: A computer program for chemically reactive flows with sprays. Technical Report LA-11560-MS, 6228444, Los Alamos National Laboratory, 1989.

Anderson, D. M., McFadden, G. B., and Wheeler, A. A. Diffuse-Interface Methods in Fluid Mechanics. *Annual Review of Fluid Mechanics*, 30(1):139–165, 1998. 10.1146/annurev.fluid.30.1.139. _eprint: https://doi.org/10.1146/annurev.fluid.30.1.139.

Andrianov, N. *Analytical and numerical investigation of two-phase flows*. PhD thesis, Otto-von-Guericke-Universität Magdeburg, Universitätsbibliothek, 2003.

Aregba-Driollet, D. and Natalini, R. Discrete Kinetic Schemes for Multidimensional Systems of Conservation Laws. *SIAM Journal on Numerical Analysis*, 37(6):1973–2004, 2000. 10.1137/S0036142998343075. _eprint: https://doi.org/10.1137/S0036142998343075.

Baer, M. R. and Nunziato, J. W. A two-phase mixture theory for the deflagration-to-detonation transition (DDT) in reactive granular materials. *International Journal of Multiphase Flow*, 12(6):861–889, 1986.

Banks, R. B. and Chandrasekhara, D. V. Experimental investigation of the penetration of a high-velocity gas jet through a liquid surface. *Journal of Fluid Mechanics*, 15(1):13–34, 1963. 10.1017/S0022112063000021.

Becker, S., Bie, H. D., and Sweeney, J. Dynamic Flow Behaviour in Bubble Columns. *Chemical Engineering Science*, 54(21):4929–4935, 1999.

Bedford, A. *Hamilton's Principle in Continuum Mechanics*. Pitman Publishing Ltd., 1985. 10.13140/2.1.1603.4887.

Bedford, A. and Drumheller, D. S. A variational theory of immiscible mixtures. *Archive for Rational Mechanics and Analysis*, 68(1):37–51, 1978. 10.1007/BF00276178.

Berdichevsky, V. *Variational Principles of Continuum Mechanics: I. Fundamentals*, volume 5 of *Interaction of Mechanics and Mathematics*. Springer, 2009. 10.1007/978-3-540-88467-5.

Biesheuvel, A. and Wijngaarden, L. V. Two-phase flow equations for a dilute dispersion of gas bubbles in liquid. *Journal of Fluid Mechanics*, 148:301–318, 1984. 10.1017/S0022112084002366.

Blanchard, G. *Modélisation et simulation multi-échelles de l'atomisation d'une nappe liquide cisaillée*. PhD thesis, ISAE, 2014.

Bode, M., Diewald, F., Broll, D. O., Heyse, J. F., Le Chenadec, V., and Pitsch, H. Influence of the Injector Geometry on Primary Breakup in Diesel Injector Systems. In *SAE Technical Paper*, pp. 2014–01–1427, 2014. 10.4271/2014-01-1427.

Bonnet, O. Mémoire sur la théorie générale des surfaces. *Journal de l'École polytechnique*, 19(32):1–146, 1848.

Bouchut, F. On Zero Pressure Gas Dynamics. In *Advances in Kinetic Theory and Computing: Selected Papers*, pp. 171–190. World Scientific Publishing, River Edge, 1994.

Bouchut, F. Construction of BGK Models with a Family of Kinetic Entropies for a Given System of Conservation Laws. *Journal of Statistical Physics*, 95(1/2), 1999.

Bouchut, F. A Reduced Stability Condition For Nonlinear Relaxation To Conservation Laws. *Journal of Hyperbolic Differential Equations*, 01(01):149–170, 2004. 10.1142/S0219891604000020.

Bouchut, F., Jin, S., and Li, X. Numerical Approximations of Pressureless and Isothermal Gas Dynamics. *SIAM Journal on Numerical Analysis*, 41(1):135–158, 2003. 10.1137/S0036142901398040.

Bourguignon, J.-P. *Calcul variationnel*. Editions Ecole Polytechnique, 2007.

Brackbill, J., Kothe, D., and Zemach, C. A continuum method for modeling surface tension. *Journal of Computational Physics*, 100(2):335–354, 1992. 10.1016/0021-9991(92)90240-Y.

Bueno, J. and Gomez, H. Liquid-vapor transformations with surfactants. Phase-field model and Isogeometric Analysis. *Journal of Computational Physics*, 321:797–818, 2016. 10.1016/j.jcp.2016.06.008. Publisher: Elsevier BV.

Burtea, C., Gavrilyuk, S., and Perrin, C. Hamilton's principle of stationary action in multiphase flow modeling. Lecture notes, 2021.

Bussac, J. *Modélisation et simulation d'écoulements multiphasiques avec phases miscibles*. Theses, Nantes Université, 2023.

Caflisch, R. E., Jin, S., and Russo, G. Uniformly Accurate Schemes for Hyperbolic Systems with Relaxation. *SIAM Journal on Numerical Analysis*, 34(1):246–281, 1997. 10.1137/S0036142994268090. _eprint: https://doi.org/10.1137/S0036142994268090.

Cahn, J. W. and Hilliard, J. E. Free Energy of a Nonuniform System. I. Interfacial Free Energy. *The Journal of Chemical Physics*, 28(2):258–267, 1958. 10.1063/1.1744102.

Capovilla, R., Guven, J., and Santiago, J. A. Deformations of the geometry of lipid vesicles. *Journal of Physics A, Mathematical and General*, 36(23):6281–6295, 2003.

Caro, F., Coquel, F., Jamet, D., and Kokh, S. DINMOD: A diffuse interface model for two-phase flows modelling. In *IRMA Lectures in Mathematics and Theoretical Physics*, pp. 209–237. EMS Press, 2005. 10.4171/012-1/10.

Caro, F., Coquel, F., Jamet, D., and Kokh, S. A simple finite-volume method for compressible isothermal two-phase flows simulation. *International Journal on Finite Volumes*, pp. www–latp, 2006.

Castro, M. J., LeFloch, P. G., Muñoz-Ruiz, M. L., and Parés, C. Why many theories of shock waves are necessary: Convergence error in formally path-consistent schemes. *Journal of Computational Physics*, 227(17):8107–8129, 2008. 10.1016/j.jcp.2008.05.012.

Chalons, C., Fox, R. O., Laurent, F., Massot, M., and Vié, A. Multivariate Gaussian Extended Quadrature Method of Moments for Turbulent Disperse Multiphase Flow. *Multiscale Modeling & Simulation*, 15(4):1553–1583, 2017. 10.1137/16M109209X. _eprint: https://doi.org/10.1137/16M109209X.

Chanteperdrix, Villedieu, and Vila. Un modèle bifluide compressible pour la simulation numérique d'écoulements diphasiques à phases séparées. *Preprint, ONERA report*, 2002.

Chanteperdrix, G. *Modélisation et simulation numérique d'écoulements diphasiques à interface libre. Application à l'étude des mouvements de liquides dans les réservoirs de véhicules spatiaux*. PhD thesis, ISAE, 2004.

Chanteperdrix, G., Villedieu, P., and Vila, J.-P. A Compressible Model for Separated Two-Phase Flows Computations. In *FEDSM2002*, pp. 809–816, Volume 1: Fora, Parts A and B, 2002. 10.1115/FEDSM2002-31141.

Chen, G., Levermore, C. D., and Liu, T. Hyperbolic conservation laws with stiff relaxation terms and entropy. *Communications on Pure and Applied Mathematics*, 47(6):787–830, 1994. 10.1002/cpa.3160470602.

Chern, I.-L., Glimm, J., McBryan, O., Plohr, B., and Yaniv, S. Front tracking for gas dynamics. *Journal of Computational Physics*, 62(1):83–110, 1986. Publisher: Elsevier.

Chesnel, J., Reveillon, J., Menard, T., and Demoulin, F.-X. Large Eddy Simulation of Liquid Jet Atomization. *Atomization and Sprays*, 21(9):711–736, 2011. Publisher: Begell House Type: 10.1615/AtomizSpr.2012003740.

Chiocchetti, S., Peshkov, I., Gavrilyuk, S., and Dumbser, M. High order ADER schemes and GLM curl cleaning for a first order hyperbolic formulation of compressible flow with surface tension. *Journal of Computational Physics*, 426:109898, 2021. 10.1016/j.jcp.2020.109898.

Chirco, L., Maarek, J., Popinet, S., and Zaleski, S. Manifold death: A Volume of Fluid implementation of controlled topological changes in thin sheets by the signature method. *Journal of Computational Physics*, 467:111468, 2022. 10.1016/j.jcp.2022.111468.

Coquel, F. and LeFloch, P. G. An entropy satisfying MUSCL scheme for systems of conservation laws. *Numerische Mathematik*, 74(1):1–33, 1996. 10.1007/s002110050205.

Coquel, F., Gallouët, T., Hérard, J.-M., and Seguin, N. Closure laws for a two-fluid two-pressure model. *Comptes Rendus Mathematique*, 334(10):927–932, 2002. 10.1016/S1631-073X(02)02366-X.

Cordesse, P. *Contribution to the study of combustion instabilities in cryotechnic rocket engines: coupling diffuse interface models with kinetic-based moment methods for primary atomization simulations*. PhD thesis, Université Paris-Saclay, 2020.

Cordesse, P. and Massot, M. Entropy supplementary conservation law for non-linear systems of PDEs with non-conservative terms: application to the modelling and analysis of complex fluid flows using computer algebra. *Communications in Mathematical Sciences*, 18(2):515–534, 2020. 10.4310/CMS.2020.v18.n2.a10.

Cordesse, P., Kokh, S., Battista, R. D., and Massot, M. Derivation of a two-phase flow model with two-scale kinematics and surface tension by means of variational calculus. In *Proceedings of the 10th International Conference on Multiphase Flow*, p. 7, Rio de Janeiro, Brazil, 2019.

Cordesse, P., Di Battista, R., Chevalier, Q., Matuszewski, L., Ménard, T., Kokh, S., and Massot, M. A diffuse interface approach for disperse two-phase flows involving dual-scale kinematics of droplet deformation based on geometrical variables. *ESAIM: Proceedings and Surveys*, 69:24–46, 2020. 10.1051/proc/202069024.

Courant, R. and Friedrichs, K. *Supersonic Flow and Shock Waves*. Springer, New York, 1948. Publisher: Springer.

Multiphase flows with droplets and particles. CRC Press, Boca Raton, Fla., 2. ed edition, 2012.

Curto, R. E. and Fialkow, L. A. Recursiveness, Positivity, and Truncated Moment Problems. *Houston Journal of Mathematics*, 17(4):34, 1991.

Curto, R. E. and Fialkow, L. A. The quadratic moment problem for the unit circle and unit disk. *Integral Equations and Operator Theory*, 38(4):377–409, 2000. 10.1007/BF01228605.

Curto, R. E. and Fialkow, L. A. Truncated K-Moment Problems in Several Variables. *Journal of Operator Theory*, 54(1):189–226, 2005. Publisher: Theta Foundation.

Dafermos, C. M. *Hyperbolic conservation laws in continuum physics*, volume 3. Springer, 2005.

Dal Maso, G., LeFloch, P. G., and Murat, F. Definition and weak stability of nonconservative products. *Journal de mathématiques pures et appliquées*, 74(6):483–548, 1995. Publisher: Elsevier, Paris.

Dassios, G. *Ellipsoidal Harmonics: Theory and Applications*. Number 146 in Encyclopedi of Mathematics and Its Applications. University Press, Cambridge, 2012.

Deberne, C., Chéron, V., Poux, A., and Brändle De Motta, J. C. Breakup prediction of oscillating droplets under turbulent flow. *International Journal of Multiphase Flow*, 173:104731, 2024. 10.1016/j.ijmultiphaseflow.2024.104731.

Deserno, M. Notes on Differential Geometry, 2004.

Deserno, M. Fluid lipid membranes: From differential geometry to curvature stresses. *Chemistry and Physics of Lipids*, 185:11–45, 2015. 10.1016/j.chemphyslip.2014.05.001.

Desjardins, O. and Moureau, V. Methods for multiphase flows with high density ratio. *Center for Turbulent Research, Summer Programm*, 2010:313–322, 2010.

Deuflhard, P. *Newton Methods for Nonlinear Problems: Affine Invariance and Adaptive Algorithms*, volume 35 of *Springer Series in Computational Mathematics*. Springer Berlin Heidelberg, Berlin, Heidelberg, 2011. 10.1007/978-3-642-23899-4.

Devassy, B. M., Habchi, C., and Daniel, E. Atomization Modelling of Liquid Jets using a Two-Surface Density Approach. *Atomization and Sprays*, 25(1):47–80, 2015.

Di Battista, R. Mercur(v)e, 2018.

Di Battista, R. *Towards a unified eulerian modeling framework for two-phase flow: geometrical subscale phenomena and associated highly-scalable numerical methods*. PhD thesis, Institut Polytechnique de Paris, 2021.

Dirac, P. A. M. The Lagrangian in Quantum Mechanics. *Physikalische Zeitschrift der Sowjetunion*, 3(1):64–72, 1933.

Dirac, P. A. M. An action principle for the motion of particles. *General Relativity and Gravitation*, 5(6):741–748, 1974. 10.1007/BF00761930.

Doisneau, F., Laurent, F., Murrone, A., Dupays, J., and Massot, M. Eulerian multi-fluid models for the simulation of dynamics and coalescence of particles in solid propellant combustion. *Journal of Computational Physics*, 234: 230–262, 2013. https://doi.org/10.1016/j.jcp.2012.09.025.

Downar-Zapolski, P., Bilicki, Z., Bolle, L., and Franco, J. The non-equilibrium relaxation model for one-dimensional flashing liquid flow. *International Journal of Multiphase Flow*, 22(3):473–483, 1996. 10.1016/0301-9322(95)00078-X.

Drew, D. A. Mathematical Modeling of Two-Phase Flow. *Annual Review of Fluid Mechanics*, p. 31, 1983.

Drew, D. A. Evolution of Geometric Statistics. *SIAM Journal on Applied Mathematics*, 50(3):649–666, 1990. 10.1137/0150038.

Drew, D. A. and Passman, S. L. *Theory of Multicomponent Fluids*. Number 135 in Applied Mathematical Sciences. Springer, 1999.

Drui, F. *Eulerian modeling and simulations of separated and disperse two-phase flows: development of a unified modeling approach and associated numerical methods for highly parallel computations*. PhD thesis, Université Paris-Saclay, Palaiseau, 2017.

Drui, F., Larat, A., Kokh, S., and Massot, M. Small-scale kinematics of two-phase flows: identifying relaxation processes in separated- and disperse-phase flow models. *Journal of Fluid Mechanics*, 876:326–355, 2019. 10.1017/jfm.2019.538.

Duarte, M. P. *Adaptive numerical methods in time and space for the simulation of multi-scale reaction fronts.* Theses, Ecole Centrale Paris, 2011. Issue: 2011ECAP0057.

Dufour, G. and Villedieu, P. A second-order multi-fluid model for evaporating sprays. *ESAIM: Mathematical Modelling and Numerical Analysis*, 39(5):931–963, 2005. 10.1051/m2an:2005041.

Dumouchel, C. On the experimental investigation on primary atomization of liquid streams. *Experiments in Fluids*, 45(3):371–422, 2008. 10.1007/s00348-008-0526-0.

Dunn, J. E. Interstitial Working and a Nonclassical Continuum Thermodynamics. In *New Perspectives in Thermodynamics*, pp. 187–222. Springer Berlin Heidelberg, 1986. 10.1007/978-3-642-70803-9_11.

Dunn, J. E. and Serrin, J. On the Thermomechanics of Interstitial Working. In *The Breadth and Depth of Continuum Mechanics*, pp. 705–743. Springer Berlin Heidelberg, 1986. 10.1007/978-3-642-61634-1_33.

Eckart, C. The Electrodynamics of Material Media. *Phys. Rev.*, 54(11):920–923, 1938. 10.1103/PhysRev.54.920. Publisher: American Physical Society.

Eckart, C. Variation Principles of Hydrodynamics. *The Physics of Fluids*, 3(3):421–427, 1960. 10.1063/1.1706053.

Ern, P., Risso, F., Fabre, D., and Magnaudet, J. Wake-Induced Oscillatory Paths of Bodies Freely Rising or Falling in Fluids. *Annual Review of Fluid Mechanics*, 44(1):97–121, 2012. 10.1146/annurev-fluid-120710-101250.

Essadki, M. A new high order moment method for polydisperse evaporating sprays dedicated to the coupling with separated two-phase flows in automotive engine. In *Proceedings of the 9th International Conference on Multiphase Flows*, Florence, 2016.

Essadki, M. *Contribution à la modélisation eulérienne unifiée de l'injection: de la zone dense au spray polydispersé*. PhD thesis, Université Paris-Saclay, 2018.

Essadki, M., de Chaisemartin, S., Massot, M., Laurent, F., Larat, A., and Jay, S. Adaptive Mesh Refinement and High Order Geometrical Moment Method for the Simulation of Polydisperse Evaporating Sprays. *Oil Gas Sci. Technol. – Rev. IFP Energies nouvelles*, 71(5), 2016. 10.2516/ogst/2016012.

Essadki, M., de Chaisemartin, S., Laurent, F., and Massot, M. High Order Moment Model for Polydisperse Evaporating Sprays towards Interfacial Geometry Description. *SIAM Journal on Applied Mathematics*, 78(4):2003–2027, 2018. 10.1137/16M1108364.

Essadki, M., Drui, F., de Chaisemartin, S., Larat, A., Ménard, T., and Massot, M. Statistical modeling of the gas–liquid interface using geometrical variables: Toward a unified description of the disperse and separated phase flows. *International Journal of Multiphase Flow*, 120:103084, 2019. 10.1016/j.ijmultiphaseflow.2019.103084.

Faeth, G. Spray combustion phenomena. *Symposium (International) on Combustion*, 26(1):1593–1612, 1996. 10.1016/S0082-0784(96)80383-3.

Farago, Z. and Chigier, N. Morphological classification of disintegration of round liquid jets in a coaxial air stream. *Atomization and Sprays*, 2(2):137–153, 1992.

Ferrando, D., Carreres, M., Belmar-Gil, M., Cervello-Sanz, D., Duret, B., Reveillon, J., Javier Salvador, F., and Demoulin, F. Modeling Internal Flow and Primary Atomization in a Simplex Pressure-Swirl Atomizer. *Atomization and Sprays*, 33(3):1–28, 2023. 10.1615/AtomizSpr.2022044824.

Feynman, R. P. Space-Time Approach to Non-Relativistic Quantum Mechanics. *Reviews of Modern Physics*, 20(2): 367–387, 1948. 10.1103/RevModPhys.20.367.

Fleau, S. *Multifield approach and interface locating method for two-phase flows in nuclear power plant*. Theses, Université Paris-Est, 2017. Issue: 2017PESC1081.

Forestier, A. and Gavrilyuk, S. Criterion of hyperbolicity for non-conservative quasilinear systems admitting a partially convex conservation law. *Mathematical Methods in the Applied Sciences*, 34(17):2148–2158, 2011. 10.1002/mma.1512.

Fox, R. O. Optimal Moment Sets for Multivariate Direct Quadrature Method of Moments. *Industrial & Engineering Chemistry Research*, 48(21):9686–9696, 2009. 10.1021/ie801316d.

Multiphase reacting flows: modelling and simulation. Number no. 492 in Courses and lectures. Springer, Wien ; New York, 2007.

Fox, R. O., Laurent, F., and Vié, A. A hyperbolic two-fluid model for compressible flows with arbitrary material-density ratios. *Journal of Fluid Mechanics*, 903:A5, 2020. 10.1017/jfm.2020.615.

Fox, R. O., Laurent, F., and Passalacqua, A. The generalized quadrature method of moments. *Journal of Aerosol Science*, p. 106096, 2022. 10.1016/j.jaerosci.2022.106096.

Fuster, D., Bagué, A., Boeck, T., Le Moyne, L., Leboissetier, A., Popinet, S., Ray, P., Scardovelli, R., and Zaleski, S. Simulation of primary atomization with an octree adaptive mesh refinement and VOF method. *International Journal of Multiphase Flow*, 35(6):550–565, 2009. 10.1016/j.ijmultiphaseflow.2009.02.014.

Gaillard, P. *Interfaces diffuses et flammes transcritiques LOX/H2*. PhD thesis, Universite Pierre et Marie Curie, 2015.

Gallouët, T., Hérard, J.-M., and Seguin, N. Numerical Modeling of Two-Phase Flows Using the Two-Fluid Two-Pressure Approach. *Mathematical Models and Methods in Applied Sciences*, 14(05):663–700, 2004. 10.1142/S0218202504003404. _eprint: https://doi.org/10.1142/S0218202504003404.

Gavrilyuk, S. Multiphase flow modeling via Hamilton's principle. In *Variational models and Methods in Solid and Fluid Mechanics*, number 535 in CISM Courses and Lectures, pp. 163–210. Springer, Wien ; New York, 2011.

Gavrilyuk, S. 'Uncertainty' principle in two fluid–mechanics. *ESAIM: Proceedings and Surveys*, 69:47–55, 2020. 10.1051/proc/202069047.

Gavrilyuk, S. and Gouin, H. A new form of governing equations of fluids arising from Hamilton's principle. *International Journal of Engineering Science*, p. 26, 1999.

Gavrilyuk, S. and Saurel, R. Mathematical and Numerical Modeling of Two-Phase Compressible Flows with Micro-Inertia. *Journal of Computational Physics*, 175(1):326–360, 2002. 10.1006/jcph.2001.6951.

Gavrilyuk, S. and Teshukov, V. Generalized vorticity for bubbly liquidand dispersive shallow water equations. *Continuum Mechanics and Thermodynamics*, 13(6):365–382, 2001. 10.1007/s001610100057.

Geurst, J. Variational principles and two-fluid hydrodynamics of bubbly liquid/gas mixtures. *Physica A: Statistical Mechanics and its Applications*, 135(2-3):455–486, 1986. 10.1016/0378-4371(86)90154-8.

Giovangigli, V. Kinetic derivation of Cahn-Hilliard fluid models. *Physical Review E*, 104(5):054109, 2021. 10.1103/PhysRevE.104.054109.

Giovangigli, V., Calvez, Y. L., and Nabet, F. Symmetrization and Local Existence of Strong Solutions for Diffuse Interface Fluid Models. *Journal of Mathematical Fluid Mechanics*, 25(4):82, 2023. 10.1007/s00021-023-00825-4.

Glimm, J., Grove, J. W., Li, X. L., and Tan, D. C. Robust computational algorithms for dynamic interface tracking in three dimensions. *SIAM Journal on Scientific Computing*, 21(6):2240–2256, 2000. Publisher: SIAM.

Godlewski, E. and Raviart, P.-A. *Hyperbolic Systems Of Conservation Laws*. Ellipses, 1991.

Godlewski, E. and Raviart, P.-A. *Numerical Approximation of Hyperbolic Systems of Conservation Laws*, volume 118 of *Applied Mathematical Sciences*. Springer New York, New York, NY, 1996. 10.1007/978-1-4612-0713-9.

Godunov, S. K. and Bohachevsky, I. Finite difference method for numerical computation of discontinuous solutions of the equations of fluid dynamics. *Matematičeskij sbornik*, 47(89)(3):271–306, 1959. Publisher: Steklov Mathematical Institute of Russian Academy of Sciences.

Goldman, R. Curvature formulas for implicit curves and surfaces. *Computer Aided Geometric Design*, 22(7):632–658, 2005. 10.1016/j.cagd.2005.06.005.

Gouin, H. The second gradient theory applied to interfaces: Models of continuum mechanics for fluid interfaces. In *Dynamics of Multiphase Flows Across Interfaces*, pp. 8–13. Springer Berlin Heidelberg, 1996. 10.1007/bfb0102656.

Gouin, H. *Introduction to Mathematical Methods of Analytical Mechanics*. ISTE Press/Elsevier, 2020.

Gouin, H. and Debieve, J.-F. Variational principle involving the stress tensor in elastodynamics. *International Journal of Engineering Science*, 24(7):1057–1066, 1986. https://doi.org/10.1016/0020-7225(86)90001-7.

Granger, F. *Modélisation de l'atomisation primaire d'oxygène liquide dans les flammes diphasiques des moteurs fusées à ergols liquides*. PhD thesis, ISAE, 2023.

Granger, F., Hoarau, J.-C., and Dorey, L.-H. Interface area density model for Large-Eddy Simulation of assisted atomization in fiber regime, 2023.

Grenier, N., Vila, J.-P., and Villedieu, P. An accurate low-Mach scheme for a compressible two-fluid model applied to free-surface flows. *Journal of Computational Physics*, 252:1–19, 2013. 10.1016/j.jcp.2013.06.008.

Gueyffier, D., Li, J., Nadim, A., Scardovelli, R., and Zaleski, S. Volume-of-Fluid Interface Tracking with Smoothed Surface Stress Methods for Three-Dimensional Flows. *Journal of Computational Physics*, 152(2):423–456, 1999. 10.1006/jcph.1998.6168.

Guillemaud, V. *Modélisation et simulation numérique des écoulements diphasiques par une approche bifluide à deux pressions*. PhD thesis, Université de Provence (Aix-Marseille I), 2007a.

Guillemaud, V. Modelling and Numerical Simulation of Strongly Unbalanced Two-Phase Flows. In *18th AIAA Computational Fluid Dynamics Conference*. American Institute of Aeronautics and Astronautics, 2007b. 10.2514/6.2007-3821.

Gårding, L. Problème de Cauchy pour les systèmes quasi-linéaires d'ordre un strictement hyperboliques. In *Equations aux Derivees partielles*, volume 117, pp. 33–40, Paris, 1963.

Habiballah, M., Orain, M., Grisch, F., Vingert, L., and Gicquel, P. Experimental Studies of High-Pressure Cryogenic Flames on the MASCOTTE facility. *Combustion Science and Technology*, 178(1-3):101–128, 2006. 10.1080/00102200500294486. Publisher: Taylor & Francis.

Haegeman, W. *Modèle multi-fluide à deux échelles cinématiques pour la simulation d'interface liquide gaz en propulsion solide*. PhD thesis, Institut Polytechnique de Paris, 2025.

Haegeman, W., Le Touze, C., Dupays, J., and Massot, M. Numerical Simulation of the Impact of a Gas Jet on a Free Water Surface. *Multiphase Science and Technology*, 36(1):27–48, 2024. 10.1615/MultScienTechn.2023047916Getaccess.

Hairer, E. and Wanner, G. *Solving Ordinary Differential Equations II*, volume 14 of *Springer Series in Computational Mathematics*. Springer Berlin Heidelberg, Berlin, Heidelberg, 1996. 10.1007/978-3-642-05221-7.

Harten, A., Lax, P. D., and Leer, B. v. On upstream differencing and Godunov-type schemes for hyperbolic conservation laws. *SIAM review*, 25(1):35–61, 1983. Publisher: SIAM.

Harten, A., Engquist, B., Osher, S., and Chakravarthy, S. R. Uniformly high order accurate essentially non-oscillatory schemes, III. *Journal of Computational Physics*, 71(2):231–303, 1987. https://doi.org/10.1016/0021-9991(87)90031-3.

Harten, A., Lax, P. D., Levermore, C. D., and Morokoff, W. J. Convex Entropies and Hyperbolicity for General Euler Equations. *SIAM Journal on Numerical Analysis*, 35(6):2117–2127, 1998. Publisher: Society for Industrial and Applied Mathematics.

Hausdorff, F. Summationsmethoden und Momentfolgen. I. *Mathematische Zeitschrift*, 9(1):74–109, 1921. 10.1007/BF01378337.

Helluy, P. and Seguin, N. Relaxation models of phase transition flows. *ESAIM: Mathematical Modelling and Numerical Analysis*, 40(2):331–352, 2006. 10.1051/m2an:2006015. Publisher: EDP-Sciences.

Herivel, J. W. The derivation of the equations of motion of an ideal fluid by Hamilton's principle. *Mathematical Proceedings of the Cambridge Philosophical Society*, 51(2):344–349, 1955. 10.1017/s0305004100030267. Publisher: Cambridge University Press (CUP).

Herrmann, M. Detailed simulations of the breakup processes of turbulent liquid jets in subsonic crossflows. In *11th International Annual Conference on Liquid Atomization and Spray Systems 2009, ICLASS 2009*, 11th International Annual Conference on Liquid Atomization and Spray Systems 2009, ICLASS 2009. ILASS Americas/Professor Scott Samuelsen UCI Combustion Laboratory University of California Irvine, CA 92697-3550, 2009.

Herrmann, M. A parallel Eulerian interface tracking/Lagrangian point particle multi-scale coupling procedure. *Journal of Computational Physics*, 229(3):745–759, 2010. 10.1016/j.jcp.2009.10.009.

Herrmann, M. A Dual-Scale LES Subgrid Model for Turbulent Liquid/Gas Phase Interface Dynamics. In *Volume 1: Symposia*, p. V001T21A001, Seoul, South Korea, 2015. American Society of Mechanical Engineers. 10.1115/AJKFluids2015-21052.

Hill, M. J. M. and Henrici, O. M. F. E. VI. On a spherical vortex. *Philosophical Transactions of the Royal Society of London. (A.)*, 185:213–245, 1894. 10.1098/rsta.1894.0006. _eprint: https://royalsocietypublishing.org/doi/pdf/10.1098/rsta.1894.0006.

Hoarau, J.-C., Dorey, L.-H., Zuzio, D., Granger, F., and Estivalezes, J.-L. Direct numerical simulation of a subcritical coaxial injection in fiber regime using sharp interface reconstruction. Preprint, 2023.

Hobson, E. W. *The theory of spherical and ellipsoidal harmonics*. University Press, Cambridge, 1931.

Hulburt, H. and Katz, S. Some problems in particle technology. *Chemical Engineering Science*, 19(8):555–574, 1964. 10.1016/0009-2509(64)85047-8.

Hundsdorfer, W. and Verwer, J. *Numerical Solution of Time-Dependent Advection-Diffusion-Reaction Equations*, volume 33 of *Springer Series in Computational Mathematics*. Springer Berlin Heidelberg, Berlin, Heidelberg, 2003. 10.1007/978-3-662-09017-6.

Hérard, J.-M. A three-phase flow model. *Mathematical and Computer Modelling*, 45(5-6):732–755, 2007. 10.1016/j.mcm.2006.07.018.

Hérard, J.-M. and Mathis, H. A three-phase flow model with two miscible phases. *ESAIM: Mathematical Modelling and Numerical Analysis*, 53(4):1373–1389, 2019. 10.1051/m2an/2019028.

Ishii, M. and Hibiki, T. *Thermo-fluid dynamic theory of two-phase flow*. Eyrolles, France, 1975.

Jabin, P.-E. Various Levels of Models for Aerosols. *Mathematical Models and Methods in Applied Sciences*, 12(07): 903–919, 2002. 10.1142/S0218202502001957.

Jacqmin, D. Calculation of Two-Phase Navier–Stokes Flows Using Phase-Field Modeling. *Journal of Computational Physics*, 155(1):96–127, 1999. 10.1006/jcph.1999.6332. Publisher: Elsevier BV.

Jain, M., Prakash, R. S., Tomar, G., and Ravikrishna, R. V. Secondary breakup of a drop at moderate Weber numbers. *Proceedings of the Royal Society A: Mathematical, Physical and Engineering Sciences*, 471(2177):20140930, 2015. 10.1098/rspa.2014.0930.

Jamet, D., Lebaigue, O., Coutris, N., and Delhaye, J. The Second Gradient Method for the Direct Numerical Simulation of Liquid–Vapor Flows with Phase Change. *Journal of Computational Physics*, 169(2):624–651, 2001. 10.1006/jcph.2000.6692.

Janodet, R., Guillamón, C., Moureau, V., Mercier, R., Lartigue, G., Bénard, P., Ménard, T., and Berlemont, A. A massively parallel accurate conservative level set algorithm for simulating turbulent atomization on adaptive unstructured grids. *Journal of Computational Physics*, 458:111075, 2022. 10.1016/j.jcp.2022.111075.

Jin, S. Runge-Kutta Methods for Hyperbolic Conservation Laws with Stiff Relaxation Terms. *Journal of Computational Physics*, 122(1):51–67, 1995. https://doi.org/10.1006/jcph.1995.1196.

John W. Strutt (3rd Baron Rayleigh). VI. On the capillary phenomena of jets. *Proceedings of the Royal Society*, 29 (196-199):71–97, 1879. 10.1098/rspl.1879.0015.

Jomée, G. *Simulation de modèles d'écoulements multiphasiques compressibles hors équilibre*. PhD thesis, Aix-Marseille Université, 2023.

Josiepy. HPC@Maths team, 2023. https://github.com/hpc-maths/josiepy.

Kah, D. *Prise en compte des aspects polydispensés pour la modélisation d'un jet de carburant dans les moteurs à combustion interne*. PhD thesis, Ecole Centrale de Paris, 2010.

Kah, D., Laurent, F., Massot, M., and Jay, S. A high order moment method simulating evaporation and advection of a polydisperse liquid spray. *Journal of Computational Physics*, 231(2):394–422, 2012. 10.1016/j.jcp.2011.08.032.

Kapila, A. K., Menikoff, R., Bdzil, J. B., Son, S. F., and Stewart, D. S. Two-phase modeling of deflagration-to-detonation transition in granular materials: Reduced equations. *Physics of Fluids*, 13(10):3002–3024, 2001. 10.1063/1.1398042.

Khalatnikov, I. M. *Introduction to superfluidity theory ( ).* Nauka, Moscow, 1st edition, 1965.

Khalatnikov, I. M. *Introduction to superfluidity theory.* CRC Press, Boca Raton, 1st edition, 1989.

Kleiber, C. and Stoyanov, J. Multivariate distributions and the moment problem. *Journal of Multivariate Analysis*, 113:7–18, 2013. 10.1016/j.jmva.2011.06.001.

Korteweg, D. J. Sur la forme que prennent les équations du mouvements des fluides si l'on tient compte des forces capillaires causées par des variations de densité considérables mais connues et sur la théorie de la capillarité dans l'hypothèse d'une variation continue de la densité. *Archives Néerlandaises des Sciences exactes et naturelles*, 6: 1–24, 1901.

Koshizuka, S. and Oka, Y. Moving-particle semi-implicit method for fragmentation of incompressible fluid. *Nuclear science and engineering*, 123(3):421–434, 1996.

Kreyszig, E. *Differential Geometry.* Dover, New York, 1991.

Kruzhkov, S. N. Generalized solutions of the Cauchy problem in the large for first order nonlinear equations. In *Doklady Akademii Nauk*, volume 187, pp. 29–32. Russian Academy of Sciences, 1969. Issue: 1.

Lafaurie, B., Nardone, C., Scardovelli, R., Zaleski, S., and Zanetti, G. Modelling Merging and Fragmentation in Multiphase Flows with SURFER. *Journal of Computational Physics*, 113(1):134–147, 1994. 10.1006/jcph.1994.1123.

Lafitte, P., Melis, W., and Samaey, G. A high-order relaxation method with projective integration for solving nonlinear systems of hyperbolic conservation laws. *Journal of Computational Physics*, 340:1–25, 2017. 10.1016/j.jcp.2017.03.027.

Lalanne, B., Tanguy, S., and Risso, F. Effect of rising motion on the damped shape oscillations of drops and bubbles. *Physics of Fluids*, 25(11):112107, 2013. 10.1063/1.4829366. Publisher: American Institute of Physics.

Lamb, H. *Hydrodynamics.* University Press, Cambridge, 4th edition, 1916.

Landau, L. D. and Lifshitz, E. M. *Fluid mechanics ( ).* Number 6 in Course of theoretical physics. Nauka, Moscow, 3rd ed. edition, 1986.

Landau, L. D. and Lifshitz, E. M. *Fluid mechanics.* Number v. 6 in Course of theoretical physics. Pergamon Press, Oxford, England ; New York, 2nd ed., 2nd english ed., rev edition, 1987.

Laurent, F. and Massot, M. Multi-fluid modelling of laminar polydisperse spray flames: origin, assumptions and comparison of sectional and sampling methods. *Combustion Theory and Modelling*, 5(4):537–572, 2001. 10.1088/1364-7830/5/4/303.

Laurent, F., Massot, M., and Villedieu, P. Eulerian multi-fluid modeling for the numerical simulation of coalescence in polydisperse dense liquid sprays. *Journal of Computational Physics*, 194(2):505–543, 2004. 10.1016/j.jcp.2003.08.026.

Lax, P. D. Hyperbolic systems of conservation laws II. *Communications on Pure and Applied Mathematics*, 10(4): 537–566, 1957. 10.1002/cpa.3160100406. Publisher: John Wiley & Sons, Ltd.

Le Touze, C. *Couplage entre modèles diphasiques à "phases séparées" et à "phase dispersée" pour la simulation de l'atomisation primaire en combustion cryotechnique.* PhD thesis, Université Nice Sophia Antipolis, 2015.

Le Touze, C., Dorey, L.-H., Rutard, N., and Murrone, A. A compressible two-phase flow framework for Large Eddy Simulations of liquid-propellant rocket engines. *Applied Mathematical Modelling*, 84:265–286, 2020. 10.1016/j.apm.2020.03.028.

Lebas, R., Menard, T., Beau, P.-A., Berlemont, A., and Demoulin, F.-X. Numerical simulation of primary break-up and atomization: DNS and modelling study. *International Journal of Multiphase Flow*, 35(3):247–260, 2009. 10.1016/j.ijmultiphaseflow.2008.11.005.

Letournel, R. *Reduced-order modeling and simulation of turbulent disperse two-phase flows: new theoretical and modeling approaches for reproducing intermittency, segregation and two-way coupling.* PhD thesis, CentraleSupélec, 2022.

LeVeque, R. J. *Numerical methods for conservation laws*, volume 214. Springer, 1992.

Lhuillier, D. Dynamics of interfaces and rheology of immiscible liquid–liquid mixtures. *Comptes Rendus Mécanique*, 331(2):113–118, 2003. 10.1016/S1631-0721(02)00004-9.

Lhuillier, D. Evolution of the volumetric interfacial area in two-phase mixtures. *Comptes Rendus Mécanique*, 332(2): 103–108, 2004. 10.1016/j.crme.2003.12.004.

Lhuillier, D., Chang, C.-H., and Theofanous, T. G. On the quest for a hyperbolic effective-field model of disperse flows. *Journal of Fluid Mechanics*, 731:184–194, 2013. 10.1017/jfm.2013.380.

Lin, C. C. Liquid Helium. In *Proceedings of the International School of Physics "Enrico Fermi"*, volume Course XXI, p. 93. Academic Press, 1963.

Ling, Y., Fuster, D., Zaleski, S., and Tryggvason, G. Spray formation in a quasiplanar gas-liquid mixing layer at moderate density ratios: A numerical closeup. *Physical Review Fluids*, 2(1):014005, 2017. 10.1103/PhysRevFluids.2.014005.

Liu, T.-P. Hyperbolic conservation laws with relaxation. *Communications in Mathematical Physics*, 108:153–175, 1987. Publisher: Springer.

Loison, A., Kokh, S., Pichard, T., and Massot, M. A unified two-scale gas-liquid multi-fluid model with capillarity and interface regularization through a mass transfer between scales, 2023a.

Loison, A., Pichard, T., Kokh, S., and Massot, M. Two-scale modelling of two-phase flows based on the Stationary Action Principle and a Geometric Method Of Moments, 2023b.

Marble, F. E. Dynamics of a gas containing small solid particles. In *Combustion and Propulsion*, Pasadena, 1963. Pergamon Press.

Marchisio, D. L. and Fox, R. O. Solution of population balance equations using the direct quadrature method of moments. *Journal of Aerosol Science*, 36(1):43–73, 2005. 10.1016/j.jaerosci.2004.07.009.

Markfelder, S. The Euler Equations as a Hyperbolic System of Conservation Laws. In *Convex Integration Applied to the Multi-Dimensional Compressible Euler Equations*, pp. 27–48. Springer International Publishing, Cham, 2021. 10.1007/978-3-030-83785-3_3.

Marmottant, P. and Villermaux, E. On spray formation. *Journal of Fluid Mechanics*, 498:73–111, 2004. 10.1017/S0022112003006529.

Martinez, L. G., Duret, B., Reveillon, J., and Demoulin, F. A new DNS formalism dedicated to turbulent two-phase flows with phase change. *International Journal of Multiphase Flow*, 143:103762, 2021. 10.1016/j.ijmultiphaseflow.2021.103762.

Massot, M. Eulerian Multi-Fluid Models for Polydisperse Evaporating Sprays. In , *Multiphase Reacting Flows: Modelling and Simulation*, pp. 79–123. Springer Vienna, Vienna, 2007. 10.1007/978-3-211-72464-4_3.

Massot, M., Kumar, M., Gomez, A., and Smooke, M. Counterflow spray diffusion flames of heptane: computations and experiments. *In Proceedings of the 27th Symposium International on Combustion, The Comb. Institute*, pp. 1975–1983, 1998.

Massot, M., Laurent, F., Kah, D., and de Chaisemartin, S. A Robust Moment Method for Evaluation of the Disappearance Rate of Evaporating Sprays. *SIAM Journal on Applied Mathematics*, 70(8):3203–3234, 2010. 10.1137/080740027.

Mayer, W. O. H. and Branam, R. Atomization characteristics on the surface of a round liquid jet. *Experiments in Fluids*, 36(4):528–539, 2004. 10.1007/s00348-003-0675-0.

McGraw, R. Description of Aerosol Dynamics by the Quadrature Method of Moments. *Aerosol Science and Technology*, 27(2):255–265, 1997. 10.1080/02786829708965471.

Mead, L. R. and Papanicolaou, N. Maximum entropy in the problem of moments. *Journal of Mathematical Physics*, 25(8):2404–2417, 1984. 10.1063/1.526446.

Moore, D. W. The velocity of rise of distorted gas bubbles in a liquid of small viscosity. *Journal of Fluid Mechanics*, 23(4):749–766, 1965. 10.1017/S0022112065001660.

Morel, C. *Mathematical Modeling of Disperse Two-Phase Flows*, volume 114 of *Fluid Mechanics and Its Applications*. Springer International Publishing, Cham, 2015. 10.1007/978-3-319-20104-7.

Munz, C.-D., Omnes, P., Schneider, R., Sonnendrücker, E., and Voß, U. Divergence Correction Techniques for Maxwell Solvers Based on a Hyperbolic Model. *Journal of Computational Physics*, 161(2):484–511, 2000. 10.1006/jcph.2000.6507.

Murrone, A. and Guillard, H. A five equation reduced model for compressible two phase flow problems. *Journal of Computational Physics*, 202(2):664–698, 2005. 10.1016/j.jcp.2004.07.019.

Ménard, T., Tanguy, S., and Berlemont, A. Coupling level set/VOF/ghost fluid methods: Validation and application to 3D simulation of the primary break-up of a liquid jet. *International Journal of Multiphase Flow*, 33(5):510–524, 2007. 10.1016/j.ijmultiphaseflow.2006.11.001.

Métivier, G. Remarks on the well-posedness of the nonlinear Cauchy problem. In , *Contemporary Mathematics*, volume 368, pp. 337–356. American Mathematical Society, Providence, Rhode Island, 2005. 10.1090/conm/368/06790.

Müller, C. *Spherical Harmonics*. Number 17 in Lecture Notes in Mathematics. Springer, Berlin, Heidelberg, 1st edition, 1966.

Natalini, R. Recent mathematical results on hyperbolic relaxation problems. *Quaderno IAC*, 7, 1998.

Oguz, E. *Modeling of spray polydispersion with two-way turbulent interactions for high pressure direct injection in engines*. PhD thesis, Ecole Centrale de Paris, 2014.

Orejas, J. A. Modelling and simulation of a bubble-column reactor with external loop: Application to the direct chlorination of ethylene. *Chemical Engineering Science*, 54(21):5299–5309, 1999. 10.1016/S0009-2509(99)00254-7.

O'Rourke, P. J. and Amsden, A. A. The Tab Method for Numerical Calculation of Spray Droplet Breakup. In *SAE Technical Paper 872089*, 1987. 10.4271/872089.

Osher, S. and Fedkiw, R. *Level set methods and dynamic implicit surfaces*. Number 153 in Applied mathematical sciences. Springer, New York Berlin Heidelberg, 2003.

Parés, C. Numerical methods for nonconservative hyperbolic systems: a theoretical framework. *SIAM Journal on Numerical Analysis*, 44(1):300–321, 2006. 10.1137/050628052.

Pelanti, M. Arbitrary-rate relaxation techniques for the numerical modeling of compressible two-phase flows with heat and mass transfer. *International Journal of Multiphase Flow*, 153:104097, 2022. 10.1016/j.ijmultiphaseflow.2022.104097.

Perigaud, G. and Saurel, R. A compressible flow model with capillary effects. *Journal of Computational Physics*, 209(1):139–178, 2005. 10.1016/j.jcp.2005.03.018.

Perrier, V. and Gutiérrez, E. Derivation and Closure of Baer and Nunziato Type Multiphase Models by Averaging a Simple Stochastic Model. *Multiscale Modeling & Simulation*, 19(1):401–439, 2021. 10.1137/19M1306609. Publisher: Society for Industrial and Applied Mathematics.

Perthame, B. Boltzmann Type Schemes for Gas Dynamics and the Entropy Property. *SIAM Journal on Numerical Analysis*, 27(6):1405–1421, 1990. 10.1137/0727081. _eprint: https://doi.org/10.1137/0727081.

Petitpas, F., Franquet, E., Saurel, R., and Le Metayer, O. A relaxation-projection method for compressible flows. Part II: Artificial heat exchanges for multiphase shocks. *Journal of Computational Physics*, 225(2):2214–2248, 2007. 10.1016/j.jcp.2007.03.014.

Pilch, M. and Erdman, C. Use of breakup time data and velocity history data to predict the maximum size of stable fragments for acceleration-induced breakup of a liquid drop. *International Journal of Multiphase Flow*, 13(6):741–757, 1987. 10.1016/0301-9322(87)90063-2.

Plesset, M. S. and Prosperetti, A. Bubble Dynamics and Cavitation. *Annual Review of Fluid Mechanics*, 9(1):145–185, 1977. 10.1146/annurev.fl.09.010177.001045. Publisher: Annual Reviews.

Plümacher, D., Oberlack, M., Wang, Y., and Smuda, M. On a non-linear droplet oscillation theory via the unified method. *Physics of Fluids*, 32(6):067104, 2020. 10.1063/5.0007341.

Pope, S. B. The evolution of surface in turbulence. *International Journal of Engineering Science*, 26(5):445–469, 1988. https://doi.org/10.1016/0020-7225(88)90004-3.

Popinet, S. Gerris: a tree-based adaptive solver for the incompressible Euler equations in complex geometries. *Journal of Computational Physics*, 190(2):572–600, 2003. https://doi.org/10.1016/S0021-9991(03)00298-5.

Popinet, S. and Zaleski, S. A front-tracking algorithm for accurate representation of surface tension. *Int. J. Numer. Meth. Fluids*, 30:775–793, 1999.

Prosperetti, A. Viscous effects on perturbed spherical flows. *Quarterly of Applied Mathematics*, 34(4):339–352, 1977. 10.1090/qam/99652.

Prosperetti, A. A generalization of the Rayleigh–Plesset equation of bubble dynamics. *The Physics of Fluids*, 25(3):409–410, 1982. 10.1063/1.863775.

Ramshaw, J. D. and Trapp, J. A. Characteristics, stability, and short-wavelength phenomena in two-phase flow equation systems. *Nuclear Science and Engineering*, 66(1):93–102, 1978. Publisher: Taylor & Francis.

Ransom, V. H. and Hicks, D. L. Hyperbolic two-pressure models for two-phase flow. *Journal of Computational Physics*, 53(1):124–151, 1984. https://doi.org/10.1016/0021-9991(84)90056-1.

Raviart, P.-A. and Sainsaulieu, L. A Non-Conservative hyperbolic system modeling spray dynamics. Part I. Solution of the Riemann Problem. *Mathematical Models and Methods in Applied Sciences*, 5(3):297–333, 1995.

Reitz, R. D. and Bracco, F. B. On the Dependence of Spray Angle and Other Spray Parameters on Nozzle Design and Operating Conditions. In *SAE Technical Paper*, p. 790494, 1979. 10.4271/790494.

Risso, F. The mechanisms of deformation and breakup of drops and bubbles. *Multiphase science and technology*, 12 (1), 2000.

Risso, F. Agitation, Mixing, and Transfers Induced by Bubbles. *Annual Review of Fluid Mechanics*, 50(1):25–48, 2018. 10.1146/annurev-fluid-122316-045003.

Roe, P. L. Approximate Riemann solvers, parameter vectors, and difference schemes. *Journal of computational physics*, 43(2):357–372, 1981. Publisher: Elsevier.

Rudman, M. A volume-tracking method for incompressible multifluid flows with large density variations. *International Journal for Numerical Methods in Fluids*, 28(2):357–378, 1998. 10.1002/(SICI)1097-0363(19980815)28:2<357::AID-FLD750>3.0.CO;2-D.

Rusanov, V. V. The calculation of the interaction of non-stationary shock waves with barriers. *Zhurnal Vychislitel'noi Matematiki i Matematicheskoi Fiziki*, 1(2):267–279, 1961. Publisher: Russian Academy of Sciences, Branch of Mathematical Sciences.

Sakano, Y., Nambu, T., Mizobuchi, Y., and Sato, T. Evaluation of three-dimensional droplet shape for analysis of the crossflow-type atomization. *Mechanical Engineering Journal*, 9(1):21–00378–21–00378, 2022. 10.1299/mej.21-00378.

Salmon, R. Practical use of Hamilton's principle. *Journal of Fluid Mechanics*, 132:431–444, 1983. 10.1017/S0022112083001706. Publisher: Cambridge University Press.

Samurai. HPC@Maths team, 2023.

Saurel, R. and Abgrall, R. A Multiphase Godunov Method for Compressible Multifluid and Multiphase Flows. *Journal of Computational Physics*, 150(2):425–467, 1999. 10.1006/jcph.1999.6187.

Saurel, R., Gavrilyuk, S., and Renaud, F. A multiphase model with internal degrees of freedom: application to shock–bubble interaction. *Journal of Fluid Mechanics*, 495:283–321, 2003. 10.1017/S002211200300630X.

Saurel, R., Le Métayer, O., Massoni, J., and Gavrilyuk, S. Shock jump relations for multiphase mixtures with stiff mechanical relaxation. *Shock Waves*, 16(3):209–232, 2007. 10.1007/s00193-006-0065-7.

Saurel, R., Petitpas, F., and Abgrall, R. Modelling phase transition in metastable liquids: application to cavitating and flashing flows. *Journal of Fluid Mechanics*, 607:313–350, 2008. 10.1017/S0022112008002061.

Saurel, R., Petitpas, F., and Berry, R. A. Simple and efficient relaxation methods for interfaces separating compressible fluids, cavitating flows and shocks in multiphase mixtures. *Journal of Computational Physics*, 228(5):1678–1712, 2009. 10.1016/j.jcp.2008.11.002.

Saurel, R., Chinnayya, A., and Carmouze, Q. Modelling compressible dense and dilute two-phase flows. *Physics of Fluids*, 29(6):063301, 2017. 10.1063/1.4985289.

Scardovelli, R. and Zaleski, S. Direct Numerical Simulation of Free-Surface an Interfacial Flow. *Annual Review of Fluid Mechanics*, 31(1):567–603, 1999. 10.1146/annurev.fluid.31.1.567.

Schmidmayer, K., Petitpas, F., Daniel, E., Favrie, N., and Gavrilyuk, S. A model and numerical method for compressible flows with capillary effects. *Journal of Computational Physics*, 334:468–496, 2017. 10.1016/j.jcp.2017.01.001.

Schmüdgen, K. *The Moment Problem*, volume 277 of *Graduate Texts in Mathematics*. Springer International Publishing, Cham, 2017. 10.1007/978-3-319-64546-9.

Schwinger, J. Energy and Momentum Density in Field Theory. *Phys. Rev.*, 130(2):800–805, 1963. 10.1103/PhysRev.130.800. Publisher: American Physical Society.

Sedov, L. I. Mathematical Methods for Constructing New Models of Continuous Media. *Russian Mathematical Surveys*, 20(5):123, 1965. 10.1070/RM1965v020n05ABEH001191.

Seguin, N. *Modélisation et simulation numérique des écoulements diphasiques*. PhD thesis, Université de Provence, 2002.

Seppecher, P. Second-gradient theory: Application to Cahn-Hilliard fluids. In *Solid Mechanics and Its Applications*, pp. 379–388. Kluwer Academic Publishers, 2002. 10.1007/0-306-46946-4_29.

Serre, D. *Systems of Conservation Laws 1: Hyperbolicity, entropies, shock waves*. Cambridge University Press, 1999.

Serre, D. Systems of Conservation Laws: A Challenge for the XXIst Century. In , *Mathematics Unlimited — 2001 and Beyond*, pp. 1061–1080. Springer Berlin Heidelberg, Berlin, Heidelberg, 2001. 10.1007/978-3-642-56478-9_54.

Serre, D. Systems of conservation laws with dissipation. Lectures notes, 2008.

Serre, D. The structure of dissipative viscous system of conservation laws. *Physica D: Nonlinear Phenomena*, 239 (15):1381–1386, 2010. 10.1016/j.physd.2009.03.014.

Serrin, J. Mathematical Principles of Classical Fluid Mechanics. In , *Fluid Dynamics I / Strömungsmechanik I*, pp. 125–263. Springer Berlin Heidelberg, Berlin, Heidelberg, 1959. 10.1007/978-3-642-45914-6_2.

Sethian, J. A. *LevelSet Methods and Fast Marching Methods : Evolving interfaces in computational geometry, fluid mechanics, computer vision, and materials science*. Cambridge Monographs on Applied and Computational Mathematics. Cambridge University Press, 1999.

Shapiro, A. H. and Erickson, A. J. On the Changing Size Spectrum of Particle Clouds Undergoing Evaporation, Combustion, or Acceleration. *Transactions of the American Society of Mechanical Engineers*, 79(4):775–788, 1957.

Sharma, S., Pratap Singh, A., Srinivas Rao, S., Kumar, A., and Basu, S. Shock induced aerobreakup of a droplet. *Journal of Fluid Mechanics*, 929:A27, 2021. 10.1017/jfm.2021.860.

Shinjo, J. and Umemura, A. Simulation of liquid jet primary breakup: Dynamics of ligament and droplet formation. *International Journal of Multiphase Flow*, 36(7):513–532, 2010. 10.1016/j.ijmultiphaseflow.2010.03.008.

Shu, C.-W. and Osher, S. Efficient implementation of essentially non-oscillatory shock-capturing schemes. *Journal of computational physics*, 77(2):439–471, 1988. Publisher: Elsevier.

Shukla, R. K., Pantano, C., and Freund, J. B. An interface capturing method for the simulation of multi-phase compressible flows. *Journal of Computational Physics*, 229(19):7411–7439, 2010. 10.1016/j.jcp.2010.06.025.

Smoller, J. *Shock Waves and Reaction—Diffusion Equations*. Springer New York, 1994. 10.1007/978-1-4612-0873-0. ISSN: 0072-7830 Publication Title: Grundlehren der mathematischen Wissenschaften.

Stieltjes, T.-J. Recherches sur les fractions continues. In *Annales de la Faculté des sciences de Toulouse: Mathématiques*, volume 8, pp. J1–J122, 1894. Issue: 4.

Strang, G. On the Construction and Comparison of Difference Schemes. *SIAM Journal on Numerical Analysis*, 5 (3):506–517, 1968. 10.1137/0705041.

Sussman, M. and Puckett, E. G. A Coupled Level Set and Volume-of-Fluid Method for Computing 3D and Axisymmetric Incompressible Two-Phase Flows. *Journal of Computational Physics*, 162(2):301–337, 2000. 10.1006/jcph.2000.6537.

Sussman, M., Smereka, P., and Osher, S. A Level Set Approach for Computing Solutions to Incompressible Two-Phase Flow. *Journal of Computational Physics*, 114(1):146–159, 1994. 10.1006/jcph.1994.1155.

Sweby, P. K. High Resolution Schemes Using Flux Limiters for Hyperbolic Conservation Laws. *SIAM Journal on Numerical Analysis*, 21(5):995–1011, 1984. 10.1137/0721062.

Tadmor, E. A minimum entropy principle in the gas dynamics equations. *Applied Numerical Mathematics*, 2(3): 211–219, 1986. https://doi.org/10.1016/0168-9274(86)90029-2.

Teshukov, V. and Gavrilyuk, S. Kinetic model for the motion of compressible bubbles in a perfect fluid. *European Journal of Mechanics - B/Fluids*, 21(4):469–491, 2002. 10.1016/S0997-7546(02)01195-0.

Theofanous, T. G., Tu, J. P., Dinh, A. T., and Dinh, T. N. The boiling crisis phenomenon Part I: nucleation and nucleate boiling heat transfer. *Experimental Thermal and Fluid Science*, 2002.

Tkachenko, S., Gavrilyuk, S., and Massoni, J. Extended Lagrangian approach for the numerical study of multidimensional dispersive waves: Applications to the Serre-Green-Naghdi equations. *Journal of Computational Physics*, 477:111901, 2023. 10.1016/j.jcp.2022.111901.

Tomar, G., Fuster, D., Zaleski, S., and Popinet, S. Multiscale simulations of primary atomization. *Computers & Fluids*, 39(10):1864–1874, 2010. 10.1016/j.compfluid.2010.06.018.

Toro, E. F. *Riemann solvers and numerical methods for fluid dynamics: a practical introduction*. Springer, Dordrecht ; New York, 3rd ed edition, 2009. OCLC: ocn401321914.

Toutant, A. *Modélisation physique des interactions entre interfaces et turbulence*. PhD thesis, Institut National Polytechnique de Toulouse, 2006.

Trotter, H. F. On the product of semi-groups of operators. *Proceedings of the American Mathematical Society*, 10 (4):545–551, 1959.

Truesdell, C. *Rational Thermodynamics*. McGraw-Hill, 1969.

Truskinovsky, L. Kinks versus shocks. In , *Shock induced transitions and phase structures in general media*, volume 52 of *The IMA Volumes in Mathematics and its Applications*. Springer Verlag, 1991.

Uhlmann, M. An immersed boundary method with direct forcing for the simulation of particulate flows. *Journal of computational physics*, 209(2):448–476, 2005. Publisher: Elsevier.

Uhlmann, M., Derksen, J., Wachs, A., Wang, L.-P., and Moriche, M. 5 - Efficient methods for particle-resolved direct numerical simulation. In , *Modeling Approaches and Computational Methods for Particle-Laden Turbulent Flows*, Computation and Analysis of Turbulent Flows, pp. 147–184. Academic Press, 2023. https://doi.org/10.1016/B978-0-32-390133-8.00013-X.

Unverdi, S. O. and Tryggvason, G. A front-tracking method for viscous, incompressible, multi-fluid flows. *Journal of computational physics*, 100(1):25–37, 1992. Publisher: Elsevier.

Urick, R. J. and Ament, W. S. The Propagation of Sound in Composite Media. *The Journal of the Acoustical Society of America*, 21(2):115–119, 1949. 10.1121/1.1906474. Publisher: Acoustical Society of America.

Vallet, A. and Borghi, R. Modélisation eulerienne de l'atomisation d'un jet liquide. *Comptes Rendus de l'Académie des Sciences - Series IIB - Mechanics-Physics-Astronomy*, 327(10):1015–1020, 1999. 10.1016/S1287-4620(00)87013-1.

Vallet, A., Burluka, A. A., and Borghi, R. Development of a Eulerian Model for the "Atomization" of a Liquid Jet. *Atomization and Sprays*, 11(6), 2001. 10.1615/AtomizSpr.v11.i6.20.

Van Leer, B. Towards the ultimate conservative difference scheme. V. A second-order sequel to Godunov's method. *Journal of Computational Physics*, 32(1):101–136, 1979. 10.1016/0021-9991(79)90145-1.

Vaudor, G., Ménard, T., Aniszewski, W., Doring, M., and Berlemont, A. A consistent mass and momentum flux computation method for two phase flows. Application to atomization process. *Computers & Fluids*, 152:204–216, 2017. 10.1016/j.compfluid.2017.04.023.

Vié, A., Chalons, C., Fox, R., Laurent, F., and Massot, M. A multi-Gaussian quadrature method of moments for simulating high Stokes number turbulent two-phase flows. In *Annual Research Brief of the Center for Turbulence Research - Stanford University*, pp. 309–320. Center for Turbulence Research - Stanford University, 2012.

Vié, A., Laurent, F., and Massot, M. Size-velocity correlations in high order moment methods for polydisperse evaporating sprays: Modeling and numerical issues. *Journal of Computational Physics*, 237:177–210, 2013. 10.1016/j.jcp.2012.11.043.

Wallis, G. B. *One-dimensional two-phase flow*. McGraw-Hill, New York, 1st edition, 1969.

Wargnier, Q., Faure, S., Graille, B., Magin, T., and Massot, M. Numerical Treatment of the Nonconservative Product in a Multiscale Fluid Model for Plasmas in Thermal Nonequilibrium: Application to Solar Physics. *SIAM Journal on Scientific Computing*, 42(2):B492–B519, 2020. 10.1137/18M1194225.

Warncke, K., Gepperth, S., Sauer, B., Sadiki, A., Janicka, J., Koch, R., and Bauer, H.-J. Experimental and numerical investigation of the primary breakup of an airblasted liquid sheet. *International Journal of Multiphase Flow*, 91:208–224, 2017. 10.1016/j.ijmultiphaseflow.2016.12.010.

Williams, F. A. Spray Combustion and Atomization. *The Physics of Fluids*, 1(6):6, 1958.

Wolfram Research, I. Mathematica, Version 13.3, 2023.

Wood, A. B. *A Textbook of Sound: Being an Account of the Physics of Vibrations with Special Reference to Recent Theoretical and Technical Developments*. G. Bell and Sons Ltd., London, 1st edition, 1930.

Yuan, C. and Fox, R. Conditional quadrature method of moments for kinetic equations. *Journal of Computational Physics*, 230(22):8216–8246, 2011. 10.1016/j.jcp.2011.07.020.

Yuan, C., Laurent, F., and Fox, R. An extended quadrature method of moments for population balance equations. *Journal of Aerosol Science*, 51:1–23, 2012. 10.1016/j.jaerosci.2012.04.003.

Zamansky, R. Z., De Bonneville, F. L. R., and Risso, F. Turbulence induced by a swarm of rising bubbles from coarse-grained simulations. *arXiv preprint arXiv:2312.09600*, 2023.

Zehner, P. and Kraum, M. Bubble columns. *Fluid Dynamics*, 10:3, 2000.

Zuzio, D., Estivalezes, J.-L., Villedieu, P., and Blanchard, G. Numerical simulation of primary and secondary atomization. *Comptes Rendus Mécanique*, 341(1):15–25, 2013. https://doi.org/10.1016/j.crme.2012.10.003.

ECOLE
DOCTORALE
DE MATHEMATIQUES
HADAMARD

Titre: Modélisation Eulérienne multi-fluide unifiée à deux échelles des écoulements diphasiques à phases séparées et dispersées

Mots clés: Écoulements diphasiques, Modelisation deux-échelles, Géométrie de l'interface, Description cinétique via la méthodes aux moments géométrique (GeoMOM), Calcul variationnel, Régularisation de l'interface

Résumé: Les écoulements diphasiques liquide-gaz sont présents dans de nombreuses applications industrielles telles que la propulsion aérospatiale, l'hydraulique nucléaire ou les colonnes à bulles dans l'industrie chimique. La simulation de ces écoulements est d'un intérêt primordial pour leur compréhension et leur optimisation. Cependant, la dynamique de l'interface séparant le gaz du liquide peut avoir une dynamique multi-échelle et rend alors sa simulation trop coûteuse en calcul dans un contexte industriel. Une classe de modèles - dits multi-fluides - sont moins coûteux pour des régimes particuliers de dynamique d'interface, par exemple lorsque les fluides s'écoulent de part et d'autre d'une unique interface lisse dans un régime séparé ou lorsque l'un des deux fluides est sous formes d'inclusions (gouttes ou bulles) portées par l'autre fluide dans un régime dispersé. Le couplage de ces modèles a été proposé pour des écoulements multi-échelles comme l'atomisation liquide, mais un tel couplage est souvent difficile à mettre en place du point de vue de la modélisation physique ou de ses propriétés mathématiques. Cette thèse répond à cette problématique en proposant un cadre de modélisation unifiée à deux échelles ainsi que des schémas numériques robustes. Les principales contributions liées à cette modélisation sont : 1- La combinaison de modèles multi-fluides compressibles de la littérature, adaptés soit au régime séparé soit au régime dispersé, en un modèle multi-fluide unifié à deux échelles grâce au principe d'action stationnaire de Hamilton ; 2- Le couplage local des modèles avec un transfert de masse inter-échelle régularisant l'interface à grande échelle en conservant l'énergie capillaire et modélisant les phénomènes de régime mixte présents dans l'atomisation primaire ; 3- L'amélioration des modèles à petite échelle pour les régimes dispersés en ajoutant la dynamique de quantités géométriques pour des gouttes oscillantes ou des bulles pulsantes, construites comme des moments d'une description cinétique. D'un point de vue numérique, des schémas volumes-finis adaptés aux systèmes de lois de conservation avec relaxations ont été implémentés dans le solveur open-source `Josiepy`. Enfin, des simulations démonstratives des propriétés de régularisation du modèle sont proposées sur des configurations numériques conduisant à des dynamiques d'interface multi-échelles.

Title: Unified two-scale Eulerian multi-fluid modeling of separated and dispersed two-phase flows

Keywords: Two-phase flows, Two-scale modelling, Interface geometry, Kinetic description via Geometric Method of Moments (GeoMOM), Variational methods, Interface regularization

Abstract: Liquid-gas two-phase flows are present in numerous industrial applications such as aerospace propulsion, nuclear hydraulics or bubble column reactors in the chemical industry. The simulation of such flows is of primary interest for their understanding and optimization. However, the dynamics of the interface separating the gas from the liquid can present a multi-scale dynamics and thus makes simulations of industrial processes computationally too expensive. Some modelling efforts have been conducted on the development of cheaper multi-fluid models adapted to particular interface dynamics regime, e.g. in the separated regime where the fluids are separated by a single smooth surface or in the disperse regime where there are inclusions of one fluid carried by the other. Attempts of coupling between these models have showed some progress to simulate multiscale flows like atomization, but usually have physical or mathematical drawbacks. This thesis then pursues the goal of proposing a unified two-scale modelling framework with appropriate numerical methods adapted to this multiscale interface dynamics which goes from a separated to a disperse regime. The main contributions related to this modelling effort are : 1- The combination of compressible multi-fluid models of the literature adapted to either the separated or the disperse regime into a unified two-scale multi-fluid model relying on Hamilton's Stationary Action Principle; 2- The local coupling of the models with an inter-scale mass transfer both regularizing the large-scale inter face and modelling mixed regime phenomena such as in primary break-up; 3- Enhancing the small-scale models for the disperse regimes by adding the dynamics of geometric quantities for oscillating droplets and pulsating bubbles, built as moments of a kinetic description. From the numerical perspective, finite-volume schemes and relaxation methods are used to solve the system of conservative laws of the models. Eventually, simulations with the open-source finite solver `Josiepy` demonstrates the regularization properties of the model on a set of well-chosen numerical setups leading to multi-scale interface dynamics.

Institut Polytechnique de Paris
91120 Palaiseau, France